

Andrzej M. Pawlak

SENSORS AND ACTUATORS IN MECHATRONICS

Design and Applications



Taylor & Francis
Taylor & Francis Group

SENSORS AND ACTUATORS IN MECHATRONICS

Design and Applications

SENSORS AND ACTUATORS IN MECHATRONICS

Design and Applications

Andrzej M. Pawlak



Taylor & Francis

Taylor & Francis Group

Boca Raton London New York

CRC is an imprint of the Taylor & Francis Group,
an Informa business

CRC Press
Taylor & Francis Group
6000 Broken Sound Parkway NW, Suite 300
Boca Raton, FL 33487-2742

© 2007 by Taylor & Francis Group, LLC
CRC Press is an imprint of Taylor & Francis Group, an Informa business

No claim to original U.S. Government works
Printed in the United States of America on acid-free paper
10 9 8 7 6 5 4 3 2 1

International Standard Book Number-10: 0-8493-9013-3 (Hardcover)
International Standard Book Number-13: 978-0-8493-9013-5 (Hardcover)

This book contains information obtained from authentic and highly regarded sources. Reprinted material is quoted with permission, and sources are indicated. A wide variety of references are listed. Reasonable efforts have been made to publish reliable data and information, but the author and the publisher cannot assume responsibility for the validity of all materials or for the consequences of their use.

No part of this book may be reprinted, reproduced, transmitted, or utilized in any form by any electronic, mechanical, or other means, now known or hereafter invented, including photocopying, microfilming, and recording, or in any information storage or retrieval system, without written permission from the publishers.

For permission to photocopy or use material electronically from this work, please access www.copyright.com (<http://www.copyright.com/>) or contact the Copyright Clearance Center, Inc. (CCC) 222 Rosewood Drive, Danvers, MA 01923, 978-750-8400. CCC is a not-for-profit organization that provides licenses and registration for a variety of users. For organizations that have been granted a photocopy license by the CCC, a separate system of payment has been arranged.

Trademark Notice: Product or corporate names may be trademarks or registered trademarks, and are used only for identification and explanation without intent to infringe.

Library of Congress Cataloging-in-Publication Data

Pawlak, Andrzej M.
Sensors and actuators in mechatronics : design and applications / Andrzej M. Pawlak.
p. cm.
Includes bibliographical references and index.
ISBN-13: 978-0-8493-9013-5 (alk. paper)
ISBN-10: 0-8493-9013-3 (alk. paper)
1. Mechatronics. 2. Optical detectors. I. Title.

TJ163.12.P39 2006
621--dc22

2006004129

Visit the Taylor & Francis Web site at
<http://www.taylorandfrancis.com>

and the CRC Press Web site at
<http://www.crcpress.com>

To my wife Ewa

The Author



Andrzej M. Pawlak, Ph.D., (Fellow IEEE), was born and educated in Poland. He obtained his M.S. in 1971 from the Technical University of Poznan. He did postgraduate study at the Warsaw University of Technology and obtained his Ph.D. in electrical engineering in 1981 from the Silesian University of Technology, Gliwice. His years of engineering and technology experience stem from his work at the Hitachi Poland and Japan manufacturing plants and his 20 years of research on electromechanical and electromagnetic devices at General Motors and subsequently Delphi, all of which contributed to his solid background of industrial expertise. His works on stepper motors, magnetic sensors, rotary actuators, and fast-acting solenoids are frequently cited worldwide.

Most of Dr. Pawlak's 70 scientific publications, patents, and patent applications are related to sensors and actuators. A number of them have found industrial applications in mechatronic systems with significant scientific, engineering, and economical impact on the automotive industry and beyond, with tremendous overall business value to Delphi and General Motors. Dr. Pawlak was honored with one of the highest number of individual awards in General Motors and Delphi history, including four prestigious "Boss" Kettering Awards for his accomplishments. He was the first individual from the automotive industry to receive the Respectable Achievement Award of the Industrial Research Institute.

Dr. Pawlak has contributed to the initial scientific analysis and design of several unique electromagnetic and electromechanical devices. An actuator he invented for the Magnasteer® system led to the development and the first industrial application of neodymium-boron-iron ring magnets with radial orientation, which are now commonly found in a variety of industrial applications and consumer products. Dr. Pawlak is a frequent invited keynote speaker and panelist at professional conferences and congresses worldwide. This book is the culmination of his research findings and award-winning solutions for industrial applications over the last 20 years.

Preface

The importance of mechatronic devices — both the application of electromagnetic and electromechanic devices in industry and their impact on emerging technologies — has increased dramatically in recent years. Significant advances in control technologies based on microprocessors and the substantial cost reduction of high-performance hard and soft magnetic materials have changed the face of the world of technology.

In particular, the automotive industry has shifted from mechanical and hydraulic systems and components to mechatronic systems based on electromagnetic and electromechanical devices. Servo motor design and optimization techniques used in industrial applications are well established and described elsewhere in the literature. This book discusses several perhaps less-elaborate families of modern electromechanical actuators and magnetic sensors in industrial applications: magnetic sensors, linear and latching solenoid actuators, stepper motors, rotary actuators, and other special magnetic devices. This book is intended to fill the gap in devising and designing optimization of mechatronic devices in modern industry applications. Each chapter examines a variety of magnetic sensors and electromechanical actuator analyses and designs, supported by numerical problems for mechatronic system applications in the automotive industry and beyond. The primary focus is on automotive applications, with more general discussions of studies of electromagnetic and electromechanical designs, analyses, optimization, and tests, including material and application aspects.

This book will be valuable to all those whose interests and job responsibilities are related to mechatronic systems and, in particular, magnetic sensors and electromechanical actuators. The intention of this book is to bring readers closer to the state of the art, to help them understand device functions and features, and to provide design guidance to meet specific, and sometimes extreme, industrial requirements. The focus on electromagnetic and electromechanical devices is natural because they are based on my inventions. I share my unique experiences as a design and manufacturing engineer, a researcher, and an inventor to help explain my way of thinking, which led to the development and successful industrial implementation of hundreds of millions of sensors and actuators in modern industrial mechatronic systems. I hope that this book will serve as a textbook for students and as a design handbook for engineers and will stimulate innovations in the field. I also want to share business and social aspects of the technology development process to help explain what it takes to successfully develop world-class technology.

Most of the research content of this book was developed at General Motors and Delphi Corporation in collaboration with divisional and outside partner teams. Much of the content of this book was published previously in the form of professional papers and conference presentations and is now used with the kind permission of Delphi Corporation. I would like to express my gratitude to those who contributed to those papers, including Dr. Alex Alexandridis, David Graber, Dr. Bruno Lequesne, and Takeshi Shirai, as well as to all the researchers, technicians, draftsmen, and other individuals from product lines for their support, constructive comments, and excellent work. I also thank my daughter Patrycja for her efforts to make this book reader-friendly and my wife Ewa for the impressive cover concept. Finally, this book would not have been possible without fruitful discussions with Dr. Thomas Nehl of Delphi and the continuous encouragement of Professor Tadeusz Glinka of the Silesian University of Technology.

Andrzej M. Pawlak

Symbols and Abbreviations

Symbols

a	Acceleration.
a_o	The polynomial component.
a_1	The dimension of the tooth; polynomial component.
a_2	The dimension of the tooth; polynomial component.
a_3	The dimension of the tooth; polynomial component.
a_n	The polynomial component.
\underline{a}_x	A unit vector in the vertical (x) direction.
A	The area of each component; the active sensor surface area.
\underline{A}	The magnetic vector potential.
A_f	The peak value of the line current density.
A_g	The effective surface of a tooth.
A_m	The magnet surface area.
A_m'	The effective magnet surface area.
$A_{T_{avg}}$	The average tooth cross-section area.
A_δ	The area of the main air gap.
$A_{\delta b}$	The area of the back air gap.
AT_2	The magnet's value of magnetomotive force at the working point.
AT_4	The magnet's maximum value of magnetomotive force.
AT_D	The value of magnetomotive force drop in the back walls.
AT_{Fe}	The value of magnetomotive force drop in the iron.
AT_L	The value of magnetomotive force drop in the side walls.
AT_{L1}	The value of magnetomotive force drop in the side walls of external lap-joint stator.
AT_{L2}	The value of MMF drop in the side walls of internal lap-joint stator.
AT_T	The value of magnetomotive force drop in the claw poles.
AT_δ	The value of magnetomotive force drop in the main air gap.
$AT_{\delta b}$	The value of magnetomotive force drop in the parasitic air gaps.
b_{p1}	The tooth width at the tip.
b_{p2}	The tooth width at the bottom.
B	The magnetic field density.
B_D	The flux density in the back walls.
B_g	The flux density in the air gap.
B_L	The flux density in the side walls.

B_{in}	The flux density in the inner gap.
B_{\max}	The maximum flux density.
B_{mean}	The mean value of the flux density.
B_{\min}	The minimum flux density.
B_{out}	The flux density in the outer air gap.
B_r	The remanent flux density of the magnet.
B_{rx}	The remanent magnetic flux density in the radial direction.
B_{ry}	The remanent magnetic flux density in the tangential direction.
B_t	The total flux density.
B_T	The flux density in the tooth.
B_δ	The flux density in the air gap.
$B_{\delta b}$	The flux density in the back air gap.
c	The viscous damping coefficient.
C	The maximum value of load that can be applied.
d	A skin depth.
D	The viscous damping coefficient.
D_c	The cylinder inside diameter.
D_m	The magnet outside diameter.
D_{pm}	The magnet outside diameter.
D_{RI}	The rotor inside diameter.
D_{RO}	The rotor outside diameter.
D_{SI}	The stator inside diameter.
D_{SO}	The stator outside diameter.
D_{SO1}	The lap-joint stator outside diameter.
D_{SO2}	The lap-joint inside stator outside diameter.
D_δ	The average diameter of the air gap.
e	The voltage generated in the coil.
e_s	The applied voltage.
E	The sensor signal.
E_{V1}	The back electromotive force coil 1.
E_{V2}	The back electromotive force coil 2.
f	The frequency.
f_{el}	The electrical frequency of the sensor signal.
f_{mech}	The mechanical frequency of the sensor signal.
f_p	The cycle frequency.
F	The uniform flux in the magnetic core.
F	A new function as defined in Equation 5.80.
F	The Lorentz forces.
F_a	The force developed in the armature.
F_{AR}	The armature reaction.
F_{pl}	The spring preload.

F_{m1}	The magnetic force component.
F_{m2}	The magnetic force component.
F_{mag}	The magnetic force.
F_{mech}	The net mechanical accelerating force.
F_{spg}	The total spring force.
F_t	The one-pole-pitch (tooth-pitch) magnetic force.
F_T	The magnetic force. The total magnetic force.
F_{vdg}	The viscous damping force.
g	Acceleration.
g_b	The back air gap.
G_u	The motor permeance.
h	The valve height.
h_c	The coil height.
h_s	The magnet stroke.
H_c	The coercive force of the permanent magnet.
H_D	The field strength in the back walls.
H_L	The field strength in the side walls.
H_T	The field strength in the tooth.
i	The winding current.
i_k	The current in the k coil.
i_s	A current in the coil.
$i(t)$	The winding current that is a function of time.
I	The current in the stepper motor coils.
I_1	The supplied current (constant) in coil 1.
I_2	The supplied current (constant) in coil 2.
I_c	The coil thickness.
I_f	The root-mean-square value of the phase current.
I_n	The nominal current in the coil.
I_S	The current in the coil.
I_{S1}	The current in coil 1.
I_{S2}	The current in coil 2.
I_{Sk}	The current in the k coil.
$I_{w'}$	The current in an equivalent coil.
J	The rotor inertia.
J_{add}	The additional inertia.
J_c	The coupling inertia.
J_M	The motor (rotor) inertia.
$\overline{J_{pm}}$	The equivalent permanent magnet current density.
$\overline{J_s}$	The external source current density.
k	The thermal dissipation coefficient of the material; a spring constant; a force constant.

k_{1F}	The ratio of the tooth-to-pole active areas at one coil energized.
k_{2F}	The ratio of the tooth-to-pole active areas for both coils energized.
k_a	The effective magnet area factor.
k_m	The effective flux length in the magnet factor.
K	A static torque coefficient at constant nominal voltage.
K_{1T}, K_1	The static torque coefficient that is a function of flux ϕ_1 .
K_{2T}, K_2	The static torque coefficient that is a function of flux ϕ_2 .
K_m	The mutual torque constant.
K_{V1}	The static torque coefficient that is a function of flux ϕ_1 .
K_{V2}	The static torque coefficient that is a function of flux ϕ_2 .
l	The length of each component.
l_2	The dimensions of the tooth dimension.
l_a	The dimensions of the tooth dimension.
l_d	The stator dimension.
l_{d0}	The stator two pole-pair section length.
l_{d1}	The stator dimension.
l_{d2}	The stator dimension.
l_{Fe}	The length of the magnetic path in the iron.
l_m	The average flux length in the magnet.
l_m'	The effective flux length in the magnet.
l_{mat}	The material thickness of the stator elements.
l_o	The total stator thickness.
l_{o1}	The total length of the tooth.
l_{pm}	The length of the permanent magnet.
l_{pm}'	The effective length of the permanent magnet.
l_{s1}	The lap-joint inside stator length.
l_{s2}	The lap-joint outside stator length.
l_{s3}	The overlap length.
l_{ST}	The tooth length.
l_{ST}'	The effective tooth length.
L	A self-inductance of coils.
L_1	A self-inductance coil 1.
L_2	A self-inductance coil 2.
L_{sk}	A self-inductance of the k coil.
L_{sw}	A mutual inductance.
L_y	The rectangular core of length in the y direction.
L_w	A self-inductance of an equivalent coil.
L_{ws}	A mutual inductance.
m	The total mass of all moving parts; the number of subdivisions in the coil region; the reciprocal of the skin depth.
m	The iron (real) permeability; the electron mobility; viscosity.

m_f	The multiplying factor for the International System of Units unit A/cm.
m_ϕ	The multiplying factor for the International System of Units unit Wb/cm.
M_c	The closing moment due to pressure.
M_m	The closing magnetic moment.
M_{m1}	Component 1 of the closing magnetic moment.
M_{m2}	Component 2 of the closing magnetic moment.
M_{m3}	Component 3 of the closing magnetic moment.
M_o	The opening moment due to pressure.
M_p	The total pressure moment.
n	The number of stator coils.
n_o	The velocity of rotor in r/min.
N	The number of turns of the coil.
N_1	The number of turns of stator coil 1.
N_2	The number of turns of stator coil 2.
N_f	The number of turns per phase.
N_i	The magnetomotive force.
N_o	A fixed number of pulses applied to the motor.
N_t	The number of teeth of the exciter wheel.
p	The number of magnet pole pairs or sensor sections; pressure.
P	The number of poles; permeance of the magnetic circuit.
P_1	The pole head end leakage permeance.
P_2	The pole side leakage permeance.
P_3	The pole body permeance.
P_4	The semicircular cylinder leakage permeance.
P_5	The corner pole head leakage permeance.
P_6	The pole body permeance.
P_7	The back air gap semicircular cylinder leakage permeance.
P_8	The pole body leakage permeance.
P_{\max}	The maximum permeance.
P_{\min}	The minimum permeance.
P_b	The butt-joint permeance.
P_c	The power loss due to the winding resistance.
P_e	The eddy current loss.
P_{em}	The rate of energy conversion (electromagnetic power).
P_{em}	The electromagnetic power.
P_{Fe}	The iron permeance.
P_{Fea}	The apparent iron permeance.
P_g	The lap-joint back air gap permeance.
P_{mech}	The net mechanical power.
P_r	The rate of change in the stored magnetic energy (reactive power).
P_s	The source power.

P_{spg}	The eddy spring power.
P_t	The total power.
P_δ	The main air gap permeance.
P_{vdg}	The viscous damping power.
$P1$	The elementary section permeance.
$P(\theta)$	The permeance.
q	The electron charge.
r	The disk radius.
r_1	The dimensions of the tooth.
r_2	The dimensions of the tooth.
R	The resistance of coils.
R_1	The resistance of coil 1.
R_2	The resistance of coil 2.
R_b	The reluctance of the back air gap.
R_c	The total ohmic resistance.
R_{c1}	The core reluctance.
R_{c2}	The core reluctance.
R_{c3}	The core reluctance.
R_e	The reflected resistance due to induced eddy current.
R_{ex}	The exciter wheel radius.
R_{Fe}	The reluctance of the iron.
R_{g1}	The air gap reluctance.
R_{g2}	The air gap reluctance.
R_H	The Hall constant of the material.
R_p	The plunger reluctance.
R_{peak}	The magnet-width/tooth-pitch ratio.
R_δ	The reluctance of the main air gap.
$R1$	The elementary section reluctance.
s	The distance, deflection, or position of the moving armature.
\dot{s}	The velocity of the armature.
s_v	The sensor signal sensitivity.
s_ϕ	The electromagnetic efficiency of the sensor configuration.
S	The stepping rate; the surface of integration or the device sensitivity; the surface of the electromagnet.
S_D	The cross section area of the one-pole-pair section.
S_{pm}	The magnet surface.
$S_{T_{avg}}$	The average cross section of the tooth.
t	Time.
t_2	The armature opening time.
t_3	The bottom plate thickness.
t_4	The armature closing time.

t_4	The disk armature thickness or start of armature motion.
t_{45}	The time for armature to reach force of 200N.
t_o	The voltage pulse width.
t_{rp}	The total travel time of solenoid.
T	The total static torque developed by the stepper motor; the period equal to the tooth pitch; temperature.
\bar{T}	The Maxwell stress tensor in dyadic form.
T_1	The stepper motor torque due to coil 1.
T_2	The stepper motor torque due to coil 2.
T_A	The reluctance torque, part A .
T_B	The reluctance torque, part B .
T_C	The synchronous torque.
T_d	The stall torque at zero speed.
T_D	The torque developed by the stepper motor.
T_F	The torque due to a friction.
T_L	The load torque.
T_{Li}	The load torque at i position.
T_{\max}	The maximum torque developed by the stepper motor.
$T_{1\max}$	The maximum torque due to coil 1.
$T_{2\max}$	The maximum torque due to coil 2.
T_N	The available net torque.
T_T	The total torque.
T_t	The pole-pitch (tooth-pitch) torque.
U_1	The voltage applied to coil 1.
U_2	The voltage applied to coil 2.
V	The electric voltage; volume.
\bar{V}	The velocity of the field point.
V_c	The volume of the cylinder for one cycle.
V_H	The voltage across the chip.
V_r	The total required volume.
V_s	The sensor volume.
W	The magnet width; magnetic energy.
W_m	The coenergy stored in the air gap.
W_{mag}	The total magnetic energy.
$x(t)$	The position of the moving part.
α	The electrical angle; the mechanical angle between two stators; the angle between flux and magnetizing force; pivot offset.
α_u	The magnet load line angle.
β	The temperature coefficient for the magnet material.
$\dot{\gamma}$	The sheer rate.
δ	The size of air gap; a position error; the Hall angle.

δ_b	The size of back air gap (parasitic).
ΔB	The flux density difference.
ΔS	The stepping rate.
Δt_n	The zero crossing time interval.
$\Delta\alpha$	The change in the rotor position.
$\Delta\theta$	The temperature rise.
$\Delta\phi$	The flux linkage change.
ξ	The B/A ratio of maximum torque values A and B of two consecutive steps.
θ	The mechanical angle position; sensor or rotor position.
$\theta(t)$	The location of the trailing edge of the core at time t .
λ_t	The total flux linkage of the winding.
$\lambda(i, x)$	The equivalent flux linkage of the winding.
μ_o	The permeability of the air equals $4\pi \times 10^{-7}$ H/m.
ρ	The resistivity of the iron.
s	The location of any point on the active sensor surface area.
σ	The material conductivity.
τ	The sheer stress; the stator pole pitch.
τ_o	The pole pitch; yield stress.
v	The material reluctivity.
v	The sensor signal; voltage generated in a sensor coil.
v_1	The sensor signal; signal component of coil 1.
v_2	The sensor signal; signal component of coil 2.
v_d	The voltage generated in a coil of the distributed sensor.
v_{\max}	The sensor signal characterized by the maximum flux density B_{\max} .
v_{\min}	The sensor signal characterized by the minimum flux density B_{\min} .
v_n	The noise signal.
v_s	The sensor signal.
v_s	The induced signal in the sensor coil.
ϕ	The magnetic flux embraced by the coil; flux in the air gap with the armature reaction.
ϕ_1	The magnetic flux in air gap 1.
ϕ_1	The magnetic flux embraced by coil 1.
ϕ_{1m}	The magnetic flux embraced by coil 1 for a single pole-pair section.
ϕ_2	The magnetic flux in air gap 2.
ϕ_2	The magnetic flux embraced by coil 2.
ϕ_{2m}	The magnetic flux embraced by coil 2 for a single pole-pair section.
ϕ_i	The flux linkage in any of the N turns of the coil.
ϕ_k	The flux linkages of the k coil.
ϕ_m	The median magnetic flux embraced by the coil for a single pole-pair section.
ϕ_m	The maximum magnetic flux in the air gap without an armature reaction.
ϕ_{\max}	The flux linkage for the maximum permeance position.

ϕ_{\min}	The flux linkage for the minimum permeance position.
ϕ_o	The total flux developed by permanent magnet without an armature reaction.
ϕ_p	The magnetic flux embraced by the p single pole-pair section.
ϕ_s	The flux linkages in the stator.
$\phi_{T^{\circ}C}$	The magnetic flux in the air gap at temperature $T^{\circ}C$.
ϕ_w	The flux linkages in the rotor.
ϕ_{ws}	The flux per pair of teeth.
$\Phi_k(x'', y'')$	The k th magnetic vector potential of one coil side.
$\Phi_k(x', y')$	The k th magnetic vector potential of the other coil side.
ψ	The flux linkage; the rotor position in electrical degrees.
ψ_{c1}	The rotor command position for step 1.
ψ_{c2}	The rotor command position for step 2.
ψ_c	The rotor command position.
ψ_i	The rotor i position in electrical degrees.
ψ_k	The flux linkages of the k coil.
ψ_s	The flux linkage in the stator.
ψ_w	The flux linkage in the rotor.
ω	The angular speed.
ω_{el}	The electrical angle speed of the motor (rotor).
ω_{mech}	The mechanical angle speed of the motor (rotor).
$\dot{\omega}_{mech}$	The mechanical angular acceleration of the motor (rotor).

Subscripts

a	Area.
avg	Average.
A	Part A.
AR	Armature reaction.
$ASIC$	Application specific integration circuit.
b	Back air gap.
B	Part B.
c	Coercive, winding resistance.
C	Part C.
d	Distributed; stall at zero speed.
D	Back walls; developed.
e	Eddy current.
el	Electrical.
em	Electromagnetic.
ex	Exciter wheel.
f	Magnetomotive force.

$1F$	One coil energized factor.
$2F$	Two coils energized factor.
F	Friction.
Fe	Ferromagnetic.
g	Tooth, claw pole.
H	Across the chip.
i	By i turn (any of the turns).
k	The k coil.
L	Load; side walls.
$L1$	Side walls of external lap-joint stator.
$L2$	Side walls of internal lap-joint stator.
Li	Load at i position.
m	Maximum; magnetic; median.
mag	Magnetic.
max	Maximum.
1_{\max}	Maximum at coil 1.
2_{\max}	Maximum at coil 2.
$mech$	Mechanical.
min	Minimum.
N	Net.
o	In the air; without armature reaction; per pole pair.
p	Single pole-pair section.
$p1$	Width at the tip.
$p2$	Width at the bottom.
pl	Preload.
pm	Permanent magnet.
RI	Rotor inside.
RO	Rotor outside.
r	Remanence; reactive.
rx	In the tangential direction.
ry	In the radial direction.
sk	The stator k coil.
s	Stator; spring.
$s3$	Stator overlap.
spg	Spring.
sw	Rotor stator.
$S1$	Stator (coil) 1.
$S2$	Stator (coil) 2.
SI	Stator inside.
SO	Stator outside.
$SO1$	Joint stator inside.

<i>SO2</i>	Joint stator outside.
<i>ST</i>	Stator tooth.
<i>t</i>	Total, teeth.
<i>T</i>	Tooth; claw poles.
<i>T_{avg}</i>	Average tooth area.
<i>T°C</i>	At temperature of.
<i>v</i>	Sensor signal.
<i>w</i>	Rotor; rotor's equivalent coil.
<i>ws</i>	Stator rotor.
<i>V1</i>	Electromagnetic force coil 1.
<i>V2</i>	Electromagnetic force coil 2.
δ	Air gap.
δ_b	Back (parasitic) air gap.
<i>vdg</i>	Viscous damping.
ϕ	Flux; magnetic.
<i>x</i>	In the <i>x</i> direction.

Abbreviations

ABS	Antiskid braking system.
AC	Alternating current.
AWG	American wire gauge.
BH	Magnetization curve.
DC	Direct current.
EGR	Exhaust gas recirculation.
EMF	Electromotive force.
FE	Finite element.
GM	General Motors.
GMR	Giant magnetoresistive.
H	Samarium-cobalt magnets.
HDDR	Hydrogenation-disproportionation-desorption-recombination.
HS	Neodymium magnets.
HVAC	Heating, ventilating, air-conditioning.
ID	Inside diameter.
IP	Intellectual property.
IPO	Initial public offering.
MMF	Magnetomotive force.
MOSFET	Metal oxide semiconductor field effect transistor.
MQ1	Magnequench 1.
MQ2	Magnequench 2.

MQ3	Magnequench 3.
MR	Magnetoresistive.
NI	Ampere-turns.
OD	Outside diameter.
p-p	Signal peak-to-peak.
PM	Permanent magnet.
PSSM	Passive solid-state magnetic.
PWM	Pulse-width modulation.
rpm	Revolutions per minute.
R&D	Research and development.
TC	Traction control.
TFM	Transverse flux motors.
VC	Venture capital.
VR	Variable reluctance.
VSM	Vibrating sample magnetometer.
YBM	Ferrite magnets.
YCM	Alnico magnets.
2D	Two-dimensional.
3D	Three-dimensional.

Contents

1	Introduction	1
1.1	Classification of Sensors and Actuators	2
1.1.1	Magnetic Sensors	2
1.1.2	Linear and Latching Solenoid Actuators	3
1.1.3	Stepper Motors	5
1.1.4	Special Magnetic Devices	7
1.1.5	Rotary and Linear Actuators	8
1.2	Magnetic Materials and Technology	8
1.2.1	Soft Magnetic Materials	9
1.2.2	Hard Magnetic Materials	12
1.2.3	Coating Technologies	15
1.2.4	Magnetic Materials Market and Applications	16
2	Magnetic Sensors.....	21
2.1	Theory of Magnetic Sensors	23
2.2	Magnetic Sensor Analysis	24
2.3	VR Sensors	26
2.3.1	Conventional VR Sensors	27
2.3.2	High Performance VR Sensors	32
2.3.3	Sensors with Inserted Magnets	36
2.3.4	Front-Mounted-Magnet Sensors	43
2.3.5	Sensors with E-Shaped Magnetic Structure	45
2.3.6	Sensors with U-Shaped Magnetic Structure	46
2.3.7	Multiple Magnets VR Sensors	53
2.3.8	Dual-Magnet Sensors	53
2.3.9	Dual Sensor Arrangement	61
2.3.10	Distributed VR Sensors	63
2.4	Solid-State Sensors	70
2.4.1	Solid-State Sensor Analysis	71
2.4.2	Solid-State Sensor Design	72
2.4.3	Solid-State Sensor Test Results	75
2.5	Magnetic Sensor Applications	77
2.5.1	Magnetic Speed Sensor Requirements	77
2.5.2	Magnetic Speed Sensor Applications	78
2.5.3	Magnetic Position Sensor Applications	79
2.6	VR Sensor Noise	81
2.6.1	Math Model and Noise Analysis	81
2.6.2	Noise Problem Solutions	82
	Example 2.1	85
	Example 2.2	86
	Example 2.3	88

3 Linear Actuators	89
3.1 Mathematical Model for Linear Actuators	89
3.1.1 Symmetrical Analysis of Electromagnetic Devices.....	90
3.1.2 Electrical Network Equations.....	92
3.1.3 Mechanical Equations	94
3.1.4 Magnetic Forces	96
3.1.5 PWM Analysis.....	97
3.1.6 Solenoid Analysis and Simulations	102
3.2 Fast-Acting Actuators.....	106
3.2.1 Disk Solenoids.....	106
3.2.2 Plunger Solenoids.....	108
3.2.3 Ball Solenoids	110
3.2.4 Conical Solenoids	112
3.2.5 Optimization of Fast-Acting Actuators.....	115
3.3 Applications of Solenoid Actuators	118
3.3.1 Long Stroke Solenoid Fuel Pump.....	118
3.3.2 Gasoline Injectors	121
3.3.3 Natural Gas Injectors	125
3.3.4 Diesel Fuel Injectors	131
3.3.5 Compressor Solenoid Valves	137
3.3.6 Transmission Solenoids	140
Example 3.1	149
Example 3.2	151
4 Latching Linear Actuators	155
4.1 Latching Relays	155
4.1.1 Dynamics of Latching Relays.....	157
4.1.2 Bipolar Latching Relays.....	159
4.1.3 Unipolar Latching Relays.....	163
4.1.4 Latching Relay Analysis	165
4.1.5 Latching Relay Analysis and Tests	168
4.2 Latching Solenoids.....	173
4.2.1 Latching Solenoids with Moving Magnets	174
4.2.2 Latching Solenoids with Stationary Magnets	182
4.3 Latching Solenoid Applications.....	189
Example 4.1	190
5 Stepper Motors	191
5.1 Principles of Operation	191
5.2 Static Analysis of Stepper Motor.....	196
5.2.1 Static Torque Analysis.....	196
5.2.2 Magnetic-Circuit Analysis.....	201
5.2.3 Magnet Operating Point.....	207
5.2.4 Temperature Effect	210
5.2.5 Armature Reaction Effect	210
5.2.6 Experimental Results of Static Performance.....	211
5.3 Dynamic Analysis of Stepper Motor	217
5.3.1 Math Model of the Dynamic Operation.....	218
5.3.2 Stepper Motor Dynamic Simulation	221
5.3.3 Validation of the Dynamic Model	223

5.3.4	Effects of Various Parameters on Stepper Motor Performance	226
5.3.5	Experimental Results of Dynamic Performance	231
5.3.6	Evaluation of Viscous Damping Coefficient	233
5.3.7	Effects of Load Torque on Stepper Motor Performance	237
5.3.8	Stepper Motor Inductance in Dynamic Operation	242
Example 5.1:	Magnetic-Circuit Calculations.....	250
Example 5.2:	Static Torque Calculations	256
Example 5.3:	Magnetic Flux Calculations	257
6	Special Magnetic Devices.....	261
6.1	Magnetic Valves	261
6.1.1	Background.....	262
6.1.2	Heart Valve Requirements	262
6.1.3	Heart Valve Design Concept	265
6.1.4	Mathematical Model and Simulations	265
6.1.5	Optimized Design.....	269
6.1.6	Comparison and Test Results	272
6.2	Heart Pump.....	273
6.2.1	Heart Pump Requirements	274
6.2.2	Heart Pump Design Concept.....	275
6.2.3	Analytical Simulations and Optimized Design.....	275
6.3	Magnetorheological Fluid Solenoids	281
6.3.1	Background.....	281
6.3.2	Magnetorheological Fluid Solenoid Actuator.....	283
6.3.3	MR Fluid Applications	284
Example 6.1	287
Example 6.2	288
Example 6.3	288
7	Rotary Actuators	291
7.1	Disk Rotary Actuators	292
7.1.1	Disk Rotary Actuator Analysis.....	293
7.1.2	Disk Rotary Actuator Design	298
7.1.3	Disk Rotary Actuator Excitation Electromagnetic Circuit.....	298
7.1.4	Disk Rotary Actuator Toothed Magnetic Part	299
7.1.5	Disk Rotary Actuator PM.....	300
7.1.6	Disk Rotary Actuator Test Results.....	302
7.2	Claw Pole Rotary Actuators.....	304
7.2.1	Claw Pole Rotary Actuator Analysis.....	306
7.2.2	Claw Pole Rotary Actuator Design	309
7.2.3	Claw Pole Rotary Actuator Excitation Electromagnetic Circuit.....	309
7.2.4	Claw Pole Actuator Toothed Magnetic Part	310
7.2.5	Claw Pole Actuator PM.....	310
7.2.6	Claw Pole Rotary Actuator Test Results.....	313
7.3	Cylindrical Rotary Actuators	316
7.3.1	Cylindrical Rotary Actuator Analysis	317
7.3.2	Cylindrical Rotary Actuator 2D Analysis.....	318
7.3.3	Cylindrical Rotary Actuator 3D Analysis and Test Results	322
7.3.4	Cylindrical Rotary Actuator Design.....	325
7.3.5	Cylindrical Rotary Actuator PM.....	326

7.3.6	Cylindrical Rotary Actuator Excitation Electromagnetic Circuit	332
7.3.7	Cylindrical Rotary Actuator Toothed Magnetic Structure.....	332
7.4	Rotary Actuator Applications	333
7.4.1	Disk Rotary Actuator Application	335
7.4.2	Claw Pole Rotary Actuator Application.....	336
7.4.3	Cylindrical Rotary Actuator Application	338
	Example 7.1	342
	Example 7.2	343
	Example 7.3	343
8	Addendum.....	345
8.1	Technology Development	345
8.1.1	Partnership.....	345
8.1.2	Competitiveness.....	346
8.1.3	Persistence.....	347
8.1.4	Technical Growth.....	348
8.2	Technology Valuation	349
8.2.1	Technical Attributes.....	349
8.2.2	Business Attributes.....	353
8.2.3	Financial Attributes	354
8.2.4	Technology Ranking.....	355
	Bibliography.....	357
	Index.....	363

1

Introduction

Mechatronics is the synthesis of mechanical engineering and electronics, two distinct technology areas that overlap in the design of complex systems. It is a synergetic combination of precision mechanical engineering, electronic control, and system thinking in the design of product and process (Alciatore and Histand 2003, Baumann et al. 2000, Bishop 2002, Triantafyllou et al. 1999). Sensors and actuators convert energy in mechatronics systems and the magnetic circuit seems to be the best medium for such a conversion (White and Woodson 1959). Therefore, the magnetic sensors and electromechanical actuators, with electromagnetic circuits that are electronically controllable, such as stepper motors, magnetic sensors, rotary actuators, linear solenoids, and other special devices with smart materials chosen for and described in this book, are critical components of mechatronic systems (Delphi 2002). This book discusses several families of modern electromagnetic and electromechanical devices in industrial applications and is devised to guide the reader in analysis and design optimization (Baumann et al. 2000, Bishop 2002, Box et al. 1969, Dąbrowski 1977, Fletcher 1987, Geras and Wing 1994, Kuester et al. 1973, Navarra 1990, Pawlak 1989, Piron et al. 1999, Yoon et al. 1999). The presentation of prototypes and test results along with their analyses should allow for a better understanding of the progression from concept to mass production.

The first part of this chapter categorizes and describes several key families of electromechanical and electromagnetic devices utilized in mechatronic applications. With a focus on variable reluctance (VR) sensors, it describes and categorizes different types of magnetic sensors, linear and latching solenoids, stepper motors, and different types of rotary actuators (Pawlak et al. 1997, Pawlak 1996). Special magnetic devices also are introduced, including devices with smart materials with an emphasis on biomedical applications.

Because of their simplicity, low cost, controllability, and high performance, modern electromechanical and electromagnetic sensors and actuators are finding increasing use in industrial applications (Aftonin et al. 1999, Ellis and Collins 1980, Hanitsch 1994). Proper selection of magnetic materials is a key element in electromagnetic-circuit design. Because of this, both soft and hard magnetic materials are described in the second part of this chapter (Carpenter 1989, Daido 2003, Furlani 2001, Hitachi 1999, Kasai 1992). A review of soft and hard magnetic materials includes a recommendation for different applications (Dąbrowski 1980, Geras and Wing 2002, Glinka 1995, Macoit 1999, Pawlak et al. 1999, Pawlak 2000a, Pawlak 1996, Rashidi 1982). New advancements in high-energy magnets are indicated; however, all of the applications discussed are based on commercially available magnetic materials. Furthermore, the magnetic material manufacturing technologies that should help the reader understand both the advantages and the magnetic material limitations are also discussed in this chapter.

1.1 Classification of Sensors and Actuators

The electromechanical and electromagnetic sensors and actuators such as stepper motors, sensors, rotary actuators, linear solenoids, which are electronically controllable in mechatronic systems, and other special devices with smart materials, are described and categorized in this chapter.

1.1.1 Magnetic Sensors

The magnetic sensors that are most commonly used in mechatronics systems today are VR and solid-state sensors [Hall-effect devices and magnetoresistive (MR)]. They are quickly making their way to the world market (Foster 1988, Ohshima and Akiyama 1989a, Ohshima and Akiyama 1989b, Podeswa and Lachman 1989). Over the last 10 years, the number of sensors installed in the average automobile has risen from several up to the current 20. It is expected to exceed 50 units in the near future. Worldwide, the automotive sensor market is valued at \$5 billion and is expected to continue growing at an annual average rate of about 7%. Common applications for magnetic sensors include ignition timing, power sensing, valve position, current sensing, linear or rotary motion detection, speed sensing, length measurement, flow sensing, revolutions per minute (rpm) sensing, security systems, and more. Magnetic sensors are generally used to provide speed, timing, or synchronization data to a display (or control circuitry) in the form of a pulse train. Therefore, sensors for rpm and speed measurement, the two most popular applications, can be found in almost any market:

1. rpm measurement on engines for aircraft, automobiles, boats, buses, agricultural equipment, trucks, rail vehicles, as well as on motors for precision camera, tape recording and motion picture equipment, drills, grinders, lathes, automatic screw machines, etc.
2. speed measurement on processes for food, textile, woodworking, paper, printing, tobacco, and pharmaceutical industry machinery, for pumps, blowers, mixers, exhaust and ventilating fans, electric motors, and generators

Completely self-powered, VR magnetic sensors are simple, robust devices that do not require an external voltage source for operation (Pawlak et al. 1991d). They feature non-contact, error-free conversion of actuator speed to output frequency, as well as simple installation, with no moving parts. They are also usable over a wide speed range and adaptable to a wide variety of configurations. These properties have led to widespread utilization in a number of industries. As a result, VR sensors have become known by many use-related names such as magnetic pickups, speed sensors, motion sensors, pulse generators, variable reluctance sensors, frequency generators, transducers, magnetic probes, timing probes, monopoles, and pickoffs.

The drawback of VR sensors is that they generate a signal proportional to the magnetic field's rate of change. Therefore, the signal strength decreases with decreasing speed and, below a certain flux change rate, the signal disappears into the noise. At high-frequency magnetic fields, the excess output voltage of the coil also causes problems for circuit designers. The generated voltage for VR sensors is up to 4000 V, for air gaps from 0.25×10^{-3} to 3.0×10^{-3} m with coils of resistance ranging from 200 to 4000 Ω over the wide range of temperatures from -40 to $+165^\circ\text{C}$.

Analog VR sensors are passive sensors and do not require any external power source. Such a sensor generates a typically sinusoidal-like output voltage proportional to the speed of the exciter wheel. A signal level is a function of the air gap between the sensor and a toothed exciter wheel. Digital output VR speed sensors produce a digital (square wave) pulse that is directly proportional to exciter-wheel speed. The active solid-state signal conditioning integral with the sensor converts the analog VR output to digital pulses. The exciter-wheel speed sensing range is from 0.5 m/s to 40 m/s at frequencies up to 50,000 Hz.

In most applications, it is sufficient to have one voltage output; however, when speed sensor redundancy is required, multiple coil configurations are recommended. Instead of using two separate single coil sensors, multiple coil sensors accommodate redundancy needs while minimizing system costs and weight. Sensor coil options include single, dual, triple, or quad coil configurations for both redundancy and multiple readout needs, i.e., two coils for redundant speed detection and a third independent coil for ground trim, cockpit readout, etc. For multiple coil applications, output voltages for redundant applications are maintained in the event of a sensor or system fault, such as a short in the sensor harness or associated electronics, while maintaining speed detection integrity.

Neither the Hall-effect nor the magnetoresistive (MR) sensors can generate a signal voltage on their own and must have an external power source. Therefore, they are called active sensors. Solid-state sensors produce either a digital or an analog output. Digital output sensors are in one of two states — OFF or ON. Analog sensors provide a continuous voltage output, which increases with the strength of the magnetic field. There are three types of digital sensors: bipolar, unipolar, and omnipolar. Bipolar sensors require a positive magnetic field strength (south pole) to operate and a negative one (north pole) to release. Omnipolar sensors operate with either north or south poles. Unipolar sensors require a single magnetic pole (south pole) to operate; the sensor is released when the pole is removed. Analog sensors operate in proximity of either magnetic pole (Rowley and Stolfus 1990).

Hall-effect sensors are zero speed, noncontact sensors that can provide constant amplitude output over typical target speed ranges from 0 Hz to 50 kHz and even up to 100 kHz with air gaps up to 3.0×10^{-3} m. Hall-effect circuitry measures speed accurately to true zero, direction of rotation or travel, and true angular position of gear. Hall-effect devices generate a very small raw signal because of low field sensitivities (0.5 to 5.0 mV/100 Oe applied field) and the device performance is strongly temperature dependent. Hall-effect sensors feature true zero speed sensing, a wide operating voltage range from 5.0 to 24.0 V, an open collector output with sinking currents to 35 mA, and an operating temperature range up to 150°C.

Giant magnetoresistive (GMR) metal multilayer sensors, which have recently been introduced, offer improvements over galvanometric MR sensors. A new passive solid-state magnetic (PSSM) sensor technology is based on a combination of two phenomena: the magnetostrictive effect and the piezoelectric effect. In response to a magnetic field, the magnetostrictive component imparts a strain on the piezoelectric element that in turn produces an electrical output signal of the PSSM sensor. It has the potential to replace existing sensors, provided that the technology is cost-effective in mass production and would work in the harsh environment of the final product. These sensors combine the advantages of the miniature size of Hall sensors and the passive nature of VR coil devices because the PSSM sensors consume no electrical power. Both solid-state and VR sensors are described in Chapter 2.

1.1.2 Linear and Latching Solenoid Actuators

Solenoid actuators are common industrial components used in almost every industrial motion control (Boldea and Nasar 2001). Solenoids can be found in applications that

require a pinch, lock, divert, move, latch, or kicking type of functionality in a variety of industries, such as factory automation, material handling, transportation, automotive, food processing, medical equipment, agricultural equipment, vending machines, laundry equipment, construction equipment, marine, space, and aircraft. In addition, solenoid actuators are widely used in consumer markets.

A solenoid consists of a coil with magnetic wire wound on a bobbin with a moving armature and a return spring encapsulated within the housing. Depending on an armature's shape, solenoids can be categorized as plunger, disk, ball, or conical types. When electricity is applied to the coil, the resulting magnetic field attracts the armature and pulls it into the solenoid body against an armature stop, contracting a return spring. When electricity is removed, the solenoid plunger is allowed to return to its original position due to a return spring or gravity. Solenoids are typically classified as alternating current (AC) or direct current (DC), linear or rotary, or on-off vs. variable positioning. A linear solenoid can be found in either an open frame solenoid configuration, which is used for lower-cost, less-efficient applications, or a tubular solenoid, which is most often used for longer-life, higher-force applications.

Linear solenoids convert electrical energy into mechanical work via a plunger with an axial stroke in either a push or pull action. The electromotive force (EMF) is supplied by the current applied to the coil and is limited by the heat dissipation capacity of the coil. The duty cycle, or the percentage of time that the solenoid is powered, is therefore a crucial factor in solenoid selection; the less time a solenoid needs to be powered, the more time it has to cool, and thus it can be used with a higher rated current, providing more force. The same solenoid design can have widely varying force ratings associated with different duty cycles. Continuous duty solenoids are rated for a 100% duty cycle. In general, this duty cycle will have the lowest force ratings.

Industrial work solenoids can be designed to accept the attachment of the load to the pulling or pushing end of the plunger. For some applications, the plunger assembly is designed to accept load attachments at both ends. The method of connecting the load to the industrial work solenoid must be developed with the consideration that side loads will be detrimental to solenoid life if not properly accounted for. Furthermore, if the installation causes a binding condition anywhere within the required operating stroke, excessive wear and reduced operating life will result.

Solenoid actuators transform electrical energy into mechanical energy. Depending on function, there are three types of solenoid actuators: rotary solenoid with shaft rotary motion, linear solenoid with linear motion, and holding solenoid with holding force. A rotary solenoid is an electromechanical device that converts linear motion to rotary motion by virtue of three ball bearings that travel down inclined raceways. When the coil is energized, the armature assembly is pulled toward the stator and rotated through an arc determined by the coining of the raceways. Linear solenoids are subdivided into:

- Single-acting linear solenoids — solenoid force developed in one direction, return action is effected mechanically, e.g., with a coil
- Two-directional linear solenoids — motion is effected by specifically energizing the respective coil
- Bistable solenoids — switching is effected with a current impulse of varying polarity, the end positions are maintained without current

A linear solenoid has three important characteristics: stroke, pull-in force, and relative duty cycle. Stroke is the distance by which the armature should be moved. The pull-in force is defined as the force available before the movement starts. The relative duty cycle

represents the relation of switch-on time to operational cycle time. A solenoid rated for a 100% duty cycle may be energized at its rated voltage (current) continuously, because its total coil temperature will not exceed the maximum allowable ratings (Class A 105°C, Class B 130°C, Class F 155°C, and Class H 200°C, all at an ambient temperature of 25°C). Less than a 100% duty cycle falls into the category of intermittent duty cycle that has an associated allowable “on” time, which must not be exceeded. For the same solenoid, intermittent duty coils provide considerably higher forces than continuous duty coils.

Linear solenoids are available in various types and sizes for the widest range of stroke lengths, force capabilities, and duty cycles (Pawlak et al. 1988). The line of linear solenoids includes specially engineered types for standard, intensive, heavy-duty applications, as well as bistable linear solenoids and self-holding latching solenoids designed for low energy consumption. Rotary solenoids provide rotation angles of 45°–90°.

A proportional solenoid is a linear actuator with a fixed range of travel where the value of the input signal corresponds to the solenoid travel distance. The proportional solenoids can control position in a precise manner. Solenoids also may be designed for simple on-off applications, acting much like relays. For example, they are used this way in starters and door locks. Pulse-width modulated (PWM) linear solenoids are used to operate pistons and valves for accurate control of fluid pressure or flow in applications such as transmissions and fuel injection. Transmissions require accurate and smooth control of pressure on clutches to change gears and to control the locking torque converter. Electronically controlled transmissions may contain more than eight linear solenoids, all of which require smooth, accurate control. Common-rail diesel fuel-injection applications, with pressures in excess of 13.8×10^3 kPa, may require one linear solenoid per cylinder — and one at the fuel pump — to adjust pressure accurately to maintain predictable injector fuel flow. The linear solenoid’s position is controlled in a feedback loop. For example, a valve’s downstream pressure can be monitored and used as a feedback signal to compare with the set point, adjusting the PWM duty cycle to control the solenoid. However, it may be difficult, impractical, or very costly to measure the downstream pressure. A practical alternative is to establish the position of the solenoid by measuring the current through the solenoid. This is possible because the force imposed by the mechanical load on a solenoid is directly proportional to the magnetic field, which, in turn, is directly proportional to the current through the coil. Proportional control of the solenoid is achieved by a balance of the forces between the spring-type load and the solenoid’s magnetic field, which can be determined by measuring the current through the solenoid. Linear solenoids are described in Chapter 3.

A solenoid can also be made in a magnetic latching style (Pawlak et al. 1999). In this case, a magnet is used inside the solenoid body. When the coil is energized and the armature is pulled into the solenoid body, the magnet holds the armature in position even after the power is removed. A reverse voltage is then applied to release the armature from the solenoid body to allow it to return to the starting position. Bistable solenoids have two stable end positions that are maintained without current. Switching is effected with a current impulse of varying polarity between the two end positions. In contrast to standard linear solenoids, bistable solenoids feature three characteristic forces: pull-in force (as with standard linear solenoids), holding force with the armature fully in the home position, and holding force with the armature at start position. Latching solenoids are introduced in Chapter 4.

1.1.3 Stepper Motors

A stepper motor is an electronically operated rotary electric motor that converts electrical pulses into a mechanical rotary motion with limited-angular increments called “steps.” Each revolution of the stepper motor’s shaft is made up of a series of discrete individual

steps. A step is defined as the angular rotation produced by the output shaft each time the motor receives a step pulse. These types of motors are very popular in digital control circuits, such as robotics, because they are ideally suited for receiving digital pulses for step control. These motors are popular because they are compatible with modern digital controls. Stepper motors, also called step motors or stepping motors, have a wide presence; they are popular in machine tools, process control systems, tape and disk drive systems, and programmable controllers, to name a few (Ellis and Collins 1980, Furlani 2001).

There are three distinctive stepper motor families that vary in their design based on magnetic material selection. Perhaps the most popular family is the permanent-magnet (PM) stepper motor, which operates on the interaction between a multipole ring or thin-disk PM rotor and electromagnetic field of the stator. The rotary torque is produced the same way as in a synchronous motor with an interaction of a rotating stator flux and electromagnetically corresponding PM flux.

A claw pole stepper motor, also known as a thin-can or can-stack motor, is the most commonly used motor for low torque and low speed applications because of its low cost, simplicity, high reliability, and relatively low inertia. This motor consists of a coil, multipole ring magnet, and a claw pole stator. The teeth on the stator surface and the rotor pole faces are offset so that there will be only a limited number of rotor teeth aligning themselves with an energized stator pole. The number of teeth on the rotor and stator determine the step angle that will occur each time the step pulse is applied and the polarity of the winding is reversed. The greater the number of teeth, the smaller the step angle with typical angles of 7.5° or 15°. Claw pole stepper motors are described in Chapter 5.

The VR stepper motors have reluctance-type ferromagnetic rotors that produce reluctance torque. Unlike PM stepper motors, VR stepper motors have no residual torque to hold the rotor at one position when turned off. When the stator coils are energized, the rotor teeth will align with the energized stator poles. The dynamic behavior of magnetic flux is based on the search for a path with minimum reluctance. Therefore, this motor tends to align the rotor's center of the pole with the axis of symmetry of the stator's salient pole. By alternating the windings that are energized in the stator, the stator field changes and the rotor is moved to a new position. Usually a rotor of the reluctance motor is made out of soft iron, and the stator has multiphase windings. In order to improve the motor's performance, a stack of three motors are connected and shifted from each other to obtain a large number of steps with small angular displacements.

The structure of the hybrid stepper motor combines both the VR and active PM design and is operated under the combined principles of the PM and VR stepper motors (Crnosija 2000, Croat 1985, Russell and Lenhouts 1980). The stator core structure of a hybrid motor is essentially the same as that of a VR stepper motor. The main difference is that in the VR motor, only one of the two coils of one phase is wound on one pole. However, a typical hybrid motor has coils of two different phases wound on the same pole. The two coils at a pole are wound in a configuration known as a bifilar connection. Each pole of a hybrid motor is covered with uniformly spaced teeth made of soft steel. The teeth on the two sections of each pole are misaligned with each other by a half-tooth pitch. A typical design presents a cylindrical PM sandwiched between two VR end rotors with an offset. They offer improved performance in comparison with other families, but they are more costly.

The stator winding design can also vary. Therefore, from the controller's point of view, there are several more types of stepper motors. A bipolar stepper motor has a simple winding but a more complex controller with an "H" switch, while a unipolar stepper motor has more complex windings with a simpler controller. The bifilar windings of a stepper motor are applied to the same rotor and stator geometry as a bipolar motor, but instead of winding each coil in the stator with a single wire, two wires are wound in parallel with each other, which doubles the number of wires for the motor. The multiphase

stator winding of a stepper motor is not very popular, while the three-phase winding is. The three-phase winding is connected in the Δ and y configurations that correspond to PM motors with a small number of teeth — in this case, three.

Depending on the mode of operation, stepper motors can perform full steps, half steps, and microsteps. Half steps occur when both windings are excited with identically rated currents at the same time, while microsteps occur when currents in both windings are at different levels (Russell and Pickup 1982). This mode of operation often requires current sensing and limiting that would prevent exceeding the rated current and thermal capacity of the stepper motor. A number of limiting techniques exist, including open loop current limiters, linear current limiters, voltage limiters, one-shot feedback current limiters, or the well-known PWM technique with high frequency, which is described in Chapter 5.

1.1.4 Special Magnetic Devices

Devices with unique medical applications such as an electronically controlled heart valve or a ventricle assist artificial heart pump were selected for this review (Korane 1997, Young and Pawlak 1992, Young and Pawlak 1990, Zhao et al. 1999). The medical environment and its requirements create an unusual design challenge and allow for broadening technological horizons. The key challenges for medical applications are energy supply and heat dissipation. A long-lasting energy supply helps reduce the number of surgeries between implants while a proper heat transfer helps tissues survive longer. Maintaining the temperature rise below 3–5°C above normal body temperature (36.6°C) is critical because such a relatively small temperature increase may permanently damage exposed tissue cells. Another challenge is selecting the device location and its size. The left-ventricular assist device that provides pressures for an artificial heart can be located anywhere along the blood pipeline. Location in the pelvic area would allow anchoring the pressure chamber to the bone structure for convenient energy transfer through the skin. The size of the heart valve for the mitral valve replacement was selected for the mature human heart. Even though the heart valve final design met all the required temperature and blood pressure tests, its design has a number of deficiencies in comparison with a real human mitral valve:

- Excessive noise when in operation
- Blood cell damage, inducing blood clots
- The need to dissipate heat that may damage cells
- Large volume with its sewing ring and electromagnetic circuit
- Requires electrical energy to run
- Need for connections and leads
- Limited durability, up to 10 years

New materials and, in particular, use of smart materials also creates unusual design challenges for an engineer and allows for novel configurations. Piezoelectric, magnetostrictive, rheological, and thermoresponsive materials have perhaps the highest potential for use in mechatronic systems. Piezoelectric ceramic and polymer materials that instantly change the physical shape in response to an electrical field have potential use in actuators that control vibration in precision tools, and improve accuracy and speed of robotics, printers, and injectors. Devices with electrostrictive and magnetostrictive materials that change size in response to either electric or magnetic fields, or that can produce electrical voltage signals when stretched, can be utilized as valves and pumps or sensors.

Electrorheological and magnetorheological fluids that change their states from liquid to almost solid in the presence of electrical or magnetic fields are finding applications in dampers for automotive suspension with great potential for medical, construction, and sport utility applications, among others. Thermoresponsive materials, such as shape memory alloys that change shape in the presence of cold and heat, were found useful for automotive and aircraft parts such as couplers and thermostats. Introducing mass production applications of any of the smart materials is a great challenge and a high risk. The world's first successful industrial application of magnetorheological fluid is described in Chapter 6 (Delphi 2002).

1.1.5 Rotary and Linear Actuators

Rotary actuators, also called torque motors or torque actuators, are electromechanical devices that develop torque with limited-angular travel. Linear actuators are force motors that develop force with limited linear travel. Both linear and rotary actuators are aimed at developing high force density over the limited movement of the armature. For rotary actuators, a PM armature with multipole magnetization is sandwiched between two VR toothed stators for a high-density torque with a magnetic gearing effect. Both the inner and outer armature surfaces effectively collaborate with two active stator surfaces, while the multipole magnetization develops torque that is equivalent to a multiplicity of separate force components in each rotary actuator section (one pair pole). The required angle of rotation determines the allowable number of pole pairs for rotary actuators. A corresponding linear actuator structure with multipole magnet magnetization and an adequate number of pole-pair sections in the stators can also have travel restrictions where limited travel imposes a number of pole pairs on a "transverse flux" linear actuator (Hennenberger and Bork 1997). These structures feature contactless actuation principles with bidirectional functions of magnetic springs as well as high torque and high force density. Some configurations provide a constant torque or force, which is independent of the angular or linear position for a certain current level. Some configurations can be devised with more than one degree of mechanical freedom and inherent position sensing features.

Based on the design structure, there are three types of rotary actuators:

1. Disk rotary actuators with a multipole axially magnetized disk magnet sandwiched between two VR homopolar stators
2. Claw pole rotary actuators with a multipole ring magnet and a claw pole stator homopolar stator
3. Cylindrical rotary actuators with a multipole radially oriented ring magnet with an inside and outside VR monopolar toothed structure

These rotary actuators are well suited for applications with high torque and demanding size requirements (Pawlak 1990, Weh et al. 1990). Such actuators are found in applications in passenger vehicles, computer peripherals, automatic payment machines, laser controls, and pressure and proportional valves, as described in Chapter 7.

1.2 Magnetic Materials and Technology

The interaction of matter with an external magnetic field divides magnetic materials into three categories: diamagnets, paramagnets, and ferromagnets. The interaction is due to

the actions exerted by an external magnetic field on the matter's elementary magnetic moments, which are originated by the orbital and spin motion of the electrons. Whereas diamagnets do not respond to the presence of the external magnetic field, paramagnets are materials that weakly magnetize in the same verse as the magnetic field. Ferromagnets are materials that weakly magnetize themselves in opposite verse to the magnetic field.

Only 3 of the 116 elements of the periodic table are ferromagnetic at room temperature — Fe, Co, and Ni. The combination of these elements together or with others, although not magnetic, creates a wide range of materials. Depending on coercivity, there are two types of magnetic materials:

1. *Soft* magnetic materials — when coercivity is lower than 1000 At/m; they have the ability to amplify hundreds of thousands of times the external magnetic field.
2. *Hard* magnetic materials or PMs — when coercivity is higher than 1000 At/m; they have the ability to keep their magnetism permanently and to store in their volume hundreds of kilojoules per cubic meter of energy.

Ferromagnets are substances that can be induced to become magnetized in a magnetic field. Soft ferromagnetic materials become demagnetized spontaneously when removed from a magnetic field with a relatively small remanent magnetization. Hard ferromagnetic materials can retain their magnetism, making them useful in the production of PMs. A magnetized magnet contains a north and a south pole that develop a magnetic field. Similar magnetic poles repel and opposite magnetic poles attract. A magnetic field is a region in space where a magnetic force can be detected. The magnetic field is strongest at the poles of a magnet. Magnetic lines of force are a way of representing a magnetic field. By convention, magnetic lines of force point from north to south outside a magnet and from south to north inside a magnet. Magnetic lines of force form complete loops, which never cross.

1.2.1 Soft Magnetic Materials

Soft magnetic materials are mainly utilized in applications in which magnetic materials are needed to amplify the flux generated by an electrical current or by a PM. The principal characteristics of soft magnetic materials are remanence, coercivity, maximum and initial values of permeability, saturation value of flux density B , and coercive force H and J . Properties of different soft magnetic materials are shown in Table 1.1. Figure 1.1 presents a set of first-quadrant hysteresis loops called demagnetization curves (Allegheny 1961).

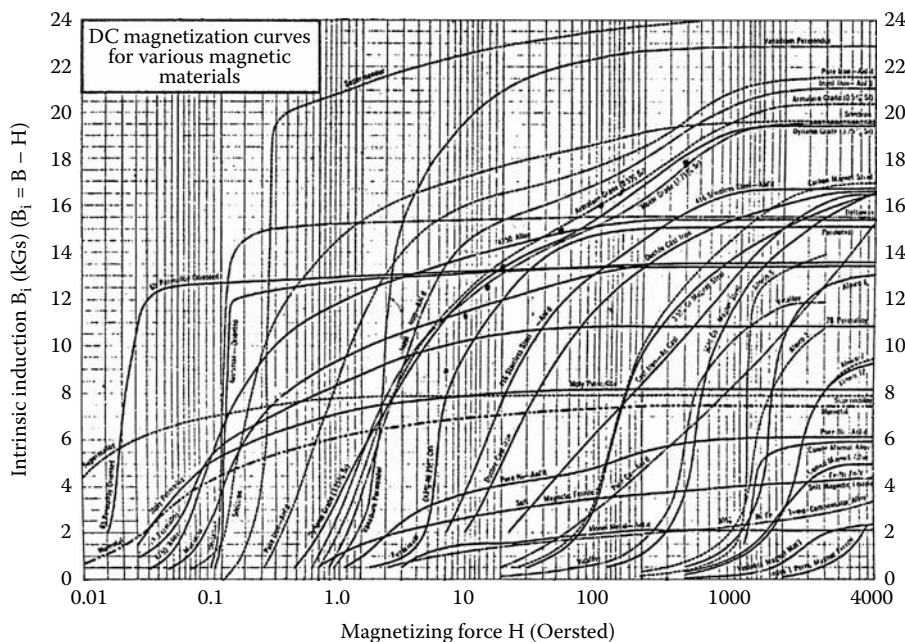
Soft iron is utilized in the form of solid bars, sheets, and, most recently, as a powder. Powder-metal soft magnetic materials also can be used in their sintered form. The development of these materials in the last decade has been spectacular due to advances in powder-metal technology. Sintered soft magnetic materials are most commonly used as pure iron, phosphorus iron, silicon-iron, and nickel-iron forms. They are applied in such devices as peripheral computer devices, printer actuators, brake assembly in disk drives, voice coil actuators, or VR sensors in the automotive industry. There are a number of technical and economic advantages for using sintered powder soft magnetic material:

- Wide range of materials available to designer
- Possibility of obtaining complex and varied shapes
- Process repeatability easily controlled by statistical methods
- Tolerance reliability
- Present magnetic characteristics close to fully dense materials

TABLE 1.1

Soft Magnetic Materials Performance Comparison

Material	Composition	B_{sat} (T)	H_c (A/m)	μ_{max} ($\times 10^{-3}$)
Pure iron	Fe (100%)	2.15	80	5
Fe-Si (nonoriented)	Fe (96%) Si (4%)	1.97	40	7
Fe-Si (grain-oriented)	Fe (97%) Si (3%)	2	8	40
Permalloy 78	Ni (78%) Fe (22%)	1.08	4	100
Supermalloy	Ni (79%) Fe (16%) Mo (5%)	0.79	0.16	1000
Mumetal	Ni (77%) Fe (16%) Mo (5%) Cr (2%)	0.65	4	100
Permendur	Fe (50%) Co (50%)	2.45	160	5
Soft ferrite	ZnFe ₂ O ₃	0.3–0.5	10–100	1.0–10.0

**FIGURE 1.1**

Magnetization curves of various soft magnetic materials. (From Allegheny Ludlum Steel Corp., *Electrical Material Handbook*, 1st ed., Allegheny Ludlum Steel Corp., Pittsburgh, 1961. With permission.)

- Possibility of material composition unattainable by other technologies
- Near integral use of material with little or no machining
- Clean, safe, nonpolluting economic production process
- Flexible production process allowing for good applications of the just-in-time lean manufacturing methods

For the applications requiring maximum induction, cobalt-iron, phosphorus-iron, and pure iron powder metal are recommended. For dynamic applications demanding rapid magnetic flux change, such as relays or injectors, the phosphorus-iron and silicon-iron materials are recommended because of their high-electrical resistivity, which suppresses the eddy currents. For the applications where high magnetic induction must be achieved in a short period of time with a low excitation current, the nickel iron with maximum permeability is recommended. Ferrous stainless steel is recommended for an application, such as wheel speed sensors in automotives, where magnetic requirements are not extreme but corrosion resistance is required. In some cases, surface coatings on nonstainless materials with better magnetic characteristics may be used for corrosion protection, as described in Section 1.2.3. If the main design issue is cost, the recommended materials are pure iron and phosphorus-iron. Complex magnetic structures can be obtained using advanced powder-metal technologies. Using sintered and extrusion methods, a variety of combinations of soft, hard, and nonmagnetic powder structures can be achieved, reducing costs for simple and elegant solutions (Chatterjee et al. 2003, Pawlak et al. 1994a, Pawlak et al. 1991d).

Two categories of soft magnetic materials can be recognized based on the DC and AC applications. DC applications of soft magnetic materials require a low coercivity H_c and a high permeability μ_{\max} . A low coercivity value is necessary to avoid remanence after the magnetic field is applied, when the power switches are off and a high value of permeability is needed to enhance the excitation field H . The most common DC applications are for electromagnets and yokes, relays, magnetic shields, electrical measuring devices, and magnetic amplifiers.

Typical materials used for DC applications are:

- Iron and low-carbon steels (maximum carbon 0.05%) — During the manufacturing operations of the device, it is necessary to avoid any mechanical deformations during the preparation of the magnetic material. Such deformation must be removed by annealing of the material in elevated temperatures typically between 750 and 900°C.
- Iron-nickel alloys (Permalloy) — Three categories of this alloy are common depending on the Ni content:
 - 36% Ni, which is a high-quality material, suitable for low-distortion transformers
 - 50% Ni, which has the maximum of J_{\max} of 1.6 T of Ni alloys and is used for tape-wound cores
 - 80% Ni, which has the higher permeability μ_{\max} (up to 300,000)
- Iron-cobalt alloys (Permandur) — Cobalt is the only element that, when alloyed with iron, increases the saturation magnetization (maximum value of 2.45 T for the 50% Fe and 50% Co). The high cost of cobalt limits this application in armatures and relay cores.

AC applications of soft magnetic materials require a low coercivity H_c and a low power loss, a high permeability μ_{\max} , and a high saturation magnetization. In AC applications, the polarity of material changes; therefore, it is important to apply a material with very thin hysteresis loops to minimize losses, with high saturation and low coercivity H_c . Typical AC applications include transformers, motors, and generators, as well as signal transmitters and receivers.

Typical materials used for AC applications are:

- Iron-silicon alloys — Iron-containing silicon has increased electrical resistivity to reduce eddy currents. A silicon content of 3% quadruples pure iron electrical resistivity. Producing grain-oriented silicon-iron increases the permeability value in the magnetic flux direction. On the other hand, the introduction of silicon in iron reduces the saturation magnetization and increases brittleness. This limits the maximum level of silicon to 4%. Finished fabricated parts must be heat treated to achieve soft magnetic characteristics. Carpenter steel is annealed at various temperatures and atmospheres. One should follow the manufacturer's instructions because the annealing temperature varies from 725°C to 1075°C. With the temperature rise, the maximum permeability of carpenter steel increases and H_c decreases for a given heat treatment (time and atmosphere). Also, the atmospheres can vary, including nitrogen-hydrogen, vacuum, and dry and wet hydrogen.
- Iron-nickel alloys (Permalloy) can be used for both DC and AC applications.
- Soft ferrites — The conductivity of metal alloys limits their utilization in frequency applications. For high-frequency applications of 1 kHz to 10 MHz Ni-Zn ferrites are utilized. Hexagonal ferrites are utilized for applications beyond 100 MHz.

1.2.2 Hard Magnetic Materials

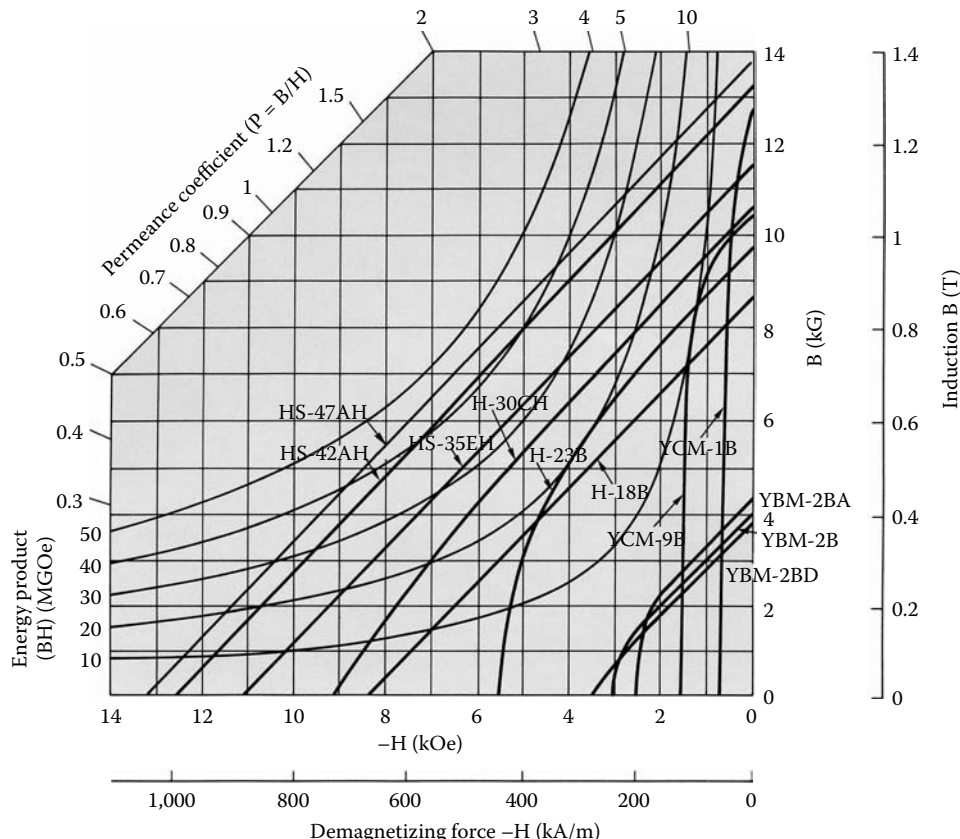
Hard magnetic materials are used as generators of the magnetic field. Hard magnetic materials have both high residual induction and high coercivity. The magnet quality depends not only on remanence B_r , coercive force H_c , and the maximum energy product BH_{max} , but also on its temperature dependence, corrosion resistance, resistivity, brittleness, and cost. Hard magnetic materials include ferrite ceramic magnets, alnico alloys, rare-earth magnets, deformation process magnets, and a bonded magnet category (Coey 1999). The properties of different hard magnetic materials, including magnetic and temperature performance of different families of hard magnet materials, are shown in Table 1.2. Figure 1.2 shows a set of demagnetization curves for different magnet materials coded by the manufacturer (Hitachi 1999): YBM ferrites, YCM alnico magnets, H-samarium-cobalt magnets, and HS-neodymium magnets. The energy product curves identify the maximum energy value for magnet materials from 10.0 to 50.0 MGOe.

Ceramic, also known as ferrite, magnets have been commercialized since the 1950s and continue to be the most widely used magnets today due to their low cost. Ferrites are produced by powder metallurgy, in the form of aggregation of single domain particles (about 1 μm) of barium ferrite $\text{BaO} \cdot 6\text{Fe}_2\text{O}_3$ or strontium ferrite $\text{SrO} \cdot 6\text{Fe}_2\text{O}_3$ (Iwasa et al.

TABLE 1.2

Magnet Performance Comparison

Material	B_r (T)	H_c (kA/m)	BH_{max} (kJ/m ³)	H_{sat} (kA/m)	B_r (%/°C)	H_c (%/°C)	T_{Curie} (°C)
Alnico	0.5–1.3	50–120	15–40	300	–0.02	0.02	900
Ferrite	0.4	150–300	25–30	800	–0.2	0.4	450
Bonded ferrite	0.2	50–200	7	800	–0.2	0.4	
NdFeB	1.1–1.2	1000–2000	250	2500	–0.1	–0.5	310
Bonded NdFeB	0.5–0.7	1000	70	2500	–0.08	–0.4	
SmCo_5	0.8–1.0	1500–2500	180	2000	–0.04	–0.04	700
$\text{Sm}_2\text{Co}_{17}$	1.0–1.1	2000	200	3500	–0.03	–0.03	800

**FIGURE 1.2**

Demagnetization curves for different PM materials. (From Hitachi Metals Ltd., Hitachi Rare-Earth Magnets, 1999. With permission.)

1981). Depending on the process, the final product could be isotropic (independent of direction) or anisotropic (having a preferred direction of magnetization). They are well suited for more corrosive environments and provide very good electrical insulation with good resistance to demagnetization. They come in blocks, disks, rings, and segments, as well as custom geometries.

Alnico magnets (general composition Al-Ni-Co) were commercialized in the 1930s and are still used extensively today. These materials span a range of properties that accommodate a wide variety of application requirements. Because alnico alloys can be cast or sintered, a variety of irregular shapes are available. They include horseshoe, pot magnets, button magnets, rotors, and chain castings. Alnico alloys exhibit high induction values, very good resistance to corrosion, excellent electrical conduction, and stability in high temperatures. The main disadvantages of these alloys are the hardness, brittleness, and ease of demagnetization.

Bonded magnets are ferrite or NdFeB magnet powder mixed with epoxy resin using techniques such as cord rolling, injection molding, or extrusion. Bonded magnets have lower magnetic properties, but they can be formed in complex shapes with the best mechanical tolerances. In recent years, there have been great improvements in the cost and performance of bonded magnets. Injection molded isotropic bonded magnets range between 5.0 and 7.0 MGOe, and injection molded anisotropic magnets range between 8.0 and 12.0 MGOe and up to 15.0 MGOe with the application of hydrogenation-

disproportionation-desorption-recombination (HDDR) of the NdFeB powder processed route (Gasiorek 1999, Tupper 1999). High-temperature polyamide NdFeB injection molding material can withstand a long-term (3000 hours) high temperature of 150°C. Compression isotropic bonded magnet energy ranges between 8.0 and 11.0 MGOe and compression molded anisotropic bonded magnet energy ranges between 16.5 and 18.3 MGOe and up to 22.0 MGOe with the application of NdFeB HDDR powder. Bonded magnets satisfy requirements in some areas where sintered magnets are not feasible. Because of this as well as their low cost and unique features, they are finding more industrial applications. Their features include:

- Precise shape and tight dimensional tolerances
- Flexibility in a wide range of magnetic property requirements
- Wide variety of shapes and sizes
- Complex shape and thin wall
- Low number of surface imperfections, such as chips, cracks, porosity, voids, and roughness
- Minimum material waste during manufacturing process
- Possible use as structural components in highly integrated structures
- Multipole orientation in anisotropic materials for improved performance over traditional orientation
- Ideal choice for ease of assembly — molding onto the flux carrier and molding onto a shaft

Neodymium-iron-boron and samarium-cobalt magnets are known as rare-earth magnets because they are both composed of materials from the rare-earth group of elements. The general composition of neodymium-iron-boron is $\text{Nd}_2\text{Fe}_{14}\text{B}$. Often abbreviated to NdFeB, neodymium-iron-boron magnets are the most recent addition to the family of modern magnet materials developed simultaneously at the General Motors Research Labs and the Sumitomo Corporation in the 1980s (Croat 1985). At room temperature, NdFeB magnets feature the highest properties of all magnet materials. Samarium-cobalt magnets are manufactured in two compositions — Sm_1Co_5 and $\text{Sm}_2\text{Co}_{17}$. The compositions are often referred to as the SmCo 1:5 and SmCo 2:17 types. $\text{Sm}_2\text{Co}_{17}$ magnets, with higher H_{ci} values, offer greater inherent stability than the Sm_1Co_5 magnets. The rare-earth magnet manufacturing process, based on a sintering operation for any magnet shape including ring magnets, is shown in Figure 1.3 (Daido 2003, Gieras and Wing 1994, Glinka et al. 2005, Hitachi 1999, Shimizu and Hirai 1990). Another technique that was applied to ring magnets is the extrusion process as shown in Figure 1.3 (Kasai 1992). Please note that the elongation of neodymium particles allows for magnetization in the direction perpendicular to elongation. Because this method provides an unutilized material at the bottom of an extrusion that has to be removed, it may be more costly in comparison with the sintered method.

This current evolution of technology in NdFeB magnets is coming from innovations in rapid solidification. New rapidly solidified alloys have been developed for sintered magnets. Because of these advancements, the existing NdFeB magnet composition is only several percent shy of its theoretical energy product limit of 64.0 MGOe. Sumitomo has reported new NdFeB magnets with an energy product record of 55.8 MGOe for Neomax 50 (Matsuura 1999).

However, some predictions indicate a magnet performance of 100.0 MGOe for composite alloys, consisting of a high magnetization component (e.g., Fe_3B or μFe) and one having large anisotropy (e.g., $\text{Nd}_2\text{Fe}_{14}\text{B}$). The new rare-earth SmFeN magnets discovered in 1990

are now commercially available. They are suitable for anisotropic bonded magnets, particularly for applications requiring better temperature stability than NdFeB, and also have potential as a second source for the fast-growing isotropic bonded magnets industry. Hybrid grades of SmFeN in combination with ferrites offer an economical solution when the properties of bonded ferrites are not satisfactory. This material requires quite a different fabrication process than other rare-earth magnets with the essential step being a gas-solid reaction at about 400°C to produce the interstitially modified $\text{Sm}_2\text{Fe}_{17}\text{N}_3$ intermetallic compound. Current value of $(BH)_{max}$ for zinc-coated powder with 10% Co substitution is 46.0 MGOe; anisotropic polymer-bonded magnets offer 22.0 MGOe (Rashidi 1999).

Magnetic nanocomposites have shown very interesting novel magnetic properties such as giant magnetoresistive and exchange-spring magnet behavior. To achieve optimized unit magnetic properties with the later family of magnetic alloys, the control of structural parameters, such as grain size, distribution of precipitated crystal in alloys, and conditions for microalloying, are extremely important. Although the use of thin film deposition techniques (sputtering, laser ablation) are much better suited to achieving better results, standard bulk processing techniques normally used for the production of nanostructure material may not be sufficient to obtain satisfactory results. Improvement of thermal stability, reduction of material cost, advancements in injection molding technology, increasing bulk density of the material, and enhancing anisotropy of these materials are challenges that lie ahead for magnet researchers.

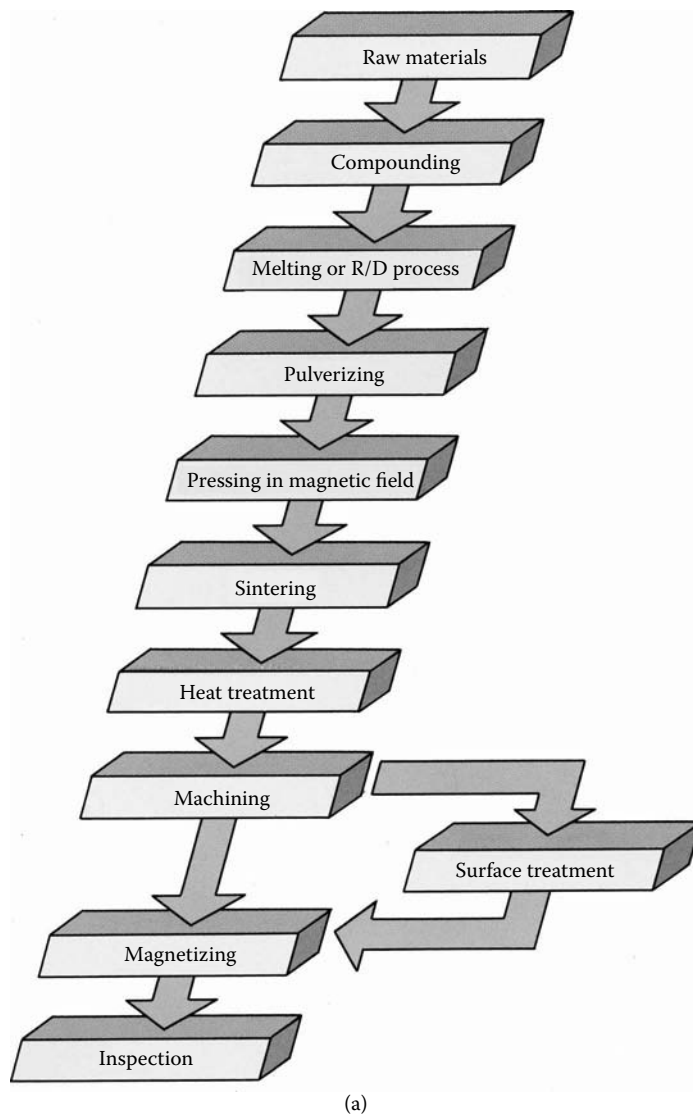
1.2.3 Coating Technologies

Corrosion continues to represent a challenging issue for magnet manufacturers because of the wide range of applications in severe environments (Mills 1999). Coating materials evolved by process improvements and are affected by the U.S. government's removal of certain chemical products from the market for environmental reasons. Coatings for sintered and bonded magnets include nickel plating organic electrocoating, spray coatings, and multiple layers of combination coatings for tough performance requirements.

Some companies developed an improved coating process where magnetic particles are encapsulated with organic coatings. Some companies developed an even more advanced coating process with precise functional characteristics by applying thin multiple coatings over individual powder particles. The layers are conformal, following the irregular contours of the magnetic powder particles. Each particle of the press-ready powder is 100% encapsulated. Benefits of this process include:

- Corrosion protection before, during, and after magnet manufacturing
- Extremely uniform metal distribution with reduced geometric or dimensional scattering
- Higher magnetic properties of the manufactured magnet
- Minimized magnetic temperature degradation associated with high-shear compounding of high-temperature injection molding operations
- Better flow characteristics — higher compaction, higher density / lower pressures, smaller cross sections, increased production rates

This coating process, therefore, allows for reducing magnet manufacturing costs by eliminating expensive compounding and blending costs, increasing production throughput, reducing rejects, and eliminating the need for secondary coatings in some applications.

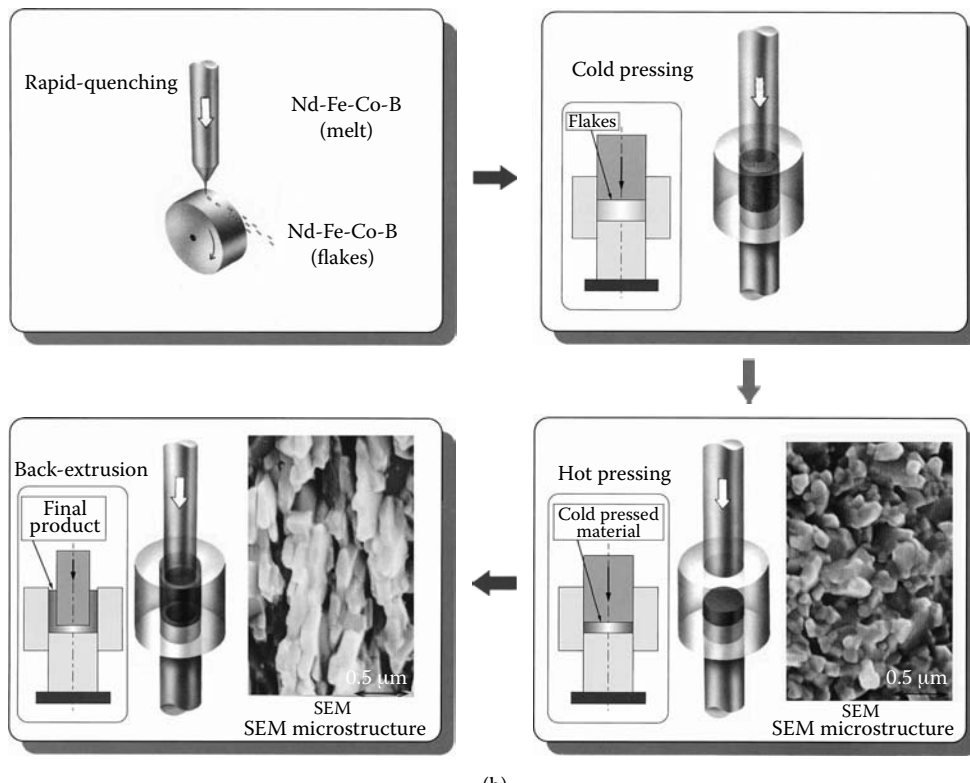
**FIGURE 1.3**

Rare-earth magnet manufacturing process: (a) sintered-based. (From Hitachi Metals Ltd., Hitachi Rare-Earth Magnets, 1999. With permission.)

1.2.4 Magnetic Materials Market and Applications

Magnets serve as essential components in almost all domestic and industrial applications in the automotive, instrumentation, production machinery, aviation, marine, and space markets. Magnets are used in computers, electric motors, loudspeakers, smartcards, cell phones, tape recorders, cameras, camcorders, compact disk players, microwave ovens, kitchen robots, refrigerators, and washers and dryers, to name a few consumer products. Their contribution is often ignored because they are built into devices and are usually out of sight.

Magnets function as transducers and energy conversion devices, transforming energy from one form to another without any permanent loss of their energy. Energy conversion devices utilize PMs to convert mechanical-to-mechanical energy as attraction and repulsion

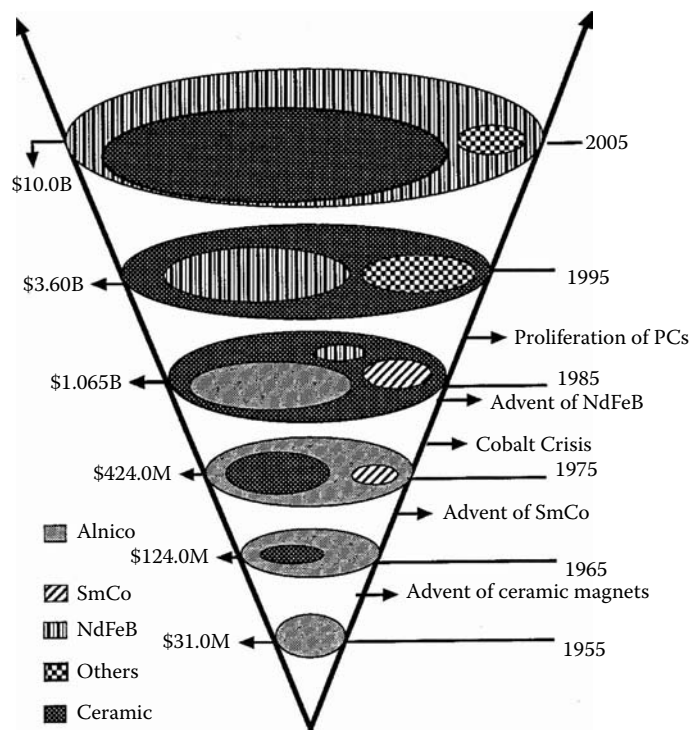
**FIGURE 1.3 (continued)**

Rare-earth magnet manufacturing process: (b) extrusion-based. (From Daido Electronics, Neoquench — DR, Radially Oriented Ring Magnets, 2003. With permission.)

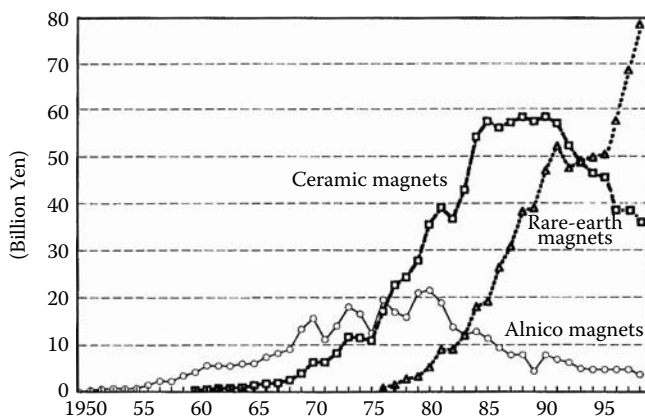
motion; mechanical-to-electrical energy as generators and microphones; electrical-to-mechanical energy as motors, loudspeakers, or charged particle deflection; mechanical energy to heat as eddy current and hysteresis torque devices and, as a special effect, devices for magnetic resonance. The development of hard magnetic materials has always advanced the development of novel electromagnetic devices (Macoit 1999, Pawlak 1995).

The PM business worldwide is now a \$10 billion industry, and it is predicted that this industry will grow at an annual average rate of 12% beyond the year 2005. Figure 1.4 shows the world PM usage coupled with milestones that changed the industry in the most profound ways and energy costs for all hard magnetic materials: ferrite ceramic magnets, alnico alloys, rare-earth samarium-cobalt and neodymium magnets and others, including the bonded magnet category (Rashidi 1999). The use of high-energy PMs made from alloys (neodymium, samarium, dysprosium, and terbium) and transition metals (cobalt and iron) have proliferated and replaced a large fraction of traditional families of PMs such as alnico and ferrites (Carsile 1986). This is because the use of rare-earth magnets in personal computers, mainframe computers, and other aspects of office automation, as well as penetration of smart devices into domestic goods, will continue at a much faster rate. It is also predicted that the second fastest growing sector of the rare-earth magnet market will be motors and actuators.

Japanese sales of PMs, as indicated in Figure 1.5, show strong rare-earth penetration in overall magnet production in Japan (Matsuura 1999). Both ceramic and alnico-based magnets show downturns but rare-earth magnets continue to show a strong increase in production, particularly in the last few years.

**FIGURE 1.4**

Growth of the PM market. (From Rashidi, S., NdFeB Opening Remarks, NdFeB '99 Conference, San Francisco, April 12–14, 1999, p. 3. With permission.)

**FIGURE 1.5**

Trend of PM production. (From Matsuura, Y., NEOMAX Update '99, NdFeB '99 Conference, San Francisco, April 12–14, 1999, p. 4. With permission.)

The overall manufacturing cost, the number of technical personnel who have been well trained and well educated at a low investment cost, and an abundance of rare-earth compounds have made China the largest manufacturer of PMs in terms of weight of production. China is known to have 60% of the world's reserve of rare-earth oxides and currently supplies about 85% of the world's rare-earth oxides' mining volume. It is

misleading to think that just the lower cost of labor has given China an edge in producing low-priced magnets. In actuality, it is a combination of low labor and overhead cost, therefore, low equipment cost as well as ready access to materials. Japan still has an edge on the total value of the magnets shipped globally. However, the Chinese cost of rare-earth powder metal used to produce equivalent quality magnets is less than half that of the Japanese.

Magnet manufacturers maintain that the following current trends in automotive system design should affect rare-earth magnet growth opportunities by increasing the penetration of electric motors in automobiles:

- Electronic control of motors — increase in integrated electronic controls for motors vs. centralized electronic control modules and growth of electronically controlled smart motors and smart systems
- Power-generation technologies — development of liquid-cooled alternators; fly-wheel-mounted, combined alternator and starter with active torque damping; and development of turbine alternator and generator strategy
- Motor technologies — development of powder-metal armature cores and hybrid PM or reluctance motors
- Minimizing parasitic engine losses — potential usage of electric-powered motors in place of hydraulics-driven and belt-driven systems, such as electric-powered oil and water pumps and electric-powered steering systems
- Worldwide supply considerations — greater market demand for “pancake” PM motors, miniaturized PM motors, and increased use of brushless PM motors
- Electrical system architecture — postponed, and perhaps still possible, introduction of 42/14 V dual system architecture, reduced cost of power electronics, growth of modularity and integrated subsystems
- Impact of modularity — modularity and large-scale system integration could result in pieces of motors assembled in modules for integrated functions

Cost, temperature, and manufacturing are the major barriers to the expanded use of neodymium magnets in automobiles:

- Cost barriers — neodymium not yet considered a ceramic replacement because of cost, system integration has potential in savings to offset system cost
- Thermal barriers — under-hood temperatures affected by engine compartment complexity, effect of operation and location of other heat-generating subsystems, component self-heating, and difficulties with predicting operating temperatures accurately
- Manufacturing barriers — feasibility of high volume production, fragile aspect of neodymium material, magnetizing and calibrating assembly, and difficulty of repair or rework

2

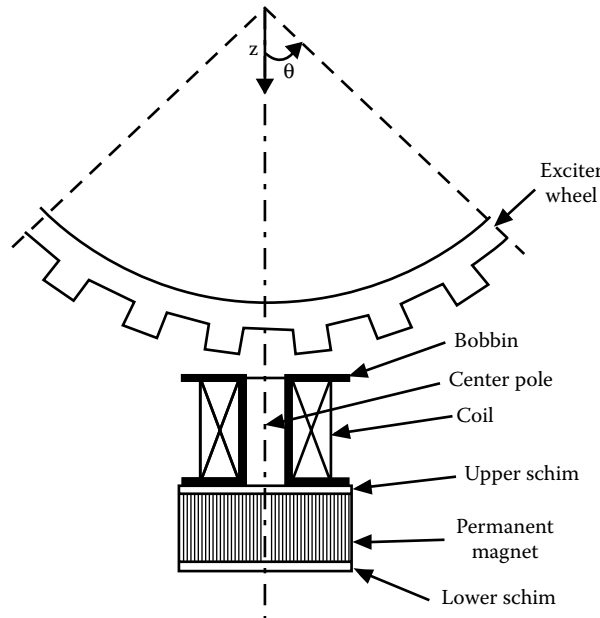
Magnetic Sensors

The market for magnetic velocity sensors is expanding rapidly, particularly in the automotive industry where they are used in a variety of mechatronic systems such as antiskid braking systems (ABS), traction control (TC), four-wheel drive systems, etc. However, as the number of applications grows, the specifications these sensors are expected to meet are becoming more and more demanding. Larger signals are required to improve signal-to-noise ratios and to relax manufacturing tolerances, thus lowering the cost. Despite the current interest in these sensors, the literature on the subject is insufficient and often limited to the description of a specific device (Foster 1988, Podeswa and Lachman 1989, Rowley and Stolfus 1990). Sometimes various technologies are compared (Ohshima and Akiyama 1989b), but because of the large number of possible approaches, the coverage of each concept remains overly general. In-depth analyses backed by theoretical frameworks are lacking, with some exceptions (Lequesne et al. 1996, Pawlak et al. 1991d, Ramsden 2001). Such analyses would allow us to understand and assess the relative importance of various design elements to the overall performance and provide the means for design optimization. They would not only be desirable, but also timely, because the emergence of new materials and manufacturing technologies holds the promise for improved configurations. This chapter attempts to fill this gap by providing both the theoretical background as well as practical optimization examples based on a number of novel sensor configurations.

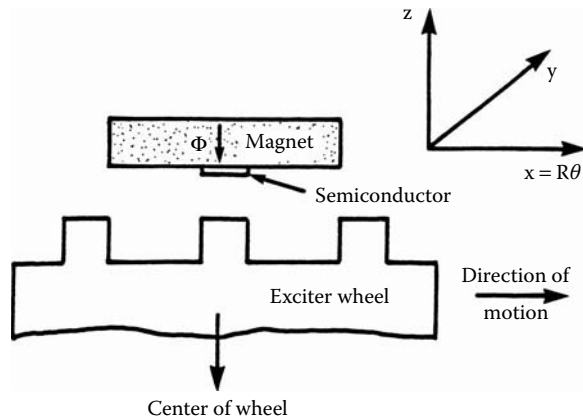
Two types of magnetic sensors based on these principles—VR sensors and galvanometric semiconductor (Hall-effect or MR) sensors—are described in this chapter. We show how recognizing this fundamental difference leads to markedly different sensor design approaches and describes modern configurations with improved performance. The analyses of magnetic sensors are based on a general theory specifically developed for these sensors. The magnetic computation uses two-dimensional (2D) and three-dimensional (3D) finite-element (FE) mathematical models, which are particularly well suited to problems involving complex magnetic configurations and the needs for the calculation of local flux densities and flux linkages. A variety of sensor examples are introduced to validate developed models and to confirm the efficiency improvements of the modern sensor structures.

The magnetic VR sensors feature a coil as a sensing device, a stationary PM operating in close vicinity of a rotary ferromagnetic wheel, sometimes called a target wheel or an exciter wheel. The outer surface of the wheel features a succession of teeth and slots which vary the magnetic permeance as the wheel rotates. This affects the magnetic flux pattern and the corresponding flux variations are sensed either by a pickup coil in the case of the VR sensor, shown conceptually in Figure 2.1, or by a galvanomagnetic semiconductor such as a Hall-effect or MR sensor, as presented in Figure 2.2. These two sensor types will be referred to as “VR sensor” and “solid-state sensor,” respectively.

PM wheels are also used instead of ferromagnetic wheels (Ohshima and Akiyama 1989a, Podeswa and Lachman 1989, Saito et al. 1988), with a solid-state device sensing the alternation of north and south poles on the magnet surface. However, these sensors can

**FIGURE 2.1**

VR sensor components. (From Lequesne, B. et al., *Transactions of IEEE/IAS*, 32(5), 1166–1175, 1996. With permission.)

**FIGURE 2.2**

Magnetic speed sensor with a semiconductor. (From Lequesne, B. et al., *Transactions of IEEE/IAS*, 32(5), 1166–1175, 1996. With permission.)

be used only in more protected environments and, because of magnet costs, the magnet wheel must be small. Their applications are, therefore, more limited and, for this reason, they were not included in this study. High-resolution sensors, such as resolvers (Ohshima and Akiyama 1989b, Podeswa and Lachman 1989) or “absolute” magnetic encoders, which rely on Permalloy-based magnetoresistors reading dense magnetic patterns (Miyashita et al. 1987, Pawlak et al. 1996, Schroeder et al. 1996), are much more expensive. They are designed differently and are beyond the scope of this chapter.

2.1 Theory of Magnetic Sensors

We first present a general theory of VR and solid-state sensors, which underscores both the similarities and differences between the two concepts. The theory is then applied to the specifics of each case. New configurations that make use of new materials and manufacturing technologies are presented. The analysis shows how the new designs can be optimized for given applications. Both the modeling approach and the superiority of the new designs are proven experimentally.

The magnetic sensors studied in this chapter depend on a stationary magnet as a source of magnetic flux and on the modulation of that flux by the movement of the exciter wheel. As the wheel rotates, the teeth, the slots, and the magnet assume various positions that can be characterized by the angular distance θ between some arbitrary location on the wheel and some other arbitrary location on the stationary magnet. The wheel rotation results in magnetic permeance variations, which can be expressed as a function $P(\theta)$.

The permeance $P(\theta)$, shown in Figure 2.3, is a periodic function with a period T equal to the tooth pitch. Its maximum and minimum values, P_{\max} and P_{\min} , correspond to magnet locations across a wheel tooth or a wheel slot, respectively. The permeance variations affect the operating point of the PM and result in flux variations that are also periodic functions with a period T .

On the surface of the sensor facing the wheel, one can define an active area A , which corresponds to the cross section of the magnetic core in the VR-sensor case (the “center pole” in Figure 2.1) or to the area of the semiconductor in the solid-state sensor case (Figure 2.2). In principle, the flux density at any point σ on A is a function not only of the sensor position θ , but also of the location of σ on A . However, variations over A are neglected in this section in order to obtain simplified formulae amenable to physical interpretation. Thus, a flux-density function $B(\theta)$, uniform over A , can be defined that corresponds to the permeance variations mentioned earlier. $B(\theta)$, like $P(\theta)$, is periodic with a period T equal to the tooth pitch and features maximum and minimum values, B_{\max} and B_{\min} , across the centers of the wheel teeth and slots, respectively.

The analysis is, therefore, based on the assumption of a uniform air gap flux-density function $B(\theta)$ over the active area A , which is commonly done in electric machine theory. Usually, this assumption leads only to neglecting harmonics. VR sensors are different,

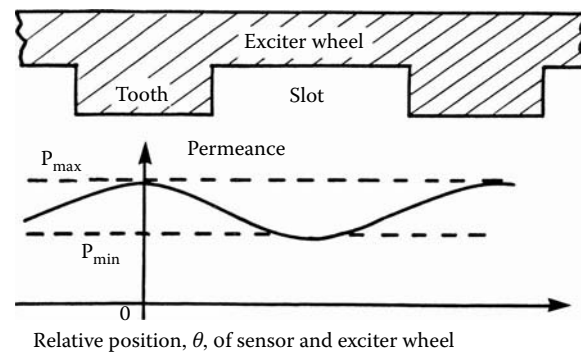


FIGURE 2.3

Exciter wheel permeance variation. (From Lequesne, B. et al., *Transactions of IEEE/IAS*, 32(5), 1166–1175, 1996. With permission.)

however, in that the useful part of their output signal is the peak-to-peak voltage and harmonics may contribute to it. More comprehensive formulae, presented in Section 2.2, are therefore needed to calculate the output signal of an actual VR sensor. They are based on flux-linkage variations for the two extreme sensor or target positions.

2.2 Magnetic Sensor Analysis

The analysis of VR and solid-state sensors presented in this chapter compares both the similarities and differences between the two concepts. For VR sensors, the sensor signal is the voltage $e(t)$ generated in the coil by the time variation of the total flux linkage ψ , given by:

$$e(t) = -\frac{d\psi}{dt} = -\frac{d}{dt} \left[\sum_{i=1}^N \phi_i \right] \quad (2.1)$$

where e is the voltage generated in the coil, N is the number of turns of the coil, ψ is the total flux linkage, and ϕ_i is the flux linkage in any of the N turns of the coil.

The flux linkages ϕ_i are the sums of the flux crossing the air gap and linking to the coil. Because VR sensors are often designed with very large air gaps in order to lower construction costs, leakage may be very large. The leakage flux varies with wheel position; therefore, its time derivative is not zero and it contributes to the useful signal as presented in Equation 2.1. However, for simplicity, these variations are neglected in this section, but they will be included in the more comprehensive expressions given in Section 2.3. Neglecting the leakage allows us to equate each flux linkage ϕ_i with a uniform flux Φ in the magnetic core:

$$\phi_i = \Phi = \int_A B(\sigma) d\sigma \quad (2.2)$$

where B is the magnetic field density, σ is the location of any point on active sensor surface area, Φ is uniform flux in the magnetic core, and A is the cross section of the active sensor surface core.

Assuming for simplicity a rectangular core of length L_y in the y direction (the y direction is defined in Figure 2.2), Φ is:

$$\Phi = L_y \int_{\theta(t)}^{\theta(t)+\delta} B(\alpha) R_{ex} d\alpha \quad (2.3)$$

where $\theta(t)$ is the location of the trailing edge of the core at time t , dimension δ is the core width in the direction θ , and R_{ex} is the exciter wheel radius.

Combining Equation 2.1 through Equation 2.3 yields:

$$e(t) = -NL_y R_{ex} \frac{d}{dt} \int_{\theta(t)}^{\theta(t)+\delta} B(\alpha) d\alpha = -NL_y R_{ex} \frac{d\theta}{dt} \frac{d}{d\theta} \int_{\theta(t)}^{\theta(t)+\delta} B(\alpha) d\alpha \quad (2.4)$$

During steady-state operation, the wheel turns at a constant velocity ω . Therefore:

$$e(t) = -NL_yR_{ex}\omega \frac{d}{d\theta} \int_{\theta(t)}^{\theta(t)+\delta} B(\alpha)d\alpha = -NL_yR_{ex}\omega [B(\theta + \delta) - B(\theta)] \quad (2.5)$$

The maximum signal attainable with a VR sensor is:

$$E = NL_yR_{ex}\omega(B_{\max} - B_{\min}) \quad (2.6)$$

where E is the maximum sensor signal, L_y is the rectangular core of length in the y direction, ω is an angular speed, B_{\max} is the maximum flux density, and B_{\min} is the minimum flux density.

The maximum sensor signal E is reached if the core width δ is such that the positions of the core edges correspond to the locations of B_{\max} and B_{\min} . In most cases, the maximum value of B is in the middle of the tooth, the minimum value is in the middle of the slot, and the distance between these two points is one half of a tooth pitch. Therefore, a magnetic core size of one half of a tooth pitch is desirable. The optimum value may differ from this value, however, because Equation 2.6 is based on two simplifying assumptions: a single function $B(\theta)$ is assumed over the sensor active area A and leakage variations are neglected. In practice, considerations other than output-signal magnitude, such as sensor volume and cost, are also taken into account. It can also be seen from Equation 2.6 that the output signal does not depend on the shape of the function $B(\theta)$, but on its maximum and minimum values. Equation 2.6 also shows that the output signal is proportional to the velocity ω . The signal, therefore, disappears at low velocity and is crucial to maximize the term $(B_{\max} - B_{\min})$ to ensure that, overall, the signal E is larger than the expected noise at the lowest specified speed. However, the signal is very large at high speeds and an over-voltage circuit protection must be included to protect the electronic circuitry.

The performance of a specific magnetic velocity sensor design requires the computation of flux densities or flux linkages. However, calculating these quantities with precision is challenging because of the complex geometry of the sensor, particularly the air gap. Therefore, conventional closed-form solutions based on reluctance paths (Roters 1967) are difficult to implement. The approach in this study was based on the more computer-intense, but more accurate, FE method.

The FE programs that are most readily available at the moment are limited to solving in two spatial dimensions. However, sensor geometries typically vary in all three dimensions. This particular issue was addressed in Sabonnadiere et al. (1989), where several methods to model a VR sensor, 3D, 2D, and tests were presented. The 2D results were processed by performing a weighted sum of results in the xz and yz planes, a technique inspired by Roters (1967). Such a summation is possible because the low level of magnetization of the ferromagnetic parts makes an assumption of linearity realistic. The results indicate that 2D results are reliable if used carefully and checked against experiments.

A 2D FE model was, therefore, selected. The test results shown in this chapter confirm that this approach is reliable qualitatively, even when computations are performed only in the xz plane without the summations proposed in Sabonnadiere et al. (1989). However, some of the experimental results given in this chapter also show that quantitative accuracy may suffer from neglecting the third dimension. Therefore, the approach presented in Rabinow (1951) remains relevant when quantitative accuracy is the prime objective. The magnetic flux density is calculated at each point of the θz plane (the θ angle is linked to the x axis by $X = R\theta$) by solving:

$$\nabla \times (v \nabla \times \bar{A}) = \bar{J}_s \quad (2.7)$$

where v is the material reluctivity, \bar{A} is the magnetic vector potential, and \bar{J}_s is the current density in the coil.

To take full account of both flux leakage and variations of the flux-density function on the sensor surface, the following formula, derived from Equation 2.1, was used for the VR sensors:

$$e(t) = -\omega \frac{d\Psi}{d\theta} \quad (2.8)$$

which requires the calculation of the flux linkage in the coil for various wheel positions, performed as follows. In the θz plane, the z axis cuts the coil into two separate areas, as presented in Figure 2.1, on either side of the magnetic core. These two coil areas are denoted by the superscripts ' and ". Each area is subdivided into m subsections and the flux linkage is obtained by performing the following summation:

$$\Psi = \frac{1}{m} \sum_{i=1}^m \left(A(\theta_i'', z_i'') - A(\theta_i', z_i') \right) \quad (2.9)$$

where A is the y component of the magnetic vector potential at the location (θ_i', z_i') or (θ_i'', z_i'') of the i th coil subsection and m is the number of subdivisions in the coil region.

In the xy plane, the y axis cuts the coil into two separate areas as presented in Figure 2.4, on the other side of the magnetic core. These two coil areas are denoted by the superscripts ' and ". Each area is subdivided into m subsections and the flux linkage is obtained by performing the following summation:

$$\Psi = \frac{N}{m} \sum_{k=1}^m \left(\Phi_k(x'', y'') - \Phi_k(x', y') \right) \quad (2.10)$$

where ψ is flux linkage, N is the number of turns of the coil, $\Phi_k(x'', y'')$ is the k th magnetic vector potential of the one coil side, and $\Phi_k(x', y')$ is the k th magnetic vector potential of the other coil side. $L1$ and $L2$ correspond to y' and y'' , respectively, and $K1$ and $K2$ correspond to x' and x'' at Equation 2.10 and Figure 2.4, respectively.

2.3 VR Sensors

VR sensors are well known for their low cost and reliability. These sensors are self-excited and, unlike solid-state sensors, they require no external voltage or current source. Conventional VR-sensor configurations, shown in Figure 2.1 and in Pawlak et al. (1991d), are, however, unable to develop high signal strength at low target-wheel speeds or with a large air gap between the sensor and the target wheel. They require a relatively large volume to accommodate a coil with a large number of turns and a large PM to develop

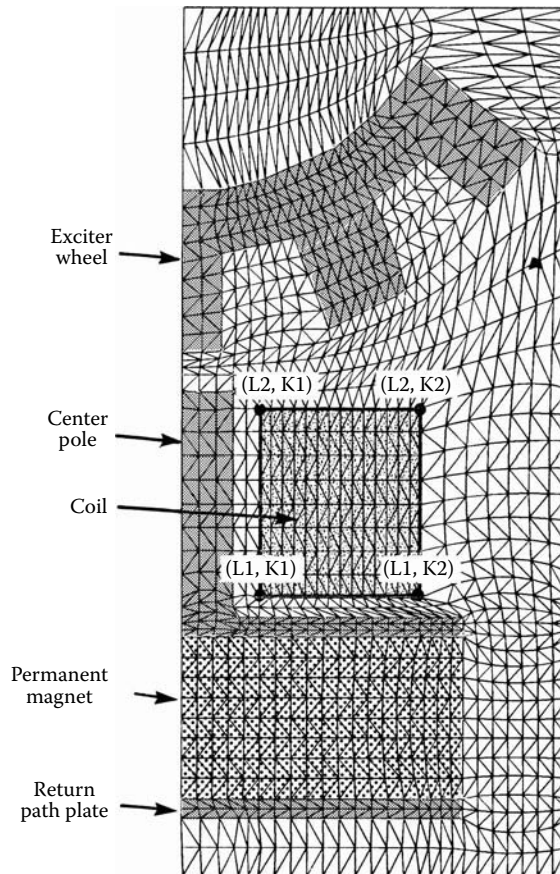


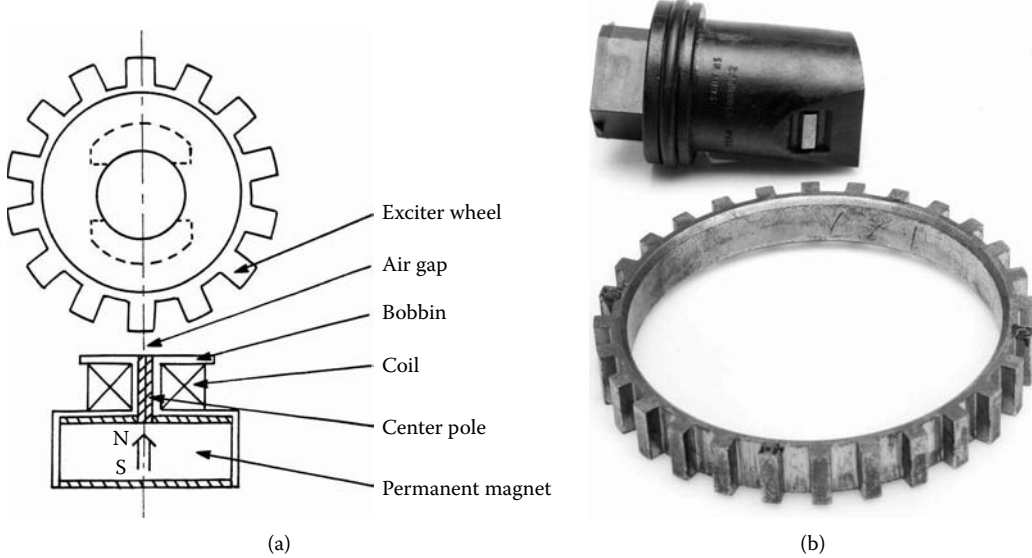
FIGURE 2.4
Sensor geometry for the FE analysis. (Courtesy of Delphi Corp.)

the required signal strength. Because the coil is large, the magnet is usually located far from the target wheel and only a small percentage of the magnet flux, as low as 5%, contributes to the signal, resulting in low signal strength. Modern VR sensor configurations offer better utilization of the flux developed by the magnet; therefore, this chapter will focus on the ways of using VR sensor improvements to reduce their volume and improve their sensitivity. It is worthwhile to improve VR sensor deficiencies because of the advantages they offer. Because of their superior reliability, low cost, and simplicity, they will always find industrial applications, especially in harsh environments.

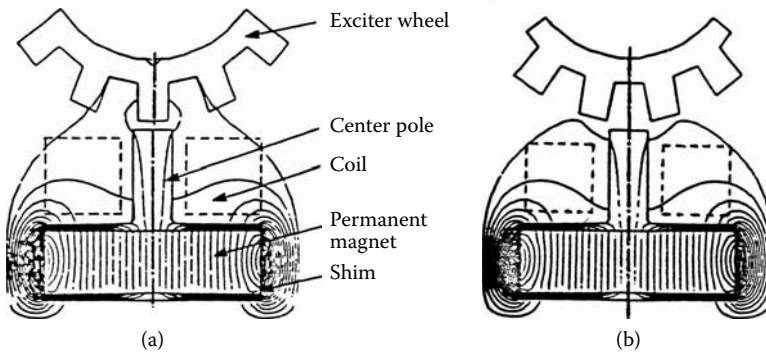
2.3.1 Conventional VR Sensors

A conventional VR speed sensor consists of a magnetic circuit, a coil, and a PM, which is located far from the exciter wheel, as shown in Figure 2.5. Conventional VR sensors feature no iron path, as shown in Figure 2.5(a). This is perceived to make the design simpler, more universal, and less expensive, but the flux is not properly guided because there is no main magnetic path. Generally, less than 5% of the magnetic flux contributes to the signal, which then relies almost entirely on the leakage flux.

Traditionally, these sensors have had a large volume to accommodate the large number of turns and a big PM necessary to develop the required signal strength. This is because

**FIGURE 2.5**

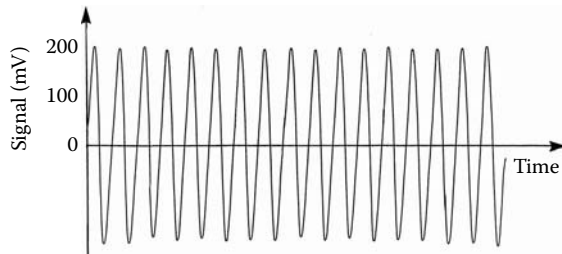
Conventional VR sensor configuration and manual transmission speed sensor example: (a) VR sensor components, (b) manual transmission speed sensor. ([a] From Pawlak, A.M. et al., *Novel Variable Reluctance Sensors*, Publ. No. 910902, Society of Automotive Engineers, Detroit, MI, 1991. With permission; [b] courtesy of Delphi Corp.)

**FIGURE 2.6**

Conventional VR sensor flux lines for two arrangements with exciter wheel for (a) maximum flux linkage and (b) minimum flux linkage. ([a] From Pawlak, A.M. et al., *Novel Variable Reluctance Sensors*, Publ. No. 910902, Society of Automotive Engineers, Detroit, MI, 1991. With permission; [b] from Lequesne, B. et al., *Transactions of IEEE/IAS*, 32(5), 1166–1175, 1996. With permission.)

of their low efficiency, since only a small percentage of the PM flux contributes to the signal development. A conventional sensor-wheel arrangement utilizes the modulation of magnetic flux by the movement of the exciter wheel, which occurs predominantly in the xy plane, as presented in Figure 2.6 for two different VR sensor arrangements with the exciter wheel. As the wheel rotates, the teeth, the slots, and the magnet assume various positions. The wheel rotation results in magnetic permeance variation, which is a periodic function with a period equal to the tooth pitch. Its maximum and minimum values correspond to maximum and minimum flux linkages in an xy plane, as presented in Figure 2.3.

By rotating an exciter wheel associated with the speed sensor, the permeance of the magnetic speed sensor changes, and this affects the magnetic flux linked to the coil. The

**FIGURE 2.7**

Sensor signal vs. time. (Courtesy of Delphi Corp.)

highest permeance occurs in the sensor-tooth position and the lowest permeance occurs in the sensor-slot position. The coil flux linkage changes due to permeance variation. The voltage signal induced by the coil (for speed or position sensor signal) is proportional to the number of coil turns, the rate of the flux-linkage change with respect to the time (Equation 2.8), as shown in Figure 2.7.

To evaluate the sensor structures, two figures of merit are defined. The first figure of merit is the sensor signal sensitivity s_v based on the signal v_s over volume V_s ratio indicating sensor electromagnetic efficiency of the investigated configuration:

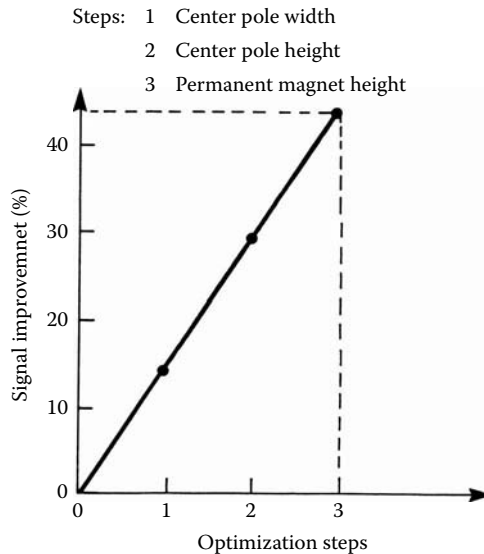
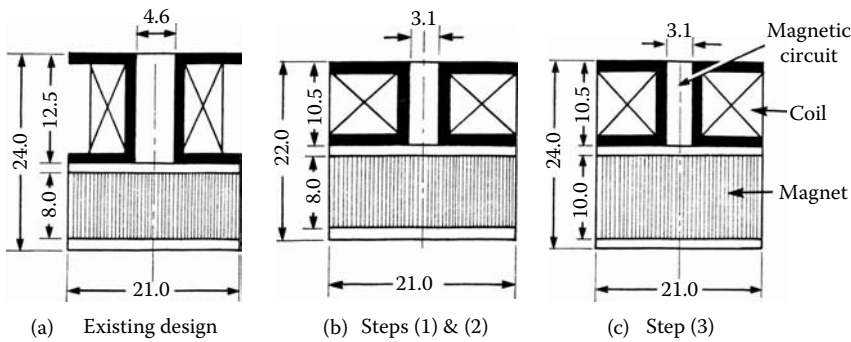
$$s_v = \frac{v_s}{V_s} \quad (2.11)$$

where s_v is the sensor signal sensitivity, v_s is the sensor signal, and V_s is the sensor volume. Sensor signal value is a measure of the sensor performance. If coupled with the sensor volume, it can be used as a figure of merit to evaluate and to compare sensor effectiveness. Quite often, requirements and, in particular, the available space envelope and exciter wheel geometry, lead to sensor configuration selection. The second figure of merit is the sensor flux sensitivity s_ϕ indicating how much the total PM flux contributes to the signal generation:

$$s_\phi = \frac{\Delta\phi}{\phi_o} \quad (2.12)$$

where s_ϕ is the sensor flux sensitivity, $\Delta\phi = \phi_{\max} - \phi_{\min}$ is the flux-linkage change defined as the difference between the magnet flux linked to the coil for the maximum permeance position and the magnet flux linked to the coil at the minimum permeance position, and ϕ_o is the total flux developed by the PM. The sensitivity s_ϕ indicates the electromagnetic efficiency of the investigated sensor configuration and maximizing its value would help achieve a magnetically efficient and highly sensitive VR sensor design. For the best design, all parasitic air gaps in the magnetic circuit should be eliminated or minimized and all available coil envelopes should be used for the coil including full utilization of the magnetic flux developed by the PM.

Utilizing effectively FE math models and an iterative design approach, the conventional sensor structure can be optimized for the best signal volume. Optimization steps must be performed at two extreme sensor-wheel positions, as presented in Figure 2.6. Figure 2.8 shows three conventional sensor geometries side by side before and after optimization with 43% signal improvement, with 40% noise reduction and cost savings for this manual transmission speed sensor, as shown in Figure 2.5(b) and Table 2.1.

**FIGURE 2.8**

Conventional sensor signal improvement for three optimization steps: (a) original design, (b) intermediate improvement, (c) final design. (Courtesy of Delphi Corp.)

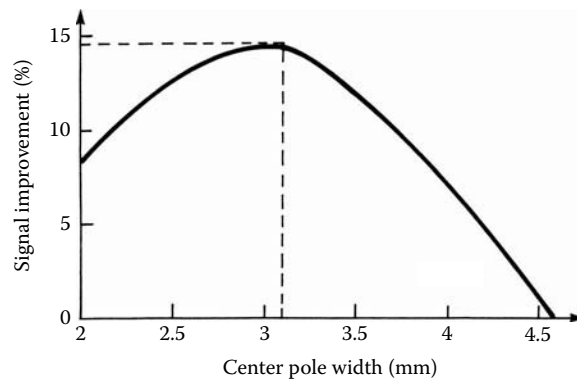
TABLE 2.1

Conventional VR Sensor Optimization Steps

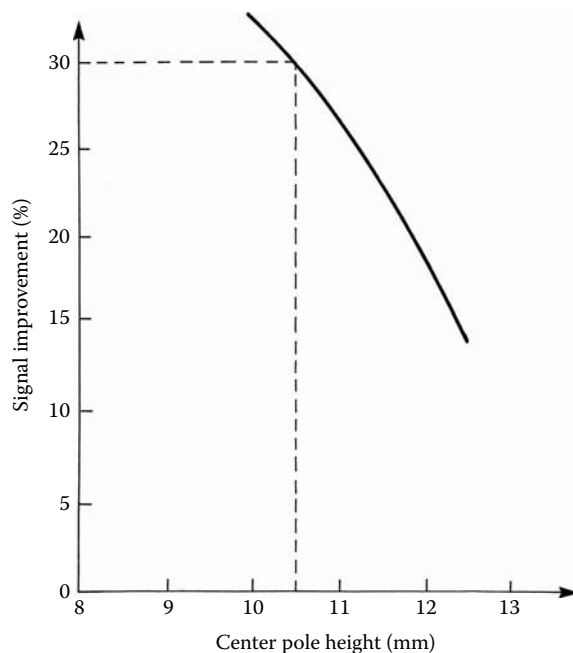
Sensor Geometry	Volume (cm ³)	Signal (V)	Signal Sensitivity (V/cm ³)
a — Original	3.96	0.364	0.092
b — Intermediate	3.63	0.473	0.13
c — Final	3.93	0.519	0.132

Source: Courtesy of Delphi Corp.

Intermediate sensor geometry includes both the center pole width and height optimization. The center pole width equal to the exciter wheel tooth width provides the highest signal value, as shown in Figure 2.5 and Figure 2.9, accounting for almost 15% of the sensor signal increase. Because space around the sensor coil was not fully utilized, the bobbin was shortened to accommodate the entire coil window with full utilization, and as a result, the sensor signal improved by another 15%, as shown in Figure 2.10.

**FIGURE 2.9**

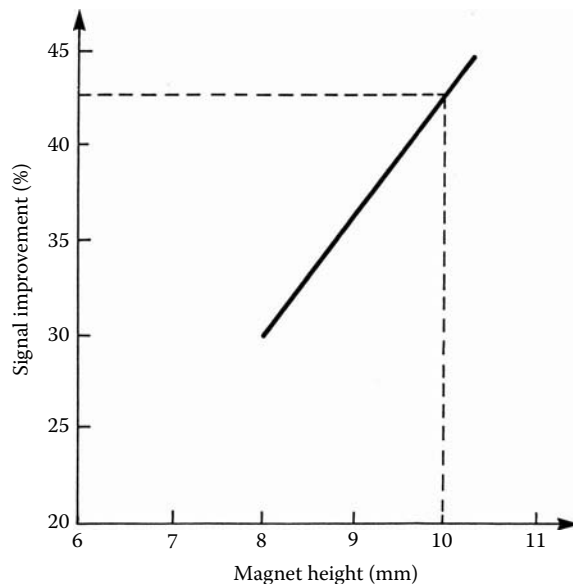
Signal vs. center pole width. (Courtesy of Delphi Corp.)

**FIGURE 2.10**

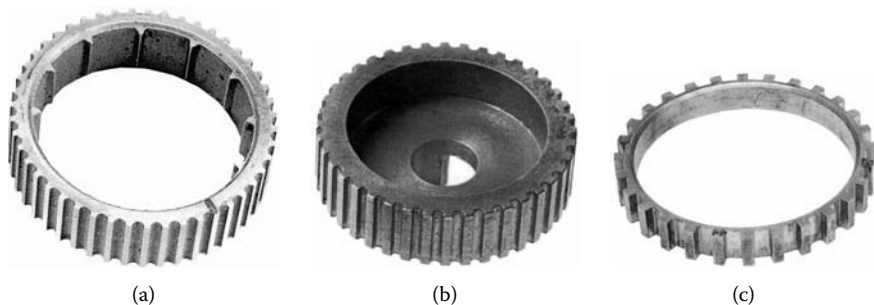
Signal vs. center pole height. (Courtesy of Delphi Corp.)

To fully utilize the sensor envelope, the sensor magnet was elongated to the original sensor height, which resulted in further signal improvement to about 10%, as shown in Figure 2.11. Combination of all improvement steps resulted in over a 40% signal gain.

Conventional VR sensors, which display low magnetic efficiency, are being replaced by much more efficient ones (Pawlak 1999b). Recent efforts are focused on new technical approaches at finding low-cost, magnetically efficient, sensitive VR structures that feature high signal strength for large air gaps with small PM volume and that address this technique for specific applications. Improved sensors have the ability to work with a variety of conventional and low-cost exciter wheels, e.g., stamped or embossed sheet metal, low- to high-density powder-metal, molded plastic with iron filler, and rolled teeth, as presented in Figure 2.12.

**FIGURE 2.11**

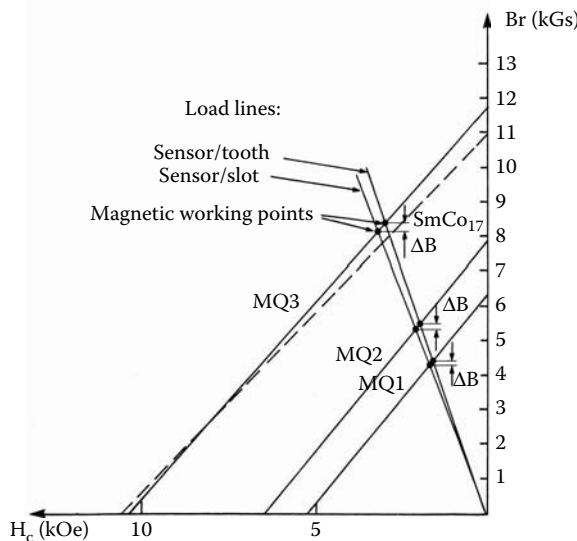
Signal vs. magnet height. (Courtesy of Delphi Corp.)

**FIGURE 2.12**

Exciter wheel configurations: (a) high-density powder, (b) low-density powder, (c) conventional machining. (Courtesy of Delphi Corp.)

2.3.2 High Performance VR Sensors

VR sensors whose configurations are different from those of conventional ones fall into the modern VR sensor category. In this category, both the distributed sensors and the stand-alone sensors are described. Recent developments in new magnetic materials and manufacturing technologies enabled the introduction of new sensor configurations and sensor wheel arrangements, which led to dramatic improvements in VR sensor performance. In particular, new PM materials with high-energy products, powder-metal manufacturing technology, bobbinless coil winding, and advanced plastic-molding technology can dramatically improve performance. Powder-metal technology allows for low-cost exciter wheels and unconventional shapes of magnetic circuit parts for the cost-efficient sensor. This technology was utilized for both the magnetic circuit and the exciter wheel for the dual-magnet sensor configuration described in Section 2.3.8.

**FIGURE 2.13**

PM working point for the extreme VR sensor positions. (From Pawlak, A.M. et al., *Novel Variable Reluctance Sensors*, Publ. No. 910902, Society of Automotive Engineers, Detroit, MI, 1991. With permission.)

Development of high-energy product PMs based on samarium-cobalt (SmCo_{17}) and based on neodymium (such as Magnequench® MQ1, MQ2, and MQ3) allowed for sensor signal improvements. The location of the magnet working point on the BH characteristics of high-energy PMs enables the generation of larger change in the flux developed by the PM in comparison with the low-energy magnets, as shown in Figure 2.13.

The rotation of the excitation wheel changes the permeance value of the magnetic circuit surrounding the PM. The minimum and the maximum permeance values for two extreme sensor positions are indicated by load lines of characteristic positions, as indicated in Figure 2.13. The lower line corresponds to sensor-slot position with minimum permeance value and the higher line corresponds to sensor-tooth position with the maximum permeance value, as presented in Figure 2.13. During the exciter wheel rotation, the PM working point changes its position. For the low- and high-energy magnets, the flux variation with the load-line changes is different, larger for the magnets with high-energy product and smaller with the low-energy product magnets, as indicated by the ΔB values in Figure 2.13. Therefore, the capability of generating not only higher flux, but also a larger difference in two extreme positions makes the high-energy magnet material more desirable for the sensor applications. Analysis and optimization studies should always start with the predetermination of the soft and hard magnetic materials used for the sensor structure. PM studies prove that the higher-energy magnets provide a higher sensor signal level. Signal level comparison for all four different magnet materials, as indicated in Figure 2.13 without additional changes, proves this point, as shown in Figure 2.14, where the highest signal level was achieved for the MQ3 material and the lowest for the MQ1 magnet material.

High-energy magnets allow for unconventional magnet geometries and locations, resulting in very large sensor signal improvements. Magnets with high-energy density permit the reduction of the magnet size, which provides greater design flexibility. In particular, the magnet can be located in the middle of the coil and in the proximity of the target wheel, instead of behind the coil as in conventional designs. That is, the magnet can be inserted in the area of the conventional center pole, such as the one shown in Figure 2.15(c). This new

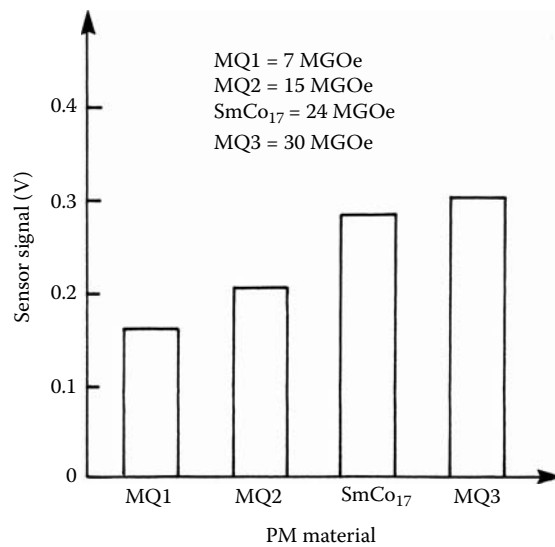


FIGURE 2.14
Sensor signal for different magnet materials. (Courtesy of Delphi Corp.)

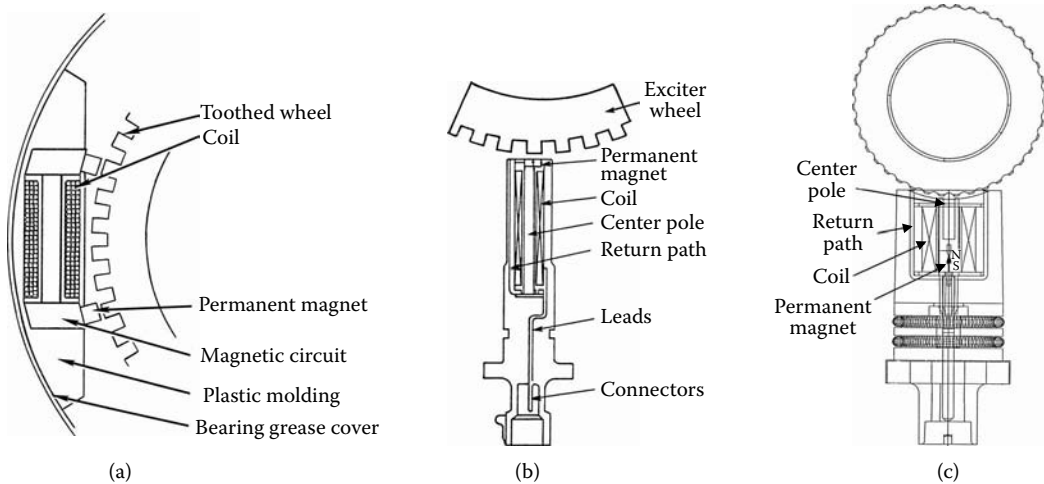


FIGURE 2.15
Sensors with unconventional magnet location: (a) two-magnet sensor, (b) front-magnet sensor, and (c) inserted-magnet sensor. ([a] From Pawlak, A.M. et al., *Novel Variable Reluctance Sensors*, Publ. No. 910902, Society of Automotive Engineers, Detroit, MI, 1991. With permission; [b] from Pawlak, A.M., *Proceedings of the NdFeB '99 Conference*, San Francisco, April 12–14, 1999. With permission; [c] courtesy of Delphi Corp.)

structure will be referred to as the “inserted-magnet” configuration. A magnet that is located closer to the target wheel is favorable because the magnetic-circuit permeance is improved, and the source of the magnetic flux is embodied within a coil, and therefore, the flux distribution affects more directly the coil.

The structure with the magnet located in close proximity to the exciter wheel will be referred to as the “front-mounted-magnet” configuration, as presented in Figure 2.15(a,b). A magnet located closer to the target wheel is also favorable because the magnetic-circuit permeance is improved and the flux distribution affects the coil more directly. Effectiveness

of front magnet location was confirmed for an automotive application of this sensor where for the same signal level, the front-mounted-magnet design allowed the reduction of a sensor volume by a factor of 4 as compared to the conventional sensor design. As this shows, the performance improvement resulting from the new magnet location is such that in many applications, it should outweigh the higher magnet-material cost. The magnet design can be considered as 2D for both the magnet width and for its height, because the axial dimension is fixed to the thickness of the exciter wheel, which is also an optimum size.

Coil turns located in the proximity of the target wheel are more directly exposed to target-wheel permeance changes and embrace more flux lines. Therefore, short and wide coil geometries are preferable to long and narrow ones. In one particular case, the signal from a conventional design was improved by 30% by changing the coil-width/coil-height ratio from 0.41 to 1.00, the coil area being kept constant. Such coil geometries are easier to implement in the front-mounted-magnet case, which is another advantage of that configuration. Coil geometries that promote close coil locations to the exciter wheel are preferable. Precision coil winding with the bobbinless technology allows for better coil packaging, including unconventional coil winding directly on the magnetic circuit. Advanced plastic-molding technology makes feasible unusual sensor configurations where parts have to be kept together, fastened to the adjacent parts, and sealed at the connectors.

Four families of modern VR sensors are described and specific examples of automotive applications of these sensors are provided:

- Sensors with an inserted magnet having improved magnetic circuit and the inserted magnet as an automotive automatic transmission speed sensor
- Sensor with front-mounted magnet featuring significant performance improvement as an automotive crankshaft position sensor with U-shaped or with E-shaped magnetic circuit for the transmission speed sensor application
- Distributed sensor with two front-mounted PMs with limited angle of exciter wheel coverage for an automotive antiskid braking system (ABS)
- Distributed sensor with ring magnet having a multiplicity of PMs with unlimited angle of exciter wheel coverage for an automotive TC system

While both inserted-magnet and front-mounted-magnet sensors are having conventional arrangements with the exciter wheel, the distributed sensors are combined with the exciter wheel in a more complex manner. Sensors with two front-mounted magnets are arranged with the exciter wheel in one 2D plane, whereas the ring magnet distributed sensors are arranged with an exciter wheel three-dimensionally. These novel sensor-excitation wheel arrangements are additional opportunities to create modern high-efficiency VR sensors.

The conventional optimization technique is based on a parametric study of selected design variables with an iterative procedure. Therefore, the best design variables (dimensions, material properties, coil, etc.) found in the first parametric study are carried on to the second iterative procedure until all design variables are optimized. The process is repeated until consecutive iterations result in no further changes in the sensor design variables.

Electromagnetic circuits of all investigated sensors were optimized using described mathematical models supported by both 2D and 3D FE magnetic field solutions. The goal of the sensor design optimization is to maximize sensor signal strength. It includes optimization of the magnetic circuit and magnetic materials selection with the best available cost-effective qualities. The design variables for the magnetic material are selected on the basis of sensor configuration, magnetic material properties, and the coil parameters subject to given constraints. The design requirements for VR sensors include an available envelope

for the sensor, the signal strength at the required exciter wheel speed range, the exciter wheel geometry and material, and the size of the air gap between the sensor and the exciter wheel. The maximum coil resistance, the acceptable electromagnetic noise signal strength, and the sensor temperature range at which sensors operate are usually determined. Additionally, the wheel-sensor arrangements, the applied technology, and the type of material used for the exciter wheel can introduce extraordinary challenges for the sensor. Table 2.9 in Section 2.5 contains examples of such requirements, concerning all four investigated sensor types, the truck transmission sensor, the crankshaft position sensor, the integral bearing speed sensor, and the distributed sensor for the ABS/TC applications.

2.3.3 Sensors with Inserted Magnets

The inserted-magnet structure falls into the modern sensor category because the magnet location allows for its efficient utilization. Figure 2.16 presents a number of different VR sensor geometries with inserted magnets. Both the sensor and magnet geometry depend on selected structure and target-wheel geometry. For sensor 1 and sensor 2 structures, the magnet thickness is the same as the thickness of the magnetic circuit, whereas for the sensor 3 to sensor 6 structures with the U-shaped central pole, magnet thickness depends upon exciter wheel tooth pole-pitch geometry. The insert-magnet structure is more flexible and provides more geometry opportunities than conventional sensors.

The objective is to identify the least complex and the most efficient sensor configuration for the given application requirements: the sensor geometry that is simple for manufacturing

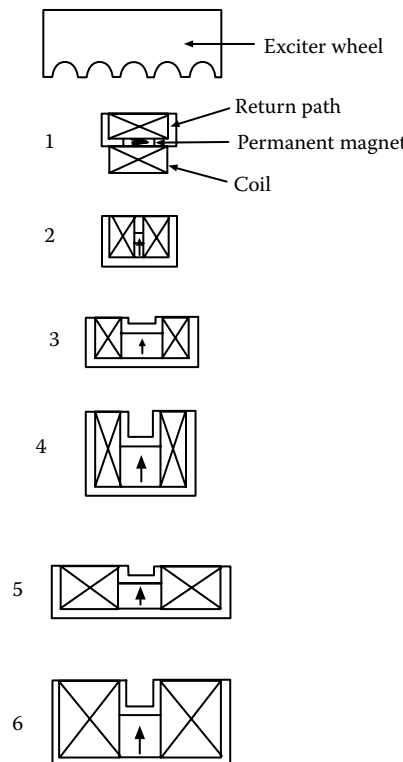


FIGURE 2.16

Inserted-magnet sensor configurations with exciter wheel segment: (1) magnet in the return path, (2) magnet in the single central pole, (3) through (6) magnet between return path and the split center pole. (Courtesy of Delphi Corp.)

TABLE 2.2
Inserted-Magnet Sensor Performance Comparison

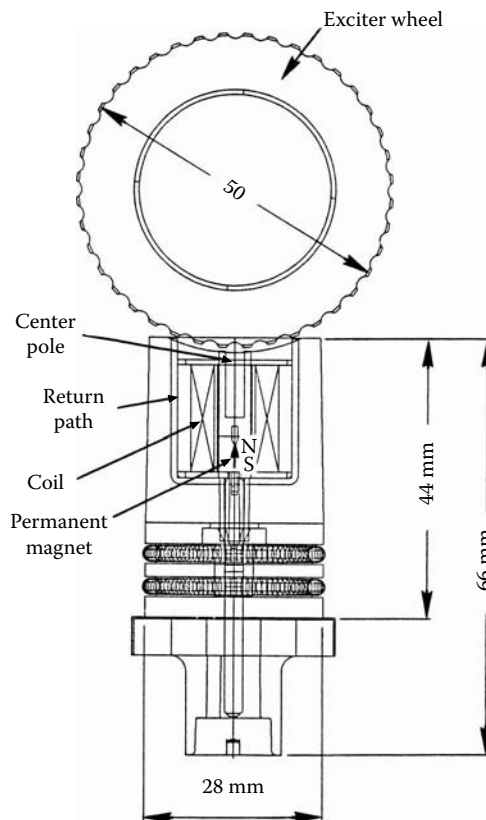
Sensor No.	Signal (V)	Volume (cm ³)	Signal Sensitivity (V/cm ³ × 10)	Flux Sensitivity (%)
1	0.052	0.702	0.74	2.2
2	0.108	1.287	0.84	1.8
3	0.445	1.859	2.39	2.1
6	0.809	3.003	2.69	1.8
5	0.548	1.638	3.34	2.7
4	0.348	1.014	3.43	3.5

Source: Courtesy of Delphi Corp.

and cost-effective. Depending on the degree of complexity, the sensor geometry could have more elements that would improve its signal strength. The investigation was performed for all geometries presented in Figure 2.16. The search should begin at the simplest structures, sensor 1 and sensor 2, and because they cannot meet performance requirements, the search should continue to incorporate more complex structures, sensor 3 through sensor 6, or investigate a different sensor family. This is because more complex structures are more difficult for manufacturing and usually require more parts, resulting in sensor cost increase. Also, the sensor reliability degrades with increased complexity of its structure. Results of this investigation are summarized in Table 2.2, which shows the performance comparison of the described sensor structures.

Table 2.2 shows the inserted-magnet sensor configurations introduced in Figure 2.16 in increasing order of sensor signal sensitivity (signal/volume ratio) from 0.74 to 0.343, as shown in Equation 2.11. The results in this table indicate that the sensor 4 configuration is the most electromagnetically efficient, providing the highest signal sensitivity of 0.343 V/cm³ and, at the same time, the best utilization of the magnet flux indicating flux sensitivity of 3.5%, as shown in Equation 2.12. The sensor flux sensitivity is quite low for all front-magnet sensor configurations, indicating that a very small part of flux developed by the magnet is utilized by the coil for signal generation. Signal strength is a function of flux-linkage variation as well as the number of coil turns (that depends on coil area), and therefore, it has the highest value for the sensor 6 configuration, which also has the highest sensor volume. The cost of the sensor is a function of sensor volume because this is an indication of the volume of magnetic and copper materials used; the sensor with the smaller volume is more cost-effective. From all these considerations the sensor 4 structure holds the best potential for further development to meet the required signal strength.

An exciter wheel for this configuration is manufactured using low-cost powder-metal technology. Because of this, the wheel has a much less distinctive tooth geometry in comparison with the conventional machining technology, and such a geometry features much less permeance variation in two extreme (poles vs. teeth and poles vs. slots) positions, as presented in Figure 2.12(b). A relatively large air gap, the teeth geometry, and low powder-metal density seriously degrade the signal; therefore, a highly sensitive sensor configuration is required for this application. Figure 2.17 shows a fully developed VR sensor based on the sensor 4 structure for an automotive truck transmission application that provides the signal output to the speedometer, cruise, and the truck transmission control system that met all signal requirements, as presented in Table 2.9. The large air gap between the sensor and the exciter wheel of 1.2×10^{-3} m is very beneficial for manufacturing because it allows the use of a wide range of mechanical tolerances that are associated with low manufacturing costs. It also drastically reduces the target-wheel vibration effect upon signal noise, improving the signal-to-noise ratio, as presented in Section 2.6.

**FIGURE 2.17**

Inserted-magnet VR sensor for truck transmission application. (Courtesy of Delphi Corp.)

The sensor configuration selected for optimization consists of the two U-shaped magnetic parts providing a flux return path of a multipole sensor configuration. The internal center pole part is made of powder-metal technology because its thickness at the bottom of the U-shape is larger than the thickness of walls. Walls with different thicknesses can accommodate better magnetic flux distribution. An axially magnetized PM made out of high-energy product samarium-cobalt material, as presented in Figure 2.13 and Figure 2.14, is located inside a coil and thus is closer to the exciter wheel in comparison with the conventional sensor magnet location. The coil is located closer to the exciter wheel than conventional sensor coil, improving its sensitivity. The entire sensor structure is encapsulated using plastic-molding technology with sealed connectors to the sensor. This sensor features a very efficient use of electromagnetic components. Both the sensor and exciter wheel were optimized using the FE method. Because the sensor structure is symmetrical, only a half of the sensor structure needs to be analyzed. Figure 2.18 shows the sensor finite-element model, with configuration, FE grid structure, and flux lines.

Sensor optimization studies were initiated with a parametric study of the exciter wheel sensor teeth dimensions. The exciter wheel teeth width was investigated, as presented in Figure 2.19. For this sensor's magnetic core thickness of 1.0×10^{-3} m, the exciter teeth width of 1.2×10^{-3} m was found to be the best, as shown in Figure 2.19. The rectangular tooth shape was found to be the best; however, this was not acceptable because a die for an exciter wheel with powder-metal technology could not be made with sharp corners due to lifetime die limitations.

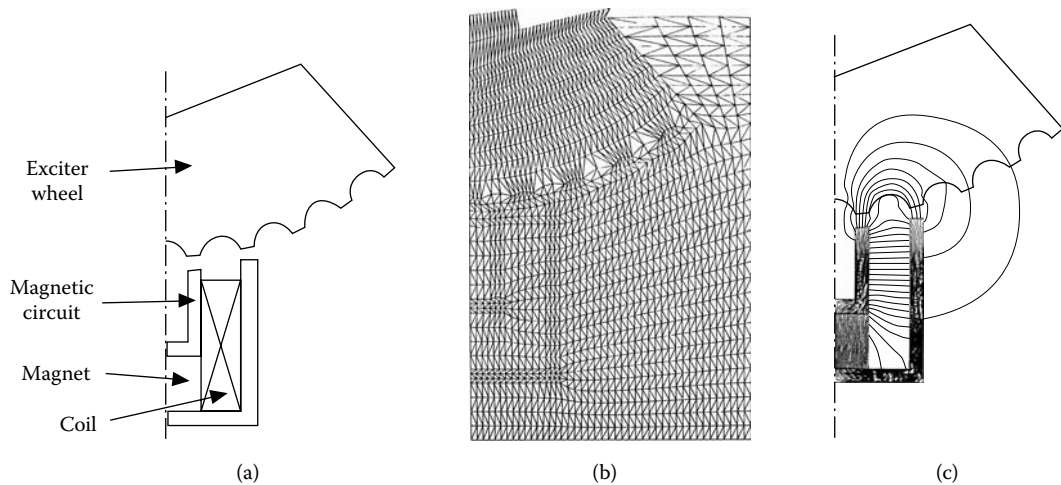


FIGURE 2.18
Inserted-magnet VR sensor FE model: (a) configuration, (b) grid, (c) flux lines. (Courtesy of Delphi Corp.)

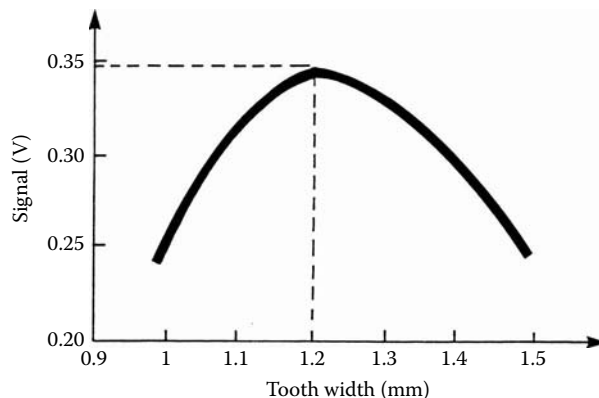
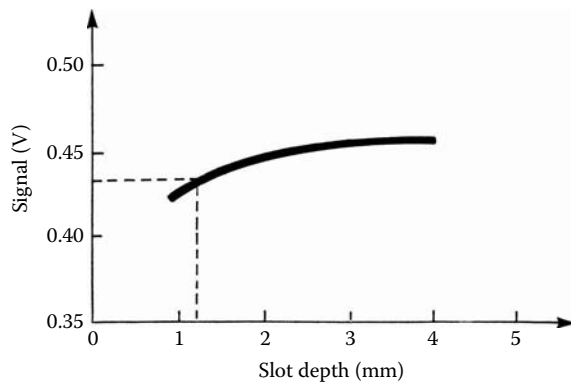


FIGURE 2.19
Sensor signal vs. exciter wheel tooth width. (Courtesy of Delphi Corp.)

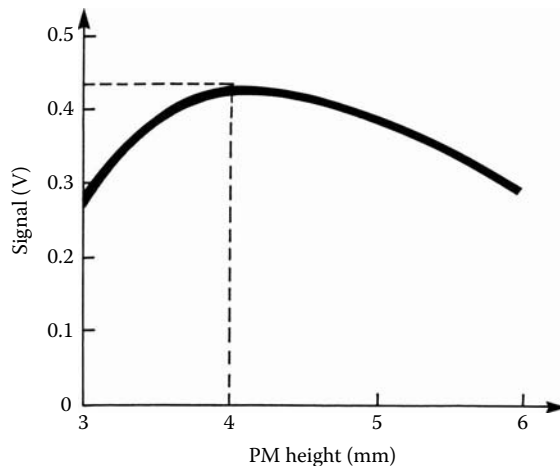
The next step was to optimize the exciter wheel. The slot depth was investigated and showed potential for further improvements for a deeper slot, as presented in Figure 2.20. Because the existing powder-metal technology limits the exciter wheel slot depth, it was not possible to utilize this approach; however, it might be possible in the future with advances in powder-metal technology.

Following this, the PM material was selected to generate high magnetic flux at given temperature requirements, as presented in Table 2.9. Implementing selected magnet material and optimizing magnet height to 4.0×10^{-3} m further increased the signal strength, as indicated in Figure 2.21. Please note that increasing magnet height and, therefore, the magnetomotive force (MMF) of a magnet or magnet strength beyond its optimum point causes signal deterioration. Therefore, there is a trade-off between magnet strength and its geometry, and hence these studies must be performed to devise proper magnet size and strength at the same time.

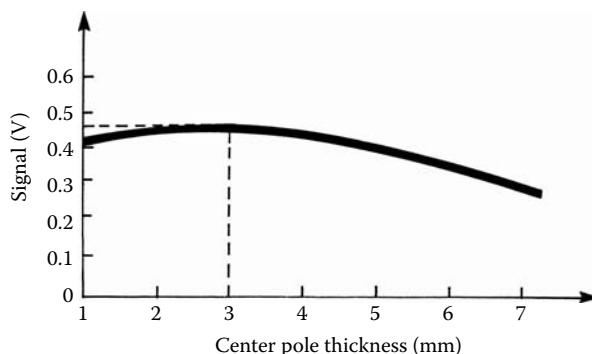
The center pole thickness parametric studies showed that 3.0×10^{-3} m thickness of the sensor center pole base further improved the signal strength, as presented in Figure 2.22.

**FIGURE 2.20**

Sensor signal vs. slot depth. (Courtesy of Delphi Corp.)

**FIGURE 2.21**

Sensor signal vs. magnet height. (Courtesy of Delphi Corp.)

**FIGURE 2.22**

Sensor signal vs. center pole base thickness. (Courtesy of Delphi Corp.)

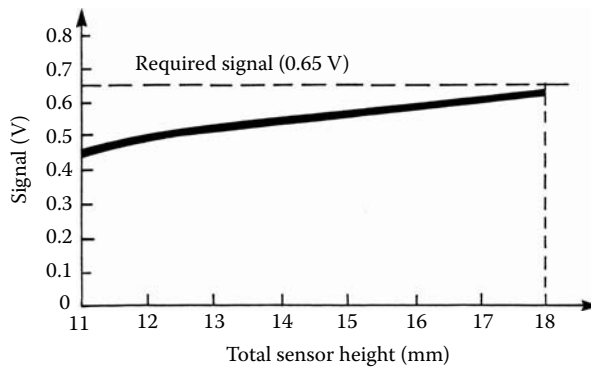


FIGURE 2.23
Sensor signal vs. total sensor height. (Courtesy of Delphi Corp.)

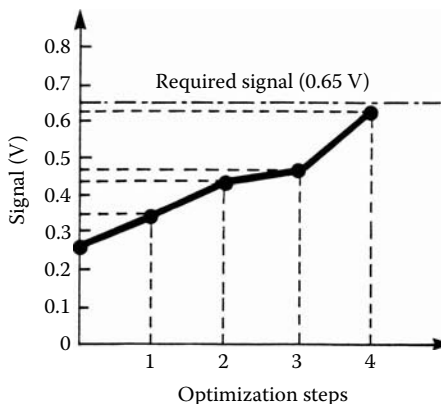


FIGURE 2.24
Inserted-magnet sensor optimization steps: (1) tooth width, (2) magnet height, (3) center pole thickness, (4) total sensor height. (Courtesy of Delphi Corp.)

It is caused by concentration of the flux lines at the base of the center pole and, consequently, flux-density saturation of this magnetic part segment that limits proper flux distribution around a coil, as presented in Figure 2.18(c). Again, there is a trade-off between saturation and proper flux distribution around a coil and further increase of the center pole base thickness would change flux distribution around a coil, causing decreased signal performance.

The total sensor height, including the magnet and center pole, was investigated. For the total unit height of 18.0×10^{-3} m the sensor signal increased to 0.63 V, which is about 97% of the required signal of 0.65 V at 25.0°C and 100 r/min, as indicated in Figure 2.23 and in Table 2.9. Sensor optimization studies were completed and, at this point, the final sensor design was good enough for the prototype design.

Figure 2.24 shows the inserted-magnet sensor optimization steps. With the consecutive iterative analysis and tests, the sensor met its signal requirements. Cost analysis showed that this sensor is cost competitive, and the sensor sensitivity is three times higher compared with the conventional sensor for this application.

Based on these optimization steps, the final dimensions of the sensor were established. Sensor components, as illustrated in Figure 2.25, were manufactured and assembled. The

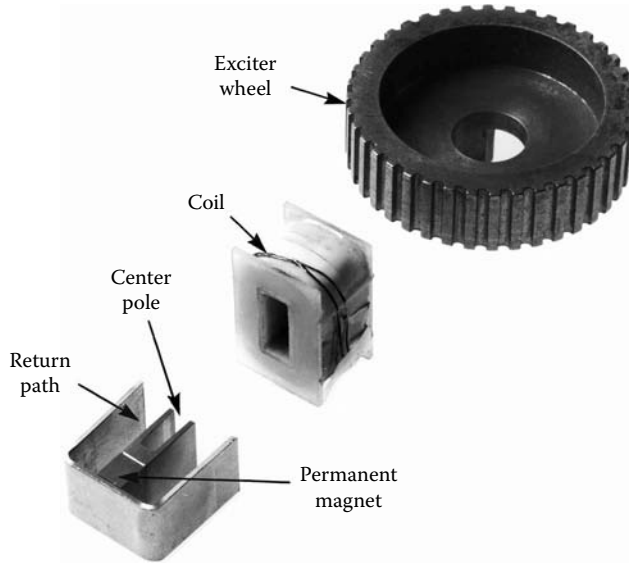


FIGURE 2.25
Inserted-magnet sensor prototype. (Courtesy of Delphi Corp.)

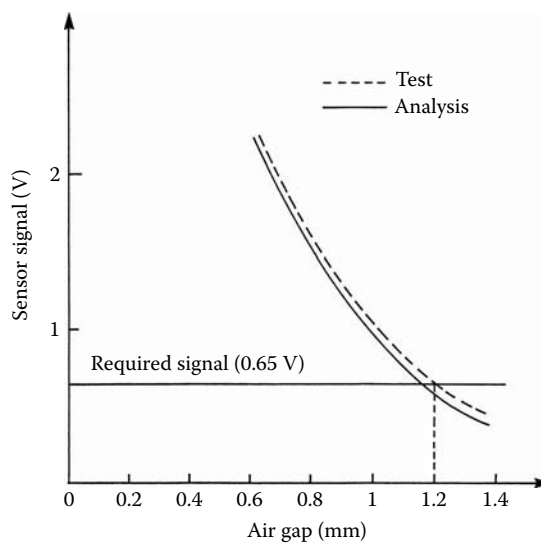


FIGURE 2.26
Inserted-magnet sensor signal vs. air gap. (Courtesy of Delphi Corp.)

exciter wheel and center pole were manufactured using powder-metal technology. Magnetic-circuit elements were devised to maintain a fixed air gap between sensor poles and the exciter wheel, allowing for the exciter wheel radius curvature, as presented in Figure 2.17.

The test results, indicated in Figure 2.26, show a very close match with analytical predictions, within 5% for the wide range of air gaps, and prove that inserted-magnet structures could be viable and practical choices for manufacturing and industrial applications.

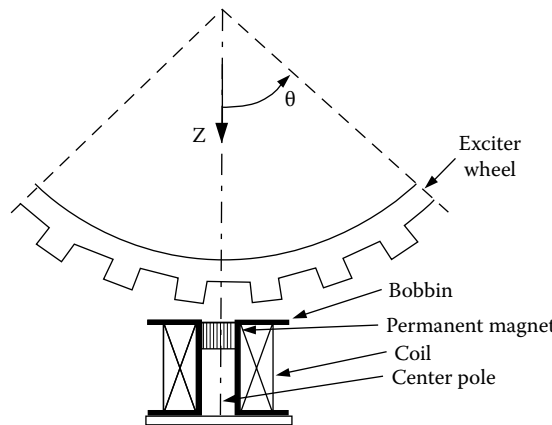


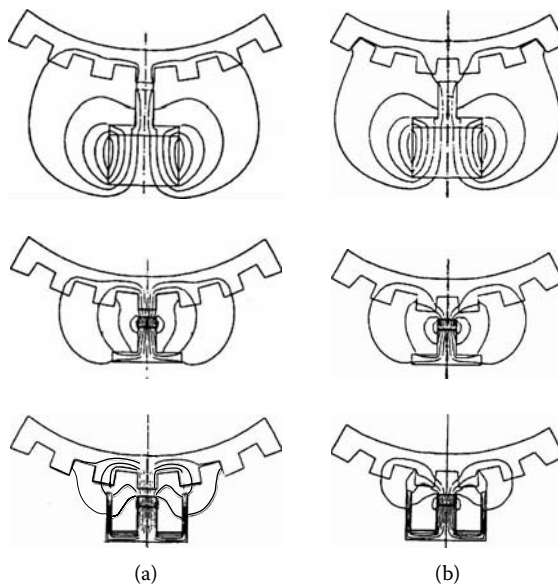
FIGURE 2.27
Front-mounted-magnet sensor with the exciter wheel. (Courtesy of Delphi Corp.)

2.3.4 Front-Mounted-Magnet Sensors

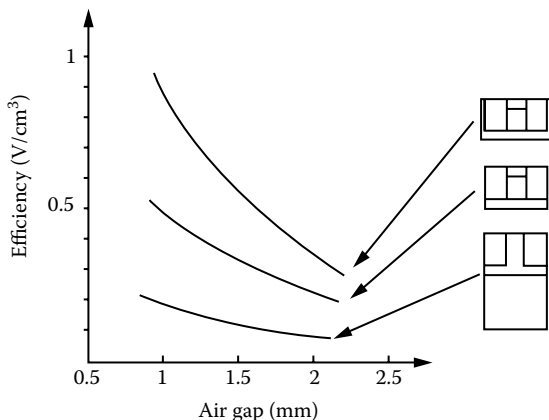
A VR sensor configuration with a PM located in the proximity of the exciter wheel is defined as a front-mounted-magnet sensor, as presented in Figure 2.27. This sensor configuration has a PM centrally located with a center pole and a back shim that construct only a partially magnetic flux return path. The magnetic circuit is partial because it does not provide the full path for the magnetic flux return path from the magnet to the center pole and further to the exciter wheel and back to the magnet. The portion from the magnetic shim to an exciter wheel is missing in the same way as it is for the conventional VR sensors, as demonstrated in Figure 2.28. The magnet location in the air gap is directly affected by the exciter wheel reluctance, which in turn affects the level of the magnetic flux developed by the magnet and its distribution. The front-mounted-magnet sensor signal performance is superior to the conventional sensor performance with the same volume because more flux lines generated by the PM contribute to the signal generation.

Figure 2.28 shows the magnetic flux distribution for the conventional sensor, the front-mounted-magnet sensor with a partial magnetic return path and the front-mounted-magnet sensor with an E-shaped magnetic return path with the same air gap for the two extreme positions with the maximum and minimum flux linkages. The E-shaped sensor structure provides the missing link by the addition of the magnetic return paths linking the back shim with an exciter wheel. Note the difference in the magnetic flux distribution around a coil window area. The coil of the front-mounted-magnet sensor with a partial magnetic return path is linked to the magnetic flux more effectively than the coil of the conventional structure, and almost all generated flux lines of the E-shaped structure with a fully developed magnetic return path are linked to a coil. Therefore, the signal of the front-mounted-magnet sensor with a partial magnetic return path is superior to the performance of conventional structures, and the signal of the front-mounted-magnet sensor with a full magnetic return path is superior to the performance of the front-mounted-magnet sensor with a partial magnetic return path. The signal-to-volume ratio for conventional and front-mounted-magnet sensors as a function of the air gap is shown in Figure 2.29.

Table 2.3 shows the performance comparison for the conventional, front-mounted-magnet sensor without a magnetic return path and a front-mounted-magnet sensor with an E-shaped magnetic return path at 1.5×10^{-3} m of air gap. The front-mounted-magnet sensor with a partial magnetic return path features more than twice the signal sensitivity with

**FIGURE 2.28**

Flux-lines distribution of the front-mounted-magnet sensors and conventional sensor for (a) maximum flux linkage and (b) minimum flux linkage. (From Pawlak, A.M., *Proceedings of the NdFeB '99 Conference*, San Francisco, April 12–14, 1999. With permission.)

**FIGURE 2.29**

The signal/volume ratio vs. air gap for front-mounted-magnet and conventional sensors. (Courtesy of Delphi Corp.)

over 50% better flux efficiency utilization than a conventional sensor having the same coil parameters, and a front-mounted-magnet sensor with an E-shaped magnetic return path features more than four times higher signal sensitivity with almost 90% better flux efficiency utilization, as presented in Table 2.3.

Because of this, for practical applications, however, the front-mounted-magnet sensor structure should always have a full return path for the magnetic flux. The return path enhances the flux level and guides the flux for better coupling with the coil turns. There are two basic shapes of the return magnetic path: an E-shaped structure that surrounds a

TABLE 2.3
VR Sensor Comparison

Sensor Geometry and Performance	Volume (cm ³)	Signal (V)	Signal Sensitivity (V/cm ³ × 10)	Flux Efficiency (%)
Conventional geometry	3.231	0.39	0.12	0.72
Front-mounted no-return path	1.385	0.44	0.32	1.1
Front-mounted E-shaped	1.385	0.74	0.54	1.35

Source: Courtesy of Delphi Corp.

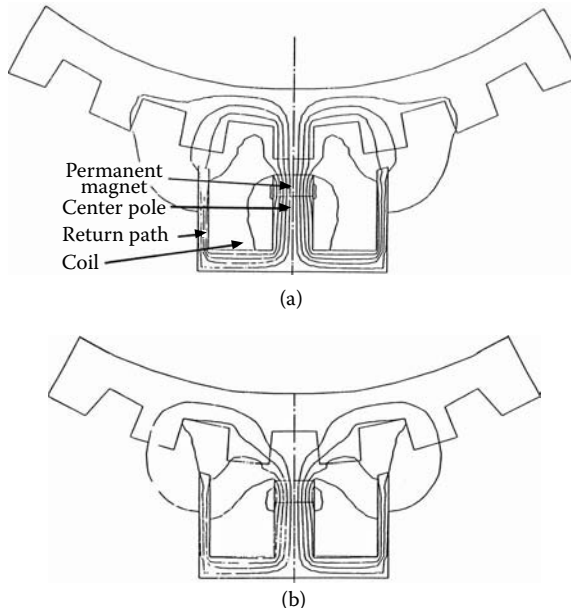


FIGURE 2.30

Magnetic flux distribution of the front-mounted-magnet sensor with E-shaped structure: (a) minimum flux linkages, (b) maximum flux linkages. (From Pawlak, A.M., *Proceedings of the NdFeB '99 Conference*, San Francisco, April 12–14, 1999. With permission.)

coil entirely, which has already been introduced, and a U-shaped structure that supports only one coil side with the magnetic return path, which will be discussed in Section 2.3.6.

2.3.5 Sensors with E-Shaped Magnetic Structure

In an application where there is sufficient space for a wide sensor with a relatively wide exciter wheel, the sensor with an E-shaped structure offers an efficient magnetic configuration. It extends between three (or more) exciter wheel teeth, where the exciter wheel geometry dictates the sensor width. Figure 2.30 shows the magnetic flux distribution of this structure for two extreme sensor-wheel positions. In contrast to a U-shaped front-mounted sensor, both sides of the coil of the E-shaped structure contribute equally to the signal generation because its structure is symmetrical.

The signal efficiency of the front-mounted-magnet sensor with an E-shaped magnetic structure is superior to the front-mounted-magnet sensor with a partial magnetic return path, as shown in Figure 2.29, for a sensor signal efficiency across any practical air gap size. For the E-shaped structure, the return path geometry is fixed by the exciter wheel

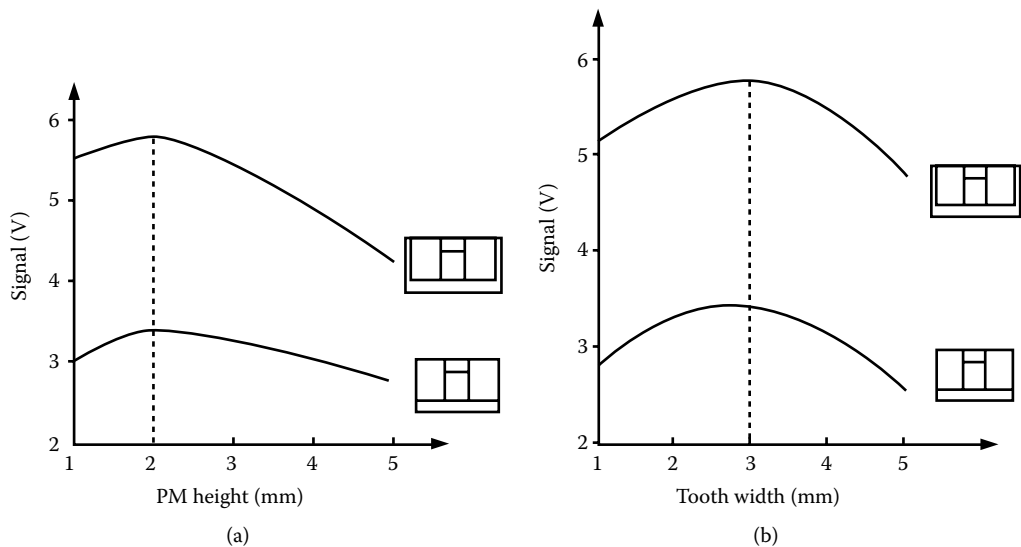


FIGURE 2.31
Magnet optimization for front-mounted-magnet sensors: (a) signal vs. PM height, (b) signal vs. tooth width. (Courtesy of Delphi Corp.)

tooth pitch, where the center of the return path geometry meets the corresponding tooth center, as presented in Figure 2.30. Therefore, optimization of the E-type magnetic structure focuses on the geometry of the center pole and the magnet.

Figure 2.31(a) shows the magnet optimization for the E-shaped structure and, for comparison purposes, also for the front-mounted-magnet sensor with a partial magnetic return path. The optimum heights of both magnets are the same and equal to 2.0×10^{-3} m, but they provide different magnet utilization and signal sensitivity due to the difference in magnetic configuration, as presented in Table 2.3. The optimum magnet and center pole widths for the front-mounted-magnet sensor with a partial magnetic return path and front-mounted-magnet sensor with an E-shaped magnetic return path are the same and correspond in this case to the width of the exciter wheel tooth of 3.0×10^{-3} m, as presented in Figure 2.31(b).

Both analyses, one for the magnet height and the other for the center pole or magnet width, indicate that there is only one set of magnet width and height dimensions that would provide the best sensor signal performance for a given exciter wheel's tooth geometry across the entire air gap range. The magnet or center pole width must be equal to the exciter wheel's tooth width for the discussed sensor structures, and that is also true for other sensor structures.

2.3.6 Sensors with U-Shaped Magnetic Structure

U-shaped structure is defined as a VR configuration having a PM in proximity to the exciter wheel and a single return magnetic path also facing the exciter wheel, as presented in Figure 2.32. Such a sensor structure requires less space compared with the E-shaped structure because it extends between two teeth only and can be devised for very limited space requirements, such as for a crankshaft position application. However, unlike the U-shaped structures, where only one side of coil is affected by teeth permeance variations, the E-shaped configuration provides better utilization of magnetic structure, resulting in superior signal performance.

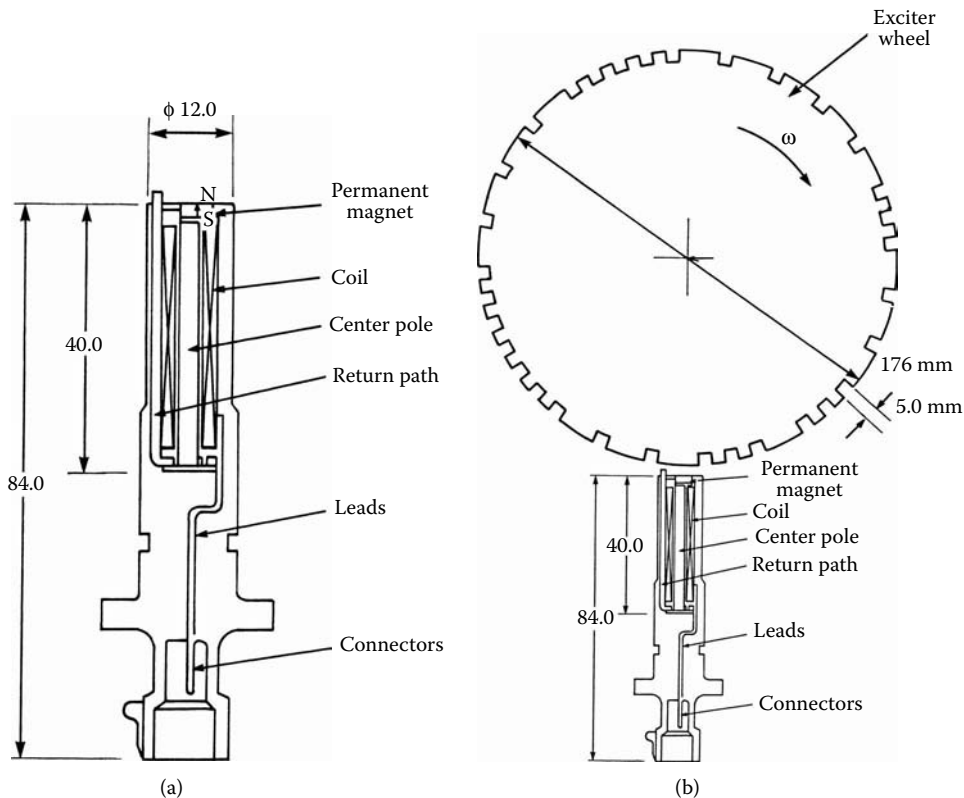


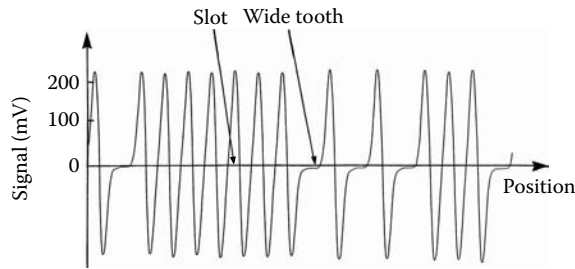
FIGURE 2.32

Front-mounted-magnet sensor with U-shaped magnetic structure: (a) sensor structure, (b) sensor-wheel arrangement. (Courtesy of Delphi Corp.)

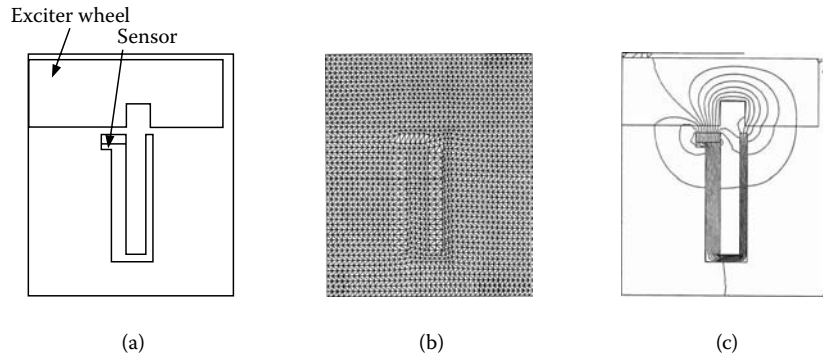
The VR front-mounted-magnet sensor consists of a PM, a U-shaped magnetic circuit, and a coil with a bobbin, as shown in Figure 2.32. The bobbin supports both the coil and the PM. Polarization of the magnet is perpendicular to the exciter wheel surface. The rectangular magnetic element under the PM collects the magnetic flux and through the magnetic center pole connected with the magnetic return path directs the flux back to the exciter wheel. The coil assembly has cylindrical symmetry, and the PM and the magnetic return path have rectangular geometry. The axis of symmetry and the center of the PM are offset in order to provide an optimum flux-linkage change at the extreme exciter wheel positions.

The sensor signal is presented in Figure 2.33. The maximum signal value of 224.0 mV was obtained at the exciter wheel speed of 30.0 r/min and an air gap of 0.2×10^{-3} m with no load. This signal is utilized as a position sensor where the real position of the exciter wheel is indicated by zero crossing of the signal at the narrow and wide teeth. Determining an optimum geometry for this nonsymmetrical structure is more complicated than for the symmetrical one. The entire sensor has to be modeled to obtain the magnetic field solution using the finite-element model, as shown in Figure 2.34, where the sensor configuration, meshing for the FE model, and the resultant flux lines are presented.

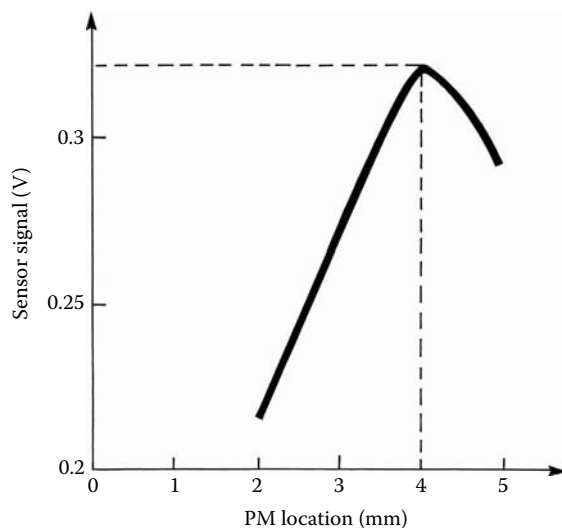
Parametric studies for this sensor configuration led to optimized position of the PM location in respect to the U-shaped magnetic circuit. Figure 2.35 identifies the distance of 4.0×10^{-3} m between the PM and the return path, which provides the maximum flux change linked to the coil in two extreme sensor-wheel positions for the exciter slot width of 5.0×10^{-3} m as

**FIGURE 2.33**

Front-mounted-magnet sensor with U-shaped magnetic structure. (Courtesy of Delphi Corp.)

**FIGURE 2.34**

Sensor FE model: (a) configuration, (b) grid, (c) flux lines. (Courtesy of Delphi Corp.)

**FIGURE 2.35**

Sensor signal vs. magnet location. (Courtesy of Delphi Corp.)

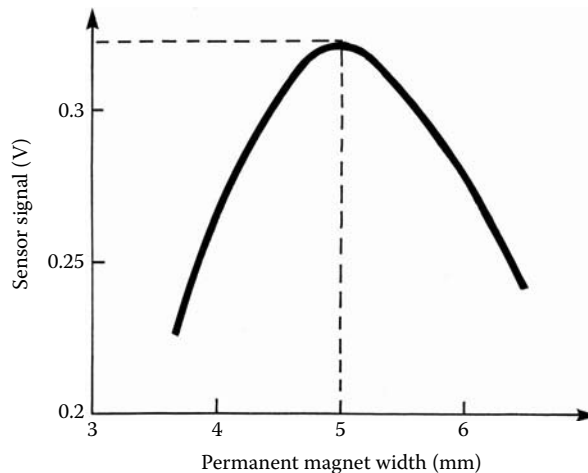


FIGURE 2.36
Sensor signal vs. magnet width. (Courtesy of Delphi Corp.)

shown in Figure 2.32(b). Please note that the width of the exciter wheel's regular tooth is also 5.0×10^{-3} m. In order to utilize this geometry, the PM must be located asymmetrically to the coil, as shown in Figure 2.35.

The PM location closer to the return path increases the amount of the magnetic flux linked to the coil, but reduces flux linkages in its two extreme positions, thus decreasing the sensor signal. On the other hand, the larger distance of the PM from the return magnetic circuit reduces the amount of the magnetic flux linked to the coil but enhances the change of the magnetic flux linkages in the extreme positions. Therefore, there is a trade-off location where flux reduction and increase of the flux-linkage change counterbalance. Because the location of the PM depends on its dimensions, the width of the PM also has to be optimized. The PM width affects the average value of the developed flux and, therefore, the flux linking to the coil. However, the flux distribution changes and this affects the flux linkages as well. For the PMs wider than the wheel slot opening, the level of the linkages increases, but the flux-linkage change for the two extreme positions decreases. Therefore, the sensor signal strength is reduced.

For the PMs narrower than the wheel slot opening, the level of the linkages reduces, but the flux-linkage change for the two extreme positions decreases even more. Therefore, the PM width equal to the slot opening is an optimum solution for this configuration. Figure 2.36 shows the results of this investigation. A PM width bigger as well as smaller than slot opening decreases the flux change and causes signal strength reduction. Therefore, a width opening of 5.0×10^{-3} m is an optimum dimension.

The PM is axially magnetized. Therefore, its height affects the total MMF of the PM. This affects the flux level and the flux linked to the coil. The height of the PM affects the coil location and its distance to the exciter wheel. For the long PM, the coil is further removed from the exciter wheel, where for the short one, the coil is closer to the exciter wheel. Therefore, the flux distribution is different in both cases. The coil location closer to the exciter wheel is preferable because in this position the coil is more sensitive to the flux, while the longer PM can generate more flux. Again, there is a trade-off for the length of the PM to produce the higher flux-linkage change for a given sensor geometry and magnet material. Figure 2.37 shows the optimum magnet height for this sensor geometry. A thickness of 2.0×10^{-3} m was selected because it provides the best signal generated for this geometry.

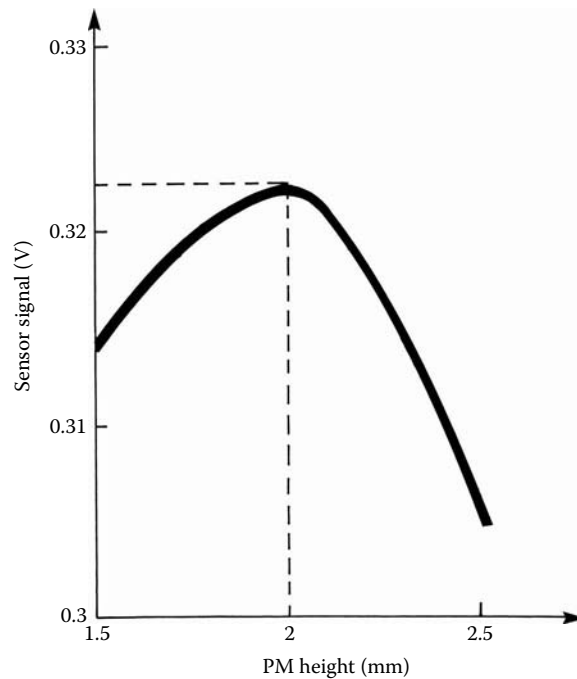


FIGURE 2.37
Sensor signal vs. magnet height.

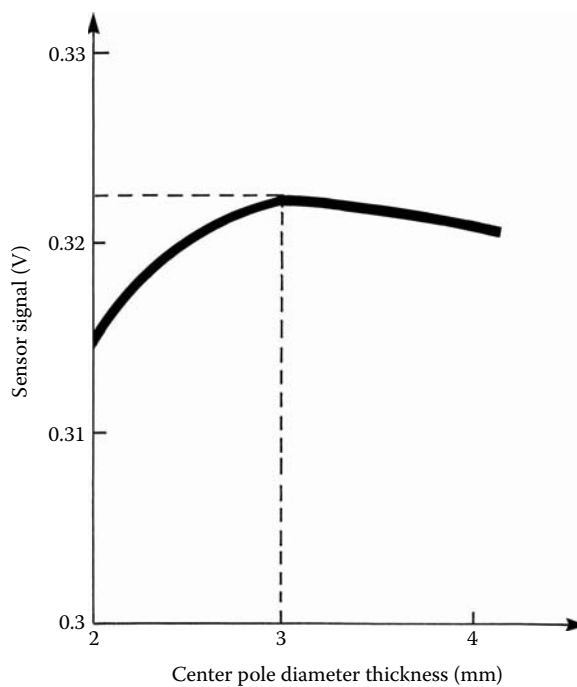
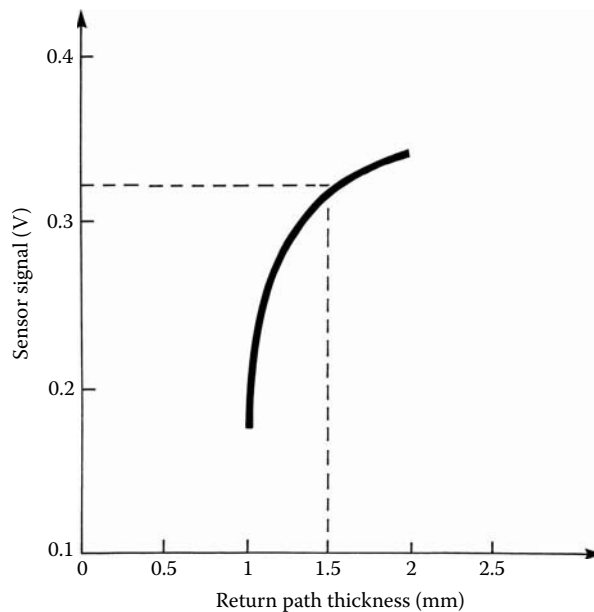


FIGURE 2.38
Sensor signal vs. center pole thickness.

**FIGURE 2.39**

Sensor signal vs. return path thickness. (From Lequesne, B. et al., *Transactions of IEEE/IAS*, 32(5), 1166–1175, 1996. With permission.)

The magnetic-circuit thickness for the center pole and the return magnetic-circuit optimized values are presented in Figure 2.38. A round center pole geometry allows for the use of regular coil winding technology, whereas rectangular return magnetic-circuit geometry allows for the minimization of the sensor thickness while providing a sufficient cross-sectional area of the magnetic flux. Note, in Figure 2.39, that reduction of the return path thickness beyond 1.0×10^{-3} m results in rapid signal loss, and increase of the thickness beyond 1.5×10^{-3} m results in moderate signal improvement. The center pole with 3.0×10^{-3} m outside diameter (OD) and 1.5×10^{-3} m thickness of the return magnetic circuit were selected because they provide the highest signal level for the given geometry.

Implementation of the magnetic return path to the sensor structure significantly improves the sensor signal strength. With the higher magnetic-circuit permeability, the flux level increases. This is because of the flux leakage reduction and the higher magnet working point that effects the slope of the magnetic-circuit permeance. The magnetic return path also changes the flux distribution, especially in the area of the coil, which additionally improves the sensor signal strength. Conventional VR sensors feature no iron return path, as presented in Figure 2.1. This is perceived to make design simple, more universal, and less expensive, but the flux is not properly guided, with significant flux leakages, because there is no main magnetic circuit that would provide a magnetic path. Sensor structures that provide a return magnetic path feature minimum flux leakages. Finally, the total sensor height and the coil geometry were optimized to ensure the required signal, as presented in Figure 2.40.

For the 25.0×10^{-3} m total sensor height, the peak-positive signal reached a value of 0.325 V, which is about 103% of that required for this application. The optimization process requires iterations until there is no further improvement in signal performance. Consequently, models with the optimized structures were built and tested, as presented in Figure 2.41.

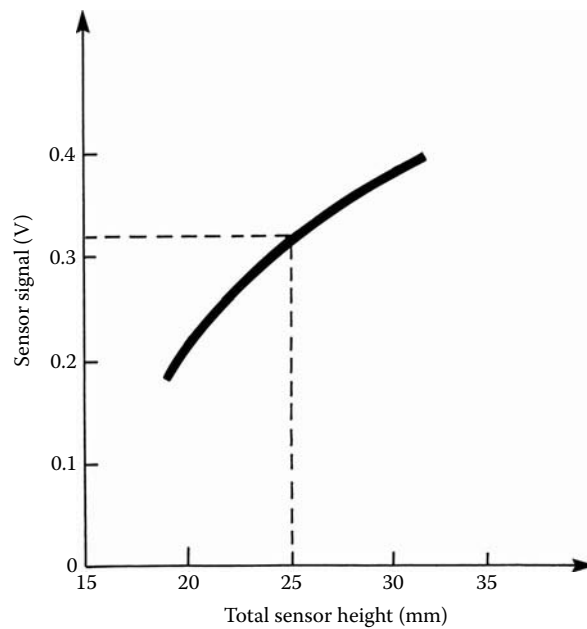


FIGURE 2.40
Sensor signal vs. total sensor height.

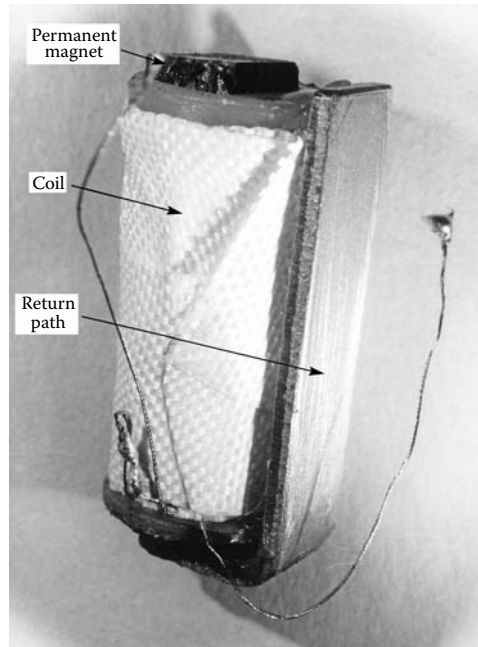


FIGURE 2.41
The U-shaped sensor model.

Figure 2.42 shows the signal performance as a function of the air gap. It matches the investigation with a load of $10\text{ k}\Omega$, and the no-load performance is satisfactory and met requirements for the crankshaft position sensor application, as presented in Table 2.9. The no-load test results also show a close match with the analytical analysis.

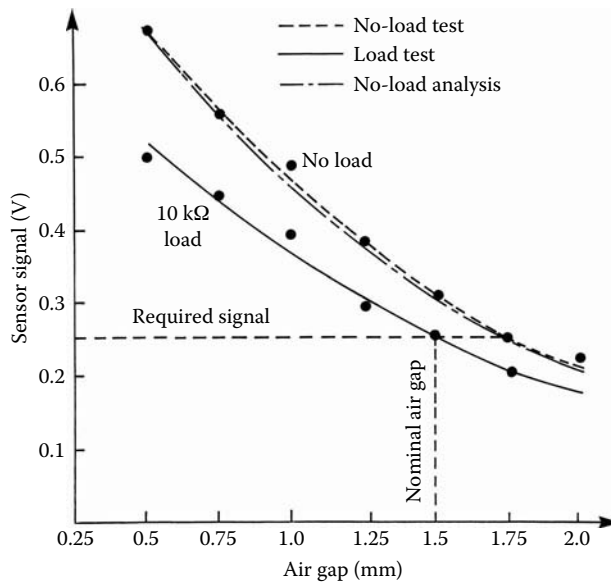


FIGURE 2.44
Sensor signal vs. air gap test and analysis.

2.3.7 Multiple Magnets VR Sensors

A need to boost sensor performance that provides a high signal at a low speed of the exciter wheel led to the development of the VR sensor configuration with multiple magnets (Pawlak et al. 1991d, Pawlak and Shirai 1988, Pawlak et al. 1991a, Pawlak et al. 1991b, Shirai and Pawlak 1995a, Shirai and Pawlak 1995b). Such a requirement for a sensor performance came from an automotive application for the ABS. The particularly difficult sensor environment with high ambient temperature around the brakes led also to the selection of magnet material that is stable at elevated temperatures. Consequently, the two-magnet partially distributed sensor led to the magnetically distributed ring-shape sensor with a multipole magnet that would fit best and could be integrated within the bearing grease cover. This sensor is very desirable for manufacturing because only radial air gaps and radial tolerances are involved, unlike other sensors where an axial air gap is present. The sensor's magnetic distribution nature would also help compensate for the radial tolerances, as noted during the lumped element sensor's development, as presented in Section 2.3.9 and Section 2.6.

2.3.8 Dual-Magnet Sensors

The very tight envelope for a VR sensor structure within a grease cover of the wheel bearing led to the development of a magnetically partially distributed sensor structure with two magnets. Figure 2.43 shows a VR sensor structure with two magnets distributed along the teeth of the exciter wheel.

Magnets are mechanically attached to both ends of the magnetic circuit with one coil placed between magnets. Both magnets are in close proximity to the exciter wheel, which is right at the air gap, having in this design an unconventional sensor-wheel arrangement. Conventionally, all VR sensors are arranged in the same manner with respect to the exciter wheel, where the sensor pole is placed against the tooth of the exciter wheel for the

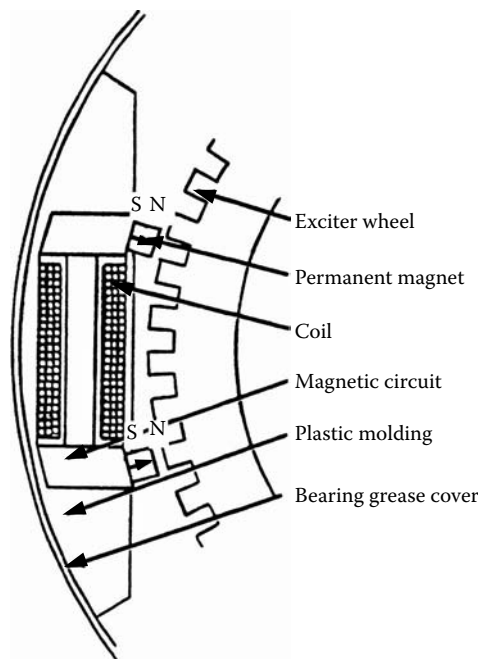


FIGURE 2.43

Two-magnet VR sensor with an exciter wheel.

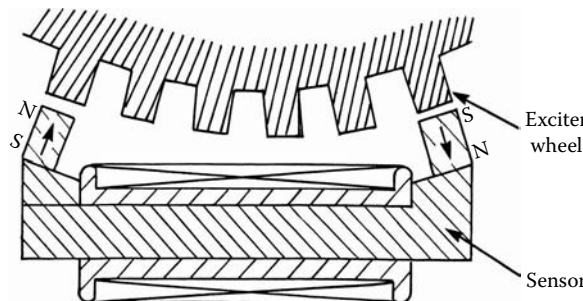


FIGURE 2.44

Conventional sensor-wheel arrangement for two-magnet VR sensor with supportive magnetization. (From Lequesne, B. et al., *Transactions of IEEE/IAS*, 32(5), 1166–1175, 1996. With permission.)

maximum magnetic permeance. When the exciter wheel rotates one pole pitch, the pole is located against a slot for the maximum permeance. The sensors utilize the difference between the maximum and the minimum magnetic permeance positions to develop the signal. To utilize the conventional sensor-wheel arrangement for the sensor with more than one pole, all of them must be positioned against the teeth of the exciter wheel at the maximum sensor position; for the minimum permeance position, they must be positioned against the exciter wheel slots. These two positions provide the highest magnetic flux-linkage variation and the maximum sensor signal of the conventional sensor arrangement, which requires that PMs must be polarized in the supporting direction in order to develop the sensor signal, as presented in Figure 2.44.

Figure 2.44 shows the front-mounted-magnet sensor with two magnets. This sensor consists of a coil, a magnetic circuit, and two PMs located in proximity of the exciter wheel.

The magnetic core consists of three elements: a cylindrical central rod and two rectangular magnet supporters on both sides of the rod. For the sensor, which is designed without a bobbin, the magnetic core made out of soft iron must have at least two separate parts in order to assemble the coil. For the bobbinless coil design, where the coil is placed directly on the insulated (blue-coated) central rod, the magnetic core can be made out of one part using a powder-metal technology. The PM's shape is rectangular or trapezoidal depending on the method used for PM attachment to the magnetic core. The trapezoidal magnet is desirable, holding magnets attached to the magnetic core using a plastic-molding technology; although, a rectangular magnet shape can be used if magnets are glued to the magnetic core. For this configuration, high-energy magnets are desirable and, depending on the application and operating temperature, the magnet material can be neodymium or samarium-cobalt-based.

Analysis of the VR two-magnet sensor configuration requires the investigation of the signal generated in the coil. For analytical purposes only, it is assumed that the coil is split into two identical coils, each equal to one half of the original coil and both connected in a series to make a full coil. It is also assumed that both PMs assigned as PM 1 and PM 2 with identical geometry and material properties having the same distance to the exciter wheel's teeth are capable of generating identical flux ϕ_1 and ϕ_2 , respectively. In such a case, the total signal is a superposition of the signal components with appropriate phase and polarization as indicated below:

$$v = v_1 + v_2 \quad (2.13)$$

where v , v_1 , and v_2 are the sensor signal, the signal component of coil 1, and the signal component of coil 2, respectively. With the assumption of the sinusoidal permeance variation, both signal components v_1 and v_2 can be expressed as:

$$v_1 = -\frac{d\phi_1}{dt} \times \sin \theta \quad (2.14)$$

$$v_2 = -\frac{d\phi_2}{dt} \times \sin \theta \quad (2.15)$$

where ϕ_1 is a magnetic flux embraced by coil 1, ϕ_2 is a magnetic flux embraced by coil 2, and θ is the sensor or rotor position. Combining Equation 2.13 with Equation 2.15, the total signal strength becomes:

$$v = -\left(\frac{d\phi_1}{dt} + \frac{d\phi_2}{dt} \right) \times \sin \theta \quad (2.16)$$

If $\phi_1 = \phi_2$, the total signal is:

$$v = -2 \frac{d\phi_1}{dt} \times \sin \theta \quad (2.17)$$

Figure 2.45 presents the sensor arrangement that corresponds to Equation 2.17 with the same flux sign for both PMs as they support each other. The signal components for magnets are arranged in the same manner with respect to the exciter wheel teeth. The total signal

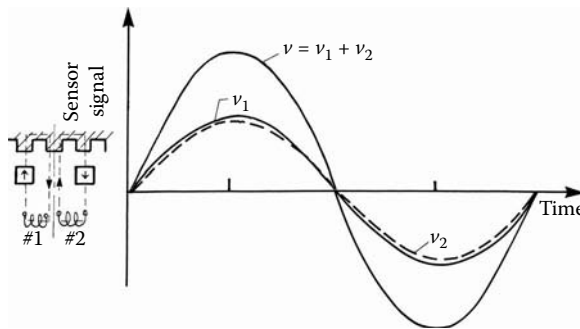


FIGURE 2.45

Sensor signal for the conventional sensor-wheel arrangement for two-magnet VR sensor with supportive magnetization. (From Pawlak, A.M. et al., *Novel Variable Reluctance Sensors*, Publ. No. 910902, Society of Automotive Engineers, Detroit, MI, 1991. With permission.)

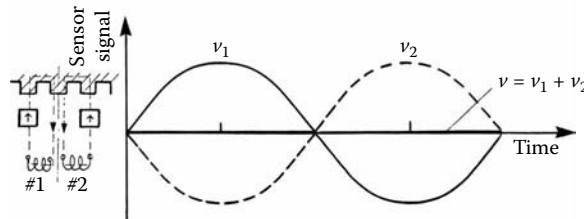


FIGURE 2.46

Sensor signal for the conventional sensor-wheel arrangement for two-magnet VR sensor with non-supportive magnetization. (From Pawlak, A.M. et al., *Novel Variable Reluctance Sensors*, Publ. No. 910902, Society of Automotive Engineers, Detroit, MI, 1991. With permission.)

reaches its maximum value in this arrangement. The use of a return path and a front-mounted-magnet approach led to a novel configuration, shown in Figure 2.45. It features two “supportive magnets” in a series in the magnetic circuit. This design provides a high output signal despite the relatively small sensor height required by this application.

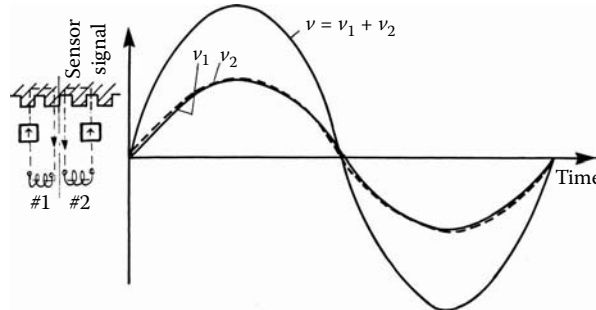
If the direction of magnetization of magnet 2 is reversed by 180° , then the magnetic flux ϕ_2 generated by this magnet is changing its sign. Therefore, the signal v_2 component can be expressed as:

$$v_2 = \frac{d\phi_2}{dt} \times \sin \theta \quad (2.18)$$

Combining Equations 2.13, 2.14, and 2.18, the total signal strength becomes:

$$v = -\left(\frac{d\phi_1}{dt} - \frac{d\phi_2}{dt} \right) \times \sin \theta \quad (2.19)$$

Figure 2.46 presents the sensor arrangement that corresponds to Equation 2.19 with the opposite flux signs because the PMs do not support each other. The signal components for magnets are arranged in the same manner with respect to the exciter wheel teeth. The total signal reaches its maximum value in this arrangement. If $\phi_1 = \phi_2$, the total signal is zero, as presented in Figure 2.46.

**FIGURE 2.47**

Sensor signal for the nonconventional sensor-wheel arrangement for two-magnet VR sensor with nonsupportive magnetization. (From Pawlak, A.M. et al., *Novel Variable Reluctance Sensors*, Publ. No. 910902, Society of Automotive Engineers, Detroit, MI, 1991. With permission.)

Figure 2.47 shows a nonconventional sensor-wheel arrangement, where one of the magnets is facing a tooth and the other is facing a slot. For this arrangement, the sensor's PMs are assembled with opposite polarization and, therefore, facing the exciter wheel with the same polarities. If the magnetization of the PM 2 and its location change in comparison with the base design, as shown in Figure 2.47, then the signal sign and phase of coil 2 will change while the other components remain the same as the base design. Therefore, the signal v_2 component can be expressed as:

$$v_2 = -\frac{d\phi_2}{dt} \times \sin(\theta + 180) \quad (2.20)$$

Combining Equations 2.13, 2.14, and 2.20, the total signal strength becomes:

$$v = -\left(\frac{d\phi_1}{dt} + \frac{d\phi_2}{dt} \right) \times \sin \theta \quad (2.21)$$

If $\Phi_1 = \Phi_2$, the total signal is:

$$v = -2 \frac{d\phi_1}{dt} \times \sin \theta \quad (2.22)$$

If the direction of magnetization of magnet 2 is reversed by 180° , then the magnetic flux ϕ_2 generated by this magnet is changing its sign, as presented in Figure 2.48. Therefore, the signal v_2 component can be expressed as:

$$v_2 = -\frac{d\phi_2}{dt} \times \sin(\theta + 180) \quad (2.23)$$

Combining Equations 2.13, 2.14, and 2.23, the total signal strength becomes:

$$v = -\left(\frac{d\phi_1}{dt} - \frac{d\phi_2}{dt} \right) \times \sin \theta \quad (2.24)$$

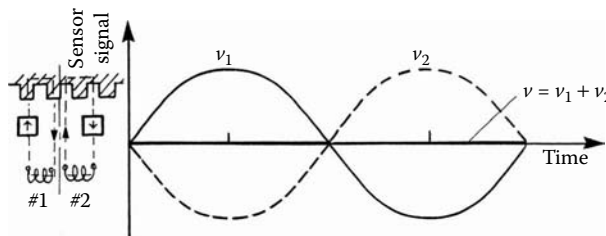


FIGURE 2.48

Sensor signal for the nonconventional sensor-wheel arrangement for two-magnet VR sensor with supportive magnetization. (From Pawlak, A.M. et al., *Novel Variable Reluctance Sensors*, Publ. No. 910902, Society of Automotive Engineers, Detroit, MI, 1991. With permission.)

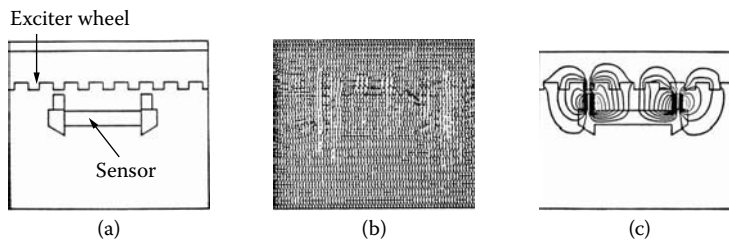


FIGURE 2.49

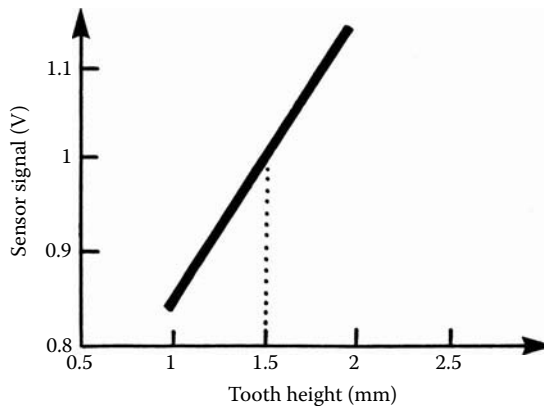
Two-magnet VR sensor FE model: (a) configuration, (b) grid, (c) flux lines. (From Pawlak, A.M. et al., *Novel Variable Reluctance Sensors*, Publ. No. 910902, Society of Automotive Engineers, Detroit, MI, 1991. With permission.)

Figure 2.48 presents the sensor arrangement that corresponds to Equation 2.24 with the opposite flux signs because these PMs do not support each other. The signal components for magnets are arranged in the same manner with respect to the exciter wheel teeth. The total signal reaches its minimum value in this arrangement. If $\phi_1 = \phi_2$, the total signal is zero.

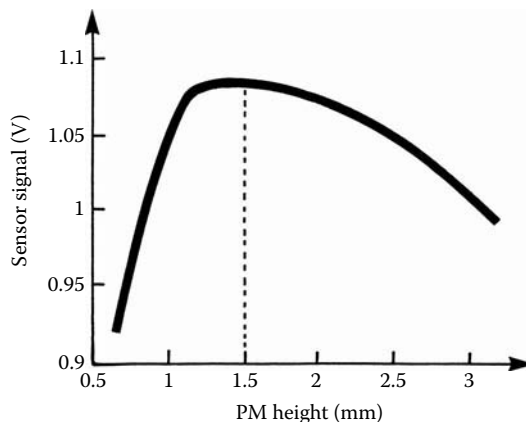
Thus, depending on the sensor-wheel arrangement, a sensor signal could be the maximum or zero. The signal developed by the sensor equals zero for both the conventional sensor-wheel arrangement with nonsupportive magnets and the sensor structure with supporting magnets and nonconventional sensor-wheel arrangement. Conversely, maximum signal strength can be obtained for both the conventional sensor-wheel arrangement and supportive magnets as well as the nonconventional sensor-wheel arrangement with nonsupportive magnets configuration. This structure was analyzed and designed using the FE technique. Assuming that the exciter radius is very large, Figure 2.49 shows the sensor configuration, mesh structure, and the flux lines.

Optimization of the exciter wheel and the sensor was conducted in the same manner as other sensor structures. This sensor configuration was optimized with the limitations that the total sensor height and width were restricted by the existing grease cover dimensions. First, the exciter wheel was optimized. Then the tooth height was investigated, indicating significant sensor improvement potential for higher teeth, as shown in Figure 2.50. Because powder-metal technology limits the exciter wheel slot depth, it was not possible to entirely utilize this gain. Again, it may be used in the future with further advances in powder-metal technology.

The PM height, which affects the total MMF developed and, consequently, the flux level and the signal strength, was also optimized. Implementing the selected magnetic material and optimizing PM height to 1.5×10^{-3} m, the signal strength improved about 8%, as shown in Figure 2.51.

**FIGURE 2.50**

Two-magnet VR sensor signal vs. exciter wheel tooth height. (From Pawlak, A.M. et al., *Novel Variable Reluctance Sensors*, Publ. No. 910902, Society of Automotive Engineers, Detroit, MI, 1991. With permission.)

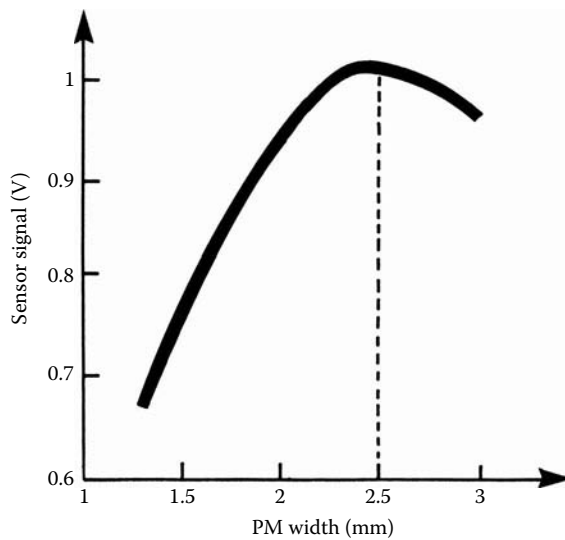
**FIGURE 2.51**

Two-magnet VR sensor signal vs. PM height. (From Pawlak, A.M. et al., *Novel Variable Reluctance Sensors*, Publ. No. 910902, Society of Automotive Engineers, Detroit, MI, 1991. With permission.)

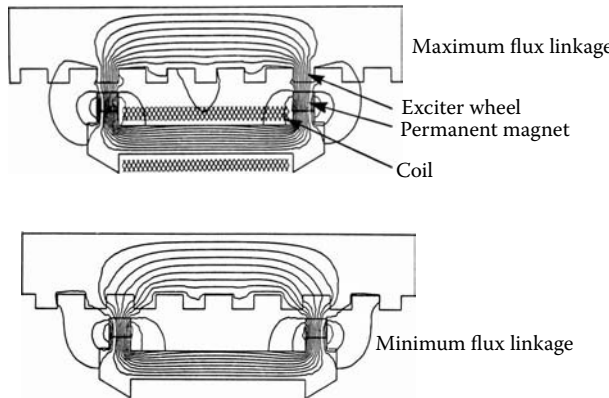
As proven previously for the front-mounted-magnet sensors, the width of the magnet has to be related to the exciter wheel tooth-slot width. Therefore, a PM width equal to the slot opening is the best dimension for this configuration. A PM width different from the exciter wheel tooth-slot width decreases the magnetic flux change, resulting in signal strength reduction, as presented in Figure 2.52. A variation of 40% of the magnet width can cause about 30% signal reduction.

For the conventional sensor-wheel arrangement and positive magnet polarization, the main magnetic path crosses both magnets, the central rod, and the exciter wheel. The entire magnetic flux links the coil, as presented in Figure 2.53. Only a small amount of the leakage flux is utilized for the signal generation.

For the nonconventional sensor-wheel arrangement, the sensor PMs are assembled with opposite polarization, facing the exciter wheel with the same polarities. The arrangement with opposite magnet polarization provides lower flux but much improved flux variations, thus enhancing the sensor signal strength. In this case, the magnets are offset by one half of a tooth pitch as compared to the design shown in Figure 2.55. Such an arrangement of

**FIGURE 2.52**

Two-magnet VR sensor signal vs. PM width. (From Pawlak, A.M. et al., *Novel Variable Reluctance Sensors*, Publ. No. 910902, Society of Automotive Engineers, Detroit, MI, 1991. With permission.)

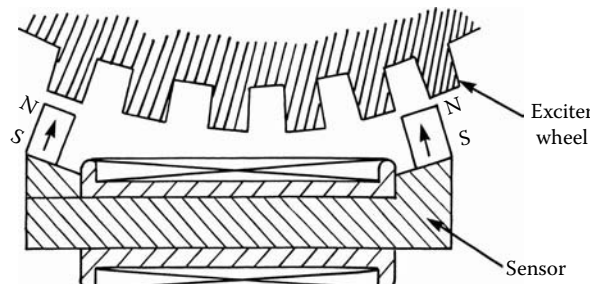
**FIGURE 2.53**

Flux lines of the two-magnet VR sensor with supportive magnetization and conventional sensor-wheel arrangement. (From Pawlak, A.M. et al., *Novel Variable Reluctance Sensors*, Publ. No. 910902, Society of Automotive Engineers, Detroit, MI, 1991. With permission.)

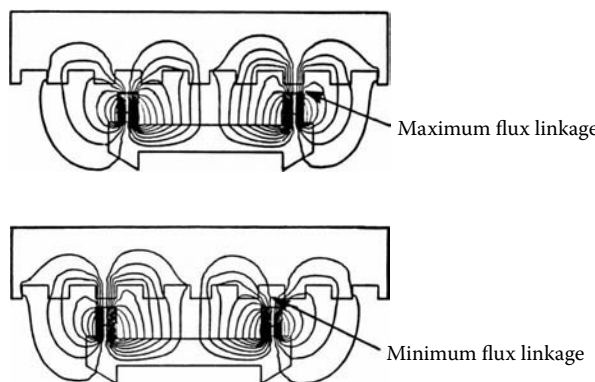
magnet polarization is nonsupporting for the magnetic flux; therefore, the magnetic flux links the coil from each magnet with different directions, as presented in Figure 2.53. The performance of the sensor was further improved, by a factor of 2.0, by assembling the magnets with opposite polarization, thus facing the target wheel with the same polarity but with a nonconventional sensor-wheel arrangement, as presented in Figure 2.54.

In this case, each of the magnets has its own magnetic path for the magnetic flux. A substantial amount of the magnetic flux is utilized for the signal generation.

There is significant difference in magnetic flux distributions for the supportive and nonsupportive magnet sensor arrangements. Because of the magnetic flux linking, the coil for the nonsupportive magnets is more sensitive for the exciter wheel position compared with the supportive magnet arrangement. Therefore, as shown in Figure 2.56, the sensor

**FIGURE 2.54**

Nonconventional sensor-wheel arrangement of the two-magnet VR sensor with nonsupportive magnetization. (From Lequesne, B. et al., *Transactions of IEEE/IAS*, 32(5), 1166–1175, 1996. With permission.)

**FIGURE 2.55**

Flux lines of the two-magnet VR sensor with nonsupportive magnetization and nonconventional sensor-wheel arrangement. (From Pawlak, A.M. et al., *Novel Variable Reluctance Sensors*, Publ. No. 910902, Society of Automotive Engineers, Detroit, MI, 1991. With permission.)

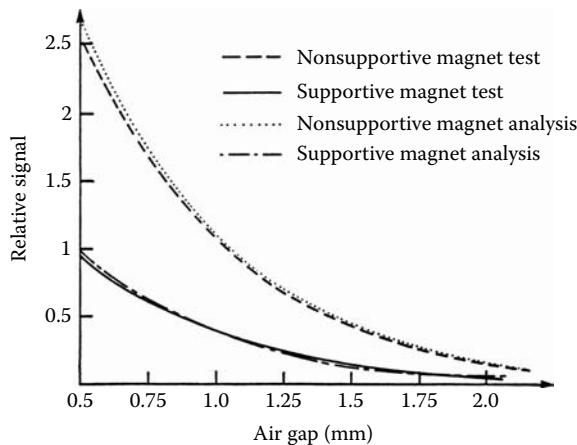
signal performance is superior to that of a sensor with the supportive magnets. The figure also shows an excellent correlation between the tests and the analysis based on an FE mathematical model.

Test results very closely match this analysis, within 5% for the wide range of air gaps, as shown in Figure 2.56. This also confirms that the signal sensor for nonconventional arrangements is superior to the conventional arrangement over the wide range of air gaps between the sensor and the exciter wheel. Vehicle performance evaluation tests, including temperature and noise tests, also indicated excellent sensor performance in automotive applications.

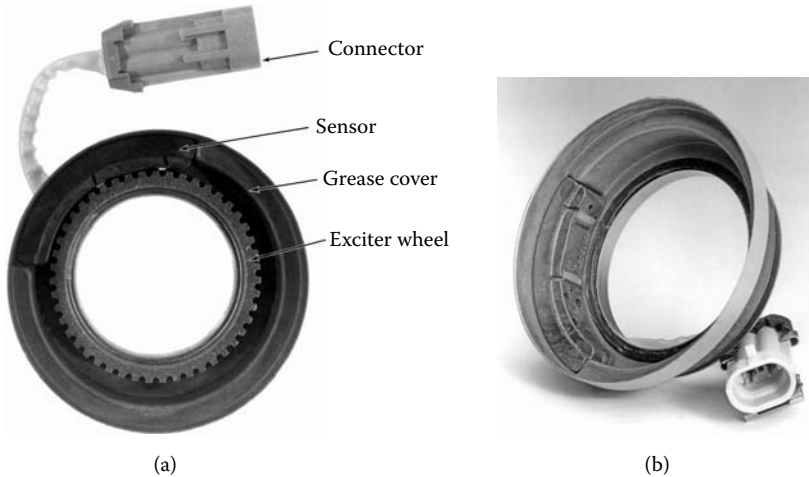
These sensors found an application in most of General Motors' passenger vehicles providing a wheel speed signal to the ABS system. Figure 2.57 shows two-magnet VR sensor components and assembly. Because this wheel sensor is located in close vicinity to the brake system where elevated temperature may be a typical sensor environment, this application requires 200°C temperature stability, and therefore, the samarium-cobalt magnet material SmCo17 was selected with 27.0 MGOe energy density.

2.3.9 Dual Sensor Arrangement

Two factors led to the development of the magnetically distributed sensor configuration. One is concerned with the shape of the wheel-bearing grease cover, where the sensor

**FIGURE 2.56**

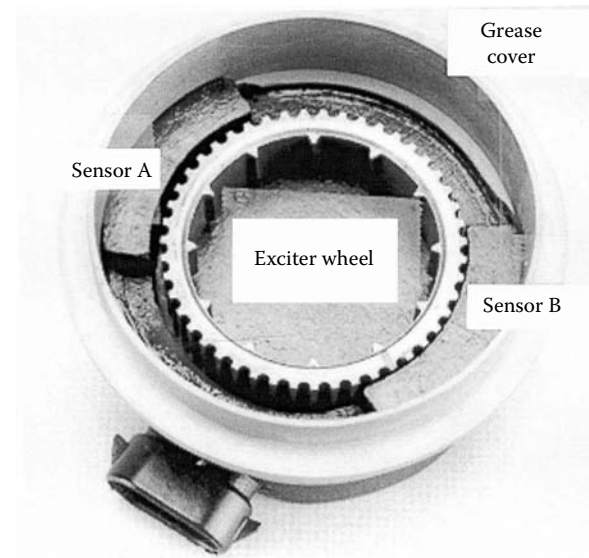
Analysis and test signal vs. air gap comparison for the nonconventional and conventional sensor-wheel arrangements of the two-magnet VR sensor. (From Lequesne, B. et al., *Transactions of IEEE/IAS*, 32(5), 1166–1175, 1996. With permission.)

**FIGURE 2.57**

Two-magnet sensor assembly: (a) sensor components, (b) sensor assembly. (Courtesy of Delphi Corp.)

would be integrated, and the second is concerned with the reduced sensitivity of the distributed sensor to the radial tolerances that offset the exciter wheel with respect to the sensor. A ring-shaped sensor would fit best and could be integrated within the bearing grease cover and its magnetic distribution nature would help compensate for the variation of radial tolerances, a deficiency that was noticed during the lumped element and partially distributed sensor's development.

In order to simulate a magnetically distributed sensor, two of the lumped element sensors (*A* and *B*) were assembled together and tested (Adams et al. 1991). Actually, the presented *A* and *B* sensors are partially distributed sensors described in Chapter 1. These sensors were assembled and electrically connected as a dual sensor arrangement 180° apart, as shown in Figure 2.58. The sensor's opposite location is selected to compensate for the offset due to tolerances of the shaft and exciter wheel. The sensor's signal vs. time

**FIGURE 2.58**

Two dual-magnet sensor arrangement. (Pawlak, A.M. et al., *Distributed Variable Reluctance Sensors*, Publ. No. 991039, Society of Automotive Engineers, Detroit, MI, 1999. With permission.)

characteristics are presented in Figure 2.59 for both the individual (A or B) and combined ($A+B$) sensor signals. Figure 2.59 also identifies both the local minimum and maximum signal values, which occur at local maximum and minimum air gaps, respectively, due to the exciter wheel offset. Table 2.4 presents the maximum and minimum signal values for both the individual (A , B) and combined ($A+B$) sensor signals obtained from the test characteristics. The data were obtained for the concentric (no offset) sensor-wheel arrangement. The combined sensor signal ($A+B$) shows only 3.1% tolerance sensitivity but individually each of the (A , B) sensors shows 14.3% and 13.5% signal variation, respectively, under the same conditions presented in Table 2.4 and Figure 2.58. The results proved the concept of the distributed sensor structure advantages. A clever solution to this problem is the distributed sensor described in Section 2.3.10.

2.3.10 Distributed VR Sensors

Distributed sensor configuration utilizes the entire exciter wheel all the time. Therefore, all tooth-pitch segments contribute to the sensor signal at any position. Conceptually, this requires the sensor to have multiple pole pairs that correspond to the exciter wheel tooth pitch. Each pole pair contributes to the signal independently under the condition that there is a common coil that collects all the signal components and the total sensor signal would be a sum of all signal vector components. Therefore, there is no signal cancellation at any time. The coil must be located in close vicinity of the flux-linkage changes and the magnetic circuit should guide the magnetic flux three-dimensionally to cross the coil. The distributed VR sensor concept presented in Figure 2.60 meets all these requirements (Pawlak 1999, Shirai and Pawlak 1993, Shirai and Pawlak 1996, Pawlak 1992a).

A distributed VR sensor features a ring structure, which consists of a coil and a multiplicity of evenly distributed magnets, as shown in Figure 2.60. In fact, the magnetically distributed sensor consists of a set of independent sensing devices, each having a PM, a section of the magnetic circuit, and a coil segment. Each of the independent sensor

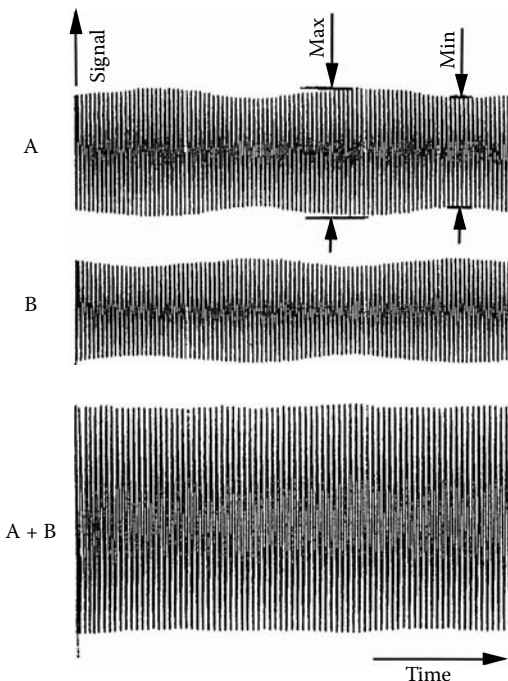


FIGURE 2.59

Dual lumped element sensor signal vs. time: (a) sensor A, (b) sensor B, (c) sensors A and B. (Pawlak, A.M. et al., *Distributed Variable Reluctance Sensors*, Publ. No. 991039, Society of Automotive Engineers, Detroit, MI, 1999. With permission.)

TABLE 2.4

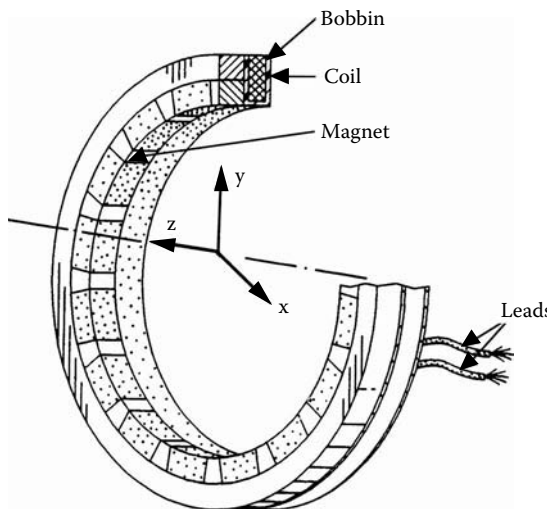
Distributed Sensor Comparison

Sensor or Signal	Maximum (V)	Minimum (V)	Location	Change (%)
Sensor A	1.26	1.09	Center	14.3
Sensor B	1.07	0.917	Center	13.5
Sensors A + B	2.15	2.22	Center	3.1

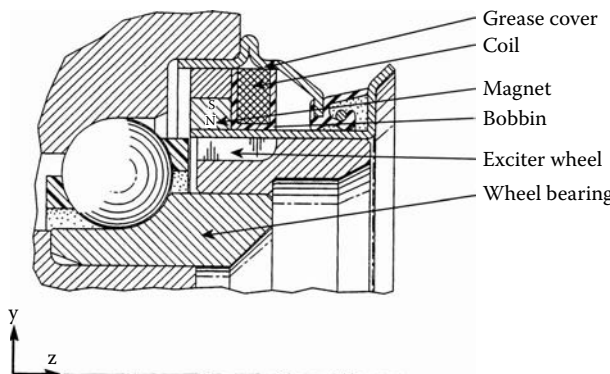
Source: Pawlak, A.M. et al., *Distributed Variable Reluctance Sensors*, Publ. No. 991039, Society of Automotive Engineers, Detroit, MI, 1999. With permission.

segments with a magnet contributes to the signal generation that enhances the total signal of the coil. The distributed sensor senses a toothed exciter wheel, which provides the VR effect on the magnetic field during rotation.

This sensor structure utilizes variation of the magnetic field three-dimensionally, rather than the conventional 2D sensor-exciter wheel arrangement, as presented in Figure 2.61 and Figure 2.62. Figure 2.61 shows the distributed sensor integrated with a wheel bearing, and Figure 2.62 identifies the magnetic flux path for this arrangement. In this structure, the flux lines are linked to the coil's turns and contribute to the signal generation along the axis of symmetry of the wheel bearing (y - z plane) rather than in a perpendicular x - y plane, which is utilized for conventionally arranged sensors. The ring-shaped distributed sensor also utilizes the modulation of that flux by the movement of the exciter wheel but in the y - z plane. The distributed sensor consists of a series of independent sections, which generate signal components. Each section facing a tooth-slot segment (one pole pitch) of

**FIGURE 2.60**

Magnetically distributed VR sensor configuration. (Pawlak, A.M. et al., *Distributed Variable Reluctance Sensors*, Publ. No. 991039, Society of Automotive Engineers, Detroit, MI, 1999. With permission.)

**FIGURE 2.61**

Distributed VR sensor-wheel assembly. (Pawlak, A.M. et al., *Distributed Variable Reluctance Sensors*, Publ. No. 991039, Society of Automotive Engineers, Detroit, MI, 1999. With permission.)

the exciter wheel makes a separate sensing device, and the continuous sensor coil is common for all of them and collects the individual sensor section's signal components in a combined total sensor signal. Therefore, such a sensor configuration allows for both the ring-shaped sensor to be integrated within the wheel bearing and to provide a magnetically distributed structure with low sensitivity to the variation of the radial tolerances. In its final design, the distributed sensor consists of two components only — a radially oriented multipole magnet and a coil. The coil's bobbin holds both the coil and the magnet. Figure 2.63 shows a picture of a distributed sensor assembled within a grease cover.

For mass production purposes, the magnet can be in the form of a multipole ring magnet molded with plastic or a multipole strip of a flexible resin-type material, which is bent to form a ring after it is magnetized. Figure 2.64 and Figure 2.65 show the sensor magnetized multipole magnet: one made using flexible magnet material, Figure 2.64, and the other with the plastic-molded multipole ring magnet, Figure 2.65. The flexible magnet, when assembled, will form a ring-shaped structure that is well integrated within the wheel

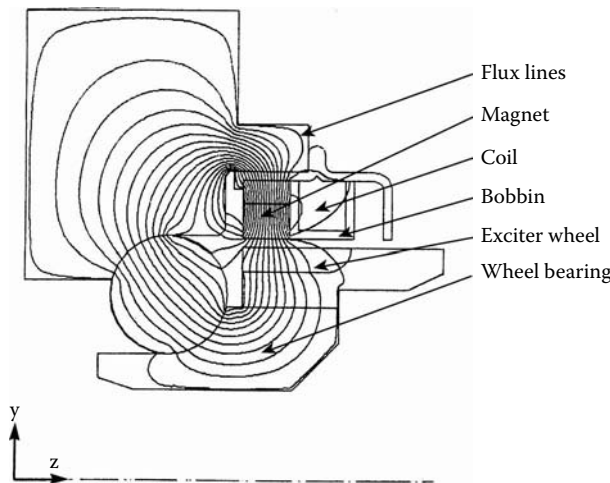


FIGURE 2.62

Flux lines of the distributed VR sensor. (Pawlak, A.M. et al., *Distributed Variable Reluctance Sensors*, Publ. No. 991039, Society of Automotive Engineers, Detroit, MI, 1999. With permission.)

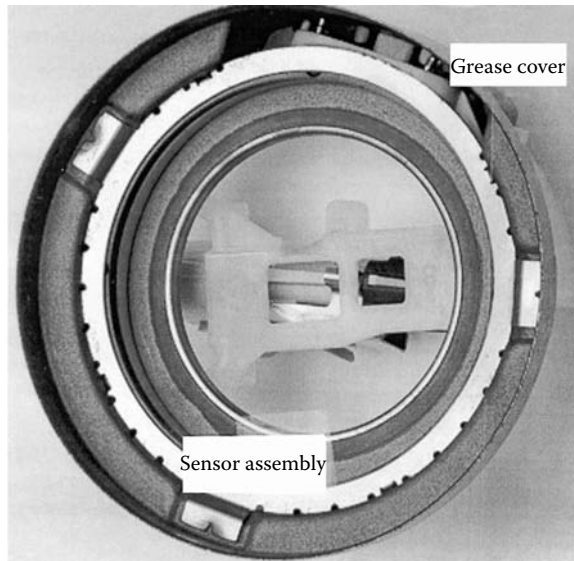
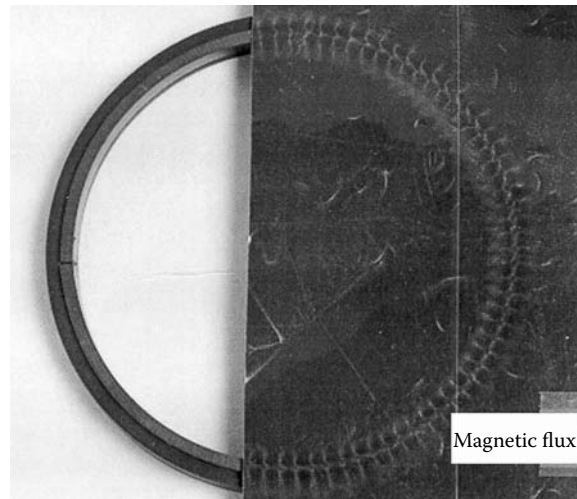


FIGURE 2.63

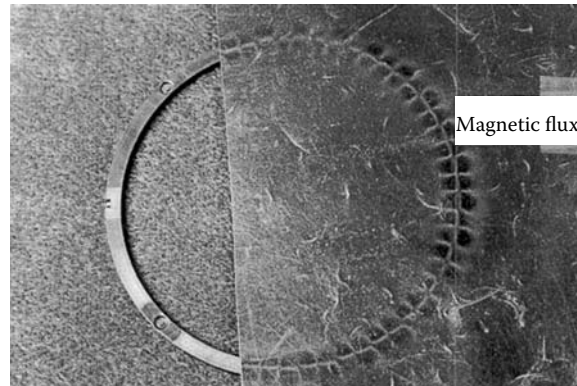
Distributed sensor assembly. (Pawlak, A.M. et al., *Distributed Variable Reluctance Sensors*, Publ. No. 991039, Society of Automotive Engineers, Detroit, MI, 1999. With permission.)

bearing grease cover. Magnetically sensitive film, which covers part of the magnet, indicates its magnetization. As shown, both the flexible and plastic-molded magnets are magnetized radially with multipole magnetization.

The flexible resin ring magnet, presented in Figure 2.64, is radially magnetized with 96 poles ($p = 48$), and the plastic-molded ring magnet is magnetized radially with 58 poles ($p = 29$), as presented in Figure 2.65. A large number of poles significantly enhances the sensor signal, which is proportional to the number of independent sections. It also helps

**FIGURE 2.64**

Flexible resin multipole ring magnet. (Pawlak, A.M. et al., *Distributed Variable Reluctance Sensors*, Publ. No. 991039, Society of Automotive Engineers, Detroit, MI, 1999. With permission.)

**FIGURE 2.65**

Plastic-molded multipole ring magnet. (Pawlak, A.M. et al., *Distributed Variable Reluctance Sensors*, Publ. No. 991039, Society of Automotive Engineers, Detroit, MI, 1999. With permission.)

reduce cost because it allows for a low-cost magnet material. In the case presented, the selected plastic-molded magnet-material energy density is less than 10.0 MGOe.

The signal of the VR sensor generated in the sensor coil is a time variation of the total flux linkage as shown in Equation 2.1, which is a function of time t and position θ , given by:

$$v(t) = -N \frac{d\phi}{dt} = -N \frac{d\phi}{d\theta} \frac{d\theta}{dt} = -N\omega \frac{d\phi}{d\theta} \quad (2.25)$$

For the distributed sensor, the total sensor signal is the sum of the separate signal components that are generated by the individual sensor sections for each of the tooth-slot segments of the exciter wheel and the corresponding magnetic flux linkages for a single pole-pair section:

$$v_d(t) = \sum_{i=1}^p v_i \quad (2.26)$$

If the sensor-wheel arrangement is not concentric for every segment, the sensor air gaps are different and every section of the sensor generates a different signal level. In particular, sections with a small air gap between the sensor and the exciter wheel embrace high magnetic flux and generate a high signal, whereas sections exposed to large air gaps generate a low signal. Generally, the flux linked to the coil (with the same number of N turns for each section) for all the sections 1, 2, ..., p is different:

$$\phi_1 \neq \phi_2 \neq \dots \neq \phi_p \quad (2.27)$$

When Equations 2.25 through 2.27 are combined, the total distributed sensor signal can be expressed as:

$$v_d(t) = -N\omega \frac{d}{d\theta} \sum_{i=1}^p \phi_i \quad (2.28)$$

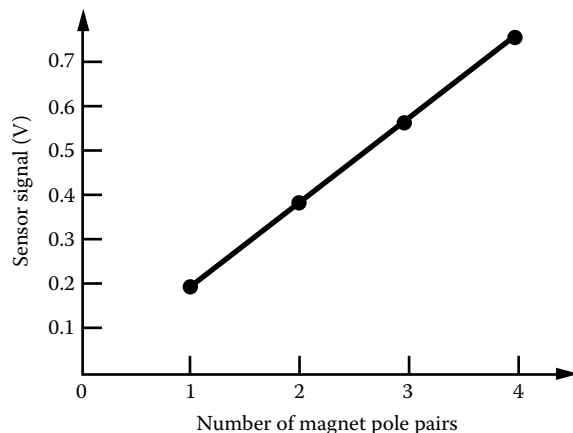
With the exciter wheel offset in the distributed sensor structure for each section, which generates a low signal, there is another section that generates a high signal. Because the total signal is the sum of all section signals and the number of sections contributing low signals is the same as the number of sections contributing high signals, the resultant total signal of the sensor is expected to be constant, as presented in Figure 2.59 ($A + B$). For the concentric sensor-wheel arrangement, all air gaps are identical and the level of the magnetic flux for all the sections 1, 2, ..., p is also the same:

$$\phi_1 = \phi_2 = \dots = \phi_p = \phi_m \quad (2.29)$$

where v_d is the voltage generated in a coil of the distributed sensor, ϕ_1 is a magnetic flux embraced by the coil 1, ϕ_2 is a magnetic flux embraced by the coil 2, ϕ_m is a median magnetic flux embraced by the coil for a single pole-pair section, ϕ_p is a magnetic flux embraced by the p single pole-pair section, p is the number of magnet pole pairs or sensor sections, ω is an angular speed, and θ is the sensor or rotor position. When Equations 2.23, 2.24, and 2.27 are combined, the total sensor signal can be expressed as:

$$v_d(t) = -N\omega p \frac{d\phi_m}{d\theta} \quad (2.30)$$

Therefore, the signal of each section is the same and the total sensor signal is proportional to the number of p sections. The total signal of the distributed sensor signal is a function of the number of turns, angular speed of the target wheel, the number of pole pairs, and the variation of the median magnetic flux for the two extreme wheel positions. Unlike the lumped element sensor, the distributed sensor is a linear function of the number of magnets (pole pairs) (compare Equation 2.25 and Equation 2.30). Therefore, for a distributed sensor, it is advantageous to employ the maximum possible number of magnet pole pairs, which provides a magnetic gearing effect. The maximum signal value can be

**FIGURE 2.66**

Distributed sensor signal vs. number of pole pairs. (Pawlak, A.M. et al., *Distributed Variable Reluctance Sensors*, Publ. No. 991039, Society of Automotive Engineers, Detroit, MI, 1999. With permission.)

TABLE 2.5
VR Sensor Signal Comparison

Sensor or Signal	Maximum (V)	Minimum (%)	Location	Change (%)
Lumped	1.88	1.26	Center	39.5
Lumped	1.6	1.01	Offset x	45.2
Lumped	1.94	0.98	Offset y	65.7
Distributed	1.67	1.5	Center	10.7
Distributed	1.39	1.39	Offset x	21.8
Distributed	1.46	1.46	Offset y	14

Source: Pawlak, A.M. et al., *Distributed Variable Reluctance Sensors*, Publ. No. 991039, Society of Automotive Engineers, Detroit, MI, 1999. With permission.

achieved for the multiplicity of magnets that are evenly distributed where one magnet pole faces a slot and another magnet with opposite magnetization faces a tooth and the number of magnets equals the number of teeth (slots) of the exciter wheel.

A number of distributed sensors were manufactured and tested. Today it is the most popular VR sensor design and has penetrated passenger vehicle markets in the millions every year. At first, all sensor magnets were assembled with segment magnets distributed symmetrically on the circumference of the sensor. All magnets with the same polarities are pointing toward the exciter wheel's teeth while the space between the magnets is facing the exciter wheel's slots. Therefore, one tooth pitch that is facing a magnet pole pitch is forming an independent sensor section. Figure 2.66 shows a sensor test that has various numbers of evenly distributed magnets. Because the characteristic presented is linear, it supports the developed mathematical model and proves that the distributed sensor signal is a function of the number of magnet pole pairs.

To verify the effect of concentricity between the sensor and the exciter wheel, as shown in Equation 2.26, both the distributed and lumped element sensors were tested. Table 2.5 shows the test results where the signal values were obtained at a constant speed of 200.0 r/min of the exciter wheel while introducing the concentric or x and y offsets of 1.0×10^{-3} m.

Results collected in Table 2.5 indicate that the percentage of the lumped element sensor signal variation is about four times that of the distributed sensor under the same sensor-wheel conditions. Therefore, one can conclude that the distributed sensor is superior to the lumped element sensor because the distributed sensor is less sensitive to the tolerance variations and provides a more stable signal in comparison to the lumped element sensor. Test results support the developed mathematical model and prove that, unlike the lumped element sensor, the distributed sensor signal is a function of a number of magnet pole pairs. The tests indicated that the percentage of the lumped element sensor signal variation is about four times of that variation for the distributed sensor under the same sensor-wheel conditions. A distributed sensor features structural simplicity and superior performance in comparison with the lumped element sensors.

2.4 Solid-State Sensors

The function of the solid-state sensors depends on the presence of the magnetic field; therefore, its effectiveness depends on the quality of the magnetic circuit. Both, the magnetoresistors and the Hall-effect generators fall into the category of the solid-state sensors (Ramsden 2001). Magnetoresistors are magnetically influenced resistors based on the InSb or NiSb material that acts on the Gaussian effect. The charge carriers that flow through the semiconductor material experience a sideways action in the presence of transverse magnetic field by Lorentzian forces. The Hall effect, named after its discoverer Edvin Hall, is the result of the Lorentzian force on electrons through the material when exposed to magnetic field B . The flow of the current without the presence of the magnetic field has a linear path and the equipotential electrical lines are perpendicular to the current flow path. In the presence of the magnetic field, the Lorentzian forces F that are affecting electrons are:

$$F = q/\sigma(j * B) \quad (2.31)$$

where F is the magnetic field of the Lorentzian forces, q is the electron charge, σ is the material conductivity, j is the current density, and B is the magnetic field density.

The cross product indicates that the force is in the direction perpendicular to the current flow and the magnetic field. The angle through the current flow is changed by the presence of the magnetic field B and is called the Hall angle θ_H . The material specifically determined by the electron mobility μ determines the Hall coefficient R_H . With the presence of the magnetic field, the equipotential lines are skewed and this generates the Hall voltage V_H across the material. The angle between the original current and that to which it charges on the introduction of the magnetic field is known as the Hall angle δ . It depends on the electron mobility μ and the magnetic field density B .

$$\tan \delta = \mu * B \quad (2.32)$$

where μ is the electron mobility and B is the magnetic field density.

For the InSb material, the exceptionally high electron mobility of $7.0 \text{ m}^2/\text{Vs}$ results in a Hall angle of $\delta = 80^\circ$ with $B = 1.0 \text{ T}$. As opposed to Hall generators, the InSb crystal has, irrespective of the low-resistive NiSb that it has alloyed into, maintained an equal distribution of the charge carriers throughout its cross section. The lengthening of the paths of

the charge carriers with increasing magnetic field results in an increase of the resistance of the magnetoresistor that is dependent on the magnetic field polarity.

Although present in all materials, the Hall effect is practical in only a few materials, where the electron mobility is high, such as gallium arsenite, indium antimonite, and with amplification done on a chip it is usable also in silicon and germanium. The result of the simultaneous action of these parameters is the generation of the voltage V_H across the chip:

$$V_H = R_H * I_1 * B/d \quad (2.33)$$

Providing the supplied current I_1 is constant and R_H is the Hall constant of the material, the resultant voltage V_H is a function of the magnetic field density B . This allows the Hall generator to be used as a sensing device commonly known as a Hall sensor or an MR sensor.

2.4.1 Solid-State Sensor Analysis

The electric characteristics of some semiconductors depends on the magnetic field to which they are exposed. In Hall-effect devices, a voltage can be measured, and in magnetoresistors, a resistance variation is observed. If such a semiconductor is located on a stationary magnet across from a moving wheel, as shown in Figure 2.2, an electric signal $v(t)$ is obtained, which reflects the permeance changes due to the wheel motion. If the size of the semiconductor were infinitely small, the signal $v(t)$ at time t would be (Lequesne et al. 1996):

$$v(t) = f[B(\theta(t))] \quad (2.34)$$

where $f(B)$ is the characteristic of the semiconductor and $\theta(t)$ is the position of the semiconductor at time t .

The semiconductor, however, encompasses some width δ and some averaging occurs over its area. The mathematics of averaging depends on the semiconductor nature and design but, in general, such averaging reduces the magnitude of the sensor's output signal. Therefore, it is preferable to have the width δ as small as is practically possible. Because it is feasible with current technology to have the width δ small compared to the wheel features, Equation 2.32 holds approximately and the sensor output can be characterized by the maximum and minimum of Equation 2.32:

$$v_{\max} = f(B_{\max}) \text{ and } v_{\min} = f(B_{\min}) \quad (2.35)$$

where v_{\max} is the sensor signal characterized by the maximum flux density B_{\max} , B_{\max} is the maximum flux density, v_{\min} is the sensor signal characterized by the minimum flux density B_{\min} , and B_{\min} is the minimum flux density.

We conclude, therefore, that the output of a solid-state sensor depends also on the maximum and minimum values of flux density and is independent of the shape of the function $B(\theta)$. This establishes a common ground between VR and solid-state sensor designs. The other conclusion, however, is that the best sensor output is obtained from the smallest value of width δ , a conclusion that makes the design of solid-state sensors differ sharply from that of VR sensors.

Note also that the output of VR sensors (Equation 2.6) is proportional to the wheel speed ω , whereas the output from solid-state sensors (Equation 2.35) is independent of speed.

This known difference (Ohshima and Akiyama 1989a, Rowley and Stolfus 1990) has important practical implications for choosing one type of sensor over the other for a particular application, but as underscored by the mathematical expressions, Equation 2.6 and Equation 2.35, it does not affect the magnetic design. In the solid-state sensor case, the flux density in the location of the semiconductor is provided by the FE software. The output from the sensor depends on the characteristic of the solid-state device. To assess performance in as general a way as possible, a figure of merit, the device sensitivity S , in percent, was defined that prorates the difference between the maximum and minimum to their mean value, as follows:

$$S = \frac{B_{\max} - B_{\min}}{B_{\text{mean}}} \quad (2.36)$$

$$B_{\text{mean}} = \frac{B_{\max} + B_{\min}}{2}$$

where S is the device sensitivity and B_{mean} is the mean value of the flux density.

2.4.2 Solid-State Sensor Design

Solid-state sensors require an external source of voltage or current, but they have the significant advantage over VR sensors in that their output signal is independent of the target-wheel speed. Also, the absence of a coil makes them more compact. Their success in the end, however, may hinge on the ability to manufacture them as inexpensively as VR sensors and, in that respect, improvements in magnetic-circuit design and sensitivity are critical for overall cost reduction. Their disadvantages include complexity, four leads, the presence of constant current source, fragility, and temperature dependence that requires stability provisions.

Unlike the VR-sensor case, the magnet size must be chosen in the solid-state sensor case to enhance the flux-density variations in one precise location, i.e., that of the semiconductor. This difference is well illustrated by studying the impact of the magnet width on sensor sensitivity, as defined in Equation 2.34, and as presented in Figure 2.67.

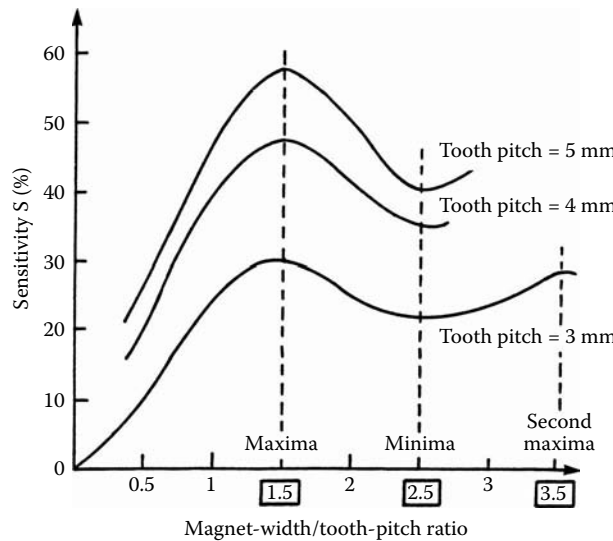
A first observation is that contrary to VR sensors, magnet widths much larger than a tooth pitch yield the best sensitivities. Another observation is the existence of sensitivity peaks that do not depend separately on magnet width and tooth pitch, but rather on their ratio. A general formula for the ratio R_{peak} yielding such a peak is:

$$R_{\text{peak}} = (1.5 + 2i) \frac{W}{T} \quad (2.37)$$

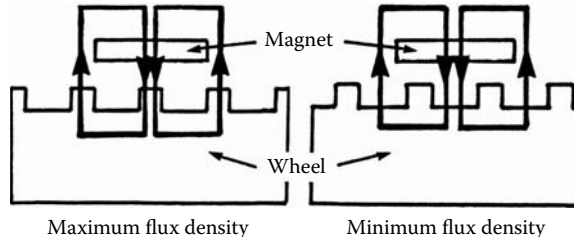
where R_{peak} is the magnet-width/tooth-pitch ratio, i is an integer, W is the magnet width, and T is the tooth pitch.

The respective locations of the magnet edge and of the wheel teeth explain the presence of sensitivity peaks and valleys. Consider the flux return paths sketched in Figure 2.68 for the case $W/T = 1.5$. The plot shows that in the maximum flux-density position, the signal is enhanced by the presence of teeth in the flux return path, and in the minimum flux-density position, it is reduced by the presence of slots near the magnet edges where the flux returns. The converse (not shown) is true for sensitivity valleys.

As shown in Figure 2.69, the concentration of magnet flux toward the teeth occurs primarily in the air gap. Figure 2.69 shows flux plots drawn from the FE calculation. The

**FIGURE 2.67**

Sensor sensitivity vs. magnet-width/tooth-pitch ratio. (From Lequesne, B. et al., *Transactions of IEEE/IAS*, 32(5), 1166–1175, 1996. With permission.)

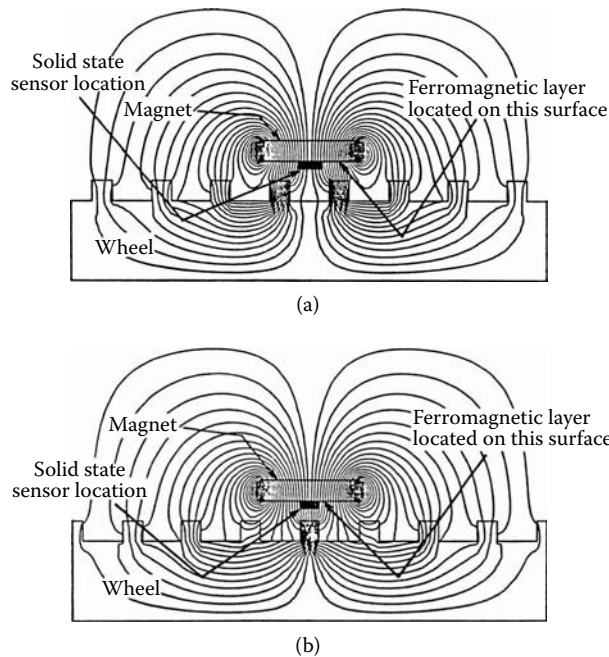
**FIGURE 2.68**

Sketch of flux paths for $W = 1.5$ T. (From Lequesne, B. et al., *Transactions of IEEE/IAS*, 32(5), 1166–1175, 1996. With permission.)

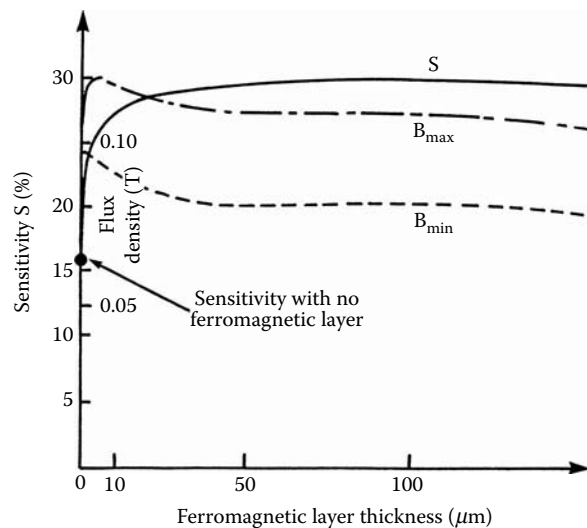
semiconductor, however, must be located close to the magnet surface to facilitate construction. Therefore, much of the flux variation bypasses the sensor and does not contribute to the signal. In order to direct more of the flux variation toward the sensing element, a thin ferromagnetic layer was added on the magnet surface (Schroeder et al. 1996). The high permeability of this layer allows for a larger flux concentration to take place between the magnet and the sensor and, therefore, enhances the signal.

Figure 2.70 plots sensitivity vs. the thickness of the ferromagnetic layer. It shows that even a very thin layer can be highly effective, almost doubling the sensitivity as compared to a similar sensor with no ferromagnetic layer. Thanks to its extreme thinness, the high permeability layer does not cause excessive leakage on the magnet edges.

In some designs, an iron member is added as a return path to the back of the PM to reduce the overall reluctance and increase the mean flux density in the sensor. However, it is interesting to note that its presence does not affect sensitivity. The same is true when the magnet thickness is increased or as the magnet material is changed from a weaker magnet material to a stronger one. These results are illustrated in Table 2.6, which shows that different designs may feature different mean flux densities B_{mean} (from 1.0 per unit

**FIGURE 2.69**

Flux plots for solid-state sensor: (a) minimum flux-density position, (b) maximum flux-density position. (From Lequesne, B. et al., *Transactions of IEEE/IAS*, 32(5), 1166–1175, 1996. With permission.)

**FIGURE 2.70**

Influence of ferromagnetic layer thickness on sensitivity. (From Lequesne, B. et al., *Transactions of IEEE/IAS*, 32(5), 1166–1175, 1996. With permission.)

[pu] to 3.1 pu) yet similar sensitivities S . This functional equivalence between iron flux guide, magnet thickness, and material strength (see, for instance, the similar values of B_{mean} and S for design 2 and design 3) is an important design tool because it allows the comparison of various options for a given application.

TABLE 2.6
Comparison of Various Designs

Design No.	Magnet Design		Output		
	Iron Flux Guide	Magnet Thickness	Magnet Strength (kJ/m ³)	B _{mean} (pu)	Sensitivity
1	No	Base	100	1	1
2	Yes	Base	100	2.1	0.96
3	No	2.5 × Base	100	2.1	0.91
4	No	Base	300	1.6	0.98
5	No	2.5 × Base	300	3.1	0.94

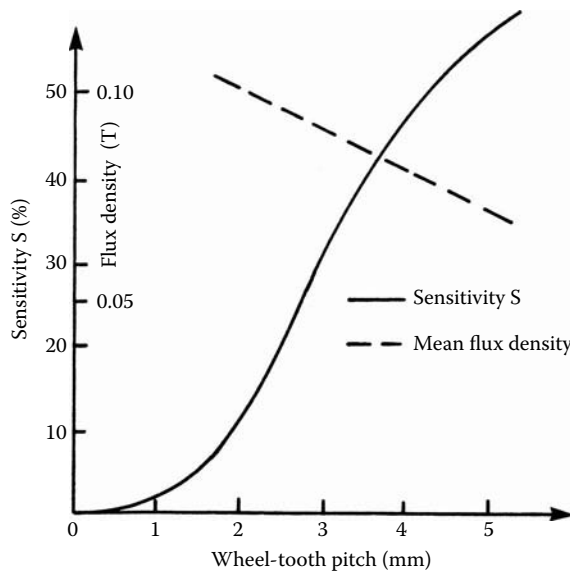


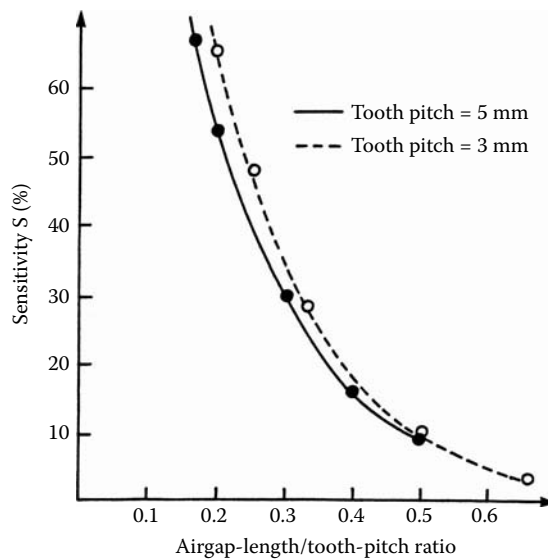
FIGURE 2.71
Influence of wheel tooth pitch on sensitivity. (From Lequesne, B. et al., *Transactions of IEEE/IAS*, 32(5), 1166–1175, 1996. With permission.)

The sensitivity of the sensor depends on the wheel-tooth pitch. If the tooth pitch is large, teeth are far from one another and the flux concentrates significantly toward any tooth located across the magnet. If the tooth pitch is small, the flux leaks toward the neighboring teeth and flux concentration occurs only to a smaller degree. Therefore, the sensitivity is higher with larger tooth pitches, as presented in Figure 2.71 (for each point in Figure 2.71, the magnet width was chosen according to Equation 2.37). The mean flux density, also shown in the figure, drops slightly as the tooth pitch increases.

Longer air gaps obviously yield smaller mean flux densities. The sensitivity also decreases with longer air gaps. The physical reasons for this are similar to those given above to relate sensitivity to tooth pitch. In fact, it can be shown that the sensitivity does not depend separately on air gap length and tooth pitch, but rather on their ratio, as presented in Figure 2.72.

2.4.3 Solid-State Sensor Test Results

Two sensors were built to check the validity of the model and the conclusions derived from it. The same magnet was equipped, in one case, with a 51×10^{-6} m thick steel layer

**FIGURE 2.72**

Correspondence between air gap and tooth pitch. (From Lequesne, B. et al., *Transactions of IEEE/IAS*, 32(5), 1166–1175, 1996. With permission.)

TABLE 2.7

Comparison Test Calculations

Sensor Design	Unit	Ferromagnetic Layer			No Ferromagnetic Layer		
		Test	Model	Difference (%)	Test	Model	Difference (%)
Maximum flux density	T	0.206	0.2028	1.6	0.207	0.2054	0.8
Minimum flux density	T	0.168	0.1693	0.8	0.183	0.1896	3.6
Sensitivity	%	20.3	18.0	11.3	12.3	8.1	34.1

Source: Lequesne, B. et al., *Transactions of IEEE/IAS*, 32(5), 1166–1175, 1996. With permission.

and none in the other case. The results are shown in Table 2.7. The computed and measured flux densities match within 4%.

The wheel in the experimental set-up was fairly deep (13×10^{-3} m) compared to the semiconductor size (less than 1×10^{-3} m deep). Therefore, the 2D approximation was a good representation of the wheel. The magnet, however, is usually small (2 or 3×10^{-3} m deep) because of its cost. A 2D model, which results in neglecting the end effects around the magnet edges in the direction perpendicular to the wheel rotation, tends, therefore, to be somewhat inaccurate. In order to assess the impact of this simplification on performance predictions, two sensors were tested which differed only by the magnet depth in the third direction. In one case, the magnet depth was 9.5×10^{-3} m, and in the other case, it was only 3.2×10^{-3} m, the deeper magnet being closest to the 2D simplification. The test data are shown in Table 2.8, along with the results of the 2D model in this case. Because the end effects constitute a reluctance path parallel with the main flux path, the consequence of their presence, as seen in Table 2.8, is to increase the mean flux density and to reduce the sensitivity, by 32% in the case studied. The impact of the end effects on the results, however, is mainly quantitative as the reluctance load that the end effects constitute for the magnet is relatively constant, regardless of the design. A 2D model, therefore, is appropriate for qualitative comparison and design selection, but not for precise quantitative prediction.

TABLE 2.8

Influence of the End Effects

Performance or Sensor Design	Shallower Magnet	Deeper Magnet	2D Model
Maximum flux density (T)	0.216	0.206	0.2028
Minimum flux density (T)	0.188	0.168	0.1693
Mean flux density (T)	0.202	0.187	0.186
Sensitivity (%)	13.9	20.3	18.0

Source: Lequesne, B. et al., *Transactions of IEEE/IAS*, 32(5), 1166–1175, 1996. With permission.

TABLE 2.9

Requirements for Sensors in Automotive Applications

Performance or Sensor Type	Inserted-Magnet Sensor Transmission Speed	Front-Magnet Sensor Crankshaft Position	Multimagnet Sensor ABS Application
Signal (p-p) V			
at 25°C	>0.65 at 100 r/min at 1.2 mm gap		
at 150°C	>0.55 at 100 r/min at 1.2 mm gap	>0.5 at 30 r/min at 1.5 mm gap >0.65 at 100 r/min	3.75, 5.5, 7.0 mV/Hz at 1.0×10^{-3} m gap
Geometry			
Diameter (m $\times 10^{-3}$)	27.0	12.0, 15.0	
Height (m $\times 10^{-3}$)	57.5	30.0, 35.0	10.0
Width (m $\times 10^{-3}$)			13.0
Length (m $\times 10^{-3}$)			25.0
Volume (m ³ $\times 10^{-6}$)	32.9	9.6	3.25
Temperature (°C)	-40 to +150	-40 to +150	-40 to +200
Speed range (r/min)	100 to 6250 <0.15 at 5000 r/min	30 to 7000 NS	42 to 5000 NS
Noise signal (V)	engine speed		
Load (kΩ)	NS	10	NS

NS = not specified.

Source: Courtesy of Delphi Corp.

2.5 Magnetic Sensor Applications

The applications of magnetic velocity sensors are increasing rapidly, particularly in the automotive industry, where they are used for ABS, TC, four-wheel drive, steering wheel and cam shaft position, etc. VR speed and position sensors are widely used in industry and, in particular, the automotive industry because of their low cost and high reliability. To date, many types of lumped element VR sensors have been utilized, but more and more modern VR sensors are used in a variety of applications.

2.5.1 Magnetic Speed Sensor Requirements

Typical VR sensor requirements for automotive applications pertain to the sensor signal, usually defined as the peak-to-peak value, its geometry, speed range, temperature range, and the acceptable noise level. Sometimes load is also specified. Requirements for four families of novel sensors utilized in automotive applications are shown in Table 2.9.

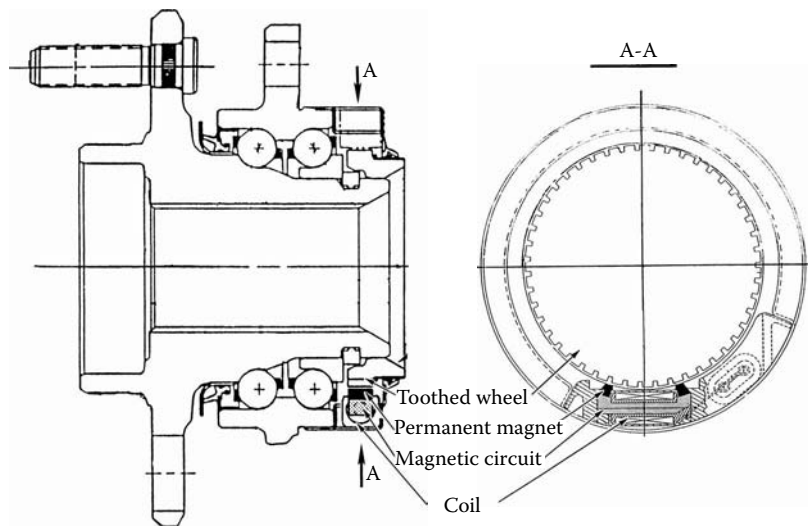


FIGURE 2.73
Two-magnet sensor integrated with the wheel bearing for ABS.

2.5.2 Magnetic Speed Sensor Applications

A need to boost sensor performance that provides high signal at a low speed of the exciter wheel led to the development of the VR sensor configuration with multiple magnets. Such a requirement for sensor performance came from an automotive application for ABS, as presented in Table 2.9. Figure 2.73 shows a two-magnet sensor applied to the wheel speed sensing application for the ABS system. The sensor fits under the grease cover that is a part of the wheel bearing and provides a signal to the ABS system. The particularly difficult sensor environment with high ambient temperature around the brakes led also to the selection of a magnet material that is stable at elevated temperatures. Consequently, the two-magnet partially distributed sensor led to the development of the magnetically distributed ring-shape sensor with multipole magnet that fits best and could be integrated within the bearing grease cover, and its magnetic distribution nature would help compensate for the radial tolerances. This enables this sensor to provide signals for both the ABS and TC system with a much more difficult requirement to meet. The magnetically distributed sensor, shown in Figure 2.74, can provide a full signal of 1.0 V at the wheel speed of 0.25 mph; however, the two-magnet sensor capability at full signal is limited to 0.9 mph vehicle speed, which is sufficient for ABS but not satisfactory for the TC.

Typical ABS system requirements vary from system to system: Bosch = 7.0 mV/Hz, GM6 = 5.5 mV/Hz, and Teves = 3.75 mV/Hz, as presented in Table 2.9. During the development of the two-magnet sensor integrated with the wheel bearing for the ABS, meeting all requirements was quite a challenge. For this modern sensor structure, shown in Figure 2.73, additional improvement was introduced by heat treatment of the magnetic parts. One should always remember to reduce mechanical stresses exerted to the magnetic parts by the manufacturing process in the form of machining or stamping operations. Proper annealing, usually guided by the material manufacturer, is a necessary element in releasing and eliminating stresses in the magnetic circuit. In this particular case, annealing of a central rod has provided performance improvement over 12% in the achieved signal value, as demonstrated in Figure 2.75, especially because cost increase per sensor is less than a penny.



FIGURE 2.74
Magnetically distributed sensor integrated with wheel bearing.

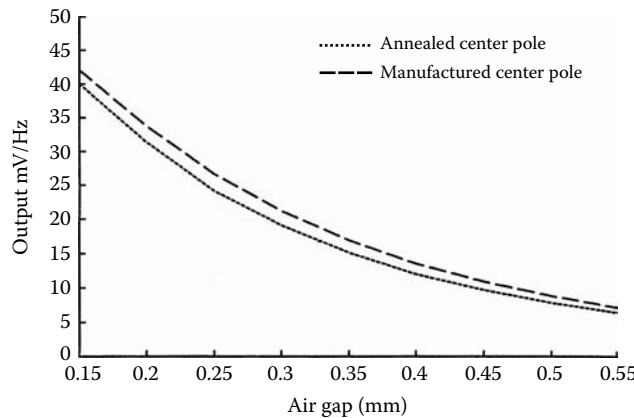


FIGURE 2.75
Output signal vs. air gap performance for the annealed center pole vs. the original manufactured center pole of the two-magnet VR sensor structure.

2.5.3 Magnetic Position Sensor Applications

The front-mounted-magnet sensor in Figure 2.76 is presented with an exciter wheel that has a particular tooth and slot pattern that would provide accurate crankshaft position. There are two such sensors adopted for this application to provide additional information on the direction of rotation. The sensor signal is presented in Figure 2.33. This signal is utilized as a position sensor where the real position of the exciter wheel is indicated by zero crossing of the signal at the narrow and wide tooth. The rotation of the wheel creates a change in magnetic flux linkage in the sensor, which generates a voltage signal based upon the flux rate change.

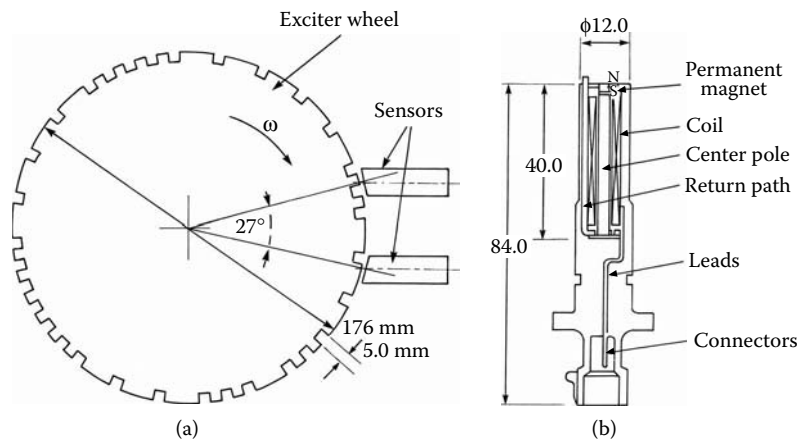


FIGURE 2.76

Front-mounted position sensor: (a) sensor-wheel arrangement, (b) front-mounted sensor.

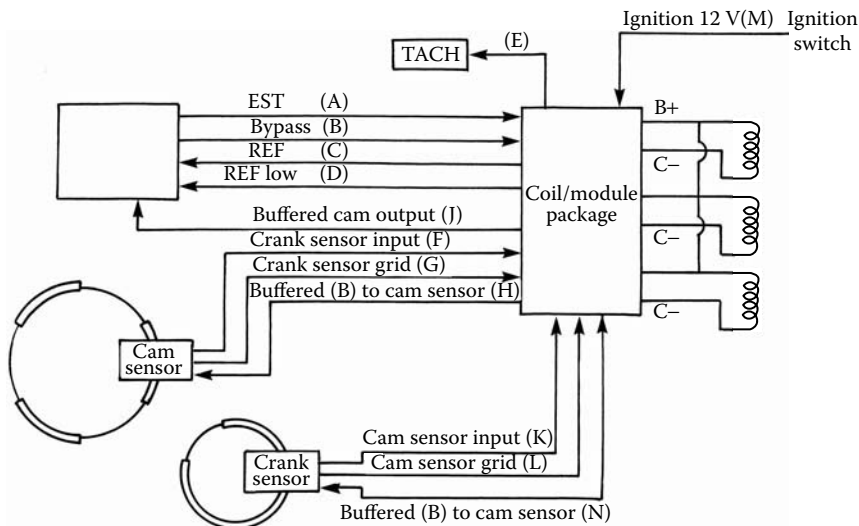


FIGURE 2.77

Crankshaft position sensor. (From Pawlak, A.M., *Proceedings of the NdFeB '99 Conference*, San Francisco, April 12–14, 1999. With permission.)

The electronic module, shown in Figure 2.77, processes the signal from the sensor to determine a crankshaft position and engine speed. It responds to voltage transmissions generated in the sensor by the slotted wheel passing by. This voltage must rise above a certain positive threshold and then move through zero volts on negative transition. The positive threshold varies from 250 mV at minimum cranking speed of 40% of the previous positive peak. The latter is to safeguard against recognition of noise at higher speeds. The module triggers off of the zero crossing of the waveform. The positive threshold is used only as an arming mechanism to filter out noise. The module counts the time between zero-crossing events of the sensor to determine the engine speed and the crankshaft position. The special slot distribution of the wheel allows recognition of the crankshaft position at its half revolution.

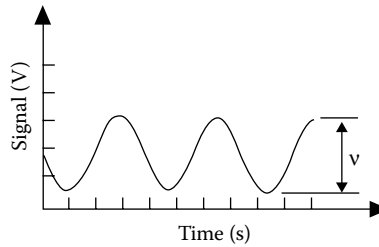


FIGURE 2.78
Sensor signal vs. time.

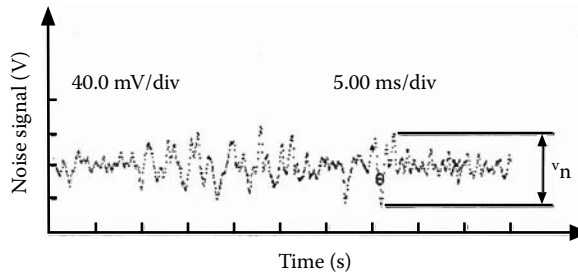


FIGURE 2.79
Noise signal vs. time.

2.6 VR Sensor Noise

In automotive applications, a VR sinusoidal sensor signal, as presented in Figure 2.78, is filtered and squared by a remote buffer circuit, whose output can be used by the speedometer, cruise control, TC, and other systems. Because it is not possible to determine the level of noise signal before the sensor is built and applied, usually it is a matter of sensor modifications after the sensor is designed and tested. Sometimes the same sensor applied to one environment's noise level is acceptable, yet in a new arrangement may not be acceptable. Noise should be measured at the worst conditions: highest temperature, highest engine rotation, and for sensor position when the flux linkages are at their maximum values (wheel tooth vs. pole tip). Under extreme conditions, the noise signal vs. time characteristic should be determined for the original sensor.

A typical example of the noise vs. time characteristic is presented in Figure 2.79. In this example, the transmission speed sensor noise signal was recorded at 5000 rpm of engine speed at transmission gear in neutral or park position. Because the vehicle is not moving, the sensor signal should be zero as well as the speedometer reading. Because the sensor indicates the noise signal, the threshold is set up for 0.15 V signal value (peak-to-peak) and no speed reading is displayed as a false speed if the noise signal is below this level.

2.6.1 Math Model and Noise Analysis

Equation 2.1 for induced signal v_s in the sensor coil can be expressed as a function of time and angular position as:

$$v_s = -N \frac{d\phi}{d\theta} \times \frac{d\theta}{dt} \quad (2.38)$$

where v_s is the induced signal in the sensor coil, N is the number of turns of the coil, θ is the angular position, and t is the time.

Substituting for $dv_s/dt = \omega$, one can see that the induced signal depends on the wheel angular speed, the number of turns N , and flux changes for different wheel positions, of which the latter is the most difficult to determine. A similar equation that describes the noise signal as a function of the relative sensor-wheel position A and time t can be expressed as follows:

$$v_n = -N \frac{d\phi}{dA} \times \frac{dA}{dt} \quad (2.39)$$

A vibration mode relative to sensor-wheel movement has three degrees of mechanical freedom, resulting in position term A , which can vary in all three coordinates:

$$A = A(x, y, z) \quad (2.40)$$

Because of the complex 3D nature of sensor-wheel interaction and geometry, an FE numerical solution of the magnetic field is necessary. Evaluation of the noise signal change has to be based on the noise-signal-to-sensor-signal ratio v_n/v_s and that sensor signal level v_s is satisfactory.

2.6.2 Noise Problem Solutions

The investigated sensor was applied to two different automotive power train transmissions, as presented in Figure 2.80. Because the axial length of the exciter wheel is different,

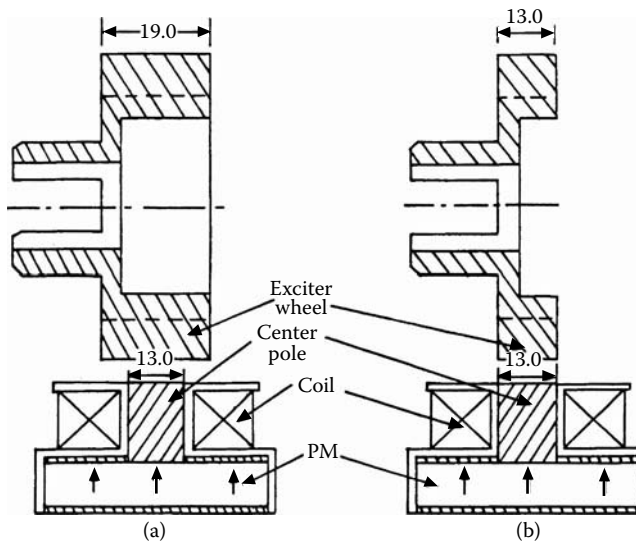


FIGURE 2.80

Sensor-wheel arrangements for two different power train transmissions: (a) wide exciter wheel, (b) narrow exciter wheel.

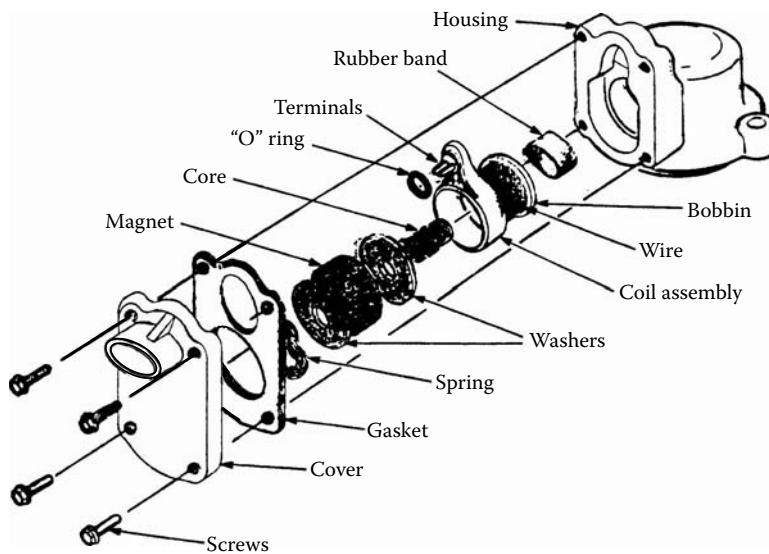


FIGURE 2.81
Transmission speed sensor components.

the transmission with the shorter exciter wheel is more sensitive to axial vibrations. Therefore, a vehicle equipped with this exciter wheel was found to have the most severe noise signal problem and was selected for experimental noise evaluation of sensor prototypes.

The voltage signal can only be generated in the coil as a result of a change in the flux linked with the coil. If the analyzed sensor is installed on a vehicle and the vehicle is stationary, this change in flux linkages can result from engine vibration, causing a relative motion between the sensor coil and the transmission speed sensor components of the sensor assembly: magnet, washers, coil and center pole, as shown in Figure 2.81, or externally between the sensor assembly and the exciter toothed wheel. Therefore, it is necessary to determine the noise contribution in each case to find the appropriate remedies. The first step is to mechanically couple, by cementing all internal sensor components, and measure noise signal on a relatively large number of sensors (50). A large number of speed sensors should be tested because of unrepeatable test conditions. In the examined case, cementing internal parts resulted in 30% of noise reduction. It was assumed that the remaining 70% of their noise is due to vibration of the exciter wheel with respect to the speed sensor assembly, as presented in Figure 2.81, which can be reduced by using tighter exciter wheel tolerances. However, cementing components and tightening the tolerances are both costly alternatives, so we started looking for other solutions.

Three areas of the sensor geometry were considered — geometry of the center pole, coil design, and air gap length. Unfortunately, any changes in the pole design that were considered show no measurable improvements in the v_n/v signal ratio. The coil design study was conducted for full available coil space (window) utilization with different coil wire sizes [American wire gauge (AWG)]. The results of these considerations are presented in Figure 2.82. The noise-to-signal ratio v_n/v is reduced for thicker wire.

The influence of the length of the air gap between the sensor and the sensor assembly was investigated. Figure 2.83 presents the results of this study. It was found that the noise decreases three times faster than the signal as the air gap increases. Therefore, this can be considered a very effective way to reduce noise. As shown in Figure 2.84, increasing the air gap from 0.9×10^{-3} m to 1.2×10^{-3} m reduces the noise from 0.5 V to the specified 0.15 V.

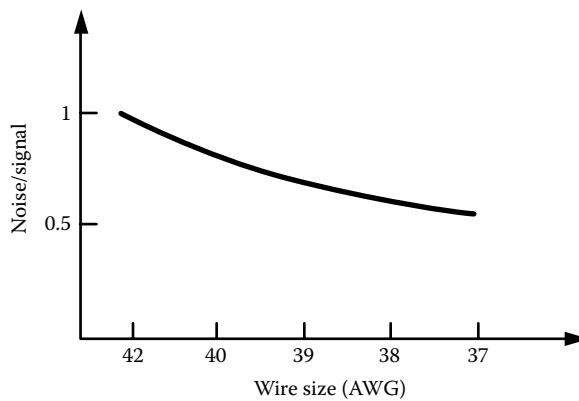


FIGURE 2.82
Noise/signal ratio vs. wire size.

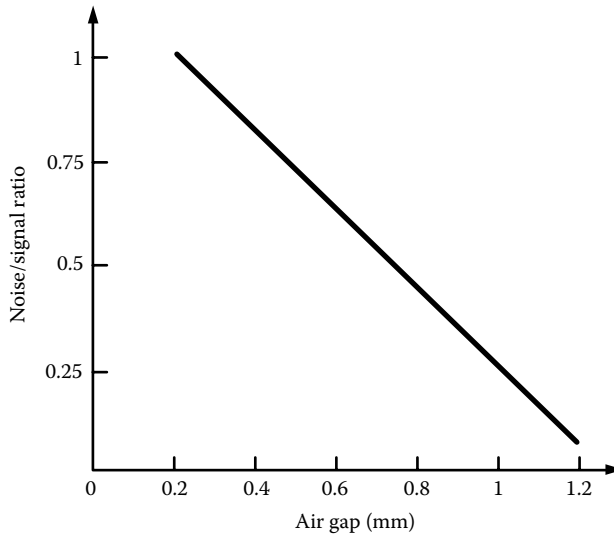


FIGURE 2.83
Noise/signal ratio vs. air gap length.

For the same change in the air gap, the signal is decreased from 0.87 V to 0.68 V, as shown in Figure 2.85.

Comparing the slopes of this characteristic indicates that the signal is less dependent on air gap changes. This can be explained by the different nature of generating signal and noise, as shown in Equation 2.37 and Equation 2.38. Even though the sensor signal level is determined by the geometry of the wheel, its angular speed, and the length of the gap, the noise is generated due to vibrations that cause variations of magnetic permeance that are independent of the wheel geometry and depend mainly on the air gap length and its variation with respect to the time. Therefore, the noise is more sensitive to air gap variation than the sensor signal.

On the basis of these results, a new air gap of 1.2×10^{-3} m was proposed to replace the existing 0.9×10^{-3} m gap. It provides a signal of 0.68 V and a reduced noise level of 0.15 V. Implementing this change does not affect the production cost and the manufacturing procedures of the device in any adversarial way. On the contrary, because of the resulting

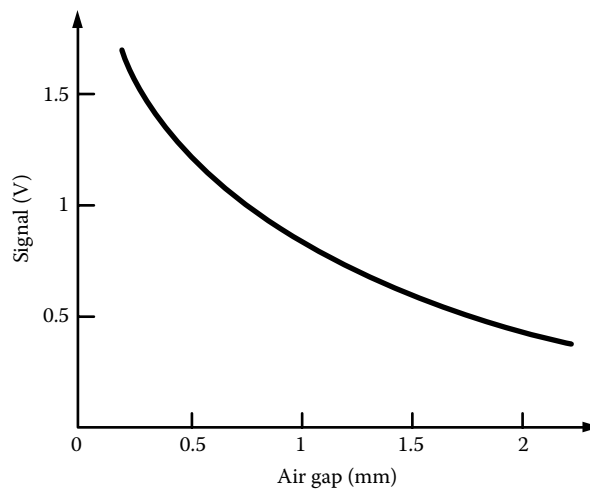


FIGURE 2.84
Noise vs. air gap length.

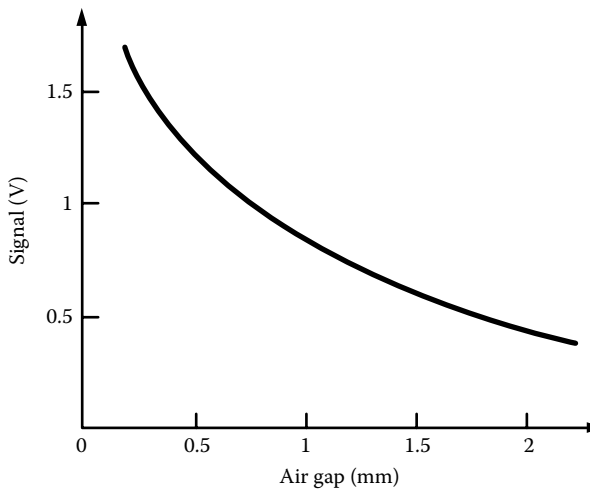


FIGURE 2.85
Sensor signal vs. air gap length.

low sensitivity to noise, the manufacturer may relax some tolerance requirements for the sensor parts and the wheel, which may lead to lower costs.

Example 2.1

Estimate the sensor signal and flux utilization of the front-magnet sensor with no changes in the coil and magnet for an E-shaped structure if the sensor with partial magnetic structure (having a central pole and shim) indicated a signal value of 0.44 V at 1.2×10^{-3} m air gap and 51 r/min exciter wheel speed.

Step 1. Calculate Signal Performance

The solution is based on Table 2.3. The signal sensitivity ratio of the E-shaped sensor to a sensor with partial magnetic structure having center pole and shim is:

$$\frac{S_{vE}}{S_{vp}} = \frac{0.54}{0.32} = 1.69$$

Because the volume of both sensors is the same, from Equation 2.11 we have:

$$\frac{S_{vp}}{S_{vE}} = \frac{V_{sp}}{V_s} \frac{V_s}{V_{sE}} = \frac{V_{sp}}{V_{sE}}$$

Substituting for the signal value, the sensor model signal of $v_{sp} = 0.44$ V and combining the calculated ratio, we have the E-shaped sensor signal estimated performance:

$$S_{vE} = \frac{0.54}{0.32} v_{sp} = \frac{0.54}{0.32} \times 0.44 = 0.743 \text{ V}$$

Verify this value for the E-shaped sensor in Table 2.3.

Step 2. Calculate Flux Efficiency

From Equation 2.12, we can estimate flux utilization:

$$s_{\phi p} = \frac{\Delta\phi_p}{\phi_o} \text{ and } s_{\phi E} = \frac{\Delta\phi_E}{\phi_o}$$

Assuming the same magnet generates the same flux ϕ_o , we can calculate the flux efficiency improvement based on the ratio from Table 2.3:

$$\frac{S_{\phi E}}{S_{\phi p}} = \frac{\Delta\phi_E}{\phi_o} \times \frac{\phi_o}{\Delta\phi_p} = \frac{1.35}{1.10} = 1.23$$

The flux utilization of the E-shaped sensor is 23% better than the sensor model and it would provide a signal of 0.743 V. This concludes the solution for Example 2.1.

Example 2.2

Calculate the two-magnet VR sensor signal for ABS and verify which of the ABS system requirements can be satisfied: Bosch = 7 mV/Hz, GM6 = 5.5 mV/Hz, or Teves = 3.75

mV/Hz. The sensor test was performed at the required air gap of 1.0×10^{-3} m with a speed of 127 r/min. The signal level, provided from Figure 2.56, is based on test results and sensor analysis. The signal of 1.1 V for nonconventional (nonsupportive magnets) and 0.4 V for conventional sensor-wheel arrangements (supportive magnets) is provided by Figure 2.56.

Step 1. Signal Calculations of Two-Magnet VR Sensor Nonsupportive Magnet Configuration

The electrical frequency of the sensor signal is:

$$f_{el} = f_{mech} \times N_t = \frac{127}{60} \times 47 = 99.48 \text{ Hz}$$

where $N_t = 47$ is the number of exciter wheel teeth. The sensor signal value of 1.1 V can be obtained from Figure 2.56 for nonsupportive magnets at the required air gap of 1.0×10^{-3} m and it corresponds to an already calculated frequency of operation:

$$1100 \text{ mV} \equiv 99.48 \text{ Hz}$$

Therefore, the signal achieved by the nonsupportive sensor at 1 Hz is:

$$v_1 = \frac{1100}{99.48} \left[\frac{\text{mV}}{\text{Hz}} \right] = 11.06 \left[\frac{\text{mV}}{\text{Hz}} \right]$$

Signal v_1 achieved by the nonsupportive sensor structure meets all requirements. This sensor has satisfied all (Bosch = 7 mV/Hz, GM6 = 5.5 mV/Hz, and Teves = 3.75 mV/Hz) system requirements.

Step 2. Signal Calculations of Two-Magnet VR Sensor Supportive Magnet Configuration

The electrical frequency of the sensor signal is:

$$f_{el} = f_{mech} \times N_t = \frac{127}{60} \times 47 = 99.48 \text{ Hz}$$

As Figure 2.56 shows, at an air gap of 1.0×10^{-3} m the signal value for supportive magnets equals 0.4 V and that corresponds to the value of frequency of operation.

Because $0.4 \text{ V} \equiv 99.48 \text{ Hz}$, the signal achieved by the nonsupportive sensor at 1 Hz is:

$$v_2 = \frac{400}{99.48} \left[\frac{\text{mV}}{\text{Hz}} \right] = 4.02 \left[\frac{\text{mV}}{\text{Hz}} \right]$$

Signal v_2 achieved by the supportive sensor structure meets only Teves = 3.75 mV/Hz system requirements. This sensor did not satisfy Bosch = 7 mV/Hz and GM6 = 5.5 mV/Hz requirements. This concludes the solution for Example 2.2.

Example 2.3

Calculate the signal value generated by the rectangular VR sensor 3 structure with inserted magnet, as presented in Figure 2.16. The FE software simulations, as presented in Figure 2.18, have provided the maximum flux-linkage value (corresponding to a tooth with maximum permeance value) of 2089×10^8 Wb/cm and the minimum flux value (corresponding to a slot with minimum permeance value) of 2029.5×10^8 Wb/cm. The sensor thickness is 1.3 cm with 4000 turns and is based on the MQ2 magnet. Assume 100 r/min speed rotation of the exciter wheel having 40 teeth.

The mechanical frequency of rotation is calculated as:

$$\omega = 2\pi f_{\text{mech}} = 2\pi \frac{100}{60} = 10.47 \text{ rad/s}$$

and the mechanical angular displacement is calculated as:

$$\Delta\theta = \frac{2\pi}{2 \times N_t} = \frac{2\pi}{2 \times 40} = 0.0785 \text{ rad}$$

The signal value can be calculated from Equation 2.25:

$$v(t) = -N\omega \frac{\Delta\phi \times 1.3}{\Delta\theta} = 4000 \times 10.47 \frac{(2089 \times 10^{-8} - 2029.5 \times 10^{-8}) \times 1.3}{0.0785} = 0.4127 \text{ V}$$

Because the flux-linkage values were provided in Wb/cm due to the FE software limitation, we need to multiply that value by the real thickness of the sensor of 1.3 cm. The calculated value of the sensor signal corresponds to the measured value of the sensor 3 structure from Table 2.2. This concludes the solution for Example 2.3.

3

Linear Actuators

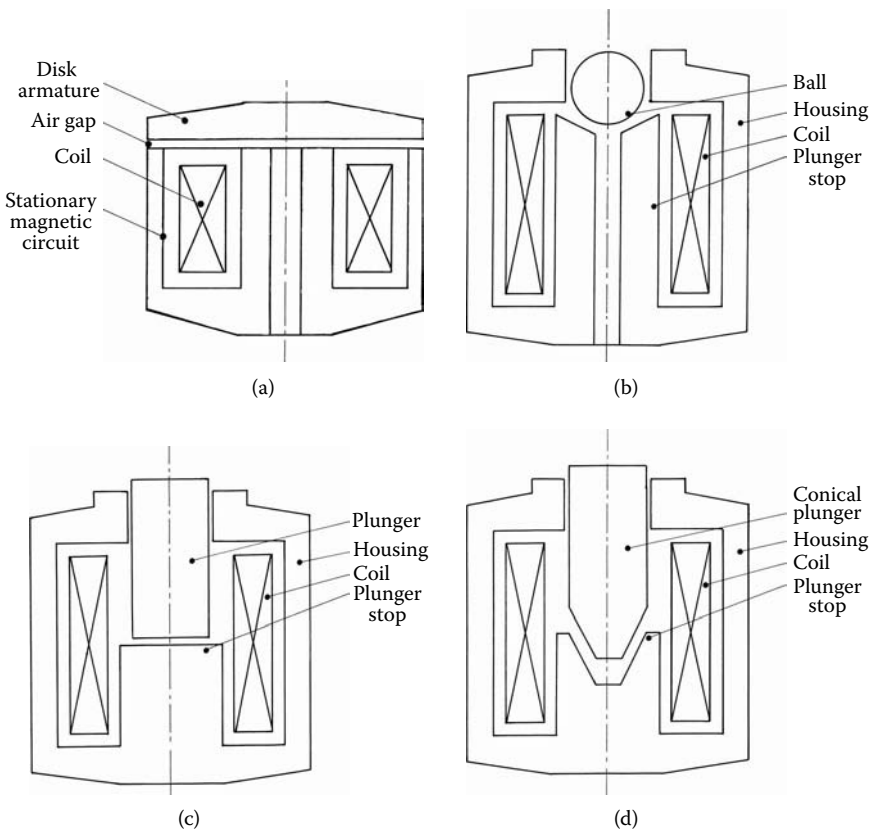
Fast-acting solenoids are finding increasingly more new industrial applications and the demand for electronically controlled magnetic linear actuators is expanding rapidly, particularly in the automotive industry. These solenoids are found in a variety of sizes, configurations, and load requirements as the use of electronics increases to replace conventional hydraulics and mechanical systems with modern mechatronics. They are utilized as fuel injectors, exhaust gas recirculation (EGR) and transmission control solenoids, fuel pumps, compressor solenoids, speed-sensitive steering system solenoids, active suspension systems, air bag deployment, etc. From the armature design point of view, linear solenoids are divided into four families of solenoid actuator geometries — solenoids with disk, plunger, conical, and ball armatures — as shown in Figure 3.1.

A variety of geometries have mixed configurations taking advantage of armature geometry features. Each of these basic geometries is discussed separately because of their different advantages, helping to serve different purposes. The selection of geometry is the first and most important step in the design application; therefore, thoroughly understanding the pros and cons of each solenoid type is critical. A conventional linear actuator consists of an armature, magnetic-circuit housing with a central rod serving as an armature stop, a return spring, and a coil.

Typically, solenoids are PWM driven and the variation of the duty cycle of the voltage applied to the solenoid results in a smooth operation. In order to obtain a wide range of duty cycle operations at a given frequency, the response time of the actuator should be minimized. It should be a design target stressed through the actuator dynamic analysis. The variables of the optimization study are the solenoid geometry, magnetic material properties, and electromagnetic circuit including coil parameters. Utilized mathematical models would couple the electrical, mechanical, hydraulic, and magnetic systems of these devices by taking into account the nonlinearity of the magnetic materials, eddy currents, and motion (Boldea 2001).

3.1 Mathematical Model for Linear Actuators

A transient 2D FE model for fast-acting PWM solenoid actuators is presented in this chapter. The unique feature of this model is the coupling of the electrical, mechanical, and magnetic systems of solenoid actuators. Transient calculations based upon 2D FE magnetic field solutions, including nonlinearity of magnetic materials, eddy currents, and motion, are compared with test results for a ball-type solenoid. Flexibility of the software allows one to apply it to any type of PWM solenoid actuator with any desired excitation profile.

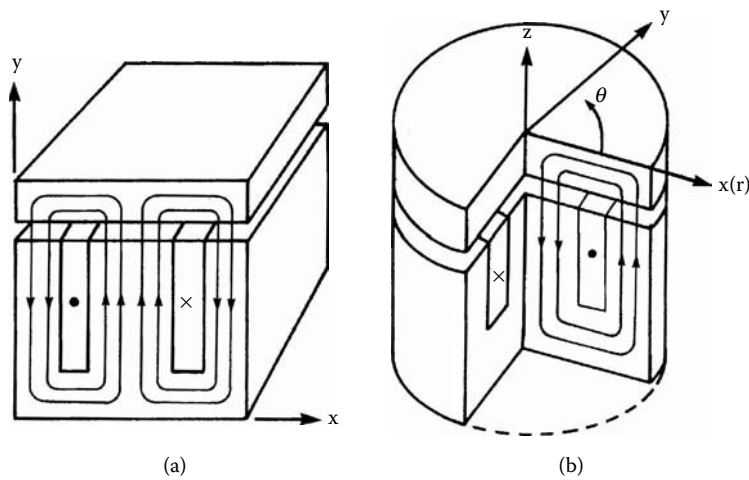
**FIGURE 3.1**

Linear solenoid actuators with different armatures: (a) disk, (b) plunger, (c) conical, (d) ball. (Courtesy of Delphi Corp.)

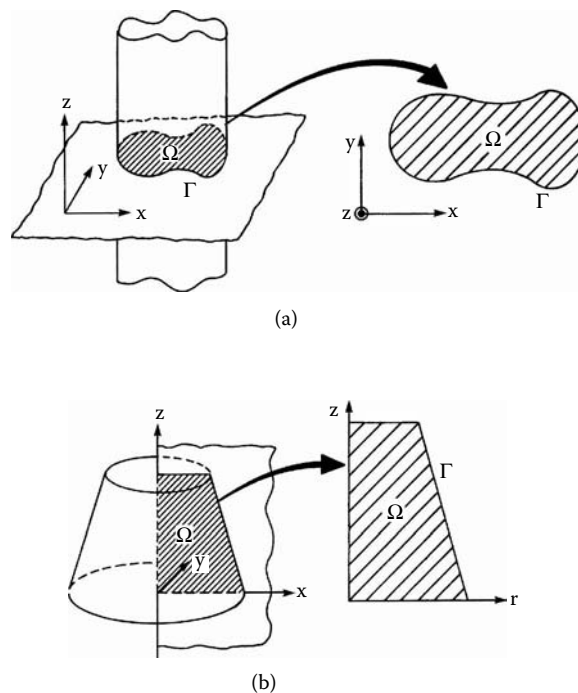
3.1.1 Symmetrical Analysis of Electromagnetic Devices

Many typical electromagnetic devices can be analyzed based on a 2D FE software system for magnetic field analysis in rectangular and cylindrical coordinates, as presented in Figure 3.2 (Nehl et al. 1988, Hammond 1978). With the assumption that end effects are negligible, it can solve field equations of both the rectangular coordinates for most of the conventional solenoids and a variety of inductors and transformers, as well as conventional rotary machines. In these devices, the high permeabilities of the magnetic cores force a majority of the magnetic flux into the x - y plane, perpendicular to the direction of excitation. For these problems it is sufficient to analyze a slice of unit thickness parallel to the x - y plane. Furthermore, if motion is restricted to the vertical (x) axis, the current densities and the vector potential are both z directed, while the magnetic flux and the flux densities lie in the x - y plane.

The majority of solenoids and injectors, as well as a large number of small inductors and transformers for power processing applications, are axisymmetric about one axis, as shown in Figure 3.2(b). In these cases, the excitation and the vector potential are cylindrical with respect to the axis of symmetry and the resulting flux and flux density exists in planes radial to the axis of symmetry. Note that fields are independent of the angle θ . Consequently, one can restrict the analysis to a pie-shaped slice of the device of unit angle in the θ direction.

**FIGURE 3.2**

Symmetrical analysis of electromagnetic devices: (a) rectangular coordinates, (b) cylindrical coordinates. (Courtesy of Delphi Corp.)

**FIGURE 3.3**

Field regions for (a) rectangular and (b) cylindrical coordinates. (Courtesy of Delphi Corp.)

Neglecting the end effect for long devices or using axisymmetry in cylindrical devices allows us to reduce a 3D geometry into a 2D region Ω with the boundary Γ , as shown in Figure 3.3. The governing field equation must be satisfied everywhere in the region Ω . In order to complete the specification for the field problem that would allow reduction of a 3D geometry into a 2D region, one must confirm that boundary conditions are specified

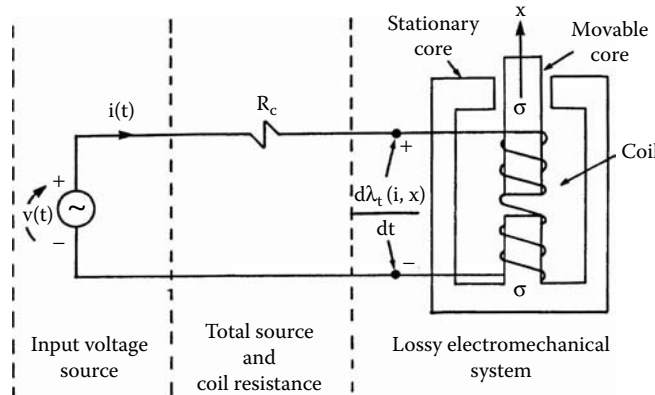


FIGURE 3.4

Lumped model parameter of a mechatronic system. (Courtesy of Delphi Corp.)

properly for zero-flux crossing (homogeneous Dirichlet), flux crossing (homogeneous Neumann), and periodicity.

3.1.2 Electrical Network Equations

In the majority of applications, the voltage applied to the terminal of a device as a function of time is specified rather than the transient current. In such cases, the field solution must be coupled to the external electrical network that provides the excitation. Problems involving mechanical motion add another source of coupling, which must be accounted for. This chapter provides equations describing the dynamics of the electrical network. This is followed by equations of motion and finally the coupling between the field equations, the electrical network, and the mechanical network, which are presented in terms of the system power balance.

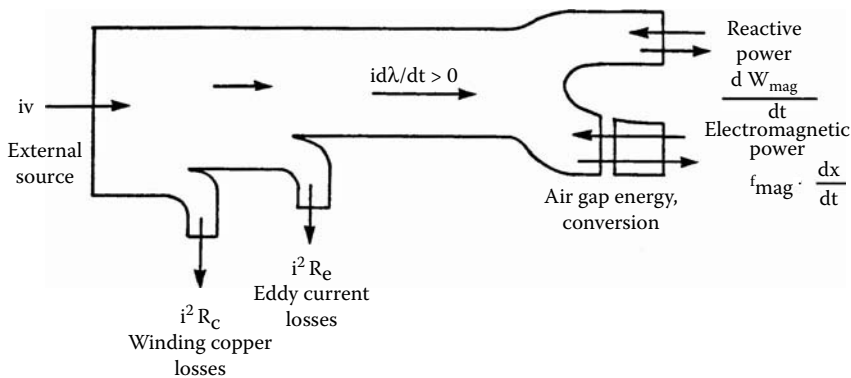
The lumped-parameter electrical network model of a single winding mechatronic (electromechanical or electromagnetic) device is shown in Figure 3.4. The model consists of three components; an ideal voltage source, a resistor, and a lossy electromechanical system. The voltage source is assumed to be a known function of time and, therefore, independent of the state of the system. The resistor accounts for the ohmic losses in the source and the winding of the device. The state of the system is governed by the differential equation that couples electric and magnetic models through the voltage equation:

$$v = iR_c + \frac{d\lambda_t}{dt} \quad (3.1)$$

where v is the specified voltage source, i is the winding current, R_c is the total ohmic resistance, and λ_t is the total flux linkage of the winding.

The time derivative of the total flux system flux linkage, given in this equation, is the total induced voltage of the device. This voltage includes components due to induced eddy currents, time variations in the applied source voltage, and motion. The total induced voltage can, therefore, be split into two components:

$$\frac{d\lambda_t}{dt} = iR_e + \frac{d\lambda}{dt} \quad (3.2)$$

**FIGURE 3.5**

Power flow diagram of an electromechanical system. (Courtesy of Delphi Corp.)

where R_e is the reflected resistance due to induced eddy currents and $\lambda(i,x)$ is an equivalent flux linkage of the winding assuming a lossless magnetic circuit.

Note that this flux linkage is a function of winding current $i(t)$ and of the position $x(t)$ of the moving part in the case of the motion problem. Substituting this expression into Equation 3.1 and multiplying both sides by the winding current i yields the instantaneous power balance of the electromechanical system as follows:

$$iv = i^2 R_c + i^2 R_e + i \frac{d\lambda}{dt} \quad (3.3)$$

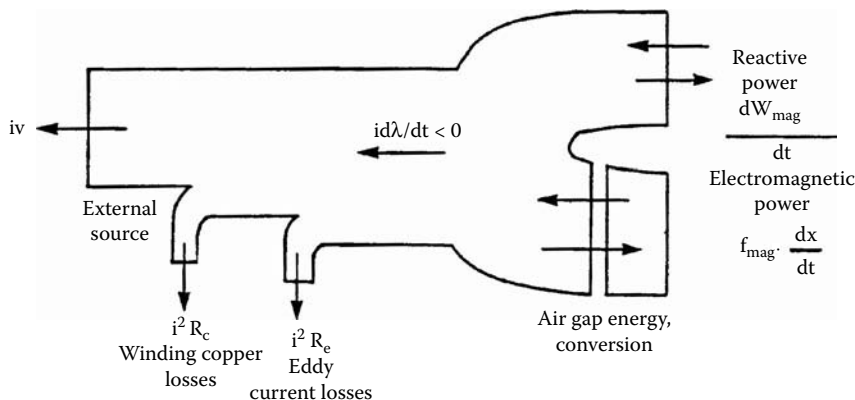
This power balance can also be expressed in terms of the rate of change of stored magnetic energy and the mechanical power (White and Woodson 1959) as:

$$iv = i^2 R_c + i^2 R_e + \frac{dW_{mag}}{dt} + F_{mag} \frac{dx}{dt} \quad (3.4)$$

where W_{mag} is the total stored magnetic energy and F_{mag} is the magnetic force on the moving part.

The interpretation of the various terms in these power balance equations is given in the two power flow diagrams of Figure 3.5 and Figure 3.6. Figure 3.5 illustrates the power flow when power is consumed by the coil. In this case, the power supplied by the external source enters on the left. The amount of input power is first reduced by ohmic or copper losses of the coil winding. Next, the total reflected eddy current losses are subtracted from this amount. The remaining power, $id\lambda/dt$, is available for conversion to mechanical output (the electromechanical power) or to produce a net rate of change in stored magnetic energy (reactive power). This situation is reversed when the power flow changes direction, that is, when the coil supplies the power to the external source, as shown in Figure 3.6. In this case, the sum of the reactive and electromagnetic powers, $id\lambda/dt$, is negative. This indicates that the coil is supplying power to the external source. Consequently, the power available at the coil terminals must be less than $id\lambda/dt$.

The relationship between the derivative terms of Equation 3.3 and Equation 3.4 can be deduced by applying the chain rule to both equations and comparing terms. This yields the following:

**FIGURE 3.6**

Power flow diagram of an electromechanical system. (Courtesy of Delphi Corp.)

$$i \frac{\partial \lambda}{\partial i} \frac{di}{dt} = \frac{\partial W_{mag}}{\partial i} \frac{di}{dt} \quad (3.5)$$

and

$$i \frac{\partial \lambda}{\partial x} \frac{dx}{dt} = \left(\frac{\partial W_{mag}}{\partial x} + F_{mag} \right) \frac{dx}{dt} \quad (3.6)$$

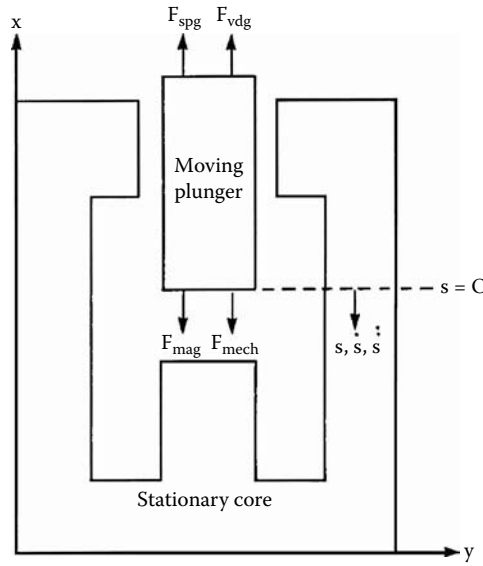
Inspection of these two equations reveals that the first represents the rate of change of the stored magnetic energy due to changes in the winding current, and the second accounts for both the energy conversion and the rate of change in the stored magnetic energy due to motion. To simplify the notation, the five power terms appearing in the system power balance, Equation 3.4, will be identified as follows:

$$P_s = P_c + P_e + P_r + P_{em} \quad (3.7)$$

where P_s is the source power, P_c is the power loss due to winding resistance, P_e is the eddy current loss, P_r is the rate of change in the stored magnetic energy (reactive power), and P_{em} is the rate of energy conversion (electromagnetic power).

3.1.3 Mechanical Equations

Problems involving mechanical motion require additional state equations to describe the dynamics of the moving masses. The motion is usually restricted to one axis and is used in the dynamic analysis of solenoids, injectors, and linear actuators. The assumed positive references for distance, velocity, and force are provided in Figure 3.7. Note that the positive direction for the position, velocity, and acceleration is in the negative x direction. It is assumed that the initial position of the moving region (plunger) is the point at which the distance s is equal to zero. The sum of all forces acting on a body along the unconstrained portion of the x axis yields the accelerating force on the body. In this region, the net

**FIGURE 3.7**

Force references for motion problems. (Courtesy of Delphi Corp.)

mechanical accelerating force is the result of the magnetic, spring, and viscous forces acting on the moving body as follows:

$$F_{\text{mech}} = F_{\text{mag}} - F_{\text{spg}} - F_{\text{vdg}} \quad (3.8)$$

where F_{mech} is the net mechanical accelerating force, F_{mag} is the magnetic force, F_s is the total spring force, and F_{vdg} is the viscous damping force.

The spring force acting on the moving part consists of two components. The first is a specified preload force, and the second is the normal spring force given by the product of the spring constant k and the deflection s . It is assumed that the deflection of the spring and the position of the moving part are identical and defined by the variable s , as presented in Figure 3.7. The magnetic force acting on the movable body can be determined by using air gap flux density or by integrating the Maxwell stress tensor over the surface of the body. Each of these methods will be discussed in Chapter 4. The calculated magnetic force F_{mag} is one component in the equation of motion that takes into account the moving mass, the spring forces, and viscous damping, as presented in Equation 3.8:

$$F_{\text{mag}} = m \frac{d^2s}{dt^2} + c \frac{ds}{dt} + ks + F_{\text{pl}} \quad (3.9)$$

where s is the position of the moving armature, m is the total mass of all moving parts including at least half of the spring mass, k is the spring constant, c is the viscous damping coefficient, and F_{pl} is the spring preload.

The instantaneous powers associated with the mechanical subsystem can be now calculated by multiplying the forces acting on the moving body by the velocity of this body. Solving Equation 3.8 and multiplying it by the velocity \dot{s} yields the power balance for the mechanical subsystem:

$$P_{em} = P_{mech} + P_{spg} + P_{vdg} \quad (3.10)$$

where P_{em} is the electromagnetic power, P_{mech} is net mechanical power, P_{spg} is the spring power, and P_{vdg} is the viscous damping power.

Comparison of the power balance for the electromagnetic and mechanical subsystems, Equation 3.7 and Equation 3.10, respectively, reveals the coupling of these systems via the electromagnetic power. This term represents the rate of energy conversion between the two systems due to the electromagnetic coupling between the stationary and moving parts of the magnetic circuit. Combining Equation 3.7 and Equation 3.10 yields the overall system power balance:

$$P_s = P_c + P_e + P_r + P_{mech} + P_{spg} + P_{vdg} \quad (3.11)$$

Note that ohmic, eddy current, and viscous damping terms must always be positive because they represent the dissipative mechanisms (sinks) of the system. The reactive, spring, and net mechanical powers, however, may be positive or negative (sinks or sources) depending on the state of the system. Conversely, the input or source power is positive when the source delivers power to the system and negative when the system delivers power to the source.

3.1.4 Magnetic Forces

The coupling between the electromagnetic and mechanical components of an electromechanical device manifests itself in the form of magnetic forces exerted on the various parts of the magnetic circuit. The dynamic simulation of such a device, therefore, requires accurate methods for calculating the magnetic force. The conventional method for calculating the force limits its range of applications and its accuracy. In this approach, it is assumed that the faces of the stationary and moving parts are parallel and that the length of the air gap (distance between the faces) is small. Under this assumption, the fields are perpendicular to the face of the moving part and the amount of fringing flux is small. Figure 3.8(a) shows a solenoid device, which satisfies these simplifying assumptions. In such cases, the magnetic force is proportional to the square of the flux density multiplied by the area of the air gap, as follows:

$$F_{mag} = \frac{B_g^2 A_g}{2\mu_0} \quad (3.12)$$

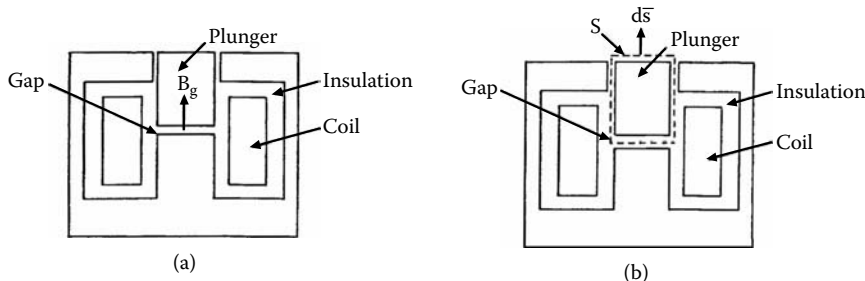


FIGURE 3.8

Comparison of methods for force calculations: (a) conventional method, (b) accurate method. (Courtesy of Delphi Corp.)

where F_{mag} is the magnetic force, B_g is the flux density in the air gap, A_g is the area of the air gap, and $\mu_0 = 4\pi \times 10^{-7} \text{ H/m}$ is the permeability of the free space (air).

Note that in this method only the main air gap field of the plunger face in Figure 3.8(a) is considered. Therefore, the influence of leakage field and “pull-back” phenomena created by the field in parasitic air gap of the plunger is ignored. This method may be used in a simple calculation based on the lumped-parameter model. The analysis of solenoids with tapered or ball-shaped plungers, for example, requires a more accurate method for force calculation, one that will take into account the total field distribution over the surface of the moving part. The magnetic force calculations are based on the Maxwell stress tensor over the surface of the plunger and along the dashed line in Figure 3.8(b), defined by:

$$F_T = \left[\iint_S \bar{T} \cdot d\bar{s} \right] \cdot \left[-\bar{a}_x \right] \quad (3.13)$$

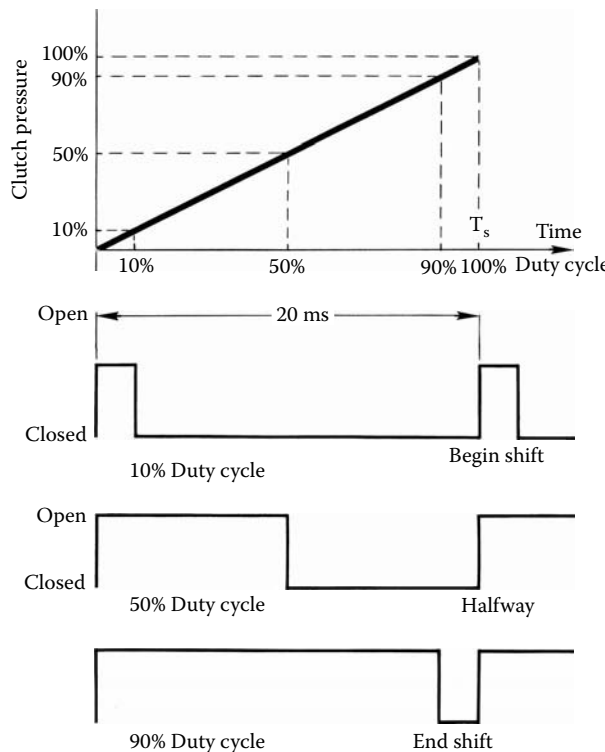
where F_T is the magnetic force, \bar{T} is the Maxwell stress tensor in dyadic form, \bar{a}_x is a unit vector in the vertical (x) direction, and S is the surface of integration.

The integral expression appearing in Equation 3.13 yields the total magnetic force exerted on the body contained within the surface of integration S . Because motion is constrained to the vertical or x axis, only the vertical component of this total force is of interest. This component of force is obtained by the dot product of the total force with the vertical unit vector, as given in Equation 3.13. The negative sign appearing in this equation is due to the assumed positive reference for the magnetic component of force, as presented in Figure 3.7. The surface of integration S completely encloses the moving part, as shown by the dashed line in Figure 3.8(b). The exact path of this integration is not important as long as the moving part is completely enclosed and the path encloses no other magnetizable regions. Therefore, the magnetic force calculated this way includes the influence of all fields impinging on the moving part.

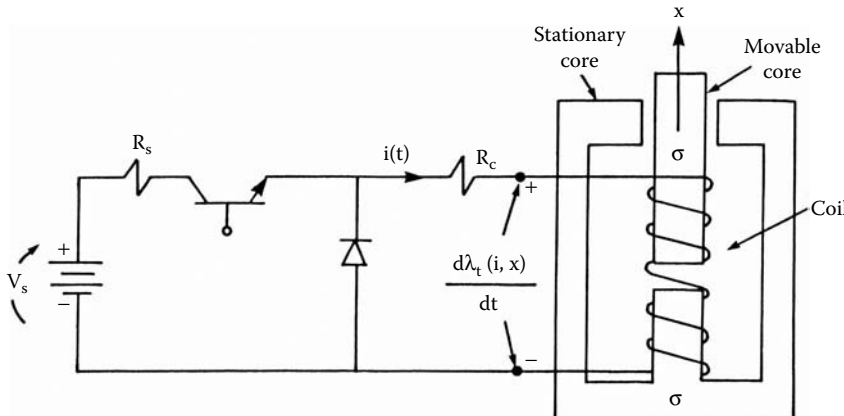
3.1.5 PWM Analysis

A PWM voltage source is required for the fast-acting solenoids to achieve smooth operation. This is particularly important to control the average value of the applied voltage and the variation of the duty cycle of the voltage applied to the solenoid. The result is smooth control of the fluid pressure. Figure 3.9 shows the variation of the fluid pressure as a function of the duty cycle and sequence of pulses applied to the solenoid with a frequency of 50.0 Hz (20.0 ms). To obtain a wide range of duty cycle operations (10–90%) at this frequency, as presented in Figure 3.9, the response time of the actuator should be less than 2.0 ms. The current level in the solenoid is controlled by superposing pulses to the applied voltage pulse having a subfrequency in the range of 500.0 Hz. These phenomena are also included in our analytical model.

The analysis of the fast-operating solenoid from the PWM voltage sources requires a mathematical model, which simulates power electronics, as well as the mechanical and magnetic systems (Demenko and Pietrowski 2004, Demenko and Sykulski 2002, Marinova et al. 2000, Nowak and Demenko 2000, Pawlak et al. 1988, Roel Ortiz et al. 2001, Nowak 1989). The 2D FE model solves the magnetic field problem by taking into account the moving armature, eddy currents, currents due to motion, and nonlinearity of the magnetic circuit. The mechanical system of the model includes the moving masses, the spring characteristics, viscous damping, and rebound decay constants. A schematic of a typical solenoid operated from a PWM controlled voltage source is shown in Figure 3.10.

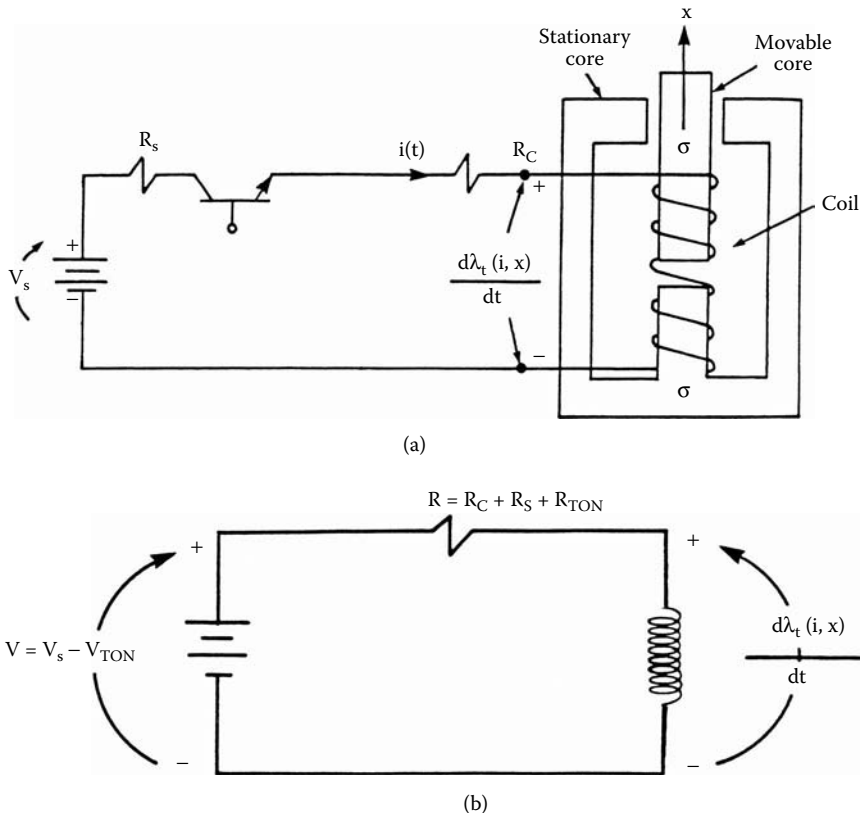
**FIGURE 3.9**

PWM to control fluid pressure. (From Pawlak, A.M. et al., *IEEE Transactions on Magnetics*, 24(1), 270–274, 1988. With permission.)

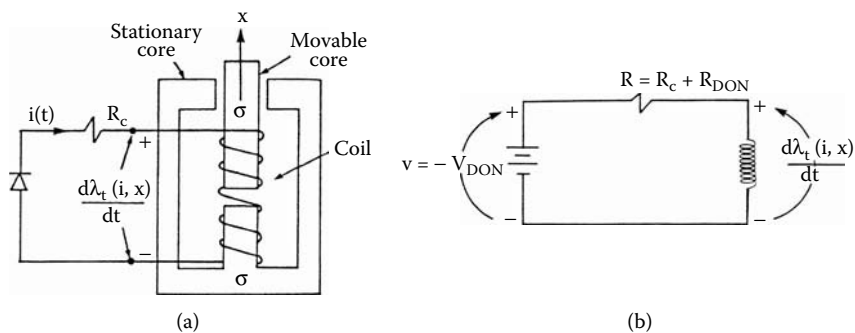
**FIGURE 3.10**

PWM voltage source operated solenoid. (From Pawlak, A.M. et al., *IEEE Transactions on Magnetics*, 24(1), 270–274, 1988. With permission.)

In automotive applications, the source is the car battery and the PWM is usually performed by a transistorized DC chopper. The power circuit switches between two states depending upon status (ON or OFF) of the chopper transistor. When the transistor is conducting (ON), the diode is reverse biased (OFF), as shown in Figure 3.11(a). In this

**FIGURE 3.11**

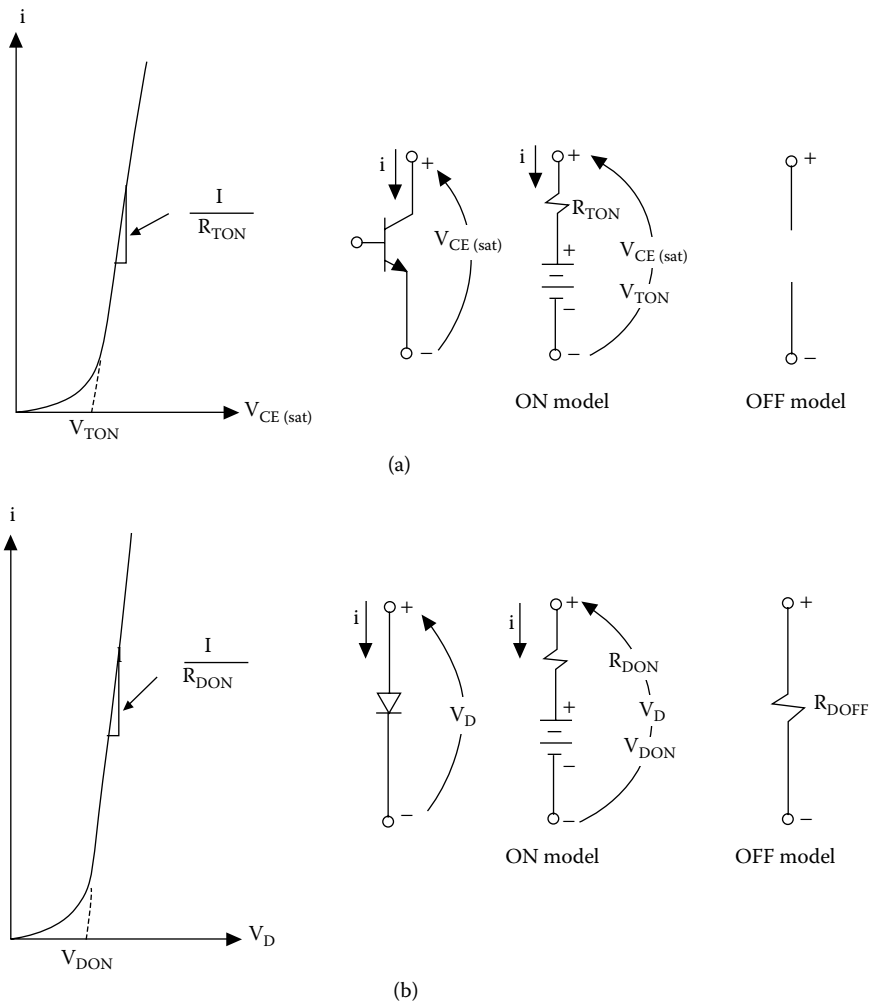
Solenoid operated from a PWM voltage source (ON state): (a) lumped-parameter model, (b) equivalent electrical network model. (From Pawlak, A.M. et al., *IEEE Transactions on Magnetics*, 24(1), 270–274, 1988. With permission.)

**FIGURE 3.12**

Solenoid operated from a PWM voltage source (ON state): (a) lumped-parameter model, (b) equivalent electrical network model. (From Pawlak, A.M. et al., *IEEE Transactions on Magnetics*, 24(1), 270–274, 1988. With permission.)

case, the DC voltage source is connected to the solenoid and the current in the coil increases provided that the source voltage is greater than the voltage induced in the coil.

The diode is forward biased (ON) whenever the transistor turns off. During this state, the source is disconnected from the solenoid, as shown in Figure 3.12(a), causing the current to decrease.

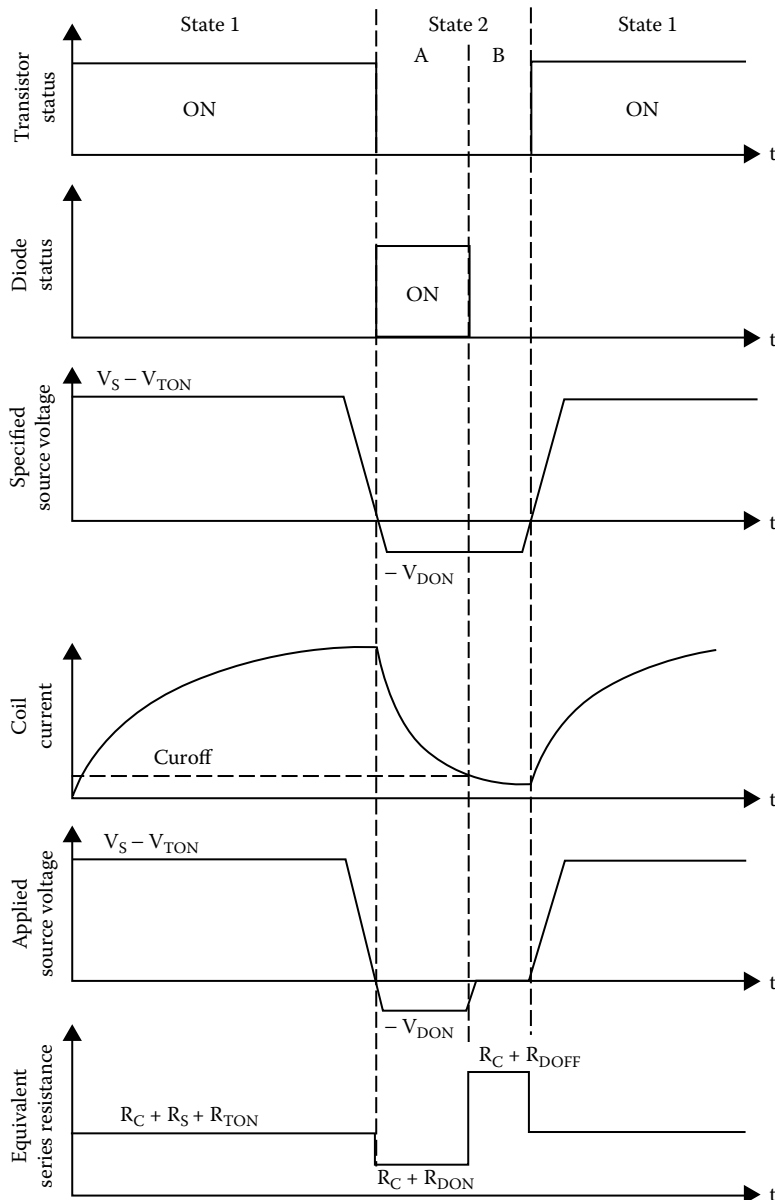
**FIGURE 3.13**

Transistor and diode models for PWM voltage source: (a) transistor model, (b) diode model. (From Pawlak, A.M. et al., *IEEE Transactions on Magnetics*, 24(1), 270–274, 1988. With permission.)

The transistors and diode models used to represent this switching action are shown in Figure 3.13(a) and Figure 3.13(b), respectively.

During the ON state, both devices are represented by a series of connected resistance and voltage source. During the OFF state, the transistor is replaced by an “open circuit,” as shown in Figure 3.13(a), thereby disconnecting the solenoid from the voltage source. The OFF state of the diode is represented by an open circuit whenever the transistor is OFF, as shown in Figure 3.13(b). The finite diode resistance is required during the OFF state of the transistor to avoid singularities with the voltage source option in the FE model.

With these simple switching models, one can replace the two states of this system, shown schematically in Figure 3.11(a) and Figure 3.12(a), with the equivalent network models of Figure 3.11(b) and Figure 3.12(b), respectively. The topologies of these network models are identical, consisting of a series of connected resistances, a voltage source, and a coil. The difference between the two models is in the values assigned to the equivalent voltage

**FIGURE 3.14**

Timing diagram for the PMW voltage source. (From Pawlak, A.M. et al., *IEEE Transactions on Magnetics*, 24(1), 270-274, 1988. With permission.)

source and resistance. The relationship between the states of the network and the equivalent voltages, resistance, and current are given in the timing diagram, Figure 3.14.

Note that the OFF state of the transistor is divided into two substates (A and B). This is necessary because a forward biased diode turns off when the current passes through zero. To simulate the behavior, the equivalent series resistance is set to a specified OFF value when the diode current drops below a specified current level CUROFF, as shown in Figure 3.14. When the diode current drops below this value, the ON diode model is replaced by the OFF diode model and the applied source voltage is set to zero.

3.1.6 Solenoid Analysis and Simulations

The typical 2D FE software system for magnetic field analysis solves Poisson's equation for the magnetic vector potential as introduced in Equation 2.7 and described in more detail in Ando et al. (2001), Ansoft (1991), Box et al. (1969), Brauer (1988), Brauer et al. (2000), Dąbrowski (1971), Demenko (1994), McBain (1981), Melgoza and Rodger (2002), Nehl et al. (1988), Silvester and Ferrari (1990), and Sykulski et al. (1995):

$$\nabla \times (v \nabla \times \bar{A}) = \bar{J}_s + \bar{J}_{pm} - \sigma \frac{\partial \bar{A}}{\partial t} + \sigma \bar{V} \times \nabla \times \bar{A} \quad (3.14)$$

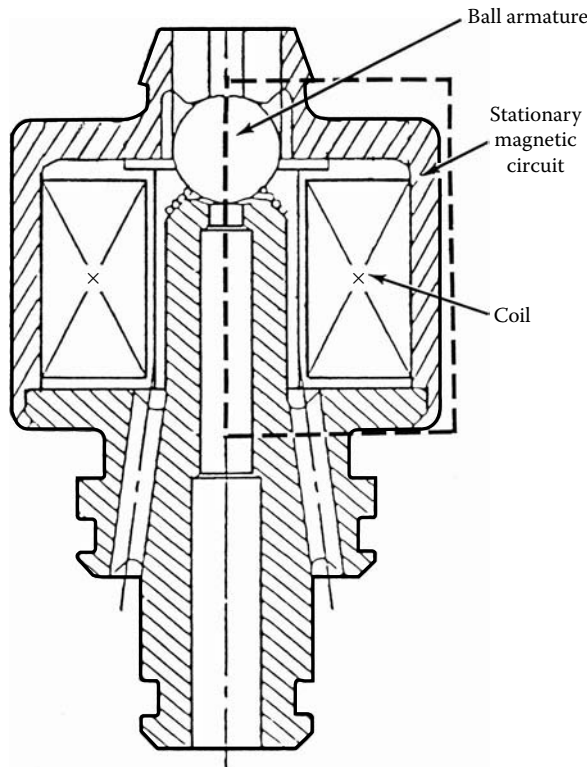
where v is the material reluctivity, \bar{A} is the magnetic vector potential, σ is the material conductivity, \bar{J}_s is the external source current density, \bar{J}_{pm} is the equivalent PM current density, and \bar{V} is the velocity of the field point.

The first term on the right-hand side of this equation is the current density due to a specified source. This includes windings excited by voltage or current source. The second term is the current density due to PMs. The third term accounts for induced currents due to possible motion of the field point with respect to the fixed coordinate reference frame.

Problems with a specified voltage source excitation require a solution of both the field problem, Equation 3.14, and the electrical network problem, Equation 3.1. This is accomplished using an iterative procedure. First, a guess at the winding current i is made based upon the value at the previous time step by means of the predictor step. Using this guess at the winding current, the field equation is solved for the vector potentials. The vector potentials are then used to calculate the total flux linkage of the winding. Using the flux linkage from the previous time step, the time derivative of the flux linkage is approximated. This information is then used to calculate the voltage v in Equation 3.1. If this voltage differs from the specified value by more than a given percentage, the winding current is recalculated using a corrector step. The iterative process is repeated until this difference meets the specified voltage tolerance. Equations 3.1, 3.9, 3.13, and 3.14 constitute a set and are solved simultaneously to obtain solutions of the dynamic behavior of the solenoid actuators.

Ball-type solenoid actuators are suitable for fluid control due to their good sealing capabilities. The solenoid, shown in Figure 3.15, has a cylindrical symmetry and consists of a ball armature, a stationary magnetic circuit, a stationary coil, and a return spring. Because of the cylindrical symmetry, only the section of the device enclosed by the dotted line in this figure needs to be modeled. The distribution of the magnetic circuit at different points in time is shown in Figure 3.16. The diffusion (penetration) of the flux into the magnetic core is clearly illustrated for these successive points in time. Actually, the ball motion does not begin until the flux penetrates the ball and the resulting force overcomes the spring preload (Bottauscio et al. 2003).

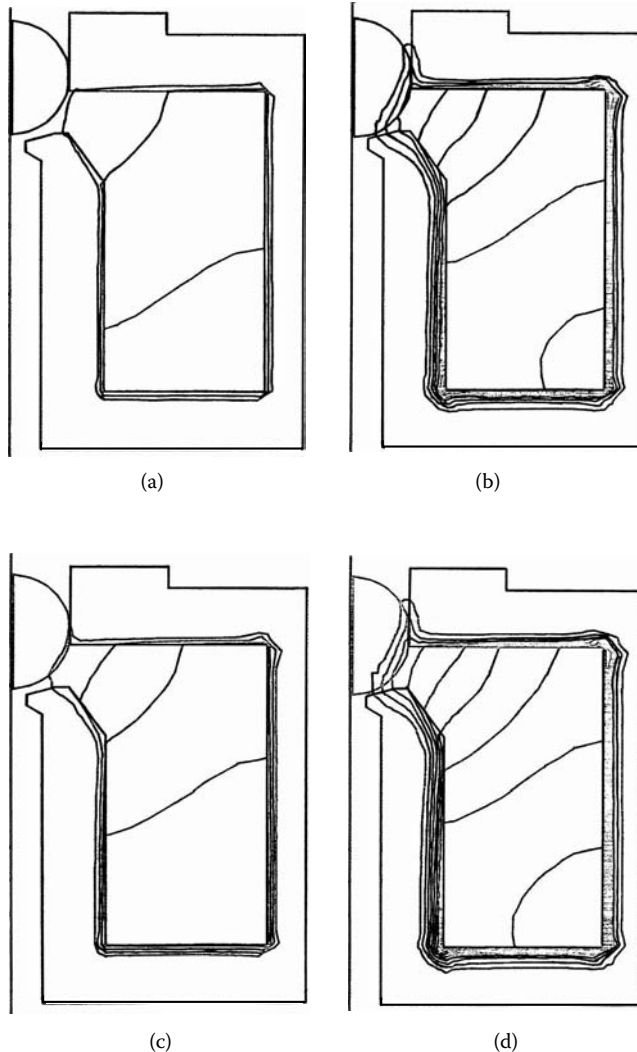
Figure 3.17 displays eight sample waveforms obtained using a software postprocessor. Included in these figures is Figure 3.17(a), which presents a specified voltage with a frequency of 50 Hz having a high subfrequency of 500 Hz imposed on a regular frequency

**FIGURE 3.15**

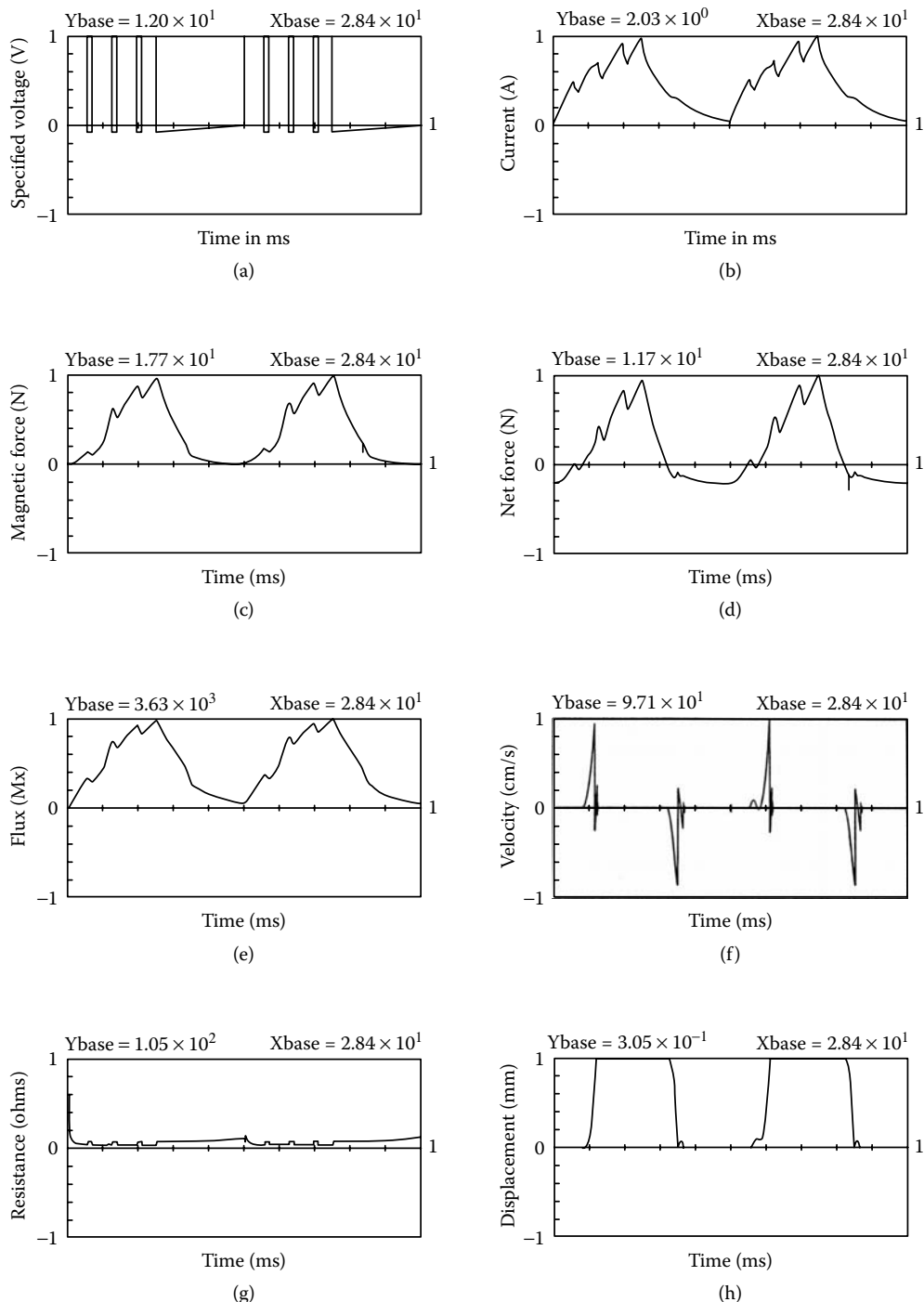
Ball-type solenoid actuator. (From Pawlak, A.M. et al., *IEEE Transactions on Magnetics*, 24(1), 270–274, 1988. With permission.)

to control the current level. Figure 3.17(b) illustrates the calculated current that shows a saw-type characteristic that limits the final current level. Both the flux crossing the main air gap and the total magnetic force on the ball shown in Figure 3.17(e) and Figure 3.17(c), respectively, have similar characteristics to the source current. The net force on the ball shown in Figure 3.17(d) is the result of the spring forces and the total magnetic forces indicating the net forces exerted on the ball with a ball velocity shown in Figure 3.17(f). The resistance vs. time and velocity vs. time are shown in Figure 3.17(g) and 3.17(h), respectively. Zero crossing of the net force identifies points where the net force changes its direction and also identifies the beginning and the end of the motion displacement, as shown in Figure 3.17(h) (Nehl et al. 1988, Pawlak 1989, Piron et al. 1999).

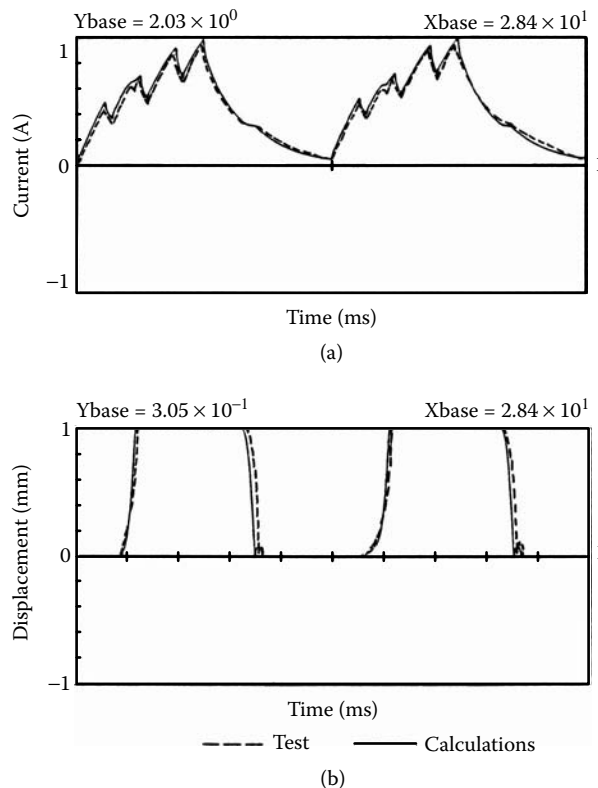
The ball-type solenoid was tested in dry conditions. With the specified voltage applied, the coil current and the armature displacement were measured using a calibrated current probe and the armature displacement was measured using a commercial proximity transducer. The test results for the current and displacement vs. time are compared with the corresponding calculated data in Figure 3.18, showing good agreement (Nehl et al. 1988).

**FIGURE 3.16**

Flux distribution of ball-type solenoid: (a) time 1.0 ms, (b) time 2.0 ms, (c) time 3.0 ms, (d) time 4.0 ms. (From Pawlak, A.M. et al., *IEEE Transactions on Magnetics*, 24(1), 270–274, 1988. With permission.)

**FIGURE 3.17**

Sample waveforms for ball-type solenoid dynamics: (a) specified voltage vs. time, (b) current vs. time, (c) magnetic force vs. time, (d) net force vs. time, (e) flux vs. time, (f) velocity vs. time, (g) resistance vs. time, (h) displacement vs. time. (From Pawlak, A.M. et al., *IEEE Transactions on Magnetics*, 24(1), 270–274, 1988. With permission.)

**FIGURE 3.18**

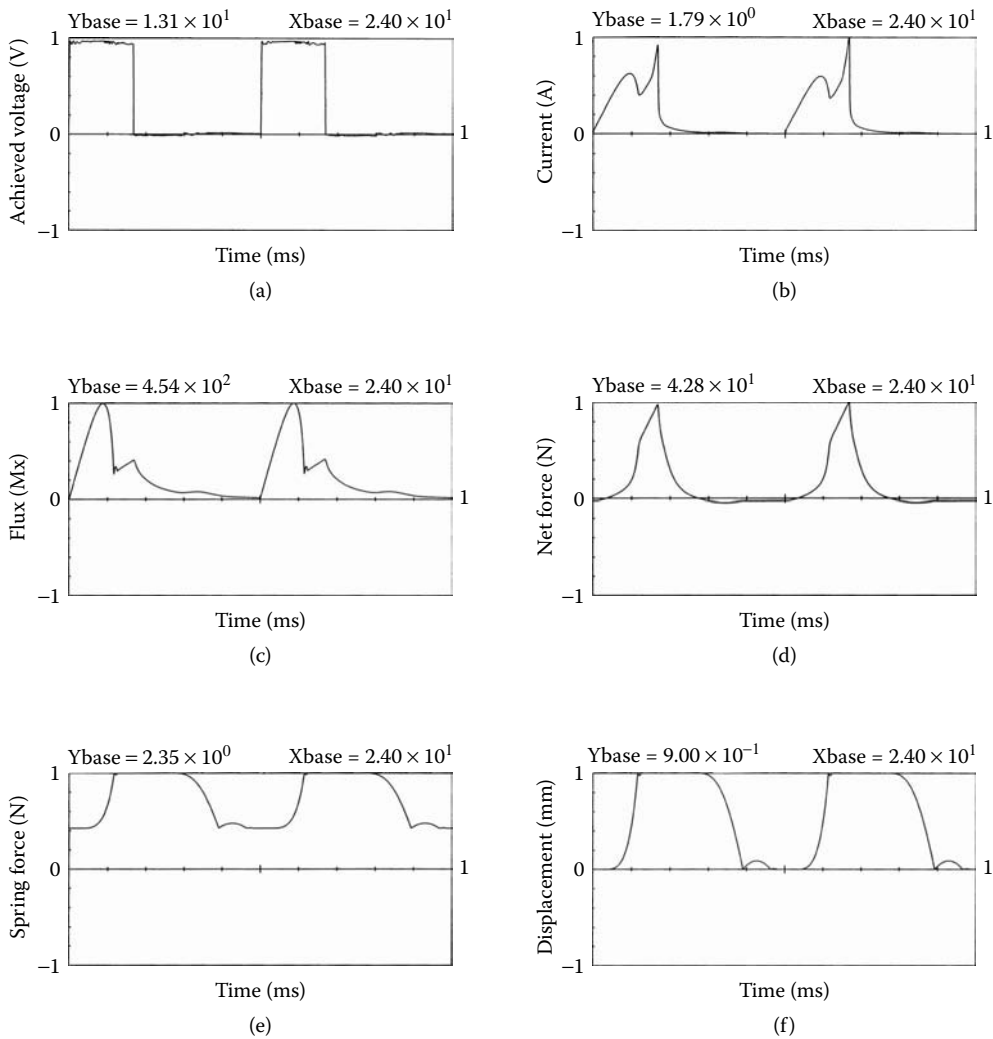
Current and displacement of ball-type solenoid analysis and test comparison: (a) current vs. time, (b) displacement vs. time. (From Pawlak, A.M. et al., *IEEE Transactions on Magnetics*, 24(1), 270–274, 1988. With permission.)

3.2 Fast-Acting Actuators

Four basic solenoid configurations with disk, plunger, conical, and ball armatures are the subjects of analysis in this chapter. Each of these configurations has unique features that predetermine applications. Pros and cons of these structures are discussed in detail. For comparison purposes, cylindrical symmetry is assigned to all the solenoid types. For the FE analysis, each solenoid is divided into a number of regions that describe the universe (air), the stationary magnetic circuit, the coil with the current source, and magnetic armature. Additionally, the main air gap region can be specified separately to maintain a linear displacement of the armature and prevent shrinking the air gap to zero, which may cause converging problems.

3.2.1 Disk Solenoids

Unlike other solenoid types, the disk solenoid configuration has double the main air gap for flux to cross, as shown in Figure 3.1(a). At the same time, it has two relatively large surfaces of inner pole and outer magnetic circuit around a coil where flux is perpendicular to its surface — at least at the small air gaps. This promotes applications with small travel

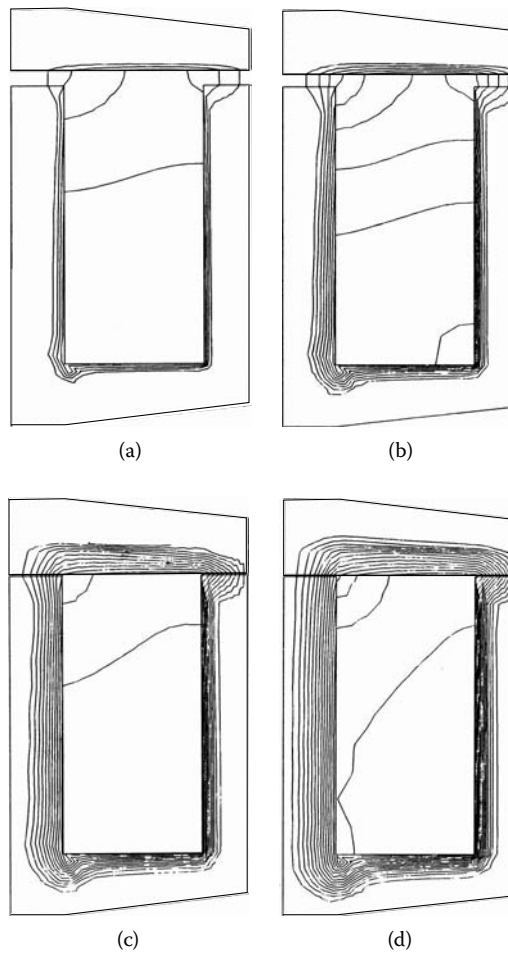
**FIGURE 3.19**

Disk solenoid magnetic flux vs. time: (a) achieved voltage vs. time, (b) current vs. time, (c) flux vs. time, (d) net force vs. time, (e) spring force vs. time, (f) displacement vs. time. (Courtesy of Delphi Corp.)

and fast action. A small travel would secure high solenoid electromagnetic efficiency, where large forces would help complete the travel distance in a relatively short period of time. Therefore, disk solenoids may find applications as injectors where all these attributes can be utilized.

The dynamic characteristics of the disk solenoid are presented in Figure 3.19(a) through Figure 3.19(f) for the input voltage, corresponding coil current, magnetic flux developed in the armature, the net force of the disk armature, the spring force, and the displacement of the armature.

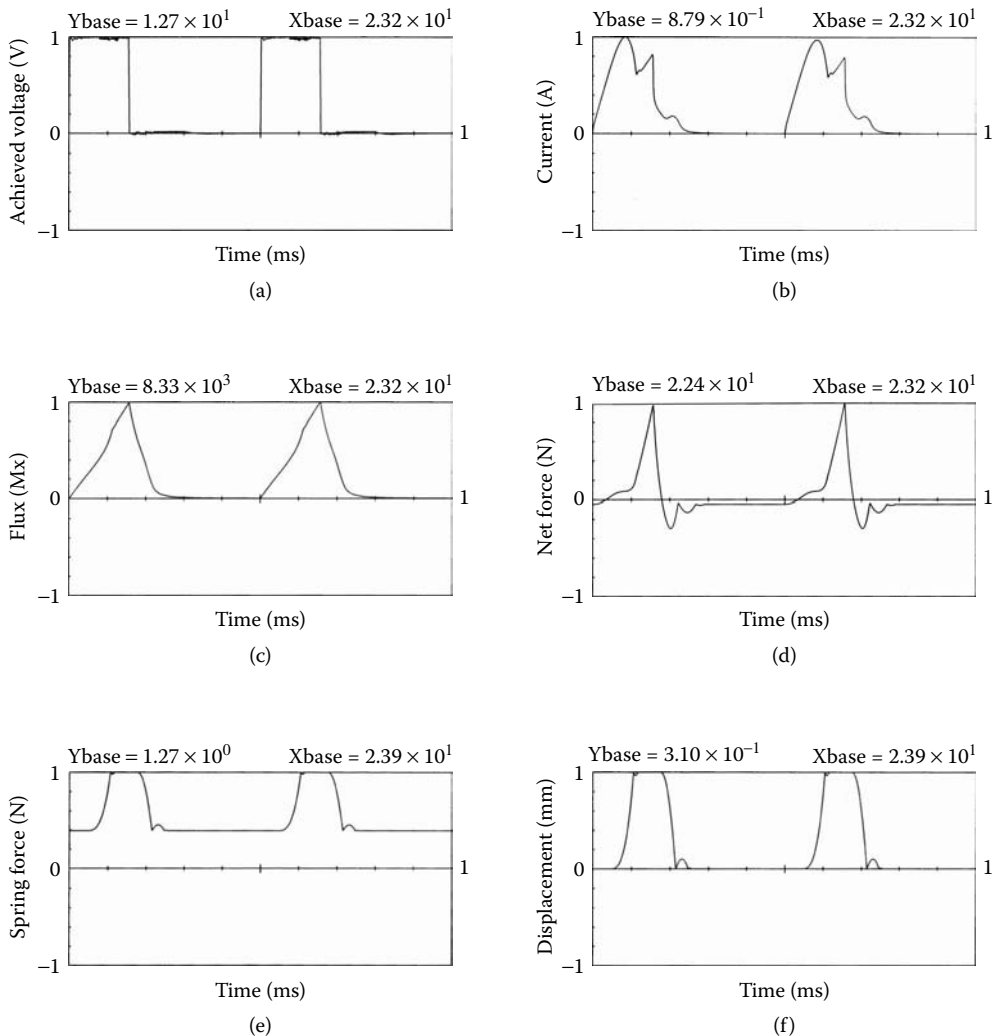
Figure 3.20 shows the magnetic flux distribution for the disk solenoid at different time intervals. Note that at the beginning of the cycle, the armature is in the upper position with low penetration of the magnetic flux within the magnetic circuit, but at the end of the cycle, the armature rests against the lower magnetic circuit with zero air gap and deep penetration of the magnetic flux within the magnetic circuit.

**FIGURE 3.20**

Dynamic characteristics of the disk solenoid: (a) flux at 1.0 ms, (b) flux at 2.0 ms, (c) flux at 4.0 ms, (d) flux at 6.0 ms. (Courtesy of Delphi Corp.)

3.2.2 Plunger Solenoids

Plunger solenoid types are the most popular solenoid configuration with a variety of applications. This is because the plunger solenoid configuration has a single main air gap for flux to cross and one parasitic air gap that is usually perpendicular to the main one. The inner pole surface of the main air gap carries the flux that is perpendicular to its surface, especially at the small air gaps where the flux crossing a parasitic air gap does not contribute to the axial forces, and in most of the cases, when the parasitic air gap is even around the axis of symmetry, these forces cancel out. This promotes applications with small travel and fast action such as injectors and other fast-acting solenoids. The plunger solenoid electromagnetic efficiency may be secured with small plunger travel and small parasitic air gap with provisions to reduce flux density in this region by elongating the parasitic gap axially.

**FIGURE 3.21**

Dynamic characteristics of the plunger solenoid: (a) achieved voltage vs. time, (b) current vs. time, (c) flux vs. time, (d) net force vs. time, (e) spring force vs. time, (f) displacement vs. time. (Courtesy of Delphi Corp.)

The dynamic characteristics of the plunger solenoid are presented in Figure 3.21(a) through Figure 3.21(f) for the input voltage, corresponding coil current, magnetic flux developed in the armature, the net force of the disk armature, the spring force, and the displacement of the armature. Figure 3.22 shows the magnetic flux distribution for the plunger solenoid at different time intervals. Note that at the beginning of the cycle, the armature is in the upper position with low penetration of the magnetic flux within the magnetic circuit. At the end of the cycle, the armature rests against the lower magnetic circuit with zero air gap and deeper penetration of the magnetic flux within the magnetic circuit, yet not as deep as in the disk solenoid case.

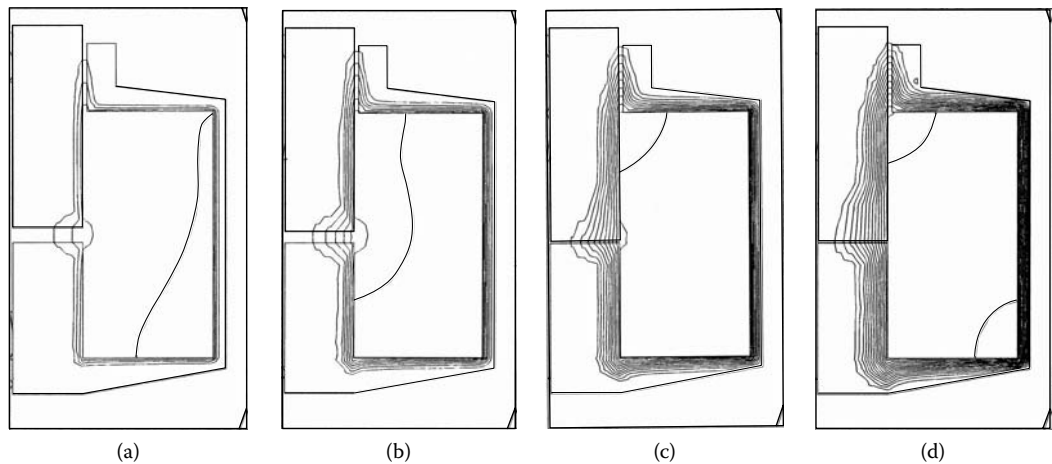
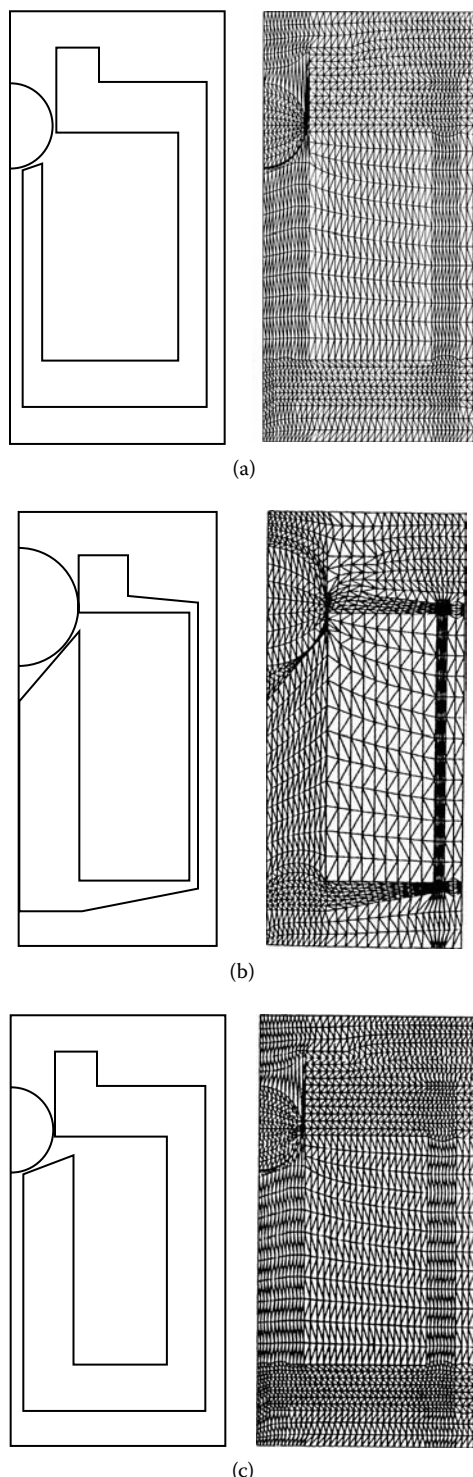


FIGURE 3.22
Plunger solenoid magnetic flux vs. time: (a) flux at 1.0 ms, (b) flux at 2.0 ms, (c) flux at 3.0 ms, (d) flux at 4.0 ms. (Courtesy of Delphi Corp.)

3.2.3 Ball Solenoids

Ball-type solenoid actuators can be applied in fluid control applications, such as automatic transmissions, due to their good sealing capabilities and response time. They are also used in applications where the ball armature, due to its inertia in a car crash, is separated from a PM ball stop and may be, therefore, used as an air bag deployment mechanism. The ball solenoid configuration has limited applications that are also more difficult to analyze because of the shape of the armature. This is a result of its uneven main air gap for flux to cross and uneven parasitic air gap, which is usually perpendicular to the main one. The inner pole surface of the main air gap carries the flux that is not perpendicular to its surface; therefore, a portion of the entire flux crosses the main air gap contributing to the axial forces. In addition, the flux crossing the parasitic air gap may not be even around the axis of symmetry, and these forces may not cancel out. This promotes only applications where the geometry of a ball can be applied in fluid dynamics. The ball solenoid electromagnetic efficiency is not very effective because its total average air gap is larger than a mechanical air gap for the axial motion. Depending on requirements and applications, three inner stop OD versions are considered, as shown in Figure 3.23.

The dynamic characteristics of the ball solenoid are presented in Figure 3.24(a) through Figure 3.24(f) for the input voltage, corresponding coil current, magnetic flux developed in the armature, the net force of the disk armature, the spring force, and the displacement of the armature. Figure 3.25 presents the magnetic flux distribution for the ball solenoid at different time intervals. Note that at the beginning of the cycle, the armature is in the upper position with low penetration of the magnetic flux within the magnetic circuit. During the consecutive steps of the cycle, flux shows deeper penetration within the magnetic circuit, and the ball armature is attracted to the inner stop.

**FIGURE 3.23**

Ball solenoid with different inner stop OD versions: (a) OD ball > OD stop, (b) OD ball = OD stop, (c) OD ball < OD stop. (Courtesy of Delphi Corp.)

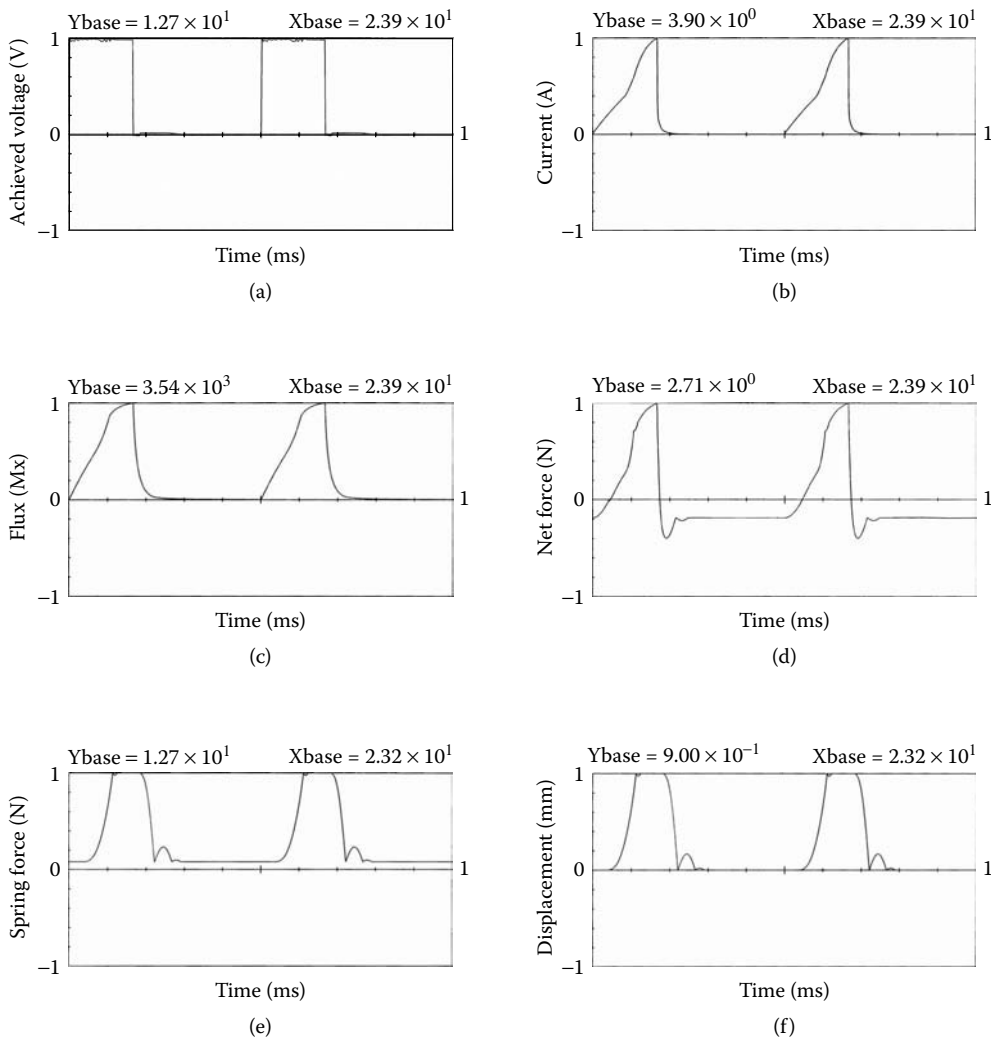
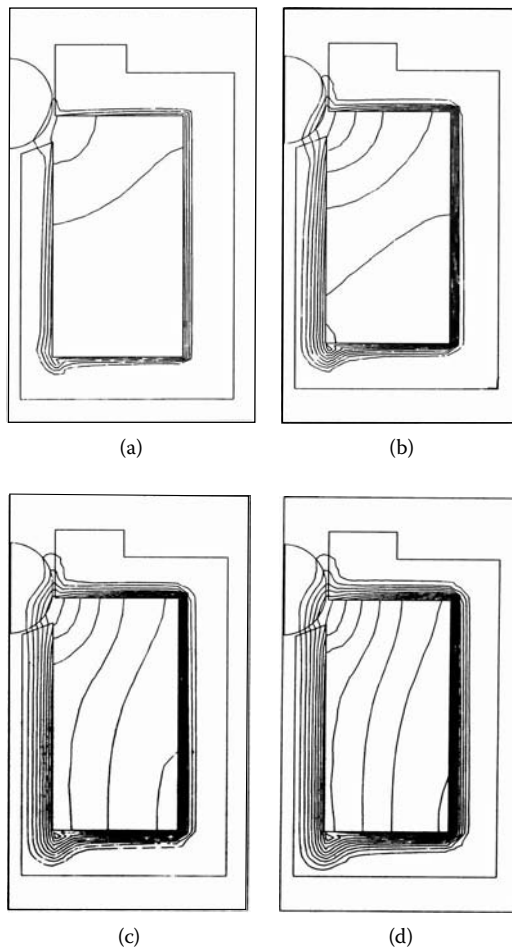


FIGURE 3.24

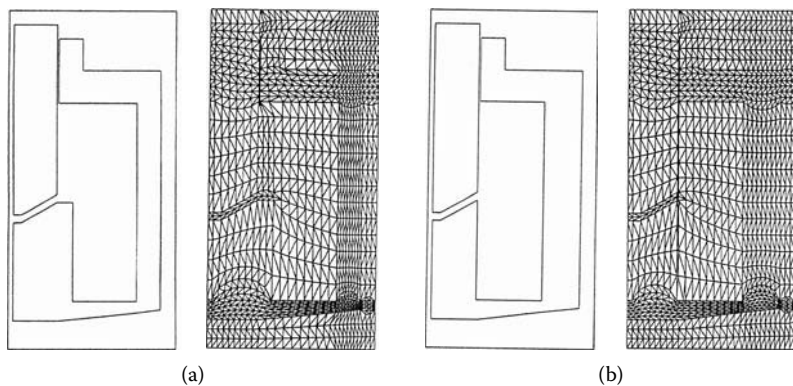
Dynamic characteristics of the ball-type solenoid: (a) achieved voltage vs. time, (b) current vs. time, (c) flux vs. time, (d) net force vs. time, (e) spring force vs. time, (f) displacement vs. time. (Courtesy of Delphi Corp.)

3.2.4 Conical Solenoids

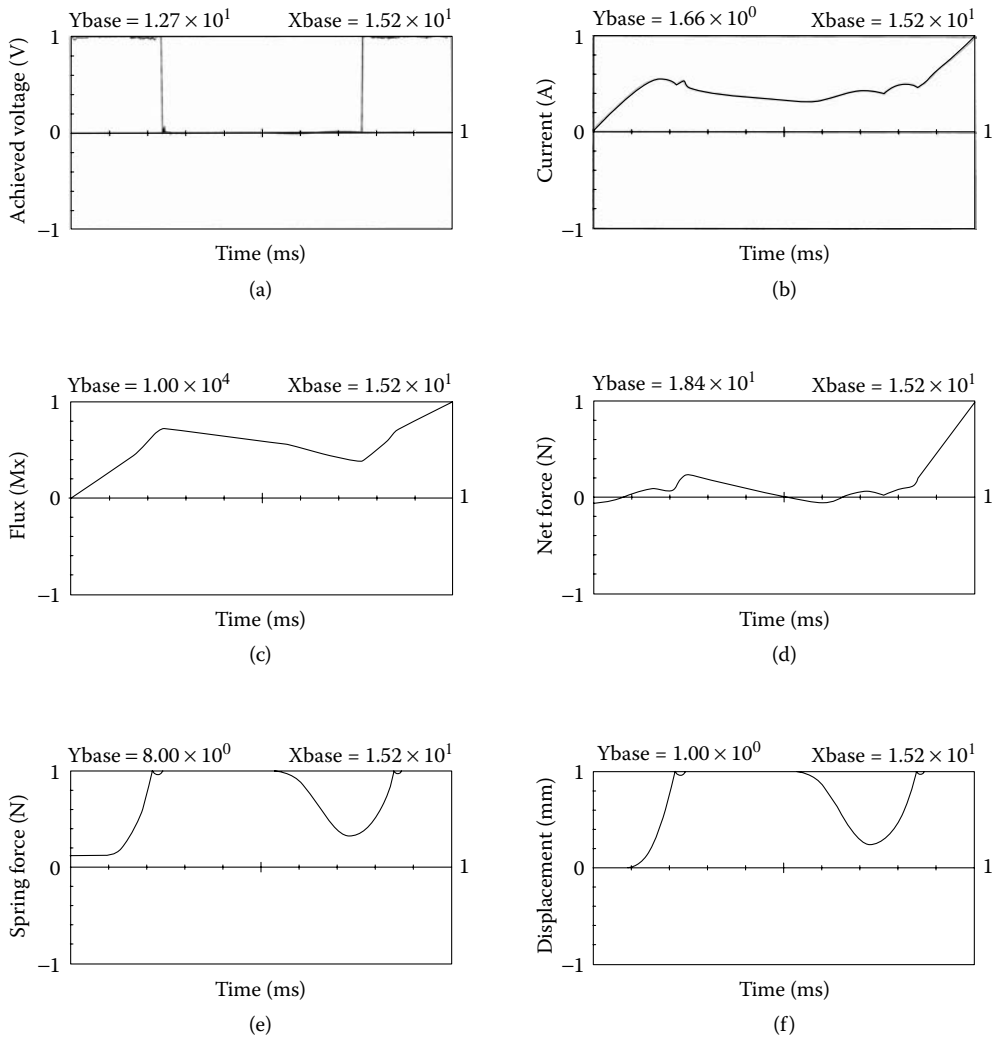
Conical solenoid actuators can be used in long stroke applications, such as in automotive door locks, due to their high force over long stroke capabilities. They can also be applied in situations where the armature can develop a relatively large force due to a smaller magnetic air gap than axial stroke. The conical solenoid configuration has limited applications in long stroke travel without fast response time. This is because the conical solenoid configuration has a single main air gap for flux to cross that is always smaller than mechanical travel distance and one parasitic air gap that is usually perpendicular to the direction of motion. The inner pole surface of the main air gap carries the flux that is perpendicular to its surface but not perpendicular to the axial motion. The flux crossing a parasitic air gap does not contribute to the axial forces, and in most cases, when the parasitic air gap is even around the axis of symmetry these forces cancel out. Depending on requirements and applications, the inner stop OD versions are considered, as shown in Figure 3.26.

**FIGURE 3.25**

Ball solenoid magnetic flux vs. time: (a) flux at 1.0 ms, (b) flux at 2.0 ms, (c) flux at 3.0 ms, (d) flux at 4.0 ms. (Courtesy of Delphi Corp.)

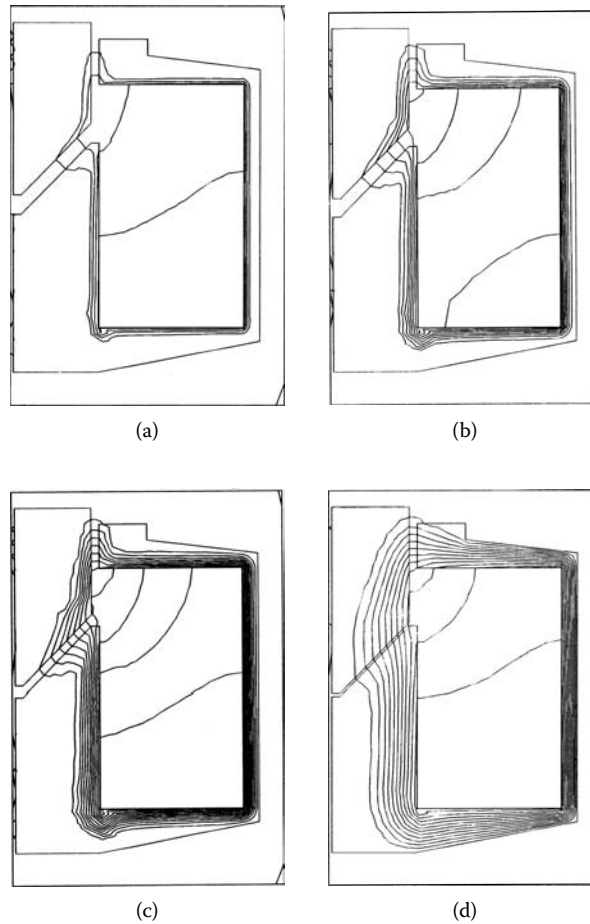
**FIGURE 3.26**

Conical solenoid with different inner stop OD versions: (a) OD conical arm < OD stop, (b) OD conical arm > OD stop. (Courtesy of Delphi Corp.)

**FIGURE 3.27**

Dynamic characteristics of the conical solenoid: (a) achieved voltage vs. time, (b) current vs. time, (c) flux vs. time, (d) net force vs. time, (e) spring force vs. time, (f) displacement vs. time. (Courtesy of Delphi Corp.)

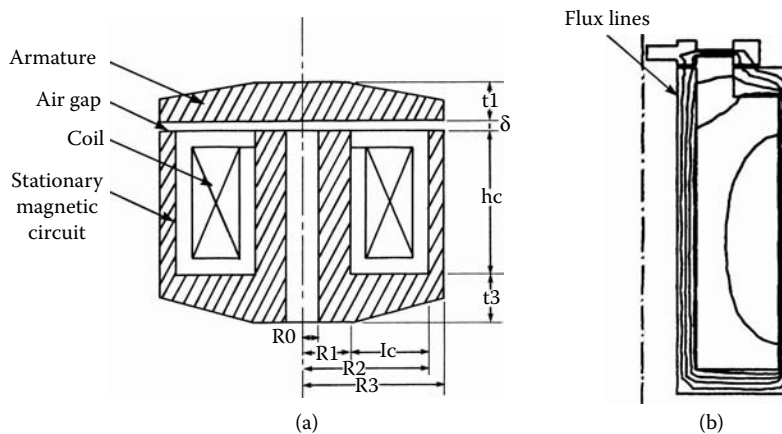
The dynamic characteristics of the conical solenoid are shown in Figure 3.27(a) through Figure 3.27(f) for the input voltage, corresponding coil current, magnetic flux developed in the armature, the net force of the disk armature, the spring force, and the displacement of the armature. As shown, the conical solenoid requires a longer period of voltage pulse than other types of solenoids to bring the armature to the rest position against the plunger stop. Figure 3.28 presents the magnetic flux distribution for the conical solenoid at different time intervals. Note that at the beginning of the cycle, the armature is in the upper position with low penetration of the magnetic flux within the magnetic circuit, although in all of the following steps of the cycle, flux shows deeper penetration within the magnetic circuit. The flux leaving the conical armature is perpendicular to the surface of the armature stop.

**FIGURE 3.28**

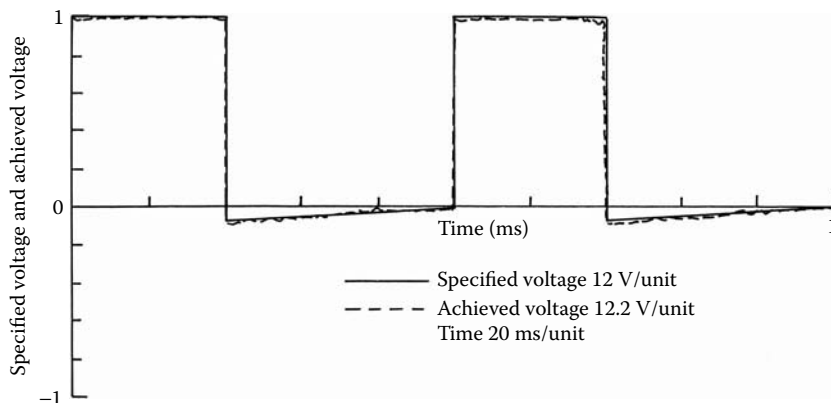
Conical solenoid magnetic flux vs. time: (a) flux at 1.0 ms, (b) flux at 2.0 ms, (c) flux at 3.0 ms, (d) flux at 4.0 ms. (Courtesy of Delphi Corp.)

3.2.5 Optimization of Fast-Acting Actuators

Optimization of an electromagnetic device is an art (Matsumoto et al. 2004, Pawlak 1989, Yoon et al. 1999). The challenge is in devising the best structure to meet all the requirements. Traditionally, optimization has been limited to a parametric study where only one parameter varies at a time, and this book is a good example of it. Optimization, however, suggests searching for a goal function, whereby all variables change and lead to achieving a goal solution. Therefore, one has to first determine a goal function and second to select all variables that can affect the selected goal function. The next step is to reduce the number of variables by subtracting from them all the requirements. Examples of such requirements may be an envelope, travel, voltage and current limitations, etc. Suppose that the subject of our optimization is a disk solenoid with the minimum mass as determined by the goal function and three variables that are not limited by any of the requirements and constraints. These variables are the thickness of the disk armature t_1 , the thickness of the bottom of the stationary magnetic circuit t_3 , and the coil window ratio defined as the coil height to its thickness h_c/l_c that affects the geometry of the stationary magnetic circuit, as presented in Figure 3.29.

**FIGURE 3.29**

Geometry and flux lines of the optimized disk solenoid: (a) geometry, (b) flux lines. (Courtesy of Delphi Corp.)

**FIGURE 3.30**

Specified and achieved voltage vs. time. (Courtesy of Delphi Corp.)

The FE analysis that is utilized for the magnetic field solutions identifies the flux path in a symmetrical portion of the disk solenoid's magnetic structure. Consequently, the voltage source is applied with the required duty cycle and one has to verify that, indeed, the achieved voltage matches the specified voltage within a reasonable error. This is shown in Figure 3.30, whereby the voltage was converging within 2% of error.

Applied voltage induces the current that in turn generates a magnetic flux in the disk armature. The current limitation affects the flux and has to be cut so as not to exceed 2.0 A. One has to make sure that the current, and consequently the flux, is not discontinued before an armature accomplishes its motion, as presented in Figure 3.31. A small dip in the current characteristic identifies the armature motion. In our case, it is visible in the second wave because both the current and flux started with higher values due to energy stored in the magnetic circuit.

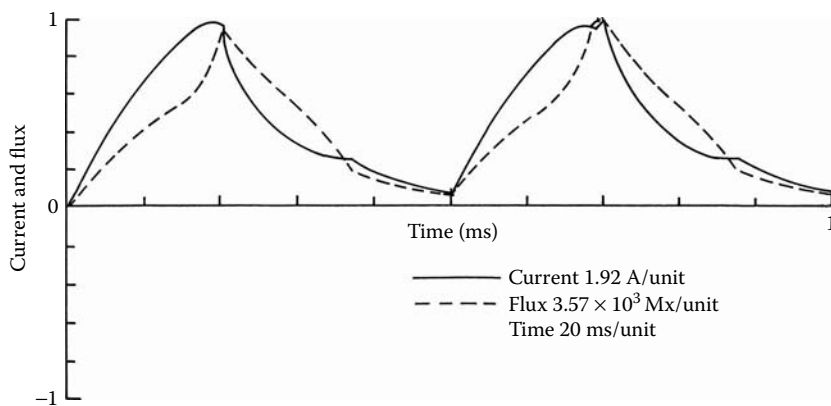


FIGURE 3.31
Current and flux vs. time. (Courtesy of Delphi Corp.)

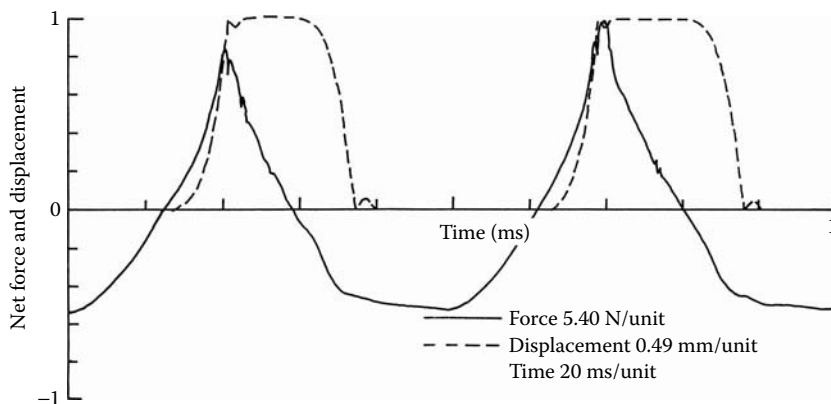


FIGURE 3.32
Magnetic force and displacement vs. time. (Courtesy of Delphi Corp.)

Flux, in turn, develops a magnetic force in the armature sufficient to move it toward to the stationary magnetic circuit. The armature movement further compresses a spring and closes the air gap to 0.49×10^{-3} m (almost to zero as the specified gap is 0.5×10^{-3} m), as presented in Figure 3.32.

With all dynamics of the disk actuator under control, one can start an optimization procedure that is continuously iterative. Such a process typically requires about 700 iterations for a simple structure. An optimization subroutine, therefore, has to be employed to do this job (Kuester et al. 1973). Results of such an optimization are presented separately for one variable, two variables, and finally for all three variables in Figure 3.33. Avoid local minima that may cause misleading results (Coulomb and Meunier 1983, Fletcher 1987, Matsumoto et al. 2004, Navarra 1990).

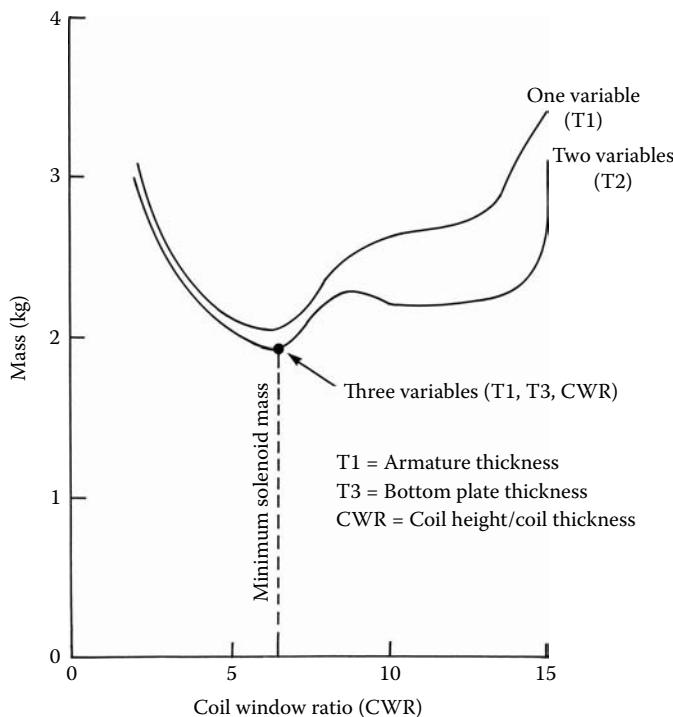


FIGURE 3.33
Disk solenoid mass optimization for three variables. (Courtesy of Delphi Corp.)

3.3 Applications of Solenoid Actuators

Solenoid actuators are the most commonly applied electromagnetic devices in the automotive industry. They are used for fast-acting operations with a short stroke, such as gasoline, natural gas, and diesel fuel injectors or compressors, fuel pumps, and transmission solenoid valves. For long stroke operations, solenoid actuators are used in solenoid fuel pumps or door locks.

3.3.1 Long Stroke Solenoid Fuel Pump

Solenoid strokes with total travel of more than several millimeters fall into the long stroke solenoid category. Most of them are conical where the total travel distance is larger than the magnetic air gap for the magnetic flux crossing. An example of this is a door lock solenoid. All other long stroke solenoids are plunger types with coil–plunger asymmetry and spring offset. A good example of this configuration is a solenoid fuel pump.

A common application of electronic fuel pumps is an automotive diesel engine. The pump has very good priming capabilities and its proximity to the engine does not obstruct the pump from drawing fuel from the tank at the rear of the vehicle and delivering it to the engine. It has few moving parts and no points exposed to wear. It provides a quiet operation with proven durability. Figure 3.34 shows a cross section of the fuel pump with no current excitation, and Figure 3.35 shows the fuel pump in two extreme positions.

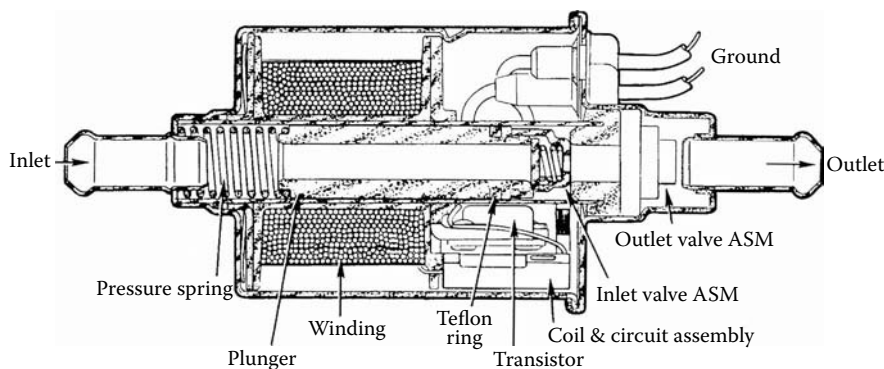


FIGURE 3.34
Solenoid fuel pump. (Courtesy of Delphi Corp.)

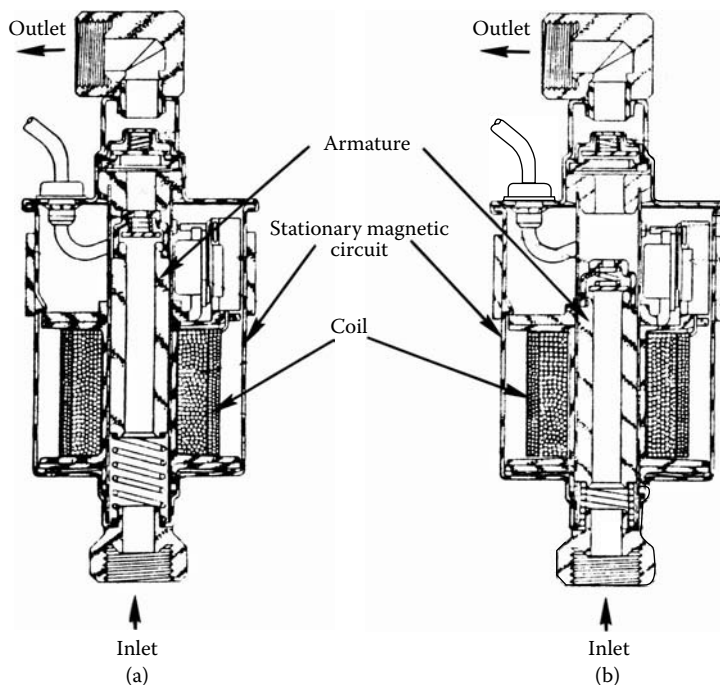
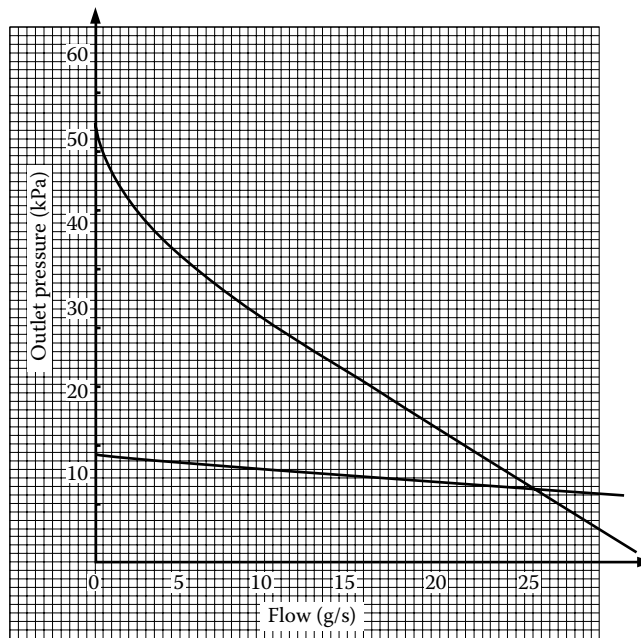


FIGURE 3.35
Solenoid fuel pump in two extreme positions: (a) current OFF and spring released, (b) current ON and spring compressed. (Courtesy of Delphi Corp.)

The pump action of the fuel pump is created by the movement of the plunger inside the cylinder, which is completely sealed against the leakage. When electrical power is applied, the resulting magnetic force pulls the plunger piston down against the pressure spring, as presented in Figure 3.35(a). The reason for this is the initial movable plunger location vs. the stationary coil that is not symmetrical to the coil and magnetic circuit. When the magnetic field is applied, it pulls the movable magnetic plunger to its center, trying to achieve the maximum magnetic permeance (and minimum magnetic reluctance) for the magnetic flux. As the plunger piston moves toward the spring, the outlet valve

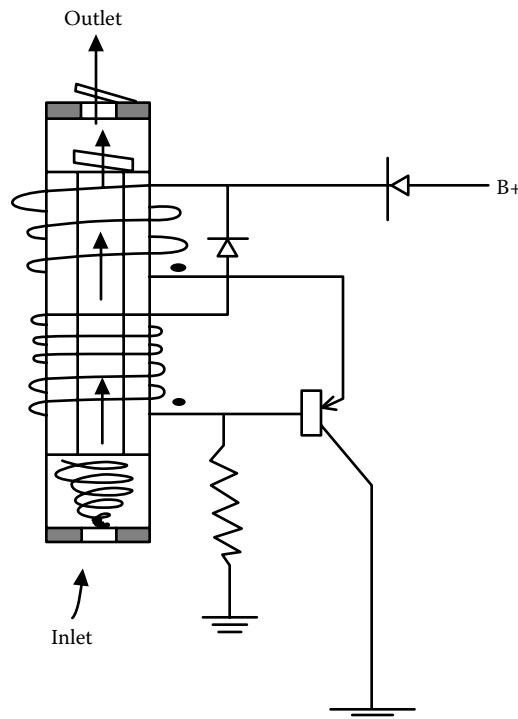
**FIGURE 3.36**

Outlet pressure vs. flow. (Courtesy of Delphi Corp.)

closes and the inlet valve opens. Fuel then enters the pumping chamber through the center of the piston. As the downward motion is completed, the magnetic field is turned off and the pressure spring forces the piston in the reverse position, as presented in Figure 3.35(b). At this time, the inlet valve closes, the outlet valve opens, and the fuel is released. This sequence occurs many times per second. As the pumping action continues, pressure on the outlet increases.

As this pressure increases, the piston stroke decreases, as presented in Figure 3.36, and only the required amount of fuel is pumped to the engine. Fuel is confined to the pump cylinder and does not enter sections of the pump that contain the coil assembly and electronics. The electronic circuit shown in Figure 3.37 indicates that the solenoid coil consists of two coils: the upper primary coil with 325 turns and wire size 12 AWG having 1.2Ω , and the lower secondary coil with 164 turns and wire size 37 AWG having 300Ω .

The purpose of the solenoid pump improvements is to increase its pressure, flow, or both. Two factors can contribute to this goal. One is to reduce the eddy currents in the movable piston and the other is to reduce the plunger inertia. The magnetic-circuit improvement can be accomplished by examining magnetic-circuit materials and, in particular, the plunger material. By replacing the low-carbon steel plunger to 2% silicon steel (Carpenter) more force can be produced by reducing eddy currents (Carpenter 1989). As changing the entire circuit would be too costly, only the plunger material should be changed. The test results of the improved device indicated improved flow by 12.8% from 15 g/s to 19.2 g/s at a pressure of 35 kPa, as presented in Figure 3.36. In addition, it required only 1.65 A of current compared with 1.85 A for the original pump, a 10.8% reduction. By changing the stroke and by raising the current to its original level, the redesigned pump has the potential for total flow improvement of 25%. In examining the coil winding, a low coil window fill factor of about 35% was identified. Increasing the coil fill factor to 50% allows shortening of the coil by 8.25×10^{-3} m. At the same time, the plunger axial size can be reduced to result in total mass reduction of 21%. With the lower

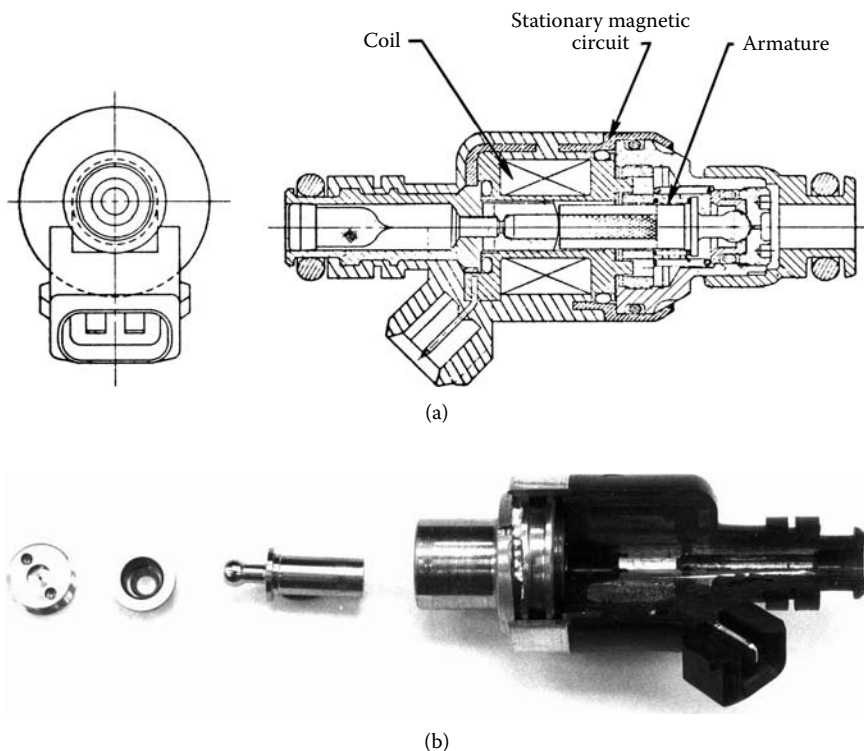
**FIGURE 3.37**

Solenoid pump drive circuit. (Courtesy of Delphi Corp.)

mass plunger, a weaker spring can be used, reducing the travel time significantly and, thus, increasing the frequency of the operation and fuel flow. These changes are well recognized and viewed as standard because they do not affect a device's size or the manufacturing process. As a result, they can be easily adopted in industry. Engineers should focus on these factors because they can bring significant improvement without any significant change to design or process.

3.3.2 Gasoline Injectors

With hundreds of millions in use annually, fast-acting solenoid actuators are by far the most popular electromechanical devices in production. They are most commonly used as natural gas, diesel fuel, and gasoline injectors. Another common use is as solenoid valves, with the most popular application in automotive transmissions. Fuel injection performs better, provides crisper throttle response, improves fuel economy, allows much easier starts especially during cold weather, and produces much lower emissions than carburetors. These advantages led to the introduction of computer-controlled engine management systems with electronic fuel injection. Gasoline-powered engines with fuel injection do not use direct injection systems, but rather indirect systems that spray fuel into either the intake manifold or head ports. The first systems introduced in the early 1980s were throttle body injection systems. The injectors spray fuel into the intake manifold, where it mixes with air and is carried through the intake runners and ports to the engine's cylinders. Nowadays, the multiport fuel injector or port fuel-injection systems are used, where a separate fuel injector is provided for each of the engine's cylinders. The injectors are mounted in the intake manifold and spray fuel into the cylinder head intake ports. In

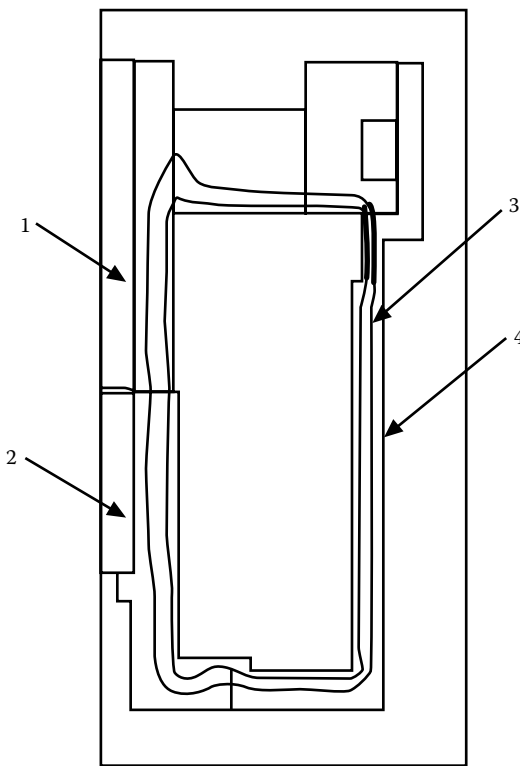
**FIGURE 3.38**

Multec port fuel injector: (a) Multec injector design components, (b) Multec distributed view components. (Courtesy of Delphi Corp.)

some injection systems, all the injectors squirt simultaneously once every engine revolution. In other systems, each injector is triggered individually as its cylinder begins the intake stroke and the intake valve opens. Sequential systems are better because they can react more quickly to changing operating conditions. For better air/gasoline control more complex air atomizer injectors are proposed (DeNagel et al. 1994).

All advanced injection systems require better dynamic injector response—the opening and closing travel time. To provide such devices, one has to use an FE tool to optimize injector dynamics. The world's first FE dynamic optimization of the fast-acting solenoid with a moving part (plunger) was applied to the Multec injector, as illustrated in Figure 3.38 (Nehl et al. 1988). Pioneer dynamic optimization of the dynamic analysis of the Multec design was performed using FE techniques including eddy currents, nonlinear magnetic materials, and motion. Proposed magnetic modifications resulted in significant improvements in performance, making Multec an extremely competitive product that for more than two decades has been manufactured with a peak volume of 50 million units annually. This dynamic optimization technique has been successfully applied to many fast-acting, solenoid-based products to improve existing and help create new designs (Matsumoto et al. 2004, Pawlak 1989, Rischmuller et al. 2000, Yoon et al. 1999).

Figure 3.39 indicates the FE analysis results for the magnetic flux distribution passing the plunger, main air gap, the plunger stop, parasitic air gaps, and the rest of the magnetic circuit. Note an additional air gap of the inside plunger insert that caused the uneven main air gap for the FE analysis.

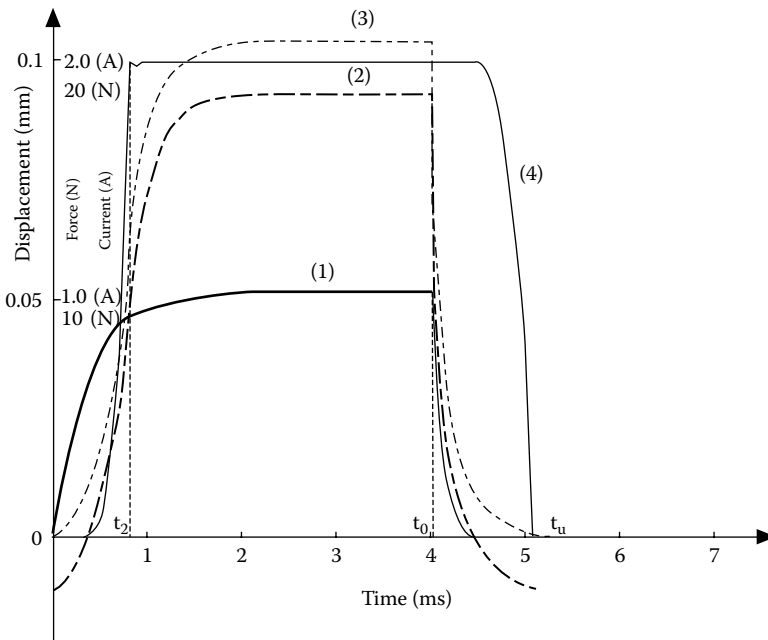
**FIGURE 3.39**

Magnetic flux lines for the Multec injector: (1) plunger, (2) plunger stop, (3) magnetic flux lines, (4) housing. (Courtesy of Delphi Corp.)

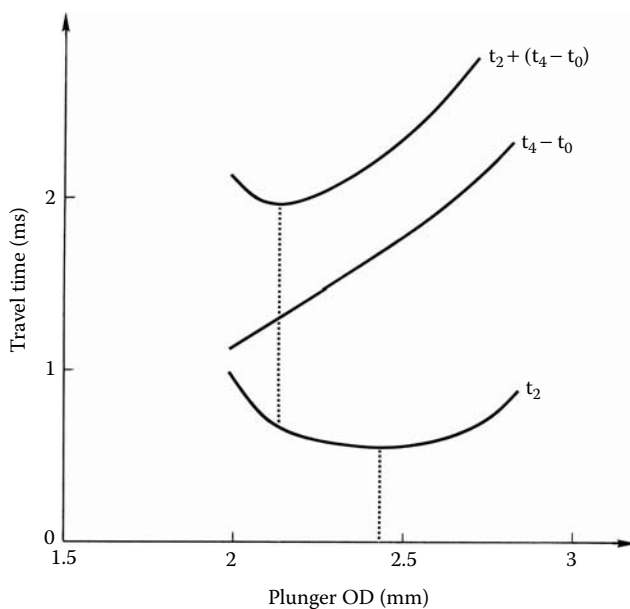
Dynamic performance of the Multec injector is illustrated in Figure 3.40. The current in the Multec coil reaches its saturation and, with constant voltage applied, it drops as soon as the voltage is discontinued. Both the magnetic and net forces resemble the current shape. As soon as the net force changes its sign from negative (due to the spring preload) to positive, the plunger starts moving until it reaches the plunger stop. When the voltage is discontinued, the net force drops, its sign changes again, and the armature then starts moving back and returns to its previous position, as shown in Figure 3.40.

The design optimization process includes changes in injector geometry and configurations to reduce magnetic saturation and flux leakage. Implementing magnetic material with higher electrical resistivity reduces eddy current effects. Incorporating the changes in the final product design significantly improved injector performance. In a Multec optimization process, several parametric studies were iteratively performed to determine the desired position of the main air gap and plunger geometry, as well as application of a high resistivity material to critical parts of the magnetic circuit.

Figure 3.41 shows the effect of changing the outside plunger diameter upon the plunger opening and closing times and on the total travel time. Table 3.1 indicates the results of this optimization. If we use optimized materials and dimensions and assume the sum of opening and closing times as a figure of merit, total travel time can be reduced by 35%.

**FIGURE 3.40**

Dynamic performance of the Multec injector: (1) current, (2) net force, (3) total magnetic force, (4) displacement. (Courtesy of Delphi Corp.)

**FIGURE 3.41**

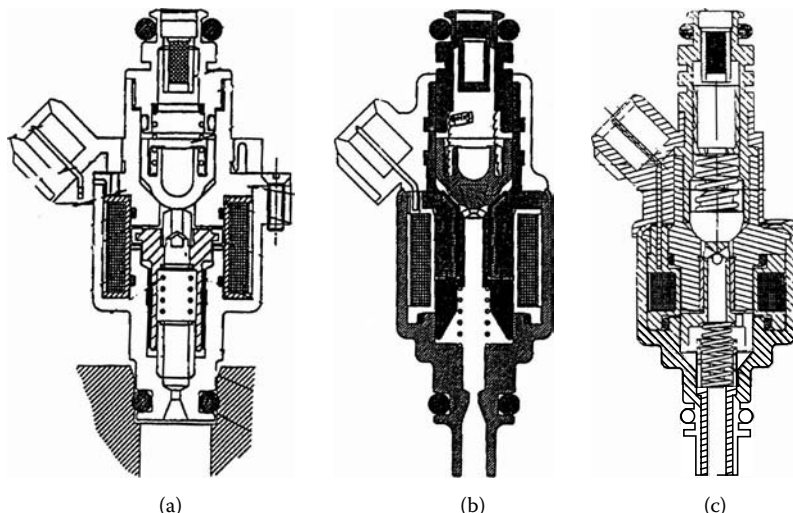
Travel time vs. plunger OD: $t_2 + (t_4 - t_0)$ = total travel time, t_2 = opening time, $(t_4 - t_0)$ = closing time. (Courtesy of Delphi Corp.)

TABLE 3.1

Multec Injector Optimization Results

Design and Performance	Opening Time (ms)	Opening Time (%)	Closing Time (ms)	Closing Time (%)	Total Travel Time (ms)	Total Travel Time (%)
Original design	1.65	0.0	1.42	0.0	3.07	0.0
New materials	1.4	15.0	1.13	20.0	2.53	18.0
New materials and dimensions	1.33	19.0	0.65	54.0	1.98	35.0
Requirements	1.5	9.0	0.9	37.0	2.4	22.0

Source: Courtesy of Delphi Corp.

**FIGURE 3.42**

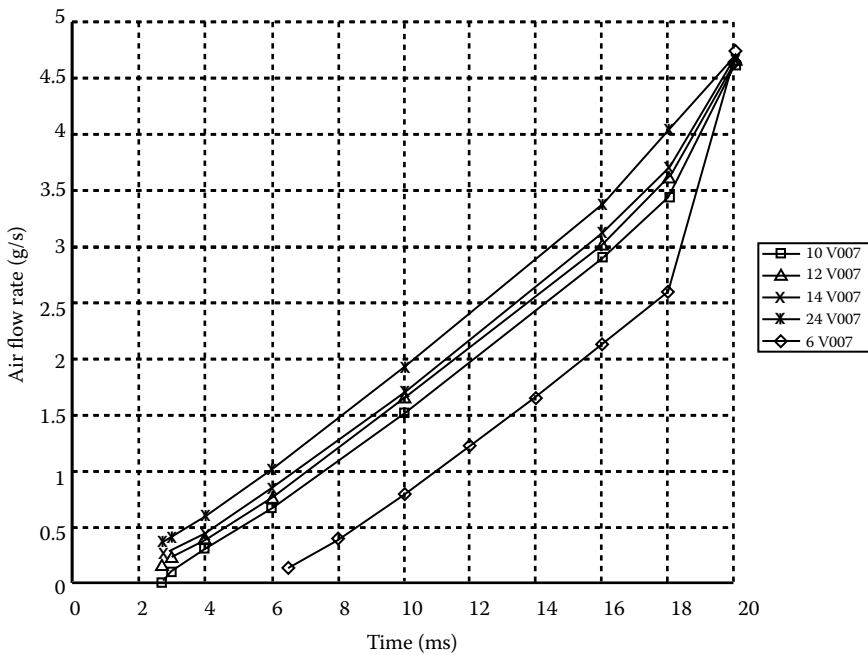
Natural gas injector designs: (a) conventional gas injector, (b) improved gas injector, (c) optimized gas injector. (Courtesy of Delphi Corp.)

3.3.3 Natural Gas Injectors

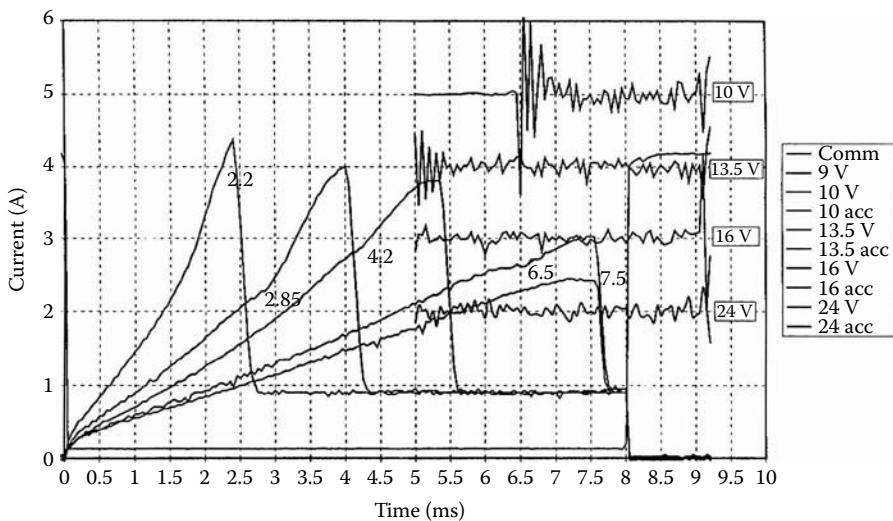
The increasing cost of gasoline is driving interest in natural gas as a less expensive energy option for automotive use. As a result, natural gas injectors are finding more and more applications in the automotive industry. Figure 3.42(a) shows a cross section of a typical natural gas injector that closely resembles a gasoline injector with its connector, coil, movable plunger, magnetic circuit, and return spring components.

Natural gas injectors have to meet natural gas requirements for automotive applications ranging from small passenger car 1.6 l engines to large truck 6.0 l engines. They have to provide the required flow rate of natural gas media under temperature and pressure requirements varied by a PWM cycle rate within a required voltage range. Figure 3.43 shows a family of natural gas flow rate characteristics ranging from 0 up to 5.0 g/s vs. PWM ranging from 2.0 to 20.0 ms for a voltage applied to a controller ranging from 6.0 to 24.0 V. The injector must perform under an ambient temperature of 21.0°C and a natural gas pressure of 414.0 kPa.

The most difficult requirement is meeting the low voltage requirement of 6.0 V because an injector has to develop sufficient force to operate under the required pressure. Figure 3.44 shows the current vs. time performance characteristic for the conventional injector

**FIGURE 3.43**

Natural gas injector flow rate vs. pulse-width performance. (Courtesy of Delphi Corp.)

**FIGURE 3.44**

Current vs. pulse-width performance of conventional natural gas injector at different voltages: 10.0 V, 13.5 V, 16.0 V, and 24.0 V. (Courtesy of Delphi Corp.)

presented in Figure 3.42(a). The figure shows that the conventional injector design did not meet this critical requirement and, in fact, stopped its operation at a voltage of 9.0 V, as presented in Table 3.2.

Because of this, a T-shaped plunger configuration was adopted, as shown in Figure 3.42(b) and Figure 3.45. For this design, almost the entire original structure of a typical

TABLE 3.2
Performance Comparison

Design	Performance Voltage (V)				
	6	10	13.5	16	24
Plunger armature opening time (ms)	none	7.5	6.5	2.85	2.2
T-shaped armature opening time (ms)	6.45	3.2	2.3	1.95	1.4

Source: Courtesy of Delphi Corp.

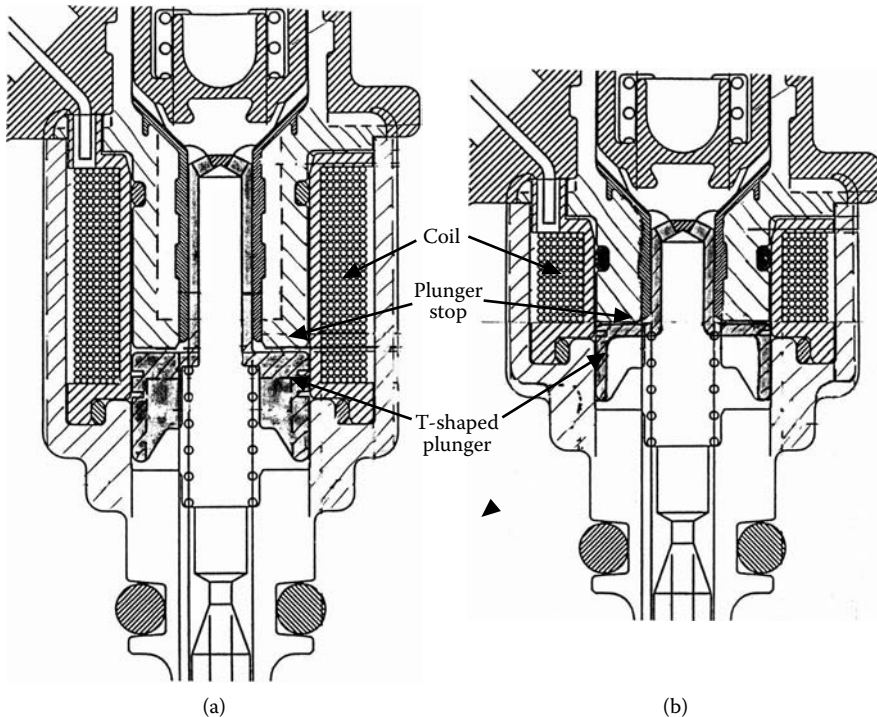
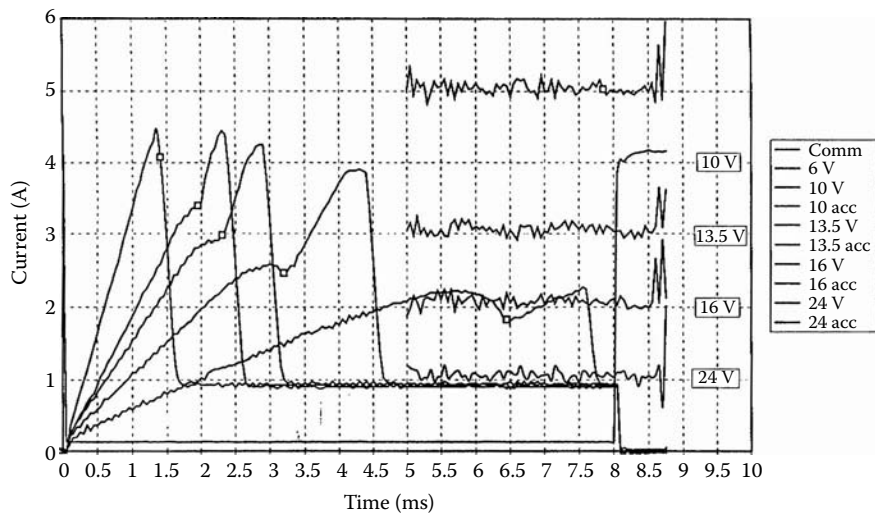


FIGURE 3.45

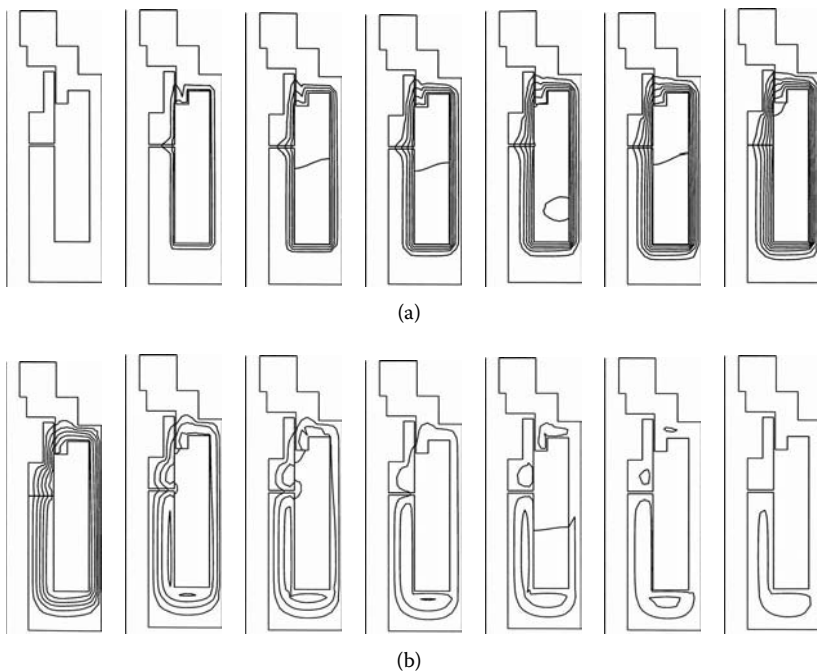
Natural gas injector with T-shaped plunger: (a) adopted T-shaped plunger, (b) optimized T-shaped plunger. (Courtesy of Delphi Corp.)

injector was preserved, except in the area of the plunger stop and the T-shaped plunger, as presented in Figure 3.45(a). The T-shaped plunger has a number of advantages over a hollow plunger armature, as presented in Figure 3.45(a). It has a relatively large active area in the vicinity of the main air gap that develops high magnetic forces and its thin walls allow for significant mass reduction and ease of manufacturing relative to the original plunger. Test results of this improved configuration are given in Figure 3.46.

The improved natural gas injector with a T-shaped armature has satisfied the low voltage requirement of 6.0 V with a response time of 6.45 ms under the required pressure of 414.0 kPa, as presented in Figure 3.46 and Table 3.2. Figure 3.46 shows the current vs. time performance characteristic for the improved injector for the entire voltage range from 6.0 to 24.0 V. Table 3.2 shows the opening time comparison for the conventional and improved solenoid configuration. At the typical automotive voltage of 13.5 V, the natural gas injector configuration with T-shaped armature has three times faster dynamic response time in comparison with the conventional hollow plunger injector design. This shows the dynamic potential of the T-shaped armatures.

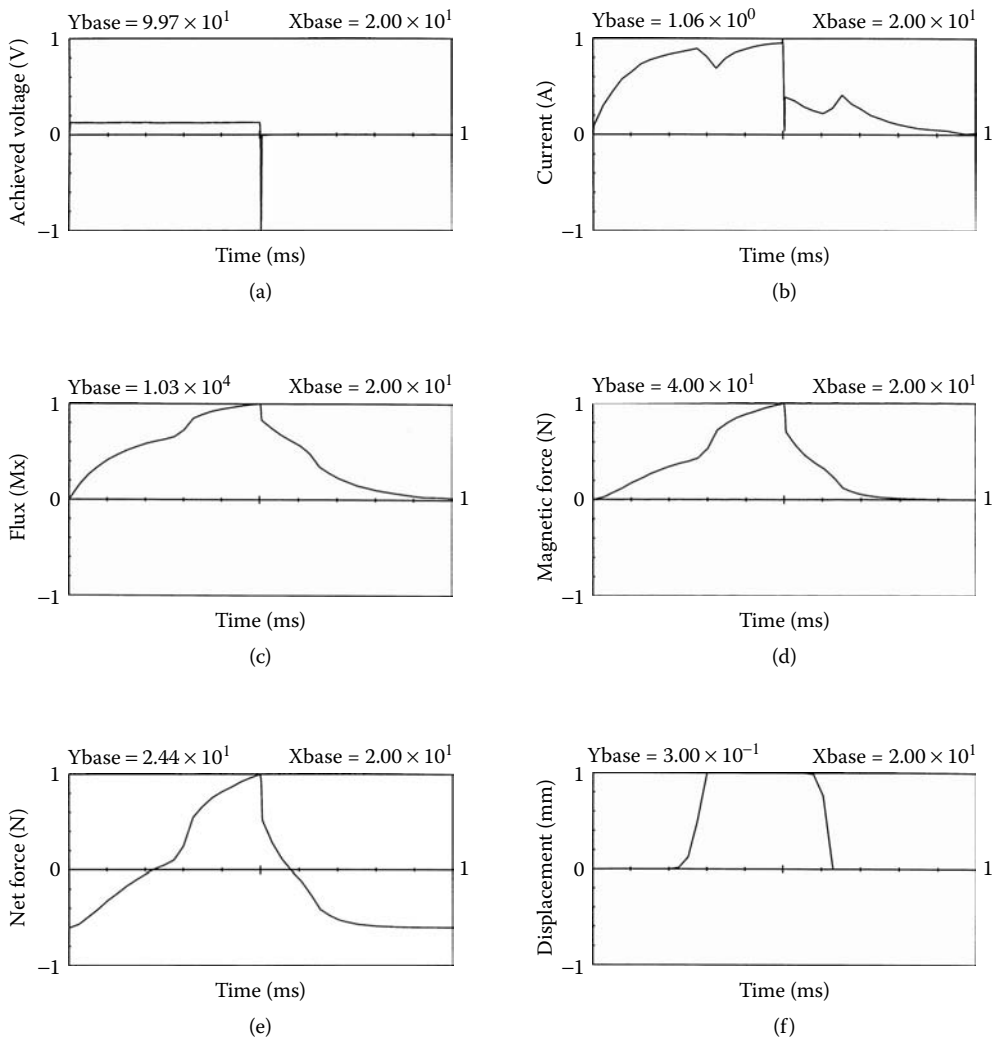
**FIGURE 3.46**

Current vs. pulse-width performance of improved natural gas injector at different voltages: 10.0 V, 13.5 V, 16.0 V, and 24.0 V. (Courtesy of Delphi Corp.)

**FIGURE 3.47**

Flux distribution of T-shaped plunger solenoid: (a) penetration of the magnetic field, (b) decay of the magnetic field. (Courtesy of Delphi Corp.)

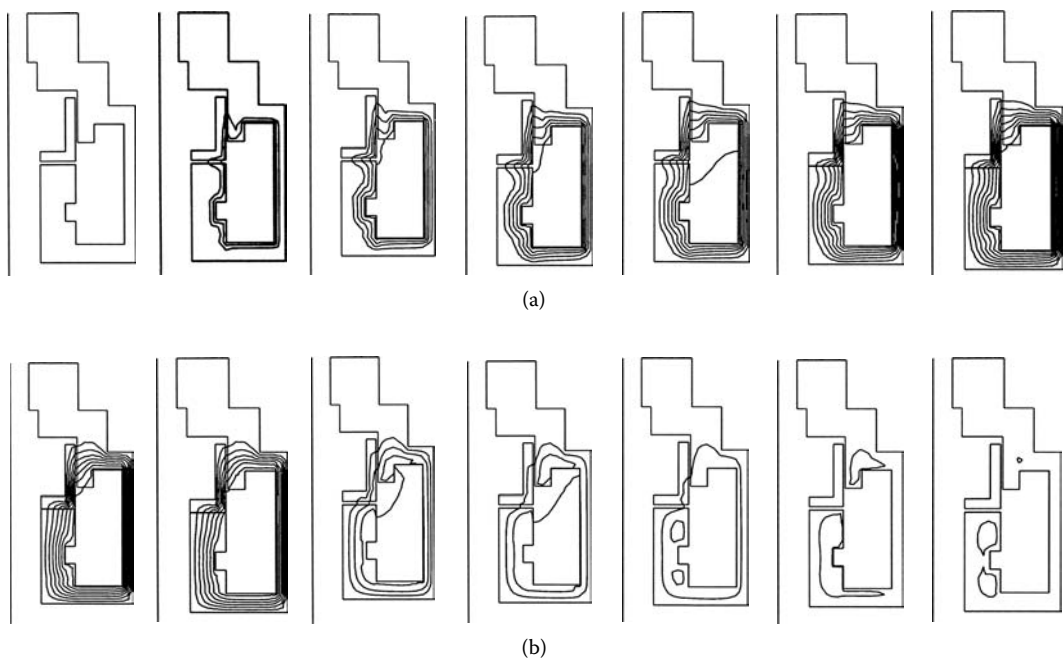
Because of the cylindrical symmetry, only one side of the device needs to be modeled. The distribution of the magnetic circuit at different points of time is shown in Figure 3.47. The diffusion (penetration) of the flux into the magnetic core is clearly illustrated at these

**FIGURE 3.48**

Dynamics of the T-shaped plunger solenoid: (a) achieved voltage vs. time, (b) current vs. time, (c) flux vs. time, (d) net force vs. time, (e) spring force vs. time, (f) displacement vs. time. (Courtesy of Delphi Corp.)

successive points of time. Actually, the armature motion does not begin until the flux penetrates the entire plunger surface at the main air gap and the resulting force overcomes the spring preload, as shown in Figure 3.47(a). Due to negative voltage spike at the end of the travel, the current is suppressed and the magnetic field is decaying faster, allowing the armature to return to its previous position, as presented in Figure 3.47(b).

Figure 3.48 displays dynamic characteristics of the T-shaped plunger solenoid. Figure 3.48(a) presents a specified voltage with a frequency of 50 Hz (20.0 ms pulse width), where the high negative voltage spike suppresses the current level. Figure 3.48(b) illustrates the calculated current that shows the effect of the negative spike that limits the decreasing current level. Both the flux crossing the main air gap and the total magnetic force on the T-shaped armature, shown in Figure 3.48(c) and Figure 3.48(d), respectively, have characteristics similar to the source current. The net force on the T-shaped armature shown in Figure 3.48(e) is the result of the spring forces and the total magnetic forces and identifies the beginning and the end of the motion displacement, as shown in Figure 3.48(f).

**FIGURE 3.49**

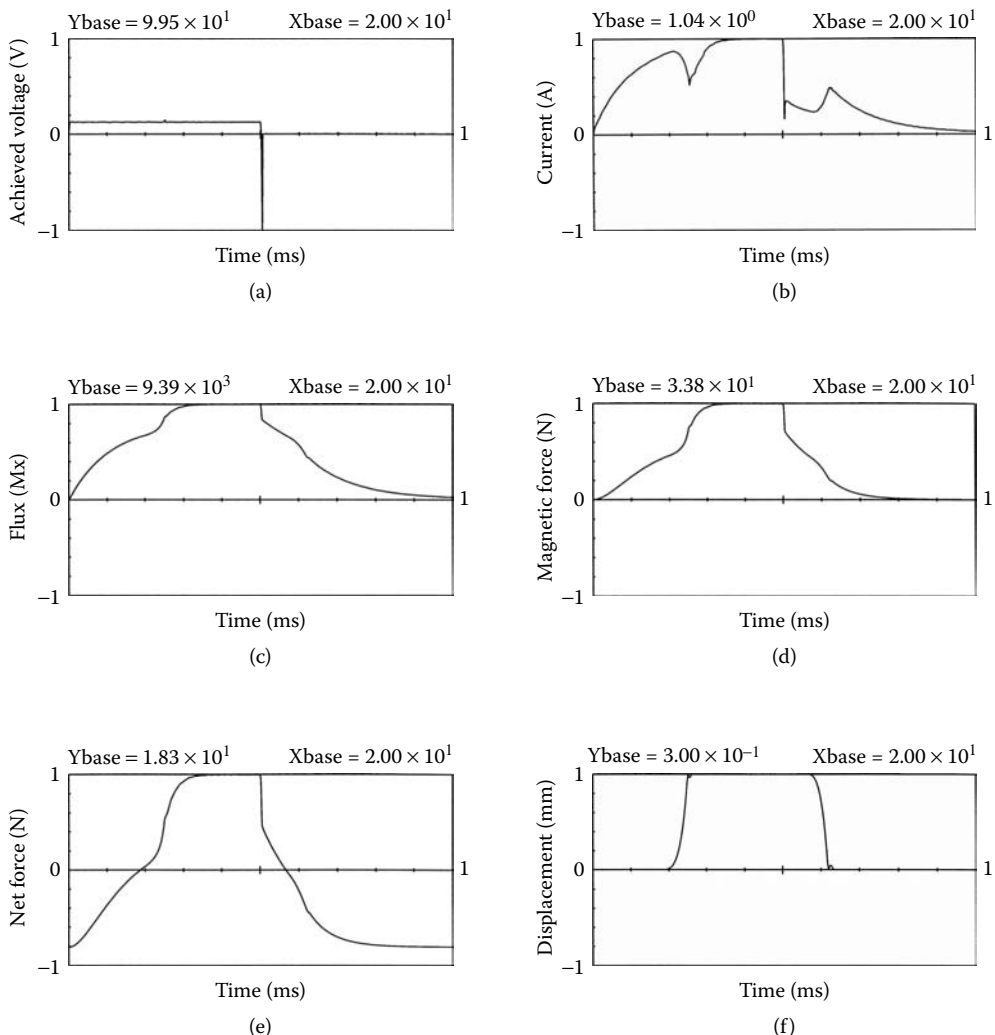
Flux distribution of optimized solenoid structure: (a) penetration of the magnetic field, (b) decay of the magnetic field. (Courtesy of Delphi Corp.)

Because the flux for the optimized injector reaches its maximum value much faster than in its previous configuration, it is possible to apply a peak and hold controller that reduces a holding current and saves energy. This is described in detail in Section 3.3.6.

Although the improved natural gas injector with a T-shaped armature has satisfied the low voltage requirement of 6.0 V, the entire magnetic circuit of the solenoid should be optimized to involve both the stationary and movable magnetic circuit as well as the coil in the optimization process. Figure 3.42(c) and Figure 3.45(b) show the optimized natural gas configuration. Both the coil and the magnetic circuit were optimized, resulting in the substantial reduction of total injector length from its original 26.7×10^{-3} m to 15.32×10^{-3} m, or 42.6%, and with a small reduction of the total OD from 25.0×10^{-3} m to 24.4×10^{-3} m. Altogether, the total solenoid volume has been reduced by 45.3%, driving its mass cost of material down substantially while improving its dynamic performance.

Again, because of the cylindrical symmetry, only one half of the device needs to be analyzed. The flux distribution of the magnetic circuit at different points in time is shown in Figure 3.49. The diffusion (penetration) of the flux into the magnetic core is clearly illustrated at these successive points in time. Actually, the armature motion does not begin until the flux penetrates the entire plunger surface at the main air gap and the resulting force overcomes the spring preload; see Figure 3.49(a). Due to negative voltage spike at the end of the travel, the current is suppressed and the magnetic field decays faster, allowing the armature to return to its previous position, as presented in Figure 3.49(b).

Figure 3.50 displays the dynamic characteristics of the optimized plunger solenoid. Included in this figure is Figure 3.50(a), presenting a specified voltage with a frequency of 50 Hz (20.0 ms pulse width) having a high negative voltage spike to suppress the current level, as shown in Figure 3.50(b). Both the flux at the main air gap and the total magnetic force on the T-shaped plunger shown in Figure 3.50(c) and Figure 3.50(d), respectively, have characteristics similar to the source current. The net force on the T-shaped armature

**FIGURE 3.50**

Dynamics of the T-shaped plunger solenoid: (a) achieved voltage vs. time, (b) current vs. time, (c) flux vs. time, (d) net force vs. time, (e) spring force vs. time, (f) displacement vs. time. (Courtesy of Delphi Corp.)

shown in Figure 3.50(e) is the result of the spring forces and the total magnetic forces and identifies the beginning and the end of the motion displacement shown in Figure 3.50(f). This dynamic performance also allows for the pick-and-hold driver that is described in detail in Section 3.3.6.

3.3.4 Diesel Fuel Injectors

The diesel fuel injector is a pressure valve with the capability of dispersing diesel fuel in required specific patterns, depending on the design of the valve nozzle. The diesel fuel injector distributes a pressurized fuel within the combustion chamber. The injector has to be able to withstand the temperature and pressure inside the cylinder and still deliver the fuel in a fine mist. Diesel engines are compression ignition engines that have no spark plugs and the diesel fuel is ignited by extreme heat and pressure. This requires a very high compression ratio (16 to 1 or higher) in the cylinders, much higher injector operating pressures (10,340 to 17,240 kPa) to overcome compression pressures in the cylinders, and

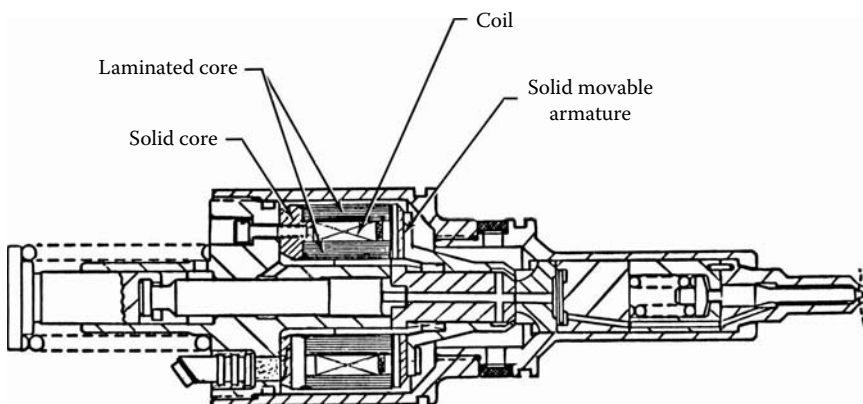


FIGURE 3.51
Electronic diesel injector. (Courtesy of Delphi Corp.)

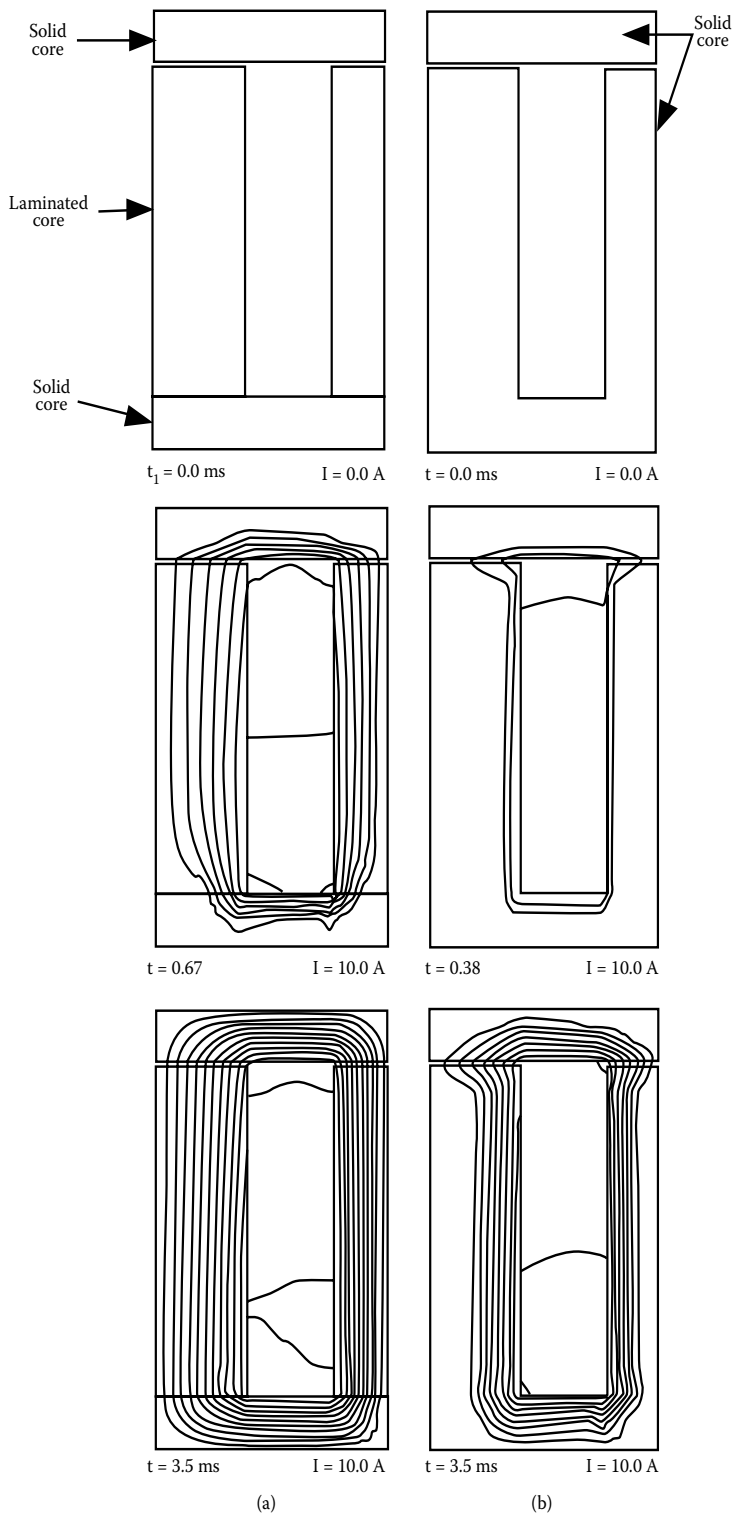
precise injector timing because diesel engine speed and power are controlled by the amount of fuel injected into the engine rather than airflow. Figure 3.51 shows a cross section of a diesel electronic injector. The actuator consists of a coil, an armature, and a magnetic circuit. The magnetic core has both laminated and solid core parts. Laminated parts are introduced in the form of a wound core to suppress eddy currents and to allow for fast penetration of the magnetic field.

Figure 3.52 shows a comparison of the penetration of the magnetic field within a laminated and solid core at the same MMF level with a current of 10.0 A. Clearly, the magnetic field penetrates much deeper into the laminated core despite the fact that both the bottom and the top (armature) parts are solid. Figure 3.53 shows the performance comparison of dynamics between the diesel injectors having partially laminated and solid magnetic cores. Figure 3.53(a) shows that the slope of the partially laminated core injector is steeper than the current slope of the injector having a solid core circuit. Because of this, the magnetic force developed by the injector with the partially laminated core is established much faster than the magnetic force of the injector having a solid core circuit; see Figure 3.53(b). Finally, the displacement performance of the armature for the injector with the partially laminated core is superior in comparison with the magnetic force of the injector having the solid core circuit, as presented in Figure 3.53(c).

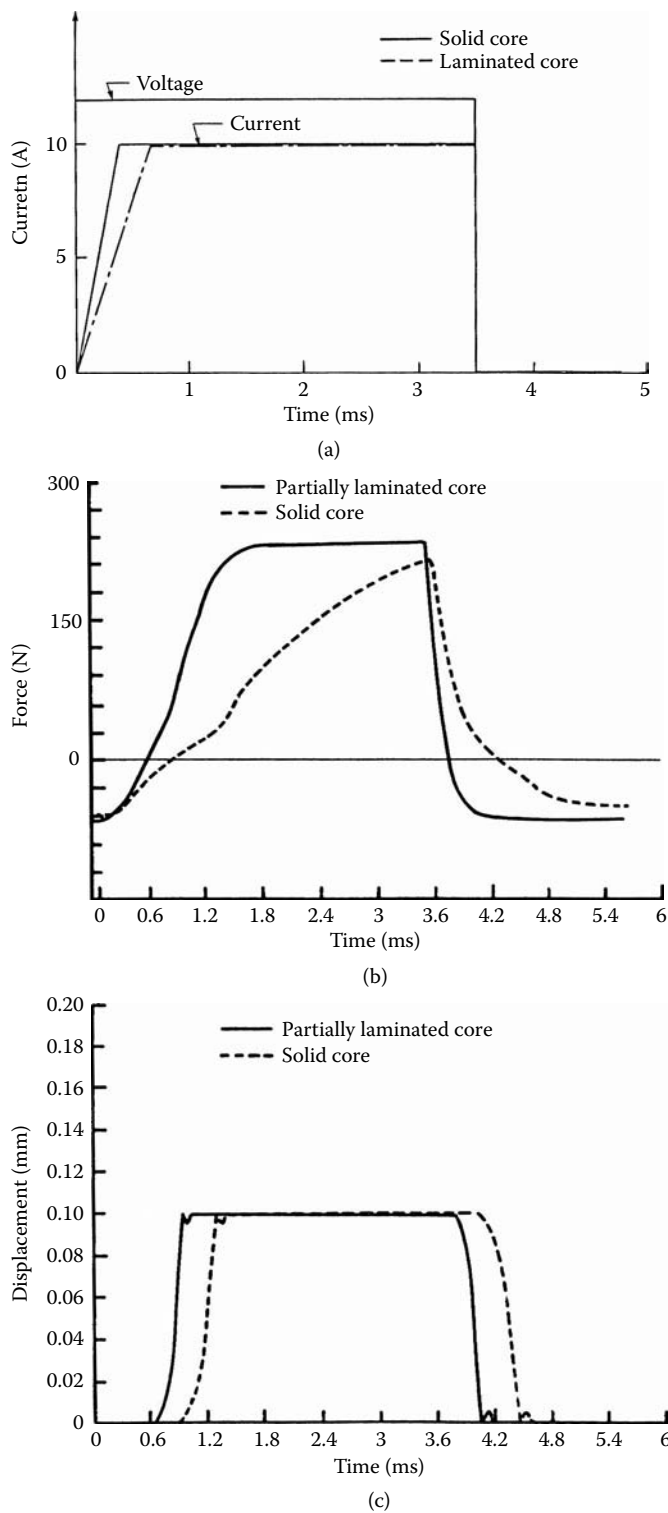
Diesel injector optimization was performed for the injector geometry introduced in Figure 3.51 for two different air gaps — a small gap of 0.11×10^{-3} m and a big gap of 0.2×10^{-3} m — and a specified plunger displacement of 0.06×10^{-3} m and 0.11×10^{-3} m, respectively. For a diesel injector, it is critical that a high armature force is established very quickly to withstand the engine's high pressure. The time to achieve the required injector force of 200.0 N in a function of coil parameters (number of turns) is analyzed. First, the current vs. time characteristics are established for both air gaps, as presented in Figure 3.54.

Dynamic response of the diesel injector for both air gaps is presented in Figure 3.55. The start time is t_1 , the opening time is t_2 , the return time is $t_4 - t_0$, the time to reach required magnetic force of 200.0 N (or 45 lb) is t_{45} , and the total travel time is $t_2 + (t_4 - t_0)$. The injector performance and details of the selected coil (gauge and turns) are presented in Table 3.3 and are also shown in Figure 3.55(a) and Figure 3.55(b).

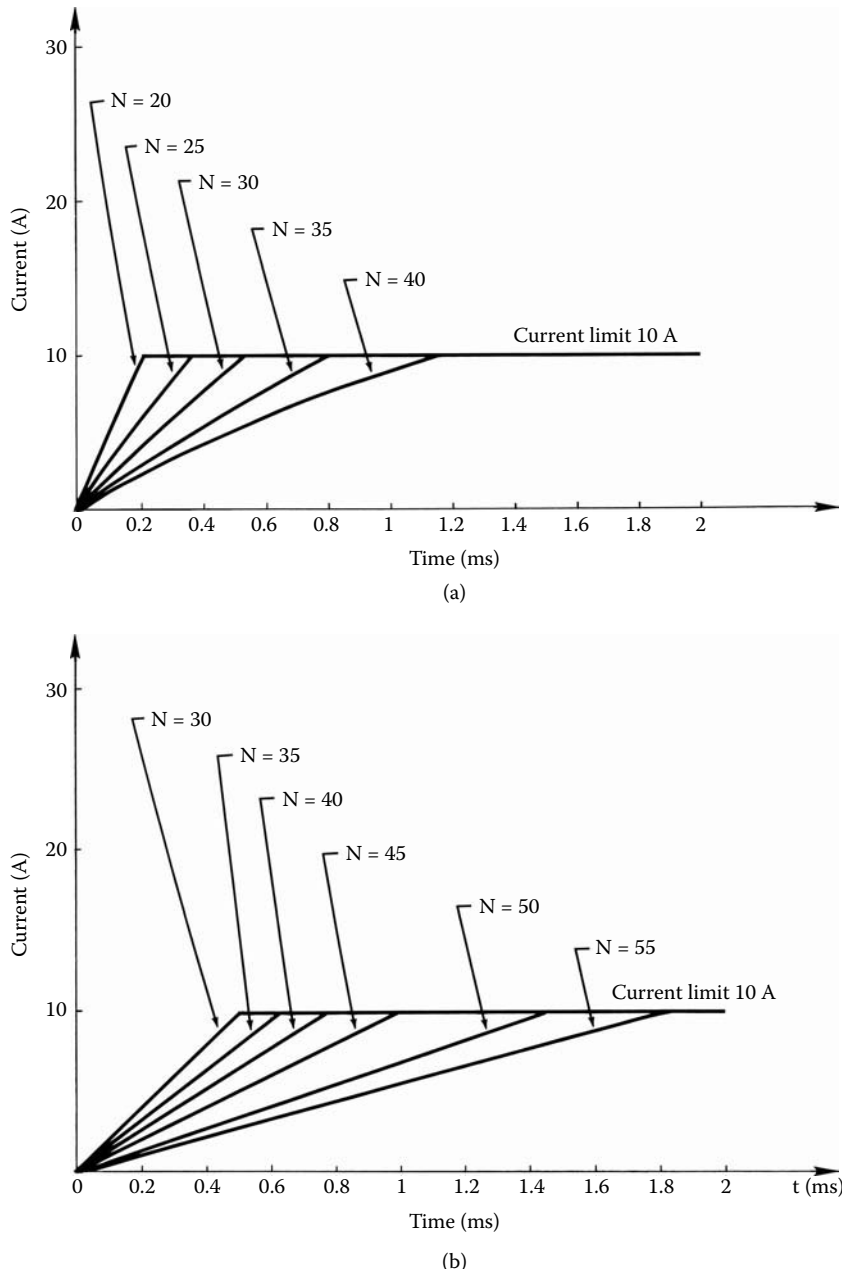
The comparison of the critical t_{45} characteristics for both air gaps is presented in Figure 3.56. By establishing different air gap openings and, therefore, different displacement distances (that provide information about an amount of fuel delivered for a given pulse width), one can determine the coil parameters, provided the other magnetic-circuit dimensions already have been optimized.

**FIGURE 3.52**

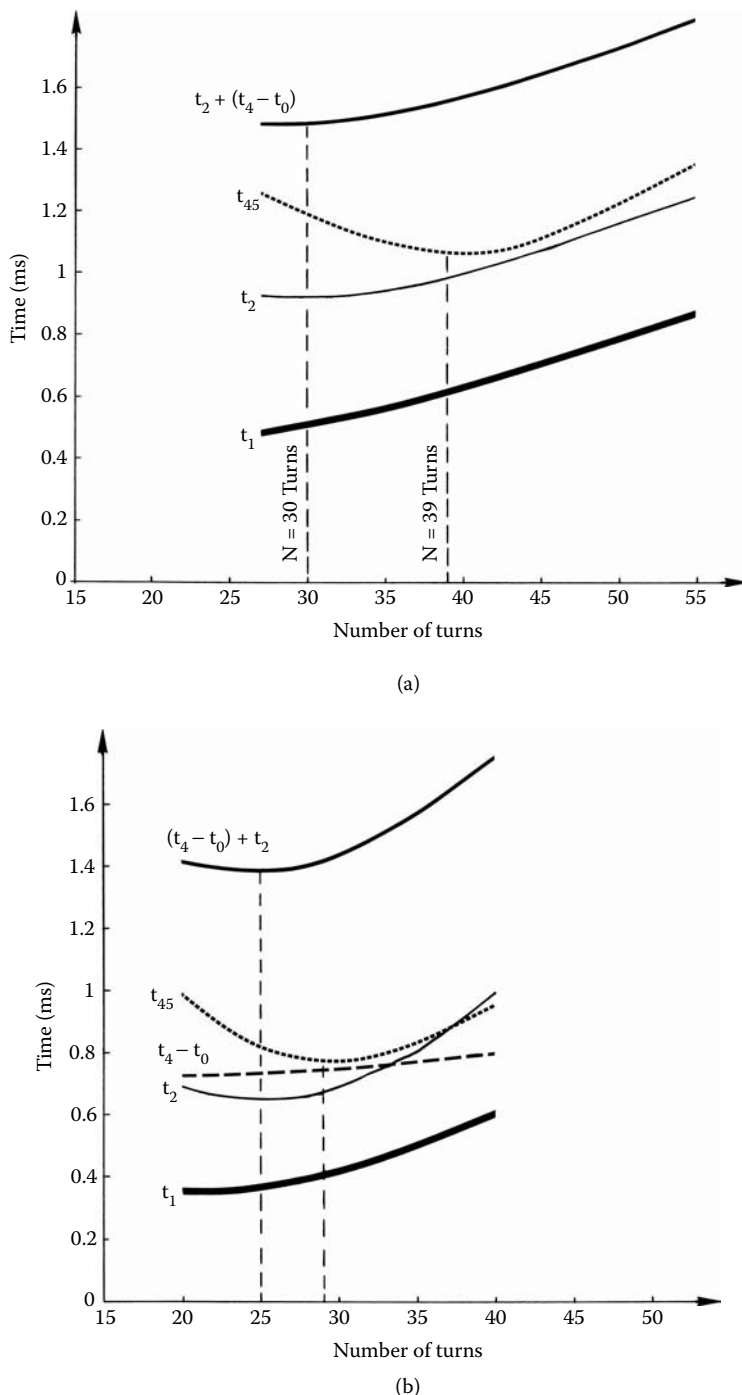
Flux lines penetration into magnetic core comparison: (a) partially laminated core, (b) solid core. (Courtesy of Delphi Corp.)

**FIGURE 3.53**

Dynamics of the diesel injector: (a) current vs. time for voltage source comparison, (b) force vs. time comparison, (c) current vs. time comparison. (Courtesy of Delphi Corp.)

**FIGURE 3.54**

Current vs. time characteristics: (a) small air gap of 0.11×10^{-3} m, (b) big air gap of 0.2×10^{-3} m. (Courtesy of Delphi Corp.)

**FIGURE 3.55**

Displacement time vs. coil turns characteristics: (a) small air gap of 0.11×10^{-3} m, (b) big air gap of 0.2×10^{-3} m. (Courtesy of Delphi Corp.)

TABLE 3.3
Performance Comparison

Air Gap ($\times 10^{-3}$ m)	Displacement ($\times 10^{-3}$ m)	Coil		Time of Response (ms)				
		N (turns)	AWG (gauge)	t_1	t_2	t_3	t_4	t_{45}
0.2	0.1	39	21	0.53	0.94	3.75	4.06	1.19
0.11	0.06	29	19	0.43	0.69	3.95	4.26	0.76

Source: Courtesy of Delphi Corp.

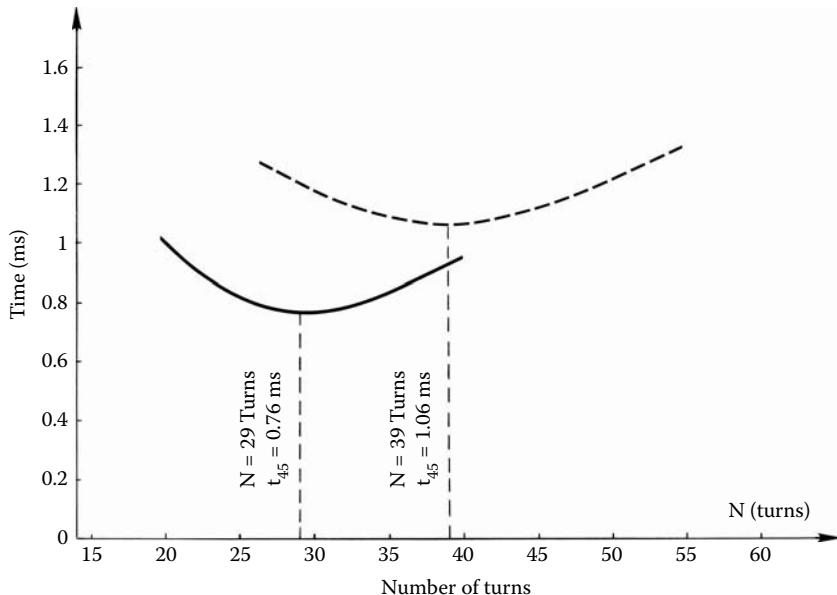
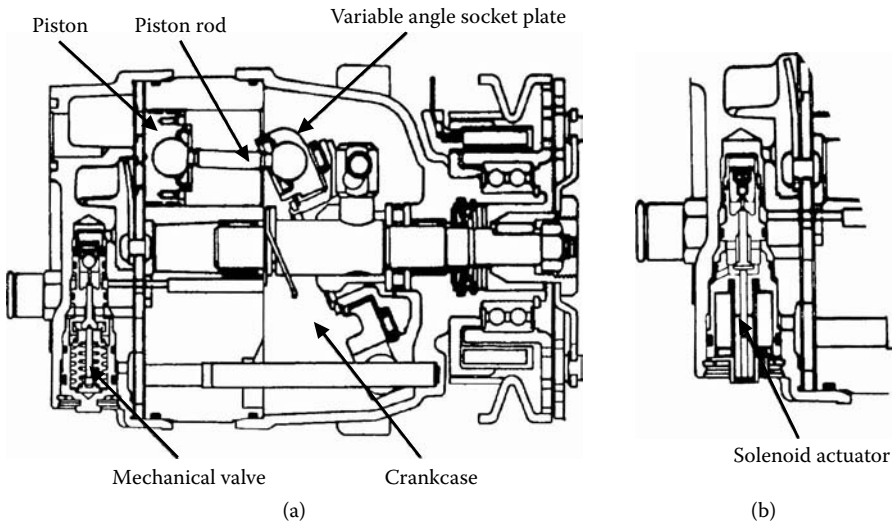


FIGURE 3.56
Time vs. coil turns for the required force of 200.0 N. (Courtesy of Delphi Corp.)

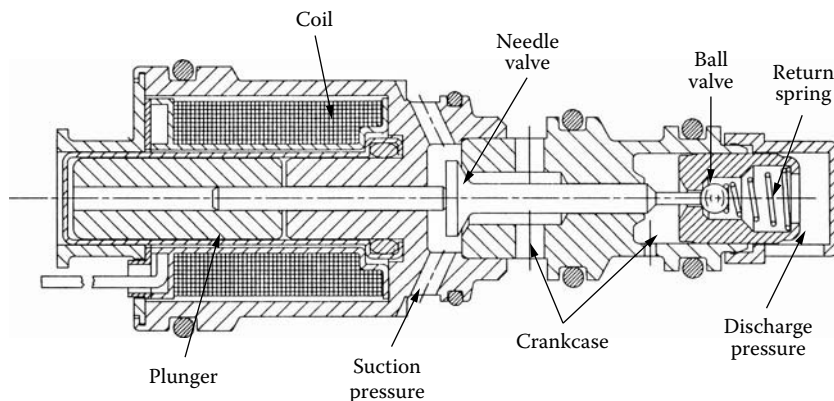
3.3.5 Compressor Solenoid Valves

Another application of the solenoid valve is an air-conditioning compressor with variable displacement. A unique feature of this compressor is that the displacement can vary depending on the cooling needs by varying the piston stroke. Changing the pressure in the crankcase of the compressor modulates the displacement. A mechanical valve senses evaporator pressure and bleeds a controlled amount of high-pressure gas into the crankcase. The amount of bleed determines the crankcase pressure and the compressor displacement, as presented in Figure 3.57(a).

A solenoid valve replaces the mechanical valve with a plunger-type solenoid actuator, as presented in Figure 3.57(b). This permits microprocessor control, resulting in greater flexibility and improved passenger comfort. By operating in pulse-width operating mode, the solenoid actuator controls the crankcase pressure between the low-pressure suction gas and high-discharge gas pressure. The pressure differential between the top and the bottom of the pistons creates a net force coupled with changes of angle of the socket plate, as presented in Figure 3.57(a). This varies the piston stroke and, thus, the displacement of the compressor.

**FIGURE 3.57**

Cross section of the variable displacement compressor: (a) mechanical pressure control, (b) solenoid pressure control. (Courtesy of Delphi Corp.)

**FIGURE 3.58**

Solenoid valve actuator. (Courtesy of Delphi Corp.)

This section describes the results of optimization of the solenoid design. In fact, two solenoid designs are obtained: one with maximum plunger force and another with the minimum current draw. Maximizing the force at the nominal current should improve valve stability and make performance less sensitive to manufacturing tolerances. However, minimizing the current draw at the nominal plunger force should simplify the driver unit and reduce its cost.

The original design of the solenoid actuator for the compressor is shown in Figure 3.58. When the coil is energized, the needle valve closes and a ball valve opens. This exposes the crankcase to a high-pressure discharge gas, which increases the crankcase pressure. When the coil is not energized, the needle valve opens by the return spring, which vents the compressor crankcase to low-pressure suction gas.

The solenoid operates at a relatively low frequency of 8.0 Hz or 125.0 ms time period. Dynamic operation of the original solenoid takes 6% of the time period and because this

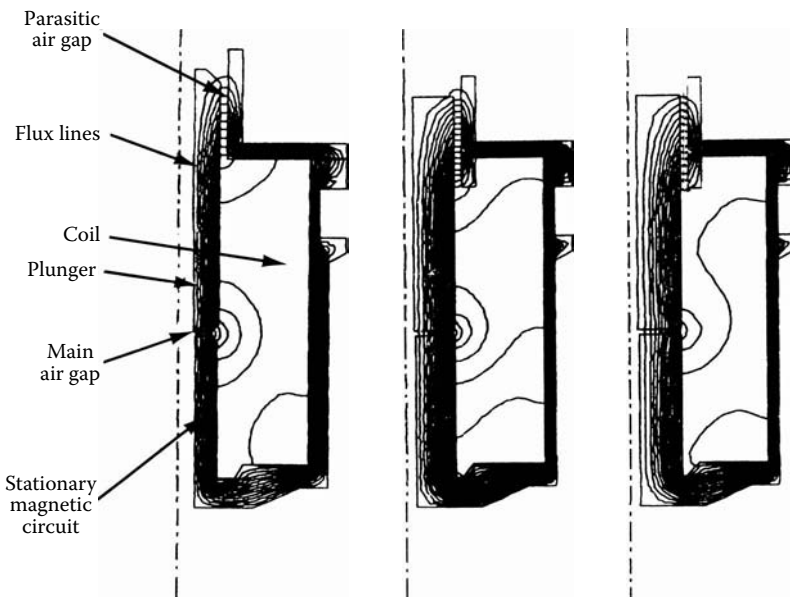


FIGURE 3.59

Flux lines for three solenoid designs: (a) original design, (b) maximum force design, (c) minimum current design. (Courtesy of Delphi Corp.)

is relatively slow, it is acceptable to optimize the static performance of the solenoid. The static performance should be optimized at worst-case operating conditions, a minimum voltage of 9.5 V and an elevated coil temperature of 120.0°C.

Before the optimization procedure, it is recommended to simulate both static and dynamic behavior of the solenoid valve, as presented in Equations 3.1, 3.9, and 3.12–3.14. The results of these simulations are helpful in the optimization steps. Because the first objective is to maximize the force of the plunger, any changes should increase the solenoid's working air gap flux density and enlarge the plunger active area according to Equation 3.12. It is best to increase flux density by reducing the flux leakage and by increasing the effective flux, eliminating flux local saturation bottlenecks. To do this, both the magnetic circuit and the coil should be considered. The optimum position of the main air gap helps achieve flux leakage reduction. Substituting the sharp corners at the plunger and the plunger stop in place of rounded corners and increasing the plunger and plunger stop ODs also help increase the total surface area. Enlarging the active surface area of the parasitic air gap by lowering the position of the magnetic flange reduces the MMF drop in this area by avoiding local saturation. Generally, all dimensions can be changed, as presented in Figure 3.59, except the outside envelope because that is usually prohibited.

For the coil optimization, the available coil space can be redesigned, as well as the wire diameter and the number of turns. The objective is to utilize fully the available coil window area. Table 3.4 combines the effect of all these steps for the solenoid valve. It compares the flux density at the three magnetic-circuit locations and certain solenoid parameters. The flux densities in the optimized designs are more uniform, which indicates better magnetic-circuit utilization by avoiding local saturations. The achieved results indicate that the maximum force design has 91% greater force than the original design with 6% less current. Minimum current versions have 56% lower current with the same force. Note that a small design difference in current (0.69 A vs. 0.65 A) is the result of designing with discrete wire gauge sizes.

TABLE 3.4

Solenoid Performance Comparison

Design	Coil Parameters		Plunger Force (N)	Flux Density			Response Time (ms)
	Current (A)	MMF (At)		Air Gap (T)	Plunger (T)	Housing (T)	
Original	0.69	572	9.81	1.3	1.8	0.4	7.7
Maximum force	0.65	532	18.7	1.4	1.6	1.1	7
Minimum current	0.31	355	9.81	1	1.1	0.9	13.5

Source: Courtesy of Delphi Corp.

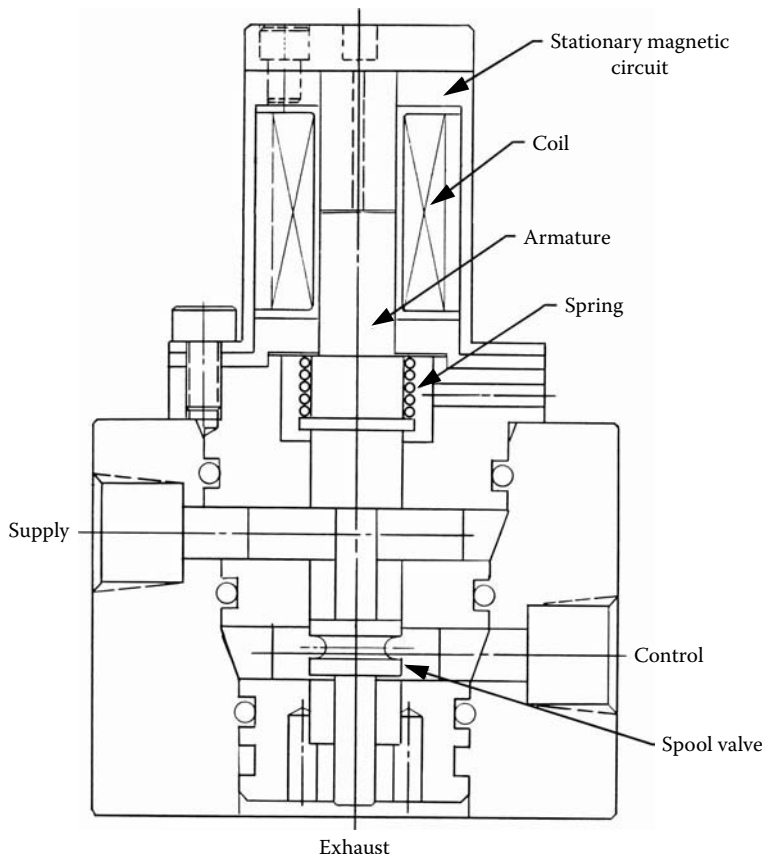
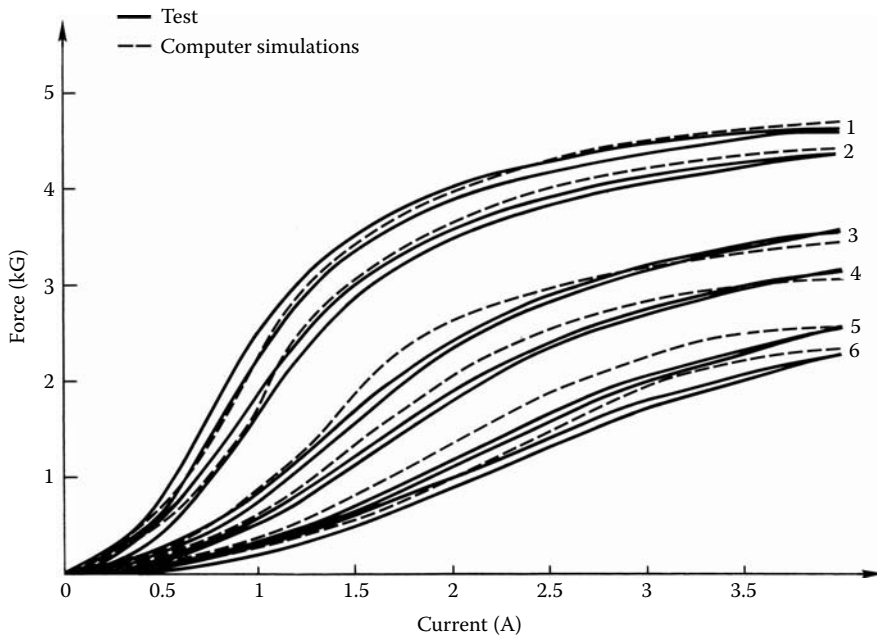


FIGURE 3.60
Transmission spool valve solenoid. (Courtesy of Delphi Corp.)

3.3.6 Transmission Solenoids

A conventional hydraulic valve body for a hydraulic transmission that used to be specially adapted for each vehicle has been replaced with a microprocessor-based solenoid valve with a controller that permits easier calibration and more precise control of shift. In addition, electronic control permits the integration of the engine and transmission computers to optimize powertrain control. An important item in developing the electronically controlled transmission is a fast-acting solenoid, as presented in Figure 3.60, to control

**FIGURE 3.61**

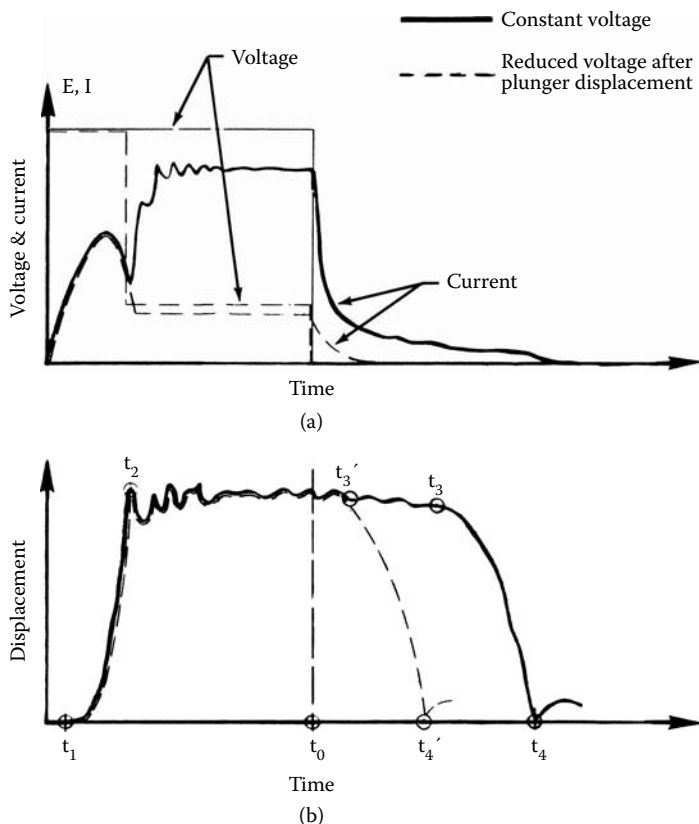
Static force vs. current for different air gaps: (1) 0.0125×10^{-3} m, (2) 0.0196×10^{-3} m, (3) 0.0367×10^{-3} m, (4) 0.049×10^{-3} m, (5) 0.0735×10^{-3} m, (6) 0.088×10^{-3} m. (Courtesy of Delphi Corp.)

clutch pressure by PWM operating a spool valve between a supply and exhaust pressures during shifting with a low current drain from the battery. Because there are as many as seven solenoids in a passenger car transmission, three of which are typically on at any one time, even a 1.0 to 2.0 A current drain has a significant impact on fuel economy, alternator size, etc.

Design and optimization of the transmission solenoid can be done using the mathematical model introduced in Section 3.1. Static analysis of the solenoid has to be performed by evaluating the plunger force at the different discrete plunger positions. The force acting on the plunger is a function of the current level and of the plunger position vs. plunger stop (value of the working air gap). Solenoid total air gap value of 0.082×10^{-3} m and maximum current value of 4.0 A can be used as maximum values for the gap position and current level, respectively. Because at least five testing points are needed to draw a characteristic, it is advisable to use six different positions from 0.0125×10^{-3} m to 0.082×10^{-3} m and six different current values from 0.0 to 4.0 A for static simulations.

Figure 3.61 shows the results of the analysis where all the characteristics were recorded for the increasing current, the lower part of hysteresis, and for the decreasing current, the upper part of hysteresis. In experiments, the test fixture should provide the same exact air gaps of the load cell to record a force at the desired current level. Because of the different current excitation, a family of the force curves is obtained as a function of current characteristics, as shown in Figure 3.61. A comparison of the test results and calculations shows good agreement. The dynamic behavior of the actuator is described in the mechanical Equation 3.9, and the electromagnetic force expressed in Equation 3.12 depends generally on all four current components, as presented in Equation 3.14.

There are two ways to operate such a solenoid actuator in the dynamic mode, as presented in Figure 3.62:

**FIGURE 3.62**

The voltage and current (a) and displacement (b) vs. time: t_1 start time, t_2 travel time up, $t_4 - t_0$ travel time down. (From Pawlak, A.M., *Proceedings of COMPEUMAG, Conference on the Computation of Electromagnetic Fields*, No. AP33, Tokyo, September 3–7, 1989. With permission.)

TABLE 3.5
Transmission Solenoid Requirements

Parameter	Unit	Requirement
Preload of the spring	N	1.785
Spring constant	$\times 10^3$ N/m	5.465
Spring mass	$\times 10^{-3}$ kg	0.75
Maximum travel	$\times 10^{-3}$ m	0.9
Holding current at full voltage pulse	A	4
Peak current at full voltage pulse	A	4
Holding current at full voltage pulse	A	1.5
Peak current at reduced voltage pulse	A	2.5

Source: Courtesy of Delphi Corp.

1. The applied voltage pulse does not change its value.
2. The applied voltage pulse has its value reduced after a certain time, generally when the plunger reaches end of the travel.

TABLE 3.6
Test and Analysis Comparison

Results	Start Time t_1 (ms)	Travel Time t_2 (ms)	Requirements t_2 (ms)
Analysis	0.99	2.98	2.0
Test	1.01	3.07	2.0

Source: Courtesy of Delphi Corp.

In the first case, the applied voltage pulse stays unchanged beyond the t_2 time, where the current reaches its maximum value, which depends only upon applied voltage and resistance of the coil. The current beyond the t_2 time is called the holding current because it works against the compressed spring and holds the plunger in the closed position. The holding current for the reduced voltage case has the lower value, and therefore, time of operation is more appropriate in any application because less energy is consumed. Moreover, because less energy is stored in the magnetic circuit, the open t_3 time and t_4 are much faster in the second mode of operation. This also permits the use of a high current to get the plunger moving and then a low current to keep the average consumption low.

Because the voltage pulse is applied with t_0 width, the current increases and the plunger starts moving in t_1 time. The travel of the plunger is accomplished in t_2 time. The current does not rise monotonically because of the change of inductance due to the shrinking air gap. Typical requirements for the transmission solenoids are presented in Table 3.5, which also includes the maximum values for the peak current and the holding current for both modes of operation.

With the proper specification and input data, one can obtain good agreement between dynamic FE simulations and test results for dry operation with 2.0% difference for the t_1 start time and t_2 travel up, as presented in Table 3.6.

For the dynamic simulations, the reduced voltage mode was used to verify dynamic performance with requirements for this mode as shown in Table 3.5. Because good agreement was obtained for the static and dynamic cases, it also proves that using proper mathematical models, dynamic behavior of the transmission solenoid can be predicted within good engineering accuracy. Figure 3.63 shows the comparison of the computer simulations and test results of the transmission solenoid.

One can optimize fast-acting solenoids through changes in the magnetic circuit and in the coil design or both. Because the magnetic circuit of the solenoid is a solid core, selecting good material with high electrical resistivity (to suppress eddy currents) and good magnetic properties (to increase magnetic flux) is recommended. A good candidate is silicon steel. In our case, Carpenter silicon steel-type "B-FM" was selected (Carpenter 1989). Optimization is an iterative process and for the magnetic circuit the first step is to consider the plunger stop position and the plunger OD. Considering these variables in the computer simulations, the appropriate plunger mass (inertia) should be taken into account. In the existing design, introduced in Figure 3.60, the plunger with a spool valve (total moving mass) weighs 11.78 g and the plunger stop is located in the center of the coil, $17.0 \times 10^{-3} \text{ m}$ from the plunger base. The computer simulations provide a response time t_2 of 2.98 ms . Figure 3.64 shows the dynamic response of the plunger for start time and the total travel time vs. plunger OD and the corresponding plunger weight.

From these results, the best OD obtained from the plunger is $11.2 \times 10^{-3} \text{ m}$. Because a bigger OD of the plunger reduces the available space for coil (as outside solenoid diameters must remain the same), a plunger OD of $10.36 \times 10^{-3} \text{ m}$ was selected because the total travel time is almost the same (2.20 ms instead of 2.18 ms). For the new diameter, its best

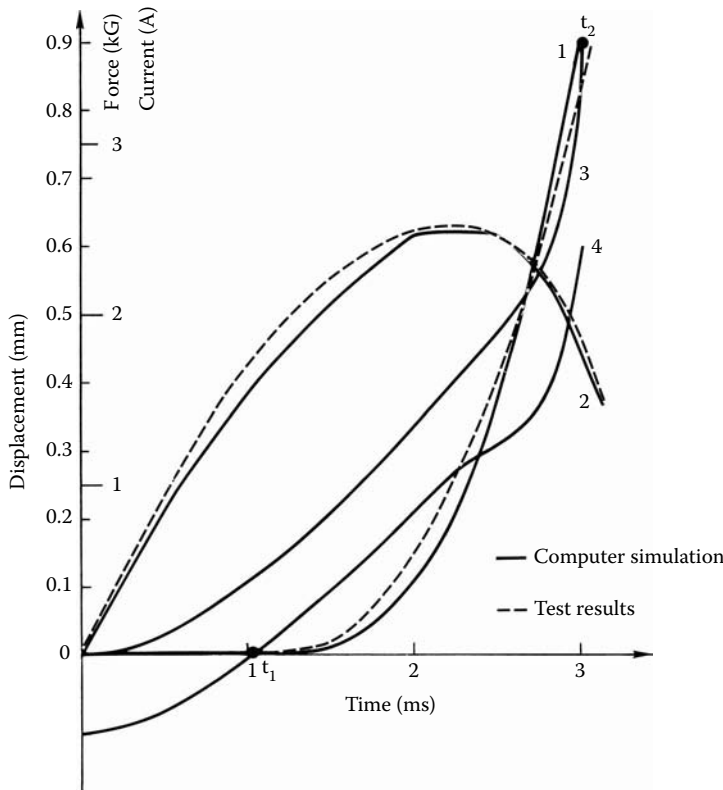


FIGURE 3.63

Dynamic simulations and test results of the transmission solenoid: (1) displacement, (2) current, (3) magnetic force, (4) plunger force. (Courtesy of Delphi Corp.)

position was optimized and compared with its previous location with the original plunger diameter, as presented in Figure 3.65.

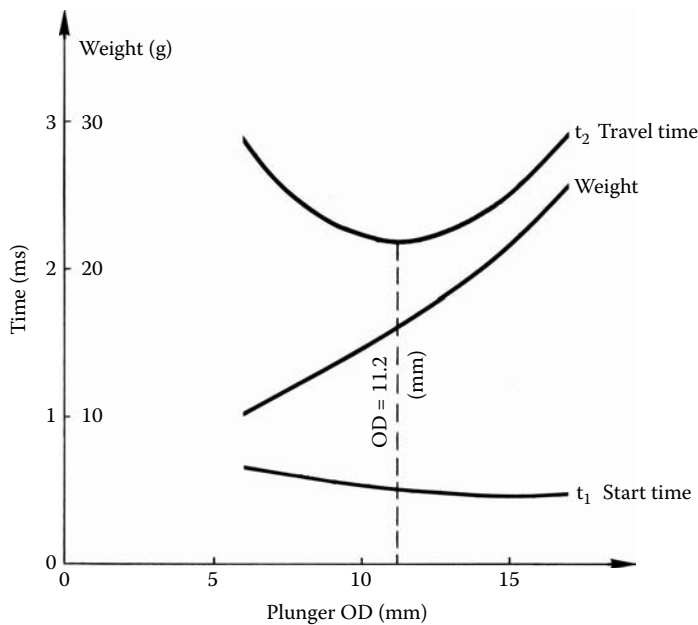
This analysis led to the conclusion that the best plunger location and diameter are a trade-off between the weight of the plunger and a magnetic flux buildup in the plunger for a given current source. Also, the best magnetic flux utilization with minimum flux leakage exists when the plunger is located in the center of the coil. By minimizing the total moving mass of the plunger, the total travel time can be reduced. One way to do this is to provide a hole in the plunger. The hole, however, affects flux distribution and decreases the active plunger surface, although the plunger weight also decreases. The hole was investigated and the results presented in Figure 3.66 show that any hole in an active plunger would increase total travel time. Therefore, this direction is not recommended.

After the best magnetic circuit is established, the coil can be optimized to increase the rate of rise of the current vs. time and reduce peak holding current, improving response time, and reducing the current drain from the battery, respectively. Based on two well-known equations that describe the slope of the current, neglecting coil resistance:

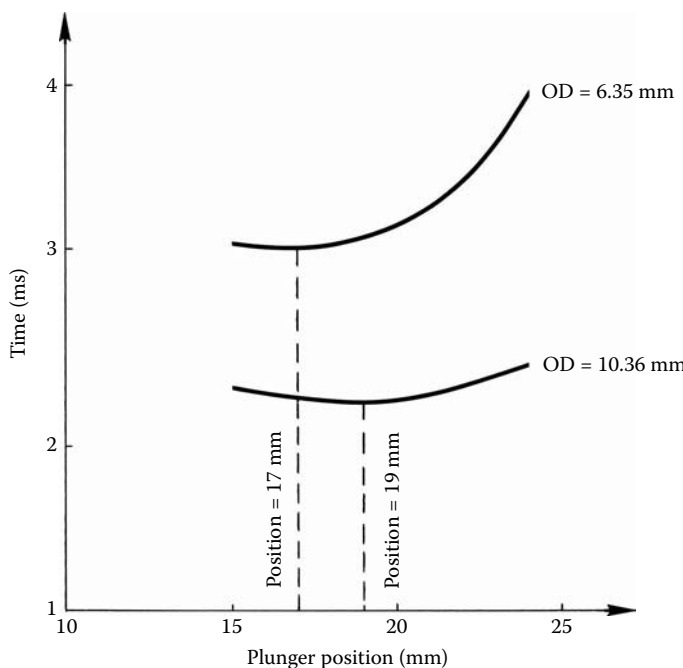
$$\frac{di_s}{dt} = \frac{e_s}{L} \quad (3.15)$$

and

$$L = \frac{N\phi}{i_s} \quad \text{or} \quad L = N^2 P \quad (3.16)$$

**FIGURE 3.64**

Plunger response and mass vs. OD. (From Pawlak, A.M., *Proceedings of COMPLUMAG, Conference on the Computation of Electromagnetic Fields*, No. AP33, Tokyo, September 3–7, 1989. With permission.)

**FIGURE 3.65**

Total travel time vs. plunger position for different ODs. (Courtesy of Delphi Corp.)

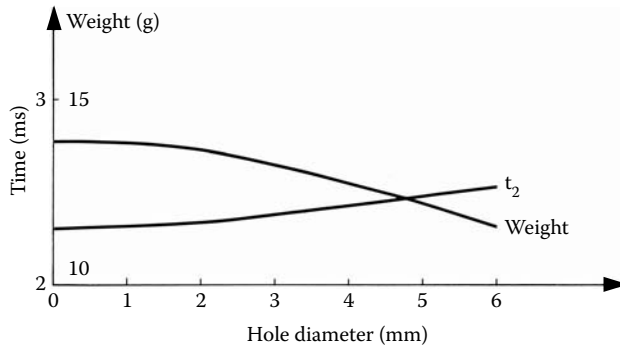


FIGURE 3.66
Total travel time and plunger mass vs. plunger hole diameter. (Courtesy of Delphi Corp.)

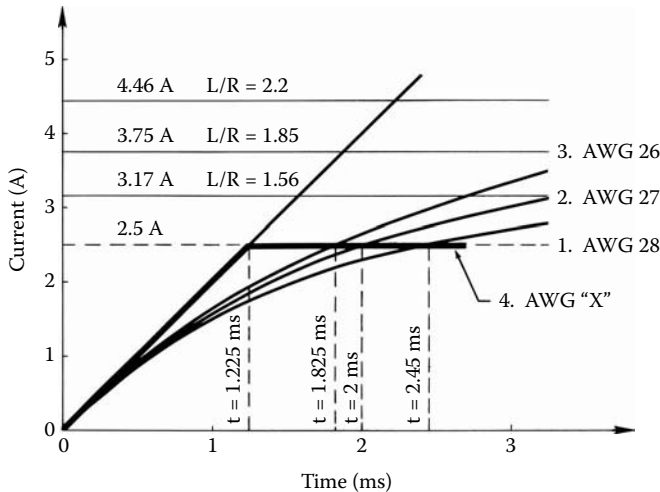


FIGURE 3.67
The current vs. time. (Courtesy of Delphi Corp.)

where i_s is a current in the coil, e_s is applied voltage, L is inductance, N is number of turns, ϕ is magnetic flux, and P is the permeance of the magnetic circuit. Taking into account the constraints, Equation 3.15, and Equation 3.16, the slope of the current can be increased if the voltage input is increased or the inductance is reduced. Increasing the voltage is not possible because of the automotive system battery voltage limitation, but one can try to reduce inductance by reducing the number of turns or changing the permeance of the magnetic circuit. The inductance of the coil may not be decreased by reducing the number of turns because this may reduce the holding force requiring an increase in holding current,

TABLE 3.7

Solenoid Performance for Different Coil Parameters

Coil and Performance (AWG)	Turns (No.)	Resistance (Ω)	Diameter ($\times 10^{-3}$ m)	Opening Time (ms)	Total Time (ms)	Time at 2.5 A (ms)
28	400	3.79	20.0	0.71	2.46	2.45
27	400	3.2	21.6	0.68	2.33	2.00
26	400	2.69	23.5	0.66	2.2	1.825
"X"	400	TBD	TBD	0.59	2.08	1.225

Source: Courtesy of Delphi Corp.

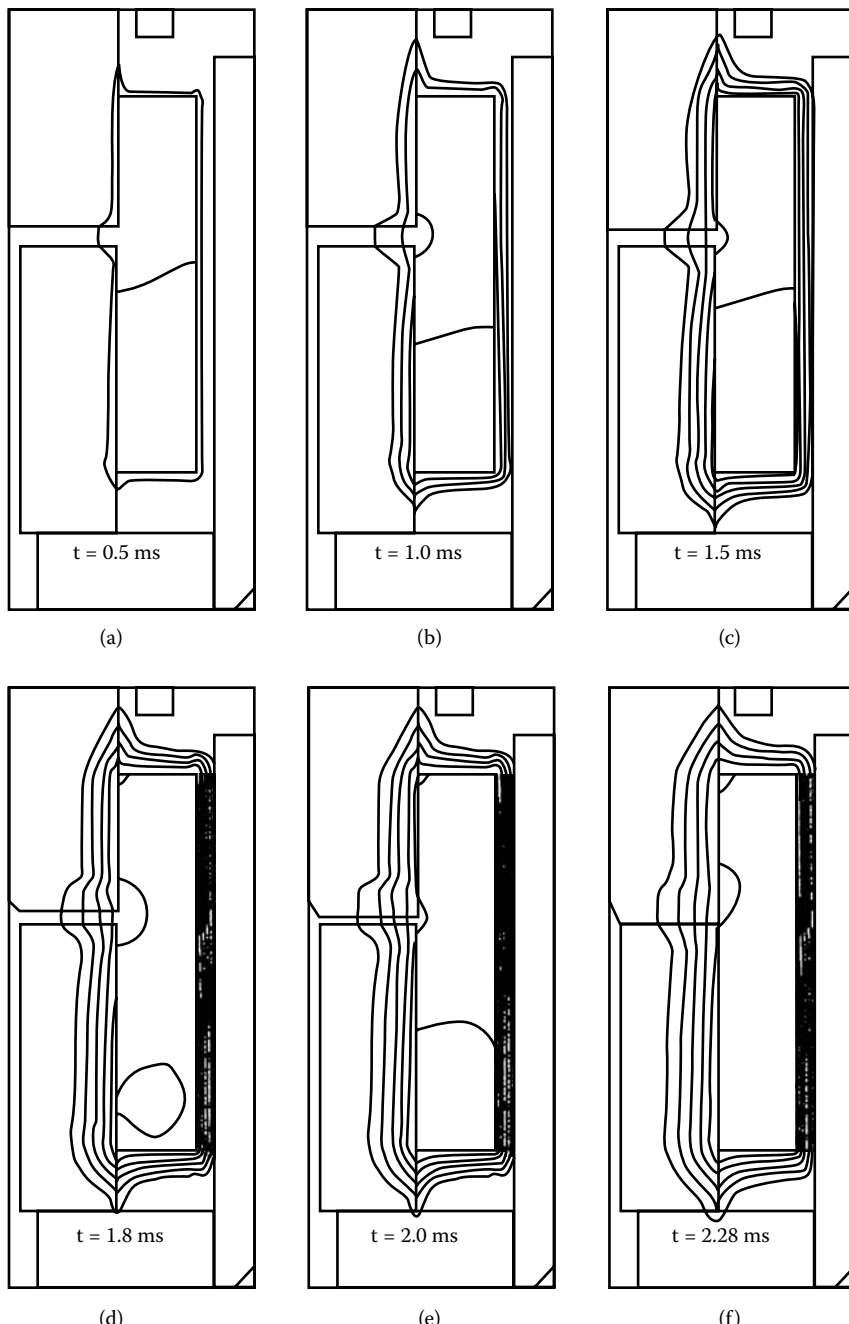
which is not possible because of the requirements presented in Table 3.5. Because of the fixed geometry, the permeance is also fixed, so changing permeance cannot change the inductance. Even so, one should not be interested in reducing permeance because it would reduce flux density and force. Therefore, the only way to change the slope of the current is to change its resistance with the same number of turns by fully utilizing available space. This can be done by changing the wire diameter and resistance at the same time. Figure 3.67 and Table 3.7 show how the diameter of wire (resistance) affected the current vs. time shape and the time when the current reaches the peak current limit of 2.5 A for the reduced voltage source. The current shapes vs. time were calculated on the basis of the inductances and resistances neglecting the eddy current effect. Therefore, these current shapes are more optimistic and reach the peak current limit faster than in the real case, as shown by the equation:

$$i_s(t) = \frac{e_s}{R} \left(1 - e^{-\frac{R}{L}t} \right) \quad (3.17)$$

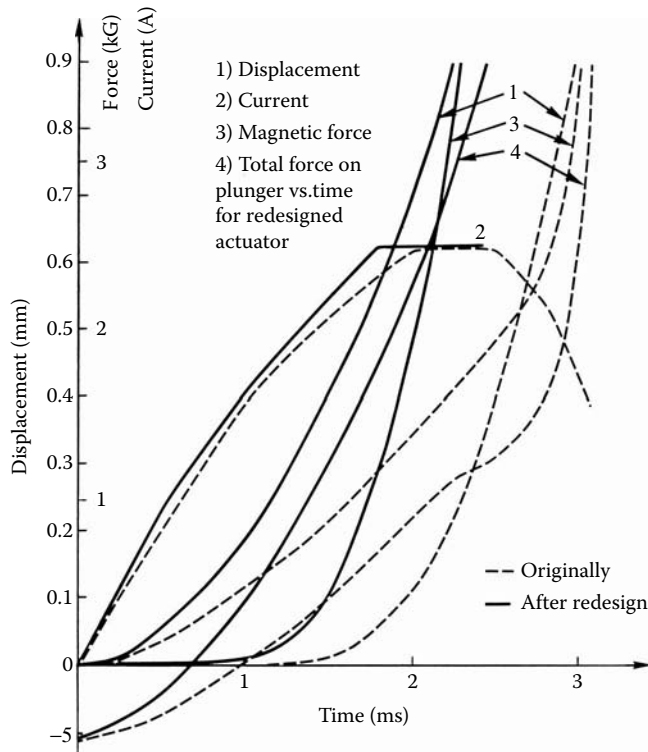
where i is the winding current and R is the coil resistance. The total travel time of 2.98 ms with the same original coil was reduced to 2.46 ms after the magnetic circuit was changed with the same coil parameters (AWG size 28 and number of turns = 400). As a result of these changes, the OD increased from 20.0×10^{-3} m to 23.5×10^{-3} m and the total travel time was further reduced to 2.20 ms, which is 26% faster than the original design. Theoretically, even by increasing wire diameter to the point where resistance is neglected (see "X" wire diameter) the current shape will change the total travel time of 2.08 ms achieved, which is still not satisfactory according to solenoid requirements, as presented in Table 3.5 and Table 3.7.

The flux lines and the displacement of the optimized solenoid are shown in Figure 3.68, where one can notice an increased number of flux lines and movement of the armature.

Figure 3.69 shows the displacement, the forces, and the current vs. time for the actuator before and after the magnetic circuit and coil optimization. The optimized actuator showed a big improvement in the dynamic response but it still does not satisfy requirements as presented in Table 3.5. Therefore, a bistable latching solenoid having a PM that provides a latching force without current application may be an option for these applications; see Chapter 4.

**FIGURE 3.68**

Flux lines vs. time with different plunger positions at dynamic operation: (a) flux at 0.5 ms, (b) flux at 1.0 ms, (c) flux at 1.5 ms, (d) flux at 1.8 ms, (e) flux at 2.0 ms, (f) flux at 2.28 ms. (From Pawlak, A.M., *Proceedings of COMPUMAG, Conference on the Computation of Electromagnetic Fields*, No. AP33, Tokyo, September 3-7, 1989. With permission.)

**FIGURE 3.69**

Dynamic analysis for the original and optimized solenoid valve: (1) magnetic force, (2) current, (3) displacement, (4) net force. (Courtesy of Delphi Corp.)

Example 3.1

Calculate magnetic flux, core and air energy, inductance, and force of the disk solenoid with simple rectangular *E-I* core based on a lumped-parameter model. *BH* characteristic is assumed linear for simplicity. Solenoid drawing, dimensions, and other solenoid parameters are provided in Figure 3.70:

Number of turns: 100

Nominal current 10 A

Permeability of air = 0.1256×10^{-5} H/m

Permeability of iron = 0.1256×10^{-2} H/m

Where the dimensions are:

$$D_1 = 20 \times 10^{-3} \text{ m} \quad H = 10 \times 10^{-3} \text{ m}$$

$$D_2 = 10 \times 10^{-3} \text{ m} \quad L = 10 \times 10^{-3} \text{ m}$$

$$D_3 = 10 \times 10^{-3} \text{ m} \quad W_1 = 10 \times 10^{-3} \text{ m}$$

$$G = 0.25 \times 10^{-3} \text{ m} \quad W_2 = 20 \times 10^{-3} \text{ m}$$

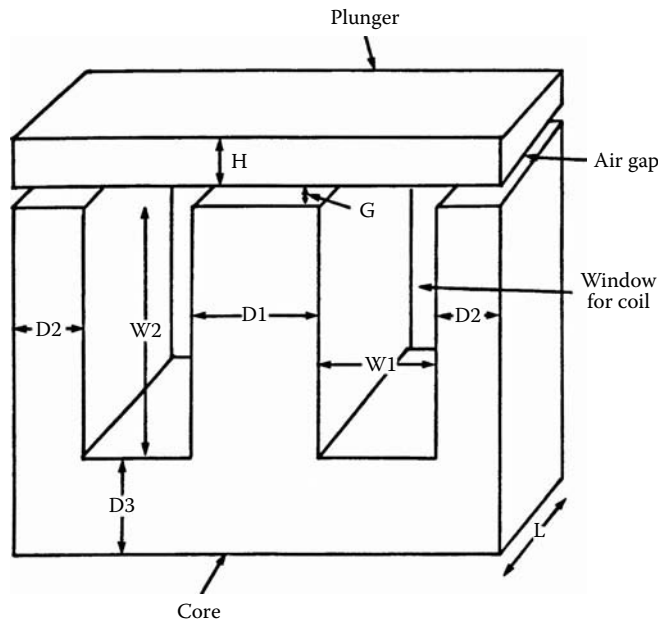


FIGURE 3.70
E-I core disk solenoid geometry. (Courtesy of Delphi Corp.)

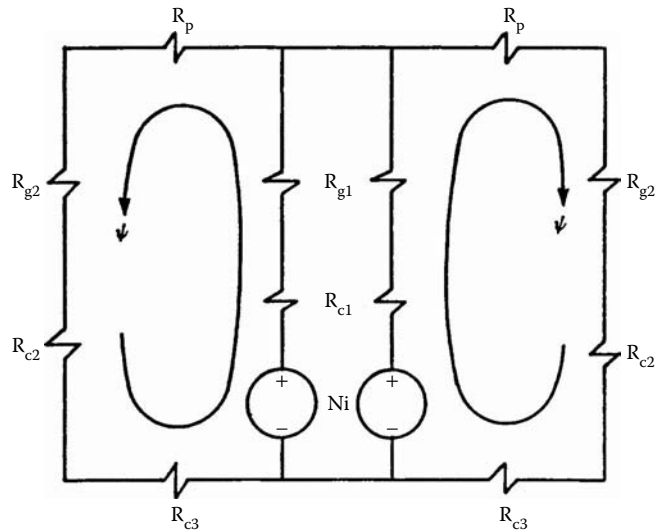


FIGURE 3.71
E-I core solenoid lumped-parameter model. (Courtesy of Delphi Corp.)

Step 1. Sketch Lumped-Parameter Model for E-I Core Solenoid, Figure 3.71

Here ϕ is the magnetic flux, Ni is the MMF, R_p is the reluctance of the plunger, R_{g1}, R_{g2} are air gap reluctances, R_{c1}, R_{c2}, R_{c3} are core reluctances.

Step 2. Calculations of the Lumped-Parameter Model; Model Description

Magnetic-circuit reluctance: $R = R_p + R_{c1} + R_{c2} + R_{c3} + R_{g1} + R_{g2} = 4.785 \times 10^6 \text{ A/Wb}$

Total reluctance: $R_T = R/2 = 2.392 \times 10^6 \text{ A/Wb}$

Magnetic flux: $\phi = \frac{Ni}{R} = \frac{1000}{4.785 \times 10^6} = 0.000209 \text{ Wb}$

Inductance: $L = \frac{N^2}{R_T} = \frac{100^2}{2.392 \times 10^6} = 4.19 \times 10^{-3} \text{ H}$

Total energy: $Energy = \frac{R_T \phi_T^2}{2} = \frac{2.392 \times 10^6 \times (2 \times 2.09 \times 10^{-4})^2}{2} = 0.209 \text{ J}$

Force: $F = \frac{B^2 A}{2 \times \mu_0} = \frac{1.324^2 \times 1 \times 10^{-4}}{2 \times 4\pi \times 10^{-8}} = 698.0 \text{ N}$

This concludes Example 3.1.

Example 3.2

Run FE analysis for the $E-I$ core rectangular solenoid presented in Example 3.1. Plot flux lines and flux distribution. Calculate flux, total air and core energy, inductance, and force of the disk solenoid, and compare with the lumped-parameter model.

Step 1. Make Assumptions and Prepare Input Data for FE Model

- The solenoid is assumed to be infinitely long (in the z direction), which means that end effects can be neglected. Consequently, the magnetic field exists in the $x-y$ plane and is independent of position along the z axis. For these reasons, the analysis can be restricted to a slice in the z direction of per unit length.
- Because the device and its excitation are symmetric about the centerline, the magnetic field, therefore, must also be symmetric around the same axis. Consequently, only one half of the device needs to be modeled, as presented in Figure 3.70.
- Assume physical and logical coordinates and mark on Figure 3.72 along with assumed relative permeabilities of the various regions.

Step 2. FE Simulations of the Solenoid's Static Parameters at MMF = 1000 At and Plot Flux Lines and Flux Distribution; Compare Data with Lumped-Parameter Calculations

Plot magnetic flux lines, Figure 3.73, and flux vs. position, Figure 3.74:

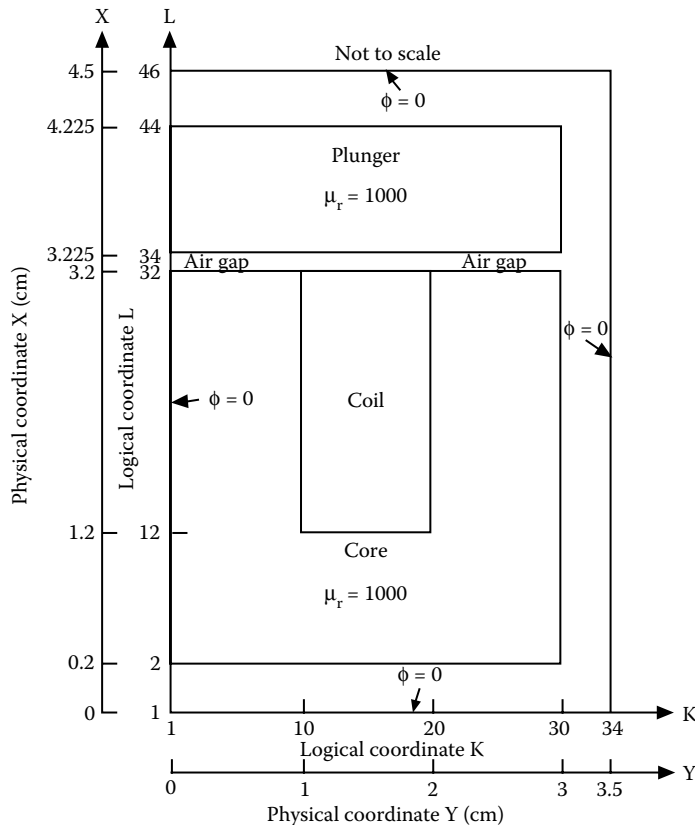


FIGURE 3.72
E-I core solenoid region to be modeled. (Courtesy of Delphi Corp.)

FE simulations results:

Flux: 0.000227 Wb

Total energy: 0.2225 J

Force: 705.4 N

Inductance: 4.45 mH

FE simulation comparison with lumped-parameter calculations:

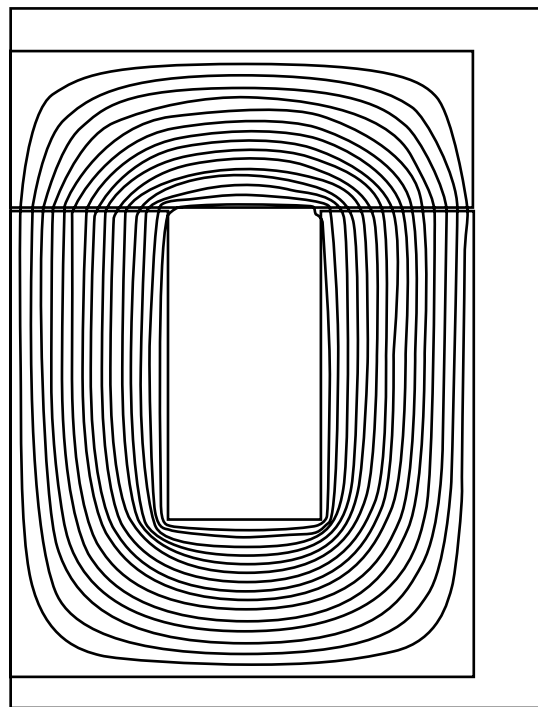
Flux: $\Delta\phi = 7.9\%$

Total energy: $\Delta E = 6.1\%$

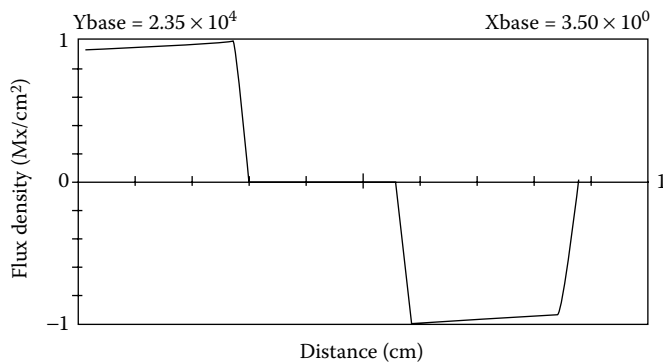
Force: $\Delta F = 1.0\%$

Inductance: $\Delta L = 5.8\%$

Comparison of the two sets of results reveals excellent agreement. One of the reasons is because the magnetic circuit is not saturated. This concludes Example 3.2.

**FIGURE 3.73**

E-I core solenoid flux lines. (Courtesy of Delphi Corp.)

**FIGURE 3.74**

E-I core solenoid flux density distribution. (Courtesy of Delphi Corp.)

4

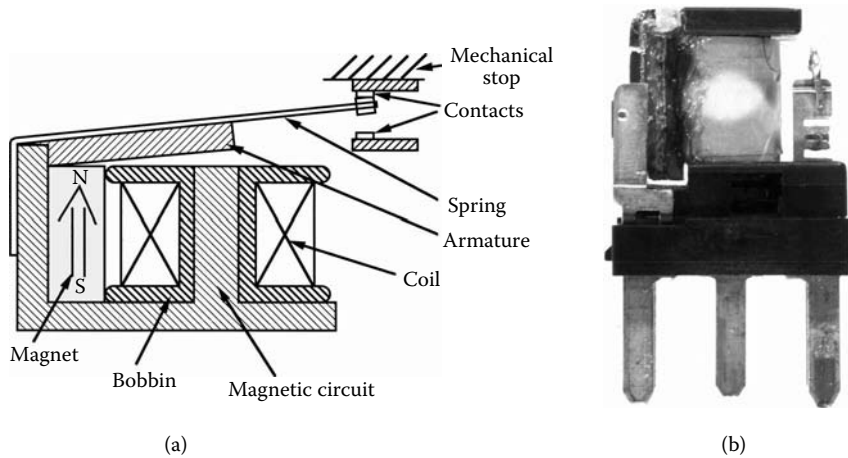
Latching Linear Actuators

Latching linear actuators represent a growing family of actuators that have latching function. The latching function can be defined as the capability of electromagnetic solenoids to maintain a last position when the power is off. There is a need for latching actuators in the industry because of their energy-saving capability. In the automotive industry, applications include injectors, relays, and fluid control solenoids. In particular, latching relay applications can result in significant energy savings in products such as daytime running lamps; fuel pumps; air-conditioning (A/C) clutch coils; heating, ventilating, air-conditioning (HVAC) blowers; engine cooling fans; and electronically operated transmission solenoids.

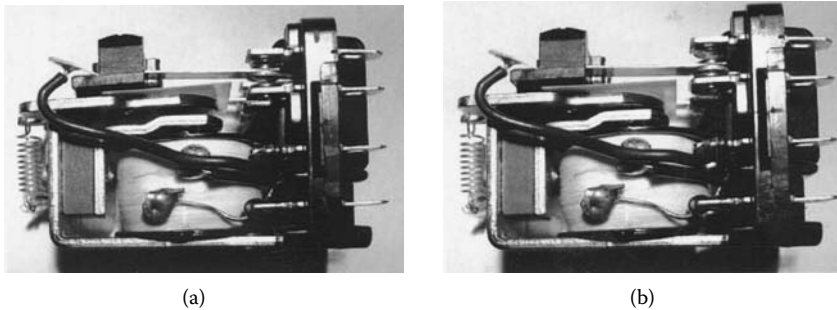
The latching function requires the presence of a PM in the magnetic circuit. It also requires that an actuator with its control circuit should have the capability to return the armature to its original position by a return spring action after the magnetic field holding the armature is dismantled (Pawlak et al. 1997, Pawlak et al. 1999).

4.1 Latching Relays

Both unipolar and bipolar latching relay configurations are discussed in this chapter. A bipolar relay consists of one coil and requires a controller having bidirectional current capabilities. This means more complex electronics, usually an H-switch allowing for bidirectional current, which is more costly than a conventional controller. A unipolar relay consists of two coils and a conventional controller with unidirectional current capabilities. The relay requires two coils, although controller capabilities are less complex compared with a bipolar relay. A conventional bipolar relay can be converted to a bipolar latching relay with the proper placement of a PM to the magnetic circuit. A conventional relay consists of a coil, a pivoted armature, and the electromagnet. For the purpose of the additional latching function, a PM is added (Pawlak et al. 1997). In this configuration, the magnet is located in a space between the coil and the magnetic circuit at the pivot point side, as shown in Figure 4.1. The figure identifies the relay components and shows a cross section of the latching relay based on the conventional relay configuration having Cartesian symmetry. The rectangular-shaped magnet has magnetization with a direction parallel to the axis of symmetry as presented in Figure 4.1(a). The external magnetic circuit is stationary and serves as the main magnetic circuit of the relay. The coil is wound on a bobbin and located around the relay's stationary magnetic core. The rectangular-shaped armature is attached to a flat return spring at the pivot, while the contacts are attached to the other side of the armature. The armature position on both sides is mechanically controlled by the contact locations and is latched on both sides due to the presence of the magnet. The spring is preloaded and with the additional force from spring compression

**FIGURE 4.1**

Bipolar latching relay based on conventional structure: (a) bipolar latching relay components, (b) conventional bipolar relay assembly model converted to latching function. (Courtesy of Delphi Corp.)

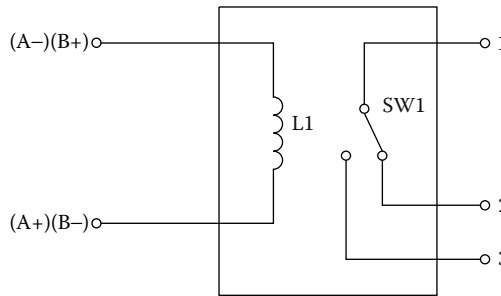
**FIGURE 4.2**

Commercial latching relay based on conventional structure: (a) unlatched position, (b) latched position.

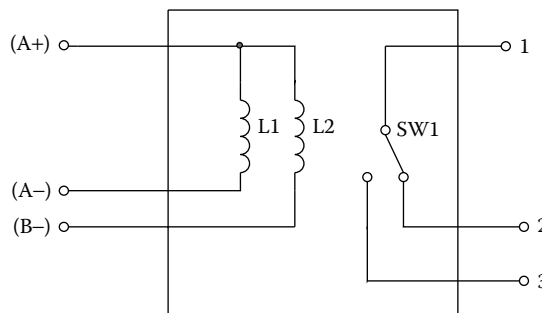
is able to return the armature. Figure 4.2 shows the commercial latching relay having one segmented coil with 10.0 A current rating in two extreme latched and unlatched positions.

Figure 4.3 illustrates the control scheme of the bipolar latching relay having one coil with two terminals and control inputs for both latch *A* and *B* positions, where electrical energy is applied for the armature movement. This controller is more complex and more expensive compared to a unipolar controller because of an H-switch allowing for the bidirectional current to change direction. As indicated by "+" and "-" polarities for latch *A* and "-" and "+" polarities for latch *B*, as shown in Figure 4.3, terminal 2 is connected for latch *A* and terminal 3 is connected for latch *B*.

Figure 4.4 shows the control scheme of the unipolar (dual input) latching relay having two coils with three terminals and control inputs for both latch *A* and *B* positions, where electrical energy is applied for armature movement. One terminal of each coil is connected to the controller ("*A*−" and "*B*−" terminals in Figure 4.4) and the other is connected to form a common terminal ("+" terminals in Figure 4.4). Both coils are energized separately, one at a time and always with the same polarity. It also shows the contact positions. When

**FIGURE 4.3**

Bipolar latching relay control schematic: L₁ is coil inductance, SW1 is an on-off switch, (1) is a common terminal, (2) is the latch A terminal, and (3) is the latch B terminal. (Courtesy of Delphi Corp.)

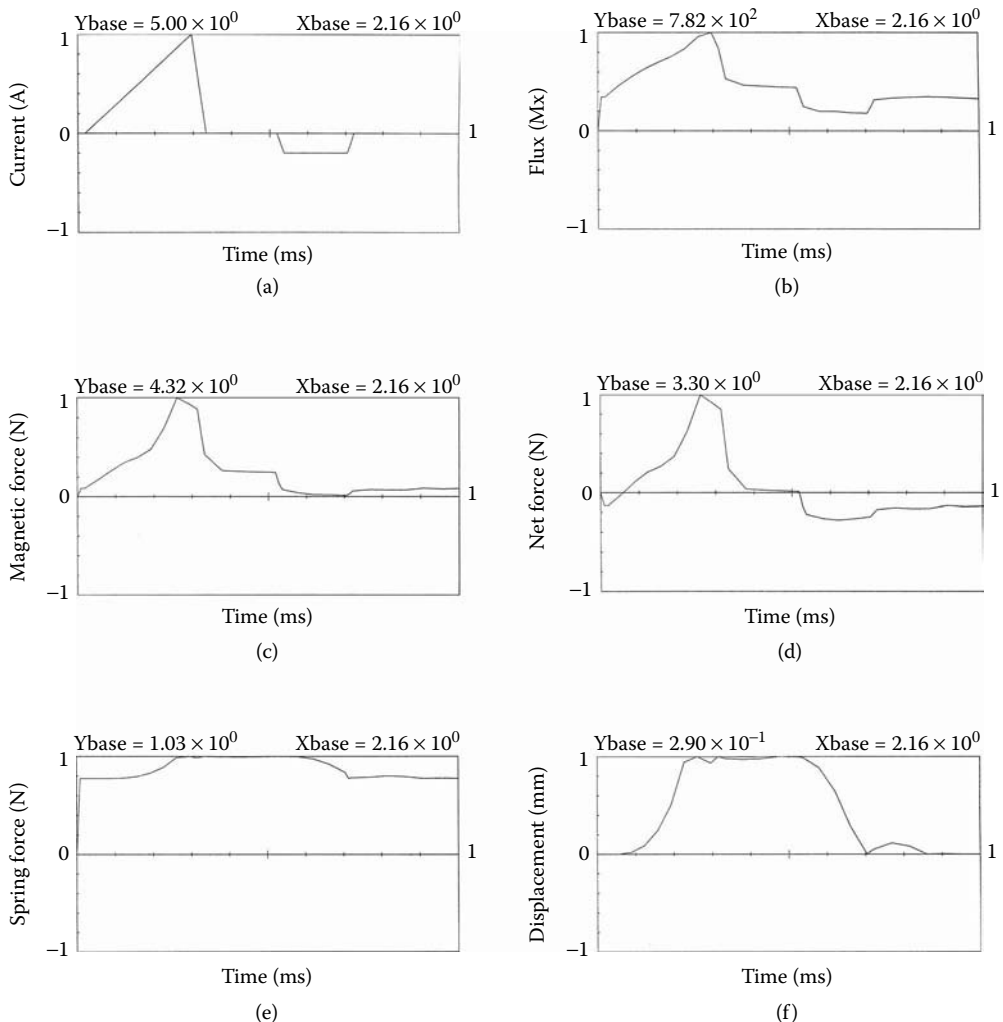
**FIGURE 4.4**

Unipolar latching relay control schematic: L₁ is coil 1 inductance, L₂ is coil 2 inductance, SW1 is an on-off switch, (1) is a common terminal, (2) is the latch A terminal, and (3) is the latch B terminal. (Courtesy of Delphi Corp.)

terminal 1 and terminal 2 are connected, the armature is in the latch A position and when terminal 1 is connected with terminal 3, the armature is in the latch B position.

4.1.1 Dynamics of Latching Relays

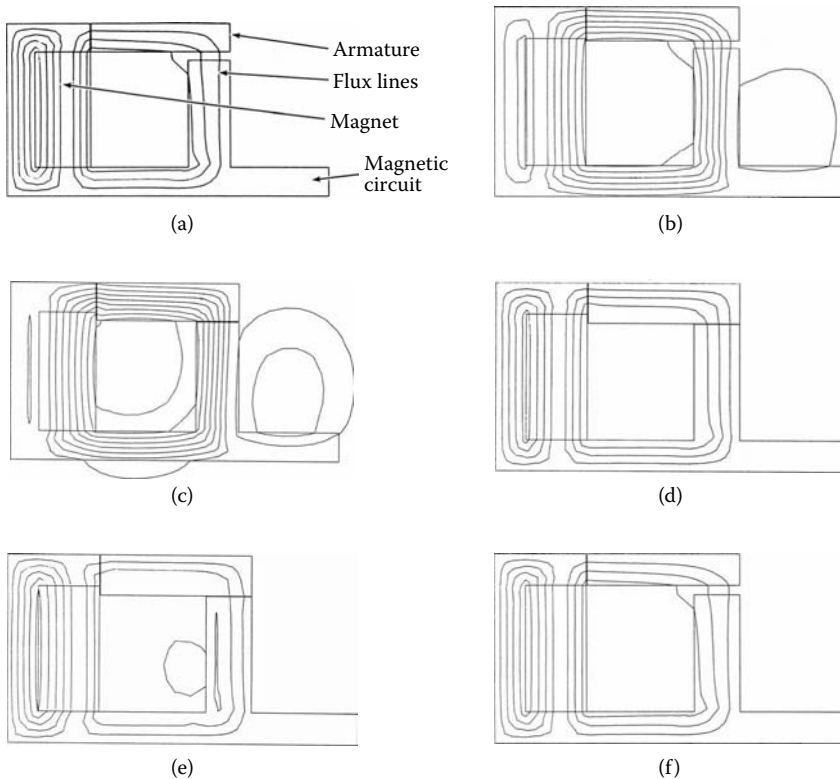
The dynamics analysis of latching relays was conducted using FE software. Because the magnetic structure of the relay has Cartesian symmetry, the pivot motion was replaced with the equivalent axial motion, where the parasitic air gap is negligible in comparison with the main working gap. Figure 4.5 shows the relay's dynamic behavior for the transient current, magnetic flux, magnetic force, spring force, net force, and displacement vs. time, respectively. The control current shown in Figure 4.5(a) identifies the proposed controlled diagram of the relay cycle. Initially, the relay is open and no voltage is applied to the coil. When the voltage is applied to the coil, the current rises, with the slope being a function of coil resistance and inductance. The current reaches its maximum value and the voltage is disconnected. At the same time, the magnetic flux builds up, as presented in Figure 4.5(b), and generates the magnetic force. Both the magnetic flux and the magnetic force are the result of magnet and coil MMFs. When the current builds up in the coil, the magnetic flux increases in the armature and, at a certain point, balances the negative spring force, as presented in Figure 4.5(d) and Figure 4.5(e). At this point, the armature starts moving and closes the air gap, as indicated in Figure 4.5(f). Then the positive voltage is discontinued and the armature stays closed due to PM MMF, which at this point is stronger

**FIGURE 4.5**

Dynamics of latching relay: (a) transient current vs. time, (b) transient magnetic flux vs. time, (c) transient magnetic force vs. time, (d) transient magnetic net force vs. time, (e) transient spring force vs. time, (f) transient displacement vs. time. (Courtesy of Delphi Corp.)

than at the beginning of the cycle because more flux lines cross the main air gap, as shown in Figure 4.6(d). Consequently, a negative voltage is applied, as presented in Figure 4.5(a), which suppresses the magnet flux lines and with the suppressed magnetic force, the spring returns the armature back to its previous position, as indicated in Figure 4.5(f) and Figure 4.6(f), and the cycle is complete.

Figure 4.6(a) through Figure 4.6(f) illustrate the relay's geometry and magnetic flux lines during the dynamic operation, previously described in Figure 4.5. Figure 4.6(a) shows the relay magnetic circuit and flux lines due to PM MMF at the beginning of the cycle at 0.1 ms with no coil excitation. A small portion of magnet flux lines crosses the air gap and the magnet force cannot move the armature. With positive current excitation, more flux is generated and the stronger magnetic force working against the spring force moves the armature, as shown in Figure 4.6(b) and Figure 4.6(c) at 0.2 ms and 0.4 ms, respectively. As illustrated in Figure 4.6(d) at 0.8 ms, with the air gap closed and no current excitation,

**FIGURE 4.6**

Magnetic flux lines for latching relay dynamic operation: (a) magnet flux lines at 0.1 ms, (b) magnet and positive current flux lines at 0.2 ms, (c) magnet and positive current flux at 0.4 ms, (d) magnet flux at 0.8 ms, (e) magnet and negative current flux at 1.2 ms, (f) magnet flux at 1.6 ms. (Courtesy of Delphi Corp.)

more flux lines are attracted toward the main air gap, generating a magnetic force sufficient to keep the armature closed and the spring suppressed. With negative current applied to the coil, the magnetic flux lines are shifted out of the air gap, as shown in Figure 4.6(e) at 1.2 ms, and the armature returns to its previous position, as shown in Figure 4.6(f) at 1.6 ms. After the negative current is discontinued, the PM restores the flux level as well as its distribution, as identified in Figure 4.6(f), at 1.8 ms, back to its original shape at the beginning of the cycle. Compare this with Figure 4.6(a). During dynamic operation, at no time is the magnet exposed to demagnetization forces. This should secure the magnet's normal operation during the entire time of relay's utilization.

4.1.2 Bipolar Latching Relays

The basic concept of a modern latching actuator with magnets in armature is presented in Figure 4.7. The latching relay consists of two components: a stationary electromagnet and a movable armature. The stationary electromagnet consists of an upper and a lower magnetic core as well as a coil with leads. The magnetic core assembly provides a mechanical stop for the armature and a sliding opening for the shaft, while providing for the coil's MMF, its primary flux conducting function. The second mechanical stop is provided by the electrical contacts, as shown in Figure 4.14. Both stops prevent the magnet from direct contact with the magnetic core, thus preventing magnet breakage. The movable

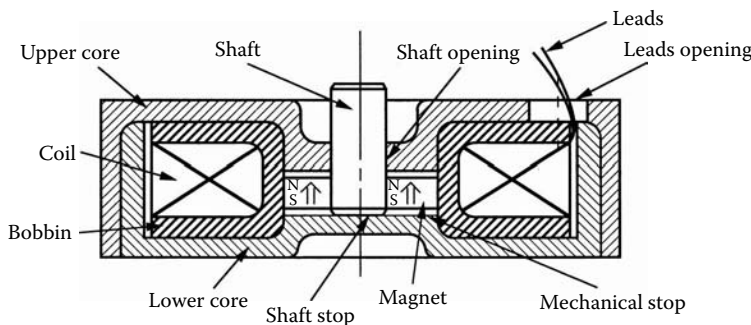


FIGURE 4.7
Bipolar latching relay structure and components. (Courtesy of Delphi Corp.)

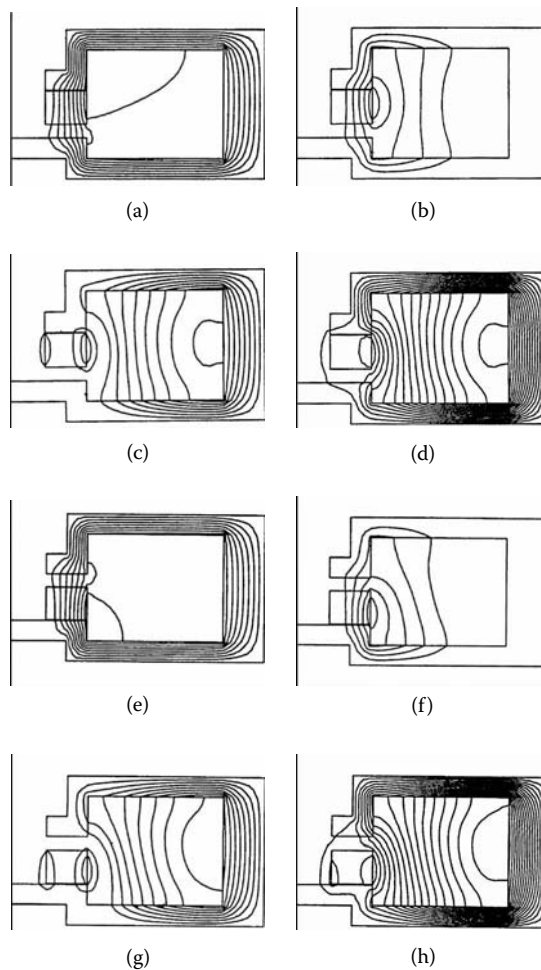


FIGURE 4.8
Bipolar latching relay with magnet in armature components and assembly. (Courtesy of Delphi Corp.)

armature consists of a PM and a shaft. The ring-shaped magnet has axial magnetization providing uniform polarity at the top and an opposite polarity at the bottom. The shaft is mechanically coupled to the ring magnet. The armature is assembled prior to the electromagnetic core assembly.

All the bipolar relay components are shown in Figure 4.7 and Figure 4.8. The armature shaft and the magnet are located inside the housing that secures the armature by providing a slide opening for the shaft and a mechanical stop for the armature. The housing consists of two ferromagnetic core parts — the lower core and the upper core — which are pressed together in the assembly process, encapsulating a coil with a bobbin and two leads. When the lower core is pressed against the upper core, the space for the armature movement is provided and determined by two mechanical stops. The opening in the housing provides a passage for the coil leads. The components presented in Figure 4.8 and Figure 4.14 show means of providing a specially shaped armature shaft that could be made out of nonmagnetic material, preferably stainless steel or plastic, where the shaft's top side would provide mechanical coupling with the ring magnet. The magnet material should be high-energy neodymium or samarium cobalt. If the magnet is based on plastic-molded neodymium, both the shaft and the magnet ring could be manufactured by the same plastic-molding process.

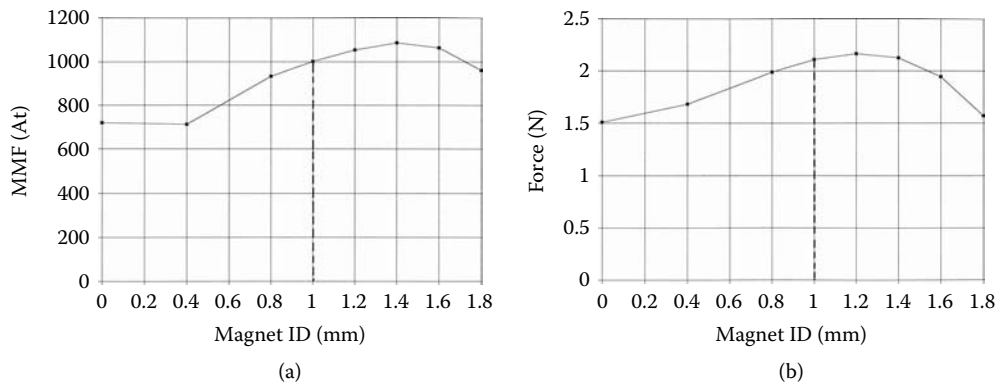
The operation of the latching relays is best demonstrated in Figure 4.9, where different stages of relay operation are illustrated by magnetic flux lines. Initially, the armature is in its upper stable equilibrium position with the presence of the magnetic flux in the magnetic

**FIGURE 4.9**

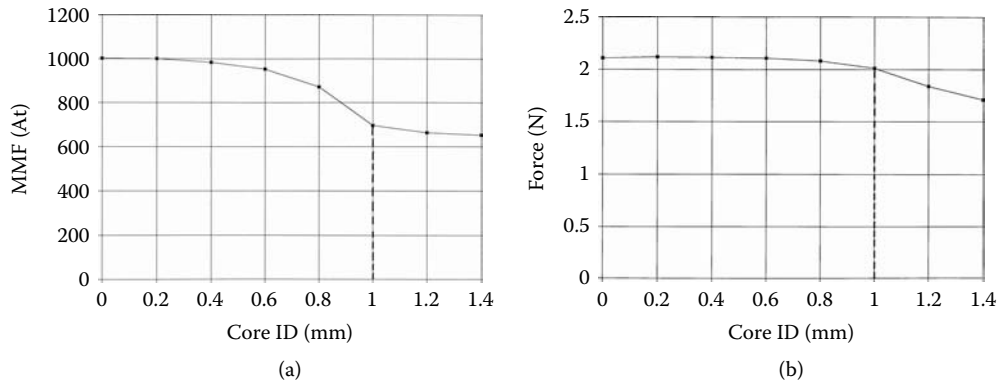
Magnetic flux lines for bipolar latching relay dynamic operation: (a) magnet flux lines at 0.0 At, (b) magnet and positive current flux lines at 100.0 At, (c) magnet and positive current flux at 200.0 At, (d) magnet and positive current flux lines at 300.0 At, (e) magnet flux lines at 0.0 At, (f) magnet and negative current flux at 100.0 At, (g) magnet and negative current flux at 200.0 At, (h) magnet and negative current flux at 300.0 At. (Courtesy of Delphi Corp.)

circuit that is only generated by the PM, as presented in Figure 4.9(a). When the current is applied to the coil, it suppresses the magnet flux lines, as shown in Figure 4.9(b) through Figure 4.9(d) with the current increased to 100.0, 200.0, and 300.0 At, respectively. At this point, the net magnetic forces change their direction and again the repulsive forces are applied, moving the armature to the bottom mechanical stop. At this time, the current is discontinued and the magnet establishes its stable equilibrium position at the bottom, as shown in Figure 4.9(e). With the opposite current applied to the coil, the entire process is reversed and the magnet is forced to move back to its original position, as presented in Figure 4.9(f) through Figure 4.9(h).

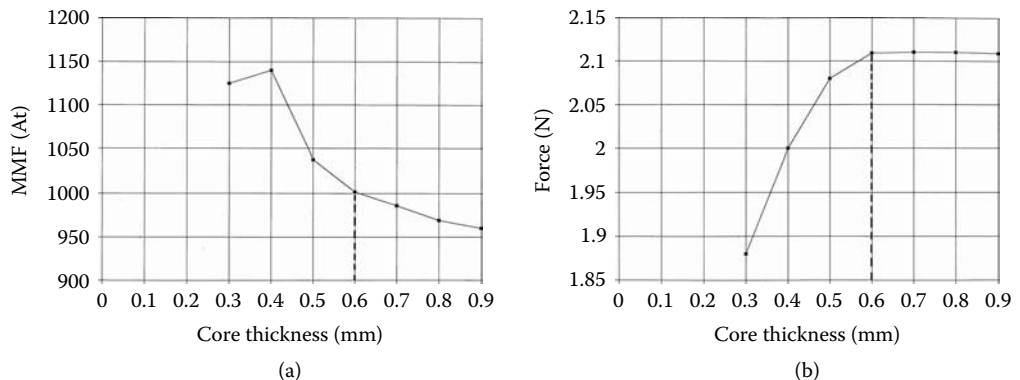
The magnet optimization studies are illustrated in Figure 4.10 through Figure 4.12. Variations in the magnet's inside diameter (ID) affect the latching force developed by the magnet. Figure 4.10(a) shows that the ring magnet develops a higher latching force compared with a disk in which the ID equals zero. There is only one ID of 1.2×10^{-3} m value for the ring magnet that will provide the maximum magnet latching force, as presented

**FIGURE 4.10**

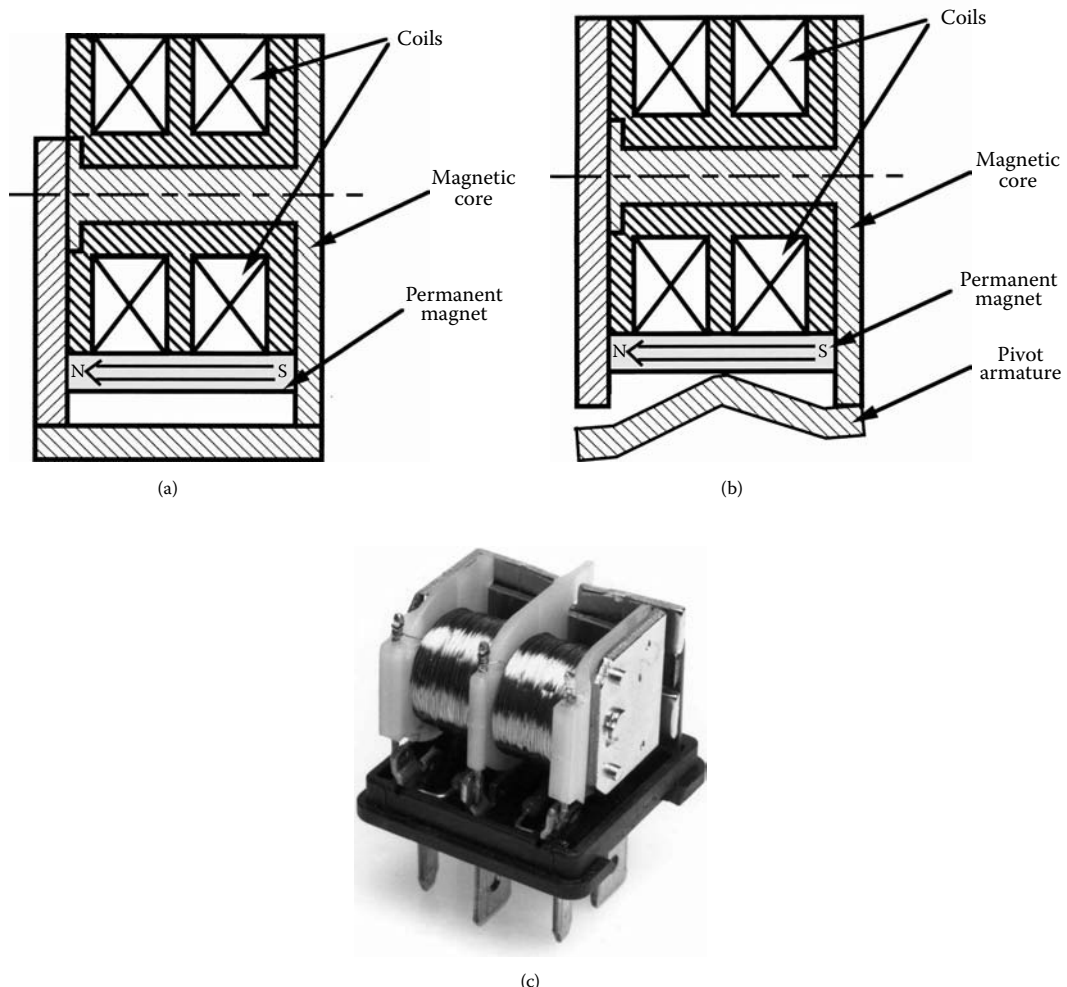
Bipolar latching relay magnet ID optimization study: (a) MMF, (b) latching force. (Courtesy of Delphi Corp.)

**FIGURE 4.11**

Bipolar latching relay core ID optimization study: (a) MMF, (b) latching force. (Courtesy of Delphi Corp.)

**FIGURE 4.12**

Bipolar latching relay core thickness optimization study: (a) MMF, (b) latching force. (Courtesy of Delphi Corp.)

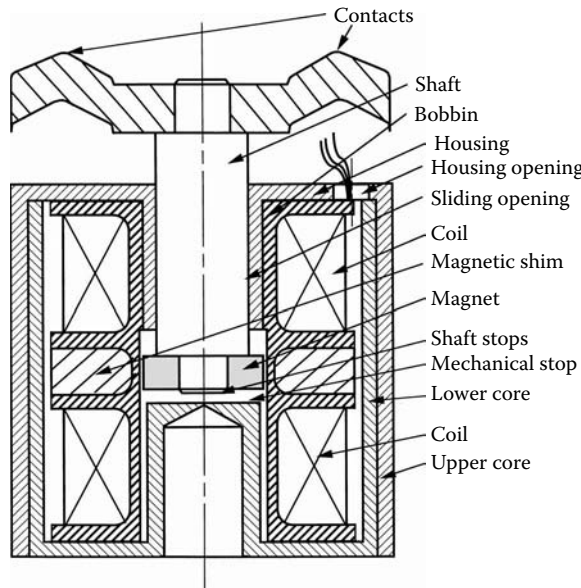
**FIGURE 4.13**

Unipolar conventional latching relay with two coils and pivot armature: (a) unipolar relay with two coils, (b) unipolar relay with two coils and pivot armature, (c) commercial unipolar relay with two coils and pivot armature.

in Figure 4.12(b). For engineering reasons, however, the 1.0×10^{-3} m value was selected, as marked in Figure 4.10(b), Figure 4.11, and Figure 4.12. These figures show the MMF and magnetic force developed in the armature as a function of the iron core thickness. Selected dimensions identified by dotted lines ensure a high relay electromagnetic performance.

4.1.3 Unipolar Latching Relays

If the latching relay presented in Figure 4.1 is duplicated to allow for the second coil to create a unipolar relay structure, it transforms to Figure 4.13. Typically, a conventional relay has a pivot action, which has to be common for both coils. Therefore, one possible solution is to introduce it at the bottom part, as shown in Figure 4.13(b). The configuration with a pivot armature is now commercially available, as illustrated in Figure 4.13(c).

**FIGURE 4.14**

Unipolar latching relay with magnet in armature structure and components. (Courtesy of Delphi Corp.)

A modern concept for unipolar configuration with a movable magnet is presented in Figure 4.14. The latching relay consists of two components: a stationary electromagnet and a movable armature. The stationary electromagnet consists of an upper and a lower magnetic core encapsulating two coils side by side. The latching function is provided by a PM that holds an armature in two stable positions without a spring.

At its latched position, the magnet provides sufficient force for the electrical contacts to be closed or open, depending on the control mode. The coils are energized to repel the magnet's armature. Therefore, when each of the coils is energized, the same polarity exists at the electromagnet's poles and the adjacent magnet side. The relay assembly provides two mechanical stops for the magnetic armature while providing a nonmagnetic contact with the magnetic core. One stop is provided by the shaft because the relay shaft extends from the magnet. The second stop is provided by the contact as it closes before the magnet armature reaches the upper magnetic pole. The movable armature consists of a PM and a shaft. The ring-shaped magnet with an axial magnetization provides a certain polarity at the top and the opposite polarity at the bottom. The shaft is mechanically coupled to the ring magnet. The armature is assembled prior to the electromagnetic core assembly, followed by the magnetic core and coils assembly, and finally a connector is permanently attached to the open side of the shaft. All the parts of the unipolar (dual input) latching relay configuration with the PM in the armature are shown in Figure 4.14. The housing in this design consists of two ferromagnetic core parts, the lower and the upper core, with relatively thin walls allowing for manufacturing using stamping technology. An armature shaft and a magnet are located inside a magnetic housing, which secures the armature by providing a sliding opening for the shaft and one mechanical stop for the armature. With this technology, an additional cylindrical part is needed to provide shaft guidance. The housing parts are pressed together in the assembly process, encapsulating a bobbin with two coils and three leads. When the lower core is pressed into the upper core, the space for the movement is provided by the introduced lower mechanical stop. The opening in the housing creates a passage for the coil leads. A magnetic shim sandwiched between

**FIGURE 4.15**

Unipolar latching relay with magnet in armature components and assembly. (Courtesy of Delphi Corp.)

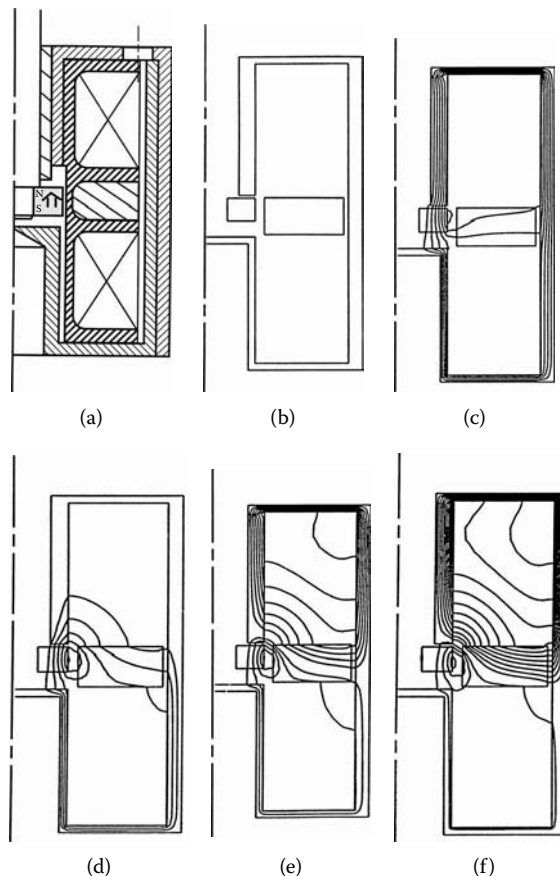
the two coils serves as an additional magnetic circuit, making this device electromagnetically efficient. The detail, presented in Figure 4.14, shows a means of providing a specially shaped armature shaft with shaft stops and contact with the stop, making the armature stop with no magnet or magnetic core contact, thus preventing the magnet from breaking. The shaft is devised such that its bottom position is longer than the magnet's thickness. The distance of the magnet to the magnetic core controls the latching force and is arranged to prevent accidental armature motion for vibration greater than the required 20g acceleration, as presented in Table 4.10. Therefore, the distance of the PM from the lower magnetic core could be different from the distance of the magnet from the upper magnetic core, which is set to provide a sufficient force on the contacts and to protect against vibration. During the lifetime of the relay, the force on the contacts increases over time; because the contact surface is losing material due to wear, the distance from the magnet to the magnetic core is decreasing, providing stronger magnetic force at the contact area. This ability of latching relays to increase contact force helps maintain low-contact resistance, the critical contact parameter. Lower contact resistance, a function of the contact force, should have a positive effect upon contact life, unlike conventional relays where the contact resistance deteriorates (increases) over time. The armature shaft should be made out of a nonmagnetic material, such as stainless steel or plastic, providing additional mechanical coupling with the ring magnet. Any desired magnet material could be utilized in this configuration, depending on the latching force requirements, preferably one based on high-energy neodymium or samarium cobalt. If the selected material is a neodymium-bonded magnet, both the shaft and the ring might be manufactured using the plastic-molded process.

4.1.4 Latching Relay Analysis

Figure 4.15 shows the unipolar relay components and assembly. The unipolar relay configuration with a magnet in an armature, having axial magnetization, is depicted in Figure 4.16(a). The magnetic flux lines in the magnetic circuit are presented in Figure 4.16(c) through Figure 4.16(f) at different dynamic operation stages. Initially, the armature is in its upper stable equilibrium position at the latch A position, as presented in Figure 4.4. When the current is applied to coil B, it is suppressing the magnetic field, as shown in Figure 4.16(c) through Figure 4.16(f). The number of magnetic flux lines increases with the increase of the MMF from 0 to 450.0 At. Figure 4.16(c) through Figure 4.16(f) show the magnet flux lines with a discrete increase of the MMF at 0.0, 150.0, 300.0, and 450.0 At, respectively.

At this point, the net magnetic force changes its direction and the repulsive force is applied, moving the armature to the bottom mechanical stop. Then current is discontinued and the magnet establishes its bottom equilibrium position at the latch B position, as presented in Figure 4.4. With the current applied to coil A, the entire process is reversed and the magnet is moved back to its original latch A position, as presented in Figure 4.4.

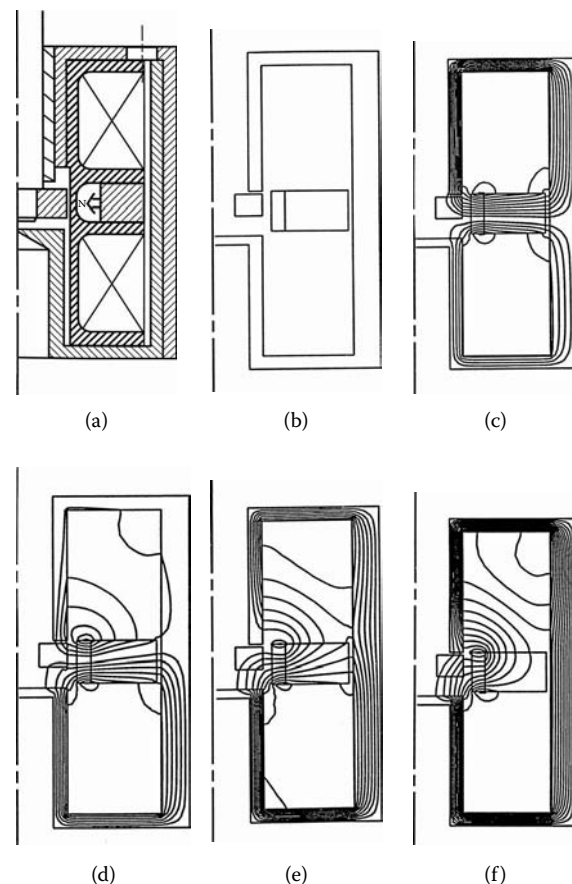
To secure magnet integrity and, therefore, the longer lifespan of the solenoid, a stationary PM location was selected, as presented in Figure 4.17(a). Consequently, Figure 4.17(c)

**FIGURE 4.16**

Flux lines for unipolar latching relay with magnet in armature: (a) relay design, (b) relay configuration, (c) magnet flux lines, (d) MMF = 150.0 At, (e) MMF = 300.0 At, (f) MMF = 450.0 At. (Courtesy of Delphi Corp.)

through Figure 4.17(f) present flux lines of the unipolar relay configuration with the stationary ring magnet position with radial magnetization, in this case, made of the neodymium MQ3. Note that different flux lines distributed between these two designs reveal much better flux utilization in the stationary magnet position configuration. As we can see here, none of the magnetic lines passes the entire housing, but in the movable magnet configuration with axial magnetization, some of the magnetic flux lines that go around the circuit contribute a net zero balance force and only saturate the circuit.

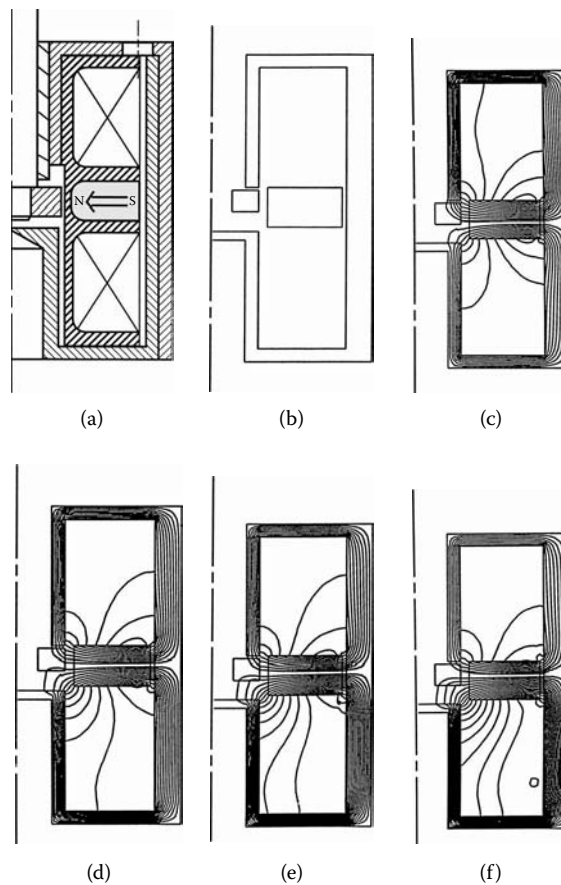
Figure 4.18 shows the unipolar relay components and assembly with a stationary MQ2 magnet. As a result of the lower MQ2 magnet's performance, it occupies the entire space between the coils compared to the configuration presented in Figure 4.17(a). The unipolar relay configuration with a magnet in the armature having radial magnetization is demonstrated in Figure 4.19(a), and the magnetic flux lines in the magnetic circuit at different dynamic operation stages are presented in Figure 4.19(c) through Figure 4.19(f). Flux distribution is similar to the unipolar relay configuration in Figure 4.17.

**FIGURE 4.17**

Flux lines for unipolar latching relay with stationary MQ3 magnet: (a) relay design, (b) relay configuration, (c) magnet flux lines, (d) MMF = 150.0 At, (e) MMF = 300.0 At, (f) MMF = 450.0 At. (Courtesy of Delphi Corp.)

**FIGURE 4.18**

Unipolar latching relay with stationary MQ2 magnet components and assembly with contacts. (Courtesy of Delphi Corp.)

**FIGURE 4.19**

Flux lines for unipolar latching relay with stationary MQ2 magnet: (a) relay design, (b) relay configuration, (c) magnet flux lines, (d) MMF = 150.0 At, (e) MMF = 300.0 At, (f) MMF = 450.0 At. (Courtesy of Delphi Corp.)

4.1.5 Latching Relay Analysis and Tests

An evaluation of latching relays can be based on electromagnetic efficiency, which is defined by the level of MMF necessary for a dynamic operation. Therefore, all analytical studies that lead to MMF reduction are very valuable and result in more electromagnetically efficient structures. Figure 4.20 shows an example of such a study where the MMF is a function of the iron thickness of the magnetic shim sandwiched between the two coils of the unipolar solenoid structure, as presented in Figure 4.14. Without iron, the MMF required is quite high at 500.0 At and, with the presence of iron, the MMF level drops significantly, to below 250.0 At for the 1.5×10^{-3} m thickness of the magnetic shim. Furthermore, shim thickness beyond 1.5×10^{-3} m does not contribute to further MMF reduction. At the same time, the force level stabilizes above 2.0 N and is also independent of the shim thickness beyond this point, as presented in Figure 4.21.

Figure 4.22 shows test results and an analysis comparison of the MMF for several investigated relay configurations. Generally, unipolar relay devices require much less MMF compared with bipolar ones: in some cases, as much as half. Because the value of a current is a function of energy consumption and the number of turns is a function of required space, from both the point of view of packaging and energy consumption, it is

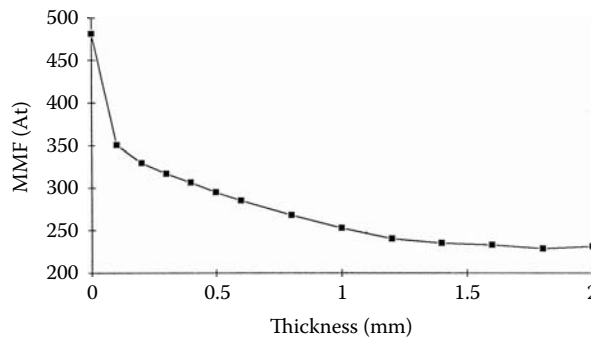


FIGURE 4.20
MMF vs. magnetic shim thickness. (Courtesy of Delphi Corp.)

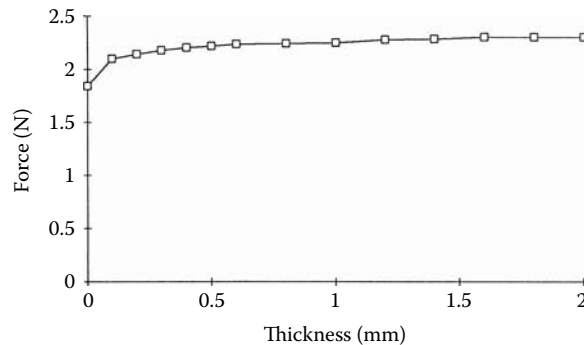


FIGURE 4.21
Force vs. magnetic shim thickness. (Courtesy of Delphi Corp.)

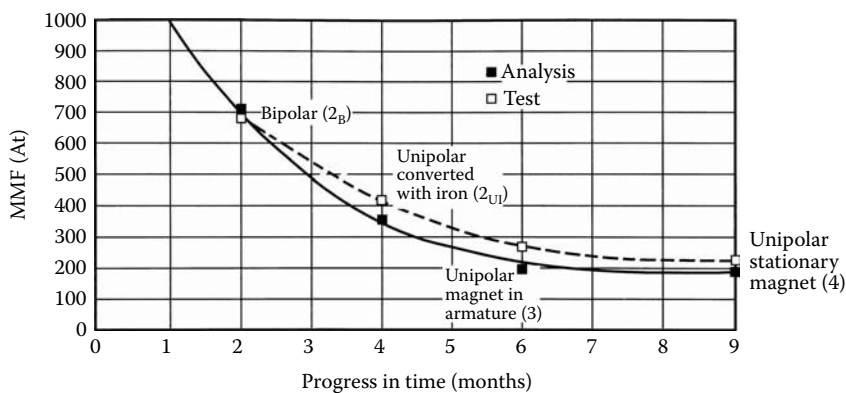


FIGURE 4.22
MMF characteristics: analysis and test comparison. (Courtesy of Delphi Corp.)

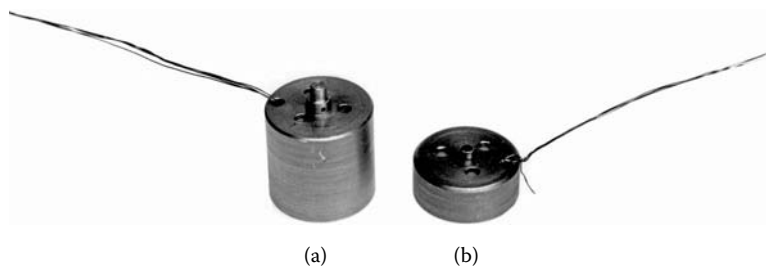
more advantageous to utilize unipolar relay structures. Because energy and packaging are two important issues for latching relays, it is advisable to focus on unipolar relays. This is also a less costly approach for the controller.

TABLE 4.1

Latching Relay Dynamic and Static Performance and Requirements

Performance	Test Results						Commercial Reference	Req.
	Conventional Stationary	Bipolar Armature	Unipolar Armature	Unipolar Stationary	Unipolar Stationary	4.13(c)		
Latching relay Magnet location	1	2	3	4	5	4.13(c)	4.13(c)	Req.
Progress step no.	4.1(b)	4.7	4.16	4.17	4.19	4.13(c)		
Figure reference	4.1(b)	4.7	4.16	4.17	4.19	4.13(c)		
Minimum voltage (V)	17.5	18.0	6.5	9.5	8.0	6.5	<7.0	
Pulse width (ms)	2.9	2.0	6.4	3.0	3.2	25.0	none	
Latching force (G)	206	193	193	127	120	152	10 g	
Armature air gap ($\times 10^{-3}$ m)	0.36	0.43	0.60	0.94	0.90	1.00	0.50	
Maximum current at 7 V(A)	0.33	2.27	0.59	0.54	0.51	0.09	<1.0	
Maximum energy fact (A \times ms)	0.96	4.50	3.80	1.60	1.60	2.25	none	
MMF at 7 V(At)	266	680	236	216	204	180	none	

Source: Courtesy of Delphi Corp.

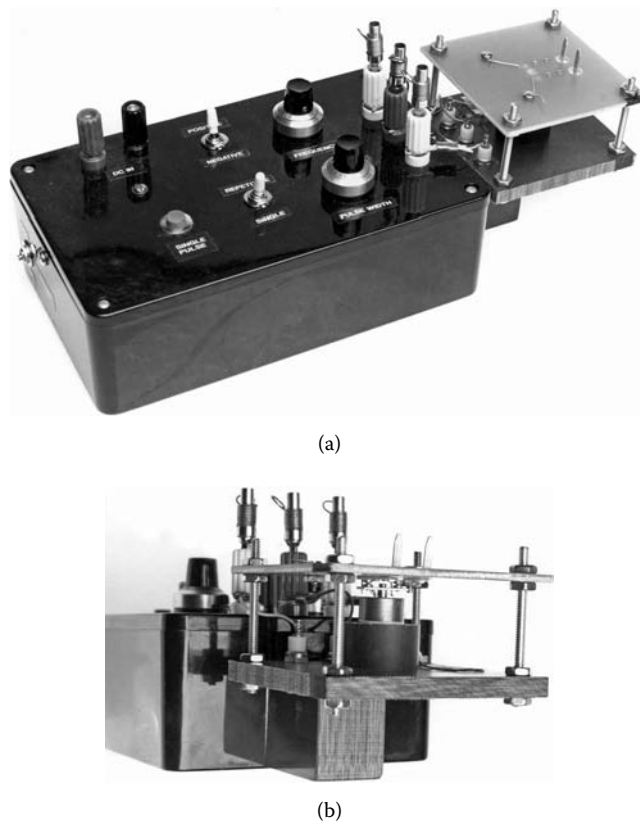
**FIGURE 4.23**

Latching relays assemblies: (a) unipolar, (b) bipolar. (Courtesy of Delphi Corp.)

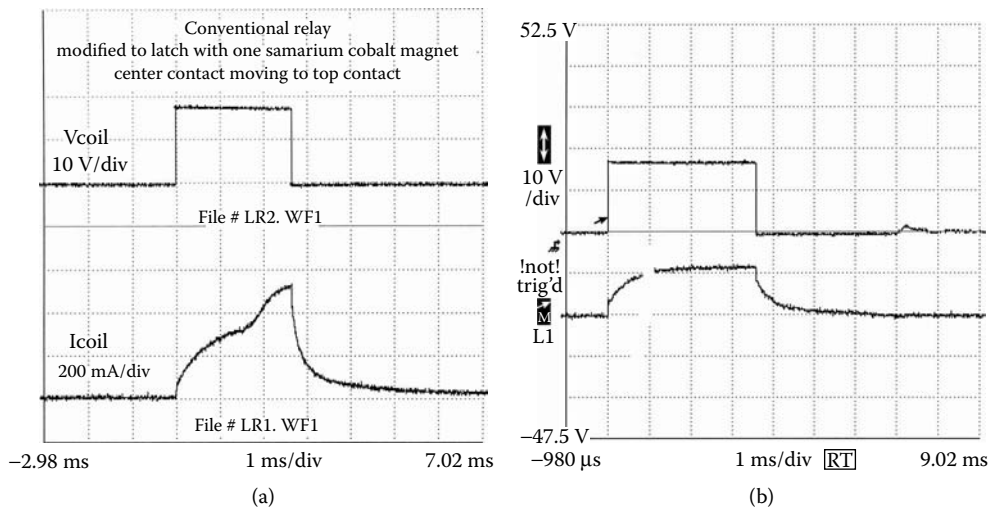
Figure 4.22 reveals the steps involved in minimizing MMF for all investigated bipolar and unipolar latching relay configurations. The beginning of the process, step (1) (Table 4.1 and Figure 4.22), indicates a conventional relay converted to a latching relay [also see Figure 4.1(b) for reference purposes only]. The next step (2_B) indicates an MMF level of 680.0 At reduced to about 400.0 At, as the unipolar relay is converted from a bipolar relay with iron at step (2_{UI}). Consequently, the MMF was reduced to about 200.0 At in step (3) and step (4) (see Figure 4.22), in the search for the most efficient electromagnetic relay.

Figure 4.23 shows two of the investigated relay assemblies, the bipolar and the unipolar models, while Figure 4.24 shows the test fixture with a unipolar model of the configurations incorporated into the test fixture. For static performance, the electromagnetic latching force was determined at the fixed air gap, which varies due to different relay designs. Dynamic tests include both the transient voltage and current, which can determine the travel time as presented in the test fixture, shown in Figure 4.24.

Figure 4.25 through Figure 4.27 present the transient voltage pulse and the transient current for all latching relays discussed above. These data help calculate the maximum energy factor and MMFs for comparison purposes. The relay's open and close travel time corresponds to the minimum input voltage pulse required to activate the relay. The minimum voltage requirement indicates the lowest input voltage signal at which the relay must operate. Figure 4.25 through Figure 4.27 show the transient current for the PWM with 20.0 ms pulse-width and nominal 12.0 V operation. All the requirements, data as well as results from static and dynamic tests of all bipolar and unipolar latching relay configurations, are shown in Table 4.1.

**FIGURE 4.24**

Voltage pulse test fixture with transient current for latching relays: (a) controller and latching relay fixture, (b) latching relay fixture. (Courtesy of Delphi Corp.)

**FIGURE 4.25**

Voltage pulse and transient current for conventional relay with magnet: (a) conventional relay with PM, (b) commercial latching relay. (Courtesy of Delphi Corp.)

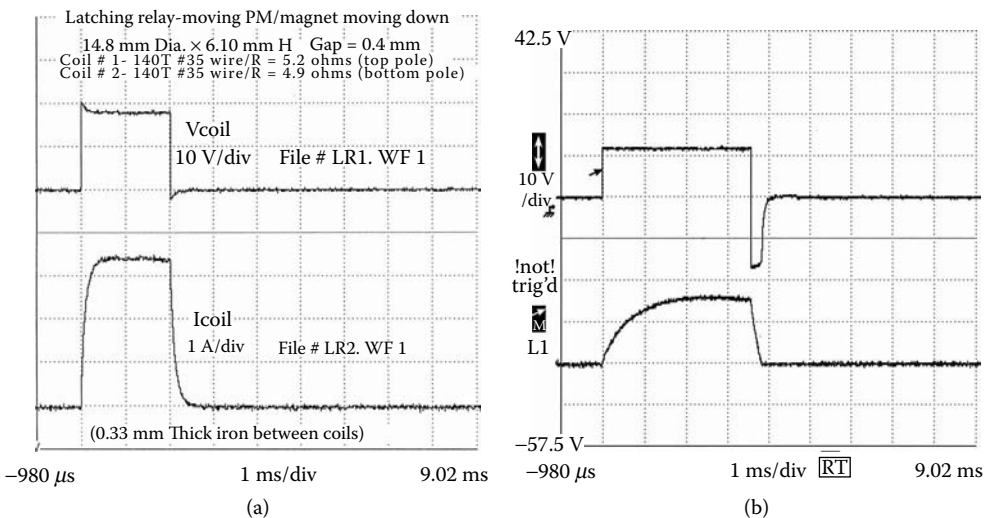


FIGURE 4.26

Voltage pulse and transient current for modern relay with PM: (a) bipolar relay with magnet in armature, (b) unipolar with MQ3 magnet in armature. (Courtesy of Delphi Corp.)

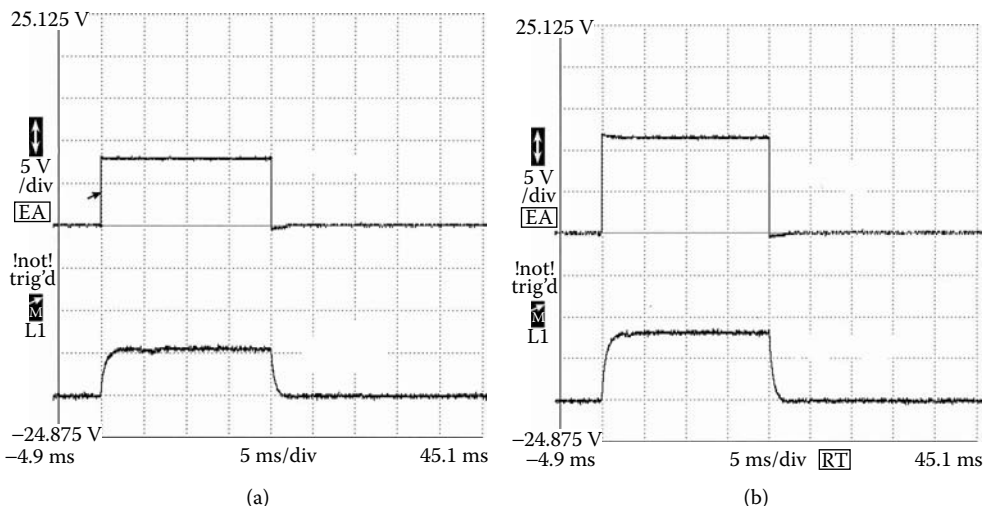


FIGURE 4.27

Voltage pulse and transient current for modern relay with PM: (a) unipolar with MQ2 stationary magnet, (b) unipolar with MQ3 stationary magnet. (Courtesy of Delphi Corp.)

Table 4.2 and Table 4.3 show a comparison of the latching relay's static and dynamic test and analysis results, respectively. The calculated and tested latching forces, MMFs and current levels, are within several percent, indicating a good correlation between the test and analytical results. The dynamics identify that for both the closing and opening, the minimum pulse width of the relay is also in correlation with the FE analysis. A reliability test was performed for a unipolar relay with a magnet in the armature. A total of 1.5×10^6 cycles at no-load condition successfully passed. Depending on the current rating, these relays also require a full current load reliability test under 10.0–25.0 A nominal current load conditions.

TABLE 4.2

Latching Static Relay Test

Performance	Test Results					
	Unipolar-No-Iron Armature (2B) MQ3	Bipolar Armature (2B) MQ3	Unipolar-Iron Armature (2UI) MQ3	Unipolar Armature (3U) MQ3	Unipolar Stationary (4U) MQ3	Unipolar Stationary (5U) MQ2
Force (G)	193	193	193	193	127	120
Air gap ($\times 10^{-3}$ m)	0.40	0.40	0.40	0.60	0.94	0.90
Current at 7 V(A)				0.59	0.54	0.51
MMF at 7 V(At)				236	216	204
Current at 12 V(A)	2.27	4.53	2.89	0.79	0.89	0.87
MMF at 12 V(At)	680	680	434	409	399	340

Source: Courtesy of Delphi Corp.

TABLE 4.3

Latching Relay Analysis

Performance	Analytical Results					
	Unipolar-No-Iron Armature (2B) MQ3	Bipolar Armature (2B) MQ3	Unipolar-Iron Armature (2UI) MQ3	Unipolar Armature (3U) MQ3	Unipolar Stationary (4U) MQ3	Unipolar Stationary (5U) MQ2
Force (G)	205	205	222	231	189	179
Air gap ($\times 10^{-3}$ m)	0.43	0.40	0.43	0.60	1.0	1.0
Current at 7 V(A)				0.60	0.47	0.48
MMF at 7 V(At)				240	189	192
Current at 12 V(A)	2.33	4.53	2.40	1.02	0.72	0.71
MMF at 12 V(At)	700	680	360	411	324	284

Source: Courtesy of Delphi Corp.

4.2 Latching Solenoids

Latching solenoids feature lower energy consumption and mass than conventional solenoids and, therefore, are used more often in applications for portable devices, such as camcorders and laptop computers, where reduction of energy consumption and low mass are particularly important. For similar reasons, latching solenoids are also very attractive for automotive component applications in spite of their more complex controller and higher cost when compared with conventional solenoids. Other potential applications include latching relays (as described in Section 4.1) and flow control solenoids for an electronically operated transmission and injectors. There are a variety of latching solenoids that can be grouped based on configuration, component location, and applications. Two families of latching solenoids can be identified based on topology and, in particular, on magnet and coil arrangements: one with a moving magnet and the other with a stationary magnet. Latching solenoids with a moving magnet are divided into two subgroups: the first group has a single magnet in the armature and the second has two or more magnets in the armature. Latching solenoids with a stationary magnet can be divided into four different subgroups: (1) a magnet located outside the main magnetic path, (2) a magnet

location parallel to the main magnetic path, (3) a magnet around the coil, and (4) multiple magnets.

4.2.1 Latching Solenoids with Moving Magnets

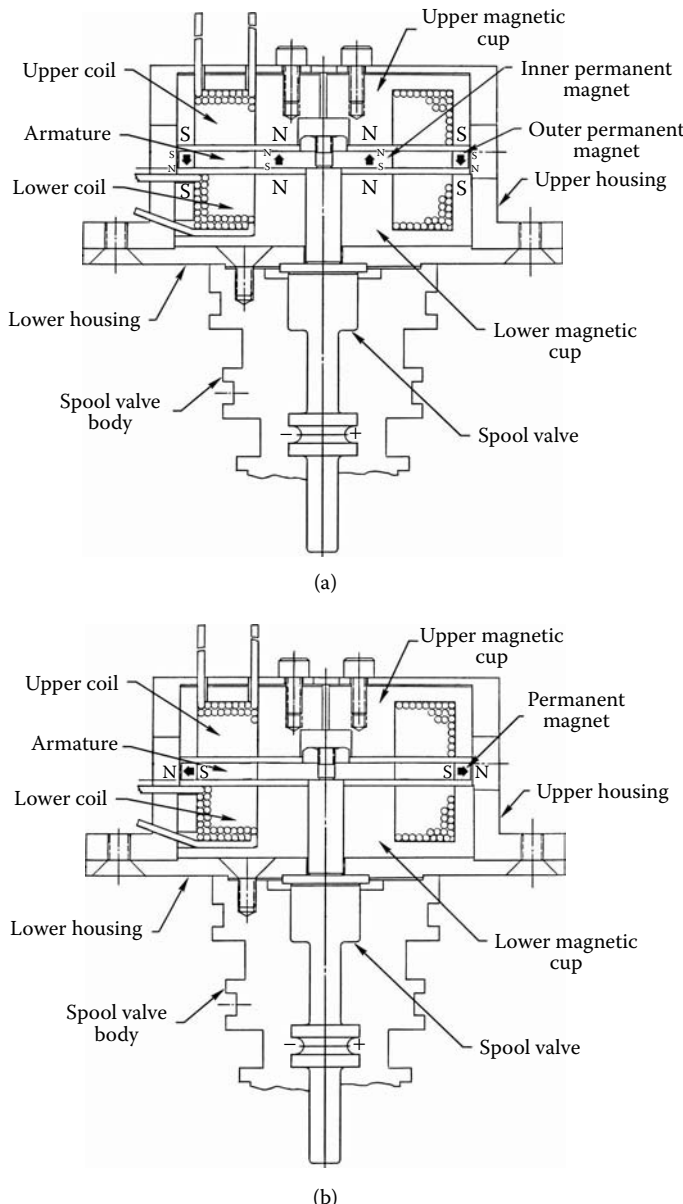
Latching solenoids with magnets in the armature with axial motion belong to the moving magnet family. Because of the brittle nature of magnet material, such a magnet location is generally not recommended for a solenoid with high durability requirements. Encapsulating the magnet in a ferromagnetic material results in higher cost and an undesirable increase of the magnetic path. Solenoids with two magnets in the armature are even more costly and more complex, having reliability deficiencies similar to solenoids with one magnet in the armature. Solenoids with magnets in a stationary magnetic circuit represent the simplest magnetic structure. In particular, solenoids with magnets located parallel to the main magnetic path, to be described in Section 4.2.2, are magnetically more efficient than those with magnets within the main magnetic path because magnets introduce a parasitic air gap, and magnets located outside or inside the main magnetic path provide magnetically efficient structures. Voice coils with the magnet around the coil imply a relatively large size of the ring magnet, which is not cost- and packaging-efficient. Solenoids with multipole magnets or coils are very complex. They are the most expensive and the most difficult to package.

A bistable, latching solenoid for automotive transmission applications with moving magnets in the armature was devised and analyzed. Latching solenoids with one magnet in a disk armature with axial motion and two independent coils are shown in Figure 4.28(b). Figure 4.28(a) presents a latching solenoid with two axially magnetized ring magnets in the armature.

A bistable, latching solenoid consists of two components: a stationary electromagnet and a movable armature. The stationary electromagnet consists of an upper and a lower magnetic core encapsulating two coils side by side. The latching function is provided by a PM that holds an armature in its two stable positions without a return spring. As a result, these solenoids are usually magnetically symmetrical. In its latched position, the magnet provides sufficient force for the spool valve to be closed or open, depending on the control mode. One coil is energized to attract the magnet's armature.

The solenoid assembly provides two mechanical stops for the magnetic armature while providing a nonmagnetic contact with the magnetic core, as presented in Figure 4.28 and Figure 4.29. One stop is provided by the upper magnetic structure, and the second stop is provided by the lower magnetic structure. The movable armature consists of a shaft and a ferromagnetic disk with one or two ring magnets attached to it. The ring-shaped magnet with radial magnetization provides one polarity at the contact with the ferromagnetic ring and the opposite polarity at the outer rim, as presented in Figure 4.28(b). The lower magnetic core is assembled to the spool valve housing with the spool valve shaft. The shaft is mechanically coupled to the disk and the ring magnet. The armature is assembled prior to the upper electromagnetic core assembly, followed by the magnetic core and coils assembly. Finally, the connector is permanently attached to the upper electromagnetic core assembly, as presented in Figure 4.30, which shows both the sub-assembly and a distributed view of all latching solenoid parts.

A variety of different magnet locations and configurations were studied and compared, as presented in Figure 4.31. Figure 4.32 shows the force developed by the latching solenoid as a function of the MMF for a variety of disk armature configurations having different magnet polarizations, geometry, and locations. For comparison purposes, all configurations have the same latching force of -1.0 N, presented in Figure 4.32, with a negative

**FIGURE 4.28**

Latching solenoid with moving magnet: (a) two magnets in armature with axial orientation, (b) one-ring magnet in armature with radial orientation. (Courtesy of Delphi Corp.)

value to indicate direction of the force. The best structure with the highest electromagnetical performance, as indicated in Figure 4.32 by curve 1, is constructed with a magnet located on the outside rim of the disk, as presented in Figure 4.28(b) and Figure 4.31(b). Configurations with two magnets and other one-magnet locations produce weaker results, as presented in Figure 4.32 curve 3 through curve 6. For comparison purposes, a solenoid with a similar structure and an all-iron armature is presented; see Figure 4.32 curve 2. It indicates that only a structure with a magnet located on the outside rim is more electromagnetically efficient

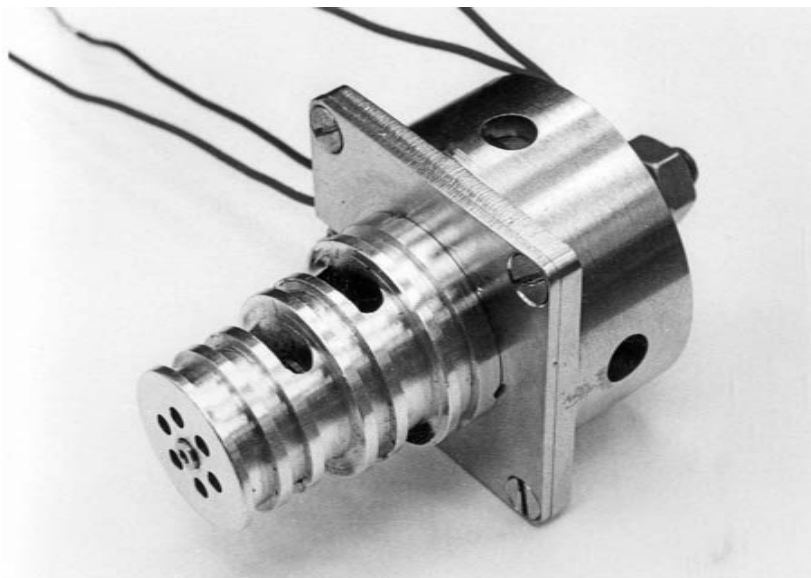
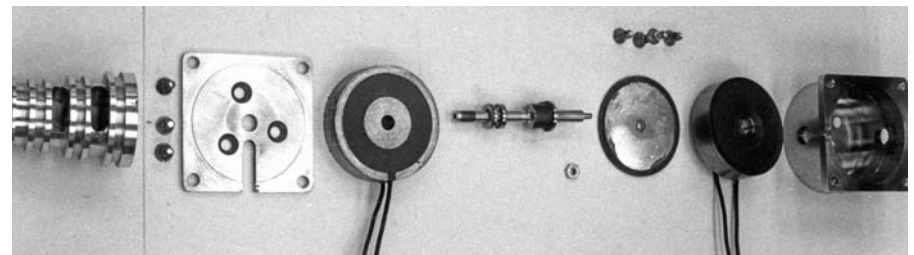


FIGURE 4.29
Latching solenoid with spool valve assembly. (Courtesy of Delphi Corp.)

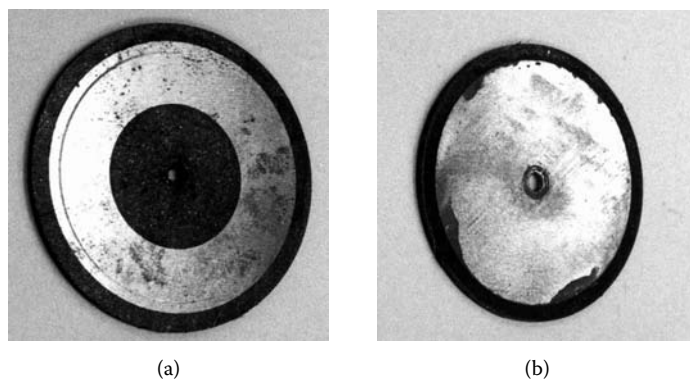


(a)

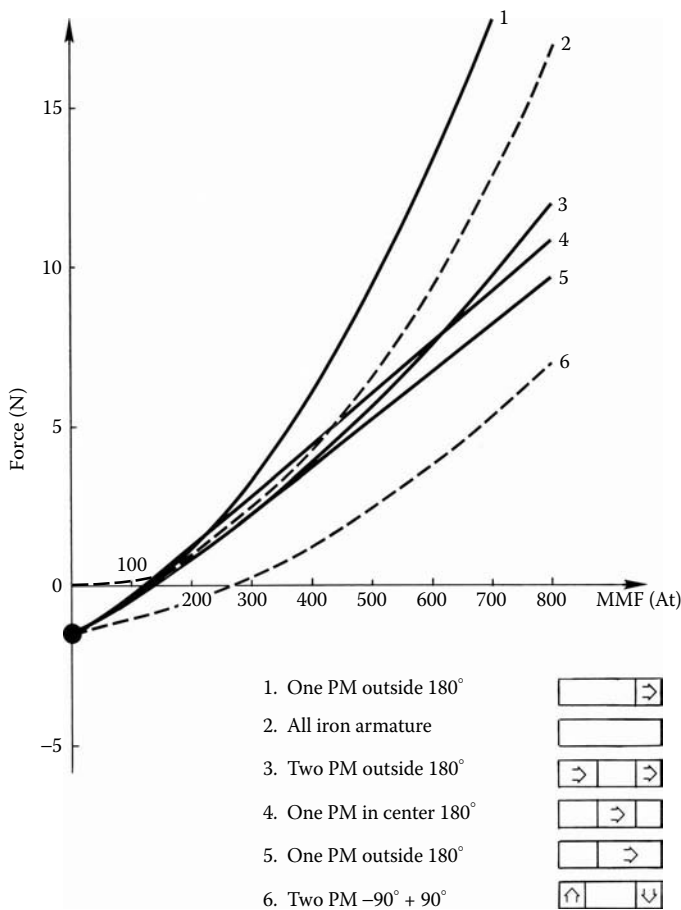


(b)

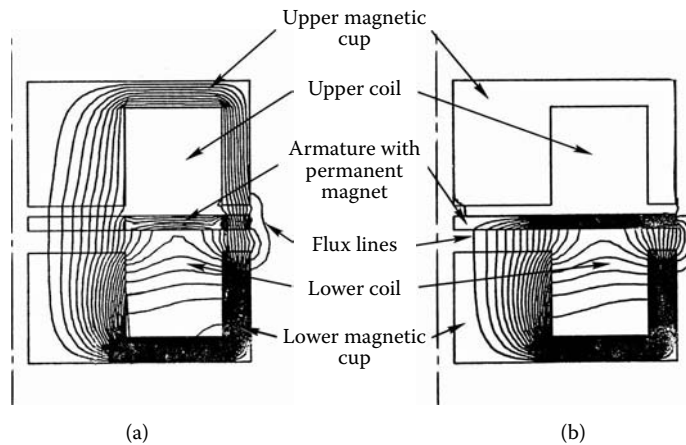
FIGURE 4.30
Components of the latching solenoid with radially magnetized magnet: (a) subassembly of the latching solenoid with moving magnet, (b) latching solenoid components. (Courtesy of Delphi Corp.)

**FIGURE 4.31**

Latching solenoid armatures with permanent ring magnets: (a) two-magnet armature, (b) one-magnet armature. (Courtesy of Delphi Corp.)

**FIGURE 4.32**

Performance of latching solenoid with variety of magnet configurations: (1) one PM outside armature with magnetization perpendicular to axis of symmetry; (2) iron armature; (3) two magnets, one inside and one outside armature with magnetization perpendicular to axis of symmetry; (4) one-magnet inside armature with magnetization perpendicular to axis of symmetry; (5) one large PM outside armature with magnetization perpendicular to axis of symmetry; (6) two magnets, one inside and one outside armature, with magnetization parallel to axis of symmetry but different in sign. (Courtesy of Delphi Corp.)

**FIGURE 4.33**

Flux lines of latching solenoids with magnet in armature: (a) two magnets, one inside and one outside armature, with magnetization parallel to axis of symmetry but different in sign as shown in Figure 4.31 (6); (b) one-magnet armature in outside rim with magnetization perpendicular to axis of symmetry as shown in Figure 4.31 (1). (Courtesy of Delphi Corp.)

TABLE 4.4

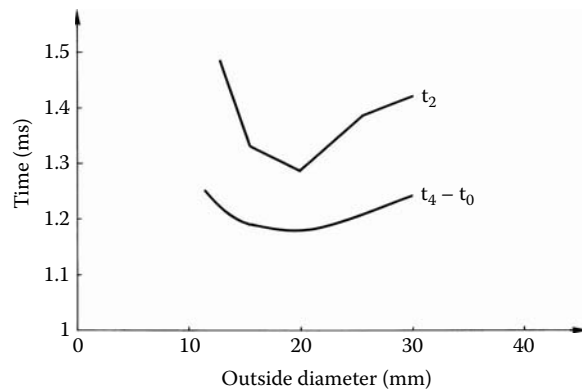
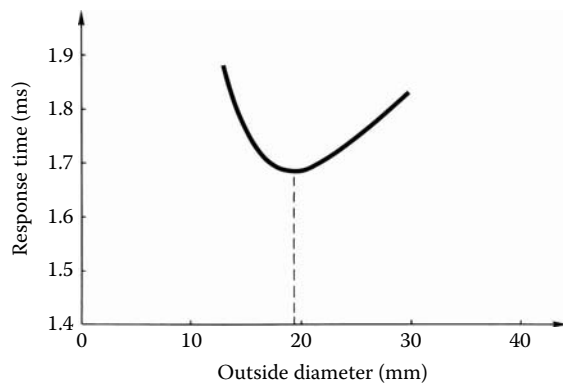
Latchung Solenoid Preload Requirements

Requirements	OD				
	30 ($\times 10^{-3}$ m)	26 ($\times 10^{-3}$ m)	20 ($\times 10^{-3}$ m)	16 ($\times 10^{-3}$ m)	12 ($\times 10^{-3}$ m)
Required preload 20g (N)	1.29	1.07	0.71	0.58	0.52
Preload analysis (N)	1.26	1.08	0.76	0.61	0.52
Mass (g)	6.58	5.45	3.63	2.96	2.64

Source: Courtesy of Delphi Corp.

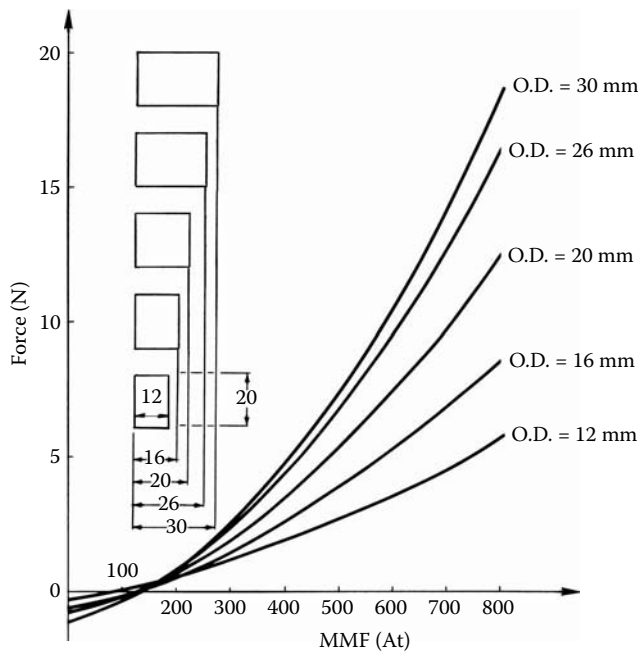
than an all-iron disk structure because magnets provide additional energy and the MMF drop due to the remote magnet location in this structure is minimized. The reason for such a significant difference in the magnetic performance between structures with a magnet located on the disk's outside rim and a structure with two magnets axially magnetized is the flux distribution when one coil is energized. Figure 4.33 presents a side-by-side comparison of both configurations, each having lower coils energized with an identical current of 10.0 A. Almost all the flux lines generated by the magnet and a coil for one-magnet configurations contribute to the force generation toward the lower magnetic cup. On the other hand, a significant portion of the flux lines for the two-magnet structure passes the upper magnetic cup contributing to the forces that would prevent armature movement toward the lower magnetic cup. Only a small portion of the flux lines contribute to force generation toward the lower magnetic cup. Therefore, there is a substantial difference in the magnetic performance of these two configurations, -1 (Figure 4.32) and -6 (Figure 4.32). Latching relay performance for other magnet locations falls in between the performance of these two structures, as demonstrated in Figure 4.32.

Design considerations are presented in Figure 4.36. Due to space requirement constraints, the solenoid height is fixed, and the OD varies from 12.0×10^{-3} to 30.0×10^{-3} m. All latching forces are indicated as 20g requirements for vibrations that for different dimensions would provide different required preloads because of different armature masses, as presented in Table 4.4. The bigger the armature and all moving mass, therefore, the more difficult the requirement is to meet, as presented in Table 4.4 and Table 4.10.

**FIGURE 4.34**Opening t_2 and closing $t_4 - t_0$ time of latching solenoid vs. OD. (Courtesy of Delphi Corp.)**FIGURE 4.35**Total travel time t_t of latching solenoid vs. OD. (Courtesy of Delphi Corp.)

FE simulations were conducted with the goal to meet or exceed preload requirements necessary for a 20g vibration. For this requirement, a parametric study was conducted to achieve the best (minimum) total travel time t_T for all designs, whereby t_T is the sum of the opening, t_2 , and the closing time, $t_4 - t_0$, for a latching solenoid. As indicated in Figure 4.34 and Figure 4.35 and in Table 4.5, the best total travel time performance can be achieved for a latching solenoid with an OD of 20.0×10^{-3} m, as presented in Table 4.5. The closing time, $t_4 - t_0$, is much more sensitive to the solenoid diameter and its inertia than the opening time, t_2 . The closing time depends also on the energy stored in the system during the time the current energizes the coil. Therefore, one has to devise an OD as small as possible to reduce the amount of iron where the energy can be stored. Concurrent with the variation of the OD, both the inertia of the armature and the force exerted on the armature, which is a function of armature's surface, are affected. Therefore, there is a trade-off between the force, inertia, and energy stored in the system, which was discussed in detail in Chapter 3.

All dimensions for this design with an OD of 20.0×10^{-3} m are presented in Figure 4.37. Neodymium MQ3 is selected for the magnet, and a silicon iron core B-FM material is selected for the armature and stationary magnetic circuit (Carpenter 1989). This soft magnetic material with high electrical resistivity would help with a transient solenoid operation suppressing eddy current effect, while a high-energy magnet would provide a small mass.

**FIGURE 4.36**

Performance of latching solenoid as a function of OD. (Courtesy of Delphi Corp.)

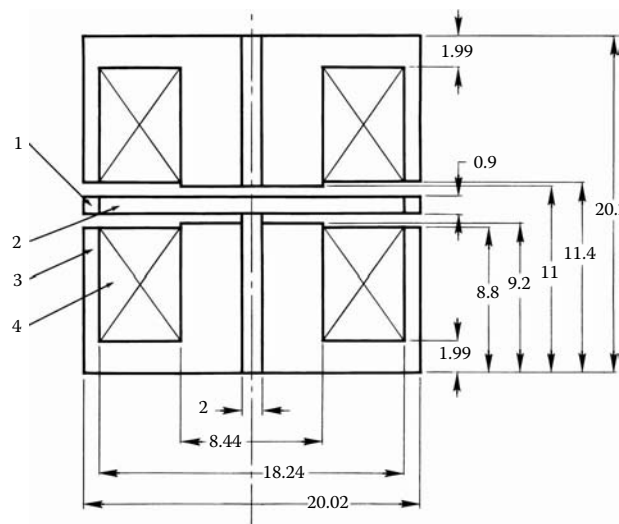
TABLE 4.5

Latching Solenoid Travel Time

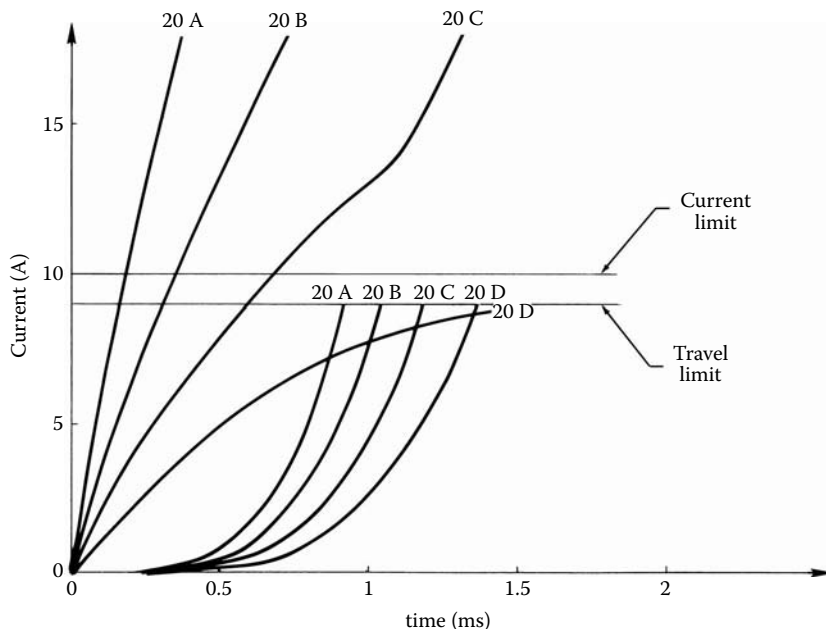
Requirements	OD				
	30.0 ($\times 10^{-3}$ m)	26.0 ($\times 10^{-3}$ m)	20.0 ($\times 10^{-3}$ m)	16.0 ($\times 10^{-3}$ m)	12.0 ($\times 10^{-3}$ m)
Opening time t_2 (ms)	0.24	0.21	0.18	0.19	0.3
Closing time $t_4 - t_0$ (ms)	1.42	1.33	1.27	1.3	1.54
Total travel time t_T (ms)	1.66	1.54	1.45	1.49	1.84
Difference (%)	14.4	6.2	0	2.7	26.9

The current and displacement vs. time characteristics for the selected OD of 20.0×10^{-3} m are shown in Figure 4.38. This figure also indicates the limits for travel and current. Four different coils were devised with different sizes from 23 to 26 AWG, having different numbers of turns to maximize the fill factor for the coil window. Only one coil met the required current limit of 10.0 A as identified by current curve 20D in Figure 4.38. This coil with $N = 130$ turns and wire size 26 AWG was selected, and is shown as coil D in Table 4.6.

Latching solenoids have to work at elevated temperatures up to 150.0°C. This affects their performance, as shown in Table 4.7, because both the magnet's resistance and PM's working point are affected. Figure 4.39 shows both the current and the displacement for the selected solenoid with OD of 20.0×10^{-3} m, identifying deterioration of solenoid dynamic performance at elevated temperature. With the proper magnet selection, only a small portion of the performance is lost, and in this case, the total travel time degradation is less than 5% of the total travel time. Therefore, this solenoid would function properly under the elevated temperature of 150.0°C. During operation, the magnet is not exposed to demagnetization forces because the external MMF flux has the same direction as the magnet magnetization.

**FIGURE 4.37**

Final dimensions of the latching solenoid: (1) ring magnet, (2) armature, (3) magnetic cup, (4) coil. (Courtesy of Delphi Corp.)

**FIGURE 4.38**

Current and displacement characteristics vs. time for latching solenoid OD of 20.0×10^{-3} m. (Courtesy of Delphi Corp.)

TABLE 4.6

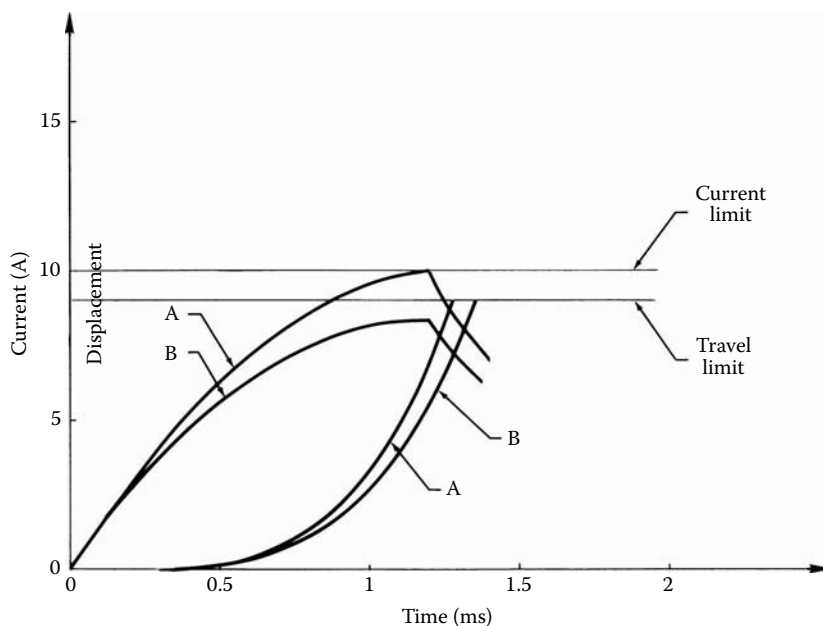
Coil Parameters for the Latching Solenoid

Coil	Turns (No.)	Gauge (AWG)	Resistance (Ω)
A	64	23	0.178
B	81	24	0.286
C	103	25	0.459
D	130	26	0.73

TABLE 4.7

Solenoid Variation vs. Temperature

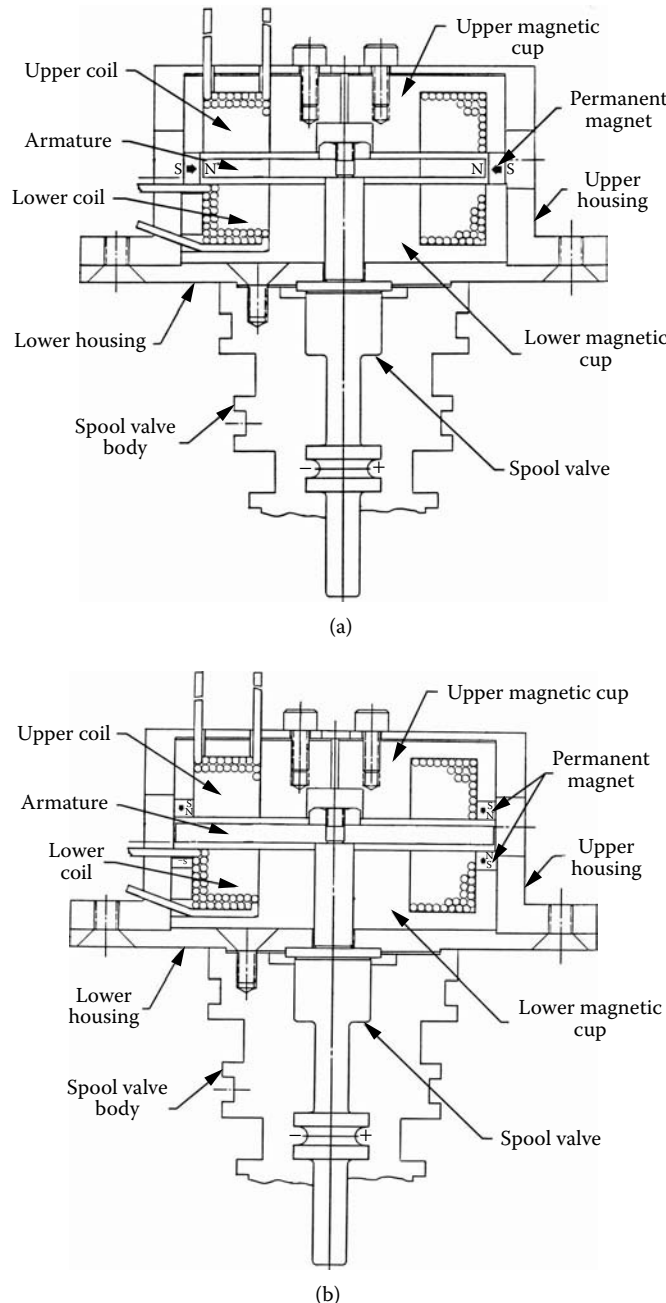
Voltage (V)	Resistance (Ω)	Temperature ($^{\circ}$ C)	Opening Time (ms)	Closing Time (ms)
12	0.645	20	0.18	1.27
12	0.926	150	0.19	1.33
6	0.645	20	0.38	2.17
6	0.926	150	0.41	2.62

**FIGURE 4.39**

Current and displacement vs. time at elevated temperatures: (a) temperature of 20.0°C , (b) temperature of 150.0°C . (Courtesy of Delphi Corp.)

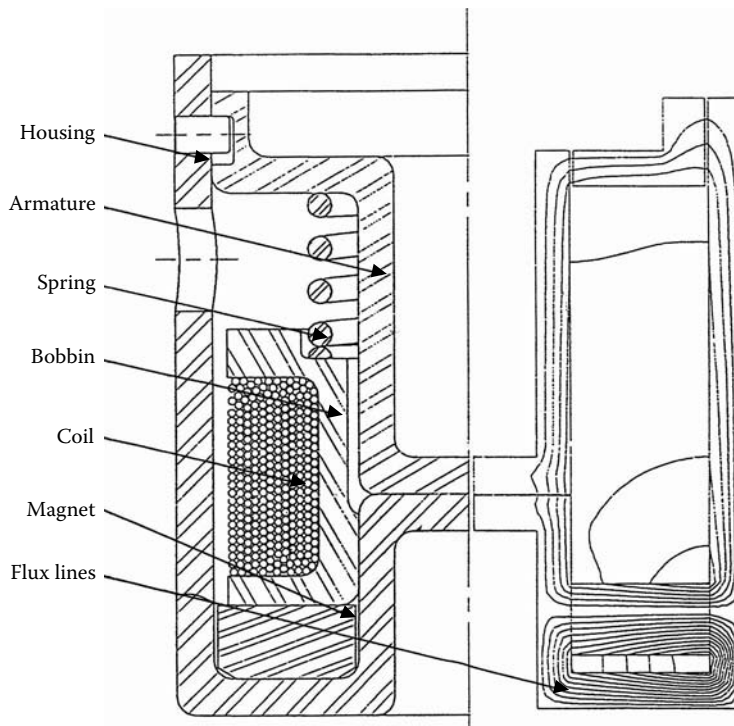
4.2.2 Latching Solenoids with Stationary Magnets

Because solenoids with magnets in a stationary magnetic circuit located parallel to the magnetic path are the most promising structures, this section focuses on and describes them in detail. They require bipolar controllers with both positive and negative current directions to energize the solenoids and to control their motion within two stable solenoid

**FIGURE 4.40**

Latching solenoids with stationary: (a) one-ring magnet with radial magnetization, (b) two-ring magnet with axial magnetization. (Courtesy of Delphi Corp.)

positions. The presence of magnet latching affects the failure mode and some provisions for this effect should be taken into consideration in the controller design. Figure 4.40 shows the cross section of the solenoids with stationary magnets located in the main magnetic path having symmetrical magnetic circuit without a return spring. The solenoid cross sections present their magnetic and nonmagnetic components that identify the magnetic

**FIGURE 4.41**

Latching solenoid configuration with magnet parallel to the main magnetic path. (Courtesy of Delphi Corp.)

flux path for both the PM and the electromagnet. The solenoid consists of a housing, a coil, an armature, and a PM.

The solenoid configuration presented in Figure 4.40(a) shows that the ring-shaped magnet is magnetized radially to provide a direction of magnetization that is perpendicular to the axis of the symmetry. The magnet is located between the coils and sandwiched between the magnetic cups. The housing is stationary and serves as the main magnetic circuit for the solenoid. Because of the magnet location, it does not provide a significant additional air gap for the electromagnet. The solenoid configuration presented in Figure 4.40(b) shows two ring-shaped magnets magnetized axially that provides direction of magnetization parallel to the axis of symmetry. The magnet is located at the outer edge of the upper and lower magnetic cups. This specific magnet location provides significant additional air gap for the electromagnet and significantly degrades the performance of solenoid.

Because of this, the solenoid configuration with a stationary magnet outside or inside the main magnetic path may be an obvious direction to avoid additional parasitic air gaps in the main magnetic circuit for the electromagnet flux. Therefore, solenoids with a magnet in the stationary circuit with a parallel location to the main magnetic circuit were selected as the most promising for further investigation. Figure 4.41 shows a cross section of the investigated configuration having cylindrical symmetry with one coil, a stationary ring magnet parallel to the main magnetic circuit, and a return spring.

One side of the solenoid identifies its components and the other shows the magnetic flux paths: a main magnetic-circuit flux path for the electromagnet and an additional magnetic path for the PM parallel to the main magnetic circuit. The coil is wound on a bobbin around the magnetic central pole. The armature is shaped with a special T shape that combines the advantages of both the disk and the plunger armature structures, as

described in Section 3.3.3. Additionally, its center pole is hollow, thus significantly reducing its mass. This particular shape allows for a small MMF drop across the parasitic air gap while maintaining high magnetic flux density in the main air gap. The armature is placed against the central spring and controlled on the other side by a pin that provides mechanical stop. The spring is preloaded and with additional force due to spring compression is able to return the armature. Because of one coil, this solenoid configuration requires controllers with both positive and negative current directions to energize the solenoid and to control its motion with two stable positions.

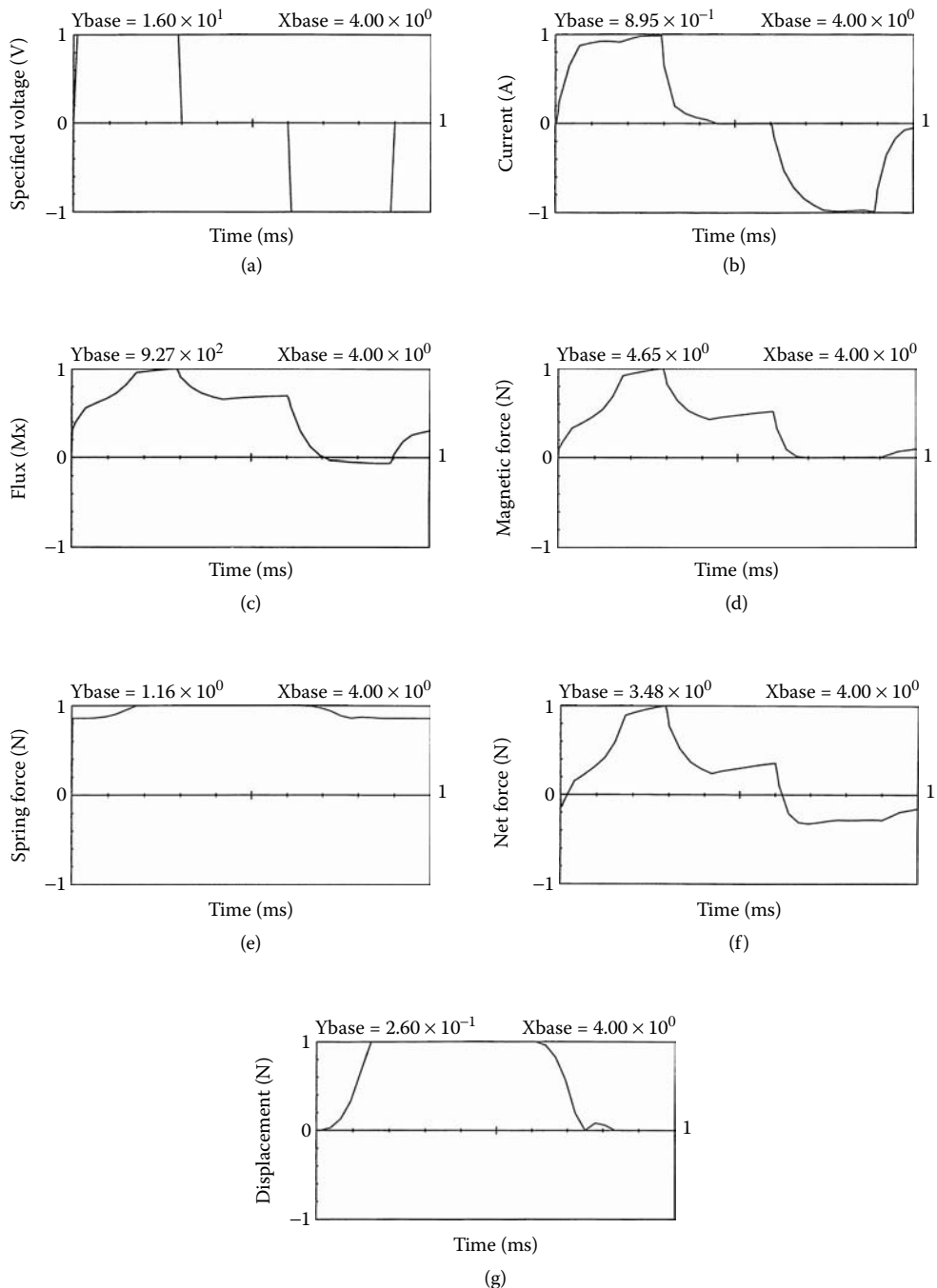
Because the solenoid configuration has a cylindrical symmetry, the dynamic analysis of this solenoid is based on 2D FE analysis, as presented in Figure 4.42. The analysis is conducted to determine the applied voltage, transient current, magnetic flux, magnetic force, net force, and displacement vs. time. The current shown in Figure 4.42(a) identifies the proposed control diagram of the solenoid cycle. Initially, the solenoid is open without any voltage applied to the coil. When voltage is applied to the coil, the current increases, as presented in Figure 4.42(b), with the slope a function of coil resistance and inductance. When the current reaches 0.85 A, the voltage is discontinued. At the same time, the magnetic flux builds up and generates a magnetic force, as presented in Figure 4.42(c) and Figure 4.42(d), respectively. Both the magnetic force and magnetic flux indicate that at the beginning of the cycle there is a certain premagnetization level due to the PM's MMF, as presented in Figure 4.42(d).

The magnet's force, however, is not able to overcome the armature spring preload, as indicated in Figure 4.42(e) and Figure 4.42(f), and the resultant beginning net force is negative, as presented in Figure 4.42(f). As the current builds up in the coil, the magnetic flux increases at the armature and, at a certain point in time, balances the negative spring force. At this point, the armature starts its travel, closing the gap, as indicated in Figure 4.42(g). The positive voltage is discontinued and the armature stays closed due to PM MMF, which is now stronger than at the beginning of the cycle because more flux lines cross the main air gap. Consequently, a negative voltage is applied, as presented in Figure 4.42(a), which suppresses the magnet flux lines, and with the suppressed magnetic force, the spring returns the armature back to its previous position, as indicated in Figure 4.42(g), and the cycle is complete.

Figure 4.43 illustrates the solenoid's geometry and magnetic flux lines during the dynamic operation previously described in Figure 4.42. Beginning the cycle without voltage excitation is shown in Figure 4.43(a) with the armature in an open position. A small portion of the magnet flux lines crosses the air gap, preventing the magnet force from moving the armature. With positive current excitation, more flux is generated and the stronger magnetic force working against the spring force moves the armature to its closed position, as shown in Figure 4.43(b).

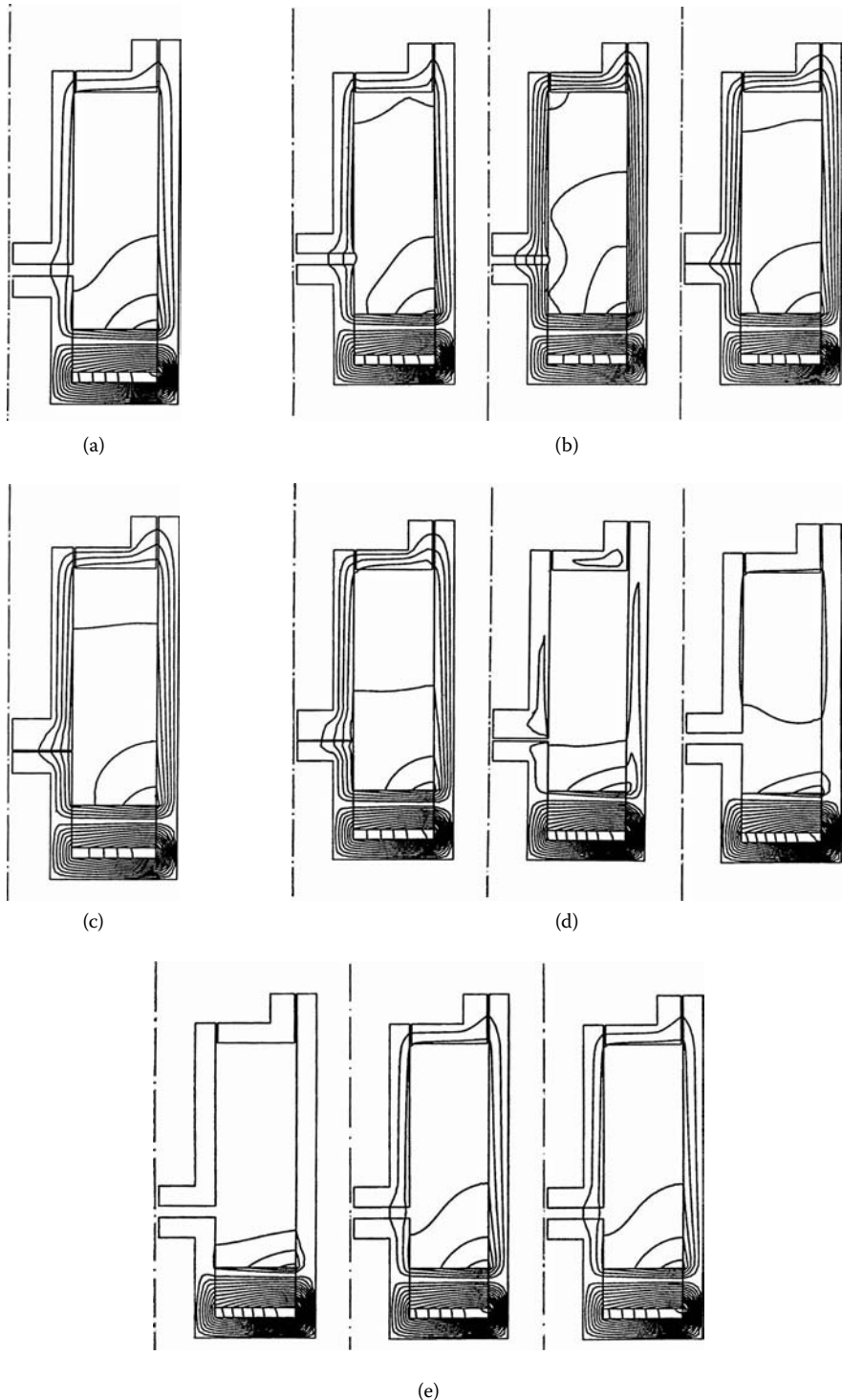
As illustrated in Figure 4.43(c), with the armature closed and no current excitation, more flux lines are attracted toward the main air gap, generating a latching magnetic force sufficient to keep the armature in a closed position compressing the spring. With a negative current applied to the coil, the magnet flux lines are shifted out of the air gap, as shown in Figure 4.43(d), and the armature is moved back to its previous open position. After the negative current is discontinued, the PM restores the flux and its distribution, as identified in Figure 4.43(e), back to its original shape as at the beginning of the cycle, as presented in Figure 4.43(a). At no time during dynamic operation is the magnet exposed to demagnetization forces. This should secure the magnet's normal operation during the entire solenoid utilization period.

Bench test of the latching models was performed for two different solenoid designs, I and II, as presented in Table 4.8. Major physical differences between these two designs as well as the static and dynamic performances of both solenoid designs are listed in Table 4.8.

**FIGURE 4.44**

Solenoid dynamic analysis: (a) voltage profile vs. time, (b) current profile vs. time, (c) flux vs. time, (d) magnetic force vs. time, (e) spring force vs. time, (f) net force vs. time, (g) displacement vs. time. (Courtesy of Delphi Corp.)

For the static performance, the electromagnetic force was determined at the fixed air gap, and both the current and the travel time were investigated for the dynamic behavior scenario. Travel time to open and close corresponds to the minimum pulse width to activate the solenoid in both the open and closed positions. Figure 4.44 shows the test results of the current vs. time characteristics for opening and closing the solenoid.

**FIGURE 4.44**

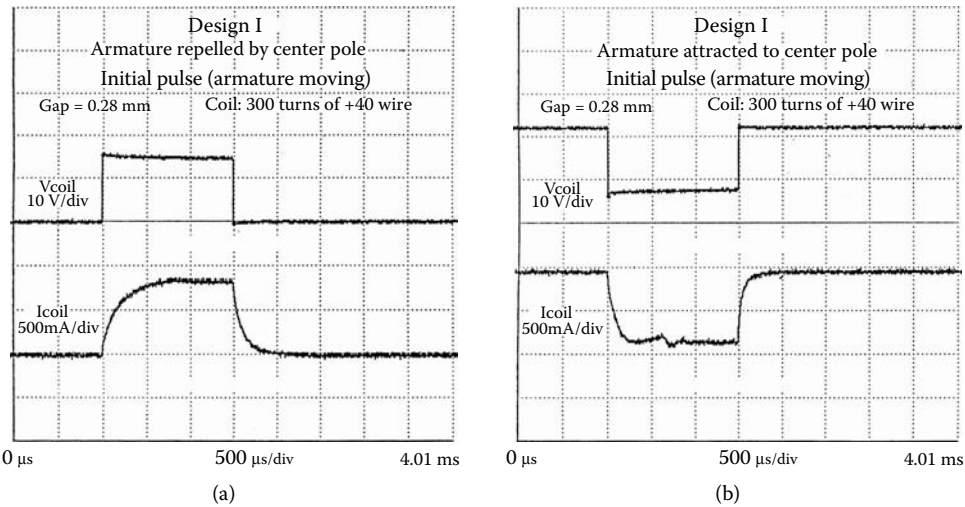
Solenoid geometry and flux-lines dynamics: (a) no voltage applied; (b) positive voltage applied, movement of the armature; (c) armature latched, no voltage; (d) negative voltage applied, movement of the armature; (e) armature unlatched, voltage discontinued. (Courtesy of Delphi Corp.)

TABLE 4.8

Latching Solenoid Designs

Performance or Design	Design I	Design II
Coil resistance (Ω)	18.1	18.2
Coil AWG 40 (no. of turns)	300	300
Solenoid OD ($\times 10^{-3}$ m)	8.0	8.6
Solenoid height ($\times 10^{-3}$ m)	8.50	13.65
Total mass (g)	2.40	5.00
Air gap ($\times 10^{-3}$ m)	0.28	0.24
Force to open (N)	2.11	3.77
Force to close (N)	0.27	0.52
Pulse width to open (ms)	0.35	0.33
Pulse width to close (ms)	0.22	0.35

Source: Courtesy of Delphi Corp.

**FIGURE 4.44**

Current test profiles in dynamics: (a) negative voltage applied, (b) positive voltage applied. (Courtesy of Delphi Corp.)

TABLE 4.9

Latching Solenoid Dynamic Test and Analysis Comparison

Performance	Test	Analysis
Max current (A)	0.85	0.89
Voltage (V)	16.00	16.00
Force to open (N)	2.11	1.93
Force to close (N)	0.27	0.41
Pulse width to open (ms)	0.35	0.33
Pulse width to close (ms)	0.22	0.19

Source: Courtesy of Delphi Corp.

Table 4.9 shows the comparison between test results and analysis for Design I. Static forces are within several percent, which indicates good correlation between test and analysis for engineering purposes. The dynamics also identify that for both closing and opening the minimum pulse width of the solenoid correlates with FE analysis.

4.3 Latching Solenoid Applications

Latching injectors, relays, and transmission solenoids have found applications in the automotive industry. Specific and recognized automotive and industrial applications for latching relays can also result in significant energy savings for automatic field watering and irrigation systems for agriculture applications and additional automotive uses, such as daytime running lamps, fuel pumps, A/C clutch coils, HVAC blowers, engine cooling fans, and electronically operated transmission solenoids.

Because the conventional latching solenoid discussed in Section 3.3.6 did not meet automatic transmission requirements, a new latching solenoid was designed, as shown in Figure 4.45. The requirements for transmission solenoids are presented in Table 4.10. At 10% duty cycle of 20.0 ms, a transmission clutch must shift, and therefore, the latching solenoid must also operate in less than 2.0 ms to meet the required duty cycle. The designed

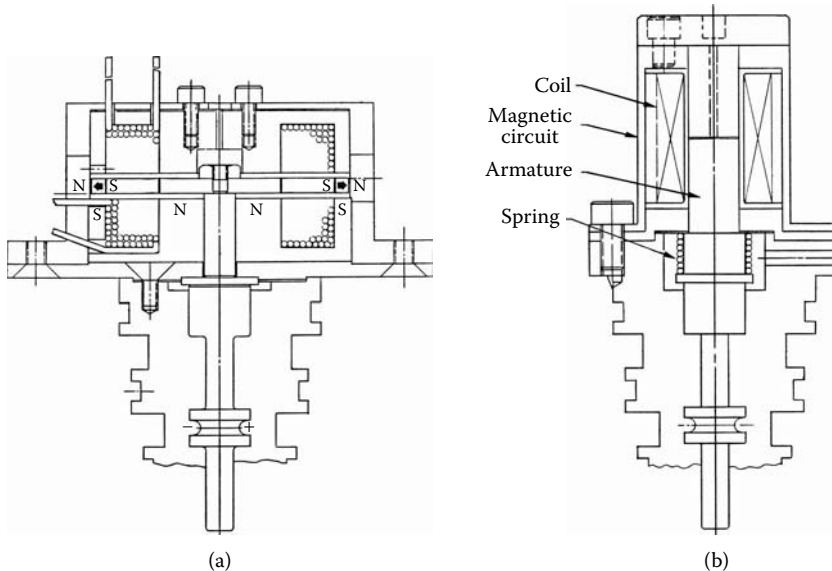


FIGURE 4.45
Solenoids for automatic transmission clutch pressure: (a) latching solenoids, (b) conventional solenoids. (Courtesy of Delphi Corp.)

TABLE 4.10
Transmission Solenoid Constraints and Requirements

Performance	Unit	Requirements
Maximum total travel time	ms	2
Total travel distance	$\times 10^{-3}$ m	1
Nominal voltage	V	6 to 16
Temperature	°C	40 to 150
Vibration	m/s^2	20g
Mass of spool valve	g	1.6
Maximum current peak	A	10
Available envelope & volume	$\times 10^{-6}$ m ³	21.7
Durability	cycles	10^{+6}

TABLE 4.11
Solenoid Performance Comparison

Performance	Unit	Conventional	Latching
Maximum total travel time	ms	3.2	2
Continuous current	A	4.0 or 1.0	0
Number of leads	#	2	3
Number of transistors	#	1	2
Transistor rating	A	4.0 or 2.5	7
Failure mode	mode	open	last

latching solenoid met all requirements and proved to be a viable option for the electronically controlled transmissions. Table 4.11 shows the comparison for the performance based on the test results for the conventional and latching solenoids for controlling the clutch hydraulic pressure application. The latching solenoid achieved 2.0 ms total travel time, and a conventional solenoid with 3.2 ms performance did not meet the requirements for a transmission application total travel time to open and close. More details on this application for conventional solenoids are given in Chapter 3.

Example 4.1

Calculate preload forces for the required 20g for all armatures discussed in Figure 4.36. Force is calculated from the following expression:

$$F = ma \quad (4.1)$$

where m is a total mass, $m = 2.64 \text{ g}$ for the OD of $12.0 \times 10^{-3} \text{ m}$ (Table 4.10); and a is acceleration, $a = 20g$ (Table 4.10), and $g = 9.806 \text{ kg/s}^2$.

Calculate the required force from Equation 4.2 and compare with Table 4.4:

$$F = 20 \text{ mg} \quad (4.2)$$

1. For OD = $12.0 \times 10^{-3} \text{ m}$ $F_{12} = 2.64 \times 10^{-3} \text{ kg} \times 20 \times 9.806 \text{ m/s}^2 = 0.518 \text{ N}$
2. For OD = $16.0 \times 10^{-3} \text{ m}$ $F_{16} = 2.96 \times 10^{-3} \text{ kg} \times 20 \times 9.806 \text{ m/s}^2 = 0.581 \text{ N}$
3. For OD = $20.0 \times 10^{-3} \text{ m}$ $F_{20} = 3.63 \times 10^{-3} \text{ kg} \times 20 \times 9.806 \text{ m/s}^2 = 0.712 \text{ N}$
4. For OD = $26.0 \times 10^{-3} \text{ m}$ $F_{26} = 5.45 \times 10^{-3} \text{ kg} \times 20 \times 9.806 \text{ m/s}^2 = 1.069 \text{ N}$
5. For OD = $30.0 \times 10^{-3} \text{ m}$ $F_{30} = 6.58 \times 10^{-3} \text{ kg} \times 20 \times 9.806 \text{ m/s}^2 = 1.290 \text{ N}$

This is the solution for Example 4.1.

5

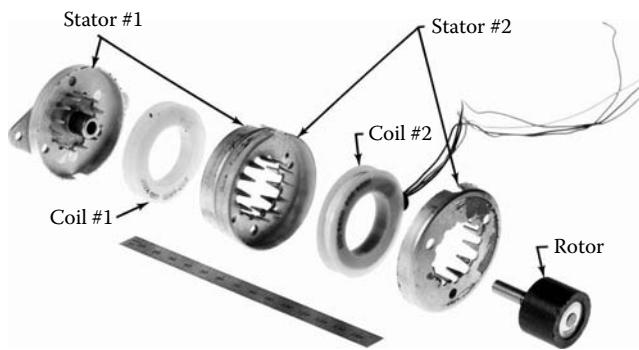
Stepper Motors

Stepper motors and, in particular, claw pole stepper motors are widely applied in industrial controls (Chirikjian et al. 1999, Floresta 1990, Kenjo 1990, Pawlak 1984, Rajagopal et al. 2003, Singh 1974). In the automotive industry, these stepper motors, often called tin-can or can-stack motors, have found a variety of applications, such as in the timing of fuel injectors or to adjust the amount of fuel going to the engine. Claw pole or interdigitated construction is used for this type of electrical machine, similar to the Lundell construction used in automotive alternators. Because this type of machine has a very complex 3D magnetic circuit, it is difficult to analyze using closed-form solutions. A 3D computer program for numerical solutions is necessary.

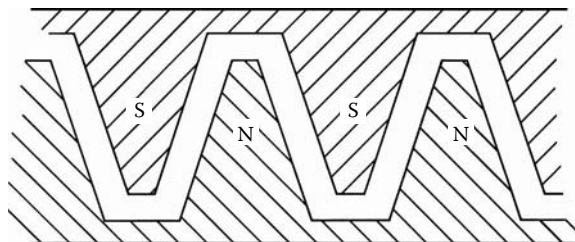
5.1 Principles of Operation

Figure 5.1 shows the various motor components necessary to produce a torque. There are two stators, each consisting of a north and a south lamination, with a coil enclosed between them and one PM rotor having P poles along the periphery. Each lamination has $P/2$ teeth which, when assembled, mesh with each other, as shown in Figure 5.1 and in a developed view in Figure 5.2 having the same number of teeth and number of magnet poles. When the coil is energized with, say, a positive current, all the teeth of the north lamination will become north poles and all the teeth of the south lamination south poles. Thus, a torque will be exerted on the rotor to align its south poles with the teeth of the north lamination and its north poles with the teeth of the south lamination, as presented in Figure 5.2. Reversing the direction of the current reverses the polarity of the stator teeth and the resultant torque moves the rotor one step. With only one stator, however, the rotor is as likely to turn backward as forward and so the second stator is introduced, physically displaced by 90 electrical degrees (one fourth of the pole pitch), as shown in Figure 5.3. It can be readily seen that positive and negative rotation can be obtained by exciting the stators in the sequence shown in Table 5.1.

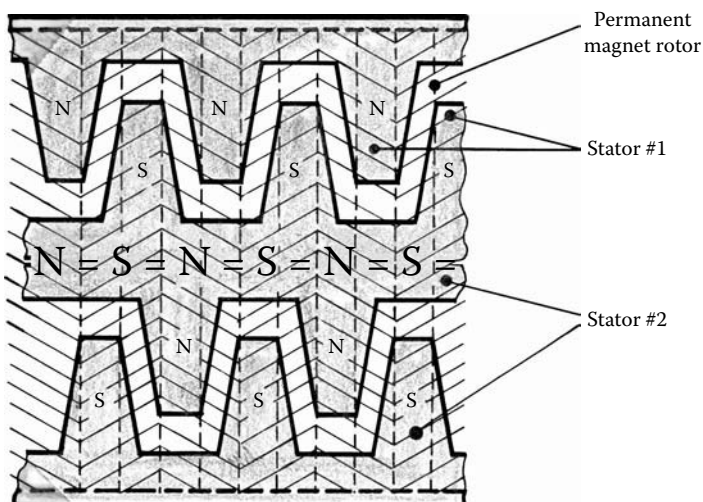
Claw pole stepper motors are divided into two types, bipolar and unipolar, depending on the number of coils. A unipolar stepper motor has four coils, and a bipolar one has only two coils, as shown in the control schematic presented in Figure 5.4. For the unipolar stepper motor, the two windings in each stator are mutually coupled. A unipolar controller driver unit, in this case, a microcontroller or application specific integrated circuit (ASIC), as shown in Figure 5.5, generates a series of pulses that are organized as a sequence of voltage pulses, as shown in Figure 5.6, which indicates that only two windings can be connected to the voltage pulses at the same time. Because each winding has a free-wheeling diode connected across it, current flows in one winding while the other winding is being switched off. The induced current in the off phase offers a damping effect to the response

**FIGURE 5.1**

Claw pole stepper motor with PM. (From Pawlak, A.M., *Proceedings of the 13th Annual Symposium on Incremental Motion Control Systems and Devices*, Champaign, IL, May 1984. With permission.)

**FIGURE 5.2**

Cross section of the claw pole stepper motor with PM. (Courtesy of Delphi Corp.)

**FIGURE 5.3**

Production of unidirectional torque energizing two stators. (From Pawlak, A.M., *Proceedings of the 13th Annual Symposium on Incremental Motion Control Systems and Devices*, Champaign, IL, May 1984. With permission.)

TABLE 5.1
Excitation Sequence

Positive rotation (left to right, Fig. 5.3)

Stator	Connection	Step				
		1	2	3	4	5
#1	A	(+)	(-)	(-)	(+)	(+)
#1	B	(-)	(+)	(+)	(-)	(-)
#2	C	(+)	(+)	(-)	(-)	(+)
#2	D	(-)	(-)	(+)	(+)	(-)

Negative rotation (right to left, Fig. 5.3)

Stator	Connection	Step				
		1	2	3	4	5
#1	A	(+)	(-)	(-)	(+)	(+)
#1	B	(-)	(+)	(+)	(-)	(-)
#2	C	(-)	(-)	(+)	(+)	(-)
#2	D	(+)	(+)	(-)	(-)	(+)

Source: Courtesy of Delphi Corp.

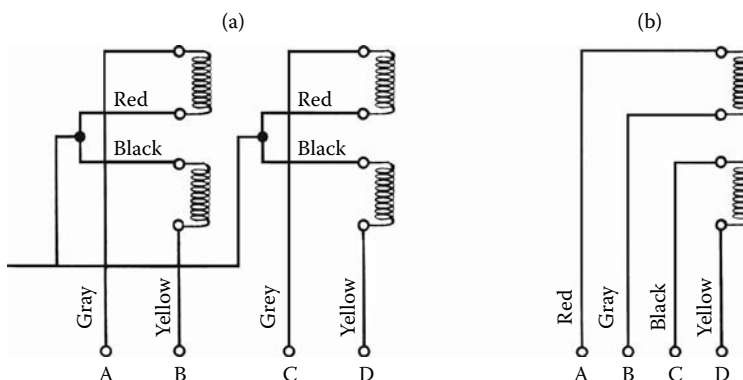
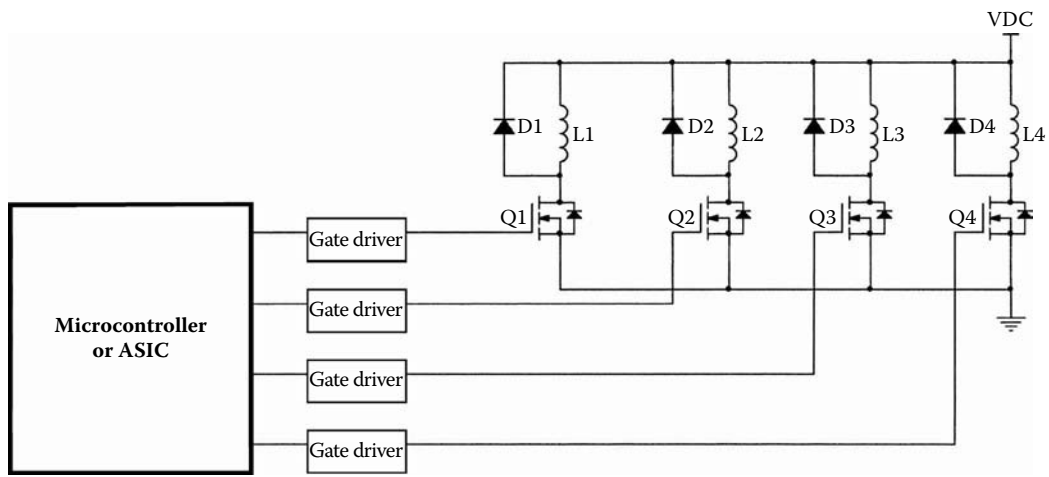


FIGURE 5.4

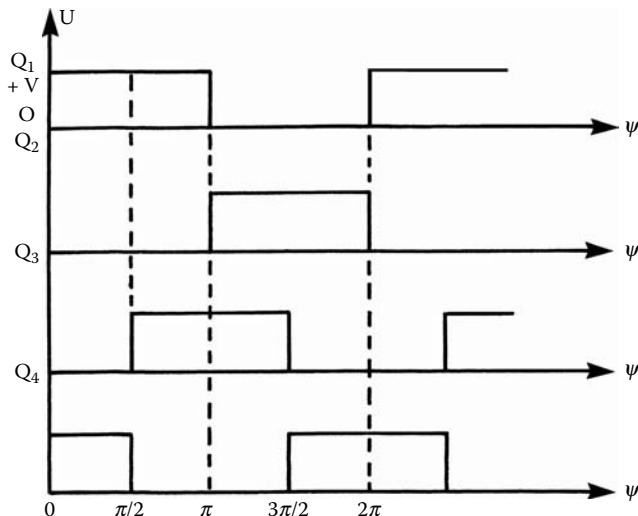
Schematic of the stepper motor with PM: (a) unipolar with four coils, (b) bipolar with two coils. (Courtesy of Delphi Corp.)

of the motor, because the current circulating in the off phase provides some retarding torque. Although this torque is small at low speeds, it becomes significant at high speeds. The circulating energy is dissipated as heat in the off phase winding. At high speed the motor heating increases. A unipolar stepper motor requires a simple drive to provide unidirectional current for its four coils (two in each stator).

It can be shown that for the same coil resistance (IR^2) loss in the stator of the unipolar motor peak, the current is only 70% that of the bipolar one. Thus, for the same stator frame and coil resistance loss, the unipolar stepper motor produces approximately 70% of the static torque in comparison with the bipolar motor. For the same torque, it is necessary to increase the stator OD for the unipolar motor and to use more copper. Hence, for the same static conditions, it is less complex and less expensive to produce a bipolar

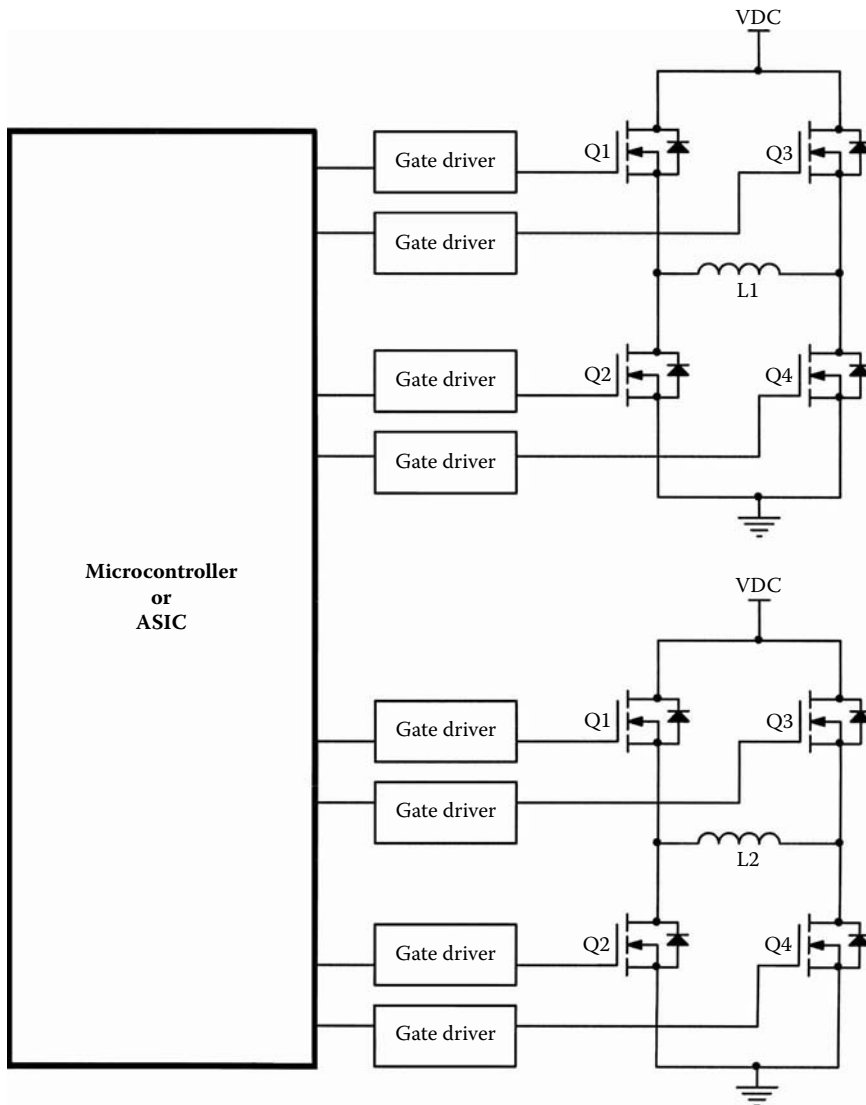
**FIGURE 5.5**

Schematic of the unipolar driver unit with microprocessor and gate drivers: D1, D2, D3, D4 are diodes in each winding from 1 to 4, respectively; L1, L2, L3, L4 are coil inductances from 1 to 4, respectively; Q1, Q2, Q3, Q4 are MOSFET switches in each side of coil 1 and coil 2, respectively; and VDC is battery voltage. (Courtesy of Delphi Corp.)

**FIGURE 5.6**

Voltage waveform for unipolar driver unit. (Courtesy of Delphi Corp.)

stepper motor than a unipolar one. However, a bipolar driver is more complicated and costly because it requires twice as many metal oxide semiconductor field-effect transistor (MOSFET) switches as the unipolar driver, as presented in Figure 5.5 and Figure 5.7. In the off phase of bipolar driver, there is no coupling and the winding current decreases

**FIGURE 5.7**

Schematic of the bipolar driver unit with microprocessor and gate drivers: L1, L2 are inductances of coil 1 and coil 2, respectively; Q1, Q2, Q3, Q4 are MOSFET switches in each side of coil 1 and coil 2; and VDC is battery voltage. (Courtesy of Delphi Corp.)

rapidly, as presented in Figure 5.8. Moreover, because the winding energy is returned to the power supply, the bipolar driver is energy efficient. In summary, the bipolar driver offers high torque at high speeds, higher efficiency, and better utilization of the motor winding compared to the unipolar driver.

Another consideration is whether a driver should be a current or a voltage source. Although a current source driver has better response, it is more costly and not very commonly used. Thus, when considering potential applications, we should focus on a bipolar driver with a voltage source.

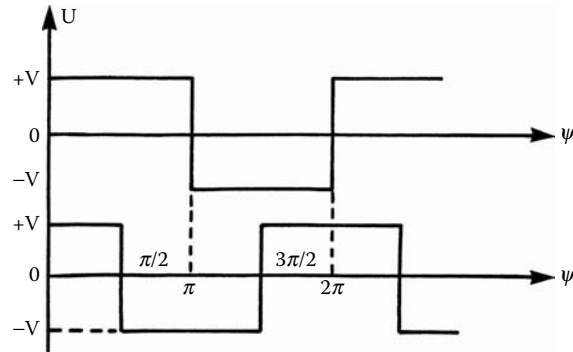


FIGURE 5.8

Voltage waveform for bipolar driver unit. (From Pawlak, A.M., *Proceedings of the 13th Annual Symposium on Incremental Motion Control Systems and Devices*, Champaign, IL, May 1984. With permission.)

5.2 Static Analysis of Stepper Motor

Because stepper motor performance characteristics cannot be described in conventional motor terms, the next sections will introduce special techniques for describing stepper motor characteristics. In this section, we will focus on the holding torque that is developed by the stepper motor in the steady state. Section 5.3 will discuss the dynamic behavior of the stepper motor, in particular, the two fundamental torque vs. speed characteristics in the dynamic mode, which can be generally expressed by their pull-out torque (start-run) curves and pull-in (start-stop) curves.

5.2.1 Static Torque Analysis

The torque developed by the stepper motor in the steady state is called the holding torque. It is the most fundamental characteristic of the stepper motor and acts in a direction to force a motor back to and hold in the zero-torque or detent position. All other torque curves, static or dynamic, have their origin in this holding torque vs. displacement characteristic.

The static torque can be calculated from the coenergy stored in the air gap W_m as a function of rotor position θ (in mechanical degrees):

$$T(\theta) = \frac{dW_m(\theta)}{d\theta} \quad (5.1)$$

The coenergy of the magnetic circuit is given by:

$$W_m(\theta) = \sum_{k=1}^{n_{ik}} \int_0^{\psi_k} \psi_k d i_k \quad (5.2)$$

where n is the number of stator coils, ψ_k is flux linkages of the k coil, i_k is the current in the k coil, $T(\theta)$ is the static torque, θ is the rotor position (in mechanical degrees), and W_m is the coenergy stored in the air gap.

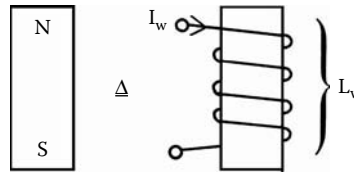


FIGURE 5.9
PM and equivalent coil. (Courtesy of Delphi Corp.)

However, $\psi_k = f(\theta)$ and $i_k = f(\theta)$ and, for the linear system, from Equation 5.1, we have:

$$T(\theta) = \frac{1}{2} \sum_{k=1}^{k=n} \left[i_k \frac{d\psi_k}{d\theta} - \psi_k \frac{di_k}{d\theta} \right] \quad (5.3)$$

For the static torque calculation, the current is either constant or zero: $-\psi_k di_k/d\theta = 0$. It can be assumed that the PM is represented by an equivalent coil with self-inductance equal to L_w carrying current I_w , as presented in Equation 5.4 and Figure 5.9.

Then the flux linkage in the stator is calculated:

$$\psi_s = \sum_{k=1}^{k=n} i_{sk} \times L_{sk} + I_w \times L_{sw} \quad (5.4)$$

And the flux linkage in the rotor is calculated:

$$\psi_w = I_w \times L_{sw} + i_{sk} \times L_{ws} \quad (5.5)$$

For $k = 1, 2, \dots, n$, where ψ_s , ψ_w are flux linkages in the stator and rotor, respectively, L_{sk} is the self-inductance of the k coil, L_{sw} , L_{ws} are mutual inductances, L_w is the self-inductance of the equivalent coil, I_{sk} is the current in the k coil, and I_w is the current in the equivalent coil.

Then the torque from Equation 5.3 through Equation 5.5 is calculated:

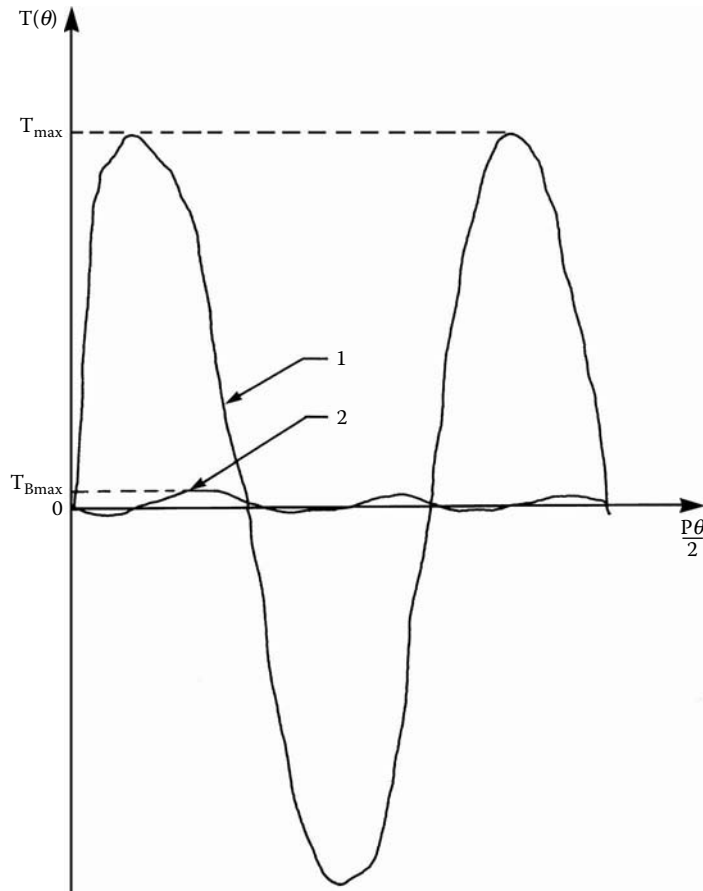
$$T(\theta) = \underbrace{\frac{1}{2} \sum_{k=1}^{k=n} I_{sk}^2 \frac{dL_{sk}(\theta)}{d\theta}}_{T_A} + \underbrace{\frac{1}{2} I_w^2 \frac{dL_w(\theta)}{d\theta}}_{T_B} + \underbrace{I_w \sum_{k=1}^{k=n} I_{sk} \frac{dL_{ws}(\theta)}{d\theta}}_{T_C} \quad (5.6)$$

where T_A and T_B are reluctance torques and T_C is synchronous torque.

However, in our case we have a smooth (cylindrical) rotor and thus:

$$\frac{dL_{sk}(\theta)}{d\theta} = 0 \quad \text{or} \quad T_A = 0 \quad (5.7)$$

As shown in Figure 5.10, the reluctance torque T_B is less than 3% of the total torque and, hence, can be neglected (Chai 1984). It should be pointed out, however, that the amplitude of T_B depends on the shape of the lamination teeth, but because the relative permeability of the magnet is the same as air, the effective air gap is large and the volume of T_B is small in this case.

**FIGURE 5.10**

Torque developed in the stepper motor: (1) total torque, (2) reluctance torque. (Courtesy of Delphi Corp.)

From the definition of inductance:

$$L_{ws}(\theta) = N \frac{P}{2} \frac{\phi_{ws}(\theta)}{I_w} \quad (5.8)$$

where $\phi_{ws}(\theta)$ is the flux per pair of teeth, P is the number of poles, N is the number of turns, I_{sk} is the current in the k coil, and I_w is the current in the equivalent coil.

In practice, it is convenient to calculate $\phi_{ws}(\theta)$ directly from the magnetic circuit, as discussed later for operating point calculations, and not to solve for L_{ws} and I_w . Substituting in Equation 5.6 and ignoring T_A and T_B , we have:

$$T(\theta) = \sum_{k=1}^{k=n} I_{sk} N \frac{P}{2} \frac{d\phi_{ws}(\theta)}{d\theta} \quad (5.9)$$

where $T(\theta)$ is the total static torque developed by stepper motor, and I_{sk} is the current in the k coil. Now for sinusoidal field distribution, the flux per pair of teeth is calculated:

$$\phi_{ws}(\theta) = \phi \cos \frac{P}{2} \theta \quad (5.10)$$

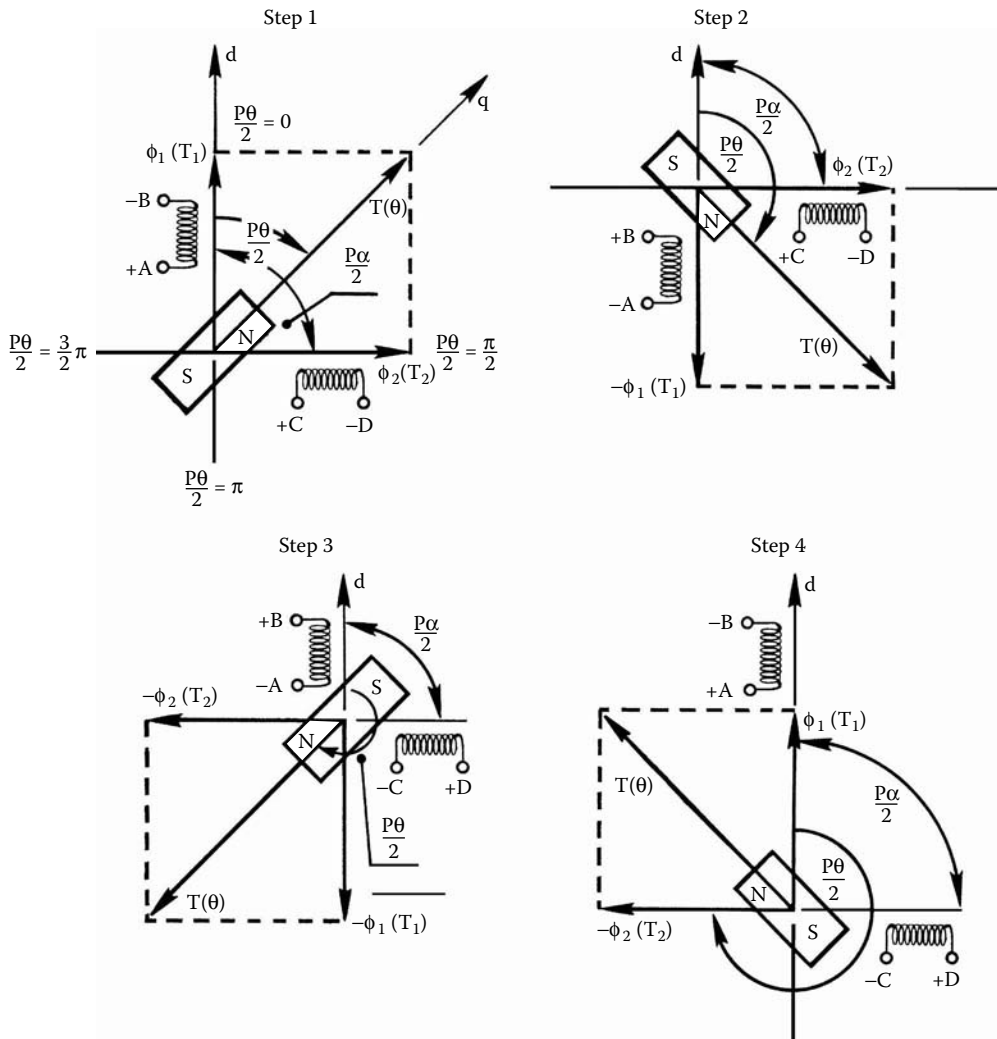


FIGURE 5.11
Position of rotor and resultant torque for four steps. (Courtesy of Delphi Corp.)

where ϕ is a flux in the air gap with armature reaction, θ is the rotor position (in mechanical degrees), and P is the number of poles.

The torque for stator 1 is given by Equation 5.6 through Equation 5.10:

$$T_1(\theta) = T_{1\max} \sin \frac{P\theta}{2} = \frac{I_{S1} N_1 \phi_1 P^2}{4} \sin \frac{P\theta}{2} \quad (5.11)$$

where ϕ_1 is the magnetic flux in air gap coil 1, $T_1(\theta)$ is the stepper motor torque due to coil 1, $T_{1\max}$ is the maximum torque due to coil 1, I_{S1} is the current in the coil 1, N_1 is the number of turns of the stator coil 1, and subscript 1 refers to the stator coil.

With a similar expression for stator 2 with phase shifted in space by a mechanical angle α (in practice $P\alpha/2 = \pi/2$) as shown in Figure 5.11:

$$T_2(\theta) = T_{2\max} \sin \frac{P\theta}{2} = \frac{I_{S2} N_2 \phi_2 P^2}{4} \sin \frac{P(\theta + \alpha)}{2} \quad (5.12)$$

where α is the mechanical angle between two stators, $T_2(\theta)$ is the stepper motor torque due to coil 2, $T_{2\max}$ is the maximum torque due to coil 2, I_{S2} is the current in the coil 2, ϕ_2 is the magnetic flux in air gap coil 2, N_2 is the number of turns of the stator coil 2, and subscript 2 refers to stator coil 2.

The total static torque developed by stepper motor is the vector sum of:

$$T(\theta) = T_1(\theta) + T_2(\theta) \quad (5.13)$$

where $T(\theta)$ is the total torque, $T_1(\theta)$ is the torque due to coil 1, and $T_2(\theta)$ is the torque due to coil 2.

For step 1 through step 4 listed in Table 5.1, only the polarity of the current changes and the torque is given by:

$$\text{Step 1: } T(\theta) = T_{1\max} \sin \frac{P\theta}{2} + T_{2\max} \sin \frac{P(\theta + \alpha)}{2} \quad (5.14)$$

$$\text{Step 2: } T(\theta) = -T_{1\max} \sin \frac{P\theta}{2} + T_{2\max} \sin \frac{P(\theta + \alpha)}{2} \quad (5.15)$$

$$\text{Step 3: } T(\theta) = -T_{1\max} \sin \frac{P\theta}{2} - T_{2\max} \sin \frac{P(\theta + \alpha)}{2} \quad (5.16)$$

$$\text{Step 4: } T(\theta) = T_{1\max} \sin \frac{P\theta}{2} - T_{2\max} \sin \frac{P(\theta + \alpha)}{2} \quad (5.17)$$

Neglecting friction, the rotor will come to rest at each step for the value of θ that makes $T = 0$. Step sizes will be uniform only when $P\alpha/2 = \pi/2$ and when $T_{1\max} = T_{2\max}$. So using Equation 5.11 and Equation 5.12, step uniformity requires the same MMF (ampere-turns) and flux in each stator as well as accurate phase shift between the two stators. The nonuniformity in step size that can be observed in some stepper motors can be due to a difference in flux level between two stators caused by an air gap in the outside of the coil where two laminations join.

Figure 5.12 shows the variation torque with rotor position assuming a sinusoidal variation in flux. In the ideal case where mechanical displacement between two stators $P\alpha/2 = \pi/2$, both stators have the same number of turns $N_1 = N_2 = N$, the same magnetic flux in the air gaps under both stators $\phi_1 = \phi_2 = \phi$, and the same current in both coils $I_1 = I_2 = I$, the peak torque is given by:

$$T_{\max} = \frac{\sqrt{2}}{4} IN\phi P^2 \quad (5.18)$$

where T_{\max} is the maximum torque developed by the stepper motor, I is the current in the stepper motor coils, ϕ is the flux in the air gap, ϕ_1 is the magnetic flux in air gap coil 1, ϕ_2 is the magnetic flux in air gap coil 2, P is the number of poles, N is the number of turns of the stator coil, I_1 is the supplied current (constant) in coil 1, I_2 is the supplied current (constant) in coil 2, N_1 is the number of turns of the stator coil 1, and N_2 is the number of turns of the stator coil 2.

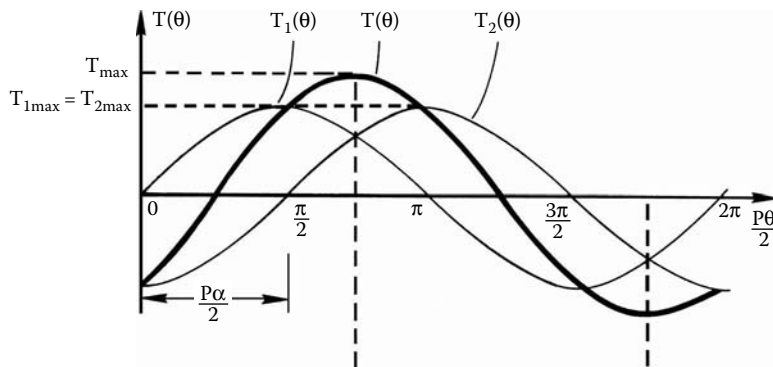


FIGURE 5.12

Static torque developed in the stepper motor. (From Pawlak, A.M., *Proceedings of the 13th Annual Symposium on Incremental Motion Control Systems and Devices*, Champaign, IL, May 1984. With permission.)

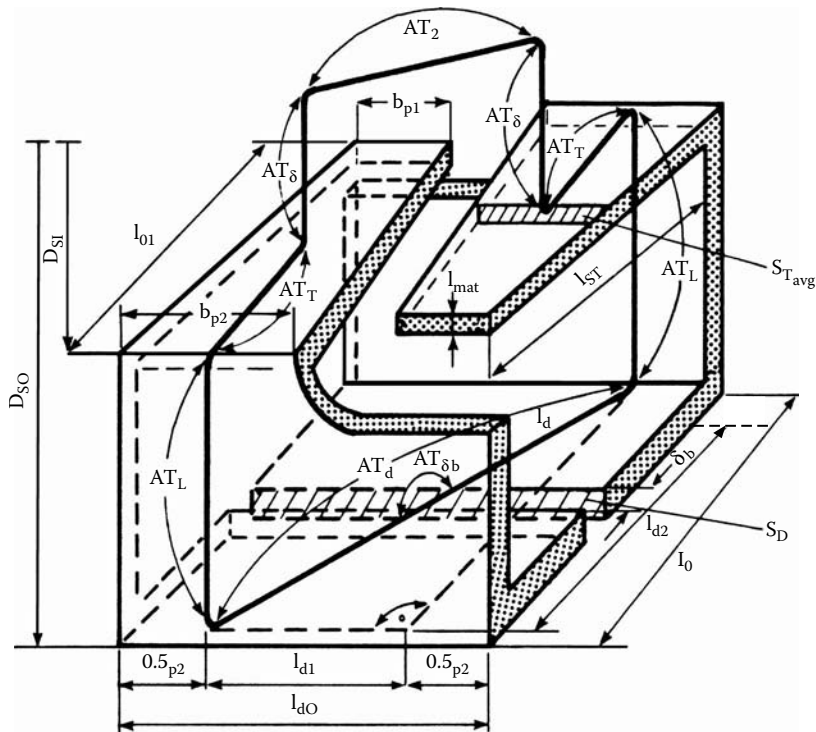


FIGURE 5.13

Stepper motor magnetic circuit for one pole-pair section. (From Pawlak, A.M., *Proceedings of the 13th Annual Symposium on Incremental Motion Control Systems and Devices*, Champaign, IL, May 1984. With permission.)

5.2.2 Magnetic-Circuit Analysis

In this section, we consider the flux produced by the magnet that crosses the air gap of the stepper motor. Figure 5.13 shows the magnetic circuit for a pair of poles with the various MMF drops and dimensions that are needed for analysis. In addition to the tooth

(AT_T) and lamination (AT_D , AT_L) components, there are the main air gap (AT_δ) and parasitic air gap at the back of the lamination ($AT_{\delta b}$).

Without a current in the stator coil, the sum of MMFs should be equal to the magnet MMF, as presented in Figure 5.13:

$$AT_2 = 2AT_T + 2AT_L + AT_D + AT_{\delta b} + 2AT_\delta \quad (5.19)$$

where AT_2 is the magnet's value of MMF at its working point, AT_T is the value of MMF drop in the claw poles, AT_L is the value of MMF drop in the side walls, AT_D is the value of MMF drop in the back walls, $AT_{\delta b}$ is the value of MMF drop in the parasitic air gaps, and AT_δ is the value of MMF drop in the main air gap.

Calculations of the MMF drops along the flux path of the claw pole stepper motor are based on geometry, material, and flux density. The flux level can be determined from the PM working point, discussed in Section 2.3.2 and described in detail in Section 5.2.3. First, we need to calculate the various MMF drops; Figure 5.14 and Figure 5.15 define various dimensions. Calculations of the MMF drop in the tooth region are based on its geometry, material, and flux density. The flux density varies from zero at the narrow end (see Figure 5.15) to $\phi/b_{p2} \times l_{mat}$ at the wide end. Using the average value of the area:

$$S_{T_{avg}} = \frac{b_{p2} + b_{p1}}{2} \times l_{mat} \quad (5.20)$$

the tooth density is:

$$B_T = \frac{\phi}{S_{T_{avg}}} \quad (5.21)$$

and the MMF drop is:

$$AT_T = H_T \times \frac{l_{01}}{2} \quad (5.22)$$

where l_{mat} is the material thickness of the stator elements, l_{01} is the total length of the tooth, b_{p1} is the tooth width at the tip, b_{p2} is the tooth width at the bottom, $S_{T_{avg}}$ is the average cross section of the tooth, B_T is the flux density in the tooth, AT_T is the value of MMF drop in the claw poles, ϕ flux in the air gap, and H_T is the magnetic field strength obtained from the BH curve of the material corresponding to B_T , as presented in Figure 5.16.

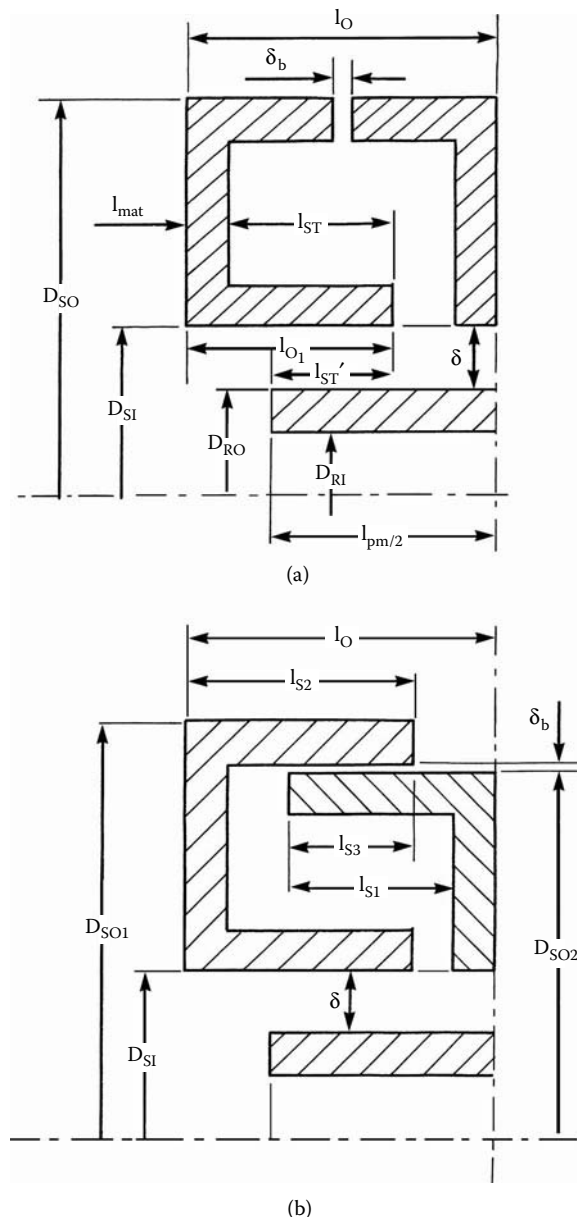
Calculations of the MMF drop in the side walls' "L" area are also based on its geometry, material, and flux density. The flux density in the side walls' "L" area is given by:

$$B_L = \frac{\phi}{b_{p2} \times l_{mat}} \quad (5.23)$$

where B_L is the flux density in side walls, b_{p2} is the tooth width at the bottom, and ϕ is the flux in the air gap with armature reaction.

The required field strength is obtained from the magnetization characteristic (see Figure 5.16) and the MMF drop AT_L is:

$$AT_L = H_L \times \frac{D_{SO} - D_{SI}}{2} \quad (5.24)$$

**FIGURE 5.14**

Two different methods of joining laminations: (a) butt joint, (b) lap joint. ([a] From Pawlak, A.M., *Proceedings of the 13th Annual Symposium on Incremental Motion Control Systems and Devices*, Champaign, IL, May 1984. With permission; [b] courtesy of Delphi Corp.)

The flux density in the "D" area is given by:

$$B_D = \frac{\phi}{l_{do} \times l_{mat}} = \frac{\phi}{\pi(D_{SO} - l_{mat}) \times l_{mat} / 2} \quad (5.25)$$

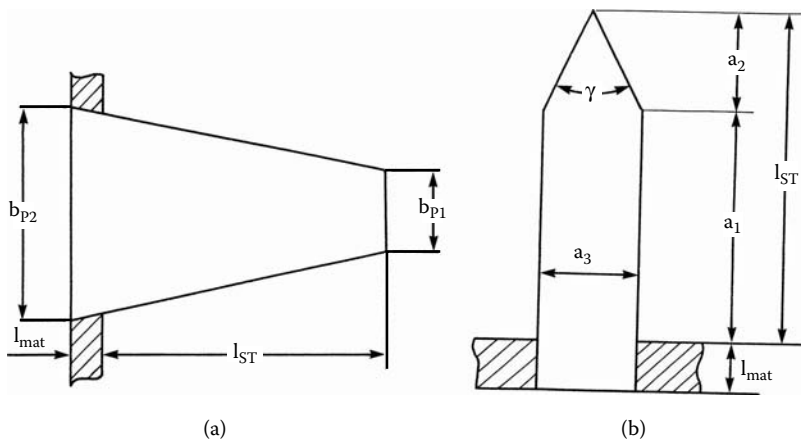


FIGURE 5.15
Tooth dimensions: (a) trapezoid sided, (b) parallel sided. (Courtesy of Delphi Corp.)

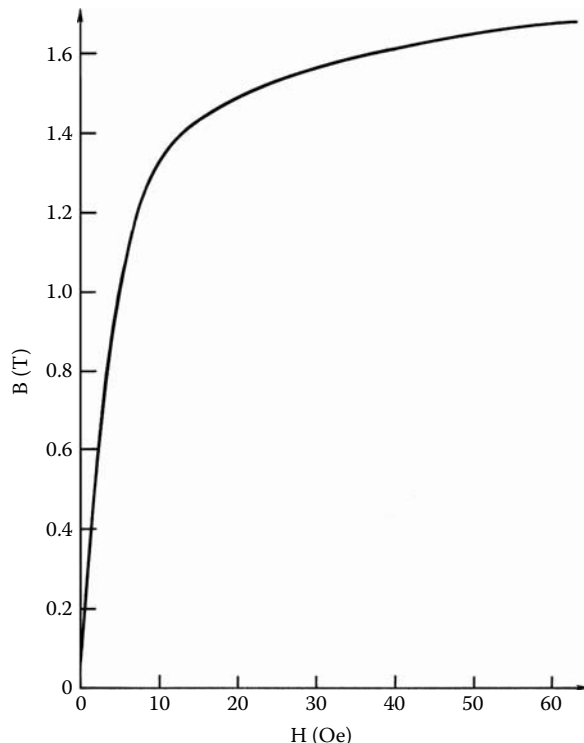


FIGURE 5.16
Magnetization characteristic of material for laminations (cold-rolled, low-carbon strip steel). (Courtesy of Delphi Corp.)

Again looking at Figure 5.16 for the field strength H_D , the MMF force drop in this section is:

$$AT_D = H_D \times l_d \quad (5.26)$$

where the total length can be obtained from Figure 5.13:

$$l_d = \sqrt{l_{d1}^2 + l_{d2}^2} \quad (5.27)$$

and

$$l_{d2} = l_o - l_{mat} \quad (5.28)$$

$$l_{d1} = \frac{\pi(D_{SO} - l_{mat})}{P/2} - b_{p2} \quad (5.29)$$

where P is the number of poles, H_L is the field strength in the side walls, H_D is the field strength in the back walls, and ϕ is a flux in the air gap with armature reaction. Other dimensions are described by Figure 5.14 and Figure 5.15: l_d is the stator dimension, l_{d1} is the stator dimension, l_{d0} is the stator two pole-pair section length, l_{d2} is the stator dimension, l_o is the total stator thickness, l_{mat} is the material thickness of the stator elements, D_{SO} is the stator OD, and b_{p2} is the tooth width.

The two stator laminations are joined at the outer diameter of the rotor using either the butt or a lap joint, as shown in Figure 5.13. For the butt-joint flux the density in the parasitic air gap is:

$$B_{\delta b} = \frac{\phi \times \frac{P}{2}}{\pi(D_{SO} - l_{mat}) \times l_{mat}} \quad (5.30)$$

In practice, cutouts are made for interlocking the laminations as well as for inserting the leads resulting in reduced joint area, as presented in Figure 5.14. For the lap joint, Figure 5.14(b), the flux density is:

$$B_{\delta b} = \frac{\phi \times \frac{P}{2}}{l_{s3} \times \pi D_{SO}} \quad (5.31)$$

where $B_{\delta b}$ is the flux density in the back air gap, l_{s3} is the overlap length, D_{SO} is the stator OD, P is the number of poles, l_{mat} is the material thickness of the stator elements, and ϕ is a flux in the air gap with armature reaction.

When $l_{s3} = l_{s1} + l_{s2} - l_o$ and the MMF drop is:

$$AT_{\delta b} = \frac{B_{\delta b} \times \delta_b}{\mu_0} \quad (5.32)$$

When there is a lap joint:

$$\delta_b = \frac{(D_{SO} - 2 \times l_{mat}) - D_{SO2}}{2} \quad (5.33)$$

where l_{s1} is the lap-joint inside stator length, l_{s2} is the lap-joint outside stator length, l_o is the total stator thickness, D_{SO} is the stator OD, D_{SO2} is the lap-joint inside stator OD, δ_b is

the size of back air gap (parasitic), l_{s3} is the overlap length, μ_0 is permeability of the air, and $AT_{\delta b}$ is the value of MMF drop in the parasitic air gap.

The MMF drop in the main air gap is based on the flux density in the main air gap:

$$B_{\delta} = \frac{\phi}{A_g} = \frac{\phi}{\frac{b_{p2} + b_{p1}}{2} \times l_{ST}'} \quad (5.34)$$

From Figure 5.14 and Figure 5.15:

$$A_g = \frac{b_{p2} + b_{p1}}{2} \times l_{ST}' \quad (5.35)$$

and

$$l_{ST}' = 1/2l_{pm} + l_{ST} + l_{mat} - l_0 \quad (5.36)$$

and the main air gap:

$$\delta = \frac{D_{S1} - D_{RO}}{2} \quad (5.37)$$

Thus:

$$AT_{\delta} = \frac{B_{\delta} \times \delta}{\mu_0} \quad (5.38)$$

where B_{δ} is the flux density in the air gap, ϕ is a flux in the air gap with armature reaction, μ_0 is permeability of the air, l_{ST}' is the effective tooth length, δ is the size of main air gap, AT_{δ} is the value of MMF drop in the main air gap, D_{RO} is the rotor OD, D_{S1} is the stator ID, l_{ST} is the tooth length, l_{mat} is the material thickness of the stator elements, l_{pm} is the length of the PM, b_{p1} is the tooth width at the tip, b_{p2} is the tooth width at the bottom, and A_g is the effective surface of the tooth.

The MMF of the PM is based on the magnet material, the effective magnet length, and the effective magnet area:

$$A_m' = k_a \times A_m \quad (5.39)$$

From Figure 5.17, we have:

$$A_m = \frac{D_{RO} - D_{RI}}{2} \times \frac{l_{pm}'}{2} \quad (5.40)$$

with:

$$k_a = \frac{A_g}{A_m} \quad \text{if} \quad A_g < A_m \quad \text{and} \quad k_a = 1 \quad \text{if} \quad A_g \geq A_m$$

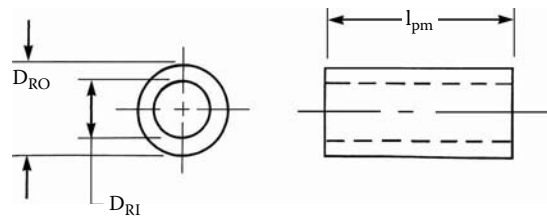


FIGURE 5.17
Magnet dimensions. (Courtesy of Delphi Corp.)

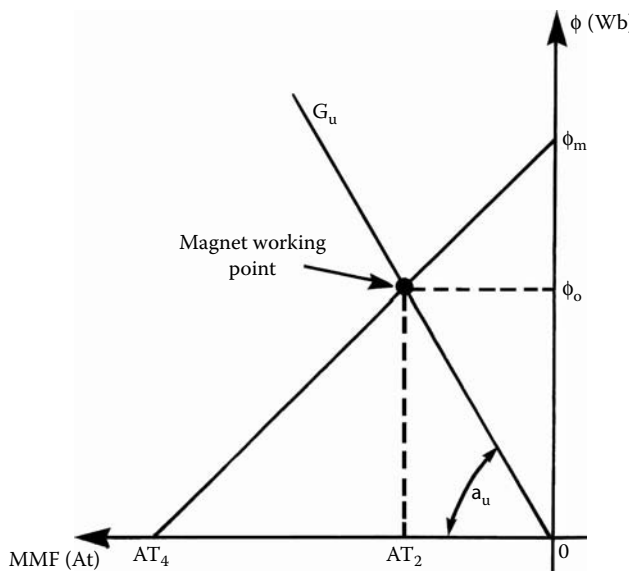


FIGURE 5.18

Magnet working point. (From Pawlak, A.M., *Proceedings of the 13th Annual Symposium on Incremental Motion Control Systems and Devices*, Champaign, IL, May 1984. With permission.)

The effective magnet length l_{pm}' depends on the relative magnitude of the stator and magnet length:

$$l_{pm}' = l_{pm} \quad \text{if} \quad l_o \geq \frac{l_{pm}}{2} \quad \text{and} \quad l_{pm}' = 2 \times l_o \quad \text{if} \quad l_o < \frac{l_{pm}}{2} \quad (5.41)$$

where l_{pm} is the length of the PM, l_{pm}' is the effective length of the PM, D_{RO} is the rotor OD, D_{RI} is the rotor ID, A_m is the magnet surface area, A_m' is the effective magnet surface area, A_g is the effective surface of the tooth, and k_a is the effective magnet area factor.

5.2.3 Magnet Operating Point

The magnet operating point can be determined from the magnet characteristic shown in Figure 5.18. Based on the assumption that the demagnetization curve is a straight line and saturation of the magnetic circuit is neglected, we have from the geometrical consideration:

$$\frac{\phi_m - \phi_o}{\phi_m} = \frac{AT_2}{AT_4} \quad (5.42)$$

where AT_2 , AT_4 are the magnet's MMFs at their working points and the maximum and ϕ_o , ϕ_m are the magnetic flux in the air gaps without armature reaction and the maximum magnet flux, respectively.

To calculate the operating point, we first assume a value for the flux per tooth ϕ . The good initial guess is the value obtained from the BH curve of the magnet using the air gap slope and multiplied by the effective magnet area. Using this flux value, the flux density and the MMF drop in the various parts of the magnetic circuit can be calculated. The total is then compared to the magnet MMF as shown in Equation 5.19, and the initial guess for ϕ can now be iterated until the right- and left-hand sides of Equation 5.19 are equal, as presented in Example 5.1.

In each section, the magnetic flux developed by the PM crosses the magnetic circuit, the main, and the parasitic air gaps. With no exciting current and no armature reaction, the PM magnetic flux in the air gaps can be determined from the magnet working point shown in Figure 5.18 and Equation 5.42:

$$\phi_o = \phi_m \left(1 - \frac{AT_2}{AT_4} \right) \quad (5.43)$$

The maximum value of the flux per tooth ϕ_m is the product of the remanent flux density B_r of the magnet and the effective surface area A_m' .

$$\phi_m = B_r \times A_m' \quad (5.44)$$

where B_r is the remanent flux density of the magnet, A_m' is the effective magnet surface area, and ϕ_m is the maximum magnetic flux in the air gap without armature reaction. The effective magnet surface A_m' depends on both the magnet and tooth surface areas as well as on the method of magnetization of the magnet.

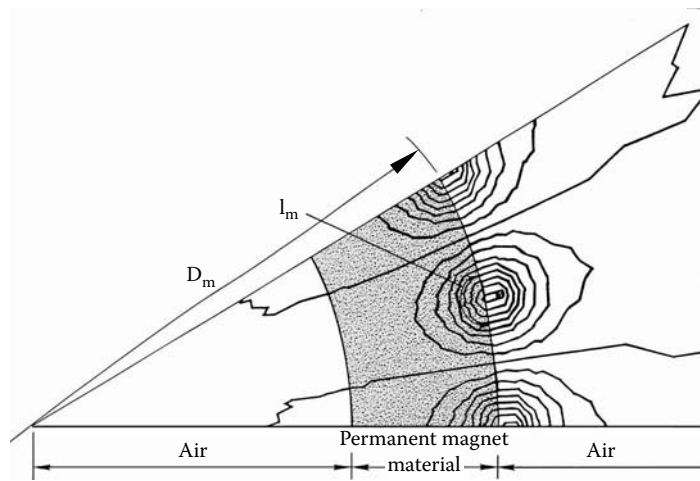
The maximum value of MMF AT_4 is the product of the coercive force of the magnet H_c and the effective magnet length l_m' :

$$AT_4 = H_c \times l_m' \quad (5.45)$$

where AT_4 is the magnet's maximum value of MMF, H_c is the magnet coercive force, and l_m' is the average line of flux in the magnet, as presented in Figure 5.19.

The exact value of the average line of flux in the magnet, l_m' , can be determined from a FE magnetic field solution. 2D FE software was used to determine the PM magnetization patterns in Figure 5.19 and to show the magnetic flux lines inside the magnet.

For this analysis, a flux plot was made using 2D FE computer simulation with real conditions provided for magnet magnetization, in this case with a magnetizing current of $I = 11,500$ A and a magnetizing wire cross section of 0.5×10^{-6} m². If one uses a 2D software for this calculation, an anisotropy factor k_m has to be taken into account because 2D software does not allow for anisotropy. Therefore, the average flux length l_m , as presented in Figure 5.19, is increased using factor k_m :

**FIGURE 5.19**

PM magnetization. (From Pawlak, A.M., *Proceedings of the 13th Annual Symposium on Incremental Motion Control Systems and Devices*, Champaign, IL, May 1984. With permission.)

$$l'_m = k_m \times l_m \quad (5.46)$$

This is defined as:

$$k_m = \frac{B_{rx}}{B_{ry_{avg}}} \quad (5.47)$$

where k_m is the effective flux length in the magnet factor, B_{rx} is the magnetic flux density in the radial direction, $B_{ry_{avg}}$ is the magnetic flux density in the tangential direction, and l_m is the average flux length in the magnet.

For the material used in our analysis, $k_m = 1.15$. This factor should be verified if 3D software is available to provide for magnet anisotropy. For the lumped-parameter model and for the magnet magnetized as shown in Figure 5.19, the following expression has been provided (Pawlak et al. 1988):

$$l_m = \frac{\pi^2 D_{RO} (2p-1)}{32p^2} \quad (5.48)$$

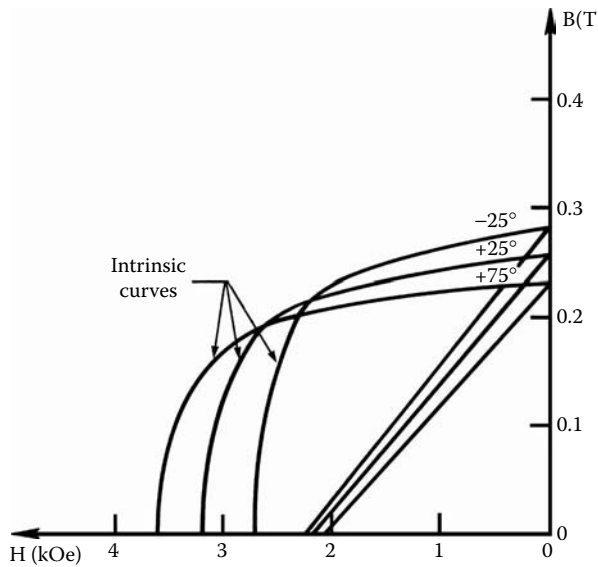
where D_{RO} is the magnet OD and p is the number of magnet pole pairs.

With the linear magnet characteristic shown in Figure 5.18, the motor permeance G_u is given by:

$$G_u = \frac{\phi_o}{AT_2} \quad (5.49)$$

And the angle α_u :

$$\alpha_u = \tan^{-1} G_u \frac{m_f}{m_\phi} \quad (5.50)$$

**FIGURE 5.20**

Magnet curves for different temperatures. (From Pawlak, A.M., *Proceedings of the 13th Annual Symposium on Incremental Motion Control Systems and Devices*, Champaign, IL, May 1984. With permission.)

where AT_2 is the magnet's value of MMF at the working point calculated from Equation 5.19, m_f is the multiplying factor for the International System of Units (SI) unit A/cm, m_ϕ is the multiplying factor for the SI unit Wb/cm, G_u is the motor permeance, α_u is a magnet load-line angle, p is the number of magnet pole pairs, D_{RO} is the rotor OD, and ϕ_o is the total flux developed by the PM without armature reaction.

5.2.4 Temperature Effect

Figure 5.20 shows BH curves for the magnet material used in our analysis of stepper motors for temperature variation from -25.0°C to $+75.0^{\circ}\text{C}$. To allow for the temperature effect properly, the magnet working point calculations should be performed using the appropriate curve. To represent this temperature effect, the following equation is used to determine $\phi_{T^{\circ}\text{C}}$:

$$\phi_{T^{\circ}\text{C}} = (1 + \beta T) \phi_{0^{\circ}\text{C}} \quad (5.51)$$

where $\phi_{T^{\circ}\text{C}}$ is the magnetic flux in air gap at temperature $T^{\circ}\text{C}$, T is temperature, and β is the temperature coefficient for magnet material. For the material used in our simulations, $\beta = -0.002$.

5.2.5 Armature Reaction Effect

In the previous sections, the ϕ_o flux value was calculated with no stator current. The effect of the armature reaction due to stator current is to reduce the air gap flux from ϕ_o to ϕ , as shown in Figure 5.21. Flux ϕ can be calculated by shifting the operating curve G_u by the MMF produced by the armature reaction F_{AR} .

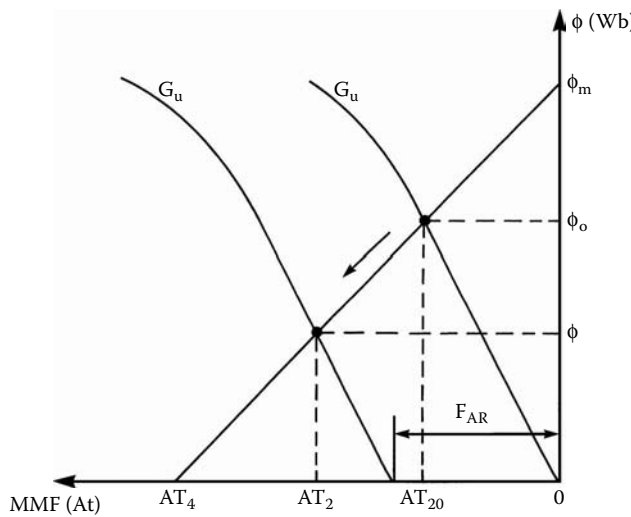


FIGURE 5.21

Determination of the magnet operating point with armature reaction. (From Pawlak, A.M., *Proceedings of the 13th Annual Symposium on Incremental Motion Control Systems and Devices*, Champaign, IL, May 1984. With permission.)

Two cases need to be considered to determine the magnet operating point with PM armature and with both stators energized. When both stators are energized, and that is normal operating mode, the armature reaction can be determined as:

$$F_{AR} = \frac{4}{\pi} NI k_{2F} \quad (5.52)$$

where NI are the coil ampere-turns, F_{AR} is the armature reaction, and k_{2F} is the ratio of the active tooth area to the magnet pole active area.

The k_{2F} is calculated as the ratio of the tooth to pole active areas for positions at the maximum value of the torque developed. When only one stator is energized, and this is an unusual mode of operation to provide half-step capability, the armature reaction can be expressed as:

$$F_{AR} = \frac{4}{\pi} NI k_{1F} \quad (5.53)$$

where k_{1F} is the ratio of the active tooth area to the magnet pole active area with only one coil energized for positions at the maximum value of the torque developed.

5.2.6 Experimental Results of Static Performance

Test results of four different stepper motors are presented and compared with analytical calculations described above. Motors were selected with a variety of sizes and significant design differences, as well as different control parameters. All motors compared vary in rated torque developed from 1.03 to 11.0 Ncm. They have different physical sizes ranging

TABLE 5.2

Claw Pole Stepper Motor Specifications

Motor	Unit	#1	#2	#3	#4
Measured torque	Ncm	11.0	7.5	1.26	1.03
DC operating voltage	V	12.0	12.0	12.0	12.0
Resistance per winding	Ω	35.0	116.0	153.0	50.0
Inductance per winding	mH	26.0	144.0	80.0	45.0
Step angle	$^\circ$	7.5	7.5	7.5	15.0
Nominal current	A	0.343	0.103	0.078	0.240
Steps per 1 revolution	#	48.0	48.0	48.0	24.0
Winding type	Type	Unipolar	Bipolar	Unipolar	Bipolar
Number of turns in a coil	#	460.0	1000.0	833.0	730.0

Source: Courtesy of Delphi Corp.

TABLE 5.3

Nominal Load Point Flux Test Results and Analytical Predictions

Motor #1			Motor #2			Motor #3			Motor #4		
Test (Mx)	Analysis (Mx)	Error (%)	Test (Mx)	Analysis (Mx)	Error (%)	Test (Mx)	Analysis (Mx)	Error (%)	Test (Mx)	Analysis (Mx)	Error (%)
291	324.3	10.4	284	315.6	10.2	81.2	89.58	9.3	112	122.1	8.1

Source: Courtesy of Delphi Corp.

from 26.25×10^{-3} m to 57.15×10^{-3} m. Two investigated motors have unipolar design with four coils and the other two have bipolar design with two coils. They have different numbers of turns and other coil parameters as well as PMs with different numbers of poles ranging from 12 to 24 (and, therefore, different numbers of steps per revolution). The different tooth shape also contributes to design variation. The summary of claw pole stepper motor specifications is provided in Table 5.2.

The magnetic-circuit cross section and tooth shapes are presented in Figure 5.22. Motor 1 and motor 3 have lap-joint stators whereas motor 2 and motor 4 have butt-joint stators. Motor 3 has a significantly different tooth shape in comparison with the other motors' tooth shapes. All sizes in Figure 5.22 are related to the largest stepper motor, and the others are presented with appropriate scale.

Table 5.3 shows some of the test results at the nominal load point together with calculated values and the percentage difference. The flux was measured by turning the motor at constant speed and measuring the induced voltage. The relationship between the flux and the voltage is developed from the flux per pair of teeth, as presented in Figure 5.12 and Equation 5.10. The peak voltage induced in the coil by turning the rotor at n_o r/min is:

$$v = N \frac{d\phi_o}{dt} = N \frac{d\phi_o}{d\theta} \frac{d\theta}{dt} \quad (5.54)$$

where from the definition:

$$\frac{d\theta}{dt} = \frac{2\pi n_o}{60} \quad (5.55)$$

Hence:

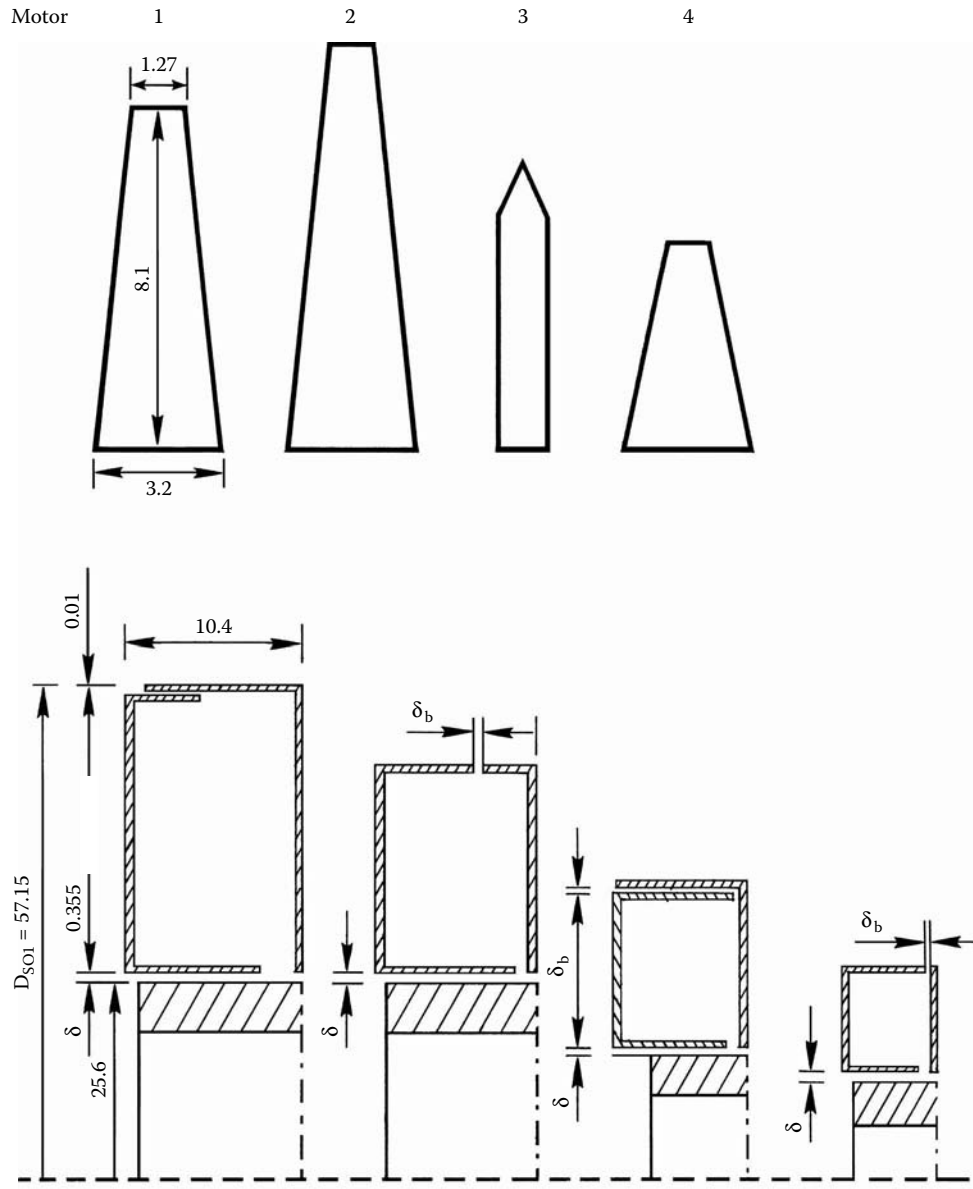


FIGURE 5.22

Tooth shape and magnetic-circuit section of tested stepper motor 1 through motor 4. (Courtesy of Delphi Corp.)

$$v = N n_o \frac{2\pi}{60} \frac{P}{2} \frac{d\phi}{d\theta} = N n_o \frac{2\pi}{60} \frac{P^2}{4} \phi_o \sin\left(\frac{P\theta}{2}\right) \quad (5.56)$$

And the root-mean-square (rms) value:

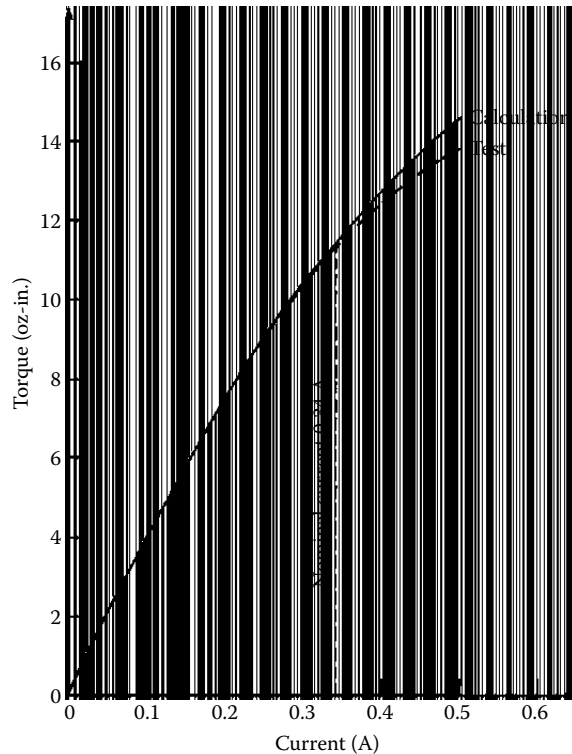
$$V = \frac{N n_o P^2}{54.019} \phi_o \quad \text{V} \quad (5.57)$$

TABLE 5.4

Static Torque Test Results

Motor #1			Motor #2			Motor #3			Motor #4		
Test (Ncm)	Analysis (Ncm)	Error (%)									
11	11.4	1.3	7.5	7.8	3.8	1.26	1.49	15.4	1.03	1.02	1
8.7	8.3	4.6	5.8	5.8	2	1.06	12.03	2.8	0.74	0.77	4.5

Source: Courtesy of Delphi Corp.

**FIGURE 5.23**

Static torque vs. current for motor 1. (Courtesy of Delphi Corp.)

where N is the number of turns of the coil, t is the time, θ is the mechanical angle position, P is the number of poles, V is the electric voltage, n_o is the velocity of the rotor in r/min, ϕ is the magnetic flux embraced by the coil, ϕ_o is the flux in the air gap with armature reaction, and v is the sensor signal.

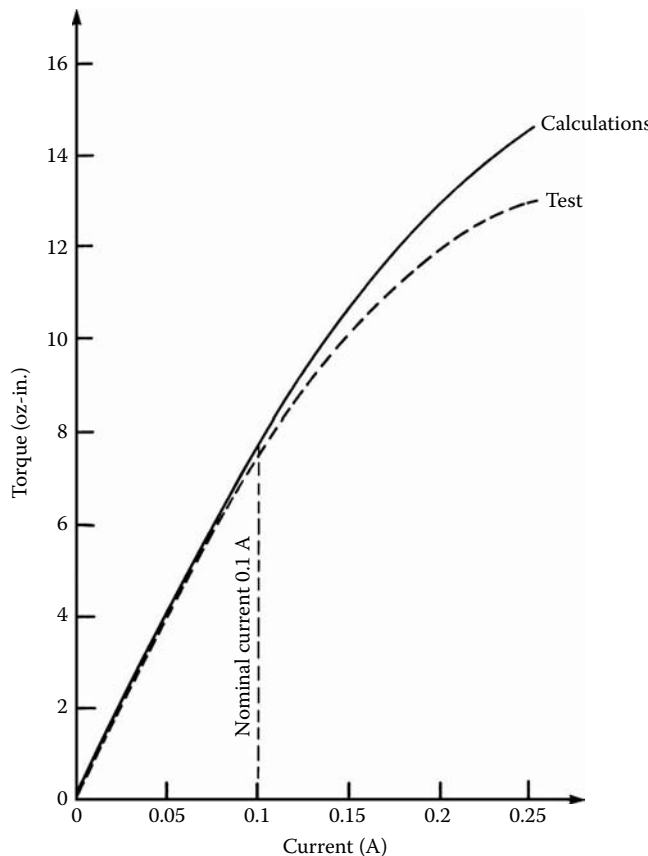


FIGURE 5.24
Static torque vs. current for motor 2. (Courtesy of Delphi Corp.)

Table 5.3 shows test results at the nominal load point together with the calculated values and the percentage difference. The flux was measured by turning a motor at a constant speed and measuring the induced voltage, as presented in Equation 5.52.

The measurement of static torque was performed by exciting the motor with a DC and then slowly turning the shaft through one complete revolution. Therefore, the torque variation is sinusoidal and the peak values were noted and the average value is used in Table 5.4. Thus, for motor 1 through motor 3, as many as 48 readings were taken and for motor 4 only 24 readings. It is necessary to take so many readings because for small motors there are variations from pole to pole not normally found in larger machines. Figure 5.23 through Figure 5.26 show the comparisons between the tested and calculated results for the static torque of each motor as a function of current. As the current is increased, the armature reaction reduces the flux and the slope of the curve is reduced. In all cases, the agreement between tests and calculations appears to be good for design purposes. To improve accuracy, the motor's physical dimensions should be measured prior to calculations to eliminate the effect of mechanical tolerances. Even small changes in critical dimensions during assembly can cause significant error.

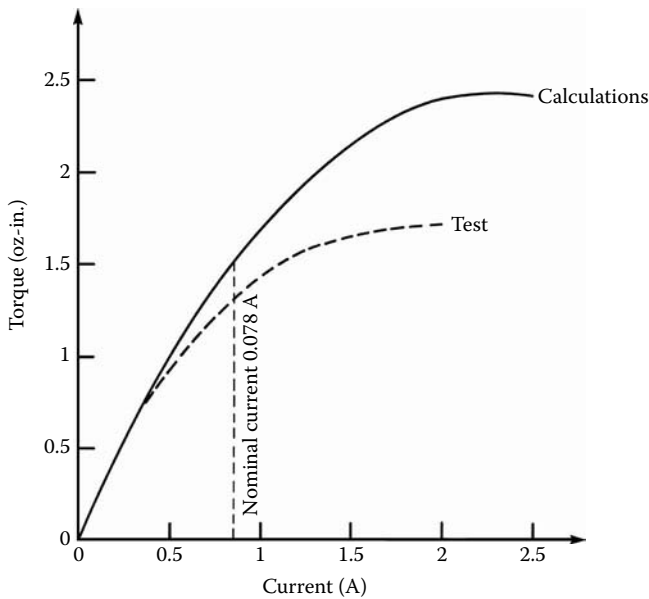


FIGURE 5.25
Static torque vs. current for motor 3. (Courtesy of Delphi Corp.)

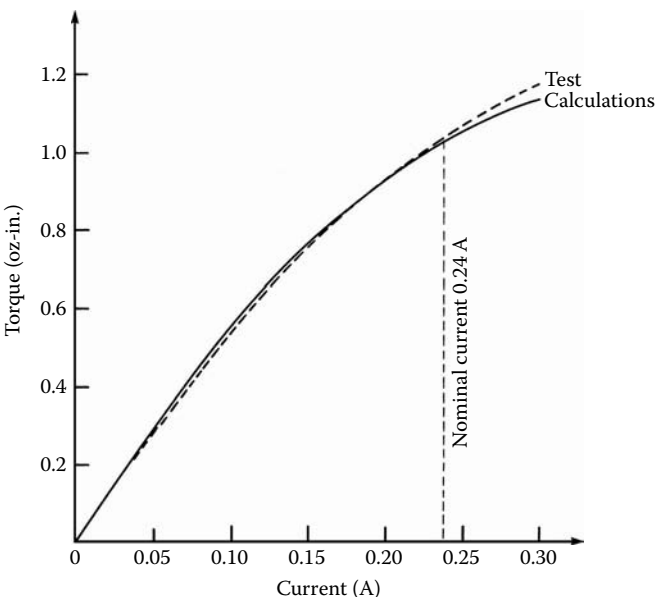


FIGURE 5.26
Static torque vs. current for motor 4. (Courtesy of Delphi Corp.)

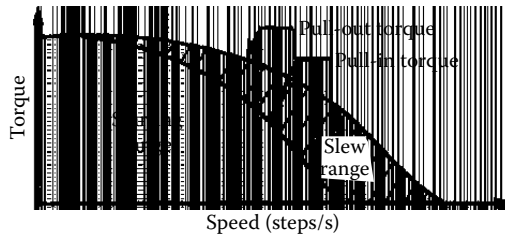


FIGURE 5.27
Stepper motor dynamic characteristics. (Courtesy of Delphi Corp.)

5.3 Dynamic Analysis of Stepper Motor

On the basis of static analysis, it is possible to derive a set of differential equations for the dynamic case. The dynamic modes use the static-displacement relationship, as well as damping torque, inertia, and other parameters. In combination with the static model, this section presents a comprehensive method for designing the claw pole stepper motor (Kuo 1982).

The two fundamental torques of a stepper motor vs. the speed characteristic in the dynamic mode of the stepper motor can generally be expressed by their pull-out torque (start-run) curves and pull-in torque (start-stop) curves (Pickup and Russell 1979, Robinson and Taft 1969, Robinson 1969, Russell and Lenhouts 1980, Russell and Pickup 1982, Singh 1974). The pull-out torque of the stepper motor indicates the maximum steady-state load torque that can be applied as the load on the stepper motor at the corresponding speeds, or stepping rates, without pulling the rotor out of synchronism with the input pulse train and stalling the motor, as presented in Figure 5.27.

The pull-out torque curves of a stepper motor do not define specific points as in the case of a DC motor. These curves simply define the region of torque-speed combinations inside which the motor will operate satisfactorily. The pull-in torque of a stepper motor is the load torque that the motor will be able to start and drive without missing steps at the indicated pulse rate (frequency). In practice, the frequency of pulses is varied to determine the maximum frequency at which the motor can both start and stop at a given frequency without error (missing two or more steps).

It should be pointed out that a stepper motor with a position sensor and closed-loop frequency control generally produces the pull-out torque vs. speed characteristic regardless of the level of stepping rate. In open-loop operations, the pull-out torque can be obtained only if the applying stepping rate command is very low. As the commanded stepping rate is increased, the torque that the motor can develop at a given speed is reduced. In the limit with a high rate of stepping command, the motor will produce the pull-in torque. The range of speed that lies between the pull-in and pull-out curves is called the slew range. Above the pull-out torque curve, the stepper motor never follows the command and never starts. Below the pull-in torque curve, the stepper motor always follows the command without stopping or missing steps, with some exceptions (Pollack 1980). Figure 5.27 shows a typical relation between the pull-in torque and pull-out torque of the stepper motor.

5.3.1 Math Model of the Dynamic Operation

On the basis of the theory presented for static analysis, it is possible to derive a set of equations for the dynamic case, as discussed below. The electromagnetic torque developed in the two coil claw pole stepper motor with a PM as described in Section 5.2 is in the form:

$$T_D(\theta) = I_{S1}N_1p^2\phi_1 \sin p\theta + I_{S2}N_2p^2\phi_2 \sin p(\theta + \alpha) \quad (5.58)$$

or

$$T_D(\theta) = I_{S1}K_{1T} \sin p\theta + I_{S2}K_{2T} \sin p(\theta + \alpha) \quad (5.59)$$

if

$$K_{1T} = N_1p^2\phi_1 \quad \text{and} \quad K_{2T} = N_2p^2\phi_2 \quad (5.60)$$

where I_{S1}, I_{S2} are the currents in the stator 1 and stator 2, respectively; N_1, N_2 are the number of the stator coils, coil 1 and coil 2, respectively; p is the number of pair of poles; ϕ_1, ϕ_2 are maximum values of magnetic flux in air gap 1 and air gap 2, respectively; θ is the mechanical angle of rotor position; T_D is the torque developed by the stepper motors; K_{1T} is the static torque coefficient that is a function of flux ϕ_1 ; K_{2T} is the static torque coefficient that is a function of flux ϕ_2 ; and α is the mechanical angle between two stators, in our case, $\pi/2$.

The electrical circuit equations for the two coils are:

$$U_1 = R_1I_1(t) + L_1 \frac{dI_1(t)}{dt} + E_{V1}(t) \quad (5.61)$$

$$U_2 = R_2I_2(t) + L_2 \frac{dI_2(t)}{dt} + E_{V2}(t) \quad (5.62)$$

Because the flux distribution in the air gap for the one stator is:

$$\phi(\theta) = p\phi_m \sin(p\theta) \quad (5.63)$$

then:

$$E_V = N \frac{d\phi(\theta)}{dt} = N \frac{d\phi(\theta)}{d\theta} \frac{d\theta}{dt} \quad (5.64)$$

From Equation 5.63 and Equation 5.64, we have:

$$E_{V1} = N_1 \frac{d\theta}{dt} \frac{d(p\phi_m \cos p\theta)}{d\theta} = -N_1p^2 \frac{d\theta}{dt} \phi_{m1} \sin p\theta \quad (5.65)$$

and

$$E_{V2} = N_2 \frac{d\theta}{dt} \frac{d(p\phi_m \cos p(\theta + \alpha))}{d\theta} = -N_2p^2 \frac{d\theta}{dt} \phi_{m2} \cos p\theta \quad (5.66)$$

because:

$$\frac{d\theta}{dt} = \omega_{mech} \quad \text{and} \quad \alpha = \frac{\pi}{2} \quad (5.67)$$

and

$$K_{V1} = N_1 p^2 \phi_{m1} \quad \text{and} \quad K_{V2} = N_2 p^2 \phi_{m2} \quad (5.68)$$

Substituting, we have the set of equations:

$$U_1 = R_1 I_1(t) + L_1 \frac{dI_1(t)}{dt} - K_{V1} \omega_{mech} \sin p\theta \quad (5.69)$$

$$U_2 = R_2 I_2(t) + L_2 \frac{dI_2(t)}{dt} + K_{V2} \omega_{mech} \cos p\theta \quad (5.70)$$

where U_1, U_2 are voltages applied to coil 1 and coil 2, respectively; R_1, R_2 are the resistances of coil 1 and coil 2, respectively; L_1, L_2 are the self-inductances of coil 1 and coil 2, respectively; E_{V1}, E_{V2} are back EMFs of coil 1 and coil 2, respectively; ϕ_{m1} is a magnetic flux embraced by coil 1 for a single pole-pair section; ϕ_{m2} is a magnetic flux embraced by coil 2 for a single pole-pair section; I_1 is the supplied current in coil 1; I_2 is the supplied current in coil 2; K_{V1} is the static torque coefficient that is a function of flux ϕ_1 ; K_{V2} is the static torque coefficient that is a function of flux ϕ_2 ; p is the number of magnet pole pairs or a sensor section; and ω_{mech} is the mechanical angle speed of the motor (rotor).

From Equation 5.60 and Equation 5.68, we have:

$$K_{1T} = K_{V1} = N_1 p^2 \phi_1 \quad \text{and} \quad K_{2T} = K_{V2} = N_2 p^2 \phi_2 \quad (5.71)$$

As discussed in the stepper motor construction section, the relation between electrical and mechanical angles is:

$$\psi = p\theta \quad \text{and} \quad \omega_{el} = p\omega_{mech} \quad (5.72)$$

where ψ is the electrical angle of motor (rotor) position, θ is the mechanical angle of motor (rotor) position, ω_{el} is the electrical angle speed of motor (rotor), and ω_{mech} is the mechanical angle speed of motor (rotor).

From Equations 5.69, 5.70, and 5.72, we have:

$$U_1 = R_1 I_1(t) + L_1 \frac{dI_1(t)}{dt} - \frac{K_1 \omega_{el}}{p} \sin \psi \quad (5.73)$$

$$U_2 = R_2 I_2(t) + L_2 \frac{dI_2(t)}{dt} + \frac{K_2 \omega_{el}}{p} \cos \psi \quad (5.74)$$

The basic mechanical equation is:

$$J \frac{d^2\theta(t)}{dt^2} + \frac{d\theta(t)}{dt} + T_F + T_L(t) = T_D(t) \quad (5.75)$$

where J is the rotor inertia, D is the viscous damping coefficient, T_F is torque due to friction, T_L is load torque, and T_D is torque developed by the stepper motor.

From Equation 5.72 and Equation 5.75, we have:

$$\frac{J}{p} \frac{d^2\psi(t)}{dt^2} + \frac{D}{p} \frac{d\psi(t)}{dt} + T_F + T_L(t) = T_D(t) \quad (5.76)$$

Equation 5.68 and Equation 5.72 through Equation 5.76 are rearranged into a set of first-order differential equations, as shown in Equation 5.77, that can be solved numerically. With an initial value of the angle $\psi = 0$ and (time = 0), we have:

$$\frac{dI_1}{dt} = \frac{1}{L_1} \left(U_1 - R_1 I_1 + \frac{K_1 \omega_{el}}{p} \sin \psi \right)$$

$$\frac{dI_2}{dt} = \frac{1}{L_2} \left(U_2 - R_2 I_2 - \frac{K_2 \omega_{el}}{p} \cos \psi \right)$$

$$T_D = -I_1 K_1 \sin \psi + I_2 K_2 \cos \psi \quad (5.77)$$

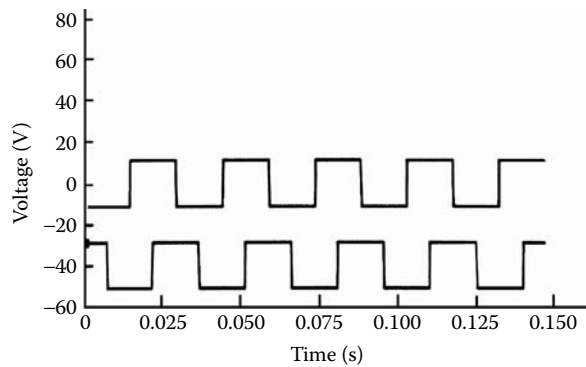
$$T = T_D - T_L$$

$$\frac{d\omega_{el}}{dt} = \frac{J}{p} \left(T_D + \frac{D}{p} \omega_{el} - T_F \right)$$

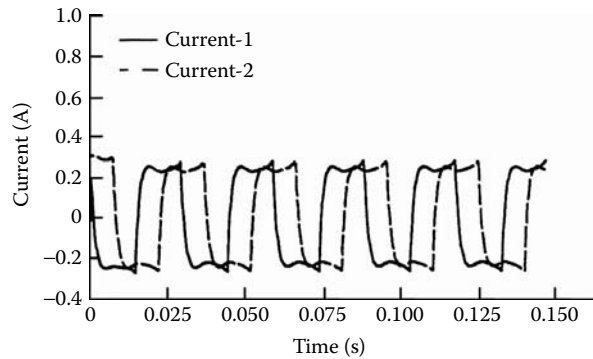
$$\frac{d\psi}{dt} = \omega_{el}$$

This set of differential equations is nonlinear because of the transcendental functions $\sin \psi$ and $\cos \psi$ as well as the presence of the product of the state variables $\omega_{el} \sin \psi$, $\omega_{el} \cos \psi$, $I \sin \psi$, and $I \cos \psi$. Moreover, the coefficients K_1 and K_2 are functions of fluxes ϕ_1 and ϕ_2 , which are nonlinear functions of currents I_1 and I_2 . Because of these nonlinearities, analytical solutions are impossible to obtain and numerical methods need to be used, such as Runge-Kutta integration (McRuer 1974).

This set of equations contains a number of the following motor parameters that can be obtained directly from the design and calculations of static analysis: number of pole pairs p , number of turns N , fluxes in the air gap ϕ_1 and ϕ_2 , inertia of rotor J , resistance and self-inductance of coils R and L , and voltage V . The magnetic fluxes in the air gap ϕ_1 and ϕ_2 , as well as self-inductances L_1 and L_2 , were described and calculated in Section 5.2. The viscous damping D and friction torque T_F can be obtained from the measurements because the methods of calculating these coefficients are not available in the literature and will be developed in the future.

**FIGURE 5.28**

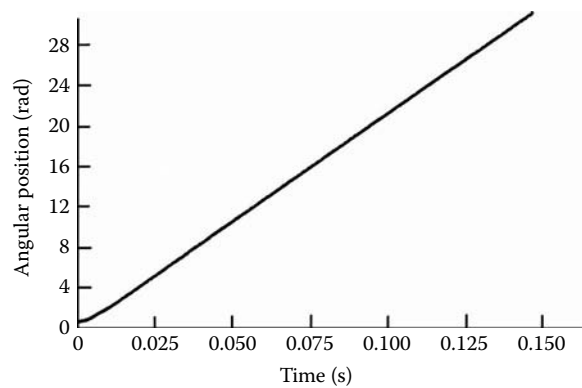
The applied voltage vs. time in two coils. (From Pawlak, A.M., *Proceedings of the 13th Annual Symposium on Incremental Motion Control Systems and Devices*, Champaign, IL, May 1984. With permission.)

**FIGURE 5.29**

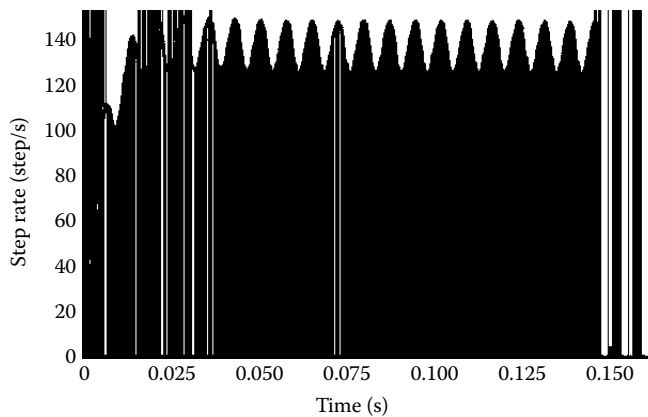
The current vs. time in two coils. (From Pawlak, A.M., *Proceedings of the 13th Annual Symposium on Incremental Motion Control Systems and Devices*, Champaign, IL, May 1984. With permission.)

5.3.2 Stepper Motor Dynamic Simulation

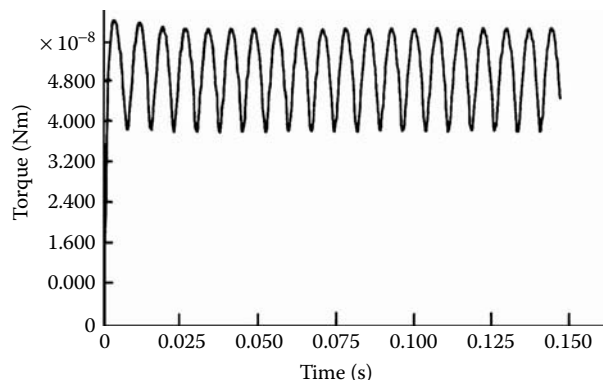
Because the dynamic torque of the stepper motor is sensitive to the $D\dot{\omega} + T_F$, it was necessary to evaluate it by measurements, as presented in Section 5.3.7. In the computer simulations, a fixed number of pulses N_o was applied to the motor at a given stepping rate S and the obtained solutions are presented in Figure 5.28 through Figure 5.32. The objective of our computations is to find the maximum stepping rate at which the motor misses not more than two of the N_o steps based on Robinson's phase-plane theory (Robinson and Taft 1969, Robinson 1969). The computer uses a special search routine called binary search to determine the maximum stepping rate at which the initial value of stepping rate commands is established. If the stepper motor follows the command, then the stepping rate is increased by an arbitrary amount ΔS . If the motor follows the higher stepping rate, then the stepping rate is increased by an amount of ΔS , and so on, until the stepper motor starts to lose steps or stops. Then the search routine subtracts half of this step command $\Delta S/2$ and so on, until the maximum stepping rate is found for a given

**FIGURE 5.30**

The position of rotor vs. time. (From Pawlak, A.M., *Proceedings of the 13th Annual Symposium on Incremental Motion Control Systems and Devices*, Champaign, IL, May 1984. With permission.)

**FIGURE 5.31**

The rotational speed of the motor vs. time. (From Pawlak, A.M., *Proceedings of the 13th Annual Symposium on Incremental Motion Control Systems and Devices*, Champaign, IL, May 1984. With permission.)

**FIGURE 5.32**

The dynamic torque of the stepper motor vs. time. (From Pawlak, A.M., *Proceedings of the 13th Annual Symposium on Incremental Motion Control Systems and Devices*, Champaign, IL, May 1984. With permission.)

TABLE 5.5
Stepper Motor Parameters

Motor	Voltage (V)	Resistance (Ω)	Inductance ($H \times 10^{-3}$)	Inertia ($kgm^2 \times 10^{-7}$)	Poles (P)	Type	Used as
#1	12.0	51.0	43.8	31.0	12	Bipolar	Bipolar
		52.5	49.3				
#3	12.0	36.2	48.5	0.6	24	Unipolar	Bipolar
		36.5	49.5				
#4	12.0	158.6	104.0	2.0	24	Bipolar	Bipolar
		162.0	117.0				

Source: Courtesy of Delphi Corp.

load torque. In our computations using Robinson's analysis, we have fixed the number of pulses N_o to be 20. The simulation stops the integration whenever the motor is losing steps or the accuracy flag is raised. Under these circumstances, a new stepping rate is commanded and a binary search is resumed until a specified accuracy is achieved. Computations include initialization of dynamic equations described by Equation 5.77, interpolation of viscous damping coefficient curve, eddy current coefficient curve, pulse function generator for the first coil (phase) and for the second coil (phase), as well as insertion of adequate friction to the calculations.

5.3.3 Validation of the Dynamic Model

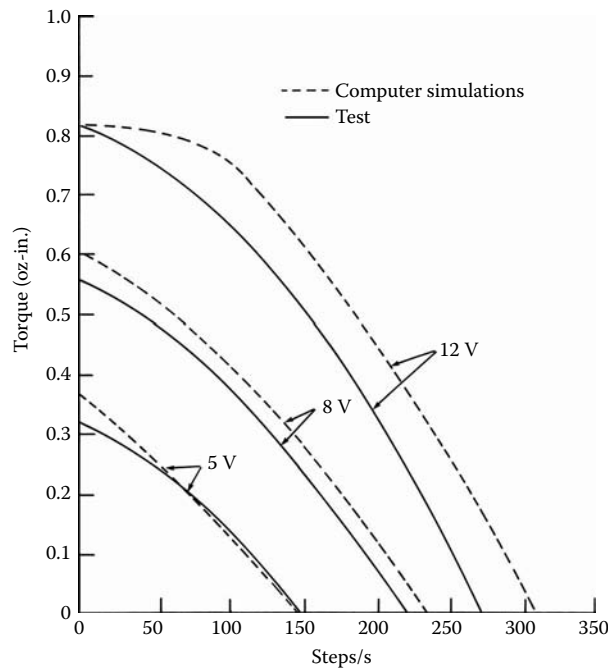
The mathematical model used in the computation of the stepper motor dynamics can be verified by comparing pull-in torque curves from the test results previously used in static analysis, as presented in Section 5.2.1. The torque parameters of these motors are presented in Table 5.5. These parameters were used for the computations, and the results are presented in Figure 5.33 through Figure 5.35.

The motors were tested using the pull-in torque measurement method described in Section 5.3.7. The computations as well as the test data are shown for three different applied voltages. For the nominal parameters, the computer program predicts test results within several percent for a wide range of stepper motor sizes. The accuracy obtained is satisfactory for such small motors and confirms that the presented dynamic analysis is useful for the stepper motor design.

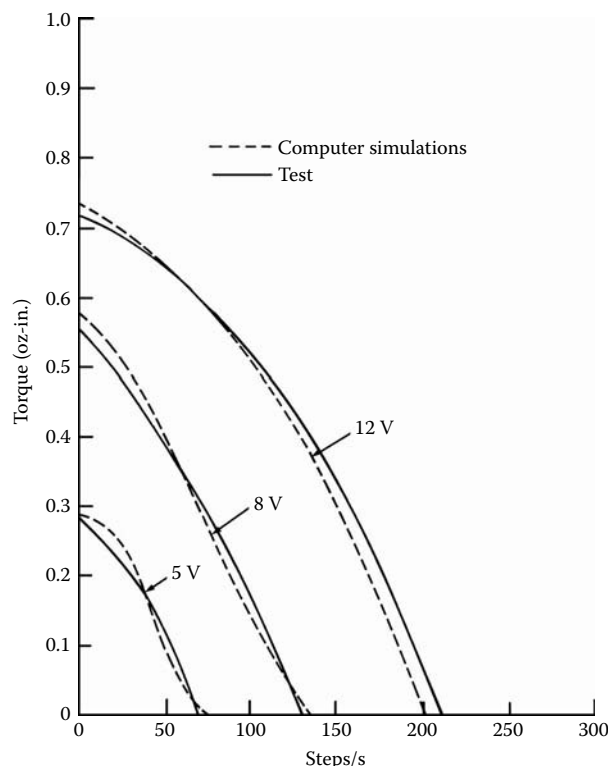
The largest difference between measured and simulated values, about 15%, occurred with the stepper motor 3, which has the biggest difference between parameters of coils, as presented in Table 5.5. Other results are within 5% and the accuracy obtained is satisfactory for such small motors.

Let us take a closer look at two characteristic pull-in torque curve points: the stall torque T_d at zero speed and no-load speed. The stall torque T_d is determined by the static torque as determined in the static torque analysis section. In an ideal case, the stall torque is equal to $1/\sqrt{2}$ of the static torque, as presented in Section 5.3.7. In practice, this value is less, as shown in Table 5.6.

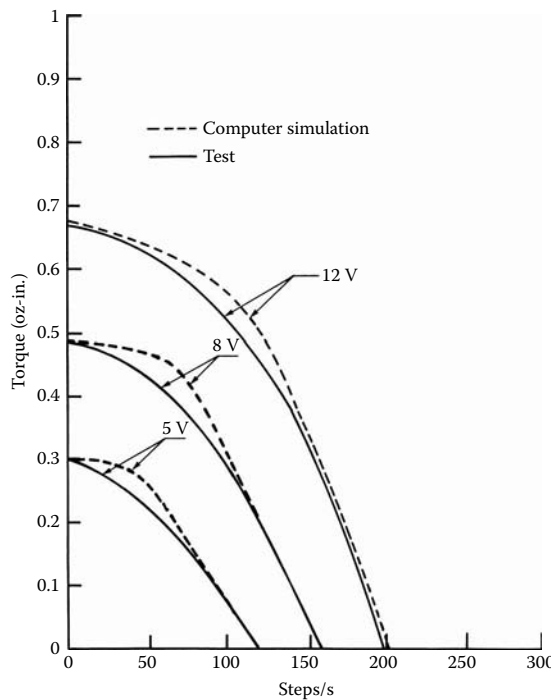
The no-load speed point of the pull-in torque depends on all parameters described in Equation 5.36. No-load characteristics are also presented for the three different sizes of stepper motors with different voltage applied in the range 0–12.0 V: one with free shaft and the other coupled to a torquemeter, as presented in Section 5.3.4. The appropriate conditions (different inertia and friction) were used to get identical conditions as in the analysis. The pull-in curves, one provided by analysis and the other from the test, are presented in Figure 5.36 through Figure 5.38.

**FIGURE 5.33**

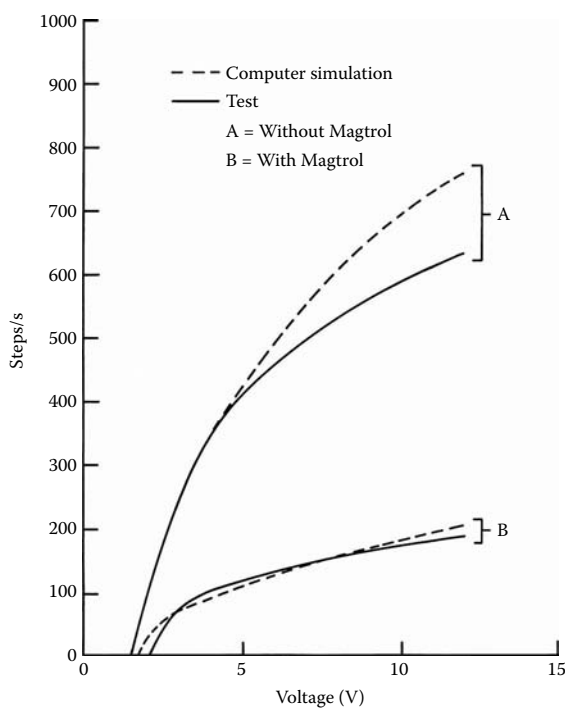
The pull-in torque for different applied voltage, motor 1. (Courtesy of Delphi Corp.)

**FIGURE 5.34**

The pull-in torque for different applied voltage, motor 3. (Courtesy of Delphi Corp.)

**FIGURE 5.35**

The pull-in torque for different applied voltage, motor 4. (Courtesy of Delphi Corp.)

**FIGURE 5.36**

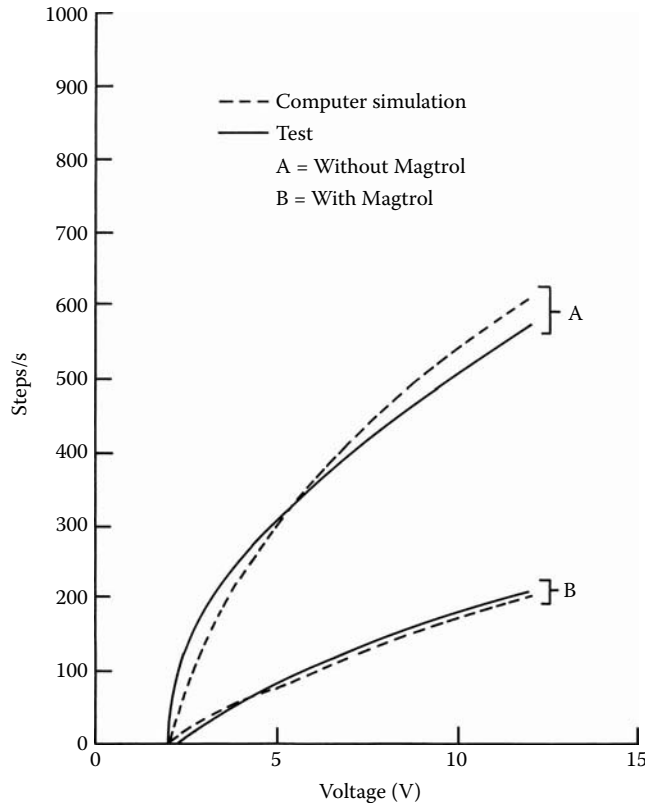
No-load speed vs. voltage characteristics, motor 1. (Courtesy of Delphi Corp.)

TABLE 5.6

The Stall Torque Comparison for Nominal Torque

Type #	T_m (Ncm)	$T_i = T_m/2^{-1/2}$ (Ncm)	T_d (Ncm)	$(Ti - Td)100\% / Ti\%$
1	7.88	5.58	5.61	0.6
3	0.859	0.608	0.508	14.7
4	0.717	0.504	0.479	5.5

Source: Courtesy of Delphi Corp.

**FIGURE 5.37**

No-load speed vs. voltage characteristics, motor 3. (Courtesy of Delphi Corp.)

For the nominal voltage of 12.0 V, the computer simulations predict no-load speeds with accuracy in the range 0–15% as compared with the test results with the free shaft and having accuracy in the range 0–12% for the stepper motor shaft coupled with a torque-meter. This is another confirmation that the math model introduced can be used for engineering design purposes.

5.3.4 Effects of Various Parameters on Stepper Motor Performance

Based on the dynamic math model presented, it is possible to test the effect of the three main parameters on the dynamic performance of the stepper motor: viscous damping D , inertia J , and the static torque coefficient K at constant nominal voltage. If these parameters are varied in the range of $\pm 40\%$, as presented in Table 5.7, we can obtain the family of pull-in torque curves, as shown in Figure 5.39 through Figure 5.41. From the curve

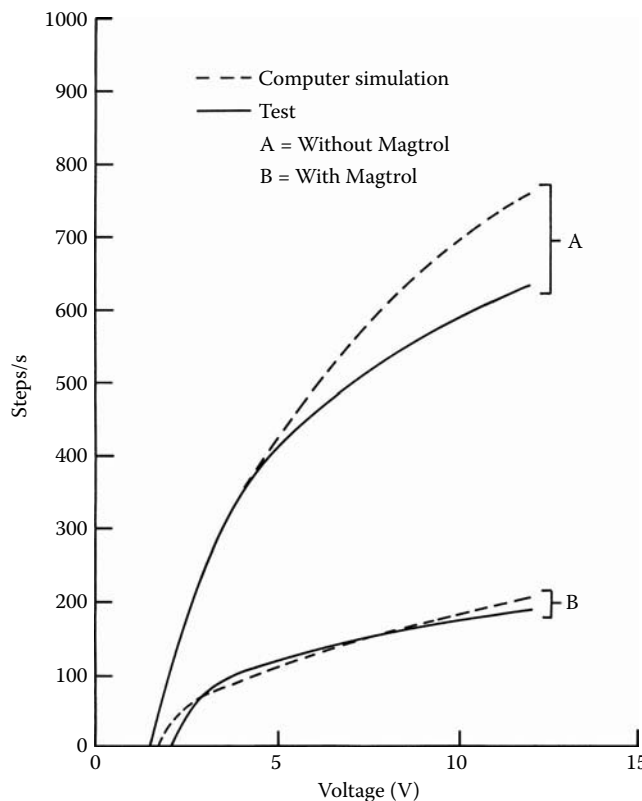


FIGURE 5.38
No-load speed vs. voltage characteristics, motor 4. (Courtesy of Delphi Corp.)

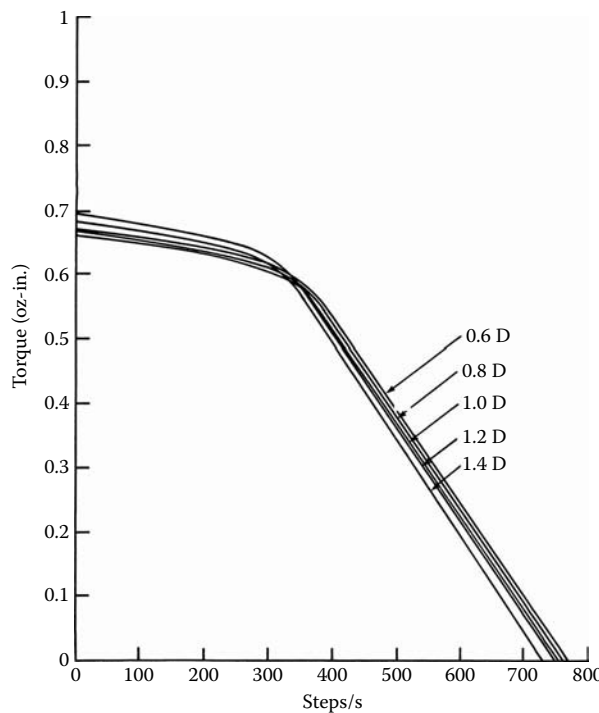
TABLE 5.7
Stepper Motor Parameter Variation for Pull in Torque

Parameter	Change in Range (from nominal)	Load Torque (Ncm)	Nominal Max Stepping Rate (steps/s)	Max Stepping Rate Change in Range (from nominal)
Inertia	$(0.6-1.4)J$	0.213	550	0.89-1.15
Damping	$(0.6-1.4)D$	0.213	550	0.89-1.15
Static torque coefficient	$(0.6-1.4)K$	0.213	550	0.89-1.15

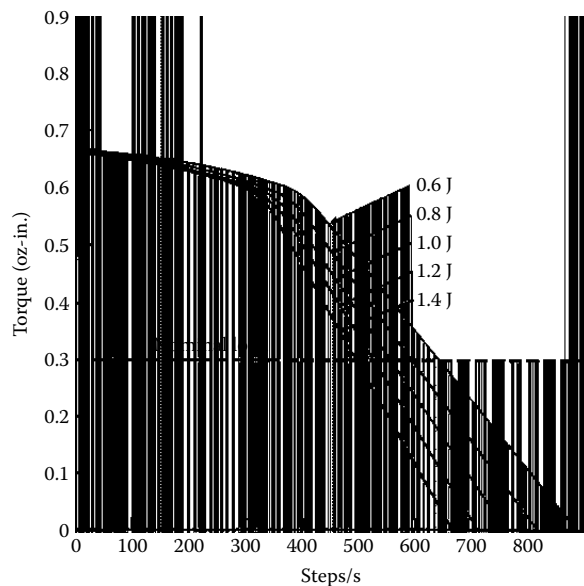
Source: Courtesy of Delphi Corp.

characteristics and from Table 5.7 we can conclude that, of the three most important stepper motor parameters, the static torque coefficient has the greatest influence on the pull-in characteristic, followed by inertia and the viscous damping coefficient.

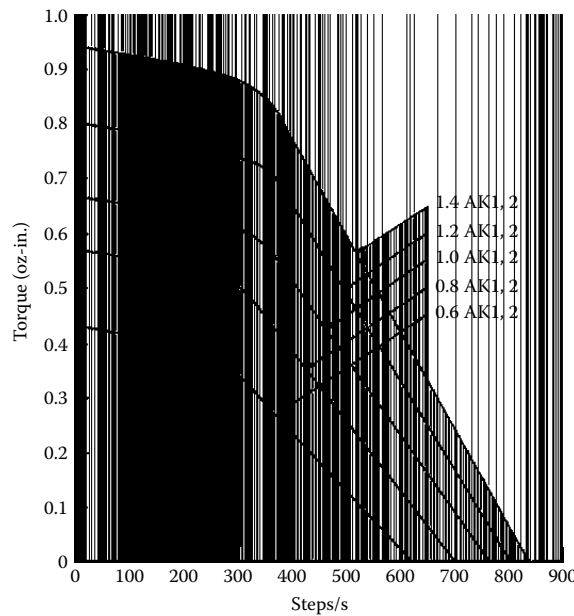
The no-load speed characteristics were simulated for the stepper motor for different applied voltages in the range 0–12.0 V. Changing viscous damping D , inertia J , and the static torque coefficient K by $\pm 40\%$, as presented in Table 5.8, at nominal step rate S , the family of no-load speed curves can be obtained, as shown in Figure 5.42 through Figure 5.44. From these characteristics showing the families of curves and from Table 5.8, we can conclude that the biggest effect on maximum stepping rate for a given nominal voltage was inertia, followed by the static torque constant and the viscous damping coefficient.

**FIGURE 5.39**

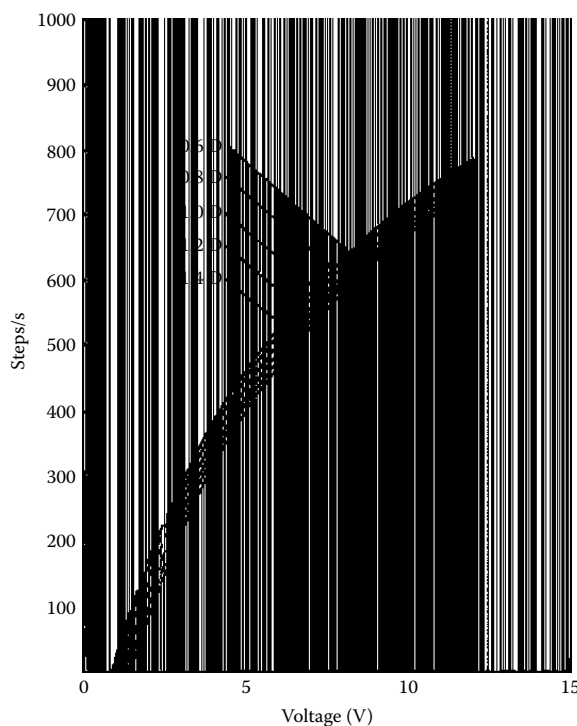
The pull-in torque for different viscous damping coefficient at nominal voltage, motor 1. (Courtesy of Delphi Corp.)

**FIGURE 5.40**

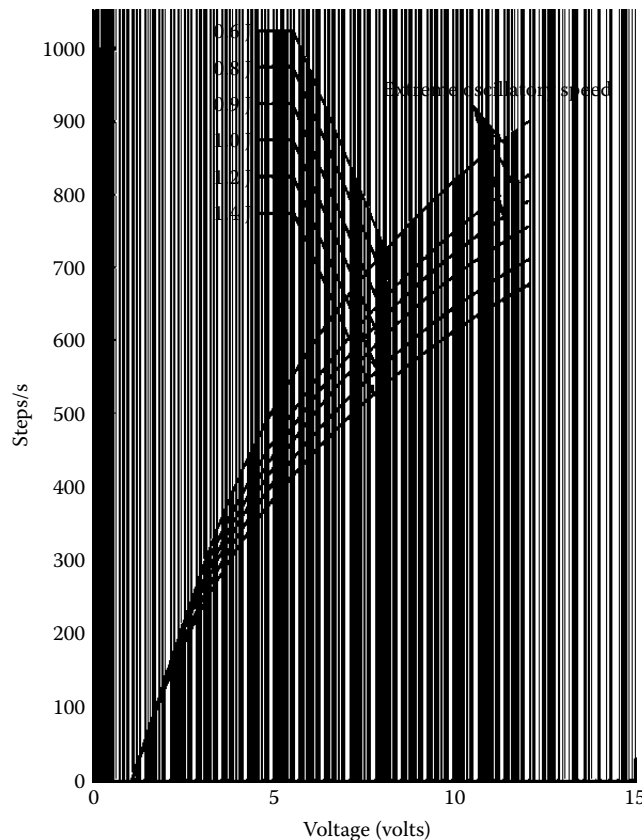
The pull-in torque for different inertia, at nominal voltage, motor 1. (Courtesy of Delphi Corp.)

**FIGURE 5.41**

The pull-in torque for different torque constant, at nominal voltage, motor 1. (Courtesy of Delphi Corp.)

**FIGURE 5.42**

Load speed vs. voltage for different viscous damping coefficient, motor 1. (Courtesy of Delphi Corp.)

**FIGURE 5.43**

Load speed vs. voltage for different inertia, motor 1. (Courtesy of Delphi Corp.)

TABLE 5.8

Stepper Motor Parameter Variation for No Load Conditions

Parameter	Change in Range (from nominal)	Voltage (V)	Nominal Max Stepping Rate (steps/s)	Max Stepping Rate Change in Range (from nominal)
Inertia	(0.6–1.4) J	10.0	695	0.89–1.19
Damping	(0.6–1.4) D	10.0	695	0.89–1.19
Static torque coefficient	(0.6–1.4) K	10.0	695	0.89–1.19

Source: Courtesy of Delphi Corp.

From the computer simulation shown in Table 5.8, as well as from the test results, it is possible to estimate the effect of these three parameters on stepper motor performance. Inertia and the static torque coefficient have the greatest effects. The viscous damping has a rather small effect. These simulations show the trend that can be useful for new design purposes. The effect of load torque upon dynamic behavior of the stepper motor is described in Section 5.3.5.

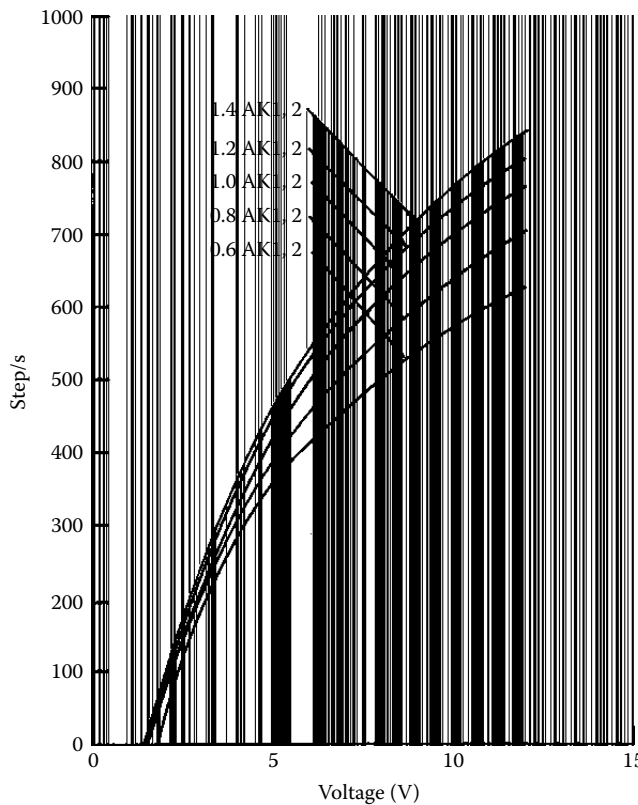


FIGURE 5.44
Load speed vs. voltage for different torque constant, motor 1. (Courtesy of Delphi Corp.)

5.3.5 Experimental Results of Dynamic Performance

Several different motors were tested and the results were compared with calculations using the theory described in Section 3.5.1. The discrepancy in the range 3–15% between the test results and computer simulations indicates satisfactory agreement and confirms that the mathematical model presented is proper. In order to obtain the pull-in characteristics (torque vs. maximum stepping rate), a generator and a bipolar driver unit need to be used to run the stepper motor and a torquemeter (such as Magtrol) to measure speed and torque. Several different torquemeters are described in the literature. Because of the difference in the viscous damping coefficient and inertia of the torquemeters, measurements for the same stepper motor give different results. For the same computer simulations, the dynamometer inertia and the amount of viscous damping must be known. One can use a different size of torquemeter. For comparison purposes, this section reviews two different sizes of torquemeter. Table 5.9 provides motor and dynamometer inertias.

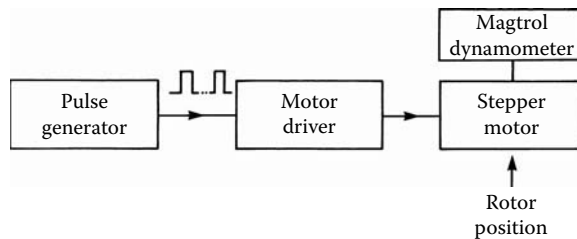
Stepper motor control can generally be classified as open-loop or closed-loop control. For the purpose of this section, open-loop control will be investigated where the phase switchings are controlled by a pulse generator that sends a sequence of pulses to the motor drive circuit. For each pulse the motor receives from pulse generator, the stepper motor makes one step. For the pulse train with uniformly spaced pulses, the repetition of pulses determines the speed of rotation of the motor. Figure 5.45 shows the block diagram with the basic elements of the open-loop stepper motor control system.

TABLE 5.9

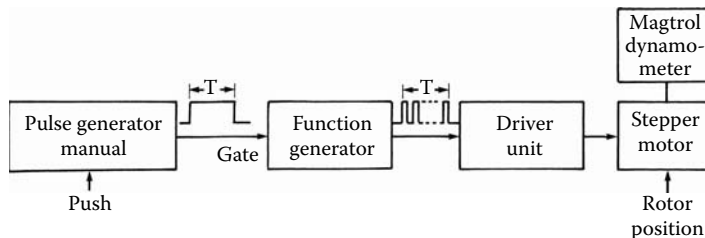
Motor and Dynamometer Inertia

Motor No.	Motor Inertia (kgm ²)	Torquemeter Rating (Ncm)	Torquemeter Inertia (kgm ²)
#1	32.0×10^{-7}	7.815	41.9×10^{-7}
#3	2.11×10^{-7}	1.777	9.51×10^{-7}
#4	0.59×10^{-7}	1.777	9.51×10^{-7}

Source: Courtesy of Delphi Corp.

**FIGURE 5.45**

An open-loop stepper motor control system. (Courtesy of Delphi Corp.)

**FIGURE 5.46**

Block schematic for pull-in torque measurement of the stepper motor open-loop stepper motor control system. (Courtesy of Delphi Corp.)

By observing the position of the marked rotor, one can readily determine if the rotor follows the command and turns through one complete revolution. Figure 5.46 shows the circuit that can be used to apply a fixed number of pulses to the driver unit from a pulse generator, causing one full revolution of the rotor.

The signal from the pulse generator is transferred to the function generator, which generates in the time T a certain number of pulses to the driver unit. Because of the construction of the used stepper motor, it was always adjusted for a 48 pulse train that gives one revolution (for motor design with $p = 12$) and 24 pulses, which gives one revolution (for motor design with $p = 6$). With any given load, by changing the time period T and keeping the same number of pulses for one revolution, one can find the minimum time period T (maximum stepping rate), where the motor is still under control (did not lose any steps). Using this process, all pull-in characteristics can be obtained.

5.3.6 Evaluation of Viscous Damping Coefficient

The method of measuring the viscous damping coefficient is based on Equation 5.76. If the motor is running at a certain speed and is suddenly disconnected from the supply, then Equation 5.76 becomes:

$$J \frac{d^2\theta(t)}{dt^2} + D \frac{d\theta(t)}{dt} + T_F = 0 \quad (5.78)$$

Separating the damping and friction components, we have:

$$D + \frac{T_F}{\frac{d\theta}{dt}} = -J \frac{\frac{d^2\theta}{dt^2}}{\frac{d\theta}{dt}} \quad (5.79)$$

A new function F is defined as:

$$F = D + \frac{T_F}{\frac{d\theta}{dt}} \quad (5.80)$$

so that:

$$F = -J \frac{\frac{d^2\theta}{dt^2}}{\frac{d\theta}{dt}} = -J \frac{\dot{\omega}_{mech}}{\omega_{mech}} \quad (5.81)$$

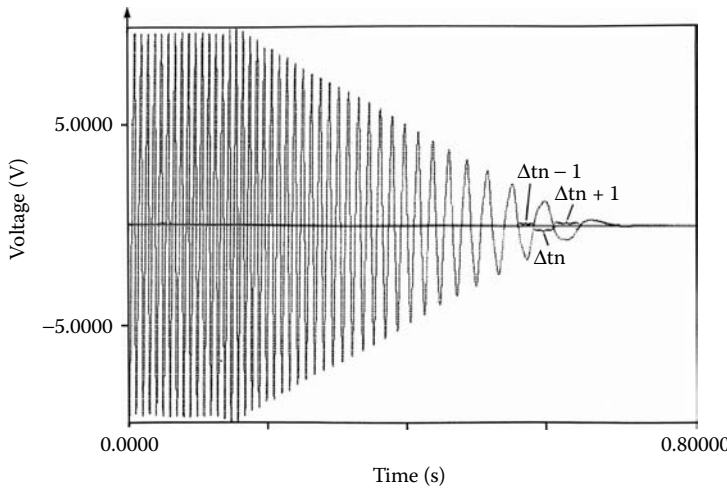
where J is the rotor inertia, T_F is the torque due to friction, D is the viscous damping coefficient, θ is the mechanical angle position, t is time, ω_{mech} is the mechanical angular speed of the motor (rotor), $\dot{\omega}_{mech}$ is the mechanical angular acceleration of the motor (rotor), and F is a new function, as defined in Equation 5.80.

Thus F can be determined by measuring the deceleration and speed of the motor as it slows down. It is apparent that if T_F is negligible:

$$F = D \quad (5.82)$$

and, hence, in the literature F is sometimes called (erroneously) the viscous damping coefficient. The voltage induced in the stator coil of the stepper motor is an accurate measure of speed. Using a processing digital oscilloscope, the induced voltage vs. speed can be very precisely recorded, as shown in Figure 5.47.

In the stepper motors that we considered the motor inertia is very small and after disconnecting the rotor stops very fast, so it was necessary to increase the inertia. This allowed us to increase the time between disconnecting from the supply and the moment the rotor comes to a stop, improving measurement accuracy. The additional inertia was 10 times bigger than the rotor inertia. Thus, the inertia in Equation 5.78 is the sum of the motor, coupling, and additional inertias:

**FIGURE 5.47**

Voltage induced in open coil of the stepper motor vs. time. (Courtesy of Delphi Corp.)

$$J = J_M + J_C + J_{add} \quad (5.83)$$

From Figure 5.47, it is easy to obtain the zero crossing time Δt_n , which indicates the change $\Delta\alpha$ in the rotor position (equal angle between two poles). Thus, for any time, it is possible to obtain the mechanical angular speed:

$$\omega_{mech} = \frac{\Delta\alpha}{\Delta t_n} \quad (5.84)$$

where $\Delta\alpha$ is the change in the rotor position, J_c is coupling inertia, J_{add} is additional inertia, J_M is motor (rotor) inertia, and Δt_n is the zero crossing time interval. Using the digital scope, it is easy to obtain very precisely the time of zero crossing, and using Equation 5.84, it is possible to obtain speed vs. time characteristics, as presented in Figure 5.48.

The next step is to use a polynomial curve fitting computer program to fit the curve to an n -order polynomial:

$$y = a_0 + a_1x + a_2x^2 + a_3x^3 + \dots + a_nx^n \cong \omega_{mech} = f(t) \quad (5.85)$$

The slope of the speed against time curve can be obtained by differentiation:

$$\frac{dy}{dx} = a_1 + 2a_2x + 3a_3x^2 + \dots + na_nx^{n-1} \cong \dot{\omega}_{mech} = f(t) \quad (5.86)$$

where a_0, a_1, a_2, a_3, a_n are polynomial components, ω_{mech} is the mechanical angular speed of the motor (rotor), and $\dot{\omega}_{mech}$ is the mechanical angular acceleration of the motor (rotor).

Using this method, which is shown in Figure 5.48, the speed vs. time characteristic is obtained and from Figure 5.47 and Figure 5.48, the function can be calculated, as shown in Figure 5.49, which can be directly used in Equation 5.81 to obtain function F . Then using Equation 5.79, the viscous damping coefficient D is obtained for three investigated motors,

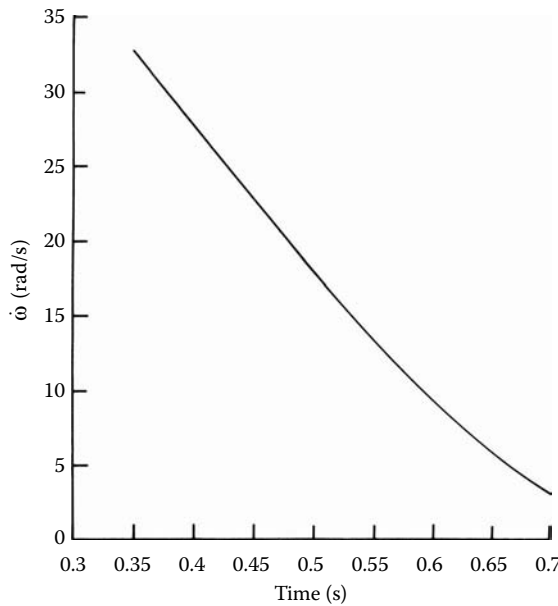


FIGURE 5.48
Speed vs. time characteristic. (Courtesy of Delphi Corp.)

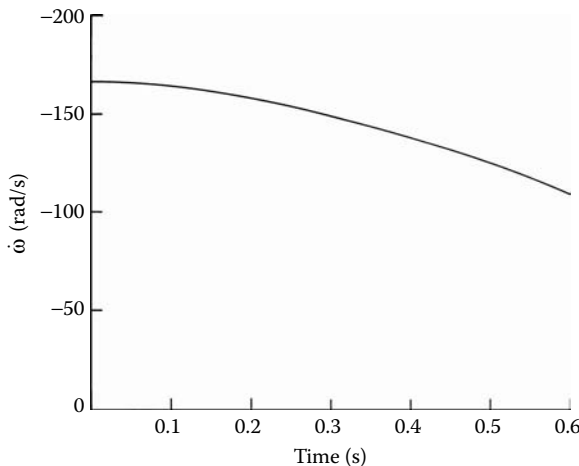


FIGURE 5.49
Deceleration vs. time characteristic. (Courtesy of Delphi Corp.)

as shown in Figure 5.50 through Figure 5.53, for given coulomb frictions, which are very small for these motors.

When the additional inertia is provided by a dynamometer, a much bigger value of damping coefficient was obtained, as shown in Figure 5.52 and Figure 5.53. This is because of the additional dynamometer damping. In the computer simulation for three investigated stepper motors, a different damping curve is given from measurements. It is very inconvenient to use the viscous damping coefficient given from measurements. To determine this curve for design data, especially in the new types of stepper motors, we should investigate this problem to obtain adequate analytic closed-form solutions.

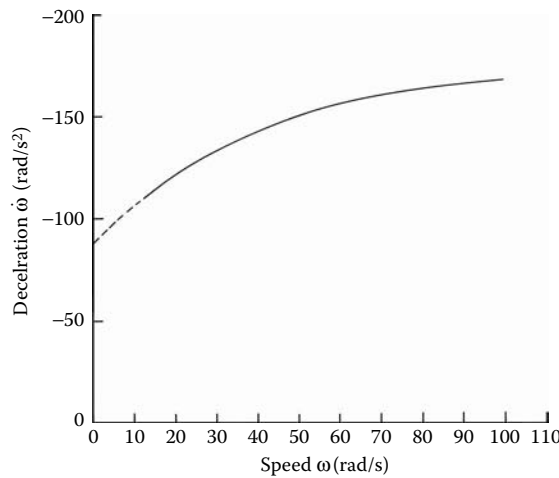


FIGURE 5.50
Deceleration vs. speed characteristic. (Courtesy of Delphi Corp.)

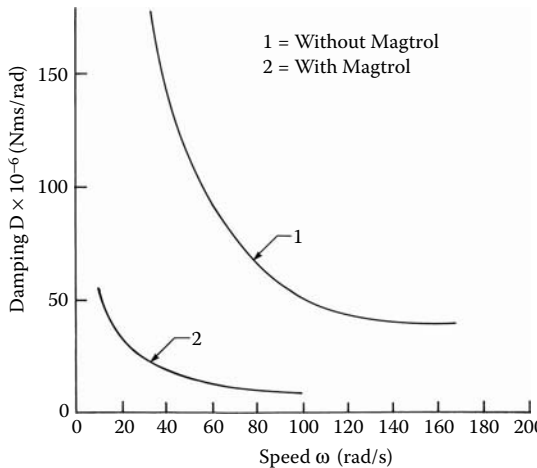


FIGURE 5.51
Damping vs. speed characteristic, motor 4. (Courtesy of Delphi Corp.)

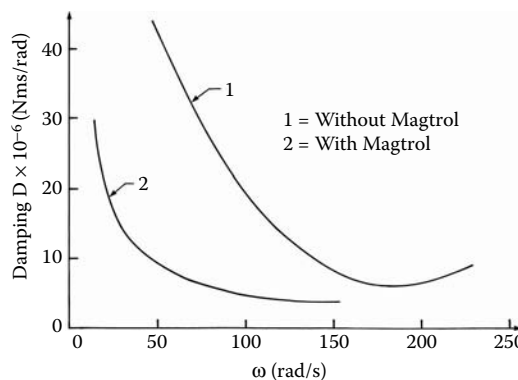
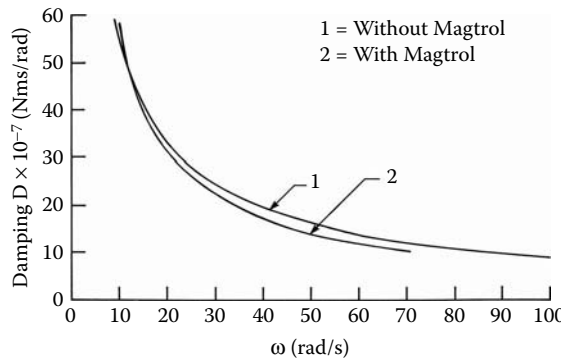
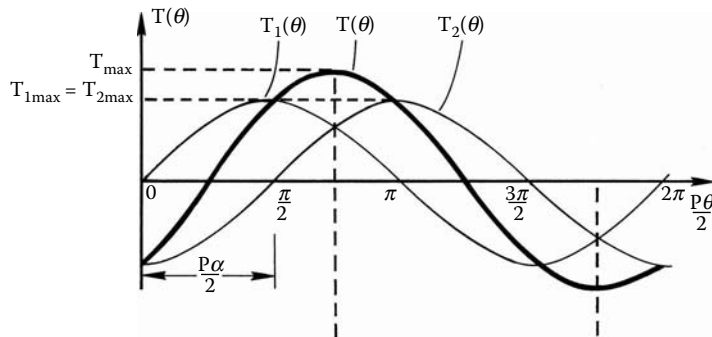


FIGURE 5.52
Damping vs. speed characteristic, motor 3. (Courtesy of Delphi Corp.)

**FIGURE 5.53**

Damping vs. speed characteristic, motor 1. (Courtesy of Delphi Corp.)

**FIGURE 5.54**

Torque developed in the stepper motor. (Courtesy of Delphi Corp.)

The unipolar driver unit gives additional electrical source damping to the closed electrical circuit when two coils are not working, as described previously. Then the same stepper motor, used once as a unipolar driver, has a different performance. This additional damping effect is not covered in this chapter.

5.3.7 Effects of Load Torque on Stepper Motor Performance

The torque developed by the stepper motor, as presented in Equation 5.14, can be written as:

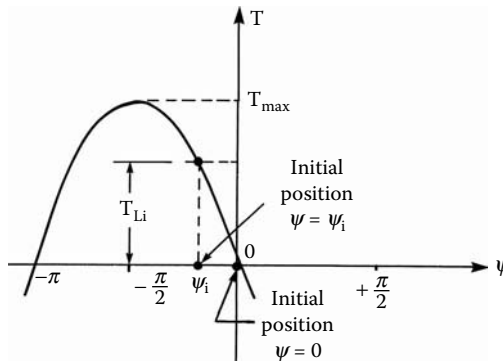
$$T_D(\theta) = T_{1\max} \sin p\theta + T_{2\max} \sin p(\theta + \alpha) \quad (5.87)$$

Shifting the origin through $3\pi/4$, for $\alpha = \pi/2$ torque is expressed by:

$$T(\theta) = T_{1\max} \sin p\left(\theta + \frac{\pi}{4}\right) + T_{2\max} \sin p\left(\theta - \frac{\pi}{4}\right) \quad (5.88)$$

The two torque components are shown in Figure 5.54.

If $T_{1\max} = T_{2\max} = T_{\max}$, then

**FIGURE 5.55**

Torque developed in the stepper motor vs. position for load $T_L = 0$. (Courtesy of Delphi Corp.)

$$T_D(\theta) = \sqrt{2} T_{\max} \sin p\theta \quad (5.89)$$

or

$$T_D(\psi) = \sqrt{2} K_T I \sin \psi \quad (5.90)$$

where $\psi = p\theta$ is the rotor position in electrical degrees. After the load is applied, the equilibrium position of the rotor changes from initial zero position $\psi = 0$ to $\psi = \psi_i$ position (with load $T_L = T_{Li}$), as shown in Figure 5.55.

Position ψ_i is expressed by:

$$\psi_i = \arcsin \frac{T_{Li}}{T_{\max}} \quad (5.91)$$

where θ is the rotor position (in mechanical degrees), p is the number of pole pairs, $T_D(\theta)$ is the torque developed by the stepper motor, $T_{1\max}$ is the maximum torque due to coil 1, ψ is the electrical angle of the rotor position, $T_{2\max}$ is the maximum torque due to coil 2, T_{Li} is a load torque at i position, and T_{\max} is the maximum torque developed by the stepper motor.

Under steady-state conditions, the applied load can be equal to the maximum torque developed by the stepper motor $T_L = T_{\max}$ and then the offset in the equilibrium position will be $\psi_i = \pi/2$. The dynamics of the stepper motor are described by:

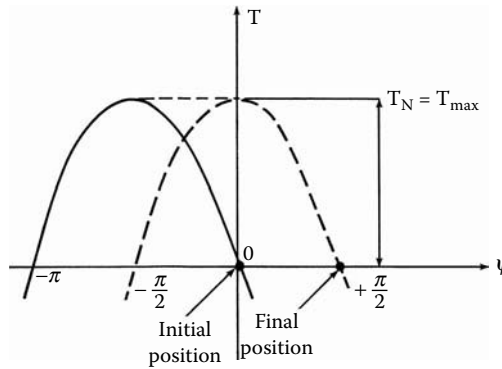
$$T_D(t) = \frac{J}{p} \frac{d^2\psi(t)}{dt^2} + \frac{D}{p} \frac{d\psi(t)}{dt} + T_F + T_L \quad (5.92)$$

Because in the equilibrium position:

$$\frac{d^2\psi(t)}{dt^2} \quad \text{and} \quad \frac{d\psi(t)}{dt} = 0 \quad (5.93)$$

then

$$T_D = T_L \quad \text{or} \quad T_{\max} \sin \psi = T_L \quad (5.94)$$

**FIGURE 5.56**

Torque developed in the stepper motor vs. position for the previous and next steps with load $T_L = 0$. (Courtesy of Delphi Corp.)

If the angle ψ_c is the rotor command position, then from Equation 5.44 we have:

$$T_{\max} \sin(\psi_c - \psi) = T_L \quad (5.95)$$

where the rotor command position $\psi_c = \pi/2$ for the next step. Thus:

$$T_{\max} \sin\left(\frac{\pi}{2} - \psi\right) = T_L \quad (5.96)$$

where J is inertia, T_D is torque developed by the stepper motor, T_F is torque due to friction, T_L is a load torque, T_{\max} is the maximum torque developed by the stepper motor, p is the number of pole pairs, ψ is the electrical angle of the rotor position, and ψ_c is the rotor command position.

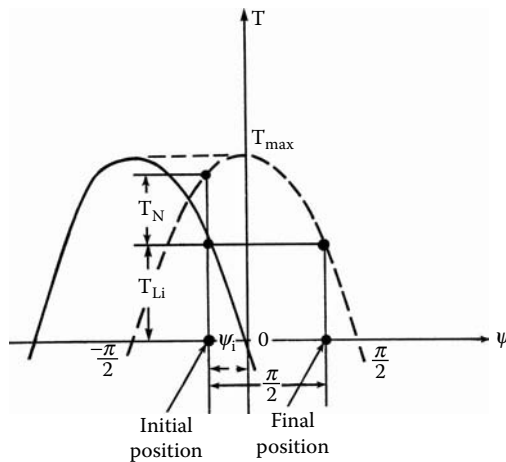
Figure 5.56 shows the initial and final equilibrium positions and the available net torque T_N for the acceleration if the load is equal to zero for the previous position of the rotor and after the applied command for the next step.

The addition of load causes an offset in the equilibrium of the rotor. Load torque also slows down the step response and the maximum stepping rate because of lower available net torque T_N for acceleration. With load torque applied, the initial position of the rotor is determined by the equilibrium point of the previous step. This effect is illustrated in Figure 5.57. The amount of the net torque available for acceleration decreases with increasing load torque until:

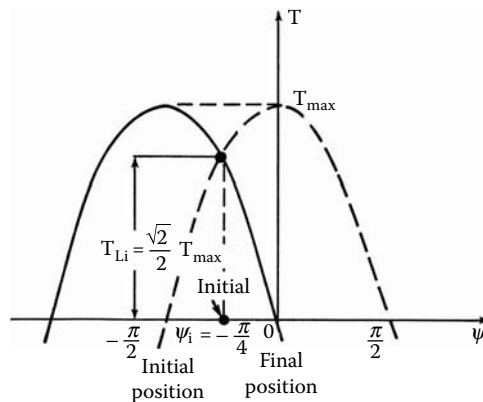
$$\frac{T_L}{T_{\max}} = \frac{\sqrt{2}}{2} \approx 0.707 \quad (5.97)$$

In this case, the rotor position offset is $\psi = \pi/4$, as shown in Figure 5.58. When the next step is commanded:

$$T_N = T_{\max} \sin\left(\frac{\pi}{2} - \frac{\pi}{4}\right) - \frac{\sqrt{2}}{2} T_{\max} = 0 \quad (5.98)$$

**FIGURE 5.57**

Torque developed in the stepper motor vs. position for the load $T_L/T_{\max} = 0.5$. (Courtesy of Delphi Corp.)

**FIGURE 5.58**

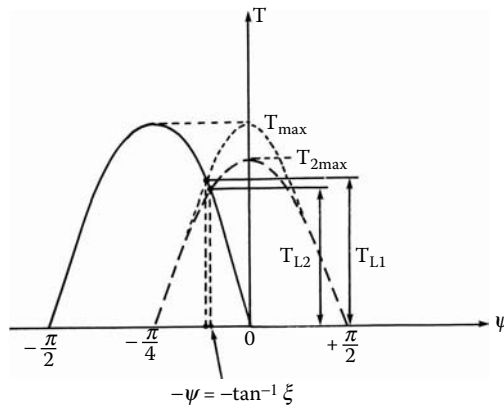
Torque developed in the stepper motor vs. position for the load $T_L/T_{\max} = \sqrt{2}/2$. (Courtesy of Delphi Corp.)

where T_N is the available net torque and T_{\max} is the maximum torque developed by the stepper motor.

Then, there is no net torque available to accelerate the motor and a step command cannot be accomplished. The motor cannot step and statistically hold a load torque equal in value to the still torque of the motor. Thus, the motor load $T_L = 0.707T_{\max}$ will cause the claw stepper motor with PM to fail to respond to a step command. This situation occurs if $T_{1\max} = T_{2\max}$, which means that the torque is developed by two coils equal to each other. But in practice, there is sometimes a big difference between them (more than 10%), which reflects the maximum load value that we can apply to the stepper motor. Figure 5.59 shows torque developed vs. position for different torque values.

Thus, we have:

$$A \sin(\psi_{c1} - \psi) - B \sin(\psi_{c2} - \psi) = 0 \quad (5.99)$$

**FIGURE 5.59**

Torque developed vs. position for different torque values. (Courtesy of Delphi Corp.)

$$A \sin(0 - \psi) - B \sin\left(\frac{\pi}{2} - \psi\right) = 0 \quad (5.100)$$

$$\sin \psi - \xi \cos \psi = 0 \quad (5.101)$$

Solving this, we have:

$$\psi = -\tan^{-1} \xi \quad (5.102)$$

which is $< \pi/2$ because $\xi = B/A < 1$.

The maximum value of load we can apply $\frac{T_D}{T_{\max}} = C$ is:

$$C = \xi \frac{1}{\sqrt{1+\xi}} = \frac{B}{A} \frac{1}{\sqrt{1+\left(\frac{B}{A}\right)^2}} \quad (5.103)$$

From Figure 5.58 and Equation 5.53, we can obtain the position error δ :

$$\delta = 2\left(\frac{\pi}{4} - \tan \xi\right) \quad (5.104)$$

where C is the maximum load value that can be applied, T_D is torque developed by the stepper motor, δ is the position error, ψ is the electrical angle of rotor position, ψ_c is the rotor command position, ψ_{c1} is the rotor command position for step 1, ψ_{c2} is the rotor command position for step 2, and ξ is the B/A ratio.

If $\psi = 0.9$, then the maximum torque value is $C = 0.6689$ compared to $C = 0.707$ determined previously (a decrease of 5.4%) and the position error δ is equal to 6.026° compared to 0° . This reduction obviously affects the dynamic response of the stepper motor.

5.3.8 Stepper Motor Inductance in Dynamic Operation

This section presents a method of determining the inductance of the claw pole stepper motor as a function of frequency (step rate). Because the claw pole stepper motor generally has a large number of poles, the magnetic field in the air gap changes sign with a frequency up to 300.0 Hz. This can significantly influence effective inductance and, therefore, the dynamics of the motor. The approach taken is to split the motor permeance into two lumped-parameter components, one for air gaps and one for the iron parts. Because of eddy currents, the iron permeance is a function of frequency, and the permeance of the air is constant. This section addresses the problem of variation in iron permeance and presents a method of calculating effective motor inductance that should enable us to better analyze the stepper motor dynamics (Pawlak 1986).

Stepper motor inductance can be calculated on the basis of design parameters available from static calculations described in Section 5.3.7. Ignoring the eddy currents, the inductance can be described as:

$$L = N^2 P \quad (5.105)$$

where N is the number of coil turns and P is the permeance of the stepper motor magnetic circuit.

Because the number of turns N is known, the only unknown term is the total permeance P . To calculate it, one must know all physical dimensions of the stepper motor, as well as the material of the magnetic circuit, the parameters of the coil, and the magnetic flux produced.

Because of the specific construction of the motor, it is sufficient to investigate one elementary section of the magnetic circuit with a pair of poles, as shown in Figure 5.13. The main path of the flux crossing this section consists of the main and the back air gaps and the iron part of the magnetic circuit. With no current in the stator coil, the sum of the MMFs should be equal to PM MMF (AT_2), as presented in Equation 5.19. Because there are p such sections in one stepper motor, the total permeance is p times the elementary section permeance:

$$P = pP_1 \quad (5.106)$$

where P is the total permeance, p is the number of pole pairs, N is the number of coil turns, and P_1 is the elementary section permeance of the stepper motor magnetic circuit.

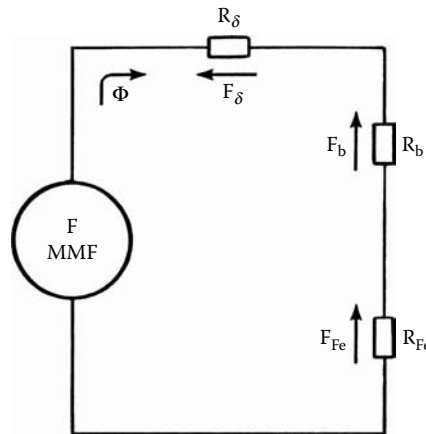
By combining Equation 5.105 and Equation 5.106, the expression for the inductance can be obtained:

$$L = N^2 pP_1 \quad (5.107)$$

The elementary section permeance P_1 can be calculated if all physical dimensions of the elementary section, shown in Figure 5.13, are known, as well as the magnetic-circuit material parameters and the magnetic flux produced. The equivalent magnetic circuit for the elementary section of the motor is shown in Figure 5.60.

The total reluctance is:

$$R_1 = R_{Fe} + R_b + R_\delta \quad (5.108)$$

**FIGURE 5.60**

Equivalent magnetic circuit. (Pawlak, A.M., *International Conference on Electrical Machines Proceedings ICEM '86*, Munich, West Germany, September 8–10, 1986. With permission.)

Because permeance is reciprocal to reluctance, the total permeance is represented as:

$$P_1 = \frac{1}{R_1} = \frac{P_{Fe}P_bP_\delta}{P_bP_\delta + P_{Fe}P_\delta + P_{Fe}P_b} \quad (5.109)$$

where R_1 is the total reluctance, and R_{Fe} , R_b , and R_δ are reluctances of the iron, back air gap, and the main air gap, respectively.

Air gap permeances are calculated on the basis of the method for estimating a permeance of probable flux paths (Chai 1986, Roters 1967). These air gap permeances remain the same during stepper motor operation and are independent of the frequency of the magnetic field. There are two air gaps in this configuration, shown in Figure 5.14, for the main and the back air gaps, respectively. The back air gap can be a butt- or lap-joint type and because of the complicated 3D geometry, as presented in Figure 5.13, the air gap permeance calculations can be simplified (Dąbrowski 1980). Air gap permeance P_δ can be calculated by considering the following paths in parallel and adding each permeance on the basis of Figure 5.61 and Figure 5.62.

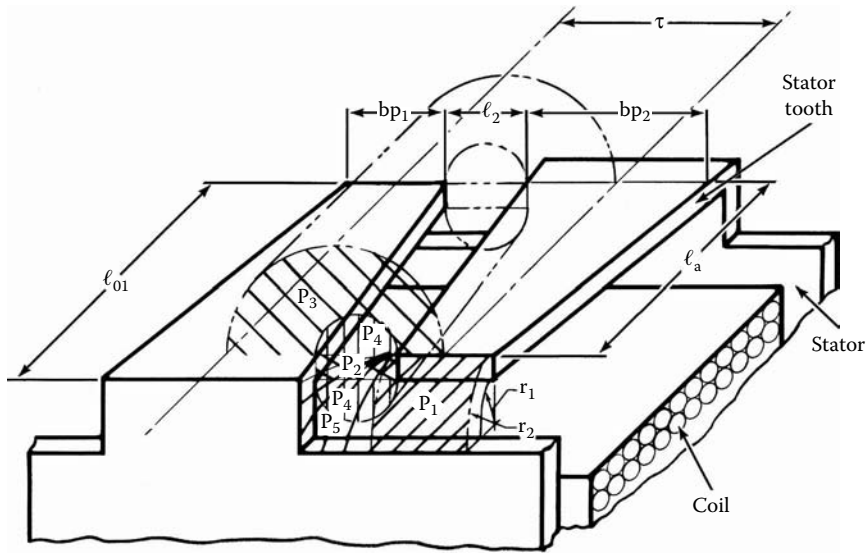
The main air gap permeance can be calculated from Figure 5.55:

$$P_\delta = P_1 + P_2 + P_3 + 2P_4 + 2P_5 \quad (5.110)$$

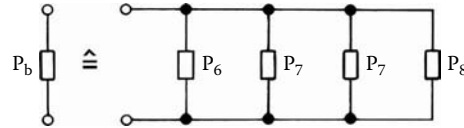
In each case, the permeance is in the form:

$$P = \frac{\mu_0 A}{l} \quad (5.111)$$

where μ_0 is the permeability of the air, which equals $4\pi \times 10^{-7}$ H/m; A , l are the area and length of each component, respectively; P is permeance; P_δ is main air gap permeance; P_1 is pole head end leakage permeance; P_2 is pole side leakage permeance; P_3 is pole body permeance; P_4 is semicircular cylinder leakage permeance; and P_5 is corner pole head leakage permeance.

**FIGURE 5.61**

Main air gap permeances. (Pawlak, A.M., *International Conference on Electrical Machines Proceedings ICEM '86*, Munich, West Germany, September 8–10, 1986. With permission.)

**FIGURE 5.62**

Schematic of the main air gap permeances. (Pawlak, A.M., *International Conference on Electrical Machines Proceedings ICEM '86*, Munich, West Germany, September 8–10, 1986. With permission.)

The components of Equation 5.110 are expressed finally in the following forms:

For pole head end leakage:

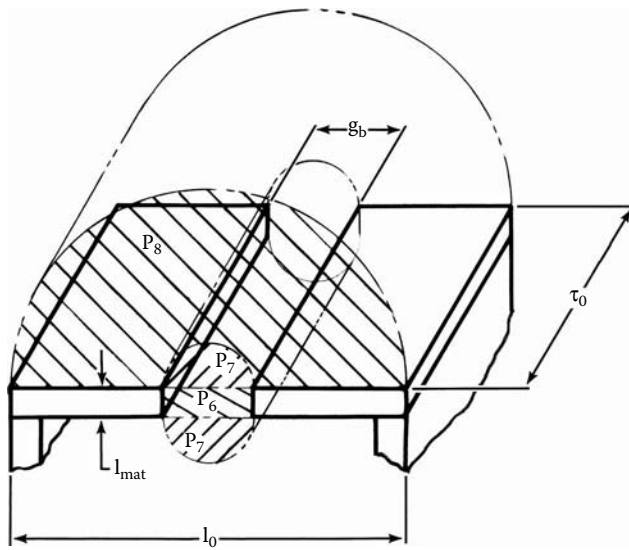
$$P_1 = \frac{2\mu_0 b_{p1}}{\pi} \ln \frac{r_1}{r_2} \quad (5.112)$$

Pole side leakage:

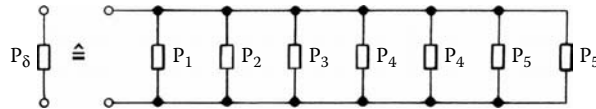
$$P_2 = \mu_0 \frac{l_a l_{mat}}{l_2 \cos \left[a \tan \left(b_{p2} - \frac{b_{p1}}{2l_{01}} \right) \right]} \quad (5.113)$$

Pole body leakage:

$$P_3 = \mu_0 \frac{l_a}{\pi} \ln \left(1 + \frac{a_3}{2l_2} \right) \quad (5.114)$$

**FIGURE 5.63**

The butt-joint air gap permeances. (Pawlak, A.M., *International Conference on Electrical Machines Proceedings ICEM '86*, Munich, West Germany, September 8–10, 1986. With permission.)

**FIGURE 5.64**

Schematic of the butt-joint air gap permeances. (Pawlak, A.M., *International Conference on Electrical Machines Proceedings ICEM '86*, Munich, West Germany, September 8–10, 1986. With permission.)

Semicircular cylinder leakage:

$$P_4 = 0.26\mu_0 l_a \quad (5.115)$$

Semicircular cylinder leakage:

$$P_5 = 0.5\mu_0 l_{mat} \quad (5.116)$$

The back butt-joint air gap can be similarly expressed on the basis of Figure 5.63 and Figure 5.64. Thus, the back-butt-joint air gap permeance is:

$$P_b = P_6 + 2P_7 + P_8 \quad (5.117)$$

where P_8 is the main air gap permeance, P_1 is the pole head end leakage permeance, P_2 is the pole side leakage permeance, P_3 is the pole body permeance, P_4 is the semicircular cylinder leakage permeance, P_5 is the corner pole head leakage permeance, and l_{mat} , l_{O1} , l_a , b_{p1} , b_{p2} , r_1 , r_2 , a_3 , l_2 represent the tooth dimensions, as presented in Figure 5.15.

The components of the Equation 5.117 are expressed in the form:

$$P_6 = \mu_0 \frac{l_{mat} \tau_o}{g_b} \quad (5.118)$$

Back air gap semicircular cylinder leakage:

$$P_7 = 0.26 \mu_0 \tau_a \quad (5.119)$$

Pole body leakage:

$$P_8 = \mu_0 \frac{\tau_o}{\pi} \ln \frac{l_o}{g_b} \quad (5.120)$$

The lap-joint back air gap permeance:

$$P_b = P_g = \mu_0 \frac{l_{s3} \tau_o}{g_b} \quad (5.121)$$

where P_b is the butt-joint permeance, P_g is the lap-joint back air gap permeance, P_6 is the pole body permeance, P_7 is the back air gap semicircular cylinder leakage, P_8 is the pole body leakage, τ_o is a pole pitch, l_o is the total stator thickness, g_b is the back air gap, l_{mat} is the material thickness, and l_{s3} is the overlap length.

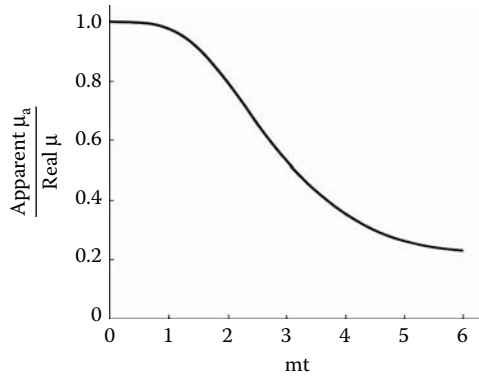
Iron permeance can be calculated in two stages, first with the constant field and next with a magnetic field changing with high frequency. For a constant magnetic field, the iron permeability can be found from the static calculations:

$$P_{Fe} = \frac{\phi}{l_{Fe}} = \mu \frac{AT_{Fe}}{l_{Fe}} \quad (5.122)$$

where P_{Fe} is the iron permeability, AT_{Fe} is the MMF drop in the iron part of the stepper motor, μ is the iron permeability, μ_a is the iron apparent permeability, l_{Fe} is the length of the magnetic path in the iron of the stepper motor, d is the skin depth, and m is the reciprocal of the skin depth d .

The expression with real permeability of the iron is valid when there are no eddy currents in the iron, or in other words, for a constant field in the iron. For the dynamic case, when the magnetic field changes with high frequency, the eddy currents come into the picture and their existence can be expressed by introducing so-called apparent permeability instead of real permeability. Assuming the real permeability of iron to be constant and all other dimensions to be large compared to the lamination thickness [considered as a thin plate problem (Guyton 1977, Moulin 1955)], the apparent permeability of the core is less than the real permeability because eddy currents set up in the laminations as shown below:

$$\left(\frac{\mu_a}{\mu} \right)^2 = \frac{2}{m^2 t^2} \frac{\cosh mt - \cos mt}{\cosh mt + \cos mt} \quad (5.123)$$

**FIGURE 5.65**

Ratio of apparent/real permeability vs. mt . (Pawlak, A.M., *International Conference on Electrical Machines Proceedings ICEM '86*, Munich, West Germany, September 8–10, 1986. With permission.)

where m is the reciprocal of the skin depth d and is a function of the real permeability μ , the frequency f , and the resistivity of the iron ρ :

$$m = \sqrt{\frac{\pi f \mu}{\rho}} = \frac{1}{d} \quad (5.124)$$

Equation 5.71 can be written in a different form:

$$\left(\frac{\mu_a}{\mu}\right)^2 = \frac{\left(1 + \frac{2m^4 t^4}{6!} + \dots\right)}{\left(1 + \frac{2m^4 t^4}{4!} + \dots\right)} \quad (5.125)$$

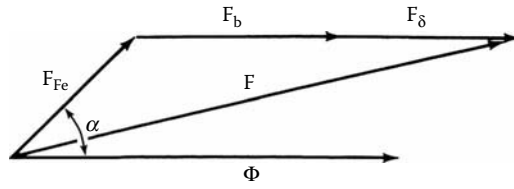
If $mt = 0$, the eddy currents are zero and the apparent permeability is equal to real permeability, or $\mu_a = \mu$. For values $mt \gg 1.0$, i.e., when the thickness of the magnetic material is greater than the depth of penetration d , the last component of Equation 5.125 $(\cosh mt - \cos mt)/(\cosh mt + \cos mt)$ tends to unity and, thus, $\mu_a/\mu = \sqrt{2}/mt$, as presented in Figure 5.65.

Eddy currents change the iron real permeability to an apparent permeability and, therefore, motor inductance changes as a function of frequency. Although a 3D FE field analysis with eddy currents would be desirable to determine the flux distribution of such a complicated machine, a simplified approach based on estimated permeance can be used because it yields acceptable results.

Thus, because of eddy currents, we define apparent iron permeance:

$$P_{Fe,a} = \frac{\mu_a}{\mu} P_{Fe} \quad (5.126)$$

Finally, for all values combining Equation 5.126 and Equation 5.123:

**FIGURE 5.66**

Phasor diagram. (Pawlak, A.M., *International Conference on Electrical Machines Proceedings ICEM '86*, Munich, West Germany, September 8–10, 1986. With permission.)

$$P_{Fe,a} = \frac{\sqrt{2}}{mt} \sqrt{\frac{\cosh mt - \cos mt}{\cosh mt + \cos mt}} P_{Fe} \quad (5.127)$$

For values $m \gg 1.0$, i.e., when the thickness of the magnetic material is greater than the depth of penetration:

$$P_{Fe,a} = P_{Fe} \frac{C}{\sqrt{f}} \quad (5.128)$$

where

$$C = \sqrt{\frac{2\rho}{\pi t^2 \mu}} \quad (5.129)$$

The resultant MMF across each element, shown in Figure 5.12, is the sum of all MMFs. The phasor diagram is shown in Figure 5.66.

For any given value of the magnetizing force, the total flux in the solid iron core can be practically independent of iron core thickness t if the frequency is high, that is $mt \gg 1.0$, and the flux lags the magnetizing force by $\alpha = \pi/4$.

$$F = \sqrt{F_{Fe}^2 + (F_\delta + F_b)^2 - 2F_{Fe}(F_\delta + F_b)\cos(\pi - \alpha)} \quad (5.130)$$

Because MMF:

$$F = \phi R1 \quad \text{or} \quad F = \phi \frac{1}{P1} \quad (5.131)$$

Combining Equation 5.130 and Equation 5.131, the total reluctance for the magnetic circuit becomes

$$R1 = \sqrt{R_{Fe}^2 + (R_\delta + R_b)^2 - 2R_{Fe}(R_\delta + R_b)\cos(\pi - \alpha)} \quad (5.132)$$

and the total section permeance is:

$$P1 = \frac{P_{Fe} P_\delta P_b}{\sqrt{P_\delta^2 P_b^2 + P_{Fe}^2 (P_\delta + P_b)^2 - 2P_{Fe} P_\delta P_b (P_\delta + P_b)\cos(\pi - \alpha)}} \quad (5.133)$$

TABLE 5.10
Computer Simulations

Design	Frequency (Hz)	μ_a (-)	P_{Fe} 10^{-8} (H)	P 10^{-8} (H)	L (mH)
#1	1	5000	28.76	56.39	36.06
	10	4942	28.43	56.38	36.05
	100	2834	16.30	55.78	35.67
	1000	799	4.59	52.39	33.5
	10000	253	1.45	43.71	27.95
#2	1	4996	10.61	1.63	82.78
	10	4583	9.74	1.61	81.89
	100	1499	3.18	1.26	63.72
	1000	474	1.01	0.70	35.51
	10000	150	9.32	0.28	14.32
#3	1	4998	10.76	0.92	153.9
	10	4781	10.29	0.92	153.5
	100	1839	3.96	0.83	138.1
	1000	566	1.22	0.59	98.2
	10000	179	0.39	0.29	49.2

Source: Pawlak, A.M., *International Conference on Electrical Machines Proceedings ICEM '86*, Munich, West Germany, September 8–10, 1986. With permission.

At low frequency, $\alpha = 0$ and the total permeance is as shown in Equation 5.56. Combining Equation 5.55 and Equation 5.80, the inductance of the motor can be expressed as:

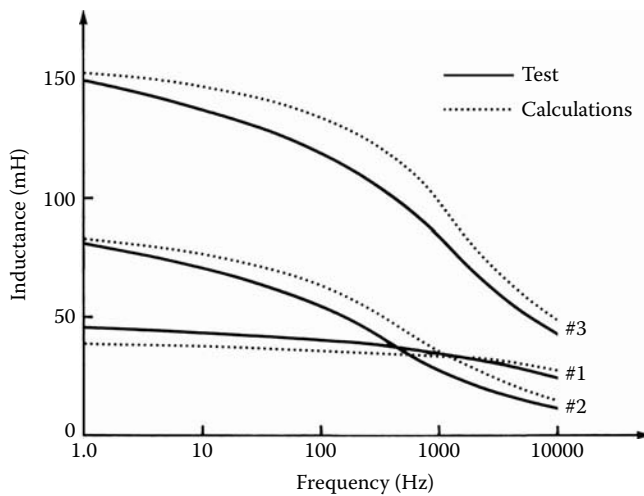
$$L = \frac{N^2 p P_{Fe} P_\delta P_b}{\sqrt{P_\delta^2 P_b^2 + P_{Fe}^2 (P_\delta + P_b)^2 - 2P_{Fe} P_\delta P_b (P_\delta + P_b) \cos(\pi - \alpha)}} \quad (5.134)$$

where P_{Fea} is the apparent iron permeance, P_{Fe} is the iron permeance, P_δ is the main air gap permeance, P_b is the butt-joint permeance, $P1$ is the elementary section permeance, R_{Fe} is the reluctance of the iron, R_b is the reluctance of the back air gap, R_δ is the reluctance of the main air gap, $R1$ is the elementary section reluctance, α is the flux and magnetizing force angle, N is the number of turns, ϕ is the uniform flux in the magnetic core, and L is the inductance of the stepper motor.

Equation 5.134 was used for our inductance calculations because the frequency is high and the stepper motor magnetic circuit can be assumed to be entirely of solid iron. The total permeance is a function of frequency and, therefore, the inductance is also a function of frequency according to Equation 5.105. Because of this, the stepper motor inductance varies during the dynamic operation.

On the basis of the theory discussed, a computer program to calculate the claw pole stepper motor inductance was written to provide a tool for quick verification. Using this program, detailed calculations were performed for the three previously investigated stepper motors, motor 1, motor 2, and motor 3, as described in Section 5.2.6. Results of computer simulations are presented as a function of frequency in Table 5.10.

The iron permeability is reduced significantly due to applied frequency and this affects motor inductance. However, these changes differ from motor to motor due to the different configurations. The inductance of motor 2 is reduced by a factor of 5 while inductance of motor 1 is only reduced by 25%. This is because the iron permeance is a big factor in the total permeance of motor 2. We can conclude that the inductance of the claw pole stepper motor configuration with a lap-joint stator is more sensitive to frequency than one with

**FIGURE 5.67**

Stepper motor inductance vs. frequency for stepper motor 1, motor 2, and motor 3. (Pawlak, A.M., *International Conference on Electrical Machines Proceedings ICEM '86*, Munich, West Germany, September 8–10, 1986. With permission.)

a butt-joint stator. The inductance was measured at different frequencies up to 10 kHz for all three stepper motors. These measurements were compared with computer simulation results and match within 15% for all cases and for the wide range of frequency, as shown in Figure 5.67. This method of calculation can be easily extended and applied to any claw pole stepper motor design configuration.

Example 5.1: Magnetic-Circuit Calculations

Calculate all magnetic parameters of the magnet working point characteristics: AT_4 , AT_2 , ϕ_m , and ϕ_o without load when $T_L = 0$. Conduct calculations for all four introduced stepper motors, as presented in Figure 5.12, based on the input data from Table 5.11. Use input data of motor 1 to demonstrate all intermediate and final steps including the magnetic-circuit calculation and collect them into Table 5.12 through Table 5.14.

Solution to Example 5.1

All calculations will be in steps. First, the magnetic circuit will be calculated in four steps with all intermediate and final result calculations summarized for all stepper motors, motor 1 to motor 4, in Table 5.12. The results of these calculations will be used for the next example where the torque with current load demagnetization effect will be calculated for all four stepper motors.

Step 1: Magnetic Calculations of PMs

Calculate the maximum value of the effective magnet length from Equation 5.48:

TABLE 5.11

Magnetic Circuit Calculations for Four Claw Pole Stepper Motors

Parameter	Unit	Motor Number			
		#1	#2	#3	#4
<i>1. Design</i>					
Number of teeth	#	24	24	24	12
Number of coil turns	#	460	1000	833	730
Wire gauge	AWG	33	35	39	35
Number of coils	#	4	2	4	2
Motor design	type	lap	butt	lap	butt
<i>2. Permanent magnet</i>					
Number of poles	#	24	24	24	12
Magnet outside diameter R_{OD}	10^{-3} m	25.578	25.578	13.97	10.33
Magnet inside diameter R_{ID}	10^{-3} m	17.272	17.272	9.525	6.36
Magnet axial length L_{PM}	10^{-3} m	18.03	18.03	12.70	10.00
Magnet remanence B_r	[T]	0.2575	0.2575	0.2575	0.2575
Magnet coercive force H_c	[Oe]	2175	2175	2175	2175
Magnet remanence temp. coefficient	% B_r /°C	-0.2	-0.2	-0.2	-0.2
Magnet coercive force temp. coefficient	% H_c /°C	-0.2	-0.2	-0.2	-0.2
<i>3. Motor component dimensions</i>					
Steel thickness	10^{-3} m	1.062	1.062	0.91186	0.63
Stator outside diameter D_{SO1}	10^{-3} m	55.02	45.339	33.0708	24.08
Stator total outside diameter D_{SO2}	10^{-3} m	57.15	45.339	34.798	24.08
Stator inside diameter D_{SI}	10^{-3} m	26.29	26.289	14.605	11.04
Stator stack thickness L_O	10^{-3} m	10.414	10.67	7.9375	5.46
Stator side thickness L_{S1}	10^{-3} m	7.874	5.316	6.48	2.527
Stator side thickness L_{S2}	10^{-3} m	8.00	5.316	7.214	2.527
Butt or lap joint air gap length δ_b	10^{-3} m	0.0102		0.00	0.405
Tooth width b_{P1}	10^{-3} m	1.27	1.117	1.27	1.00
Tooth width b_{P2}	10^{-3} m	3.20	3.175	1.27	2.798
Total tooth length L_{ST}	10^{-3} m	9.19	9.652	6.576	4.85
Segment tooth length a_1	10^{-3} m	0.00	0.00	4.6482	0.00
Segment tooth length a_2	10^{-3} m	0.00	0.00	1.016	0.00
<i>4. Performance information</i>					
Copper temperature	°C	25	25	25	25
Magnet temperature	°C	25	25	25	25
Maximum current	A	0.6	0.2	0.2	0.5
Current increment	A	0.1	0.05	0.05	0.1

Source: Courtesy of Delphi Corp.

$$l_m = \pi^2 D_m (4p - 1) / 32p^2 = \pi^2 \times 25.578 \times 10^{-3} \times (2 \times 12 - 1) / 32 \times 12^2 = 2.514 \times 10^{-3} \text{ m}$$

Because this value is estimated from a closed-form solution, Equation 5.48, and not from the 2D software, we do not use the anisotropy factor from Equation 5.46 and Equation 5.47 and, therefore, $k_m = 1.0$ and $l_m' = l_m$.

TABLE 5.12

Intermediate Magnetic-Circuit Calculations for Motors 1 through 4

Motor Number	Parameter			
	Area ($\times 10^{-6}$ m 2)	Flux Density (T)	Magnetic Length ($\times 10^{-3}$ m)	MMF (At)
<i>Motor #1</i>				
Tooth area 1	2.376	1.366	4.595	3.459
Tooth area 2	2.376	1.366	4.595	3.459
Stator side walls "L1"	3.398	0.955	13.303	4.884
Stator side walls "L2"	3.398	0.955	14.368	4.544
Stator back walls "D"	7.501	0.635	11.720	1.095
Parasitic back air gap	78.777	0.412	0.006	0.0984
Main air gap	17.469	0.186	0.355	52.514
<i>Motor #2</i>				
Tooth area 1	2.180	1.447	4.826	4.951
Tooth area 2	2.180	1.447	4.826	4.951
Stator side walls "L1"	3.226	0.978	8.509	2.974
Stator side walls "L2"	3.226	0.978	8.509	2.974
Stator back walls "D"	5.895	0.535	11.263	1.561
Parasitic back air gap	11.789	0.268	0.038	8.095
Main air gap	17.215	0.183	0.355	51.864
<i>Motor #3</i>				
Tooth area 1	1.158	0.736	3.288	0.822
Tooth area 2	1.158	0.736	3.288	0.822
Stator side walls "L1"	1.158	0.736	8.321	2.08
Stator side walls "L2"	1.158	0.736	9.185	2.296
Stator back walls "D"	3.839	2.334	8.190	0.413
Parasitic back air gap	49.839	0.018	0.0	0.0
Main air gap	5.690	0.1574	0.318	39.778
<i>Motor #4</i>				
Tooth area 1	1.196	1.020	2.425	0.907
Tooth area 2	1.196	1.020	2.425	0.907
Stator side walls "L1"	1.763	0.692	5.890	1.244
Stator side walls "L2"	1.763	0.692	5.890	1.244
Stator back walls "D"	3.868	0.316	7.811	0.536
Parasitic back air gap	7.735	0.158	0.405	50.855
Main air gap	8.337	0.146	0.355	41.362

Source: Courtesy of Delphi Corp.

TABLE 5.13

Final Magnetic Circuit Calculations for Motors #1 through #4

Parameter	Unit	Motor #1	Motor #2	Motor #3	Motor #4
Total MMF drop AT ₂	At	122.66	128.77	85.70	138.86
Total magnet MMF AT ₄	At	435.12	447.06	220.55	321.88
Maximum flux from magnet	$\times 10^{-8}$ Wb	449.8	443.29	146.52	214.67
Flux from magnet at working point	$\times 10^{-8}$ Wb	324.56	315.61	89.58	122.06

Source: Courtesy of Delphi Corp.

TABLE 5.14
Working Point Calculations

Parameter Motor	Current (A)	F_{AR} (At/m)	Flux $\times 10^{-8}$ (Wb)	Torque (Ncm)
#1	0.1	28.518	303.644	2.844
	0.2	57.037	282.955	5.301
	0.3	85.555	262.266	7.370
	0.4	114.073	241.577	9.051
	0.5	142.591	220.887	10.350
	0.6	171.11	200.198	11.250
#2	0.05	31.65	293.264	2.986
	0.10	63.3	270.92	5.516
	0.15	94.95	248.577	7.593
	0.20	126.6	226.233	9.213
	0.25	158.25	203.89	10.380
#3	0.05	24.407	79.672	0.6758
	0.10	48.814	69.758	1.184
	0.15	73.221	59.845	1.522
	0.20	97.628	49.931	1.694
	0.25	122.035	40.017	1.697
#4	0.1	45.342	104.866	0.3898
	0.2	90.684	87.671	0.6518
	0.3	136.027	70.477	0.786
	0.4	181.369	53.283	0.7923
	0.5	226.711	36.089	0.6708

Source: Courtesy of Delphi Corp.

Step 2: Maximum MMF Calculations

Calculate the maximum value of the MMF of the PM based on the magnet material and the effective magnet length from Equation 5.45:

$$AT_4 = H_c \times l_m' = 173.036 \times 10^3 \text{ A/m} \times 2.514 \times 10^{-3} \text{ m} = 435.12 \text{ At}$$

Step 3: Maximum Flux Calculations

Calculate the maximum value of the flux per tooth ϕ_m that is the product of the remanent flux density B_r of the magnet and the effective surface area A_m' ; see Equation 5.40:

$$A_m = \frac{D_{R0} - D_{R1}}{2} \times \frac{l_{pm}'}{2} = \frac{25.578 - 17.272}{2} 10^{-3} \times \frac{18.08}{2} 10^{-3} \text{ m}^2 = 37.54 \times 10^{-6} \text{ m}^2$$

The effective magnet surface A_m' depends on both the magnet and tooth surface areas, as well as on the method of magnetization of the magnet. Because $A_\delta < A_m$, then $A_m' = A_\delta$. From Equation 5.43:

$$\begin{aligned} A_\delta &= \frac{b_{p2} + b_{p1}}{2} \times \left(\frac{l_{pm}}{2} + l_{ST} + l_{mat} - l_o \right) \\ &= \frac{1.27 + 3.20}{2} \times 10^{-3} \text{ m} \times \left(\frac{18.08}{2} + 8.128 + 1.062 - 10.414 \right) \times 10^{-3} \text{ m} = 17.469 \times 10^{-6} \text{ m}^2 \end{aligned}$$

Finally, the maximum magnet flux ϕ_m can be calculated from Equation 5.44.

$$\phi_m = B_r \times A_m' = B_r \times \frac{A_\delta}{A_m} A_m = B_r \times A_\delta = 0.2575 \text{ T} \times 17.469 \times 10^{-6} \text{ m}^2 = 4.498 \times 10^{-6} \text{ Wb}$$

Step 4: Calculate MMFs along the Magnetic Flux Path

Now, calculate the MMF drops along the flux path of the claw pole stepper motor based on Equation 5.19, where there are MMF drops in the claw poles, side walls, back walls, parasitic air gaps, and main air gap. Assume a flux-density level in one area, for example, in the tooth, and calculate both Equation 5.19 and Equation 5.42, iterating the assumed flux-density values until its value would satisfy these two equations within 1% error.

Step 4.1: Tooth Area

Assume flux density B_T of 1.366 T in the tooth area, as shown in Figure 5.15. Calculating the average value of the tooth area from Equation 5.20:

$$S_{T_{avg}} = \frac{b_{p2} + b_{p1}}{2} \times l_{mat} = \frac{3.20 + 1.27}{2} \times 10^{-3} \text{ m} \times 1.062 \times 10^{-3} \text{ m} = 2.376 \times 10^{-6} \text{ m}^2$$

From Equation 5.21, the flux ϕ_o in the tooth area (and passing through the one pole-pair section) is:

$$\phi_o = B_T \times S_{T_{avg}} = 1.366 \text{ T} \times 2.376 \times 10^{-6} \text{ m}^2 = 3.2456 \times 10^{-6} \text{ Wb}$$

The MMF drop in the tooth from Equation 5.22, where $H_T = 851.2 \text{ At/m}$ is obtained from the BH curve of the material corresponding to $B_T = 1.366 \text{ T}$, as presented in Figure 5.15 is:

$$AT_T = H_T \times \frac{l_{01}}{2} = 851.2 \frac{\text{At}}{\text{m}} \times \frac{8.128}{2} \times 10^{-3} \text{ m} = 3.459 \text{ At}$$

Step 4.2: Stator Side Walls "L" Area

The flux density in the side walls "L" area is given by Equation 5.23:

$$B_L = \frac{\phi_o}{b_{p2} \times l_{mat}} = \frac{3.2456 \times 10^{-6} \text{ Wb}}{3.20 \times 10^{-3} \text{ m} \times 1.062 \times 10^{-3} \text{ m}} = 0.955 \text{ T}$$

The MMF drop in the tooth from Equation 5.24, where $H_L = 316.5 \text{ At/m}$ is obtained from the BH curve of the material corresponding to $B_T = 1.366 \text{ T}$, as presented in Figure 5.15, and the MMF drops AT_{L1} and AT_{L2} are:

$$AT_{L1} = H_L \times \frac{D_{SO1} - D_{SI}}{2} = 316.5 \text{ At/m} \times \frac{57.15 \times 10^{-3} \text{ m} - 26.29 \times 10^{-3} \text{ m}}{2} = 4.884 \text{ At}$$

$$AT_{L2} = H_L \times \frac{D_{SO2} - D_{SI}}{2} = 316.5 \text{ At/m} \times \frac{55.02 \times 10^{-3} \text{ m} - 26.29 \times 10^{-3} \text{ m}}{2} = 4.544 \text{ At}$$

Step 4.3: Stator Back Walls “D” Area

The flux density in the “D” area is given by Equation 5.25:

$$B_D = \frac{\phi_o}{l_{do} \times l_{mat}} = \frac{\phi_o}{\frac{\pi(D_{SO} - l_{mat})}{P/2} \times l_{mat}} = \frac{3.2456 \times 10^{-6} \text{ Wb}}{\left(\frac{3.14(57.15 - 1.062)}{12} \times 1.062 \right) \times 10^{-6} \text{ m}^2} = 0.2082 \text{ T}$$

Again looking at Figure 5.16 for the field strength H_D , the MMF force drop AT_D in this section can be calculated from Equation 5.26 through Equation 5.29:

$$AT_D = H_D \times \sqrt{\left(\frac{\pi(D_{SO} - l_{mat})}{P/2} - b_{p2} \right)^2 + (l_o - l_{mat})^2}$$

$$= 74.01 \text{ At/m} \times \sqrt{\left(\frac{3.14(57.15 - 1.062)}{24/2} - 3.2 \right)^2 + (10.41 - 1.062)^2} \times 10^{-3} \text{ m} = 1.095 \text{ At}$$

Step 4.4: Stator Parasitic Air Gap Area

The flux density for the lap joint from Equation 5.31 is:

$$B_{\delta b} = \frac{\phi_o P/2}{(l_{s1} + l_{s2} - l_o) \times \pi D_{SO1}}$$

$$= \frac{3.2456 \times 10^{-6} \text{ Wb} \times 24/2}{(7.87 + 8.0 - 10.41) \times 10^{-3} \text{ m} \times 55.02 \times 10^{-3} \text{ m}} = 0.412 \text{ T}$$

The MMF drop is from Equation 5.32 and Equation 5.33:

$$AT_{\delta b} = \frac{B_{\delta b} \times \frac{(D_{SO1} - 2 \times l_{mat}) - D_{SO2}}{2}}{\mu_o}$$

$$= \frac{0.412 \text{ T} \times (57.15 \times 10^{-3} \text{ m} - 2 \times 1.062 \times 10^{-3} \text{ m} - 55.02 \times 10^{-3} \text{ m})}{2 \times 4\pi \times 10^{-7} \text{ H/m}} = 0.0984 \text{ At}$$

Step 4.5: The Main Air Gap Area

The flux density in the main air gap from Equation 5.34 is:

$$B_{\delta} = \frac{\phi_o}{A_{\delta}} = \frac{\phi_o}{\frac{b_{p2} + b_{p1}}{2} \left(\frac{l_{pm}}{2} + l_{ST} + l_{mat} - l_o \right)} = \frac{3.2456 \times 10^{-6} \text{ Wb}}{17.469 \times 10^{-6} \text{ m}^2} = 0.1858 \text{ T}$$

The MMF drop in the main air gap from Equation 5.38 is:

$$AT_{\delta} = \frac{B_{\delta} \times \frac{D_{S1} - D_{RO}}{2}}{\mu_o} = \frac{0.1858 \text{ T} \times 0.5(26.29 \times 10^{-3} \text{ m} - 25.58 \times 10^{-3} \text{ m})}{4\pi \times 10^{-7} \text{ H/m}} = 52.514 \text{ At}$$

Step 4.6: MMF Calculations

The total MMF from Equation 5.19 is:

$$AT_2 = AT_{T1} + AT_{T2} + 2AT_T + AT_D + AT_{T\delta b} + 2AT_\delta = 4.884 \text{ At} + 4.544 \text{ At} + 2 \times 3.459 \text{ At} \\ + 1.095 \text{ At} + 2 \times 0.0984 \text{ At} + 2 \times 52.514 \text{ At} = 122.66 \text{ At}$$

Compare to the total MMF from the magnet operating point equation, Equation 5.42:

$$AT_2 = AT_4 \frac{\phi_m - \phi_o}{\phi_m} = 435.12 \text{ At} \times \frac{4.498 \times 10^{-6} \text{ Wb} - 3.2456 \times 10^{-6} \text{ Wb}}{4.498 \times 10^{-6} \text{ Wb}} = 121.21 \text{ At}$$

Because $AT_2 \approx \sum AT$ from Equation 5.19 and Equation 5.42 are within 1%, we can accept the calculated magnetic flux $\phi_o = 3.2456 \times 10^{-6} \text{ Wb}$ based on assumed flux density B_T of 1.366 T in the tooth area. Intermediate and final results for all four motors investigated are presented in Table 5.12 and Table 5.13, respectively.

Example 5.2: Static Torque Calculations

Calculate static torque for the four introduced stepper motors as presented in Figure 5.22 and Table 5.11 and Table 5.12. Use input data of motor 1 to demonstrate intermediate steps including the magnetic flux calculation and collect all intermediate and final calculation steps in Table 5.14. Show an example of the demagnetization BH curve for motor 1.

Solution to Example 5.2

All calculations will be in steps. First, the magnetic circuit will be calculated in step 1 through step 5 with all intermediate calculations tabularized for all stepper motors, motor 1 through motor 4, in Table 5.12. Next, the torque with current load demagnetization effect will be calculated for all four stepper motors. Final results are provided in Table 5.13.

The flux in the working air gap has to be calculated for the entire current range as described in the performance information section of Table 5.14. The flux shall be obtained from the BH characteristic, as presented in Figure 5.68, at the armature reaction corresponding to the current level. For this, the permeance coefficient slope and armature reaction have to be calculated first.

Step 1: Motor Permeance

First, calculate the motor permeance G_u given by Equation 5.49 and based on the linear magnet characteristic shown in Figure 5.61:

$$G_u = \frac{\phi_o}{AT_2} = \frac{3.2456 \times 10^{-6} \text{ Wb}}{121.21 \text{ At}} = 2.678 \times 10^{-8} \text{ Wb/A}$$

We take angle α_u from Equation 5.50:

$$\alpha_u = \tan^{-1} G_u \frac{m_f}{m_\phi} = \tan^{-1} 2.678 \times 10^{-8} \text{ Wb/A} \times \frac{39.56 \text{ A/cm}}{0.346 \times 10^{-6} \text{ Wb/cm}} = \tan^{-1} 3.0619 = 71.91^\circ$$

where the magnet MMF AT_2 is calculated from Equation 5.19 and m_f, m_ϕ are the multiplying factors to allow for SI units in Figure 5.68, in A/cm and Wb/cm.

Step 2: Working Point Flux

Working point flux can be obtained from the crossing point of the BH demagnetization curve (see Figure 5.68) and the load line with armature reaction corresponding to the current level. When both stators are energized, which is normal operating mode, the armature reaction can be determined from Equation 5.53:

$$F_{AR} = \frac{4}{\pi} NI k_{2F} = \frac{4}{\pi} \times 460 \times 0.1 \times 0.4847 = 28.402 \text{ A/m}$$

where NI are the coil ampere-turns and k_{2F} is the ratio of the tooth to pole active areas for positions at the maximum value of the torque developed. For each of the current increments from 0.1 A to 0.6 A, the flux at the working point can be determined from Figure 5.68, as presented in Table 5.14.

Step 3: Static Torque Calculation

Total MMF from Equation 5.18 and Figure 5.12 is:

$$T_{\max} = \frac{\sqrt{2}}{4} IN\phi P^2 = \frac{\sqrt{2}}{4} \times 0.1 \text{ A} \times 460 \times 3.036 \times 10^{-6} \text{ Wb} \times 24^2 = 2.844 \text{ Ncm}$$

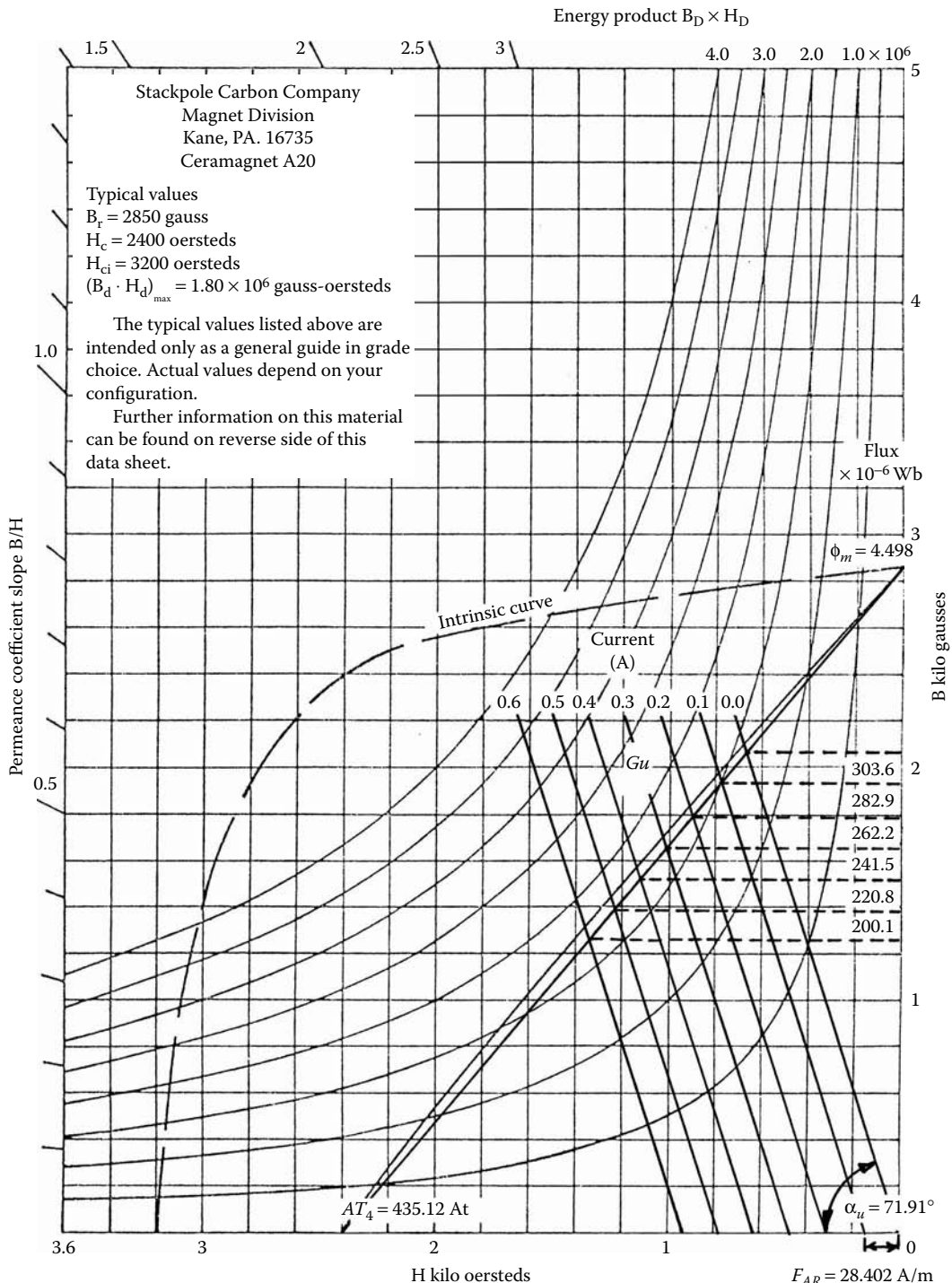
All other current points are combined in Table 5.14. This concludes Example 5.2.

Example 5.3: Magnetic Flux Calculations

Calculate the induced voltage in all four stepper motor coils. The input data for all motors are provided in Table 5.8 and Table 5.9. The tests of motor 1 through motor 4 voltage rms values $U = 2.57 \text{ V}, 5.45 \text{ V}, 1.3 \text{ V}$, and 3.925 V , respectively, were measured by turning the motors at a constant speed of 1800 rpm.

Solution to Example 5.3

From Equation 5.57, the calculated flux value from the voltage test of motor 4 is:

**FIGURE 5.68**

Magnet demagnetization curves with calculated armature reaction. (Courtesy of Ceramagnet A20, Stackpole Magnet Co., Magnet Division, Kane, PA.)

$$\phi_{\#1} = U \frac{54.019}{Nn_o P^2} = 2.57 \times \frac{54.019}{460 \times 1800 \times 24^2} = 291 \text{ Mx}$$

$$\phi_{\#2} = U \frac{54.019}{Nn_o P^2} = 5.45 \times \frac{54.019}{1000 \times 1800 \times 24^2} = 284 \text{ Mx}$$

$$\phi_{\#3} = U \frac{54.019}{Nn_o P^2} = 1.3 \times \frac{54.019}{833 \times 1800 \times 24^2} = 81.3 \text{ Mx}$$

$$\phi_{\#4} = U \frac{54.019}{Nn_o P^2} = 3.925 \times \frac{54.019}{730 \times 1800 \times 12^2} = 112.05 \text{ Mx}$$

Verify these results with Table 5.3. This concludes Example 5.3.

6

Special Magnetic Devices

The market for special magnetic devices is rapidly expanding. Growth is particularly strong in the medical area, where they are used for artificial hearts, artificial limbs, electronically operated heart valves, etc. (Glinka et al. 1995, Young and Pawlak 1990). However, as the number of applications grows, the specifications the devices are expected to meet become more and more demanding. Increasingly smaller devices are required to operate artificial hearts and limbs.

The first part of this chapter describes an electromechanical heart valve and heart pump, which are suitable to operate and control blood circulation. This electronically operated heart valve was developed to create an experimental model to study mechanisms important in pulmonary edema and heart failure (Pawlak et al. 1992, Pawlak and Young 1989). This device can control cardiac output or left atrial pressure. The heart pump described in the text was devised to maintain blood pressure and to help a person be independent of a stationary energy source. This is possible because a patient is only required to carry portable batteries that supply energy for heart operation (Lee et al. 2003, Young and Pawlak 1990).

The last part of this chapter deals with devices composed of intelligent or smart materials that are being evaluated for a variety of applications throughout the world. As basic material studies continue, an increasing number of smart materials are becoming more and more appealing. There are three known methods of controlling these materials: heat flow, electrical potential, and, the most popular, the magnetic field. These materials are divided into four categories: piezoelectric materials, magnetostrictive materials, shape memory alloys, and magnetorheological fluids.

Bringing these materials to market requires more than a clever concept and desirable applications. Above all, the devices made with smart materials must be robust and have sustained performance. Currently, low durability and excessive cost are two limiting factors for these materials. These drawbacks limit their initial introduction to niche markets with easy requirements. Therefore, the automotive market with its very severe requirements for sustained performance and low cost is a very difficult target market for intelligent materials. However, this chapter also addresses an example of a smart material (magnetorheological fluid) application in the automotive industry that can achieve sustained performance in a passenger vehicle.

6.1 Magnetic Valves

Artificial heart valves, commonly implanted in humans, are generally uncontrollable. The ability to control these valves can benefit medical research of the human heart and could be helpful in clinical cases. The controllable valve enables researchers to conduct valuable

medical studies of heart failure and related conditions involving the kidneys and lungs. Heart failure and related conditions are “a clinical problem of major importance throughout the world”; therefore, research related to these conditions is supported by the National Institutes of Health. For example, as a research tool for animal studies, the valve can be controlled so that cardiac output is reduced and pressure in the left atrium and pulmonary veins is maintained at higher than normal levels, simulating the clinical syndrome of heart failure (Young and Pawlak 1992).

A possible solution, explained in this chapter, both analytically and experimentally, is an electromagnetically controlled artificial heart valve. A mathematical model, based on FE analysis, was used to analyze electromagnetic forces exerted on a movable PM attached to the heart valve. The electromagnetically controlled heart valve configuration described represents a new family of electromechanical devices. It is based on an original concept where an electronically controlled magnetic field controls the valve position. A parametric study was conducted to optimize the geometry and performance of the heart valve to meet the requirements. A prototype unit was built to prove the concept and was tested to confirm the performance of the device.

6.1.1 Background

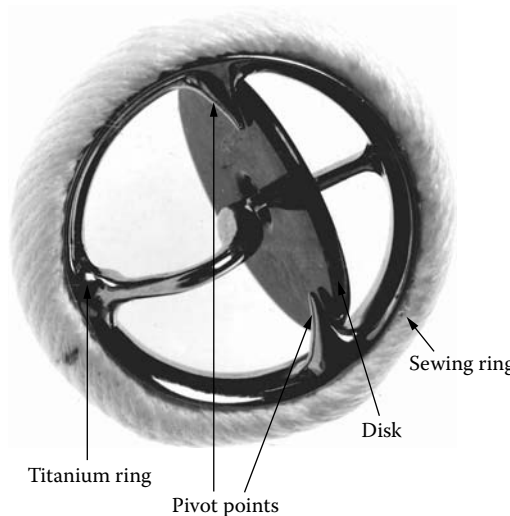
The differentiating factor of this valve is its ability to close for a certain portion of the cardiac cycle. This serves as a superior corrective device for a damaged human heart valve because prior models would simply remain open. Now, pressure in the atrium and cardiac output would be monitored at each cardiac cycle by a device reporting to a computer, which would activate the electronic regulating valve function in a manner that would maintain these variables at the desired level.

In comparison with a human heart valve, an artificial valve has considerably greater mass, causes blood cell destruction, leaks, makes noise, develops heat, and lasts a limited time. Nevertheless, commonly used artificial heart valves take the form of a caged ball, tilting disk, and bileaflet types (Chandran 1986). These valves are opened by blood flow pumped by the heart and closed by the back pressure. They also have no means of position control. The tilting disk-type valve was selected as the most suitable to accommodate an additional provision for controllability. A disk-type artificial heart valve with the tilting disk in the open position is shown in Figure 6.1.

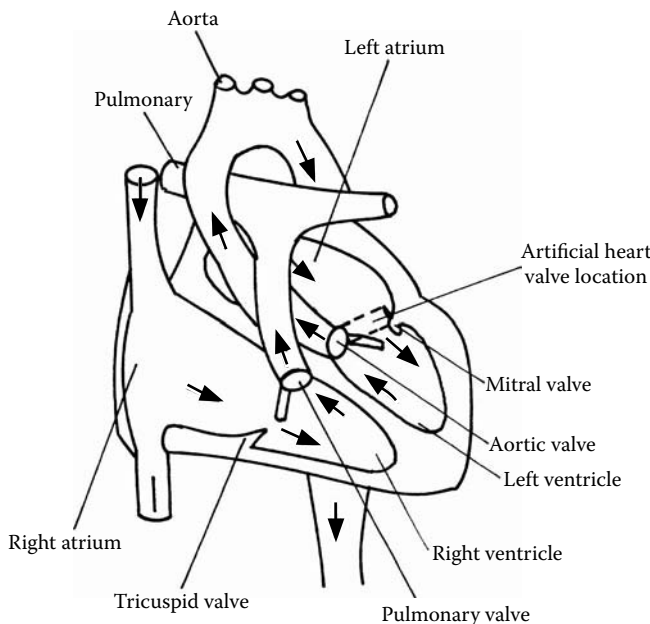
The electromechanical valve concept is based on the magnetic interaction between a PM located in the movable disk and the magnetic field produced by a stationary electromagnet located around the titanium ring and under the sewing ring, as shown in Figure 6.1. An element of dissymmetry was introduced into the PM field at the pivot support, where the holding force has its maximum value. This is because the heart valve has to remain perfectly horizontal in a fully closed position, while maintaining the blood pressure (Young and Pawlak 1992).

6.1.2 Heart Valve Requirements

A controlled heart valve has to meet four basic requirements — space, temperature, force, and duty cycle. The available space for the controllable heart valve is determined by both the size of the heart and the size of the artificial heart valve. The location of an artificial heart valve inside the human heart and the outline of the available space for the heart valve are shown in Figure 6.2. The dimensions of the available space to accommodate a controllable heart valve inside the targeted heart of a 50.0-kg sheep are a valve OD of 27.0×10^{-3} m and a valve height of 10.0×10^{-3} m.

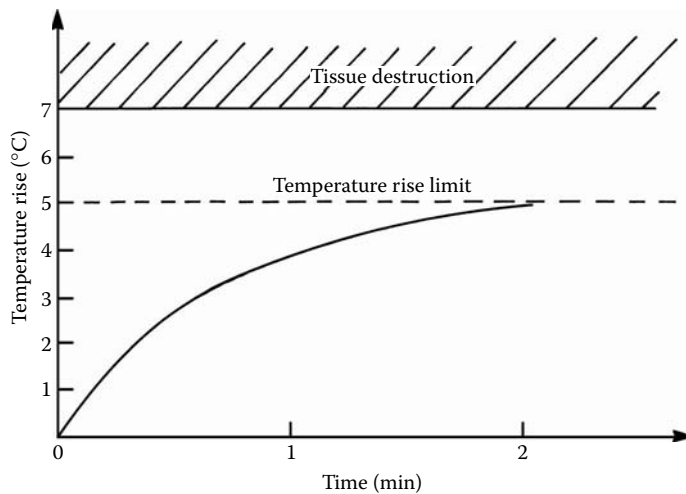
**FIGURE 6.1**

Disk-type artificial heart valve. (From Pawlak, A.M. and Young, D.B., *IEEE/IAS Transactions*, San Diego, CA, October 1–5, 1989. With permission.)

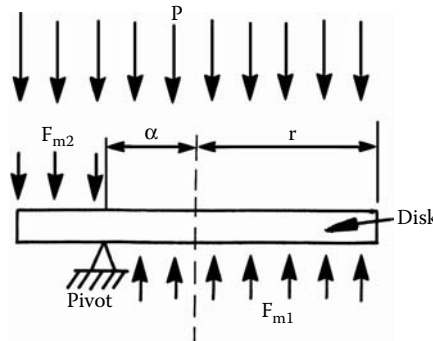
**FIGURE 6.2**

The artificial heart valve location. (From Pawlak, A.M. and Young, D.B., *IEEE/IAS Transactions*, San Diego, CA, October 1–5, 1989. With permission.)

The temperature of the electromagnetically controlled heart valve rises during operation due to copper losses in its coil. The coil temperature stabilizes when the input energy balances the dissipated heat. For a heart with a small mass, the time to reach temperature stability is about 2 min. The maximum permissible temperature rise was specified as 5.0°C .

**FIGURE 6.3**

Temperature rise vs. time. (Courtesy of Delphi Corp.)

**FIGURE 6.4**Forces exerting on the heart valve disk. (From Young, D.B. and Pawlak, A.M., *Transactions of ASAIO American Society for Artificial Internal Organs Conference*, Washington, D.C., April 17–25, 1990. With permission.)

Permanent damage to the heart tissue takes place beyond this limit, at about 7.0°C , as shown in Figure 6.3.

On command, the valve is required to develop enough force to hold the disk in a closed position against blood pressure. Because of the pivoted tilting disk structure of the valve, the effective blood pressure force acting on the disk is not simply a product of the blood pressure and the disk area. While a portion of the disk area develops positive force F_{m1} causing the valve to open, the remaining part produces a negative closing force F_{m2} , as presented in Figure 6.4. The resulting net force determines the equivalent electromagnetic force that is required to keep the valve in a closed position, against the blood pressure. This is further explained in Section 6.1.3. For example, a magnetic force of 1.08 N is required to withstand a blood pressure of 50.0 mm Hg for a valve pivot offset of 4.2×10^{-3} m and a valve radius of 8.9×10^{-3} m. A diagram of different forces exerting on the controllable heart valve disk during its operation is shown in Figure 6.4.

The length of a full cycle of the beating of the human heart depends on its pulse rate. For a typical human, the rate is 60 times per minute, which makes the length equal to 1.0 s. The pressure in the left atrium of the heart rises for 0.2 s, or 20%, of the entire cycle (Young

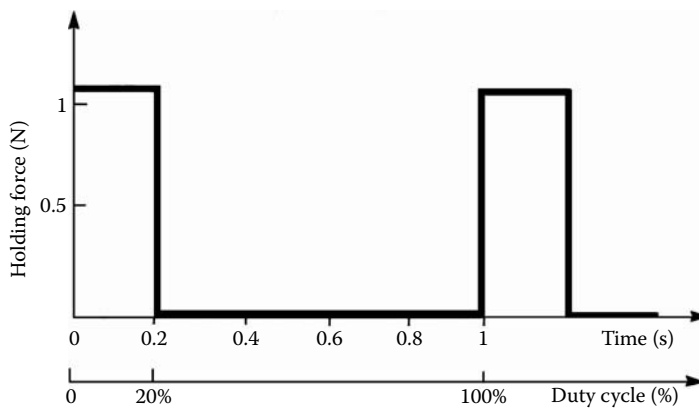


FIGURE 6.5

Heart valve force vs. time cycle operation. (From Pawlak, A.M. and Young, D.B., *IEEE/IAS Transactions*, San Diego, CA, October 1–5, 1989. With permission.)

and Pawlak 1990). During this period, the nominal current, flowing in the controlled coil, is assumed to produce the holding force required for full valve controllability, which is 1.08 N. This is shown in Figure 6.5.

6.1.3 Heart Valve Design Concept

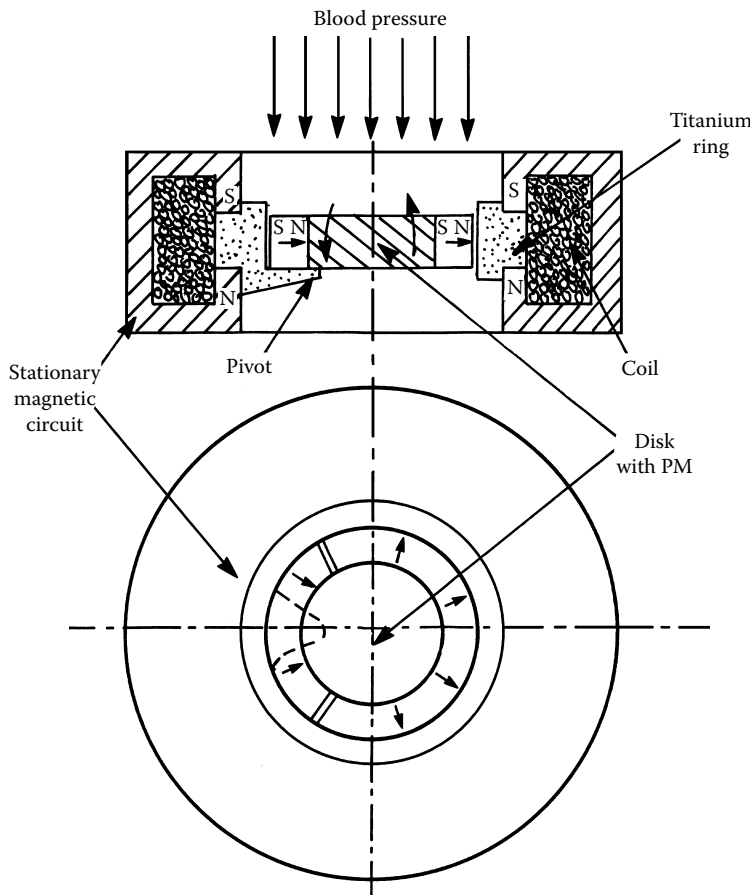
The concept of a heart valve design is based on the magnetic interaction between a radially magnetized PM ring, placed on the movable disk, and the magnetic field developed by the stationary electromagnet, placed around the titanium ring. For the heart valve to remain perfectly level while maintaining the blood pressure, the holding magnetic forces must have a different orientation at the pivot point to form a pair of forces that can withhold the blood pressure forces. This is shown in Figure 6.4. To achieve the different magnetic force directions around the pivot point, an element of dissymmetry had to be introduced into the magnetic field at the pivot support. This was accomplished by splitting the PM ring into two parts around the pivot point. To achieve a magnetic dissymmetry with full magnetic symmetry of the stationary electromagnet, both magnet ring parts were radially magnetized with different polarization. This unique configuration consists of a PM and a stationary magnetic circuit with a coil. This is shown in Figure 6.6. The polarities of the magnetic field, shown in this figure, are for the energized electromagnet and PM.

With this arrangement, the polarity of the external magnetic circuit and the PM will force the disk to close and remain closed at the level position. The holding force in this position is at its maximum value. With the reversed current direction, the polarity of the external magnetic circuit and the PM will force the disk to open. However, this function may not be used because the blood back pressure opens the valve.

The design analysis presented in this chapter is based on this concept of heart valve design. It is important to note that although this unique configuration was developed for controlling a heart valve, it has the potential to be used in other applications where control of fluid pressure and flow is desirable.

6.1.4 Mathematical Model and Simulations

The design optimization of the electromagnetically controlled heart valve requires the use of mathematical models of the electromagnetic circuit to evaluate the magnetic holding

**FIGURE 6.6**

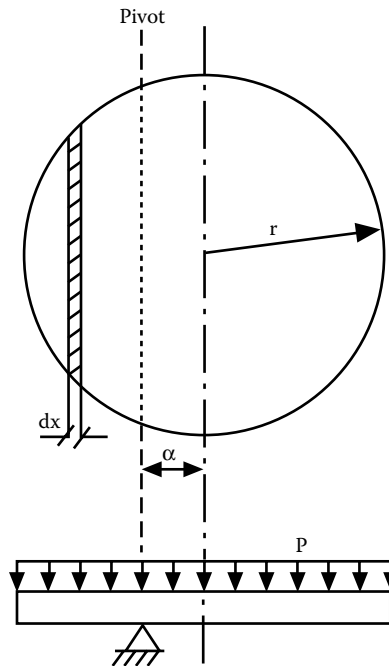
Heart valve configuration. (From Young, D.B. and Pawlak, A.M., *Transactions of ASAIO American Society for Artificial Internal Organs Conference*, Washington, D.C., April 17–25, 1990. With permission.)

force and temperature rise. The rise is due to heat dissipated by the energized coil and is critical in this application. The 2D FE software was used for modeling the magnetic field of the controlled heart valve (Nehl et al. 1988). Because of the existing axisymmetrical circuit with the disk in the horizontal position, only a radial cross section needs to be modeled to analyze the magnetic field distribution and obtain the static holding force in this position. This is indicated in Figure 6.6. The developed magnetic force with different current excitations was obtained from the Maxwell's stress tensor over the surface of the disk. It is defined by:

$$F_m = \iint_S \bar{T} \cdot d\bar{s} \quad (6.1)$$

where F_m is the magnetic force, \bar{T} is the Maxwell stress tensor in dyadic form, and S is the surface of integration.

This force assumes complete geometric and magnetic symmetry of the device. To account for the magnetic asymmetry, the force per unit length of the circumference needs to be calculated. The total magnetic force F_t can be obtained by summing up different components. This is given by Equation 6.13.

**FIGURE 6.7**

Pressure forces affecting the disk of the heart valve. (From Pawlak, A.M. and Young, D.B., *IEEE/IAS Transactions*, San Diego, CA, October 1-5, 1989. With permission.)

The total force affecting the disk of an artificial heart valve due to blood pressure can be calculated by force integration around the circumference of the disk and the moment balance around the pivot point. The disk configuration and the distribution of the pressure forces are shown in Figure 6.7.

The total pressure moment is the difference between the closing and the opening moment due to pressure:

$$M_p = M_c - M_o \quad (6.2)$$

where M_p is the total pressure moment, M_c is the closing moment, and M_o is the opening moment.

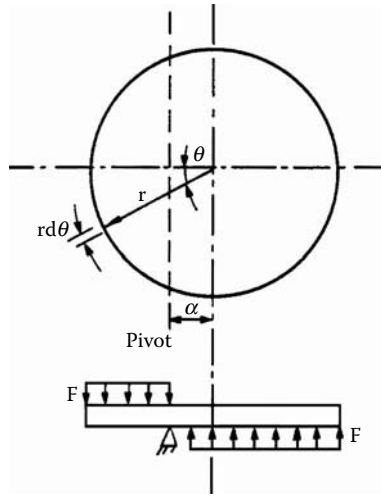
The closing moment is expressed as:

$$M_c = 2p \int_{-r}^a (r^2 - x^2)^{1/2} (x - 3) dx \quad (6.3)$$

and the opening moment is expressed as:

$$M_o = 2p \int_a^r (r^2 - x^2)^{1/2} (x - 3) dx \quad (6.4)$$

Integrating between limit values, the total pressure moment can be given by:

**FIGURE 6.8**

Magnetic forces exerting on the disk of a heart valve. (From Pawlak, A.M. and Young, D.B., *IEEE/IAS Transactions*, San Diego, CA, October 1–5, 1989. With permission.)

$$M_p = \pi r^2 \alpha p \quad (6.5)$$

The closing magnetic moment due to magnetic forces is illustrated in Figure 6.8. It is the sum of integral components:

$$M_m = 2 \left\{ \int_0^{\cos^{-1} \frac{a}{r}} dM_{m1} - \int_{\cos^{-1} \frac{a}{r}}^{\frac{\pi}{2}} dM_{m2} + \int_{\frac{\pi}{2}}^{\pi} dM_{m3} \right\} \quad (6.6)$$

where r is the radius of the disk, α is the pivot offset, and θ is the angle, which is described in Figure 6.8. F_m is the magnetic force, M_m is the closing magnetic moment, M_{m1} is component 1 of the closing magnetic moment, M_{m2} is component 2 of the closing magnetic moment, and M_{m3} is component 3 of the closing magnetic moment.

The components are:

$$dM_{m1} = F_m r d\theta (r \cos \theta - \alpha) \text{ from } \theta = 0 \text{ to } \cos^{-1} \frac{\alpha}{r} \quad (6.7)$$

$$dM_{m2} = F_m r d\theta (\alpha - r \cos \theta) \text{ from } \theta = \cos^{-1} \frac{\alpha}{r} \text{ to } \frac{\pi}{2} \quad (6.8)$$

$$dM_{m3} = F_m r d\theta (\alpha - r \cos \theta) \text{ from } \theta = \frac{\pi}{2} \text{ to } \pi \quad (6.9)$$

Integrating and clearing, the closing magnetic moment is obtained:

$$M_m = 4F_m r \left(\sqrt{r^2 - \alpha^2} - \alpha \cos^{-1} \frac{\alpha}{r} + \frac{\alpha \pi}{2} \right) \quad (6.10)$$

Solve for the force F_m around its circumference by letting:

$$M_m = M_p \quad (6.11)$$

Define the total magnetic force as:

$$F_t = 2\pi r F_m \quad (6.12)$$

By combining Equations 6.5, 6.10, and 6.12, we obtain:

$$F_t = \frac{0.5\pi^2 r^2 \alpha p}{\sqrt{r^2 - \alpha^2} - \alpha \cos^{-1} \frac{\alpha}{r} + \frac{\alpha \pi}{2}} \quad (6.13)$$

where r is the radius of the disk, α is the pivot offset, θ is the angle, F_m is the magnetic force, F_t is the total magnetic force, M_m is the closing magnetic moment, and p is the pressure.

Figure 6.9(a) shows the magnetic flux due only to the PM, and Figure 6.9(b) and Figure 6.9(c) show the resultant magnetic field due to both the PM and the stationary magnetic coil with MMF = 150.0 At and 300.0 At excitation, respectively.

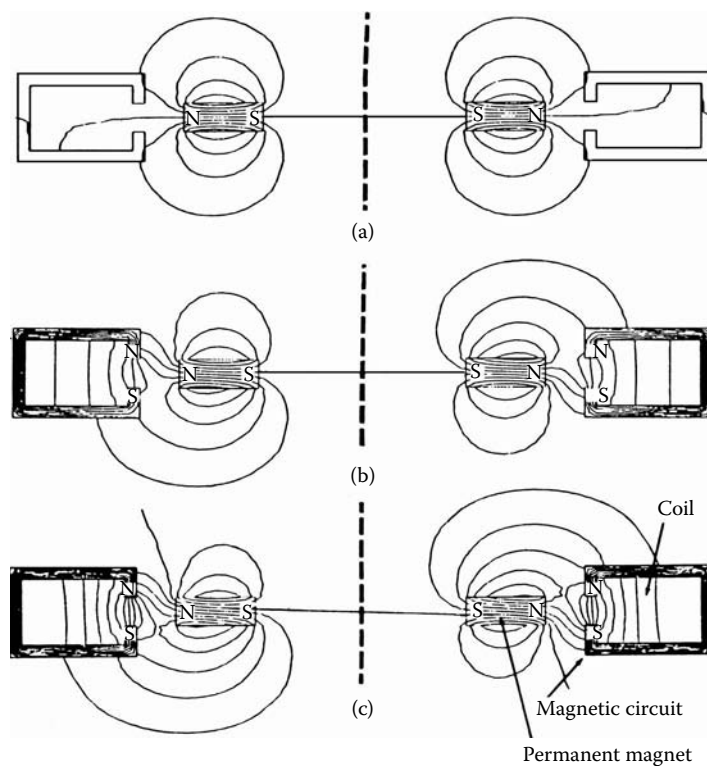
The polarities of the magnetic circuit and the flux lines indicate the magnetic force direction. The magnetic field distribution and, subsequently, the total magnetic force are calculated for different current excitations, as presented in Figure 6.10. At zero MMF of the electromagnet, the magnetic force due to the PM is zero, because the magnetic field is perfectly balanced. With higher MMF values, the external magnetic circuit of the electromagnet saturates, affecting the magnetic force.

Knowing the force required to hold the valve against the blood pressure of 50.0 mm Hg, the desired current excitation carried by the coil can be calculated. For this current, the calculations of temperature rise have to be conducted to ensure that the upper limit is not exceeded.

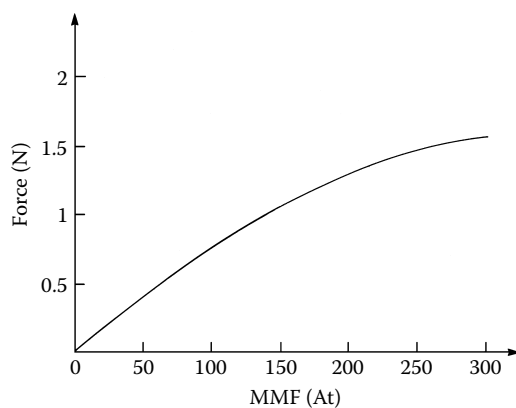
A 2D FE software can be used to evaluate the cogging forces. These forces develop due to the interaction between the PM and the magnetic core with no current excitation in the offset positions, as presented in Figure 6.11. The cogging force should not increase beyond acceptable limits, which are determined by patient comfort. A 3D magnetic field analysis is recommended for cogging force evaluation in positions different from the level position.

6.1.5 Optimized Design

The objective of design optimization is to develop the required magnetic force with the minimum coil MMF to reduce coil losses and, consequently, the coil temperature rise, without exceeding the space envelope. This is shown in Figure 6.2. To achieve this goal, aside from optimizing the geometry of the magnetic circuit and the coil, magnetic materials that have the best available qualities should be selected for the valve parts. High-density

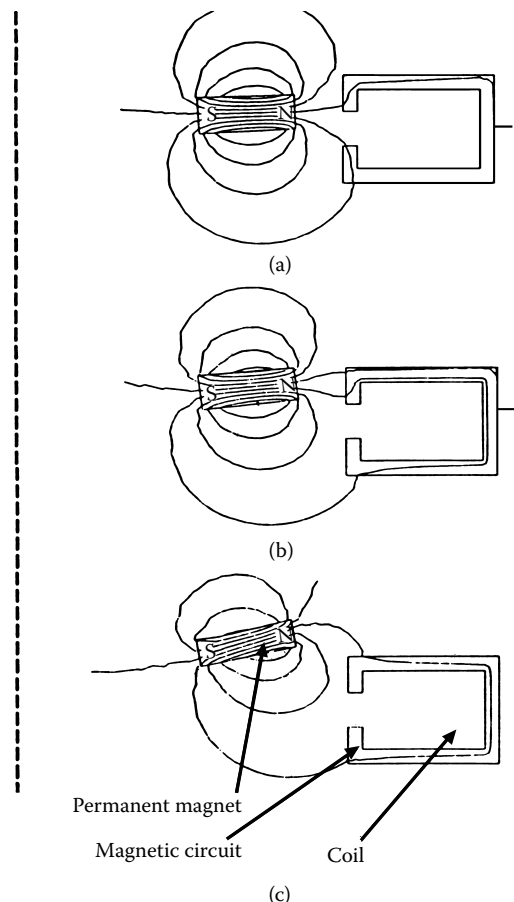
**FIGURE 6.9**

Magnetic field distribution of the heart valve for different coil excitations: (a) MMF = 0.0 At, (b) MMF = 0.150 At, (c) MMF = 0.300 At. (From Young, D.B. and Pawlak, A.M., *Transactions of ASAIO American Society for Artificial Internal Organs Conference*, Washington, D.C., April 17–25, 1990. With permission.)

**FIGURE 6.10**

Total heart valve force vs. MMF. (From Young, D.B. and Pawlak, A.M., *Transactions of ASAIO American Society for Artificial Internal Organs Conference*, Washington, D.C., April 17–25, 1990. With permission.)

energy magnets based on neodymium, such as MQ3, and the best magnetic steel for the stationary circuit, such as vanadium permandur, should be selected, as presented in Chapter 1.

**FIGURE 6.11**

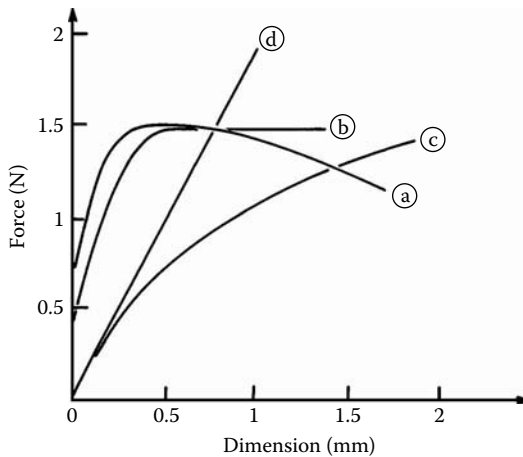
Flux distribution for the different magnet offset positions: (a) displacement 0.4×10^{-3} m, (b) displacement 0.8×10^{-3} m, (c) displacement 1.6×10^{-3} m. (From Young, D.B. and Pawlak, A.M., *Transactions of ASAIO American Society for Artificial Internal Organs Conference*, Washington, D.C., April 17–25, 1990. With permission.)

A parametric study was conducted to investigate the influence of the shape and wall thickness of the "C" core as well as the geometry of the PM. Figure 6.12(a) shows the impact of the "C" core opening on the developed force. It was found that the magnetic force has its maximum value for a "C" core with an opening equal to or slightly less than the PM thickness, in this case, 0.8×10^{-3} m.

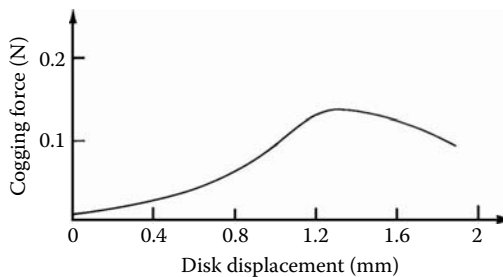
Because the magnetic force was found to increase linearly with the PM thickness keeping the constant coil MMF, as shown in Figure 6.12(d), the maximum possible magnet thickness of 0.8×10^{-3} m was selected. This is limited by the thickness of the disk (1.0×10^{-3} m) and because a certain thickness (0.1×10^{-3} m on each side of the magnet) was required to cover its surface with material to prevent blood clotting for implantable models.

PM length is limited by disk geometry, as well as by acceptable cogging forces. Increasing the PM length causes the magnetic force to first increase rapidly and then at a lower rate. This is shown in Figure 6.12(c).

By increasing the PM length up to 2.0×10^{-3} m, the total force rapidly increases up to 1.5 N. That is why this value was selected for the magnet length. Additional length increase will have a minor effect on the total force and might increase the cogging force. Values of the cogging forces for the 2.0×10^{-3} m magnet for different disk positions are given in Figure 6.13.

**FIGURE 6.12**

Magnetic force vs. dimension: (a) magnetic core opening, (b) core thickness, (c) magnet length in direction of magnetization, (d) PM thickness. (Courtesy of Delphi Corp.)

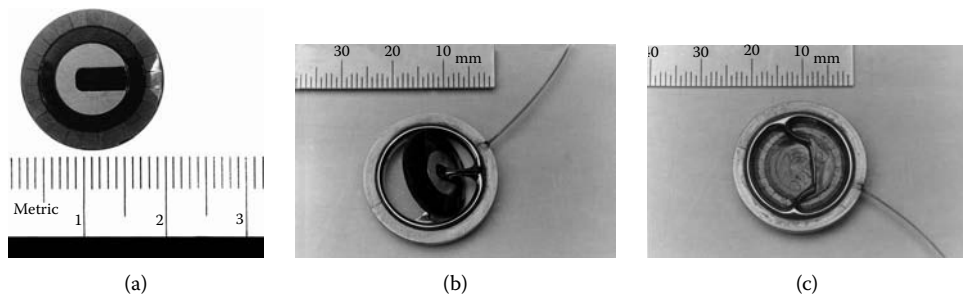
**FIGURE 6.13**

Magnetic cogging force vs. disk displacement. (From Young, D.B. and Pawlak, A.M., *Transactions of ASAIO American Society for Artificial Internal Organs Conference*, Washington, D.C., April 17–25, 1990. With permission.)

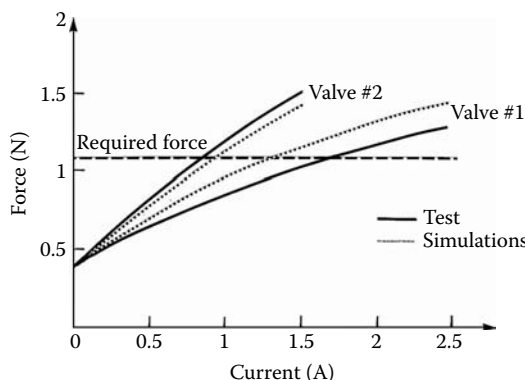
Finally, the magnetic core thickness should be optimized to provide maximum space for the coil without excessive coil saturation. The effect of core thickness on the developed force, with excitation MMF up to 200.0 A, is presented in Figure 6.12(b). It is obvious that for core thickness larger than 0.3×10^{-3} m, no appreciable increase in force is achieved. Therefore, the wall thickness of 0.3×10^{-3} m ought to be selected. This is thick enough for manufacturing, yet it provides enough space for the coil to minimize its losses.

6.1.6 Comparison and Test Results

Two different size models were manufactured, both based on the existing artificial heart valve design. During the assembly process, several compromises were made that affected the final electromagnetic force developed. The compromises concerned the valve geometry (air gap, magnet position) and magnetic material properties. The air gap in the final design had to be increased from 1.0×10^{-3} m to 1.5×10^{-3} m to accommodate the PM into the disk, thus requiring more MMF to develop the specified force. Also, the position of the PM was offset due to the concave shape of the disk. Moreover, to accommodate for the PM on the surface of such a concave disk shape, the magnet had to be split into 24 segments. This resulted in some material losses, in comparison with the full ring, as originally simulated.

**FIGURE 6.14**

Electronically controlled heart valve disk assembly: (a) disk assembly, (b) open valve assembly, (c) closed valve assembly. (Courtesy of Delphi Corp.)

**FIGURE 6.15**

Test and simulations comparison of the force vs. current. (From Young, D.B. and Pawlak, A.M., *Transactions of ASAIO American Society for Artificial Internal Organs Conference*, Washington, D.C., April 17-25, 1990. With permission.)

Also, the BH characteristic curve of the magnetic-circuit material may have been adversely altered by heating the magnetic parts to relieve the mechanical stresses of the material. The assembled electronically controlled heart valve disk and valve assembly are shown in Figure 6.14. Note the magnet segments around the disk perimeter.

The math model used here was modified to incorporate the compromises made in the design during the manufacturing process. The combined effect of all of the changes mentioned increased the cogging force and decreased the electromagnetic force for the nominal coil current. The simulation results are compared with the test results for both designs in Figure 6.15. This figure shows a good agreement between test and simulation results. It also suggests a potential for further performance improvement of geometry and magnetic materials in future design generations.

6.2 Heart Pump

A long stroke solenoid with a magnet armature concept can be adopted for the heart pump application to develop required pressure for blood circulation. The heart pump is

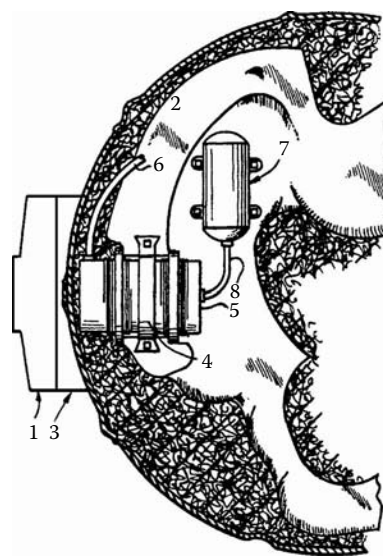


FIGURE 6.16

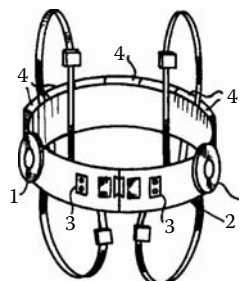
Location and components of the electromagnetically driven compressor for pneumatic artificial heart: (1) electromagnet with magnetic core and coil, (2) pelvis, (3) insulation pad, (4) cylinder holder, (5) cylinder with magnet armature, (6) tubing to artificial heart, (7) flexible bag casing, (8) tube connecting flexible storage bag and compressor cylinder.

based on a drive system for artificial hearts and left-ventricular assist devices. The drive system includes two implantable pumps driven by external electromagnets. The system consists of a pair of pumps, each coupled to a respective ventricle of an artificial heart. Each pump is mounted to the pelvic bones in the vicinity of the iliac crest, as shown in Figure 6.16. Fluid communication between the pump and its associated ventricle or left-ventricular assist device is provided by a length of flexible tubing, which extends subcutaneously up from the pump. Means are provided to enable the periodic reversal of internal system leakage and to enable replenishment of fluid lost from the system. The components of the electromagnetically driven compressor for a pneumatic artificial heart are shown in Figure 6.16. The compressor's cylinder with the magnet armature is permanently fastened to the pelvis. It faces an electromagnet from one side and a flexible storage bag on the other side. A set of tubing connects an artificial heart and a flexible storage bag. Only a thin layer of tissue and skin separates the cylinder from the electromagnet.

In its final design, the artificial heart pump needs to be totally implantable, with 10 years' life expectancy, and should allow for patient mobility. However, at present, there is no safe, available, implantable power source. Consequently, the electromagnetic heart pump must rely on an external power supply. A portable power supply enables patient mobility. The power supply, delivering electric power to a solenoid pump through the person's skin, can be worn around the waist or carried on a shoulder. Unlike this design, most of the electrically powered artificial heart designs rely on the brushless motor positioned within the thorax. The motor is mechanically coupled to a pump that pressurizes hydraulic fluid, which, in turn, activates the blood pump.

6.2.1 Heart Pump Requirements

The electromagnetic heart requirements include the development of 100.0–150.0 mm Hg of system pressure with 20.0–50.0 l/min of volume to be transferred at a frequency of 12 cycles per second. The distance between the active electromagnet and the top of the

**FIGURE 6.11**

Portable artificial heart support with electromagnets: (1) electromagnet, (2) harness, (3) switches with DC/DC converter, (4) batteries.

linear pump is 30.0×10^{-3} m. This distance corresponds to the thickness of a pad separating the electromagnet and the skin, as well as the skin and tissue that the electromagnetic field has to penetrate to operate the magnet piston. A portable battery set provides a minimum discharge time of 4 h for patient mobility. For patient comfort, the total weight of the entire system should not exceed 10.0 kg. The system includes a battery set, a DC/DC converter with controller, and two electromagnets. This system is shown in Figure 6.17.

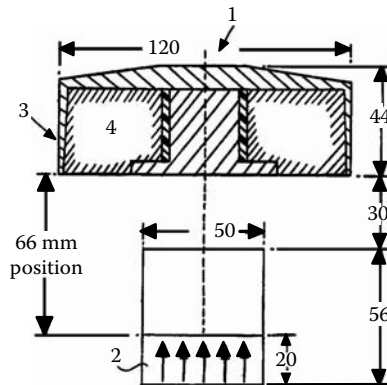
6.2.2 Heart Pump Design Concept

The investigated concept relies on the transfer of energy across the skin by an external electromagnet, which is positioned over a linear pump with an active PM piston armature implanted within the body. This concept, illustrated in Figure 6.16 and Figure 6.17, includes an electromagnet located external to the body and an implanted compressor cylinder with a magnet armature. The pump is anchored to the outside of the pelvic bone, but rests under the skin, on both sides of the body, slightly below the waist. Therefore, the pumping function is moved to the pelvic area, and the distributing heart function is maintained in the heart cavity of the chest area.

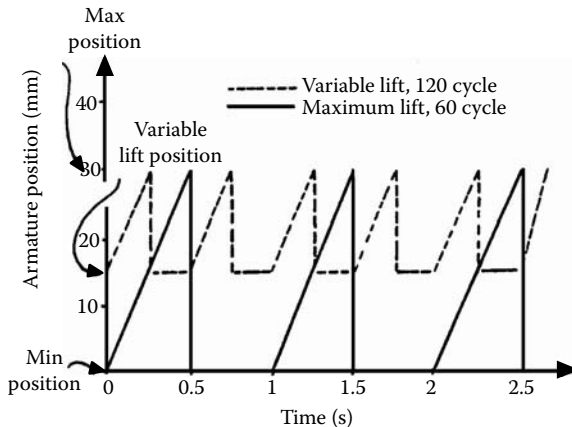
The cylinder would be connected to the pneumatic chamber of the Jarvick artificial heart by a length of flexible tubing from one side and to a flexible storage overflow bag from the other side of the pump. One of these cylinders would be implanted on each side of the body. Because there are two of the same pump, they can support each other or, in a failure mode, they can be utilized separately. An active PM movable piston armature, dynamically coupled with the magnetic field of an outside-the-body solenoid, provides linear motion activating the pumping action. An electromagnet located outside of the skin, over the cylinder, could be activated intermittently to attract the piston. When the piston is attracted to the electromagnet, it would compress the air or liquid media in the cylinder, thereby providing the force for the pumping cycle of the artificial heart. The movement of the armature piston could be reversed to aid in the filling of the heart by reversing the flow of the current in the electromagnet, thereby repelling the piston armature and reducing the pressure in the cylinder and in the artificial heart. The electromagnets could be held in place over the cylinders by a belt or girdle worn by a subject, as illustrated in Figure 6.17. Large electromagnets could be fitted in a chair or a bed, in which the patient could sit or lie, if he or she wants to rest and remove the wearable units.

6.2.3 Analytical Simulations and Optimized Design

Electromagnetic heart requirements include an electromagnet, a battery, a DC/DC converter with a controller and a heart pump system. The electromagnetic heart pump components and dimensions are shown in Figure 6.18. The distance of 30.0×10^{-3} m between

**FIGURE 6.18**

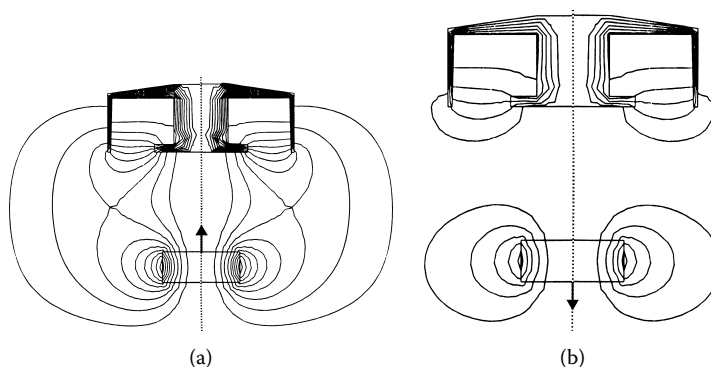
Electromagnetic heart pump configuration: (1) electromagnet, (2) PM with direction of magnetization at the bottom of the cylinder, (3) ferromagnetic housing, (4) coil.

**FIGURE 6.19**

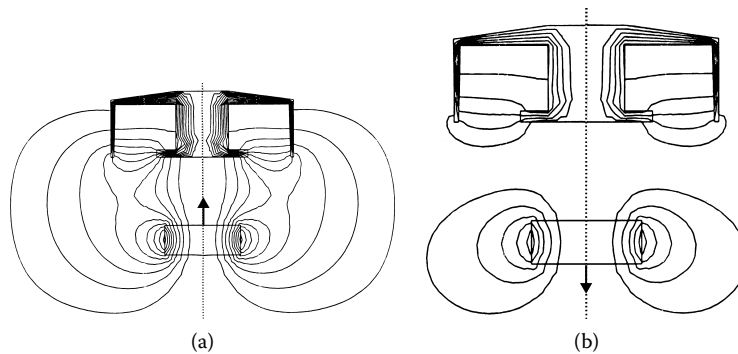
Armature position vs. time.

a cylinder and an electromagnet is required for the thickness of the skin and insulation pad with a thickness of 10.0×10^{-3} m. The large distance of the electromagnet to the armature implies a large ratio of the electromagnet diameter to the armature diameter. In our case, the ratio for original design is about 2.4. This would help secure a sufficient magnetic field penetration for the total distance between the external electromagnet and the implanted PM armature, which equals 66.0×10^{-3} m. The system has to meet all of the artificial heart requirements. Therefore, the system has to have a volume of 70.0 ml, which would be secured by cylinder size, as well as an armature stroke and pressure of 150.0 mm Hg, which is supported by a force level developed in the magnet armature. The system can operate in two armature lift modes, as shown in Figure 6.19, which illustrates a variable lift mode of operation with 120 cycles per minute and the maximum lift mode with 60 cycles per minute.

The mathematical model simulations should be approached using the cylindrical symmetry 2D FE model and the procedure described in Chapter 3. The two extreme stroke positions must be analyzed first. For an original heart pump design, these two critical points are at the top (35.0×10^{-3} m, which includes the thickness of the cylinder) and at

**FIGURE 6.20**

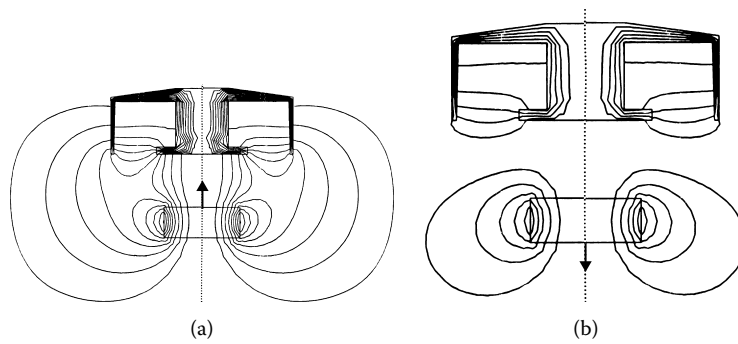
Flux lines for the heart pump at the maximum distance: (a) attractive forces, (b) repulsive forces.

**FIGURE 6.21**

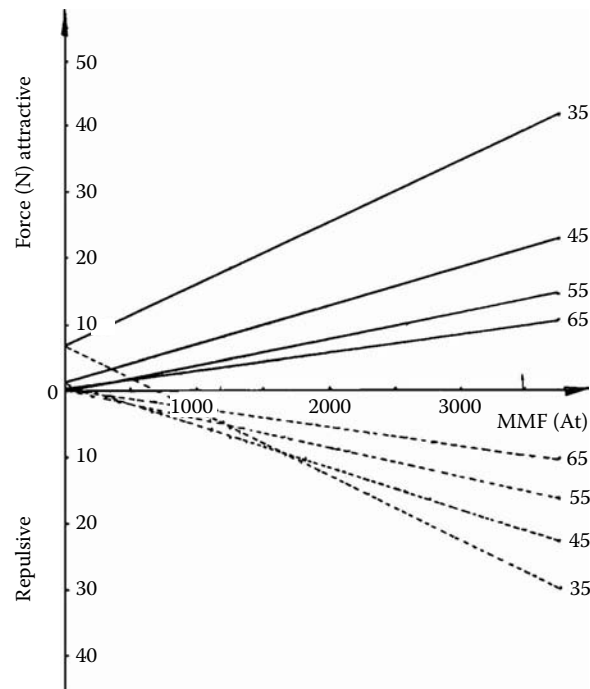
Flux lines for the heart pump at the intermediate distance: (a) attractive forces, (b) repulsive forces.

the bottom (66.0×10^{-3} m) of the armature position, as presented in Figure 6.22 and Figure 6.20, respectively. At least three intermediate points should be simulated. In our case, one median point (45.0×10^{-3} m) was simulated to obtain the magnetic force characteristics developed in the armature as a function of MMF. This is shown in Figure 6.21. All of these points contribute to the force vs. magnetomotive characteristic for both attractive and repulsive force directions. This is shown in Figure 6.23. Repulsive and attractive forces are controlled by the direction of the current. The current profile that corresponds to the pump operation and ensures smooth pump operation maintains the proper level of forces to generate adequate and stable pressure in the artificial Jarvick heart. The current rises quickly at the maximum position, developing attractive forces with the shape corresponding to the profile of the current. It changes its sign at the minimum distance, causing the force to reverse its sign. The generated repulsive force has a reduced value, which is needed to develop low off pressure for the Jarvick artificial heart. Figure 6.24 indicates the current vs. time profile. The current has to maintain the same current profiles from cycle to cycle to stabilize the pressure in the Jarvick artificial heart.

For the original design, the maximum force level of 39.3 N was achieved. This is sufficient to develop the required pressure of 150.0 mm Hg with the average power consumption of 42.0 W and the corresponding average current of 1.06 A. The force developed by the magnet armature can be expressed as:

**FIGURE 6.22**

Flux lines for the heart pump at the minimum distance: (a) attractive forces, (b) repulsive forces.

**FIGURE 6.23**

Force in armature vs. MMF at different armature positions: $35.0, 45.0, 55.0$, and 65.0×10^{-3} m.

$$F_a = p \times S_{pm} = p \times \frac{\pi D_{pm}^2}{4} \quad (6.14)$$

Pump cylinder volume:

$$V_c = \frac{V_r}{f_p} \quad (6.15)$$

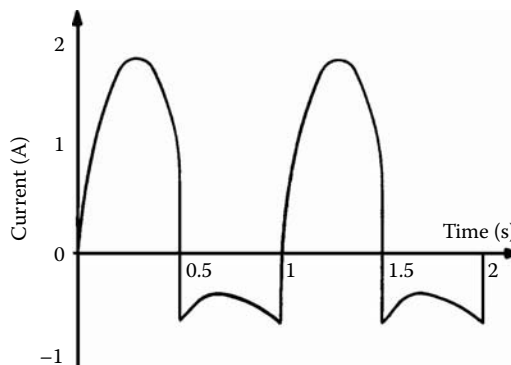


FIGURE 6.24
Current vs. time profile.

Pump cylinder ID:

$$D_c = 2\sqrt{\frac{V_c}{\pi h_s}} = 2\sqrt{\frac{V_r}{\pi h_s f_p}} \quad (6.16)$$

For this design $D_c = D_{pm}$ by combining Equation 6.14 and Equation 6.16, we have:

$$F_a = \frac{pV_r}{h_s f_p} \quad (6.17)$$

where F_a is the force developed in the armature, p is the required pressure, S_{pm} is the magnet surface, D_{pm} is the magnet OD, D_c is the cylinder ID, V_r is the total required volume, V_c is the volume of the cylinder for one cycle, f_p is the cycle frequency, and h_s is the magnet stroke.

The temperature rise in the electromagnet can be calculated from the total power P_t that needs to be dissipated over the surface of the electromagnet S , taking into account a thermal dissipation coefficient of the material k :

$$\Delta\theta = \frac{P_t}{kS} \quad (6.18)$$

The temperature rise in the original design did not exceed 130.0°C. This may be managed by using insulating materials and fins designed to dissipate excessive heat. The original pressure requirements of 150.0 mm Hg were reduced to 100.0 mm Hg. Also, the volume of 50.0 l/min at 12 cycles per second was reduced to 20.0 l/min. This is shown in Table 6.1. Additional improvements were possible because modern coil winding technology and high-energy magnetic materials with 30, 40, and 50.0 MGOe were used, as well as requirement changes. The improved design variables include armature material, stroke, and diameter, as well as the electromagnet diameter and its height. This is shown in Table 6.2. The stroke controls the volume and the maximum distance from the electromagnet. The force developed in the armature for the improved design is presented in Figure 6.25. The armature magnet diameter of 50.0×10^{-3} m was selected because the force of 26.2 N with the surface of 1962.0×10^{-6} m² can develop the required pressure.

TABLE 6.1

Design Parameters and Heart Pump Requirements

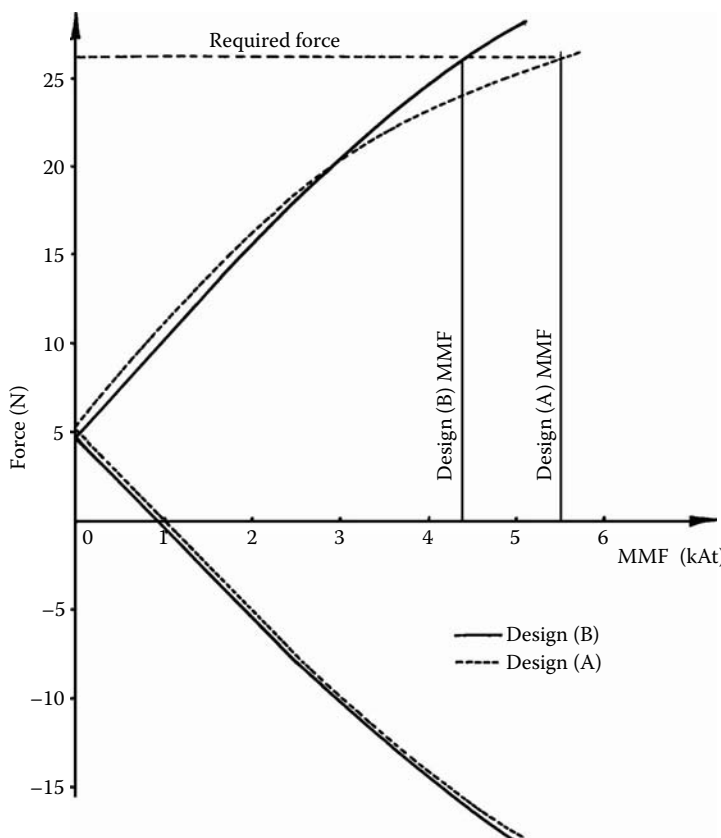
Parameter	Unit	Design		
		Original Design	Improved Design	Final Design
<i>External Electromagnet</i>				
Outside diameter OD	$\times 10^{-3}$ m	120.0	80.0	80.0
Total height	$\times 10^{-3}$ m	44.0	44.0	25.0
Coil area	$\times 10^{-6}$ m ²	1490.0	979.0	302.5
Wire diameter	AWG	24	24	29
Number of turns	#	3500	2300	3523
Coil resistance @ 20°C	Ω	39.0	22.6	129.9
Current, average	A	1.06	1.2	0.48
Current, maximum	A	1.80	2.38	0.96
Power, average	W	42.0	32.57	48.9
Temperature rise	°C	113.0	128.3	130.0
Heat sink	$\times 10^{-4}$ m ²	none	27.0	172.8
Displacement	$\times 10^{-3}$ m	35.6	14.2	22.1
Total volume	$\times 10^{-4}$ m ³	500.0	221.0	125.0
<i>Magnet Armature</i>				
Outside diameter OD	$\times 10^{-3}$ m	50.0	50.0	40.0
Total height	$\times 10^{-3}$ m	20.0	5.0	4.0
Magnet material	MGsOe	30.0	40.0	50.0
Back iron	$\times 10^{-3}$ m	no	2.0	2.0
<i>System Requirements</i>				
Cylinder volume	$\times 10^{-3}$ L	70.0	27.78	27.78
Liquid volume transfer rate	L/min	50.0	20.0	20.0
Frequency of operation	Hz	12.0	12.0	12.0
Developed pressure	mmHg	150.0	100.0	100.0
Force	N	39.3	26.2	16.75

TABLE 6.2

Design Variations

Armature		Design										
Parameter	Unit	20.0	25.0	30.0	35.0	40.0	45.0	50.0	55.0	60.0	65.0	70.0
Diameter	$\times 10^{-3}$ m	20.0	25.0	30.0	35.0	40.0	45.0	50.0	55.0	60.0	65.0	70.0
Surface	$\times 10^{-6}$ m ²	314.0	490.6	706	961.6	1256	1589	1962	2375	2862	3317	3846
Stroke	$\times 10^{-3}$ m	88.46	56.62	39.32	28.89	22.1	17.47	14.2	11.7	9.83	8.38	7.22
Force	N	4.20	6.50	9.40	12.80	16.75	21.10	26.20	31.70	37.70	44.25	51.30

For the complete final design, the armature magnet diameter of 40.0×10^{-3} m was selected because the force of 16.75 N with the surface of 1256.0×10^{-6} m² can develop the required pressure. The force developed by the armature must balance the required pressure and is a function of the cylinder volume, armature stroke, and frequency of operation. Using these dependencies, Equation 6.14 through Equation 6.17, we can calculate the design variation for different ODs of a magnet for the final design, as presented in Table 6.2. The selected stroke of 22.1×10^{-3} m provides the required volume of 20.0 l/min at 12 cycles per second. The electromagnet has a reduced diameter from the original 120.0×10^{-3} m to 80.0×10^{-3} m. In improved designs, the electromagnet height is also reduced from 44.0 $\times 10^{-3}$ m to 25.0

**FIGURE 6.25**

Test and analysis of the force vs. MMF for the heart pump improved design.

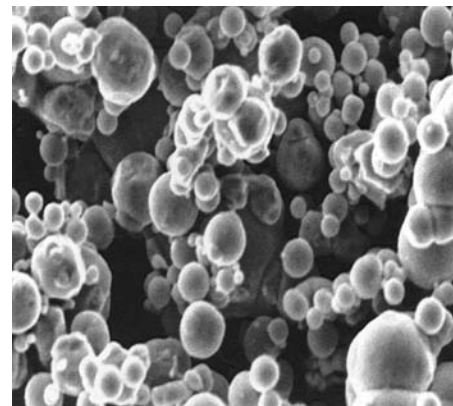
$\times 10^{-3}$ m. The final design is magnetically efficient; it has the best magnetic materials for components, as well as minimum weight and energy consumption.

6.3 Magnetorheological Fluid Solenoids

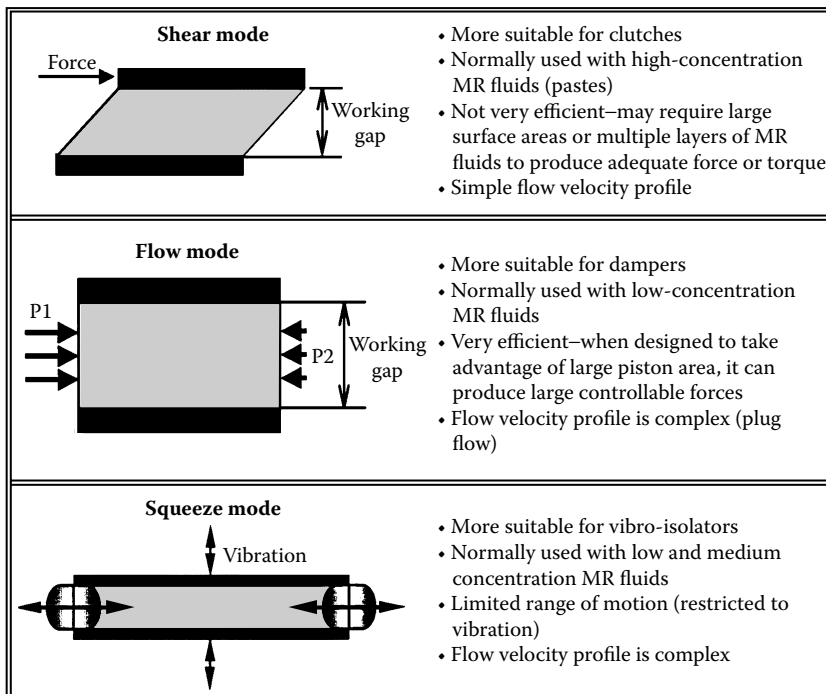
Magnetorheological fluid solenoids are solenoid actuators that collaborate with the magnetorheological fluid as an active magnetic medium to change fluid viscosity or sheer forces (Alexandridis 2000, Rabinow 1951). Although this technology was discovered half a century ago, it was not practical until the 2002 introduction of the semi-active suspension MagneRide™ system for the Cadillac STS (Delphi 2002).

6.3.1 Background

Magnetorheological fluid is a suspension of fine, magnetizable, soft iron particles in a synthetic hydrocarbon- or silicone-based fluid. Ferromagnetic particles are usually very small carbonyl iron microspheres, with a diameter size in the range of 3.0–10.0 μm . This is shown in Figure 6.26. To enhance suspension stabilization and to reduce the sedimentation effect, the surface of the particles may be chemically treated with surfactants. The base

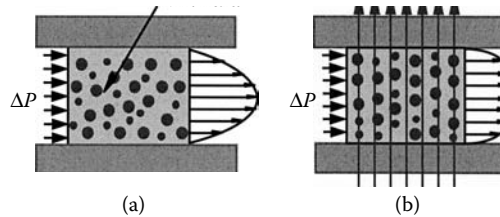
**FIGURE 6.26**

Magnetorheological fluid. (Courtesy of Delphi Corp.)

**FIGURE 6.27**

Magnetorheological fluid modes of operation: (top) shear mode, (center) flow mode, (bottom) squeeze mode. (From Alexandridis, A.A., Vehicle Electronic Systems 2000 European Conference and Exhibition, Stratford-upon-Avon, U.K., June 29–30, 2000. With permission.)

liquid is selected to ensure that the magnetorheological fluid has an appropriate operating temperature range. The percentage amount of iron particles depends on the application and may vary from about 20 to 40%. Depending on the application, to protect mechanical components such as bearings and seals, friction-reducing and antiwear additives may be included in the magnetorheological fluid formulation (Tung et al. 2002, Vardaraian et al. 2004). Depending on the application, the magnetorheological fluid devices operate in three different modes: shear mode, flow mode, or squeeze film mode, as shown in Figure 6.27

**FIGURE 6.28**

The effect of the magnetic field upon magnetorheological fluid: (a) no magnetic field, (b) magnetic field applied. (From Alexandridis, A.A., Vehicle Electronic Systems 2000 European Conference and Exhibition, Stratford-upon-Avon, U.K., June 29–30, 2000. With permission.)

(Alexandridis 2000). The sheer mode is most suitable for magnetorheological clutches and applications where magnetized particles, using their sheer forces, would connect and drag along a nondriven magnetic element. For these applications, the volume of magnetic particles is in the high percentage range. The flow mode is more suitable for active suspension applications because the pressure difference ($P_1 - P_2$) of the initiating flow is directly proportional to the fluid yield stress. The fluid yield stress, in turn, is directly controlled by the magnetic flux density. For these applications, the volume of magnetic particles is in the low percentage range. The squeeze film mode is best suited for vibration isolation devices, where small displacements are present. For these applications, the volume of magnetic particles is in the medium to low percentage range.

Without the presence of a magnetic field, magnetorheological fluid is a random dispersion of magnetizable particles and can be expressed by Newtonian rheological behavior:

$$\tau = \mu \times \dot{\gamma} \quad (6.19)$$

where τ is sheer stress, μ is viscosity, and $\dot{\gamma}$ is the sheer rate.

The application of a magnetic field affects the internal structure of the magnetorheological fluid. The magnetic field, which is perpendicular to the original flow direction of the magnetorheological fluid, aligns the magnetic particles along the lines of the magnetic force. The magnetic forces that are developed between the particles resist the sheering in the original line of flow, which is perpendicular to the magnetic field. As a result, the magnetorheological fluid behavior can now be described by Bingham plastic:

$$\tau = \tau_o + \mu \times \dot{\gamma} \quad (6.20)$$

where τ_o is yield stress.

The yield stress is directly controlled by the applied magnetic field, whereas the viscosity is not altered by the magnetic field. The magnetorheological effect is fast, with the response time much less than 1.0 ms, and reversible. Also, it is temperature independent over a wide temperature range because only the liquid phase of the magnetorheological fluid is affected by temperature changes. The effect of the magnetic field upon magnetorheological fluid is illustrated in Figure 6.28.

6.3.2 Magnetorheological Fluid Solenoid Actuator

Magnetorheological fluid dampers have been designed both as shock absorbers and as MacPherson struts for use in passenger vehicles. They are gas-pressurized, single-tube

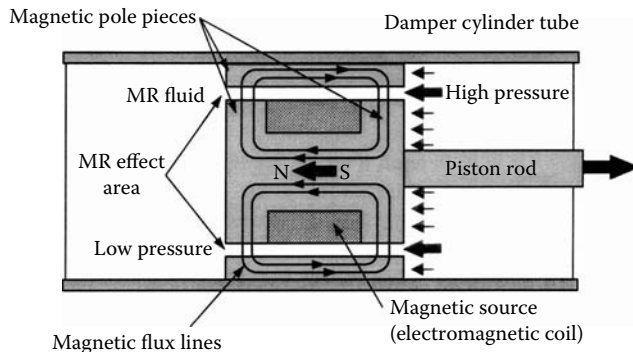


FIGURE 6.29

Cross section of the damper cylinder tube with magnetic flux lines. (From Alexandridis, A.A., Vehicle Electronic Systems 2000 European Conference and Exhibition, Stratford-upon-Avon, U.K., June 29–30, 2000. With permission.)

dampers and contain no valves of any kind. The magnetorheological fluid is separated from the nitrogen gas by a floating piston. The control of the magnetorheological fluid flow takes place in the main piston of the damper. The principle of operation, with the absence and presence of the magnetic field, is illustrated in Figure 6.28 and Figure 6.29. The MagneRide actuator is a single-tube design. The main piston incorporates an annular flow passage that can be magnetized by an electromagnetic coil. The magnetization is in the radial direction (perpendicular to the flow) and concentrated on both sides of the coil. Although the fluid spends only a very short time in the annulus, the forces measured are very close to those predicted, assuming a steady-state, laminar flow.

Typical actuator configurations of a MacPherson strut and a real shock absorber with integrated air leveling are shown in Figure 6.30. The magnetorheological fluid main piston shown in Figure 6.31 incorporates an annular flow passage, which can be magnetized by an electromagnetic solenoid with coil. The magnetization is in the radial direction (perpendicular to the flow) and concentrated on both sides of the coil. During the dynamic operation, the fluid spends only a very short time in the annulus, yet the mathematical models allow for very good predictions of the forces, assuming a steady-state, laminar flow.

The 3D mathematical models are adopted for simulations and optimization of the magnetorheological fluid solenoid actuators. Typical findings are yield stress as a function of the flux density in the magnetorheological fluid passage and magnetorheological fluid viscosity as a function of temperature without the presence of the magnetic field. This would provide an opportunity to predict the dynamic behavior of the magnetorheological fluid actuators. An example of such an analysis is shown in Figure 6.31. This example includes both the flux-density level, indicated by the gray in the graph, as well as the magnetic flux lines and directions, indicated by arrows that circulate around the field source: a coil with current. Both static and dynamic analyses are important; however, it is the dynamic behavior that is a critical feature of the magnetorheological fluid actuators.

6.3.3 MR Fluid Applications

Magnetorheological fluids are ideal media for controlled dampers and torque transfer devices. There have been a number of attempts to use this technology in a variety of applications and markets. These include washing machines, earthquake proofing buildings in construction, exercise equipment, and prosthetics in the medical industry. Attempts



FIGURE 6.30 (Color Figure 6.30 follows p. 294.)

Cutaway of the MacPherson strut and cross section of the damper cylinder tube. (Courtesy of Delphi Corp.)

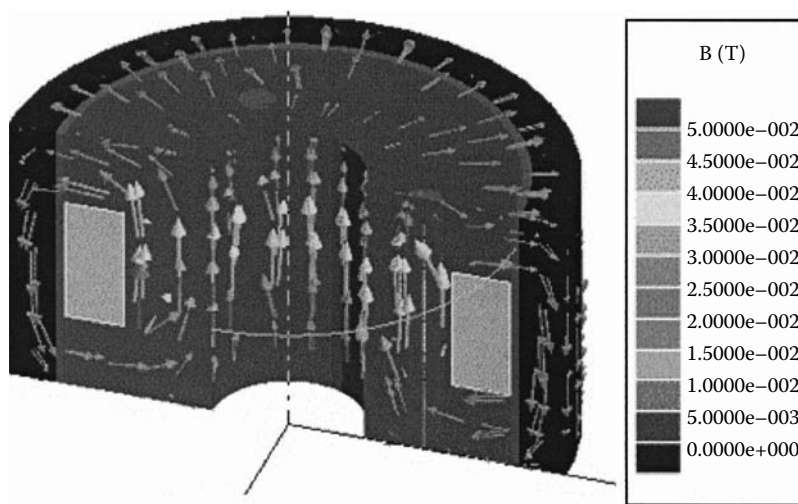
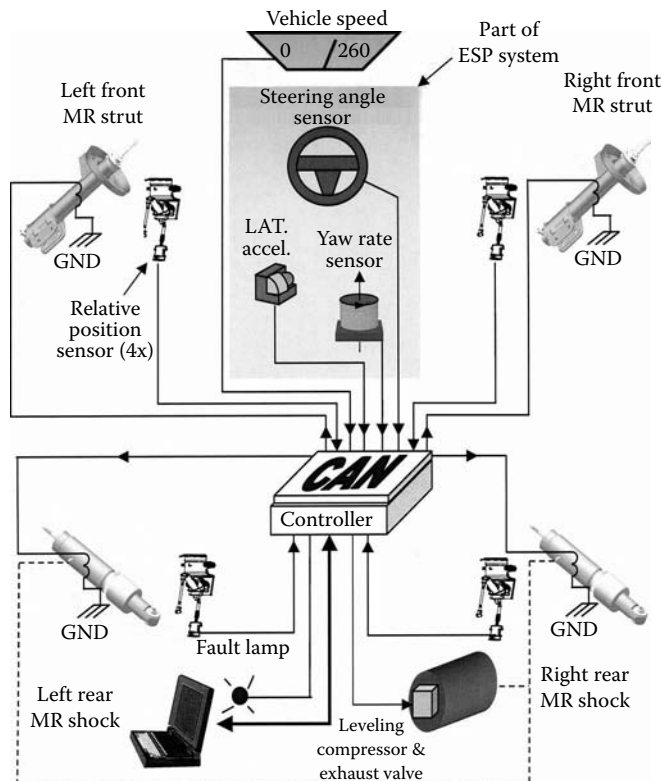


FIGURE 6.31 (Color Figure 6.31 follows p. 294.)

The 3D magnetic analysis of the magnetorheological fluid actuator. (Courtesy of Delphi Corp.)

have been made to use magnetorheological fluid in industrial and military applications, but the only successful application to date is the MagneRide system in the automotive industry. This technology is currently in production in very high-end automotive suspension systems (Delphi 2002).

As described earlier, the three areas of magnetorheological fluids applications are closely related to the magnetorheological fluid modes of operation:

**FIGURE 6.32**

MagneRide system components. (From Alexandridis, A.A., Vehicle Electronic Systems 2000 European Conference and Exhibition, Stratford-upon-Avon, U.K., June 29–30, 2000. With permission.)

1. The sheer mode is best suited for magnetorheological clutches and exercise equipment applications, where magnetized particles are using their sheer force. This mode is not very efficient because it may require very big surface areas or multiple layers of magnetorheological fluid to produce sufficient sheer or drag forces.
2. The fluid yield stress, in turn, is directly controlled by the magnetic flux density and it has a limited range of motion, restricted to the vibration. This mode is suitable for earthquake proofing buildings or engine mounts, where displacements are relatively small.
3. The flow mode is more suitable for the active suspension applications because the pressure difference ($P_1 - P_2$) of the initiating flow is directly proportional to the fluid yield stress. This mode is very efficient and it can provide large controllable forces when designed for large piston areas.

MagneRide is the first reliable, proven, mass-production system that truly utilizes the capabilities of the flow mode of magnetorheological fluid, as shown in Figure 6.32 (Delphi 2002). The result was simultaneous technical advances in intelligent materials, design optimization, and chassis control algorithms. The system provides a very wide range of damping force control with unparalleled responsiveness and high authority. The new technology overcomes the traditional trade-off between ride and handling. By enabling continuous, real-time damping control, the system increases control of vehicle motions for a flat ride and precise handling, as well as enhances road holding, for improved wheel

control and a safer, more secure ride. It also provides control — load transfer characteristics for improved road control and handling during transient maneuvers and improved road isolation — by reducing the transmission of high-frequency road disturbances through the dampers.

The MagneRide system both isolates and smooths the action of each of the tires. The combining effect is less bouncing, vibration, and noise. On gravel or slippery roads, MagneRide integrates with TC to ensure maximum stability. MagneRide works with ABS brakes to help keep the car poised and balanced for positive stopping power. The MagneRide system architecture is shown in Figure 6.32. Stand-alone operation requires four relative position sensors, vehicle speed, and steering wheel displacement. When the ABS/TC system is available, the MagneRide system controller shares the additional sensor information with other systems. If leveling is required, the MagneRide controller and sensors also handle the leveling function. The system collaborates with a number of vehicle sensors to provide input to the central controller, which independently controls each of the tires of the vehicle. The controller collaborates with the other ride and handling systems, such as ABS for braking and TC for acceleration maneuvers. The control action is executed by four MagneRide dampers.

Example 6.1

Calculate a required electromagnetic force to balance the blood pressure force against 50 mm Hg for three different valves, as described in Table 6.3.

From Equation 6.13, we can calculate the force in valve type 1:

$$\begin{aligned}
 F_{t\#1} &= \frac{0.5\pi^2 r^2 \alpha p}{\sqrt{r^2 - \alpha^2} - \alpha \cos^{-1} \frac{\alpha}{r} + \frac{\alpha\pi}{2}} \\
 &= \frac{0.5 \times \pi^2 \times 9.0 \times 10^{-3} \times 2.5 \times 10^{-3} \times 50 \times 10^{-3}}{\sqrt{(9.0 \times 10^{-3})^2 - (2.5 \times 10^{-3})^2} - 2.5 \times 10^{-3} \times \cos^{-1} \left(\frac{2.5 \times 10^{-3}}{9.0 \times 10^{-3}} \right) + \frac{2.5 \times 10^{-3} \pi}{2}} \\
 &= 0.69 \text{ N}
 \end{aligned}$$

and using the same equation for type 2 and type 3, we have $F_{t\#2} = 1.6 \text{ N}$ and $F_{t\#3} = 1.08 \text{ N}$, respectively.

TABLE 6.3

Valve Dimensions

Valve Type	Offset ($\times 10^{-3} \text{ m}$)	Radius ($\times 10^{-3} \text{ m}$)
1	2.5	9.0
2	4.9	11.0
3	4.2	8.9

Source: Courtesy of Delphi Corp.

Example 6.2

Calculate the required electromagnetic force to develop the blood pressure force against 150.0 mm Hg and 100.0 mm Hg for the original and final heart pump designs, as described in Table 6.1.

For the original design:

$$F_a = p \times \frac{\pi D_{pm}^2}{4} = 0.02 \text{ N/m}^2 \times \frac{\pi (50.0 \times 10^{-3} \text{ m})^2}{4} = 39.25 \text{ N}$$

For the final design:

$$F_a = p \times \frac{\pi D_{pm}^2}{4} = 0.01334 \text{ N/m}^2 \times \frac{\pi (40.0 \times 10^{-3} \text{ m})^2}{4} = 16.75 \text{ N}$$

Please check with the results in Table 6.1.

Example 6.3

Calculate the required cylinder volume per cycle and temperature rise for the original and final designs, as described in Table 6.1.

The original design cylinder volume supports the blood volume requirement of 50.0 l/min:

$$V_c = \frac{V_r}{f_p} = \frac{50 \times 10^3 \text{ ml}}{60 \text{ s} \times 12 \text{ [1/s]}} = 69.44 \text{ ml}$$

Final design cylinder volume was designed to support the blood volume requirement of 20.0 l/min:

$$V_c = \frac{V_r}{f_p} = \frac{20 \times 10^3 \text{ ml}}{60 \text{ s} \times 12 \text{ [1/s]}} = 27.78 \text{ ml}$$

Original design temperature rise:

$$\Delta\theta = \frac{P_t}{kS} = \frac{42.0 \times 24.5^2}{0.008 \times \left(\frac{\pi \times 120.0^2}{4} + \pi \times 120.0 \times 44.0 \right)} = 113.0^\circ\text{C}$$

Final design temperature rise:

$$\Delta\theta = \frac{P_t}{kS} = \frac{48.9 \times 24.5^2}{0.008 \times \left(\frac{\pi \times 80.0^2}{4} + \pi \times 80.0 \times 25.0 + 28.8 \times 24.5^2 \right)} = 128.3^\circ\text{C}$$

Improved design temperature rise:

$$\Delta\theta = \frac{P_t}{kS} = \frac{32.57 \times 24.5^2}{0.008 \times \left(\frac{\pi \times 80.0^2}{4} + \pi \times 80.0 \times 44.0 + 4.5 \times 24.5^2 \right)} = 130.0^\circ\text{C}$$

Check with the results in Table 6.1.

This concludes the solution for Example 6.3.

7

Rotary Actuators

Rotary actuators are electromagnetic devices developing mechanical torque with limited rotary motion. Because of their simplicity and low cost, they are finding more and more industrial applications. The demand for rotary actuators is expanding rapidly, particularly in the automotive industry, where they are being used in steering assistance, EGR, power door locks, and other applications. Some applications are more demanding, requiring an exceptionally high torque level, symmetry, and a stable equilibrium position. In particular, for steering wheel assistance, these requirements would ensure a neutral steering wheel position. This chapter describes three types of rotary actuators with multipolar PMs featuring a high force density transverse flux configuration, which performs a spring action by developing electromagnetic torques with limited-angular movement (Harris et al. 1975, Hennenberger and Bork 1997, Mercow et al. 1990, Weh et al. 1990). Because of the magnetically complicated and nonsymmetrical rotary actuator configurations, the analysis of the magnetic field for these actuators is based on FE software (Ansoft 1991, Nehl et al. 1988). The analysis, which is well supported by test results, shows that these actuators have the capability of developing symmetrical magnetic forces in both directions of rotation with a stable equilibrium position, satisfying all design requirements.

Three types of rotary actuators are described in this chapter: disk actuators with disk magnets having multipole trapezoidal-shaped magnetized poles and axial main air gaps, claw pole actuators with claw poles and radial air gaps, and cylindrical actuators with rectangular-shaped poles having radial air gaps (Pawlak and Graber 1991, Pawlak et al. 1989, Pawlak 2000b, Pawlak et al. 1995). All these rotary actuators were developed for the automotive application as a major component of the Magnasteer system, which adds an electromagnetic actuator to the conventional hydraulic power steering to provide a variable steering effort function (Gieras and Wing 2002). This system consists of an electronic controller and an actuator integrated with the hydraulic power rack and pinion gear in the form of the Magnasteer valve, as shown in Figure 7.56 and Figure 7.57 and described in Section 7.4.

For the first Magnasteer system, a disk homopolar rotary actuator was developed, built, and tested both on a bench and a Cadillac Seville, as shown in Figure 7.1 and as described in Section 7.1 (Pawlak 1990). The disk rotary actuator provided sufficient performance for the original specifications; however, in a gear assembly, the existing axial tolerances adversely affect the disk magnet manufacturability and its cost. Because of the growing interest in the system from small car manufacturers, a more compact and less costly actuator that would be less sensitive to axial tolerances needed to be developed. This led to an axial symmetry actuator configuration with a ring magnet whose performance was less sensitive to the steering gear axial tolerance variations and featured high performance with a compact geometry. To secure high-torque output, a multipole magnet structure was selected with a claw pole actuator configuration, as shown in Figure 7.20 and as described in Section 7.2 (Pawlak et al. 1991c, Pawlak 1992b). This claw pole actuator with multipole ring magnet provided higher output than a disk magnet, but did not meet the expanded

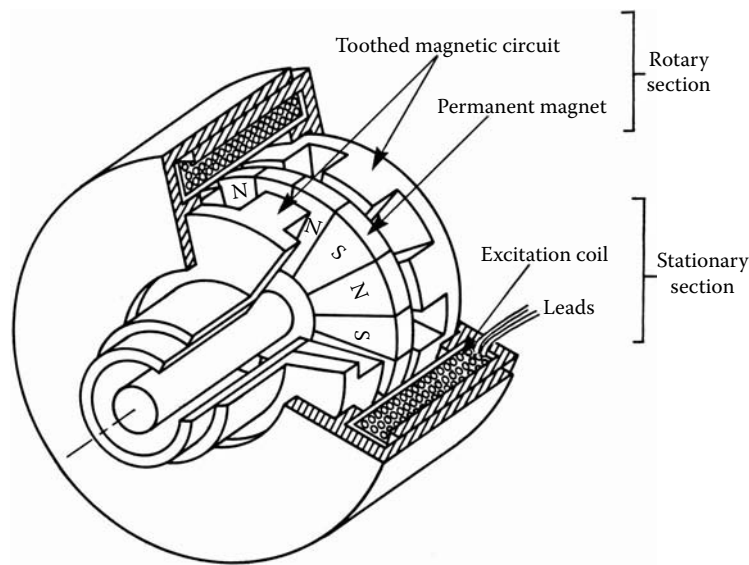


FIGURE 7.1

Disk rotary actuator configuration. (From Pawlak, A.M., *Proceedings of ICEM '90 International Conference on Electrical Machines*, Cambridge, MA, August 13–15, 1990. With permission.)

performance goals. This design greatly improved sensitivity to axial tolerances, but did not eliminate them. The prototype of the claw pole actuator appeared promising, but this configuration introduced major manufacturability difficulties when using low-cost powder-metal technology for the claw pole structure. Therefore, both disk and claw pole configuration concepts were combined — from the disk actuator came the toothed structure and from the claw pole actuator came a multipole ring magnet — to form a cylindrical rotary actuator configuration with a ring magnet and a toothed structure, as shown in Figure 7.34 and as described in Section 7.3 (Pawlak et al. 1994a, Bottauscio et al. 2005). This actuator is less sensitive to the axial tolerances and features a low-cost powder-metal toothed structure, the world's first high-energy ring magnet with multipole radial orientation, as well as a fully plastic encapsulated precision winding coil.

7.1 Disk Rotary Actuators

The disk rotary actuator consists of a stationary and a rotary section, as presented in Figure 7.1, which shows rotary and stationary components of the actuator. The rotary section consists of a multipole disk PM sandwiched between two mechanically coupled toothed magnetic elements. The number of poles of the PM depends on the required angle of limited-angular motion and has double the number of salient teeth of the toothed magnetic-circuit parts. The stationary section comprises an external magnetic circuit providing the return path for the magnetic flux produced by the stationary excitation coil. The excitation coil is placed on a stationary part and the toothed magnetic parts and PM are part of a rotary section that allows free rotation of the toothed structure. In addition to the full rotary motion of the actuator rotary section, this configuration allows for limited-angular motion of the PM disk with respect to the toothed magnetic parts. This motion is mechanically limited in both the left and right directions of rotation.

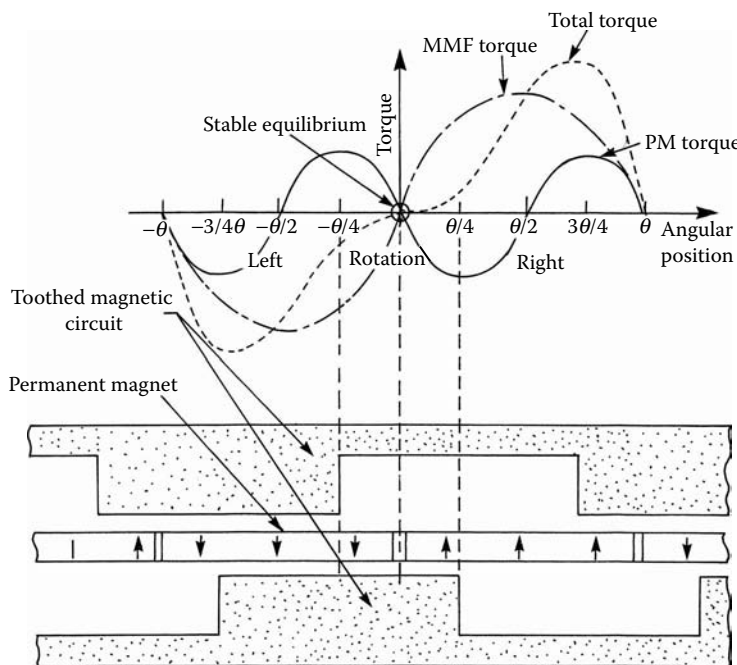


FIGURE 7.2

Stable equilibrium position arrangement. (From Pawlak, A.M., *Proceedings of ICEM '90 International Conference on Electrical Machines*, Cambridge, MA, August 13–15, 1990. With permission.)

To satisfy the symmetrical torque requirement and provide the stable equilibrium at the neutral PM position, a unique actuator magnetic-circuit configuration was devised. A stable equilibrium for both the energized coil MMF and PM was established with a half overlap arrangement, as presented in Figure 7.2, with the magnet located in the middle of this shift.

The external magnetic circuit provides the same polarity, depending on the direction of the excitation current, to all the teeth of the toothed magnetic part regardless of its angular position. This homopolar actuator configuration enables the reversal of the torque by simply reversing the direction of the excitation current. The stable equilibrium rotor position should stay unchanged with the current reversal. Unlike other electromagnetic devices, the disk rotary actuator utilizes both the external and internal PM surfaces for torque development, thus providing a high-torque density structure. Proper balance of both magnetic flux levels (flux densities) — one due to internal PM and the second due to stationary external coil — is the most important task during the actuator's design optimization. This can be achieved by establishing a magnet MMF based on the material and magnet thickness, which corresponds to the external coil MMF based on nominal current and a number of coil turns.

7.1.1 Disk Rotary Actuator Analysis

The torque developed by the actuator is a function of the coil MMF and the PM magnetic field interaction. It consists of two components: the PM VR cogging-type torque due to the magnetic structure geometry and the mutual synchronous-type torque due to interaction of the coil MMF and the magnet. The total torque is the superposition of these components:

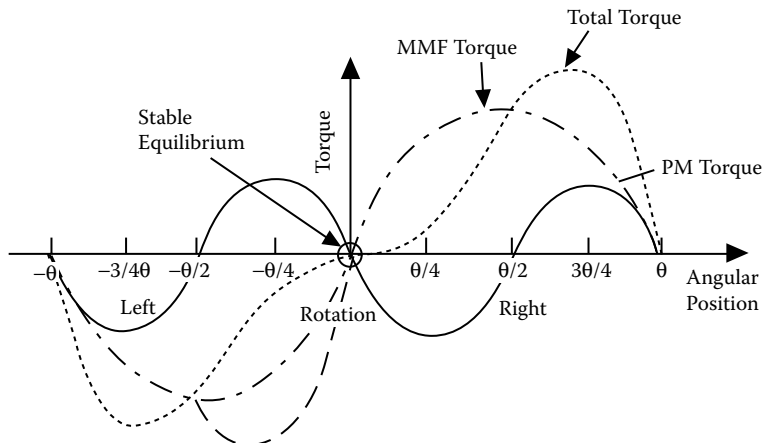


FIGURE 7.3

Disk actuator torque vs. position. (From Pawlak, A.M. et al., *Magnetic Power Steering Assist System — MAG-NASTEER*, Publ. No. 940867, Society of Automotive Engineers, Detroit, MI, 1994. With permission.)

$$T_t(\theta) = T_m(\theta) + T_c(\theta) \quad (7.1)$$

where $T_t(\theta)$ is total torque, $T_m(\theta)$ is mutual torque, $T_c(\theta)$ is cogging torque, and θ is a position angle.

The torque variation with the position is a function of claw poles geometry and the PM field distribution. For rectangular poles, sinusoidal magnet magnetization, and nominal coil excitation, the total torque can be expressed as a sum of two sinusoidal components:

$$T_t(\theta) = K_m I_n \phi \sin \theta - K_c \phi^2 \sin 2\theta \quad (7.2)$$

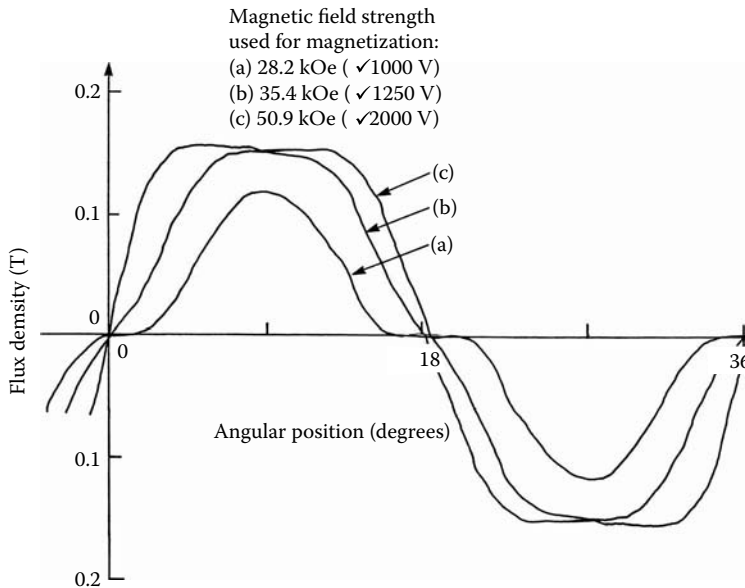
where K_m , K_c are constant for the mutual and cogging torques, respectively; I_n is the nominal current in the coil; and ϕ is the flux developed by the magnet.

Reversing the current direction, only the mutual torque components change; direction and the total torque can be expressed as:

$$T_t(\theta) = -(K_m I_n \phi \sin \theta + K_c \phi^2 \sin 2\theta) \quad (7.3)$$

The VR torque component has double the frequency of the mutual torque component and affects both the total torque profile and its maximum value, as presented in Figure 7.3. The VR torque is determined by the tooth geometry, the air gap length, and the magnet magnetization. The magnetic flux distribution of the PMs depends upon the magnet material and the applied strength of the magnetizing field, as presented in Figure 7.4.

By increasing the magnetizing field strength, the magnet flux density also increases up to the saturation level. Increasing the field further affects the magnet field distribution from sinusoidal to trapezoidal. For the stable equilibrium purpose, it was necessary to select the magnetization pattern shown in Figure 7.4(b) with small transitional slope change at the point where magnetization changes its sign at 0° , 18° , 36° , etc. The presence of the nonmagnetized neutral zone of the magnet helps secure a stable equilibrium position. The best results were obtained for the 15% neutral zone for the pole pitch, as indicated in Figure 7.4, which shows the magnetization pattern of the disk magnet. Because this

**FIGURE 7.4**

Disk magnet magnetization pattern: (a) magnetic field strength of 28.2 kOe, (b) magnetic field strength of 35.4 kOe, (c) magnetic field strength of 50.9 kOe. (From Pawlak, A.M., *Proceedings of ICEM '90 International Conference on Electrical Machines*, Cambridge, MA, August 13–15, 1990. With permission.)

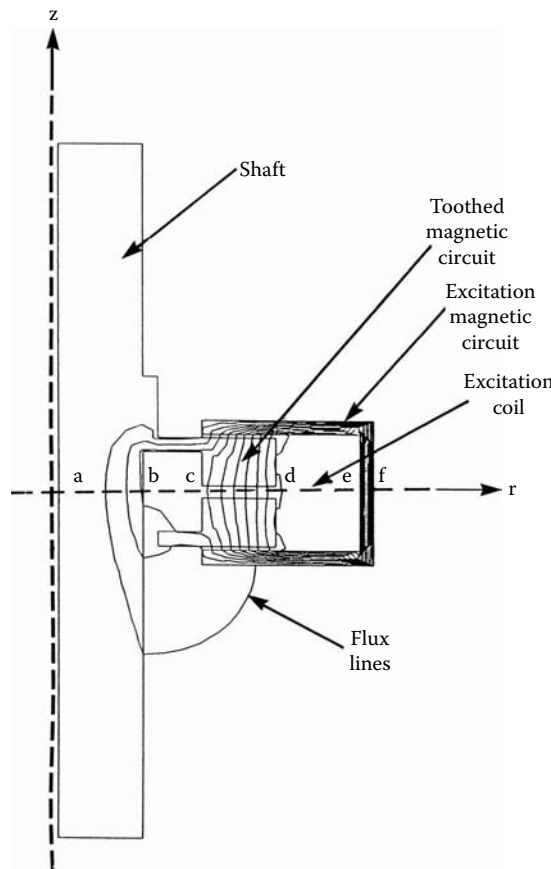
portion of magnet is not fully saturated during the magnetization process, it affects the magnet thermal stability.

Despite the complicated geometry of the actuator, it was possible to use simplified 2D FE software for magnetic field analysis. Two 2D models were analyzed, representing sections in axial and rectangular planes based on the same nominal flux density in the air gap. The FE axial plane model with cylindrical symmetry was used to determine the magnetic flux density and its distribution in the main air gaps and in the surrounding magnetic parts. Figure 7.5 shows the actuator geometry with the flux-line distribution at the nominal excitation current.

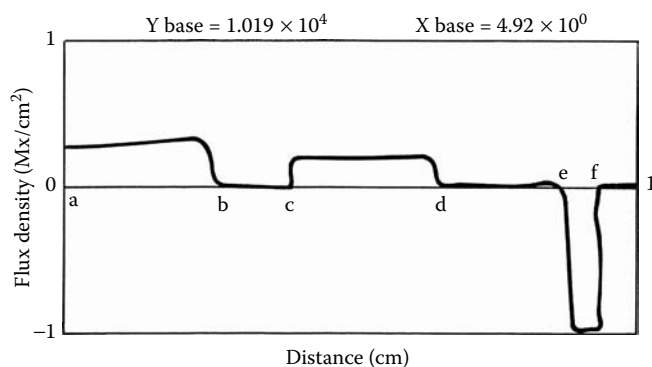
In this model, both toothed magnetic parts were replaced by magnetic rings with the assumption that teeth carry the entire magnetic flux. For the magnetic flux developed by the excitation coil (MMF), the thickness of the PM can be treated as an additional air gap added to the main air gaps. The magnet thickness, however, determines the magnet strength for a given magnet material because the magnet is axially magnetized. Therefore, there is a trade-off between magnet strength and coil field strength based on the magnet thickness, which has to be optimized.

The flux-density distribution across the actuator for the axial plane analysis is shown in Figure 7.6. It indicates that the excitation magnetic circuit (distance *e-f*), toothed magnetic circuit (distance *c-d*), and shaft (distance *a-b*) all carry part of the flux. Providing a non-magnetic shaft or large air gap between the shaft and toothed parts can reduce the flux shunting effect. The resultant air gap magnetic flux density calculated with the nominal excitation current for the cylindrical symmetry has to be transferred to the rectangular *x-y* plane.

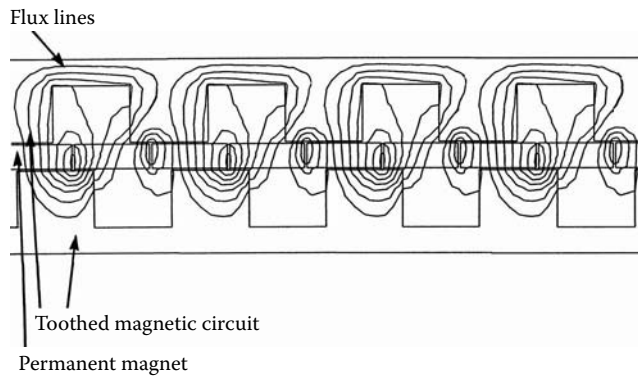
The *x-y* plane model was based on the one tooth-pitch segment with the assumption that all segments equally contribute to the torque generation, as presented in Section 7.3.2 for the Cartesian model 2D analysis. The magnetic force and torque developed by the actuator is obtained from the rectangular *x-y* plane. For the purpose of illustration, the

**FIGURE 7.5**

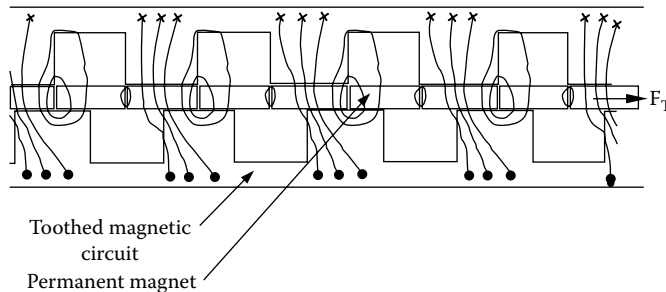
Cylindrical symmetry of the disk rotary actuator. (From Pawlak, A.M., *Proceedings of ICEM '90 International Conference on Electrical Machines*, Cambridge, MA, August 13–15, 1990. With permission.)

**FIGURE 7.6**

Flux-density distribution for the disk rotary actuator. (From Pawlak, A.M., *Proceedings of ICEM '90 International Conference on Electrical Machines*, Cambridge, MA, August 13–15, 1990. With permission.)

**FIGURE 7.7**

Magnet flux-line distribution from FE analysis. (From Pawlak, A.M., *Proceedings of ICEM '90 International Conference on Electrical Machines*, Cambridge, MA, August 13–15, 1990. With permission.)

**FIGURE 7.8**

Flux-line distribution with current excitation from FE analysis. (From Pawlak, A.M., *Proceedings of ICEM '90 International Conference on Electrical Machines*, Cambridge, MA, August 13–15, 1990. With permission.)

flux distribution in this section was repeated for the neighboring section in Figure 7.7 without coil excitation and at the stable equilibrium position and in Figure 7.8 with nominal current excitation and out of the stable equilibrium position. When the magnet is moved with respect to the toothed structure and the coil is excited, the magnetic flux-line distribution indicates the direction of the developed magnetic forces. Notice the 3D character of the coil flux distribution, as shown in Figure 7.8, and the vector resultant magnetic force F .

The magnetic force calculations are based on one tooth-pitch segment using the Maxwell stress tensor over the surface of the PM two-pole section, defined by:

$$F_T = \iint_S \bar{T} \cdot d\bar{s} \quad (7.4)$$

where F_T is the total magnetic force, \bar{T} is the Maxwell stress tensor in dyadic form, and S is the surface of integration.

The total force developed by the actuator can be calculated as a sum of the forces developed by each tooth pitch. Assuming complete geometric and magnetic symmetry of the device, the total force developed by the actuator is the superposition of the forces developed by each tooth pitch:

$$F_T = NF_t \quad (7.5)$$

where F_T is the total magnetic force developed by actuator, F_t is magnetic force developed by one pole-pitch (tooth-pitch) section, and N is the number of teeth (pole pairs).

These two models can be utilized in a parametric study to optimally select the actuator dimensions. The tooth magnetic force itself is a function of the tooth surface area and, subsequently, of the area of teeth. The total developed torque can be calculated as:

$$T_T = NT_t \quad (7.6)$$

where T_T is total torque developed by the actuator and T_t is the torque developed by one pole-pitch (tooth-pitch) section.

The one-tooth-pitch (one-pole pitch) torque developed by an independent magnetic section can be calculated as:

$$T_t = F_t R_{avg} \quad (7.7)$$

where R_{avg} is the mean radius of the actuator rotor. Combining Equation 7.6 and Equation 7.7, the total torque developed can be calculated as:

$$T_T = NF_t R_{avg} \quad (7.8)$$

Both the number of teeth and the actuator mean radius are determined by actuator geometry, and the force developed by the tooth pitch of the actuator is determined by the FE mathematical model.

7.1.2 Disk Rotary Actuator Design

With the introduced 2D FE mathematical model, one can design the disk actuator. The design optimization can be pursued by using a parametric study technique. If the goal of the actuator design is to maximize its torque (force F_T) level for the nominal current excitation, each optimization process should be followed by an iteration of the three-step parametric variations for the excitation coil (wire size, number of turns, resistance), the PM (magnetic material properties, geometry), and the magnetic circuit (geometry of the toothed structure, magnetic-circuit path, and the selected magnetic material properties).

7.1.3 Disk Rotary Actuator Excitation Electromagnetic Circuit

The excitation circuit consists of the coil and the magnetic circuit, as shown in Figure 7.9. This ring-shaped coil is placed in the stationary side of the actuator for ease of excitation without sliding contacts. Further, the external location of this electromagnetic circuit is preferable from the heat dissipation point of view, providing an increased cooling surface through the contact with the other assembly parts. The magnetic circuit consists of two pressed C-shaped rings, which fit tightly and surround the coil. The lead wires are introduced through a special cut in its external wall. The inside walls are not connected to prevent a magnetic-circuit short, and they are adjusted to match the tooth magnetic part thickness to minimize the reluctance of the parasitic air gap between the stationary core

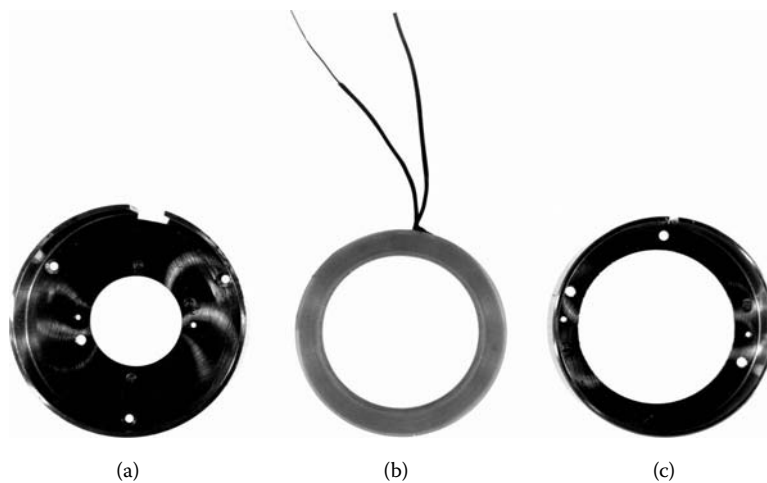


FIGURE 7.9

Disk rotary actuator excitation circuit parts: (a) magnetic housing, (b) coil, (c) magnetic housing. (Courtesy of Delphi Corp.)

and the toothed parts. Two additional magnetic parts in the shape of hollow disks are attached to the bottom and the top walls of the excitation ring to increase flux crossing area to the toothed magnetic parts and further minimize the MMF drop along the parasitic gap. The OD as well as ID of these parts corresponds to the OD of the excitation ring and the ID of the toothed parts, respectively. The cross section of the magnetic circuit is chosen to avoid local saturation.

If the voltage and the coil envelope are constrained, the coil parameters are based on the required level of MMF and the size of excitation magnetic parts determine the thermal dissipation capability of the device. In the presented example, the MMF level of the coil excitation was established at 450.0 At. The optimized excitation coil has 460 turns of the wire size 25 AWG with a bobbin. Bobbinless coil winding technology should be also considered to improve the fill factor and coil window utilization up to 15%. The dimensions of the coil and the stationary parts of the magnetic circuit are given in the cross section shown in Figure 7.15.

7.1.4 Disk Rotary Actuator Toothed Magnetic Part

The reluctance variation introduced by the toothed magnetic parts, as shown in Figure 7.10, plays an important role in the development of the actuator torque. The number of teeth (10 in this case) is determined by the maximum angular position required. The period of torque waveform is inversely proportional to the number of teeth. To achieve a maximum torque with an angular displacement of 4.5°, the desirable period between torque peaks is 9°. This corresponds to 36° pole pitch or 10 teeth, as shown in Figure 7.1. The number of teeth also affects the torque developed by the actuator. The electromagnet magnetic-circuit geometry was determined based on flux saturation levels of the different parts for the selected magnetic material. The toothed structure is similar to the VR machines where the ratio of tooth height to its width has to be optimized. Because tooth width is determined by the required angle of limited rotation, in the same way as for the number of magnet poles, the tooth height is the only variable in this ratio. As a result of this analysis, the tooth/width ratio of 0.9 was selected for nominal MMF coil excitation of 450.0 At, as presented in Figure 7.11.



FIGURE 7.10
Disk rotary actuator toothed structure. (Courtesy of Delphi Corp.)

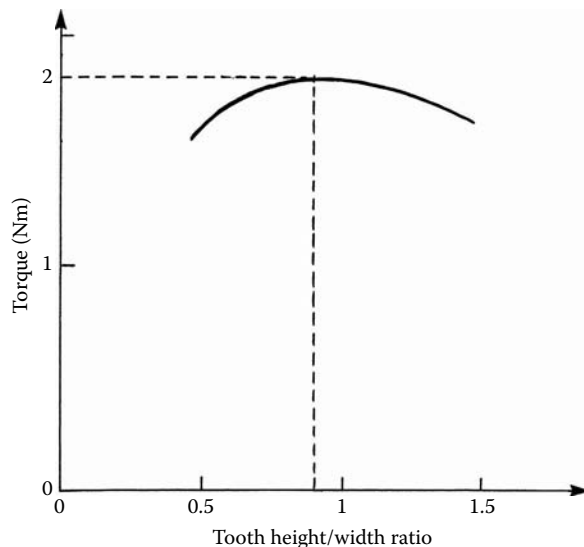
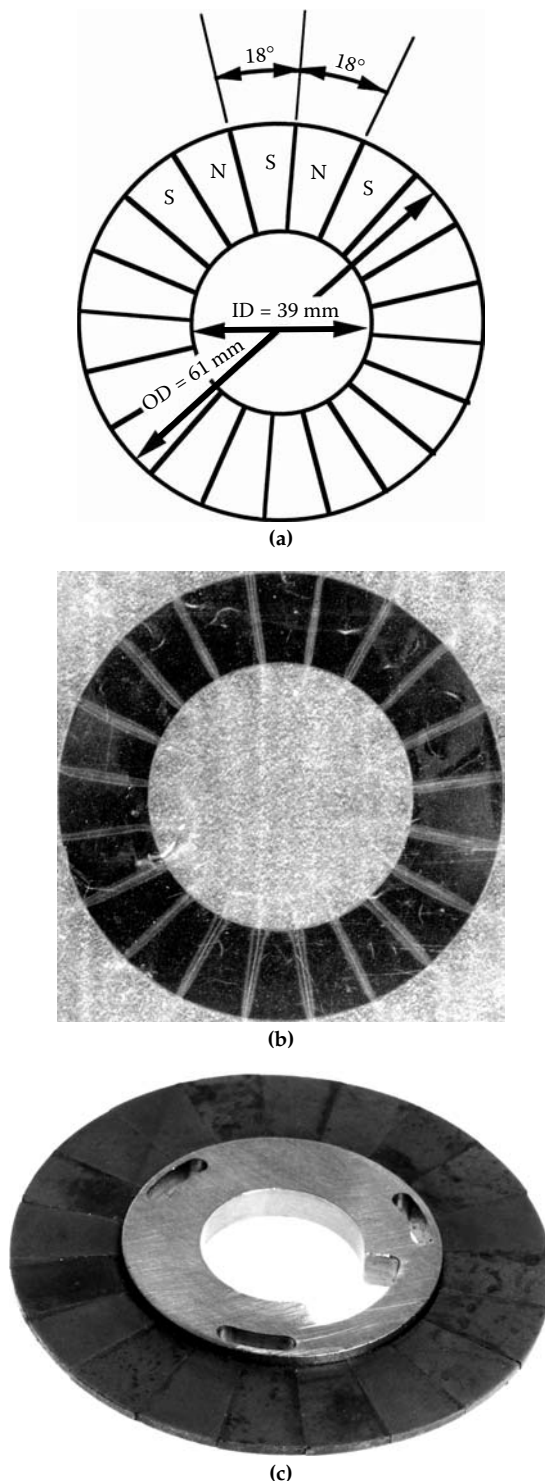


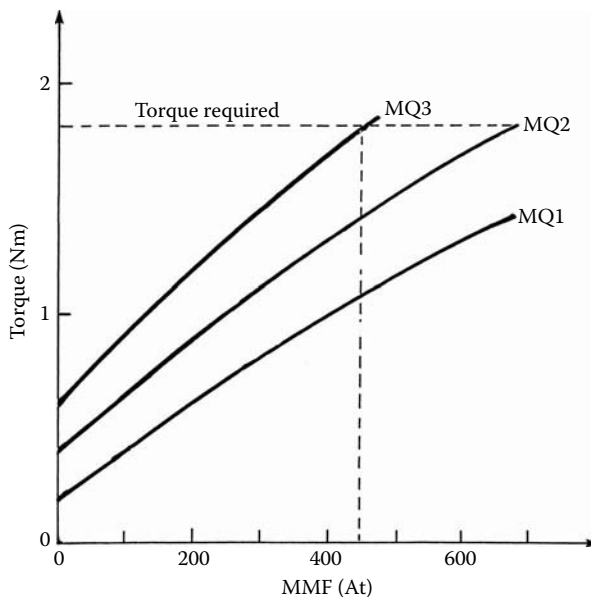
FIGURE 7.11
Disk actuator torque vs. tooth height/width ratio. (From Pawlak, A.M., *Proceedings of ICEM '90 International Conference on Electrical Machines*, Cambridge, MA, August 13–15, 1990. With permission.)

7.1.5 Disk Rotary Actuator PM

As illustrated in Figure 7.12, the PM has a disk shape with multipole axial magnetization, which shows magnet geometry, magnetization pattern, and magnet hardware model. The number of poles was established by the required angle of rotation, and the actuator geometry was determined by the magnet geometry. Both magnet thickness and material properties determine the magnet strength. Several neodymium magnets were investigated — MQ1,

**FIGURE 7.12**

Disk magnet geometry and magnetization pattern. (a) Magnet geometry, (b) magnetization pattern, (c) magnet model. ([a] From Pawlak, A.M., *Proceedings of the Permanent Magnet Systems Conference*, Atlanta, GA, September 25–27, 2000. With permission; [b] courtesy of Delphi Corp.; [c] from Pawlak, A.M., *Proceedings of IEEE/IAS '95 Conference*, Orlando, FL, October 9–13, 1995. With permission.)

**FIGURE 7.13**

Disk actuator torque vs. MMF level for various magnet materials. (Courtesy of Delphi Corp.)

TABLE 7.1
Permanent Magnet Performance

Permanent Magnet	Energy (MGoe)	Flux Density (T)	Coercive Force (CkOe)
Ferrite "Ceramic 8"	3.5	0.39	3.2
Neobond 50	4.5	0.45	4.5
Magnaquench MQ1	8	0.61	5.3
Magnaquench MQ2	15	0.8	6.5
Magnaquench MQ3	32	1.17	10.5

Source: Pawlak, A.M., *Proceedings ICEM '92 International Conference on Electrical Machines*, Vol. 1, University of Manchester Press, 1992. With permission.

MQ2 and MQ3 — see Figure 7.13 and Table 7.1 (Carsile 1986). Based on this study, the MQ3 material was selected to meet the specified torque requirement level of 1.7 Nm for the nominal coil excitation of 450.0 At and the magnet thickness of 1.3×10^{-3} m, as presented in Figure 7.14. For this excitation, the magnet was devised to meet the required torque level of 1.7 Nm, as presented in Figure 7.14. Based on actuator requirements and constraints, several magnet parameters were established. These are number of poles (20), inside and outside actuator diameters (40.5×10^{-3} m and 61.5×10^{-3} m, respectively), and the total magnet thickness (1.3×10^{-3} m), as presented in Figure 7.14 and Figure 7.15.

7.1.6 Disk Rotary Actuator Test Results

This analysis makes it possible to build disk actuator models. Figure 7.16 and Figure 7.17 show disk actuator parts and assembly, respectively. Half of the disk magnet is covered by a magnetic field indicator foil, showing the multipole magnetization with a number of pole pairs that corresponds to the number of teeth.

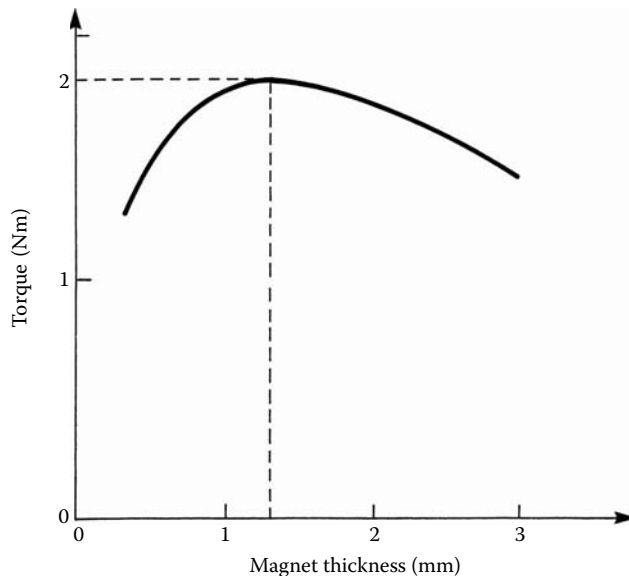


FIGURE 7.14
Torque vs. magnet thickness. (From Pawlak, A.M., *Proceedings of ICEM '90 International Conference on Electrical Machines*, Cambridge, MA, August 13–15, 1990. With permission.)

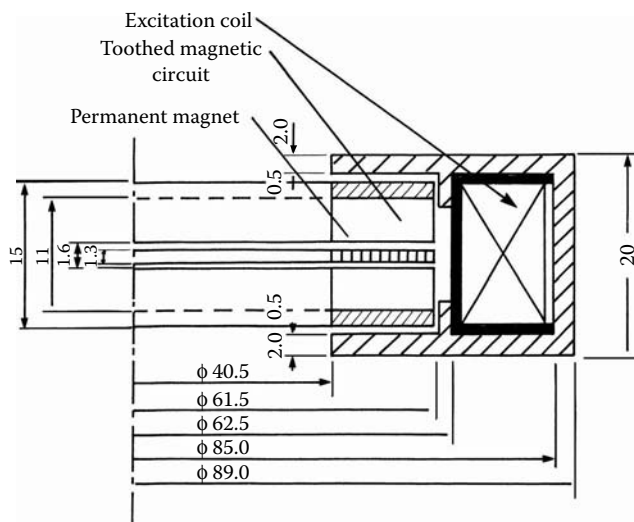
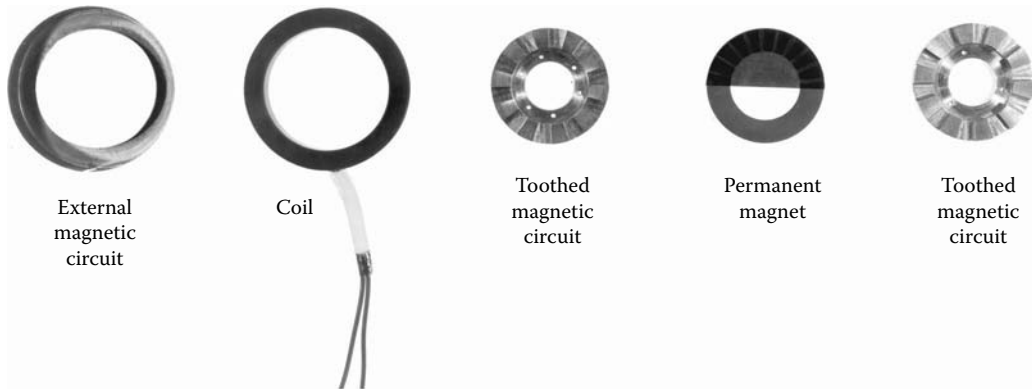


FIGURE 7.15
Disk rotary actuator geometry. (Courtesy of Delphi Corp.)

Test results from the model always provide the best evaluation of the mathematical model used for analysis. The analysis presented is well supported by test results, as shown in Figure 7.18 and Figure 7.19, where test results closely match analysis within several percent. Test results also indicated that symmetrical magnet forces in both directions of rotation were achieved with the stable equilibrium position.

Both the VR (magnet) and mutual (MMF) torque components are represented adequately in Figure 7.18 and well supported by analysis. The obtained torque level from the disk rotary actuator was satisfactory, but this configuration indicated sensitivity on the axial

**FIGURE 7.16**

Disk rotary actuator components. (From Pawlak, A.M., *Proceedings of ICEM '90 International Conference on Electrical Machines*, Cambridge, MA, August 13–15, 1990. With permission.)

**FIGURE 7.17**

Disk rotary actuator assembly. (From Pawlak, A.M., *Proceedings of ICEM '90 International Conference on Electrical Machines*, Cambridge, MA, August 13–15, 1990. With permission.)

stock-up tolerances. Therefore, for the applications where disk actuator components were applied to the system, which had difficulty maintaining the tolerance variation target, it was necessary to explore different actuator topologies with radial air gaps rather than axial air gaps. Otherwise, they can be successfully used in a variety of applications, such as the stepper motors.

7.2 Claw Pole Rotary Actuators

Claw pole rotary actuators with a multipole ring PM that develop symmetrical limited-angular movement electromagnetic torques in both the left and right directions of rotation are described in this section. The complicated 3D geometry of the actuators has a configuration similar to that of claw pole stepper motors, as discussed in Chapter 5 (Pawlak et al. 1991c, Pawlak 1992b). For simplicity, a lumped-parameter mathematical model is

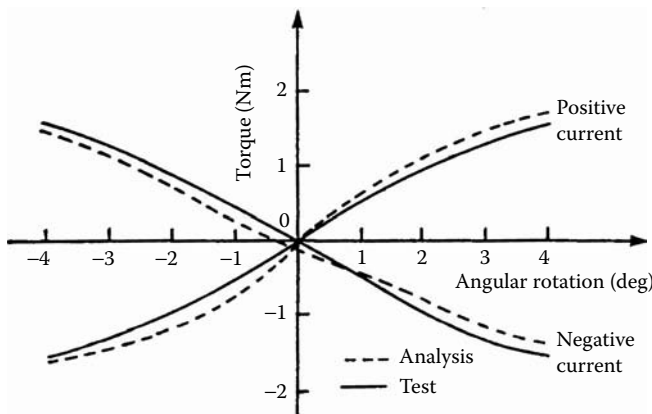


FIGURE 7.18
Disk rotary actuator torque vs. angular position comparison.

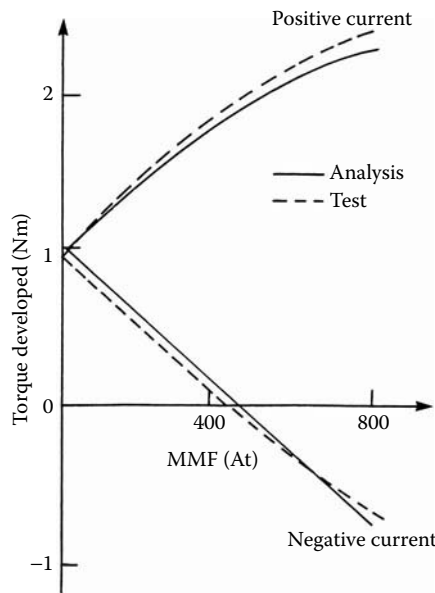
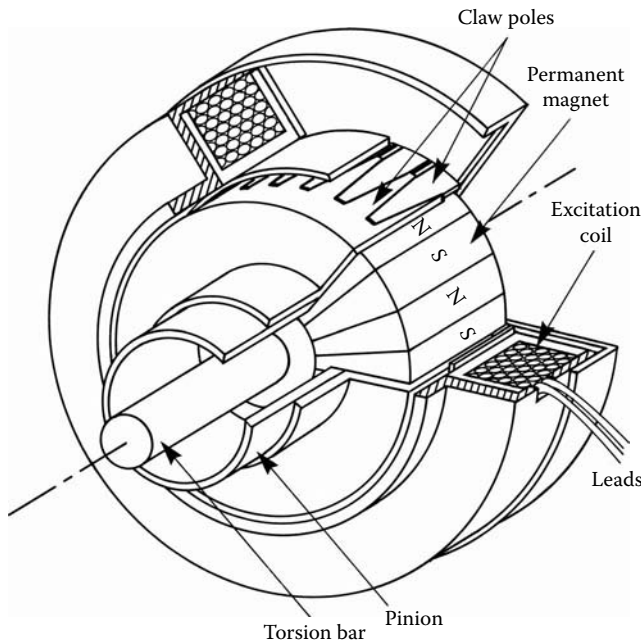


FIGURE 7.19
Disk rotary actuator torque MMF comparison. (From Pawlak, A.M., *Proceedings of ICEM '90 International Conference on Electrical Machines*, Cambridge, MA, August 13–15, 1990. With permission.)

presented to analyze and optimize this complicated structure. The predictions of the model showed good correlation with test results, as presented in Chapter 5. These actuators can be used in any application that requires both repulsive and attractive torques over a limited angle of rotary motion. Because of their homopolarity, the unlimited rotation of the rotary elements does not affect the rotary actuator capabilities of developing electromagnetic torque.

The claw pole actuator consists of two sections — a rotary and a stationary section — as presented in Figure 7.20. The stationary section is composed of an electromagnet that consists of a coil and two L-shaped magnetic core parts. The stationary location of the excitation coil allows contactless current connections. The external magnetic circuit always provides the same polarity to each claw pole section, regardless of its angular position.

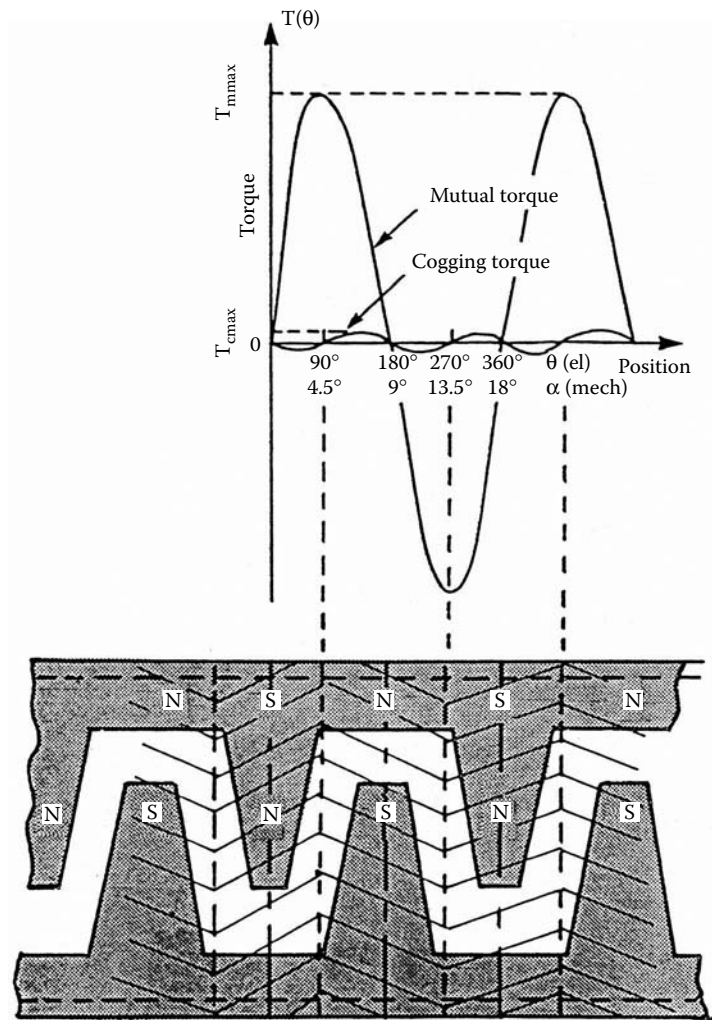
**FIGURE 7.20**

Claw pole rotary actuator. (From Pawlak, A.M., *Proceedings ICEM '92 International Conference on Electrical Machines*, Vol. 1, University of Manchester Press, 1992. With permission.)

The specific polarity of the claw pole sections depends on the direction of the excitation current and determines whether the actuator develops attractive or repulsive magnetic spring forces. Because of this, such an electromagnetic device has inherent homopolar features, which enable the reversal of torque by simply reversing the excitation current. The rotary section comprises a multipole PM ring and a claw pole magnetic core. Both the claw pole structure and the ring magnet have unlimited freedom of movement in the left and right directions of rotation. In addition to the full rotary motion of the actuator center parts, this configuration allows for a limited-angular motion of the PM ring with respect to the claw poles as required for the automotive speed-sensitive steering application, as presented in Section 7.4.3. For this application, two degrees of mechanical freedom are needed: one for rotation of a steering wheel without driver effort, and the second for a limited-angular motion steering assist when the driver applies effort to the steering wheel. This motion is mechanically limited for both directions of rotation. Unfortunately, such a mechanical separation, which is necessary to provide unlimited mechanical freedom, introduces additional parasitic air gaps in the magnetic circuit, which adversely affect the magnetic flux level. Figure 7.21 shows the distributed view of the claw poles and the corresponding torque profile. The number of poles indicates the period of the actuator torque waveform with respect to the angular position.

7.2.1 Claw Pole Rotary Actuator Analysis

The total electromagnetic torque is a superposition of the torques developed by each claw pole-pair section. This provides an amplification of the torque, in the form of the magnetic gearing torque effect (Pawlak 1990). The rotary actuator has to provide a required torque level, which is symmetrical in both the left and right directions of rotation. The actuator torque is developed by the interaction of the coil MMF and the PM magnetic field. The

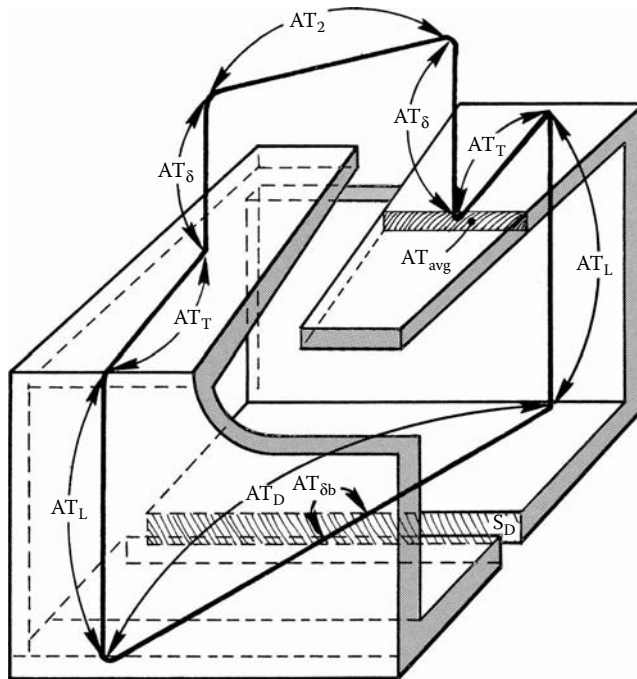
**FIGURE 7.21**

Claw pole rotary actuator torque vs. displacement. (From Pawlak, A.M., *Proceedings ICEM '92 International Conference on Electrical Machines*, Vol. 1, University of Manchester Press, 1992. With permission.)

torque variation with position is a function of the claw pole's geometry and the PM's field distribution. For claw poles with a rectangular cross section, at the nominal coil excitation and sinusoidal magnet magnetization, the total torque can be expressed as the sum of two sinusoidal components — mutual torque $T_m(\theta)$ and cogging torque $T_c(\theta)$ components — as presented in Equation 7.1. For claw pole actuators, the maximum value of the cogging torque is only a few percent of the maximum value of the mutual torque, as described in Chapter 5 and presented in Figure 5.9; therefore, for engineering purposes, the cogging torque component is negligible (Chai 1984). The mutual torque developed by the claw pole actuator is the sum of the torques developed by each claw pole section. The mutual torque constant K_m is:

$$K_m = 0.25Np^2I_n \quad (7.9)$$

Therefore, the total torque developed by the actuator is:

**FIGURE 7.22**

Claw pole section with magnetic flux path. (From Pawlak, A.M., *Proceedings ICEM '92 International Conference on Electrical Machines*, Vol. 1, University of Manchester Press, 1992. With permission.)

$$T_T(\theta) = T_m(\theta) = 0.25Np^2I_n\phi\sin\theta \quad (7.10)$$

where T_T is total torque developed by the actuator, N is the number of coil turns, p is the number of poles, K_m is the mutual torque constant, I_n is the nominal current in the coil, ϕ is the flux in the air gap with armature reaction, and θ is the mechanical angle position.

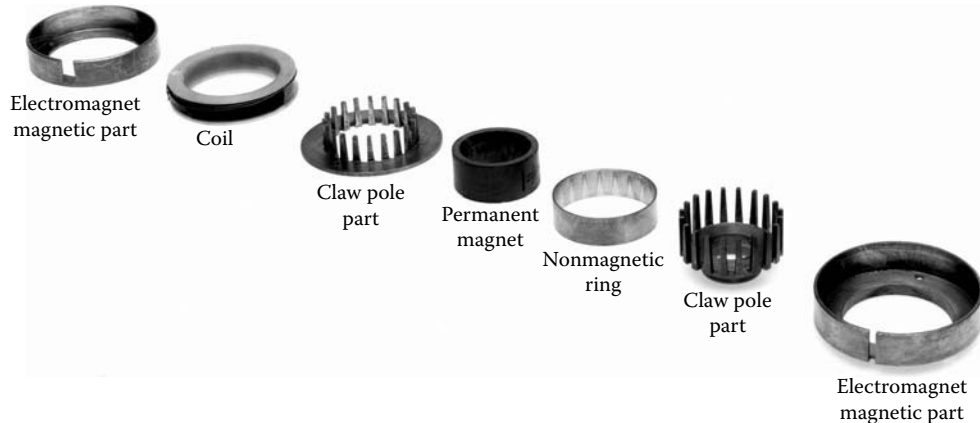
All the parameters of Equation 7.10 can be defined from the actuator requirements, except the magnetic flux. To determine the magnetic flux, the claw pole actuator should be considered as a series of independent claw pole sections, each having one pole pair with an independent magnetic flux path, as presented in Figure 7.22.

In each section, the magnetic flux developed by the PM crosses the magnetic circuit and the main and the parasitic air gaps. With no exciting current and no armature reaction, the PM magnetic flux ϕ can be determined from the magnet working point described in detail in Section 5.2.3 by combining Equation 5.19 with Equation 5.43 through Equation 5.46 and Equation 5.48:

$$\phi = B_r A_m' \left[1 - \frac{8p^2(2AT_T + 2AT_L + AT_D + AT_{\delta b} + 2AT_{\delta})}{0.96\pi^2 D_m (2p-1) k_m H_c} \right] \quad (7.11)$$

The magnetic flux and all MMF drops were determined with an iterative process to satisfy all pertinent equations, based on the geometry and magnetic material properties. Finally, combining Equation 7.9 and Equation 7.10, the total torque developed can be expressed as:

$$T_t(\theta) = 0.25Np^2I_nB_rA_m' \left[1 - \frac{8p^2(2AT_T + 2AT_L + AT_D + AT_{\delta b} + 2AT_{\delta})}{0.96\pi^2 D_m (2p-1) k_m H_c} \right] \sin\theta \quad (7.12)$$

**FIGURE 7.23**

Distributed view of the claw pole actuator. (From Pawlak, A.M., *Proceedings ICEM '92 International Conference on Electrical Machines*, Vol. 1, University of Manchester Press, 1992. With permission.)

where B_r is the remanent flux density of the magnet, A_m' is the effective magnet surface area, p is the number of magnet pole pairs, I_n is the nominal current in the coil, ϕ is the flux in the air gap with armature reaction, θ is the mechanical angle position, and AT_T , AT_L , AT_D , $AT_{T\delta b}$, AT_δ , and AT_2 are MMF drops in the claw poles, side walls, back walls, parasitic air gaps, main air gap, and magnet working point MMF, respectively.

This set of equations was used to devise an algorithm and a custom computer software that provides the capability of performing parametric studies of the magnetic flux and torque developed.

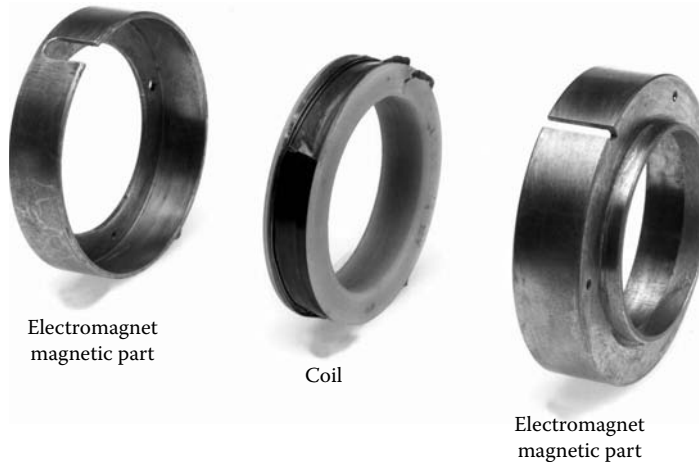
7.2.2 Claw Pole Rotary Actuator Design

The final claw pole actuator design was optimized based on the required actuator envelope, temperature, and the nominal current level for the selected magnetic materials. Figure 7.23 shows the distributed view of the final actuator design. It consists of an excitation electromagnetic circuit, two claw pole magnetic parts, and a ring PM with multipole magnetization.

7.2.3 Claw Pole Rotary Actuator Excitation Electromagnetic Circuit

The excitation electromagnetic circuit consists of a coil and a magnetic-circuit core. The coil has 200 turns with wire size 21 AWG. The nominal current of claw pole design is restricted to 3.0 A. Therefore, during the test, the nominal MMF value of 600.0 At is applied to verify the achieved nominal torque level. The ring-shaped electromagnetic excitation circuit is stationary and, therefore, is excited through two leads without slip rings. The external location of this electromagnet is preferred for heat transfer reasons because such a location increases the area of heat dissipation through its attachment to the stationary housing. The magnetic circuit consists of two L-shaped rings that fit tightly and surround the coil, both having a special cut in the external walls to allow for lead passage, as presented in Figure 7.24.

The outside walls are adjacent to provide a large cross section for the magnetic circuit. Their height is matched to the claw pole magnetic part thickness to allow for maximum area of the parasitic air gap, thereby minimizing the MMF drop along this gap. The claw

**FIGURE 7.24**

Claw pole rotary actuator electromagnet parts. (From Pawlak, A.M., *Proceedings ICEM '92 International Conference on Electrical Machines*, Vol. 1, University of Manchester Press, 1992. With permission.)

pole's shape and dimensions play an important role in the development of the electromagnetic torque, and they are related to the magnet pole dimensions. These dimensions were optimized to maximize the torque at the nominal current.

Figure 7.25 shows a cross section of the actuator parts. The magnetic circuit consists of two pressed L-shaped rings that fit tightly and surround the coil with an opening for the leads passage. The outside walls are adjacent to provide a bigger cross section for the magnetic circuit and their height is related to the claw pole magnetic part thickness to maximize the flux crossing the parasitic air gap. Both sides of the L-shaped parts are enlarged to increase the flux crossing area to the claw pole magnetic parts and to minimize the MMF drop along the parasitic air gap. Figure 7.25 also identifies the final dimensions of the stationary electromagnet.

7.2.4 Claw Pole Actuator Toothed Magnetic Part

Both the geometry (claw pole surface area and mean radius) and the number of teeth affect the total torque level, which is a superposition of the torque developed by each pole-pair section of the actuator. The distributed view of the final claw pole design is shown in Figure 7.26.

The shape and dimensions play an important role in the development of the electromagnetic torque and are related to the magnet pole dimensions. These dimensions should be optimized to maximize the torque at a given MMF level. The number of poles (40) indicates the period of the actuator torque waveform with respect to its angular position. Both geometry (claw pole surface area and mean radius) and the number of teeth affect the torque developed by the actuator. Figure 7.27 shows the final claw pole shape and dimensions with 20.0×10^{-3} m actuator axial length and 2.0×10^{-3} m material thickness.

7.2.5 Claw Pole Actuator PM

Figure 7.28 shows the ring PM with its geometry, magnetization, and hardware. The magnet has multipole arc magnetization with the number of poles equal to the number

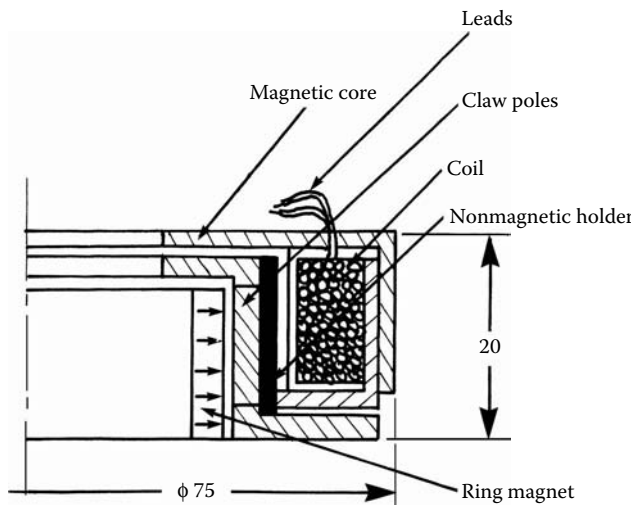


FIGURE 7.25
Claw pole rotary actuator cross section. (Courtesy of Delphi Corp.)

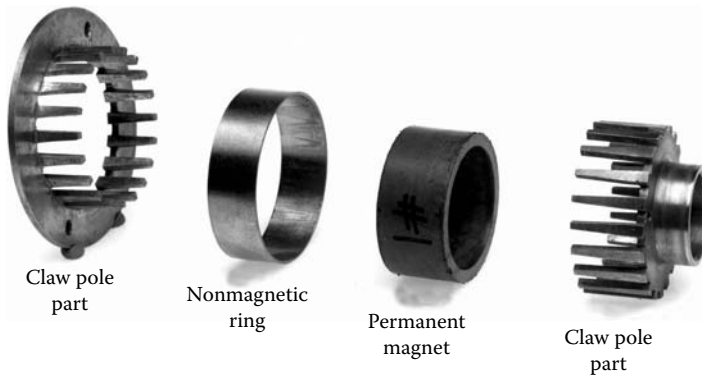
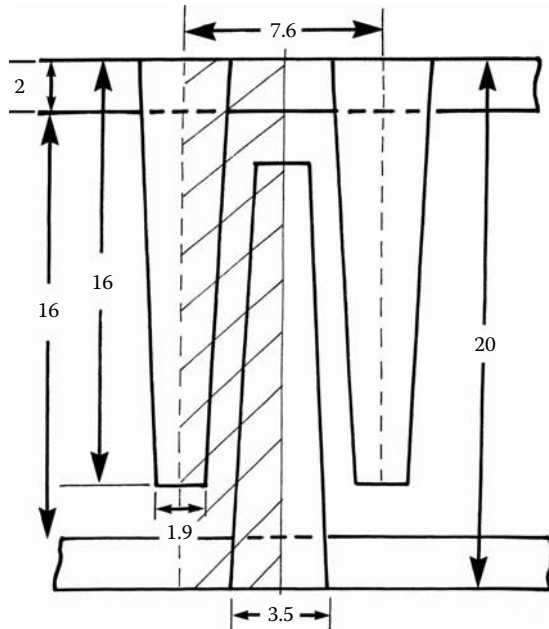


FIGURE 7.26
Claw poles with PM. (From Pawlak, A.M., *Proceedings ICEM '92 International Conference on Electrical Machines*, Vol. 1, University of Manchester Press, 1992. With permission.)

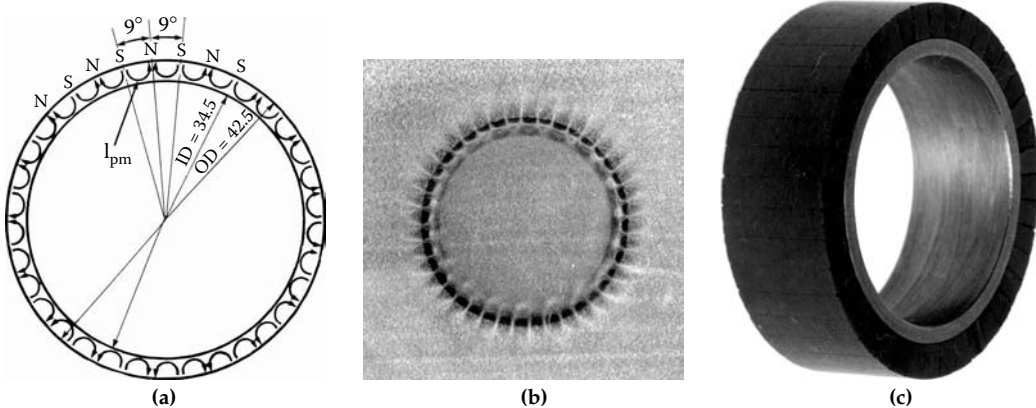
of claw poles. The size and geometry of the ring corresponds to the claw poles. The PM is made as one piece and magnetized in a custom-made magnetizing fixture. Figure 7.28 shows the magnet geometry, the magnetic field pattern of the magnetized magnet ring, which is indicated by a magnetic film, and the magnet hardware model.

The multipole ring PM is located under the claw poles and the number of magnet poles corresponds to the combined number of claws from both claw pole parts. The magnetized ring magnet has a sinusoidal distribution of flux density along its active surface, as shown in Figure 7.29.

Twenty pole pairs ($P = 40$ poles) were selected for the multipole magnet magnetization to best utilize the relatively small mechanical angle rotation of 4.5° . The relation between mechanical and electrical angles of rotation is:

**FIGURE 7.27**

Claw pole teeth dimensions. (Courtesy of Delphi Corp.)

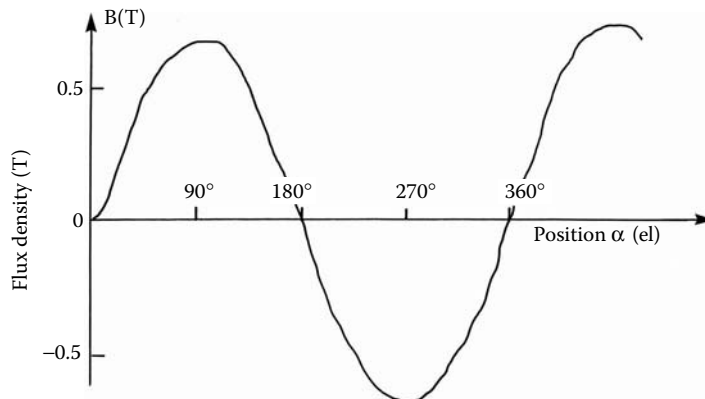
**FIGURE 7.28**

Ring PM with magnetization pattern. (a) Magnet geometry, (b) magnetization pattern, (c) magnet model. ([a] From Pawlak, A.M., *Proceedings of IEEE/IAS '95 Conference*, Orlando, FL, October 9–13, 1995. With permission; [b] from Pawlak, A.M., *Proceedings ICEM '92 International Conference on Electrical Machines*, Vol. 1, University of Manchester Press, 1992. With permission; [c] courtesy of Delphi Corp.)

$$\alpha = \frac{P\theta}{2} \quad (7.13)$$

where θ is a mechanical angle, α is an electrical angle, and P is the number of poles.

Thus, for the mechanical angle of $\theta = 4.5^\circ$, the number of poles $P = 40$ corresponds to an electrical angle of $\alpha = (40 \times 4.5^\circ)/2 = 90^\circ$, at which point the sinusoidal flux distribution provides a maximum flux-density value. Because the actuator's torque characteristic is

**FIGURE 7.29**

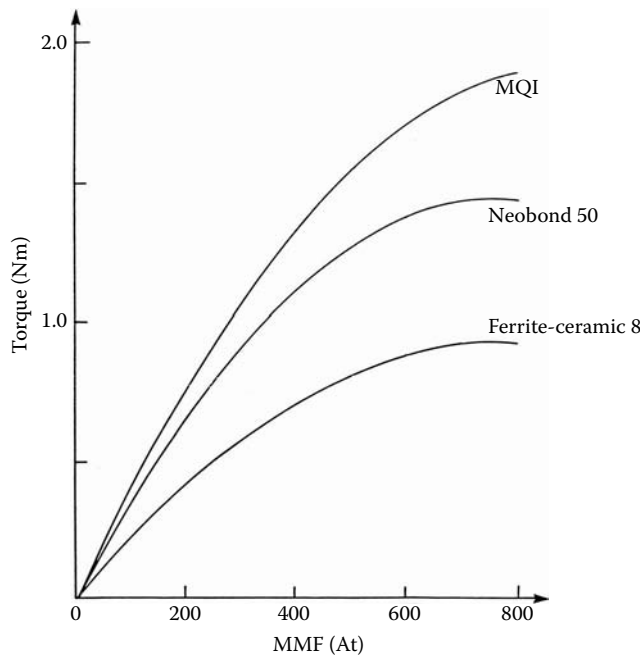
PM flux-density distribution. (From Pawlak, A.M., *Proceedings ICEM '92 International Conference on Electrical Machines*, Vol. 1, University of Manchester Press, 1992. With permission.)

affected by the magnetic flux distribution along the PM, the maximum torque value corresponds to the mechanical angle of 4.5° . For the internal arc magnetization of the ring magnet, no iron ring for magnetic flux return is required. The thickness and material of the PM were selected to provide the field strength necessary to develop the required torque in interaction with the electromagnet. Several magnet materials were investigated — Ferrite Ceramic 8, Neobond 50, and Magnequench MQI — as presented in Table 7.1. For the original design the Ferrite Ceramic 8 magnet material was used. Analysis indicated that this design is capable of developing a 0.88 Nm torque at the nominal MMF of 600.0 At and displacement of 4.5° . Upgrading the magnet material to Neobond 50 improved the torque level to 1.38 Nm, which still did not satisfy the requirements. By changing the magnet material to MQI, the torque further improved to 1.67 Nm, as shown in Figure 7.30, which satisfied the torque requirements. Therefore, neodymium magnet-material Magnequench MQI was selected for the final actuator design with dimensions identified in Figure 7.28.

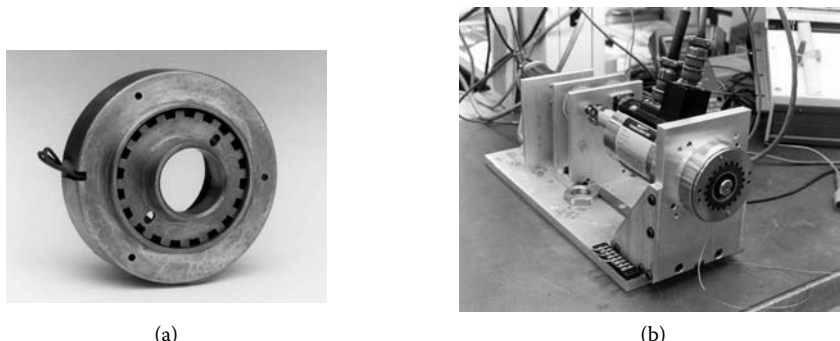
7.2.6 Claw Pole Rotary Actuator Test Results

For the final actuator design, the PM was made of a solid ring and magnetized using a custom magnetizing fixture. The claw pole magnetic parts were machined, although, for the mass production purposes, powder-metal technology should be used to reduce the cost of manufacturing. The electromagnet parts were also machined, although, for the mass production, these parts would be stamped from sheet metal to minimize the manufacturing cost. Figure 7.31(a) shows the assembly of the final actuator design. Figure 7.31(b) shows the test fixture with the attached final actuator assembly.

All actuator models were assembled and tested by the torquemeter test fixture to obtain torque-position characteristics, as presented in Figure 7.31(b). This test fixture has a torque gauge and a position sensor directly connected with a x - y plotter. Results of the torque test and the analytical predictions are compared as presented in Figure 7.32. Figure 7.32 presents such a comparison showing good correlation between the test and the mathematical model over the entire range of the excitation current. At the nominal MMF of 600.0 At, the test torque value differs less than 16.0% from the predicted torque value. Neglecting the cogging torque contributed to this discrepancy, although the cogging torque value is less than 10% of the nominal torque level. Thus, for the engineering design purposes, the

**FIGURE 7.30**

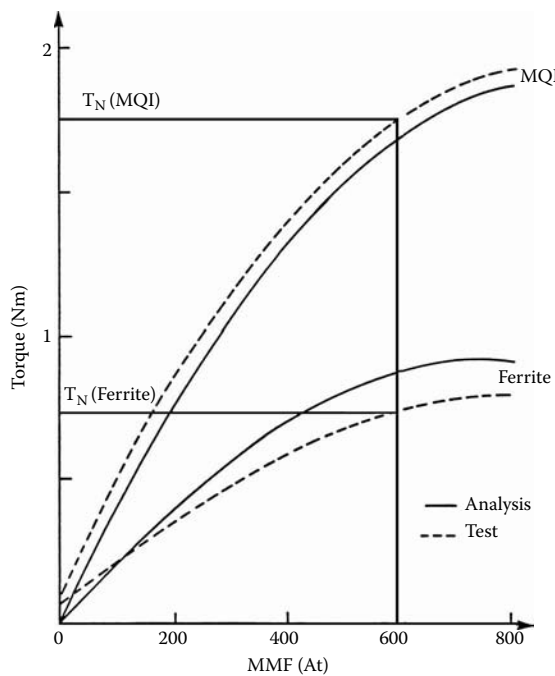
Torque vs. current analysis. (From Pawlak, A.M., *Proceedings ICEM '92 International Conference on Electrical Machines*, Vol. 1, University of Manchester Press, 1992. With permission.)

**FIGURE 7.31**

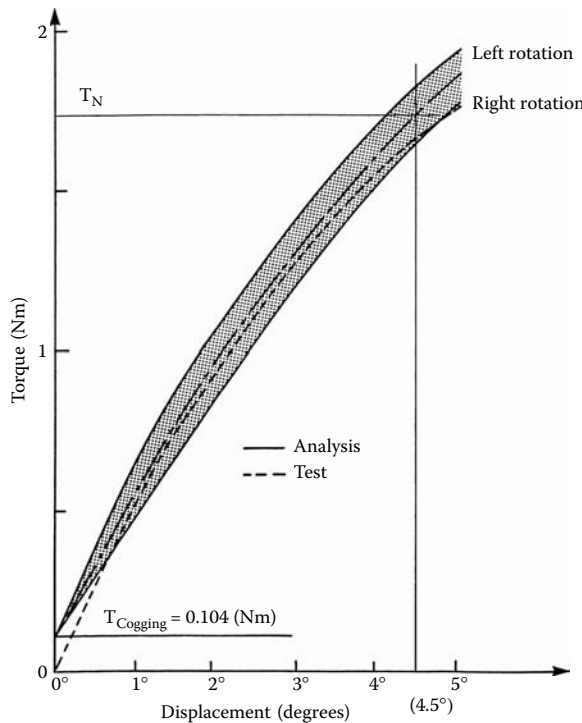
Claw pole actuator assembly and test fixture: (a) final assembly, (b) test fixture with claw pole actuator. ([a] From Pawlak, A.M., *Proceedings ICEM '92 International Conference on Electrical Machines*, Vol. 1, University of Manchester Press, 1992. With permission; [b] courtesy of Delphi Corp.)

developed mathematical model is quite satisfactory. If more accurate estimates are required, a 3D FE mathematical model must be used.

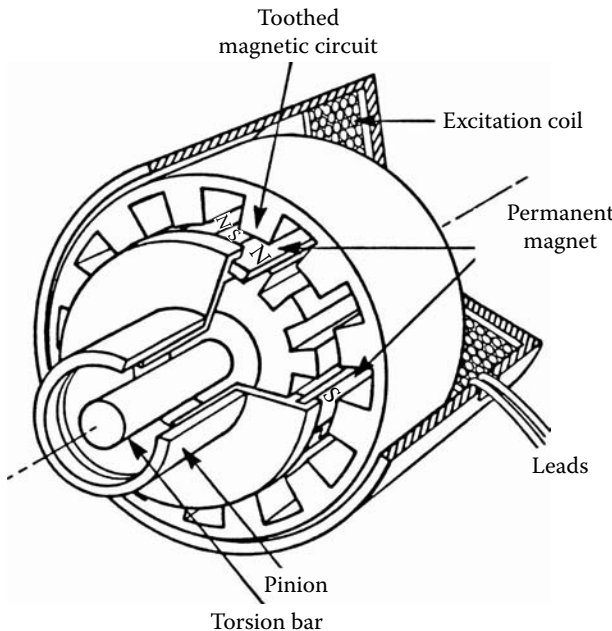
Test results of the torque-position characteristic are presented in Figure 7.33 for both left and right directions of rotation showing satisfactory torque symmetry and good correlation with analytical predictions. At a position of 4.5° , this system provides 1.74 Nm of torque variation, which is high, considering the relatively low magnet energy density and additional parasitic air gaps. Our tests showed that the actuator achieved the required controllability, torque level, and symmetrical variable effort for both the left and the right directions of rotation. It develops attractive and repulsive electromagnetic torques with limited-angular movement in both the left and right directions of rotation. Actuator performance was well supported by test results.

**FIGURE 7.32**

Torque vs. current for claw pole actuator. (From Pawlak, A.M., *Proceedings ICEM '92 International Conference on Electrical Machines*, Vol. 1, University of Manchester Press, 1992. With permission.)

**FIGURE 7.33**

Torque vs. displacement for claw pole actuator. (From Pawlak, A.M., *Proceedings ICEM '92 International Conference on Electrical Machines*, Vol. 1, University of Manchester Press, 1992. With permission.)

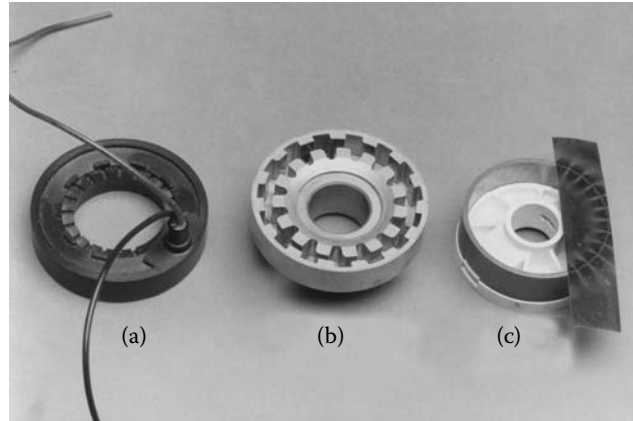
**FIGURE 7.34**

Cylindrical rotary actuator. (From Pawlak, A.M. et al., *Magnetic Power Steering Assist System — MAGNASTEER*, Publ. No. 940867, Society of Automotive Engineers, Detroit, MI, 1994. With permission.)

7.3 Cylindrical Rotary Actuator

This section describes a modern homopolar rotary actuator with a ring radially magnetized multipolar PM featuring a high-force density, transverse flux configuration, which performs a spring action by developing electromagnetic torques with limited-angular movement (Gieras and Wing 2002, Hennenberger and Bork 1997, Weh et al. 1990). The rotary actuator investigated features high-performance torque output because the actuator's topology provides a magnetic torque gearing effect (Harris et al. 1975, Hennenberger and Bork 1997, Mercow et al. 1990). The torque level is proportional to the number of independent magnetic sections, which are equal to the number of stator teeth or magnet pole pairs. Therefore, the total force developed by the actuator is the sum of the forces developed by each tooth-pitch section (Pawlak 1990). The homopolar rotary actuator consists of three basic components: a stationary electromagnet, a rotary toothed pole structure, and a rotary multipolar PM ring, as presented in Figure 7.34 and Figure 7.35.

The stationary electromagnet is composed of an external magnetic circuit and a precision wound coil fully encapsulated in a plastic molding. The stationary coil location enables brushless current connections, essential for reliability. The toothed pole structure is manufactured as a single piece using advanced powder-metal technology, which allows the two concentric VR ferromagnetic toothed structures to be attached together by a nonmagnetic disk. The high-energy neodymium PM ring with energy density of 32 MGoe and

**FIGURE 7.35**

Cylindrical rotary actuator parts: (a) coil, (b) toothed structure, (c) magnet and magnetization pattern. (Courtesy of Delphi Corp.)

multipolar radially oriented magnetization was developed for the purpose of this actuator, as presented in Chapter 1. This actuator features high torque output because its multipolar structure provides a magnetic torque gearing effect with the high-density transverse flux configuration utilizing both the outside and the inside magnet surfaces, similar to the transverse flux motors (TFMs) (Gieras and Wing 2002, Hennenberger and Bork 1997, Weh et al. 1990).

The PM is located inside the toothed structure with the number of pole pairs corresponding to the number of teeth. In the TFM, at the constant ratio of ampere-turns NI to OD or ID, the line current density can be increased by increasing the number of pole pairs. The peak value of the line current density of a single phase in the TFM is:

$$A_f = \frac{\sqrt{2}I_f N_f}{2\tau} = \frac{p2I_f N_f}{\pi D_\delta} \quad (7.14)$$

where A_f is the peak value of the line current density, I_f is the rms value of phase current, N_f is the number of turns per phase, D_δ is the average diameter of air gap, τ is the stator pole pitch, B_δ is the flux density in the air gap, and p is the number of pole pairs.

Because the force density (shear stress) is proportional to the product of $A_f B_\delta$, the electromagnetic torque of the TFM is proportional to the number of pole pairs (independent sections). Therefore, similar to the rotary actuators, the TFM motor's torque is proportional to the number of poles. This actuator's topology provides a magnetic torque gearing effect; therefore, configurations based on the transverse flux topology are well suited for the gearless electromechanical drives.

7.3.1 Cylindrical Rotary Actuator Analysis

The external magnetic circuit provides the same polarity, depending on the direction of the excitation current, to both the inner and the outer toothed poles regardless of its angular position. This homopolar actuator configuration enables the reversal of the torque by simply reversing the excitation current. Both the toothed pole structure and the ring

magnet have unlimited freedom of movement in both the left and right directions of rotation. In addition to the full rotary motion of the actuator center parts, this configuration allows for a limited-angular motion of the PM ring with respect to the toothed poles.

To satisfy a desirable symmetrical torque requirement and provide a stable equilibrium at the neutral PM position, a unique arrangement of the magnetic circuit was devised. A stable equilibrium for both coil MMF and magnet was established with a half-tooth overlap arrangement and with the magnet located in the middle of this shift, as shown in Figure 7.7. The specific location of the different actuator parts, indicated in Figure 7.7, is essential to provide a stable equilibrium position for the PM in its neutral position. The pole teeth on both sides of the magnet are offset by one-half of a tooth width, and the PM pole is centered over the overlapped teeth part in the stable equilibrium position because in this arrangement all forces exerted on the PM are balanced at both directions of the coil excitation. If the PM rotor is moved to the left or to the right of this neutral position, a net reluctance force is produced to return it to the stable position. When the magnet is moved with respect to the toothed structure and the coil is excited, the magnetic flux-line distribution indicates the direction of the developed magnetic forces. Note the 3D character of the coil flux distribution, as shown in Figure 7.8.

Similar to the disk rotary actuator, the cylindrical actuator configuration utilizes both the external and internal PM surfaces for torque development, thus providing a high-torque density structure. Proper balance of both magnetic flux levels (flux densities) — one due to the internal PM and the second due to the stationary external coil — is the most important task during the actuator design optimization. This can be achieved by establishing a magnet MMF based on material and magnet thickness, which corresponds to the external coil MMF based on the nominal current and the number of coil turns. The torque developed by the actuator is a function of the coil MMF and the PM magnetic field interaction. The total actuator torque consists of two components: the PM VR cogging-type torque and the mutual synchronous-type torque due to the interaction of the coil MMF and the magnet. The total torque developed is a superposition of these components as described in Equation 7.1 through Equation 7.3, and presented in Figure 7.3.

7.3.2 Cylindrical Rotary Actuator 2D Analysis

The 2D FE software package was used to analyze this complicated, nonsymmetrical structure (Ansoft 1991, Nehl et al. 1988). The magnetic force calculations can be done based on 2D analysis using a basic actuator section extending over one tooth-pitch segment, as presented in Pawlak (1990), or based on the 3D analysis for the entire model or wedge model of the actuator, as discussed in Section 7.3.3. Two 2D models will be analyzed, representing the Cartesian model in a rectangular plane and cylindrical model sections in the axial plane, as presented in Figure 7.36 and Figure 7.37, and Figure 7.38, respectively.

The magnetic force and torque developed by the actuator are obtained from the x - y plane, as shown in Figure 7.36. Some assumptions are made in this model. First, the total force developed is the superposition of component forces developed by one-pole-pitch section and, therefore, only one such component needs to be analyzed. Second, the appropriate excitation electromagnetic-circuit geometry is introduced with adequate coil and sectional magnetic flux crossing areas to secure the proper flux densities.

With the assumption that the magnet radius is very large, the x - y plane is comparable to the disk Cartesian model presented earlier. The force equations, Equation 7.5 through Equation 7.8, developed for disk magnets correspond to the cylinder magnet analysis. Because of this, the same force equations will govern the Cartesian analysis of the cylindrical actuators, provided that appropriate actuator's dimensions and physical parameters

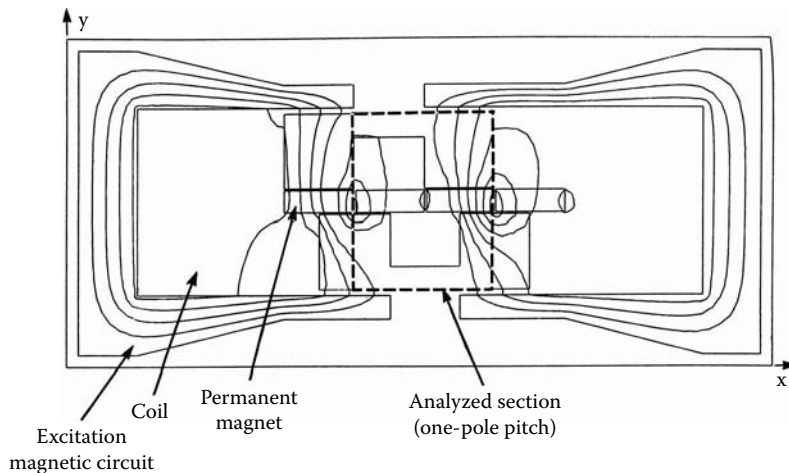


FIGURE 7.36
Cartesian actuator with the flux lines. (Courtesy of Delphi Corp.)

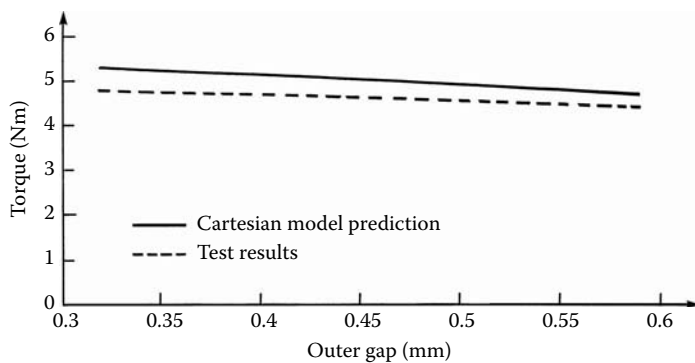
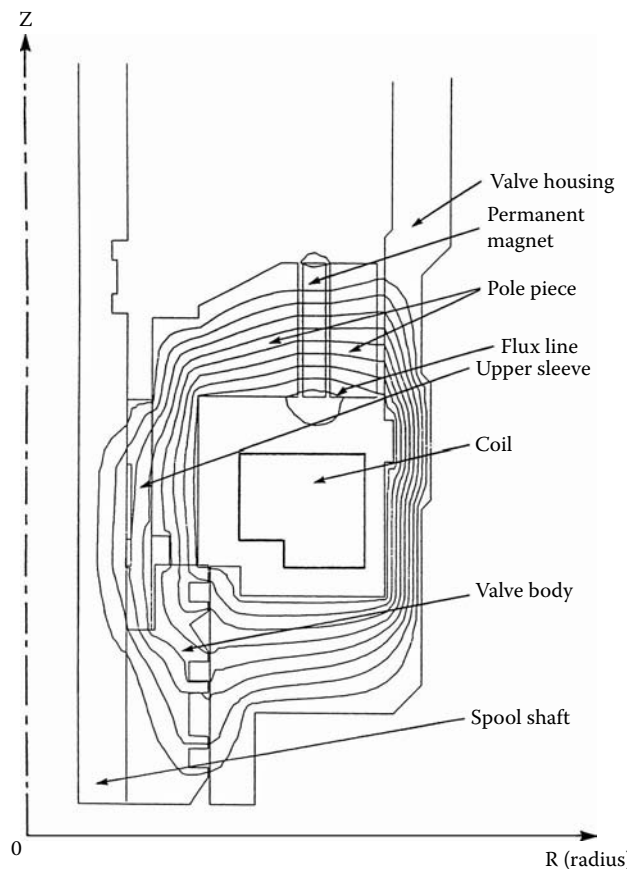


FIGURE 7.37
Torque values from the Cartesian analysis and test comparison. (From Pawlak, A.M. et al., *Proceedings of the IEEE/IAS '94 Conference*, Vol. 1, Denver, CO, October 2–6, 1994. With permission.)

are used. The stable equilibrium position discussions of the disk magnet configuration are comparable to the stability of a ring magnet because they were derived from the Cartesian analysis.

Evaluations of the force and torque developed by the actuator are based on the Cartesian symmetry model for the one-pole pitch of the actuator (indicated by a dotted line in Figure 7.36). This value is used to compute the torque produced by the entire actuator, as described in Section 7.1.1 for the disk actuators. The Cartesian model preprocessor, which was developed to simplify these calculations, allowed for simple modification of magnet position (distance from the actuator's centerline, not circumferential position of segments), thickness, and actuator air gaps. Four physical variables were considered in the x - y analysis: magnet inner radius, magnet outer radius, inner gap width, and outer gap width. The inner pole radius and the outer pole radius were calculated from the magnet and air gap information. The Cartesian model was validated against the actual data. Two magnets of nominal size and strength and two toothed structures having similar physical properties were used in the test. A three-step procedure was devised in which the gap between the magnet ring and the outer pole (outer gap) was increased, while the gap between the

**FIGURE 7.38**

Cylindrical model of actuator with flux lines.

magnet ring and the inner pole (inner gap) was held constant. Each pole was measured using a coordinate measuring tool, then tested for torque output with each magnet, at $\theta = 4^\circ$ of the valve angle of rotation. Nominal currents of $+3$ A for positive and -3 A negative excitation were applied. Then each pole's outer teeth were machined to increase the outer gap, then tests were conducted again. This step was repeated once more, for a total of three outer gaps per pole. Outer gap dimensions were increased from 0.3×10^{-3} m to 0.6×10^{-3} m, while the inner gap remained unchanged during testing. The inner gap measured 0.5×10^{-3} m. Each outer gap iteration for each pole was tested twice with each magnet. Validation of the Cartesian model was done by comparing the total torque predicted by the model with the actuator's total torque. Total torque from testing is the sum of the average of the left and right turn torques at nominal positive and negative currents. Because the model was for the one-pole pitch, the total torque that the actuator would develop had to be computed, as presented in Example 7.1. Comparison of the test results and analytical results from the Cartesian model are presented in Figure 7.38 and show the same trend with a discrepancy that does not exceed several percent. The total torque developed by the actuator is described in Equation 7.6 through Equation 7.8. The calculated torque level is in close agreement with test results, as presented in Figure 7.37. This figure also shows the invariance of the torque level with the changes in the main air gap variation. This is because the magnet thickness is a part of the main air gap because this actuator utilizes both the inside and the outside magnet surfaces.

Force and torque cannot be calculated directly using the cylindrical model, but the torque level can be estimated. The force developed by the actuator (and so the torque) is proportional to the square of the flux level in the air gaps. To account for both the inner and outer gap, a total flux-density level was computed:

$$B_t^2 = B_{in}^2 + B_{out}^2 \quad (7.15)$$

where B_t is the total flux-density level, B_{in} is the flux density in the inner gap, and B_{out} is the flux density in the outer air gap.

The force developed by the actuator is then:

$$F_T = kB_t^2 \quad (7.16)$$

where F_T is the total force and k is a coefficient of proportionality. Finally, the total torque level is calculated as:

$$T_T = F_T \times R_{avg} \quad (7.17)$$

where T_T is the total torque, and R_{avg} is the average radius of the magnet ring.

The average radius of the magnet ring can be obtained from the magnet geometry whereas the total force is based on the 2D x - y model analysis.

The axial cross section or cylindrical symmetric model of the cylindrical actuator shown in Figure 7.38 was created to study the flux pattern and flux density as it traveled through the actuator. Flux density was studied as the material and geometry of the actuator were varied. The effect of these changes was evaluated by measuring the flux density in the air gaps between the magnet and the pole piece. This is an indicator of the torque that the actuator can develop, but assumptions had to be made regarding the flux, which travels between the teeth of the pole piece but not through the circuit. This is the reason why the Cartesian model also should be created. Seven physical variables are considered: magnet inner radius, magnet outer radius, magnet bottom position, magnet length, inner gap width, outer gap width, and outer pole radius. The inner pole radius and the outer pole radius were calculated from the magnet and air gap information.

The cylindrical model was validated against the actual data in the same manner as explained in the above discussion about the Cartesian model. The analytically predicted torque level was compared to the actuator's output torque test results to validate the cylindrical model. The torque level is proportional to the sum of the squares of the inner and outer gap flux-density levels, as presented in Equation 7.13 through Equation 7.15. Flux density measured at the surface of the magnet, halfway along its axial length, is used in these calculations, as presented in Example 7.2. Figure 7.39 indicates that, as expected, both the analytically predicted and tested torque levels decrease when the outer gap is increased. Although the torque level shown in Figure 7.39 is calculated for the nominal inner gap of 0.5212×10^{-3} m, two other air gaps were also considered.

The inner gap of 0.5212×10^{-3} m provided the smoothest results, as presented in Figure 7.40. The results of analysis using inner gaps of small elements required by these small inner gaps are the cause of these erratic results because mathematical conversion is harder to achieve when small elements are used in the model. If erratic results occur, more analyses should be conducted in the surrounding region to determine the true performance of the device.

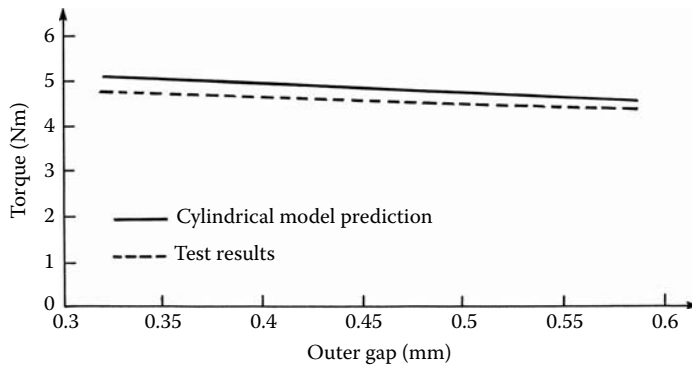


FIGURE 7.39
Torque values from the cylindrical analysis and test comparison.

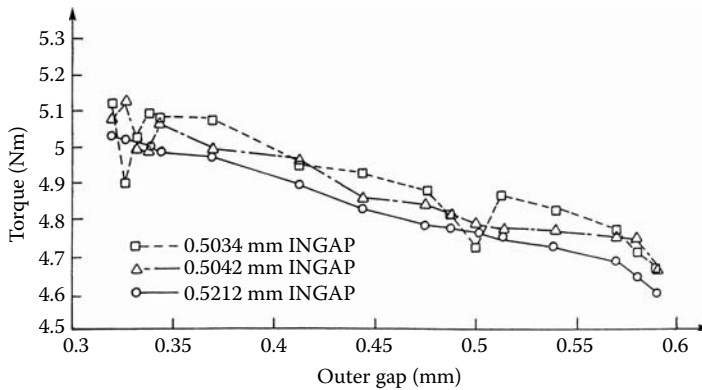


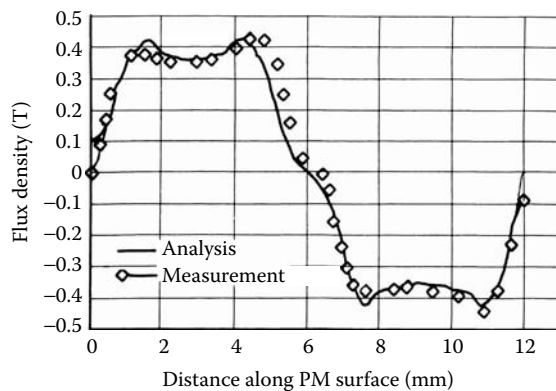
FIGURE 7.40
Torque values from the cylindrical model analysis for different inner gap values.

7.3.3 Cylindrical Rotary Actuator 3D Analysis and Test Results

Because of the magnetically complicated and nonsymmetrical rotary actuator configuration, the analysis of the actuators is based on 3D FE software. The analysis, which is well supported by test results, shows that symmetrical magnetic forces in both directions of rotation were achieved with a stable equilibrium position, satisfying all design requirements. More accurate analysis was obtained using the 3D FE software applied to the full or wedge models (Ansoft 1991, Pawlak et al. 1995). In these models, torque calculations are based on the virtual work principle using the local Jacobian derivative (Coulomb and Meunier 1983):

$$T_T(\theta) = \frac{dW(\theta, i)}{d\theta} \Big|_{i=const} \quad (7.18)$$

In this approach, the moving object is not actually rotated during the force computation and, hence, requires only one field solution. Only those tetrahedra that lie along the outside surface of the object need to be virtually distorted for these calculations. Therefore, the virtual torque is given by the change in coenergy of these tetrahedra.

**FIGURE 7.41**

PM flux-density distribution. (From Pawlak, A.M. et al., *Proceedings of the IEEE/IAS '94 Conference*, Vol. 1, Denver, CO, October 2–6, 1994. With permission.)

The 3D software we used does not have the ability to provide the proper ring magnet magnetization pattern produced by the magnetizer. Therefore, precise flux-density measurements were used to ensure proper representation of the multipolar ring magnet magnetization. In the magnetizer, the magnet is attached to a retainer on one side, resulting in a unique magnetizing coil structure that produces magnetization that is different for both the inside and the outside surfaces, as well as the north and south poles of the magnet. Fictitious oval-shaped magnet poles, as presented in Figure 7.43, were used to simulate the real field shape, as shown in Figure 7.41.

The computed flux distribution and its level of magnetization as well as a very important nonmagnetized zone show an excellent correlation with test results. With proper magnet flux-density representation, the electromagnetic torques were calculated for the complete, full actuator model for both the left and right directions of rotation. Figure 7.42 shows the 3D rotary actuator geometry for the full model with the major magnetic components identified. Note the oval-shaped magnet poles that are required to ensure the proper magnetic flux-density distribution. Figure 7.43 shows the flux-density distribution for the entire rotary actuator geometry of the full model.

For the full model, the magnetic torque was calculated for the entire range of magnet rotation of $\pm 4.0^\circ$. Figure 7.44 shows the results of this analysis where the corresponding test data taken under the same current and displacement conditions show good correlation between the full model and the test results. This accuracy is similar to that of the 2D model. However, the 3D modeling provides additional information about the stable equilibrium position and takes into account the irregularities of the tooth structure, which is not possible with the 2D model.

The discrepancy between the predicted and tested stable equilibrium position is due to the workstation operational memory limitation used at the time of these simulations that only allowed a single field solution (using about 100,000 tetrahedra) at each simulated point with no possibility for further adaptive mesh refinement due to time and swap space limitations. Therefore, the wedge model, which modeled only one fifth of the full model and, hence, could permit adaptive mesh refinement improvement, was used. In the wedge model, a repeatable, symmetrical magnetic-circuit part was used for the rotary actuator. The periodicity in the actuator was exploited by using matching boundary conditions for the model. Figure 7.45 shows the 3D rotary actuator geometry for the wedge model, and Figure 7.46 shows the flux-density distribution for the wedge model.

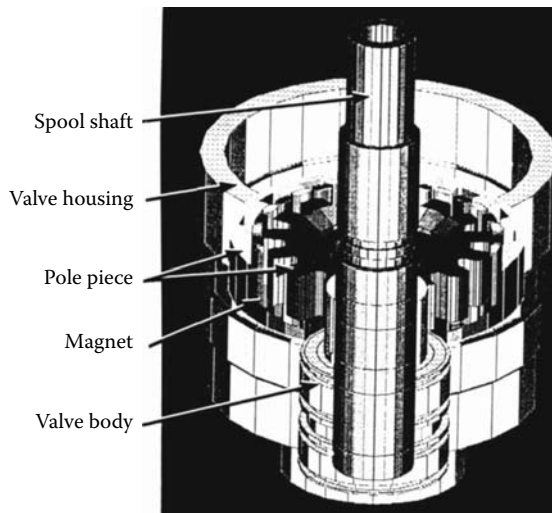


FIGURE 7.42 (Color Figure 7.42 follows p. 294.)

A 3D actuator geometry for the full model. (From Pawlak, A.M. et al., *Proceedings of the IEEE/IAS '94 Conference*, Vol. 1, Denver, CO, October 2–6, 1994. With permission.)

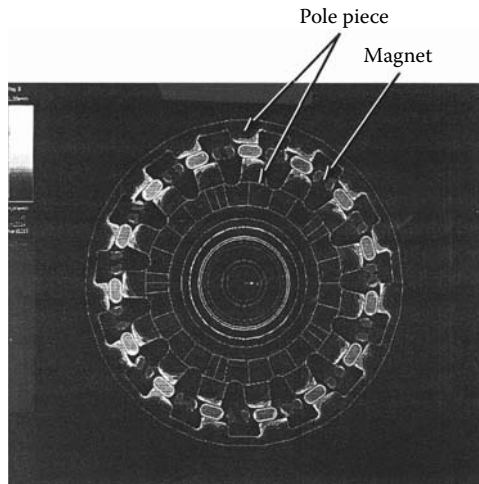
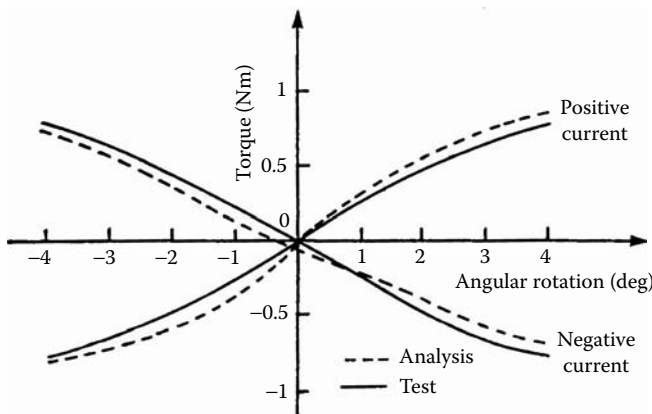


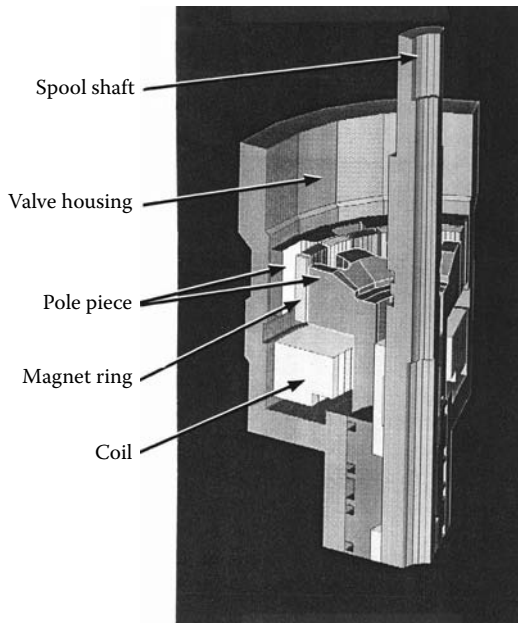
FIGURE 7.43 (Color Figure 7.43 follows p. 294.)

Full model flux-density distribution. (From Pawlak, A.M. et al., *Proceedings of the IEEE/IAS '94 Conference*, Vol. 1, Denver, CO, October 2–6, 1994. With permission.)

Results of the torque computation as a function of rotary magnet position up to $\pm 2.0^\circ$ for the wedge model are shown in Figure 7.47. Note the torque symmetry for both the left and right directions of rotation and the stable equilibrium position, which is very close to the center of rotation. Corresponding test data taken under the same current and displacement conditions show good correlation, within several percent, between the wedge model and the test results. The improvement in results is due to the fact that the final solution in the wedge model is based on three adaptive mesh refinements, the energy error metric to the solution being progressively reduced with each refined mesh.

**FIGURE 7.44**

Torque vs. angular position for the full model comparison with the test results. (From Pawlak, A.M. et al., *Proceedings of the IEEE/IAS '94 Conference*, Vol. 1, Denver, CO, October 2–6, 1994. With permission.)

**FIGURE 7.45 (Color Figure 7.45 follows p. 294.)**

A 3D wedge model actuator geometry. (From Pawlak, A.M. et al., *Proceedings of the IEEE/IAS '94 Conference*, Vol. 1, Denver, CO, October 2–6, 1994. With permission.)

7.3.4 Cylindrical Rotary Actuator Design

Validation of the 3D FE model, based on both test and analytical results, proved the model to be useful for engineering design purposes. Using this mathematical model, parametric studies were performed to optimize the geometry of the rotary actuator. The goal of the actuator design optimization was to maximize the torque developed for nominal coil excitation current. The optimization follows an iterative process, with each iteration consisting of a three-step parametric study for the excitation coil (wire size, number of turns,

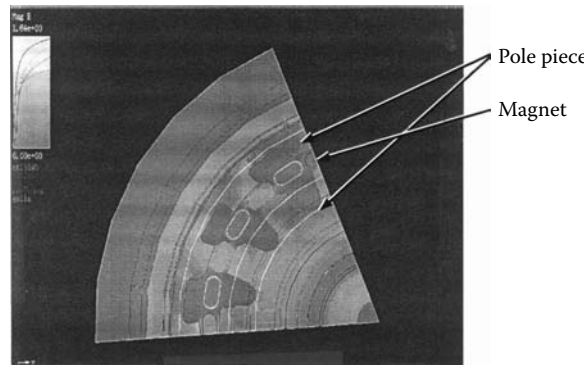


FIGURE 7.46 (Color Figure 7.46 follows p. 294.)

Wedge model flux density. (From Pawlak, A.M. et al., *Proceedings of the IEEE/IAS '94 Conference*, Vol. 1, Denver, CO, October 2–6, 1994. With permission.)

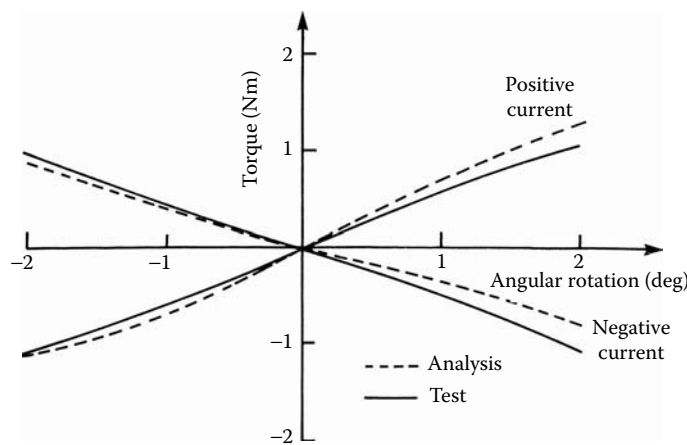


FIGURE 7.47

Torque vs. angular position for the wedge model. (From Pawlak, A.M. et al., *Proceedings of the IEEE/IAS '94 Conference*, Vol. 1, Denver, CO, October 2–6, 1994. With permission.)

resistance), the PM (material magnetic properties, geometry), and the magnetic circuit (geometry of the toothed structure, magnetic-circuit path). For the excitation coil, the nominal voltage and the coil size were predetermined by the electronic controller and envelope size specifications. The coil MMF was determined from the selected coil parameters, based on the thermal dissipation capacity at a given operating temperature. Validation of the 3D FE model based on both test and analytical results proved this model to be useful for engineering design purposes.

7.3.5 Cylindrical Rotary Actuator PM

The novel technology of ring neodymium magnets with radial orientation was developed by Hitachi and Daido of Japan in the early 1990s for the cylindrical rotary actuators for the Magnasteer system. Hitachi mastered the sintered method while Daido utilized the plastic flow of the neodymium magnets for the back extrusion method; see Chapter 1 for details on magnet manufacturing technologies (Daido 2003, Hitachi 1999). Figure 7.48 shows radially oriented ring magnet geometry, multipole magnetization pattern, and

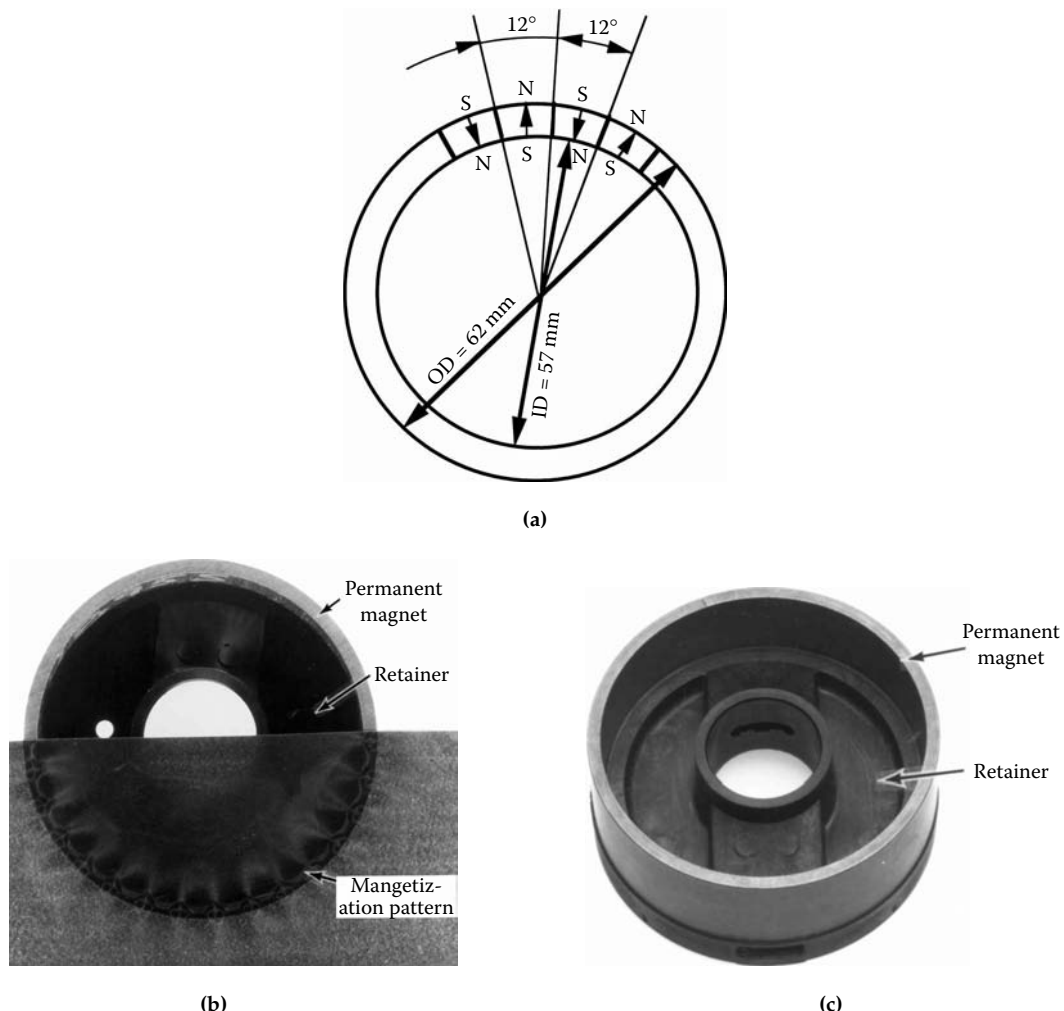
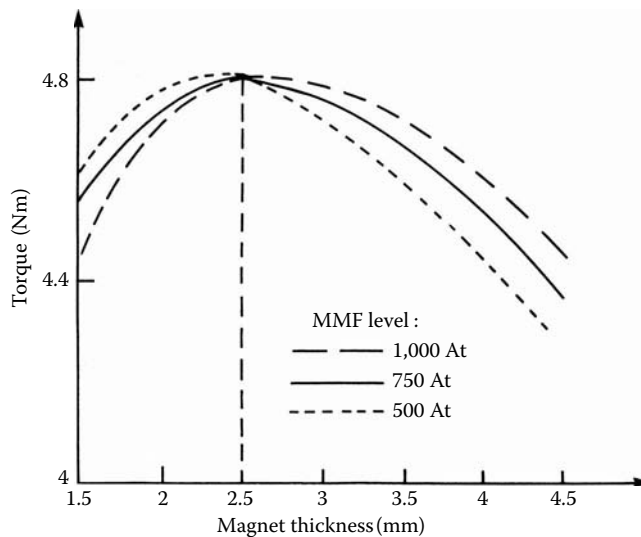


FIGURE 7.48

Ring neodymium magnet with radial orientation. (a) Magnet geometry, (b) magnetization pattern, (c) magnet model. ([a] Courtesy of Delphi Corp.; [b] from Pawlak, A.M. et al., *Magnetic Power Steering Assist System — MAGNASTEER*, Publ. No. 940867, Society of Automotive Engineers, Detroit, MI, 1994. With permission; [c] from Pawlak, A.M., *Proceedings of the Permanent Magnet Systems Conference*, Atlanta, GA, September 25–27, 2000. With permission.)

magnet final model structure. This magnet is the world's first successful development of high-energy radially oriented ring magnet applied for mass production.

PM parameters were established based on actuator requirements and constraints. The number of poles (30), equal to the number of teeth and slots, was determined by the required angle of rotation, and the actuator geometry was determined by the specified envelope size. The ring PM with multipole radial magnetization is inserted between two magnetic pole pieces and, similar to disk configuration, the number of magnetic poles is equal to double the number of magnetic poles and the magnetic poles are shifted by half of the pole pitch to provide an additional stable equilibrium position of the magnet. Similar to the disk actuator with the coil excitation, all poles on one side of the cylindrical actuator assume the same polarization, which is different for each side acting as a homopolar structure. Depending on the polarity, the actuator generates attractive or repulsive forces.

**FIGURE 7.49**

Magnet thickness study. (From Pawlak, A.M. et al., *Proceedings of the IEEE/IAS '94 Conference*, Vol. 1, Denver, CO, October 2–6, 1994. With permission.)

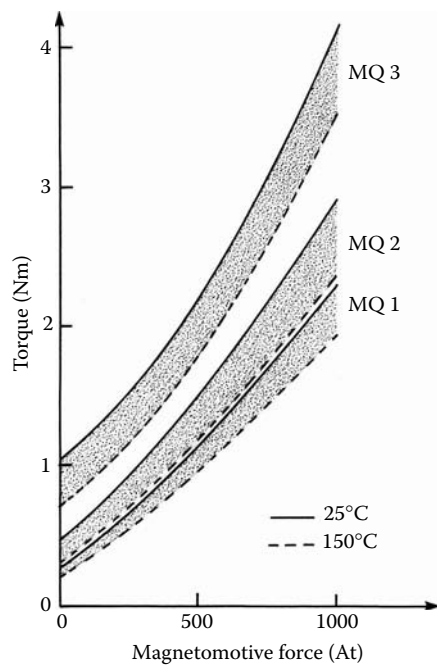
When the coil is energized, part of the magnet is exposed to the magnetizing MMFs, while the other part is exposed to the demagnetizing forces.

The PM is made as one piece and magnetized in a custom-made magnetizing fixture to secure both the required magnetic field shape and required neutral zone to secure a stable equilibrium position of the rotor. It has a complicated shape because a retention ring prevents a penetration of the magnetizing fixture inside the magnet, thus making outer and inner magnetizing field shapes different. Also the magnetic field shape is different for both north and south polarities because of the magnetizing fixture geometry limitations.

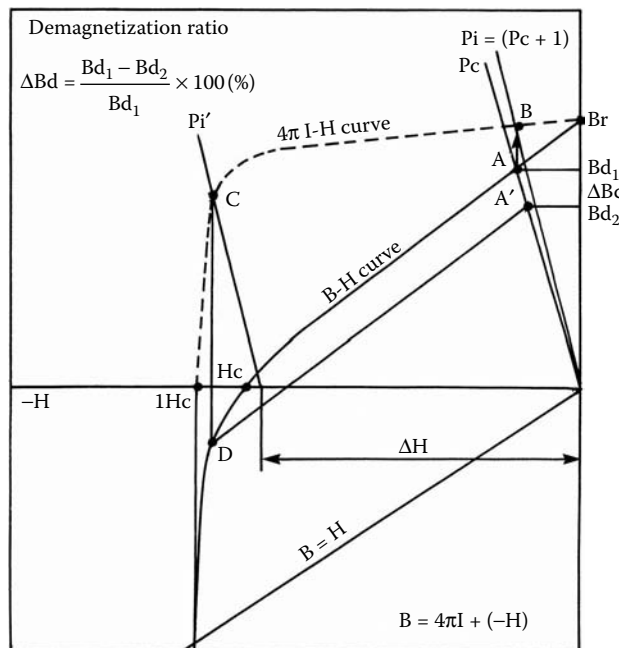
The thickness of the PM is an additional air gap added to the main air gaps for the magnetic flux developed by the excitation coil. Such a large total air gap adversely affects the magnetic flux level in the main air gaps, thus affecting the force developed. The magnet thickness, however, determines the magnet strength for a given magnet material, because the magnet is radially magnetized. Therefore, there is a trade-off between magnet strength based on the magnet thickness and coil field strength based on the MMF level. Based on the magnet thickness parametric study conducted for the three different MMF levels, the thickness of 2.5×10^{-3} m was selected, as shown in Figure 7.49.

Several neodymium-based Magnaquench (Carsile 1986) magnet materials were investigated — MQ1, MQ2, and MQ3, or their equivalents — with 8, 15, and 32 MGOe energy products, respectively, as presented in Figure 7.50 and Table 7.1. Figure 7.50 also shows the temperature effect upon torque performance between 25°C and 150°C. The demagnetization ratio for the multipole ring magnet was established from the magnet working point analysis under its nominal working conditions with the maximum temperature of 150°C and the maximum demagnetizing MMF current of 900.0 At to secure stable magnet performance. This technique, which uses the *BH* demagnetization curves for the PM material with the presence of an external magnetic circuit, is illustrated in Figure 7.51.

The magnet working point *A* is located at the intersection of the demagnetization *BH* curve and the total permeance curve P_C of an assembled and nonenergized actuator. This point is transferred to point *B* on the intrinsic curve and shifted by external demagnetization field

**FIGURE 7.50**

Actuator torque vs. MMF. (From Pawlak, A.M. et al., *Proceedings of the IEEE/IAS '94 Conference*, Vol. 1, Denver, CO, October 2-6, 1994. With permission.)

**FIGURE 7.51**

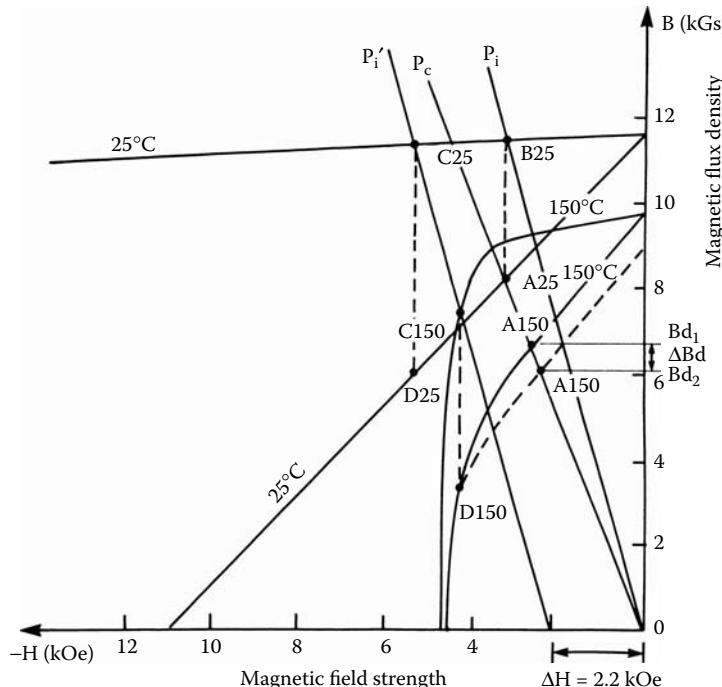
External field demagnetization analysis. (Courtesy of Delphi Corp.)

TABLE 7.2

Magnet Working Point Values

Point	Units	A25-Test	B25	C25	D25-Test	A150	A'150
Flux density	T	0.82	1.16	1.14	0.61	0.67	0.61
Demag. ratio	%	8.96					
External field	kOe	2.20					

Source: Pawlak, A.M., *Proceedings of IEEE/IAS '95 Conference*, Orlando, FL, October 9–13, 1995. With permission.

**FIGURE 7.52**

External field demagnetization analysis. (From Pawlak, A.M., *Proceedings of IEEE/IAS '95 Conference*, Orlando, FL, October 9–13, 1995. With permission.)

value of ΔF to the point C . From this, the point D on the demagnetization curve is determined. From this point, the recoil curve parallel to the BH curve intersects the magnet working point under demagnetization A' . The difference between these two points A and A' provides the value of the investigated demagnetization ratio ΔB_d . Both $A25$ and $D25$ (points A and D at 25°C) points are taken from the test, as presented in Table 7.2 and Figure 7.52.

The rotary actuator applied to automotive applications must be able to operate at temperatures up to 150°C without significant performance degradation over the life of the actuator. The magnets must not only withstand temperatures up to 150°C , but they must also retain their magnetic flux when exposed to that temperature to the maximum reverse magnetic field $-H_{max}$ generated within the actuator. An aging test that simulates the most stringent conditions of the magnet's working environment can be devised. In the course of aging for 1000 h in a 150°C oil bath, the magnetic flux density decreased during the exposure of the maximum reverse field $-H_{max}$. The flux loss under the combined

TABLE 7.3

Magnetic Properties of Test Magnets at Room and Elevated Temperatures Prior to Aging

Permanent Magnet	Flux Density 25°C	Flux Density 150°C	Energy (MGOe) 25°C	Energy (MGOe) 150°C	Coercive Force H _c (kOe) 25°C	Coercive Force H _c (Oe) 150°C	Coercive Force H _c (kOe) 25°C	Coercive Force H _c (kOe) 150°C	Max Rev Force H _{max} (kOe) 150°C
MQ1	0.56	0.46	6.8	4.3	13.4	7.2	4.8	3.7	0.77
MQ2	0.8	0.67	13.4	8.6	17.4	7.7	6.7	5.1	1.05
MQ3	1.08	0.93	23.7	15.1	14.1	4.8	9	4.6	0.25

Source: Courtesy of Delphi Corp.

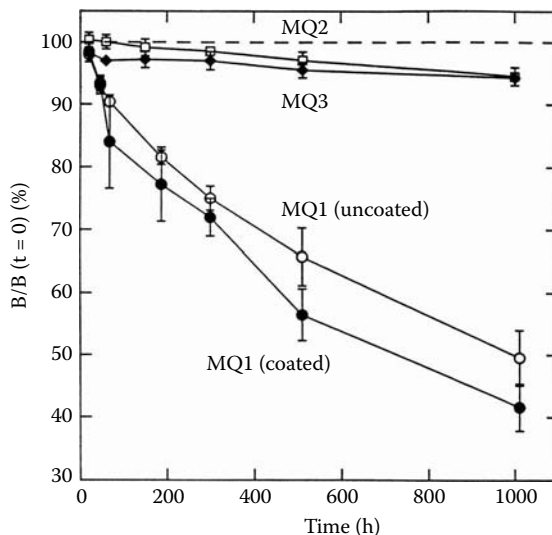


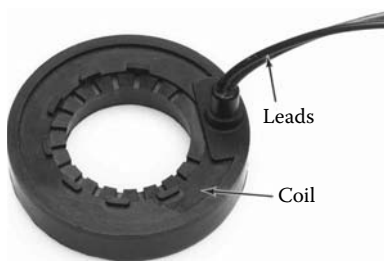
FIGURE 7.53

Aging losses for neodymium magnets. (From Pawlak, A.M., *Proceedings of IEEE/IAS '95 Conference*, Orlando, FL, October 9–13, 1995. With permission.)

design extremes of temperature and reverse field is the measure of magnetic aging performance. Magnet stability studies were conducted for the three fully magnetized magnets for each type: bonded MQ1 with and without coating, hot pressed MQ2, and die upset MQ3, as described in Table 7.3. Magnets were aged in hydraulic power steering oil at 150°C for 1000 h. At intervals during aging, the magnets were removed from the oil bath and each magnet was placed in a vibrating sample magnetometer (VSM) equipped with an oven heated to 150°C. A flow of inert argon gas through the oven protected the magnets from oxidation during the measurements. The magnetization $4\pi M$ and the magnetic flux density B were measured over the portion of the BH curve experienced by the magnet in operating actuator, that is, out of a maximum reverse field:

$$B = 4\pi M \quad (7.19)$$

The effect of aging for the time t is measured as the magnetic flux density B at $-H_{max}$ and 150°C relative to its value at the same applied field and temperature prior to aging. Figure 7.53 forms the central result of this test. The vertical axis is the magnetic flux density at $-H_{max}$ and 150°C after aging time as a percentage of its unchanged value. The MQ1 magnets

**FIGURE 7.54**

Rotary actuator coil. (From Pawlak, A.M. et al., *Magnetic Power Steering Assist System — MAGNASTEER*, Publ. No. 940867, Society of Automotive Engineers, Detroit, MI, 1994. With permission.)

lost 10% of their initial flux after only 70 h of aging and experienced a 55% degradation after 1000 h. A polymer coating provided no additional protection from aging. The bonded magnets are unsuitable for this application. The MQ2 and MQ3 magnets, in contrast, show flux losses of only about 6% after 1000 h and are considered suitable for this application.

Both the disk and ring magnets have proven high performance when applied to the rotary actuators. In particular, the ring magnets with multipole radial magnetization show superior performance. The ring magnets based on NdFeB using both sintered and quench die upset technologies were successfully developed and their first application was in electromagnetic rotary actuator devices for the Magnasteer system. Since then, they have found many applications in other electromagnetic devices, such as stepper motors, brushless motors, etc. (Miller 1989).

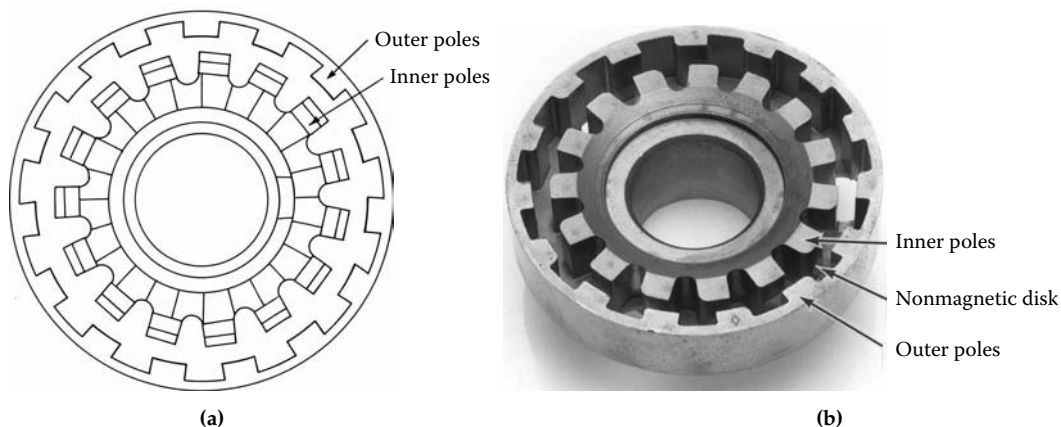
7.3.6 Cylindrical Rotary Actuator Excitation Electromagnetic Circuit

The coil is also manufactured using advanced precision winding technology and is overmolded with plastic. For the overmolding process, a golf ball technique was utilized to secure perfect sealability of the plastic around the coil. This is important to prevent a potential leak problem because the coil is submerged in the steering fluid all the time. Figure 7.54 shows the final overmolded coil for the rotary actuator.

7.3.7 Cylindrical Rotary Actuator Toothed Magnetic Structure

The reluctance variation introduced by the toothed magnetic structure, shown in Figure 7.55, plays an important role in the development of the actuator torque. Tooth and slot dimensions are related to the magnet pole dimensions. These dimensions were optimized to maximize torque at a given MMF level. The number of teeth (15) indicates the number of independent magnetic sections that develop electromagnetic torque, as presented in Equation 7.5 through Equation 7.7. Both the geometry and the number of teeth affect the torque developed by the actuator, which is a superposition of the torque developed by each pole pair for the actuator with cylindrical symmetry. They also indicate the period of the actuator torque waveform with respect to the angular position.

Low-cost, high-density powder-metal technology was used in the manufacturing of the magnetic toothed structure. Both the external and internal teeth are made out of magnetic powder, and the connecting plate is made of nonmagnetic stainless steel powder. All three parts are made in one pressing process, thus reducing the number of parts and improving manufacturing precision. This is the world's first part made as a solid piece out of both

**FIGURE 7.55**

Pole piece toothed structure: (a) toothed structure geometry, (b) toothed magnetic structure. ([a] Courtesy of Delphi Corp.; [b] from Pawlak, A.M. et al., *Magnetic Power Steering Assist System — MAGNASTEER*, Publ. No. 940867, Society of Automotive Engineers, Detroit, MI, 1994. With permission.)

magnetic and nonmagnetic powder metal. Figure 7.55 shows the final magnetic tooth shape and elements.

The pole piece was developed in an iterative process of FE analysis and modification of actual parts. The modifications are related to magnetic performance as well as the stable equilibrium position requirement for this actuator, as described in the application section (Section 7.4). They are based on radial relation of the inner to outer poles, axial relation of the inner to the outer pole teeth, and to the poles' tooth width-slot relation. Stable equilibrium requirements resulted in inner and outer pole rounds, as seen in Figure 7.55(b). The inner to outer pole relationship is a key part in developing a system that has coincident stable null (equilibrium) positions for positive, negative, and zero currents. The poles are set slightly over 50% tooth centerline overlap. This additional overlap helped make the system more stable in the equilibrium position. It also improved the linearity of the left and right torques and improved the actuator's working mechanical angle from 3° to 4° . A system of inner and outer poles acting on the ring PM is inherently nonsymmetrical mechanically and magnetically. The magnetic circuit must be modified to compensate for the mechanical nonsymmetry. To perform the compensation, the outer tooth radial depth was reduced about 55% and the inner radial depth was increased approximately 15%, as presented in Figure 7.55(a) and Figure 7.55(b). The original assumption of the same width for the inner and outer pole teeth was reconsidered to favor pie-shaped teeth. As a result, the outer teeth were widened to accomplish this, which showed immediate function improvement. Inner and outer teeth rounds also were introduced to further improve actuator performance in the stable equilibrium position and the torque symmetry in both the left and right rotations.

7.4 Rotary Actuator Applications

The rotary actuators presented were developed and found successful applications in the automotive industry, paving the road for modern electromagnetic devices and impacting the automotive industry by introducing electromagnetic devices to predominantly mechanical and hydraulic systems, such as the automotive speed-sensitive steering assist

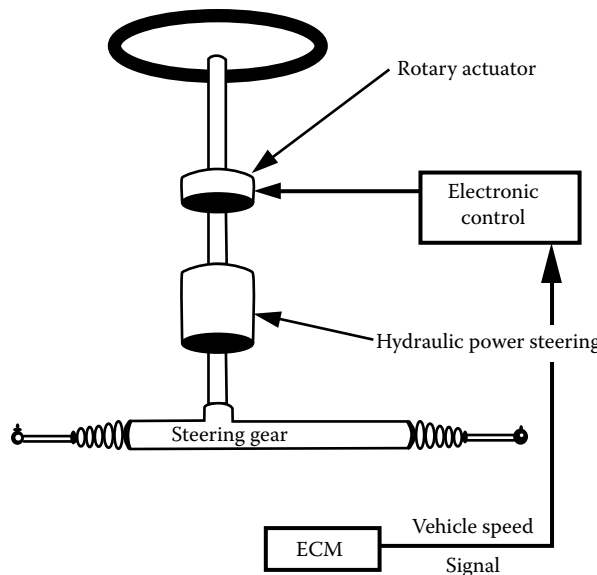


FIGURE 7.56

Schematic of the speed-sensitive steering assist Magnasteer system. (From Pawlak, A.M. et al., *Magnetic Power Steering Assist System — MAGNASTEER*, Publ. No. 940867, Society of Automotive Engineers, Detroit, MI, 1994. With permission.)

Magnasteer system, as shown in Figure 7.56 (Pawlak 1992, Pawlak et al. 1994b, Pawlak et al. 1994a, Gruber 1989, Eckhard 1992).

All commonly used speed-sensitive steering systems and power steering assist systems for cars are based on hydraulics. These systems change the pressure or modulate the flow of the conventional hydraulic power steering system. They require some means of actuation in the form of an electromagnetic device, such as a solenoid actuator, working as a flow or pressure regulator or brushless motor driving a hydraulic pump. Usually they are PWM controlled by a microprocessor. The common approach may use electronically controlled hydraulics, a power steering pump with a linear actuator, a hand-wheel speed sensor, a power gear with a specially modified valve, or any combination of the above. Based on vehicle speed and the signal from a hand-wheel sensor, if used, the controller varies the steering assist by pulse-width modulating the current in the actuator, thereby generating variable levels of steering assistance at varying vehicle speeds. The Magnasteer system simplifies the variable steering assist function and is based on electronically controlled rotary actuators, as presented in Figure 7.57.

The rotary actuators were adopted to provide additional control of the hydraulic power steering valve, which is the result of an electronically controlled vehicle-speed- and valve-position-dependent electromagnetic torque developed by the rotary actuator that acts by adding to or subtracting from that of the torsion bar. The electromagnetic torque varies with the torsion bar rotation and enhances the torsion bar effective torque for highway speed vehicle operations while reducing it for low speed parking maneuvers, as shown in Figure 7.58.

The angle of the mechanical rotation of a torsion bar is limited by the attached valve rotation angle to $\pm 7^\circ$; however, the valve and an actuator are optimized for efficient control of motion up to 4.5° in the left and the right directions of rotation that provides the optimum hydraulic pressure vs. effort.

This simple system does not require additional components, such as sensors, hydraulic pumps, or additional hydraulic plumbing. Furthermore, this system does not interfere

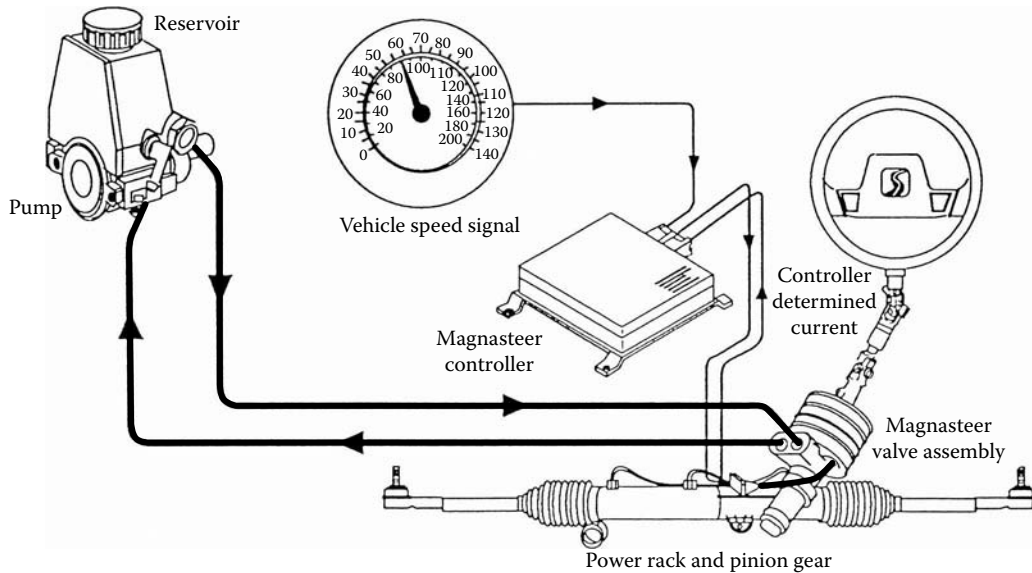


FIGURE 7.57
Magnasteer system components. (Courtesy of Delphi Corp.)

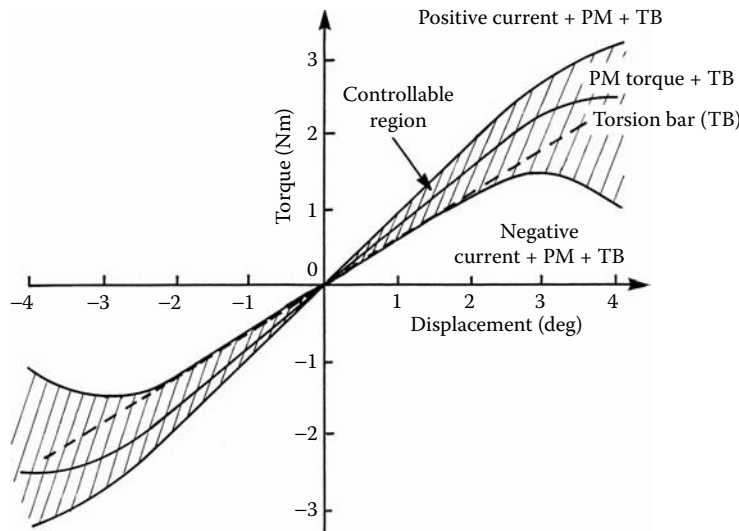
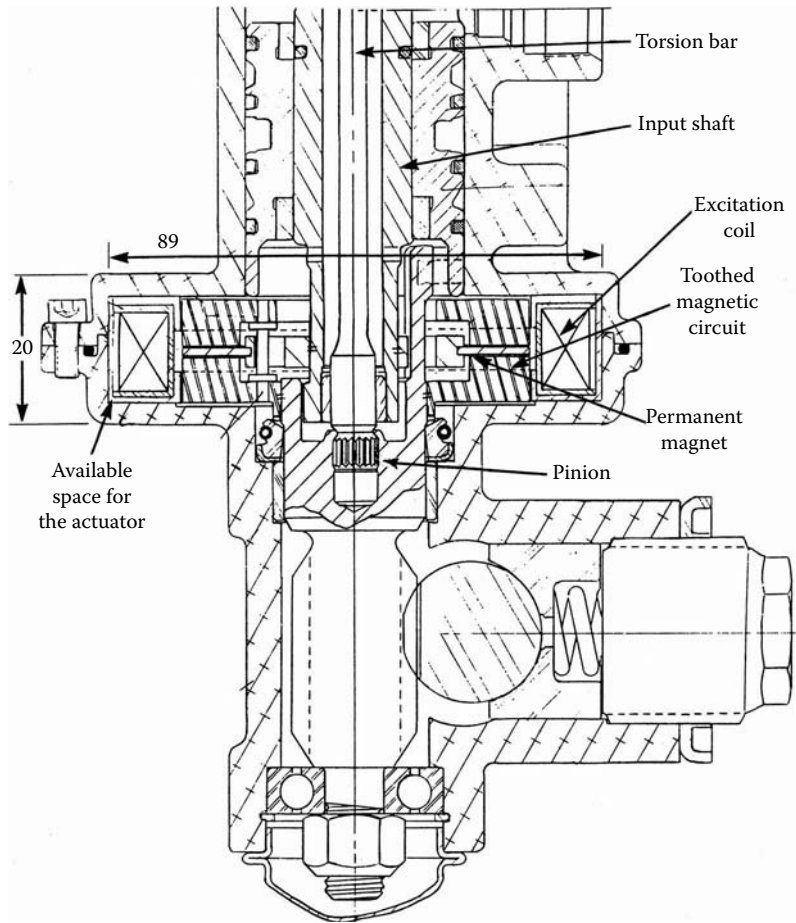


FIGURE 7.58
Torque vs. rotation angle. (From Pawlak, A.M. et al., *Proceedings of the IEEE/IAS '94 Conference*, Vol. 1, Denver, CO, October 2–6, 1994. With permission.)

with the existing hydraulic system. Moreover, the rotary actuator can be accommodated in the available existing space around the steering gear and, thus, can be used without any major steering system changes.

7.4.1 Disk Rotary Actuator Application

The early version of the speed-sensitive steering system components and location within a rack and pinion steering for the disk rotary actuator is shown in Figure 7.59 (Zuraski

**FIGURE 7.59**

Disk rotary actuator integrated with Magnasteer system components. (Courtesy of Delphi Corp.)

1989). The disk rotary actuator fits in the required envelope of $OD\ 89 \times 10^{-3}\ m$ and axial height $20 \times 10^{-3}\ m$. The stationary section is attached to the valve housing and is a part of the main magnetic circuit. The rotary section is attached to the movable valve parts. The toothed magnetic parts are mechanically coupled to the lower portion of the torsion bar through the pinion, and the PM is attached to the upper portion of the torsion bar through the input shaft, as presented in Figure 7.59. The presence of the parasitic air gaps, as presented in Figure 7.1 and Figure 7.59, allows for full rotary motion of the actuator components in the housing and for a limited-angular motion of the PM (attached to the input shaft) with respect to the toothed magnetic parts (attached to the pinion).

7.4.2 Claw Pole Rotary Actuator Application

The claw pole actuator basic geometry for the improved speed-sensitive steering application is shown in Figure 7.60. In this arrangement, however, both working areas of the PM and claw poles are limited, because only 79% of the active magnet and claw poles are utilized.

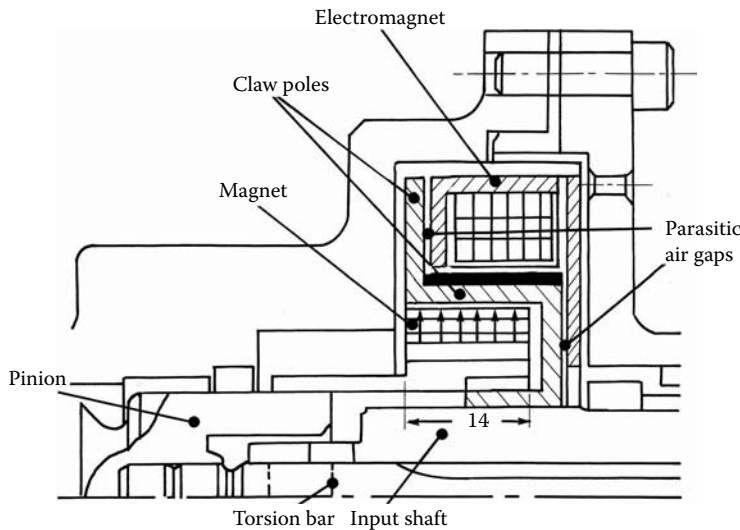


FIGURE 7.60
Base claw pole actuator assembly. (Courtesy of Delphi Corp.)

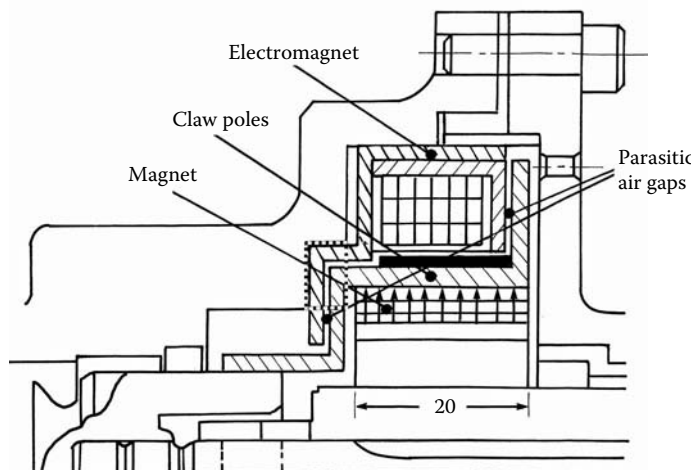
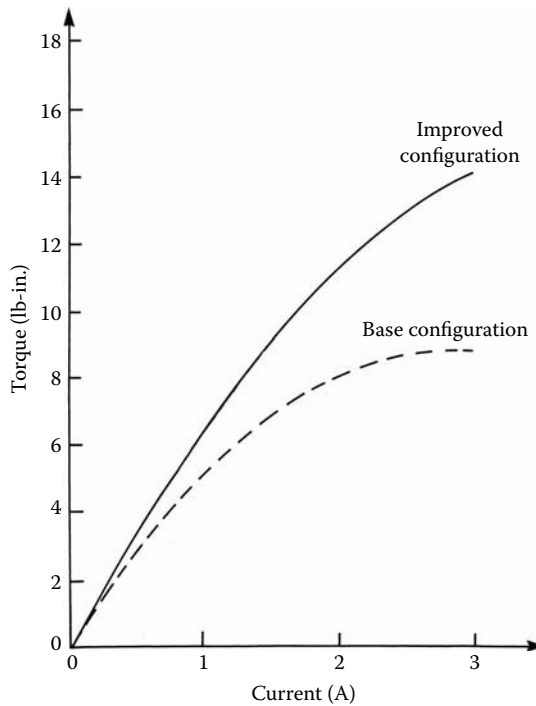


FIGURE 7.61
Improved claw pole actuator assembly. (Courtesy of Delphi Corp.)

An improved actuator configuration can be obtained by a special rearrangement wherein the magnet is attached to different assembly components, as shown in Figure 7.61. This arrangement fully utilizes the working space under the claw pole structure. The axial length of the PM was increased from 14.0×10^{-3} m to 20.0×10^{-3} m and the effective claw pole length was enlarged from 9.8×10^{-3} m to 20.0×10^{-3} m. Because certain measures were taken to decrease the MMF drop at the parasitic air gaps, it was necessary to increase the actuator package by a small volume, as represented by the dotted line in Figure 7.61. The thickness of the magnetic circuit is designed to avoid local saturations and, therefore, to enhance the magnetic flux performance.

**FIGURE 7.62**

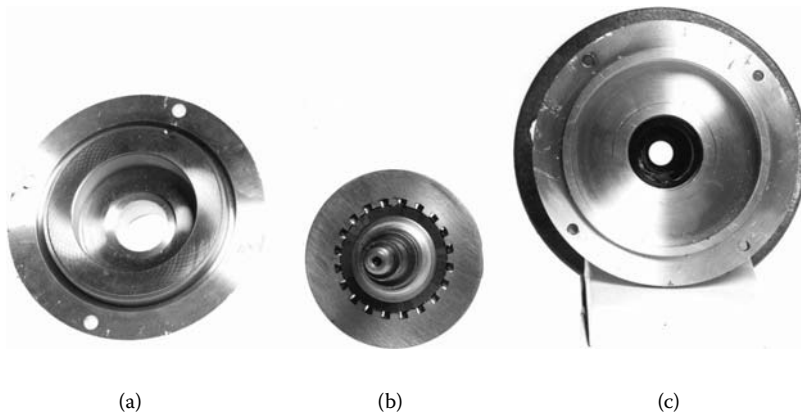
Torque vs. current for the base and improved claw pole actuator configurations. (Courtesy of Delphi Corp.)

Figure 7.62 shows analytical predictions of the torque developed for both the base and improved claw pole configurations. The improved torque performance is 60% higher in comparison with the base actuator at the nominal current of 3.0 A and with an angular displacement of 4.5°; however, its total envelope has exceeded the originally specified axial height of 20×10^{-3} m, as indicated by the dotted line in Figure 7.61. The improved configuration offers higher torque, but requires some additional space which, in this particular application, was not acceptable for the conventional steering gear design for which this actuator was adopted. Side elements are two-component housing for the center claw pole rotary actuator assembly. Figure 7.64 shows the final integration with the hydraulic valve component shown in detail in Figure 7.59 and Figure 7.63.

7.4.3 Cylindrical Rotary Actuator Application

A cylindrical actuator coupled with speed-sensitive steering Magnasteer system components is presented in Figure 7.58. The PM is attached to the input shaft and the toothed magnetic parts are attached to the pinion. Therefore, the toothed magnetic parts are mechanically coupled to the lower portion of the torsion bar through the pinion, and the PM is attached to the upper portion of the torsion bar through the spool shaft, as presented in Figure 7.65.

Figure 7.66 shows how the rotary actuator fits into the conventional hydraulic steering gear. The stationary section is attached to the valve housing and is a part of the main magnetic circuit. The rotary section is attached to the movable valve parts. In addition to the full rotary motion of the actuator components in the housing, this configuration allows for a limited-angular motion of the PM (attached to the input shaft) with respect to the toothed magnetic parts (attached to the pinion). Driver steering is normally controlled by

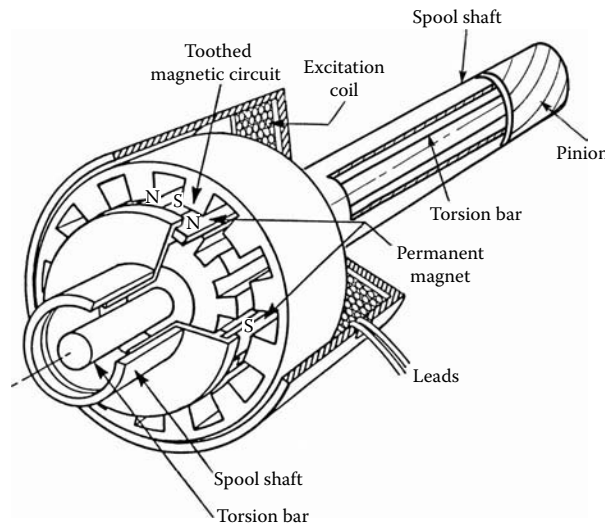
**FIGURE 7.63**

Claw pole actuator components for the speed-sensitive steering application: (a) magnetic housing, (b) claw pole stators with magnet armature on shaft, (c) magnetic housing. (Courtesy of Delphi Corp.)

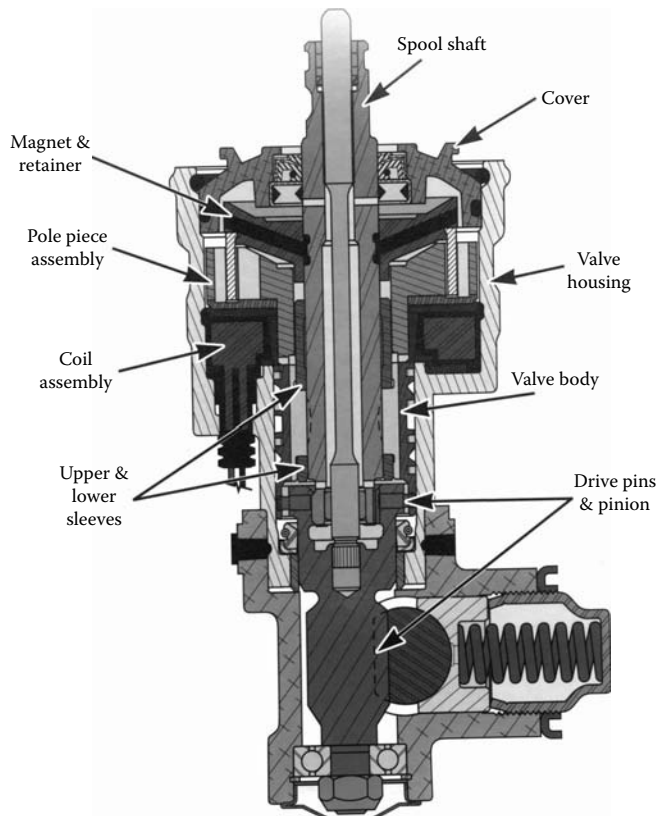
**FIGURE 7.64**

Speed-sensitive steering system assembly with claw pole actuator. (Courtesy of Delphi Corp.)

the torsion bar stiffness. The torsion bar twist is limited mechanically to $\pm 7^\circ$, but it is sufficient to control the motion up to $\pm 4.5^\circ$ in both right and left directions. Magnasteer performance requirements are combined in Table 7.4. They address three areas: average performance torque range at the constant current level in a coil, performance symmetry defined as a difference between the right rotated torque and left rotated torque, and the stable equilibrium position defined as a difference between zero cross of the torque-angle curves with the current in the coil +3.0 A and -1.5 A.

**FIGURE 7.65**

Cylindrical actuator coupled with Magnasteer system components. (Courtesy of Delphi Corp.)

**FIGURE 7.66 (Color Figure 7.66 follows p. 294.)**

Magnasteer system components. (From Pawlak, A.M. et al., *Magnetic Power Steering Assist System — MAGNA-STEER*, Publ. No. 940867, Society of Automotive Engineers, Detroit, MI, 1994. With permission.)

TABLE 7.4
Magnasteer® Requirements

Performance	Current (A)	Rotation Angle (degree)	Average Torque Range (Nm)
Torque	3	4	1.78–1.90
	-1.5	4	1.76–1.88
	3	2	1.08–1.2
	-1.5	2	0.98–1.1
Symmetry	3	4 and 2	0.12
	-1.5	4 and 2	0.12
Stability (null)	3 and -1.5	0.1	0

Source: Courtesy of Delphi Corp.

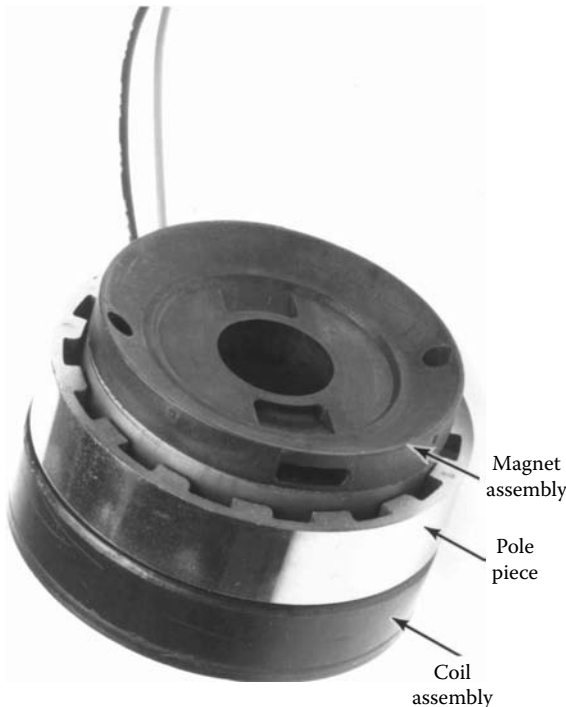
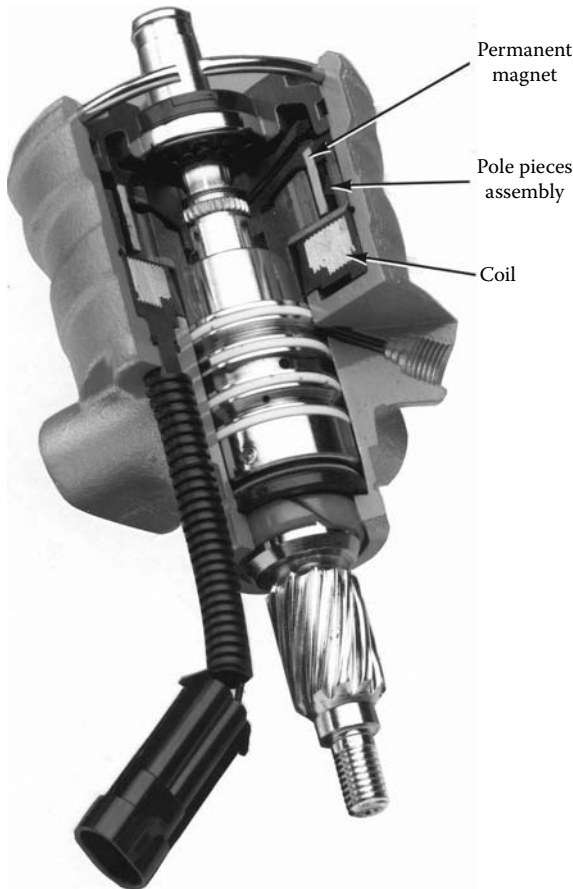


FIGURE 7.67
Coupled rotary actuator components. (Courtesy of Delphi Corp.)

The applied cylindrical rotary actuator consists of three integrated elements: a ring magnet, a toothed structure, and a coil. Figure 7.67 shows all three components combined together. In this arrangement, the coil is located below the magnetic structure of the cylindrical rotary actuator, significantly reducing the OD of the actuator to 78.0×10^{-3} m with an increased axial length of 45.0×10^{-3} m.

All actuator components are fully integrated within a rack and pinion gear, where a number of structural and hydraulic parts have more than one function. For instance, the housing, in addition to its important structure function, is an essential part of the magnetic flux path. The cross section of the assembled Magnasteer system is shown in Figure 7.68, where all components of the rotary actuator are identified.

**FIGURE 7.68**

Magnasteer system assembly. (From Pawlak, A.M. et al., *Magnetic Power Steering Assist System — MAGNASTEER*, Publ. No. 940867, Society of Automotive Engineers, Detroit, MI, 1994. With permission.)

After the introduction of the system to the Oldsmobile Aurora in the mid-1990s, many other cars, including the Cadillac line and the Chevy Corvette, accommodated the system. With advanced controls, the system is still in production almost a decade after its introduction.

Example 7.1

Calculate the total torque of the cylindrical actuator using results from the Cartesian 2D FE analysis for the cylindrical actuator having the average radius $R_{avg} = 29.76 \times 10^{-3}$ m, 15 pole pairs, and a magnet length in the gap of 14.0×10^{-3} m. The force values per one-pole pitch and per 1.0×10^{-3} m magnet length are at the nominal positive current of 3.0 A $F_{X(+3A)} = -234.2$ N/m/pole pair and at the nominal negative current of -3.0 A $F_{X(-3A)} = 601.6$ N/m/pole pair.

The force per pole pair can be calculated as:

$$\Delta F_X = |F_{X(+3A)}| + |F_{X(-3A)}| = |-234.2 \text{ N/m/pole pair}| + |601.6 \text{ N/m/pole pair}| = 835.8 \text{ N/m/pole pair}$$

This is multiplied by the length of the magnet in the gap to arrive at F_t , the one-tooth-pitch (pole-pair) force:

$$F_t = 835.8 \text{ N/m/pole pair} \times 14.0 \times 10^{-3} \text{ m} = 11.701 \text{ N/pole pairs}$$

The total force F_T due to the entire actuator is simply F_t due to the one-pole pitch multiplied by the number of pole pairs, as presented in Equation 7.5:

$$F_T = N \times F_t = 15 \text{ pole pairs} \times 11.701 \text{ N/pole pairs} = 175.52 \text{ N}$$

Multiplying this by the average radius of the magnet yields total torque from Equation 7.6:

$$T_T = F_T \times R_{avg} = 175.52 \text{ N} \times 29.76 \times 10^{-3} \text{ m} = 5.22 \text{ Nm}$$

The total torque level is $T_T = 5.22 \text{ Nm}$. This concludes Example 7.1.

Example 7.2

Calculate the total torque using results from the cylindrical 2D FE analysis for the cylindrical rotary actuator having the force constant $k = 2.0 \text{ N/kGs}^2$ and the average radius $R_{avg} = 29.76 \times 10^{-3} \text{ m}$. The flux-density values calculated at the inner gap and outer gap will be used, $B_{in} = 6.43 \text{ kGs}$ and $B_{out} = 5.92 \text{ kGs}$, respectively.

The torque level can be computed in this way from Equation 7.15:

$$B_t^2 = B_{in}^2 + B_{out}^2 = (6.43 \text{ kGs})^2 + (5.92 \text{ kGs})^2 = 76.39 \text{ kGs}$$

The force constant $k = 2.0 \text{ N/kGs}^2$.

The total force is calculated from Equation 7.16 as:

$$F_T = k \times B_t^2 = 2.0 \text{ N/kGs}^2 \times 76.39 \text{ kGs}^2 = 152.78 \text{ N}$$

and the total torque T_T is calculated from Equation 7.17 as:

$$T_T = F_T \times R_{avg} = 152.78 \text{ N} \times 29.76 \times 10^{-3} \text{ m} = 4.55 \text{ Nm}$$

Because R_{avg} and k do not change with changes in the inner gap and outer gap, for torque level calculations, B_t^2 was used to compare results from analysis using the cylindrical model, yielding sufficient engineering accuracy. This concludes Example 7.2.

Example 7.3

Calculate the maximum torque for the claw pole rotary actuator, for the nominal current of 3.0 A, with a position of 4.5° for the mechanical disk magnet having 40 poles and a magnetic flux of $3.036 \times 10^{-6} \text{ Wb}$.

Calculate the electrical angle of the magnet position from Equation 7.13:

$$\alpha = \frac{P\theta}{2} = \frac{40 \times 4.5^\circ}{2} = 90^\circ$$

The maximum torque value is at $\alpha = 90^\circ$. Therefore, the total torque level T_{\max} from Equation 7.10 is:

$$T_T(\theta) = 0.25Np^2I_n\phi \sin 90^\circ = 0.25 \times 300 \times 3.0 \times 5.476 \times 10^{-6} \times 40^2 = 1.971 \text{ Nm}$$

This concludes Example 7.3.

This chapter addresses two fundamental questions that every technology development faces: What does it take to develop a technology? If successfully developed, what is it worth? The author has attempted to answer both question by sharing with the reader his experiences with technology development and its valuation. This chapter describes how to evaluate, select, and develop world-class technologies. The author's experience comes from a number of successfully developed technologies that have found application in the automotive industry and from his entrepreneurial experience with technology management and commercialization.

8.1 Technology Development

Successful implementation of technology requires more from a researcher than new ideas — it requires partnership, competitiveness, persistence, and technical growth. Technology development takes hard work, persistence in the face of obstacles, and the ability to perceive and seize new opportunities. A key element of this approach is to closely involve product and manufacturing engineers from the operating units at every stage of research and development (R&D). Key players include not only the researcher, but also the product engineer, the manufacturing engineer, and the suppliers. With this approach, the development team confronts issues of technical feasibility, market demand, manufacturability, and affordability at the earliest stages of R&D. By addressing these issues early, the chances for technology implementation can grow exponentially, benefiting both the customer and the company's bottom line. The author has drawn upon his experience with research projects that have gone into mass production to identify actions researchers and engineers can take. These actions are discussed briefly in this chapter.

8.1.1 Partnership

Even before the project is defined, it is important to have personal contact with people in the company's operating units who are potential R&D partners. Researchers need to go out frequently, meet with people, gain their acceptance, and, most importantly, obtain an understanding of their needs and problems. In establishing these relationships, it is also important to connect with the appropriate level of engineering force. One needs to be closely aligned with people who would join a team working on a project.

As soon as the idea of a particular project has been developed, it is important to get everyone intensely involved as early as possible. This is a crucial period in the life of a

project. It is a time when a team can generate a rich mixture of ideas and concepts within a shared context because the team has developed a clear idea of the goal and what is required to achieve that goal. Even though communication at the earliest stages of a project is crucial, there are tremendous advantages to having a continual interchange of ideas as development proceeds. First, everyone must feel ownership and take ongoing responsibility for the project. Even more important, contributions from a team represent all the various stakeholders who will change and enrich the development. A researcher tends to concentrate on function, and product and manufacturing engineers will be focused on form as well as function. It is essential to include manufacturing interest early in the life of a project so one can devise ways to make manufacturing as easy as possible and with the least cost incurred. The concept for manufacturing in the early stage is far better than design for manufacturing at the prototype stage because this approach offers fewer constraints. This is most effectively done as design progresses, rather than later when the final design has already been chosen. At this stage, people can share ideas and a team can be formed to develop a vision of a new technology concept. If one would form a team at this stage, there is a good chance of assembling a strong, well-prepared team with expertise in all the areas required for development. Establishing a feeling of shared ownership is so critical to successful technology development that it cannot be emphasized enough. But partnership should extend beyond responsibilities. Credit must also be shared with every member of the team. For instance, if innovation is patentable, all team members should contribute to its solution and file jointly. When documenting research, the team members should collaborate on papers. The collaboration will often extend beyond the project and lead to future opportunities for cooperation.

8.1.2 Competitiveness

Because competition is so intense today and tomorrow will be even more so, one has to make projects highly marketable by always aiming for world-class performance. If one aims for what is world-class performance today, however, the development will fail. One has to set sights on where one thinks world-class performance will be when the project matures. In the case of the automotive industry, that target is 3–5 years down the road because that is the time it will take to develop a new system, and that is when the system will face competition from other technologies. To secure a vision of world-class performance, one needs to employ, or in some cases develop, state-of-the-art technology to enrich one's concept. In this way, one is virtually guaranteeing that the project will be at the frontier of the field and ahead of the competition. Competition, of course, is internal and external. Internal competition is something one has to face every day. For every project, there are various groups working on different concepts to achieve the desired function and results. Although the author's primary field of expertise is electromagnetics, he is competing with others who are working with mechatronics system concepts that are based on hydraulics, pneumatics, or mechanical systems. This is just a fact of development. But if a team is set up properly and has clear-cut goals and milestones, then it can win in this first hurdle of competition. External competition is less friendly. In this field, competition from abroad — the Far East and Europe — is fierce and relentless, so it is very important for a team to keep abreast of all the latest developments in the required areas of expertise.

Another way to stay competitive is to use the best analytical tools available to help create, evaluate, and improve a system. Engineers are very fortunate today to have a growing body of sophisticated mathematical software and tools with which to design and optimize a system's structure and even predict its static and dynamic behavior. With these tools, one is able to move the prototype-building stage with a concept that has been

analytically validated. In my experience, the end result of this approach is a prototype that works like one thinks it will — not only on a lab bench but also in a real environment. For the automotive application, the environment is a vehicle, which must behave properly and give good performance in a wide variety of automotive requirements. Demonstrating an operating prototype assembled within the vehicle is essential to a project's success; it is the sales device with which the team sells its product to the operating divisions. A crucial selling point is manufacturability. To gain acceptance, a system must be simple, robust, and easy to manufacture at a good price. But remember, simplicity does not have to extend to the concept. The concept can be quite sophisticated from the scientific point of view. The Magnasteer system is a case in point. This is a variable-effort steering system, described in detail in Chapter 7, which made its debut on GM's 1994 Oldsmobile Aurora and won *Popular Science's* 100 Best of What's New Award. Magnasteer is based on a concept that is quite sophisticated and advanced technologically, but also quite simple to manufacture. This did not come about without a lot of effort. The heart of the system is a rotary actuator, which initially had 17 parts. In the course of development, the Magnasteer team was able to reduce that number to three essential parts. The team achieved this significant improvement by using newly developed state-of-the-art technologies in conjunction with the team process.

8.1.3 Persistence

The author encourages all research and application engineers who wish to see their technology development in mass production to stay with the project and follow their operating partner's time line closely. In the research environment, the Magnasteer team has a newly acquired appreciation of the pressure and tensions that are part of the everyday lives of product and manufacturing engineers. As researchers far removed from the rough-and-tumble manufacturing world, the team did not always understand that if it failed to meet the deadline, the project could be moved from the front to the back burner or even canceled. People in the operations process have very little time — almost none — to deal with research issues that arise as development progresses. It is up to the researcher to follow the project very closely, watching the time line and providing research support as the project is being implemented.

Here are ways in which the researcher can support team members who are involved in operations and manufacturing:

- Defend the project against competition. Expect it to be challenged at every stage of development, not only at the concept stage but all the way from concept development to start of production.
- Resolve problems in a timely fashion in all phases. From concept to production, the researcher should help the manufacturing personnel achieve the highest possible yield. This is vital to ensuring financial success. The finest, most advanced technology in the world will not be deemed a success if it is too costly, and manufacturing is a big part of the cost.

Because new development implies new technology, the operations partners probably will not have the expertise to overcome all the technical obstacles that arise. They are devoting most of their effort to moving up the learning curve to achieve a high manufacturing yield. Researchers, meanwhile, have those good analytical tools when difficulties arise. They may also possess superior knowledge of the system's behavior. To assist manufacturing

development, researchers can support the project by doing parametric studies to evaluate different processing scenarios, conditions, or materials.

Flexibility is an important attribute of a successful development team. Here the author would like to differentiate between persistence and stubbornness. A prudent, persistent team will try to foresee and then avoid obstacles and roadblocks as its project progresses. But a stubborn team will attempt to directly challenge and overcome obstacles. Persistence is desirable, but stubbornness tends to be counterproductive. Everyone knows what happens when one pushes against the wall. Either one forces the break or the project fails. Flexibility is very important in technology development, although sometimes it seems to cause delay. It improves the chances for success.

When the team first developed the Magnasteer project, for example, it had several competing concepts for the rotary actuator. The team started with a disk design, but this design caused a problem in terms of manufacturing tolerances. Then the team switched to a claw pole design with state-of-the-art powder-metal technology. This solution proved too costly. Finally, the team combined elements of both types of design and developed a cylindrical rotary actuator. The team did not try to force its first design or its second. Instead, the team was flexible and continued to try new approaches. The payoff was an optimal design structure that could be manufactured easily.

8.1.4 Technical Growth

Expanding one's area of expertise is one of the most critical factors for improving the probability of success. Some companies allow researchers a percentage of their time to devote toward "homework" before they actually gear up to do a project. The nice thing about the concept bubble-up period is that one can investigate several potential projects at one time. When one begins to show more promise than the others, researchers can then narrow their focus to the one with the greatest potential. The value of this approach is that it pays off as technical issues arise in the course of development. Researchers should devote some time to exploring new areas and reviewing the literature and existing patents so they can understand the current state-of-the-art technology. Only at this point can one reasonably expect to build one's own vision of the world-class system.

When the author became a researcher, he worked on stepper motors. He switched to fast-acting solenoids, such as fuel injectors, then moved to magnetic sensors. His next area was rotary actuators and, most recently, latching solenoids. In between, he developed an electronically operated heart valve, left-ventricular assist devices for artificial hearts, and many special electromechanical devices. Each time he moved to a new area he was the new kid on the block, but he was able to enhance his value as he progressed in each area by drawing upon his previous experience, in addition to using his underlying expertise in electromagnetics as a foundation and framework.

Researchers cannot be afraid to put their credibility on the line. They cannot expect an operating division, and especially those within it who oversee its financial apparatus, to invest millions of dollars in development unless the researchers can convince them that they thoroughly believe in it. If team members put everything they can into a new system or technology, they will not be afraid to put their credibility on the line — and even stake their reputations on it. The key characteristic of a strong team is confidence. This is essential if one hopes to move from development to production.

The author has outlined some actions that allowed development teams in which he participated to move a technology development to mass production. But the key point behind all these actions is this: Do not ignore the all-important bottom line. To make an impact there, the team needs to be committed, competitive, persistent, and to believe in

the value of technical growth. If a team has all these elements, there is no doubt it will be quite successful at developing and implementing new technology with its customers.

8.2 Technology Valuation

Because a large number of new technologies are created every day, it is critical to understand the value of technology in focusing on developing the most promising ones. The intention of this section is to identify the critical technology value features from a commercialization point of view, particularly these technology features that may not be apparent. The following describes technology value features that are critical for commercialization in a competitive global market.

Technology commercialization is the process of bringing a selected technology to market through development and marketing, which recognizes and addresses specific market needs. The selection of technologies for commercialization that best satisfy market needs is critical for the success of new business. This is in tandem with the dynamics of innovation that "occur when there is a matching of a new or emerging need with an existing or emerging technology" (Myers and Marquis 1996). Therefore, technology valuation and ranking is an important task during the technology development process before its commercialization. Product development is changing now from a fixed process-based approach to more flexible and dynamic information-driven methodologies. Product development must be faster, cost-effective, and effectively utilize human, material, and financial resources to eliminate bottlenecks, information gaps, rework cycles, and wasted efforts. The technology value ($V_{\%}$) consists of technical technology attributes ($T_{\%}$), business case attributes ($B_{\%}$), and financial attributes ($F_{\%}$):

$$V_{\%} = T_{\%} + B_{\%} + F_{\%} \quad (8.1)$$

In a *strong market*, about 40% of the technology value is credited to technical attributes, 45% to business case attributes, and 15% to financial attributes. In the presence of a *soft market*, about 25% of the technology value is credited to technical attributes, 65% to business case attributes, and 10% to financial attributes, as in Table 8.1. Therefore, both technical and financial attributes may be perceived as less important factors because one can change a financial partner and replace technology more easily than alter market forces.

8.2.1 Technical Attributes

The technical attributes (T) are composed of expertise, technology development, novelty, and intellectual property (IP). All of these elements address the technical merit of the technology. Enabling technologies are the best springboards for a new business venture because they can generate a variety of applications satisfying needs in different market segments. Thus, corporations should develop their core competency and expertise around enabling technologies, not product applications. The company's expertise and technology development level depends on the complexity of technology, the completeness of the technology, and the technical outlook. A company's expertise is usually based on its core business with know-how in a particular technology and a technology domain that is composed of synergistic technologies. Therefore, it is typically easy to assess if the technology is conceptually simple or complex, as well as to recognize the degree of difficulty to execute

TABLE 8.1

Technology Criteria Weights

Attributes	Criteria	Weights
Technical merits	Expertise and outlook	25%
	Novelty and stage	
	IP value	
	Total technical merits	
Business case	Breadth of applications	65%
	Value proposition	
	Market size	
	Competition or barriers to entry	
Financial	Company strategy	10%
	Total market or business case	
	Capital investment required	
Total financial		

Source: Pawlak, A.M., *International Conference on Electrical Machines Proceedings ICEM '04*, Technical University of Lodz, Krakow, Poland, September 8–10, 2004. With permission.

it. A selected technology can be compared with alternative technologies that are able to provide the same or similar functions. The trouble comes when a company is commercializing the technology without core expertise in the technology domain where the technology resides. Some companies, such as the 3M Corporation, for example, believe that organic growth around core technologies tends to be more successful than acquisitions of technologies beyond the company's core competency.

3M's technology map around the subject area of nonwoven enabling technology is presented in Figure 8.1. The creation of a technology map starts with the enabling components in core domains. Technology domains such as telecommunications, wireless, mechatronics, controls, materials, electronics, optics, software, and database capture a number of enabling and synergetic subject areas. Nanotechnology and genomics represent new technology domains that are fast growing and foster many activities that can be recorded as IP directed toward commercialization of the specific technology. IP mapping provides a better understanding of the competitive position and the technology edge. The strength of the technology domain within an organization that is planning to commercialize technology is critical. Domain strength can be assessed by a presence of synergetic technologies in the selected technology domain.

Completeness of the technology addresses the technology gap issue, which must be closed to bring technology to a market-ready condition. It reflects the company's expertise level, as well as its available material, financial, and human resources ready to deal with the gaps. The outlook for the technology pertains to existing R&D programs as well as to whether the technology is in an active R&D stage or not. Current R&D activities help to address commercialization issues with new market applications by reducing technology to practice. Usually, technologies aimed at one market's needs must to be developed further to meet other markets' needs. Quite often one or more development partners are needed with expertise in a subject technology and in targeted markets. Novelty of technology is also a key attribute of the technology valuation process. Novelty criteria include the maturity stage of technology development, ease of use, elegance, pioneering, and uniqueness.

Technology maturity describes the three stages of technology development. The first stage of technology development is the concept. This stage is completed when the concept is proven. The second stage is preproduction prototyping and includes performance and cost validation. This stage is completed when prototypes are fabricated and tested. The

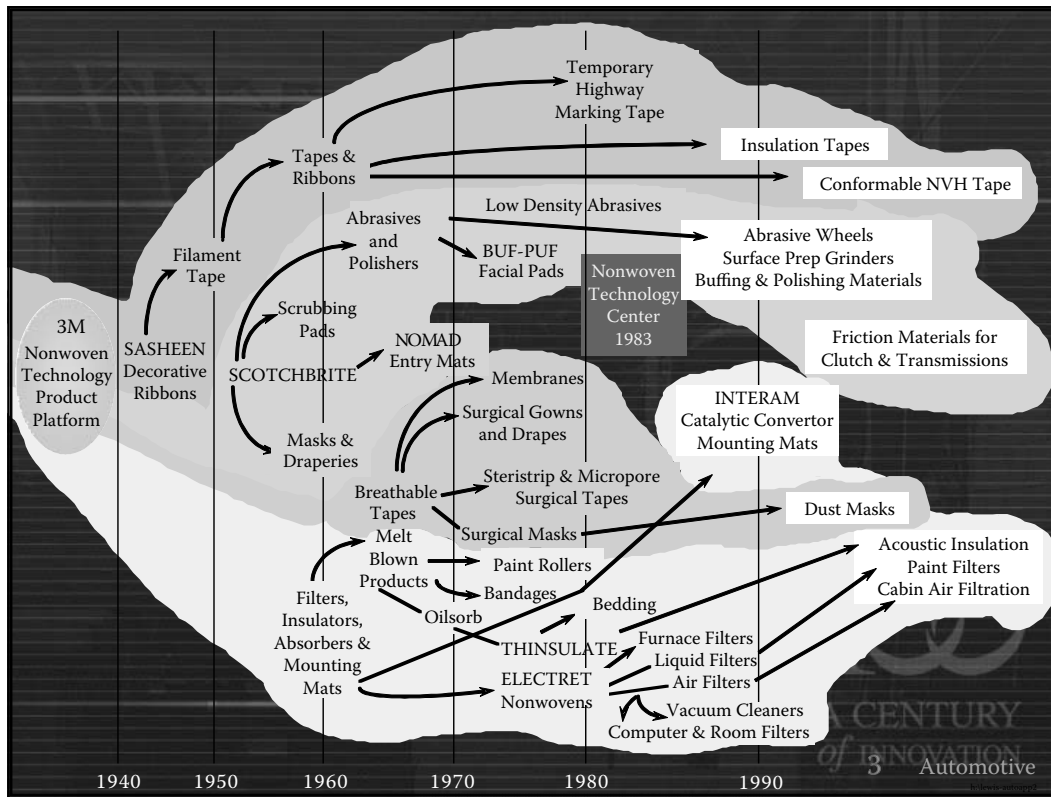


FIGURE 8.1 (Color Figure 8.1 follows p. 294.)

Example of organic technology growth at the 3M Corporation. (Image published with permission of 3M.)

third stage of technology maturity is reached with mass production in place and market-ready applications. Most universities and R&D organizations create technologies in the early stage, which often includes only proof of the concept. Corporations with R&D and advanced engineering arms complete both the concept and preproduction prototype stages, and the company's product engineering advances technology to the mature stage with mass production in place.

Ease of use and technology elegance, attributes that make it simple for manufacturing, are the most difficult attributes of technology to attain. Simplicity of manufacturing helps achieve a high production yield, improves product reliability, and reduces manufacturing cost. Product elegance is related to the "coolness" of technology.

Pioneering and uniqueness of technology are attributes that describe the novelty of the technology. There are two kinds of technologies in this category. The first is an incremental technology that incrementally improves a current process or product. The second kind is a disruptive technology that disrupts the current process or product by creating a new paradigm. Ideally, new business should be based on technology with a disruptive nature because of a high payoff potential. Only one out of eight new emerging businesses is based on disruptive technologies, yet they generate three quarters of the total revenue. In comparison to existing technologies, disruptive technology offers the best business opportunities based on superior performance, simplicity, and competitive cost. Clayton Christensen (1997) claims, "Disruptive technologies typically offer a fundamentally new benefit in a simpler, cheaper and easier to use system that appeals to a specific, often low-end

market segment. This benefit becomes the source of competitive advantage when the disruptive technology improves and enters the mainstream market.”

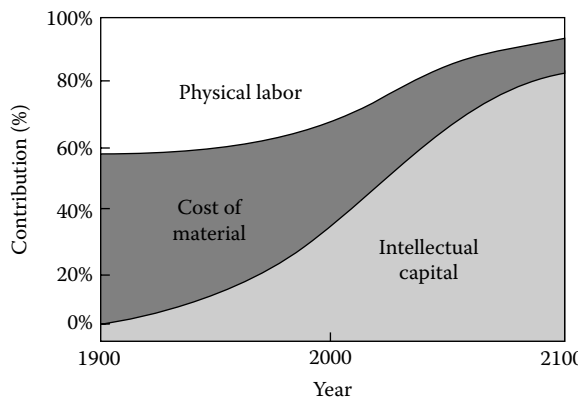
An excellent example of a unique and elegant technology is the Magnasteer system, described in Chapter 7 (Pawlak 1994a). The rotary actuator, a major component of the system, consists of only three elements: a ring magnet, a toothed structure, and a coil. All components were made in a pioneering way. The multipole permanent radially oriented ring magnet based on neodymium is the world’s first successful development with high-energy density (>30.0 MGoe). In the early 1990s, both Hitachi and the Daido Corporation, in cooperation with General Motors Research Labs, simultaneously and independently developed a PM ring structure for the Magnasteer system. Hitachi further refined and incorporated the sintering method in its ring magnet. Daido developed and used the extrusion technique in its ring magnet (Daido 2003, Iwasa et al. 1981, Kasai 1992).

The pole piece assembly for the Magnasteer system was developed in the early 1990s as a single part using high-density powder-metal technology. The powder-metal part is a single solid structure that consists of two magnetic parts bonded with a nonmagnetic connecting plate. This was also the world’s first successfully made powder-metal part combining both magnetic and nonmagnetic powder. Because the Magnasteer system is submerged in steering fluid, the excitation coil was overmolded in plastic using a special golf ball overmolding technique to prevent system leakage. Because all three Magnasteer elements were based on emerging technologies, this system has been very successful in the automotive industry. Some of the developments for the Magnasteer system, such as the high-energy radially oriented ring magnet, have found a variety of applications in brushless motors and beyond.

The IP value of technology is another critical element in technology valuation. IP addresses technology ownership that is based on IP content and more specifically on its claims. IP has different strengths ranging from weak to strong. Strong IP exists when a company owns core patents in the subject area. Weak IP position is present when the competition owns core patents. Shared IP exists when both parties own shares of the IP of a core technology. The extent of IP ownership also determines the “insurance” value of a technology in the assertion process. The IP content is the starting point of due diligence for technology commercialization. This includes an inventory of the patents issued, patent applications, a company’s record of inventions, trade secrets, and defensive publications, as well as the history of patenting, including notes and written comments from the patent examiners.

A product value consists of three components: cost of material, physical labor, and intellectual capital. In the mid-19th century, most of a product’s cost resulted from material and physical labor costs rather than intellectual capital. By the beginning of the 20th century, as more sophisticated design configurations and systems began to emerge, the relative contributions of the three components started to shift, as presented in Figure 8.2 (Pawlak 2000b).

In the mid-20th century, product complexity still remained relatively low, so the value of the knowledge component continued to be low in comparison with the value of material and labor. In the last 50 years, however, the importance of the knowledge component has drastically increased while the material cost has somewhat diminished in importance (e.g., plastic is replacing metal and wood and sand is the inexpensive base for integrated circuit chips). For the microchip, raw materials represent about 1% of its cost and traditional labor accounts for another 5%. Therefore, most of its value resides in the knowledge component that is directly related to IP that also includes IP value of capital equipment and software. Different forms of IP — such as patents or trade secrets — can protect this technology attribute. Creating new business around selected technology requires access to its IP; thus, IP management is key to modern business development. Universities,

**FIGURE 8.2**

Relative contributions of product value components over time. (From Pawlak, A.M., *Fostering Creativity in the New Millennium, Research Technology Development*, Vol. 43(6), Industrial Research Institute, New York, November–December 2000. With permission.)

industrial, and government research institutions, as well as companies with R&D, place an emphasis on IP management. These activities include IP generation, protection, IP database processing and storage, as well as commercialization activities such as licensing, donations, and new venture creation.

8.2.2 Business Attributes

Business case attributes (*B*) are the major contributors to the technology value. They include breadth of application, value proposition, market, barriers to entry, and strategic positioning. These attributes are the key elements for investment decision in new ventures by venture capital (VC) firms.

Breadth of application is composed of several elements that address the range and variety of market applications. It embraces the technology applicability, potential market technology targets, and time frame of technology development. Breadth of application is an important attribute of technology value especially for enabling technologies that can support a variety of different applications to many market segments. An excellent example of this is the kinetic spray metal coatings technology, which has the ability to generate a number of different applications for the variety of goods and markets. Sometimes, however, there is a narrow technology that is able to support a limited number of applications in one market segment. A good example of a narrow technology is the Magnasteer system, which provides a speed-dependent variable-effort function for steering only in the automotive market segment. Market recognition provides an opportunity to allocate potential technology applications in recognized market segments for replacement of existing products with similar functions or to add new functions to existing products.

Time frame is a critical value measure for bringing technology to market in a timely manner. This is particularly important for incremental technologies where time-to-market is critical. Additional unforeseen technology development or problems with a timely execution of successive stages may result in delays in bringing technology to market on time.

Value proposition is an important factor to attract potential customers. It is perceived that a 1:3 value proposition is a convincing fact to customers. This means that an emerging product to the market with the same functions and performance as an existing product in the market, but with cost reduced to one third of the original product cost should be

able to replace the existing one. The value proposition has to be convincing and its estimation should be based on the mass production cost with a high target yield. A good example of a convincing value proposition could be a night vision system for the automotive industry. The market is ready to accept such as a system for about one quarter of the existing price (1:4 value proposition). However, the low-cost technology does not exist yet and its development may be high risk.

Market criteria include market size, market maturity, customer base, and market drivers. Market size determines a business opportunity for technology because with a big market even a small percentage of penetration of the market can be substantial. For example, the PM market is about \$10 billion and the market size for machining is \$200 billion. Therefore, the potential revenue for entering the magnet market with the same percentage of market penetration is two orders of magnitude smaller than the same penetration of the machining market. It is also important what the market geographical location is and what penetration of a market can be achieved with commercialized technology.

Barriers criteria include entrenched competitors, competing technologies, dependencies (including need of a partner), and sustainability of position. The presence of existing competitors in the market makes a venture much more difficult. Even more difficult and risky is the presence of any technology that may replace selected technology. Particularly vulnerable is software-based technology because it can sometimes be replaced without hardware changes. Usually a single technology is not sufficient to make a product; thus there is often a need for synergetic technologies and partners with know-how willing to bring synergetic technology to the table.

Strategic positioning criteria include a company's support and business model. The best company support is when the selected technology is synergetic with the existing company strategy and supports the company's technology domains and its core knowledge. Therefore, it is advantageous to commercialize technologies that were developed for the core business of the company and can be utilized in other markets. A good example of this is magnetorheological fluid technology (see, for example, Alexandridis 2000). It was developed for a prime suspension of a passenger vehicle and with the introduction of this technology in 2002 to the Cadillac Seville and 2003 to the Chevrolet Corvette, now it can be used for vibration control in a variety of applications, in construction, the military, medical, toys, white goods, and many other markets.

A variety of business models are available for the commercialization of technology. Each model is unique and addresses technology technical attributes and market forces. Most new businesses begin by developing technologies in a commercial space or available basement or garage space. In the corporate world, the best approach is to nurture an emerging venture until the market is ready to accept it. This can be done externally in partnership with a venture partner or internally as an organic growth. In general, venture partners are seeking an equity stake in the new company with 5–7 years exit strategy as an initial public offering (IPO), merger, or acquisition.

With the mature technology development, the process is simplified, but dealing with the early stage of technology development may require joint development with venture partners. New business success requires market recognition, finances, and "A-level" management. It is perceived that the *A* team with *B* technology has better chances for success than the *B* team with *A* technology.

8.2.3 Financial Attributes

Financial attributes (*F*) include the investment required, significance of risk, potential revenue, and expected profitability. Required investment is the funding level required to

commercialize the technology to bring it from the concept stage to mass production. When investment is very large, in the hundreds of millions of dollars, VCs typically like to diversify investment exposure by inviting more financial partners. Risk must be assessed for both the technology and the market. Sometimes technology is high risk but the market risk is low because of significant market pull. Potential revenue and potential profitability will indicate where the new technology is placed in a given market segment. In some markets, profitability is high (such as the medical or pharmaceutical industry) while profitability for other markets is low (such as the automotive industry) and expectations should be adjusted with respect to a targeted market segment for an apple-to-apple comparison.

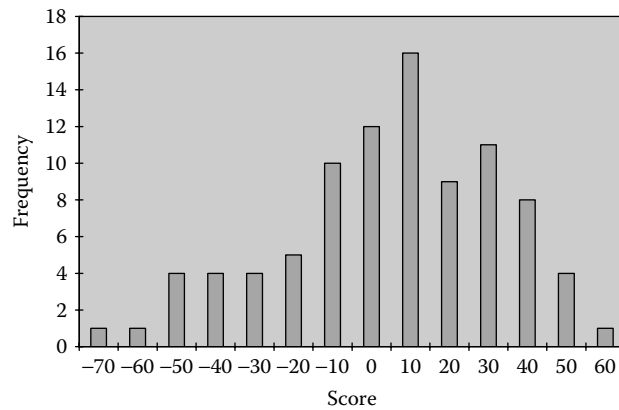
8.2.4 Technology Ranking

The first step of the technology valuation process is to investigate the IP status of the reviewed technologies. Providing that IP coverage exists and is broad enough, the next step includes the inventor's identification and discovery of any potential internal conflicts. At this stage, it can be decided whether to drop a technology from the list (~45%), merge technologies with other existing technologies based on their synergy (~10%), decide to follow up in next 12 months (~20%), or evaluate further (~25%). A decision to drop a technology from the list is often based on limited or no IP coverage. Sometimes technologies are dropped due to their narrow potential application or insufficient expertise level at a company. A follow-up decision is usually due to delays in patent issue.

Research of the technology background is the next step of the process. This includes the collection of the market data and investigation of competing technologies. The interview of inventors follows this step. The validation of the value proposition and understanding current state-of-the-art status is the final step. When the process has been completed, the results are compiled in a database, which is then used in a math model to determine technology ranking. In previous discussions, benchmarking with world-class companies identified technology attribute criteria. The criteria are weighted as shown in Table 8.1 to reflect their relative importance.

Scores for each of the attributes were assigned on a scale from 0 to 10. For better visualization, scores were assigned from -5 to +5 points for visualization purposes. The total score for a given technology can be between a maximum of +100 and a minimum of 100. This measure has been applied to all reviewed technologies in the IP portfolio in all technology domains. All technologies in this portfolio were subjected to the portfolio prioritization process for appropriate ranking.

Figure 8.3 shows the distribution of weighted ranks for the example IP technology portfolio. The average score is 9.3 and the median score is 11. The frequency indicates how many technologies achieved a given score. Distribution resembles a near-normal distribution for about 100 technologies. With more technologies, the distribution would be more symmetrical. Of course, we should focus only on those technologies with the highest ranking with enabling features and disruptive nature. The disruptive technologies would most likely score the highest ranking but only about 14% of all emerging technologies fall into this category, and most developed technologies feature incremental improvements only. Although it is usually very difficult to develop and bring them to market, the disruptive technologies carry the best payoff of 75% of the total revenues.

**FIGURE 8.3**

Technology value distribution. (Pawlak, A.M., *International Conference on Electrical Machines Proceedings ICEM '04*, Krakow, Poland, September 8–10, 2004. With permission.)

Bibliography

Adams, J.M. et al. (1991). Two Variable Reluctance Sensor Arrangement, Research Disclosure R-3339, October 1991.

Aftonin, A.A. et al. (1999). Electronically Commutated Disc Permanent Magnet Motors (in Russian), presented at International Conference on Unconventional Electromagnetic and Electric Systems, UEES '99, St. Petersburg, Russia.

Alciatore, D.G. and Histan, M.B. (2003). *Introduction to Mechatronics and Measurement Systems*, 2nd ed., Colorado State University, Fort Collins.

Alexandridis, A.A. (2000). MagneRide: Magneto-Rheological Fluid-Based Semi-Active Suspension System, presented at the Vehicle Electronic Systems 2000 European Conference and Exhibition, Stratford-upon-Avon, U.K., June 29–30.

Allegheny Ludlum Steel Corp. (1961). *Electrical Material Handbook*, 1st ed., Allegheny Ludlum Steel Corp., Pittsburgh, PA.

Ando, R. et al. (2001). Development of a simulation method for dynamic characteristics of fuel injector, *IEEE Transactions on Magnetics*, 37(5), 3715–3718.

Ansoft Corp. (1991). Maxwell 3D field simulator, *Users Reference*, Ansoft Corp., Pittsburgh, PA.

Baumann, B.M. et al. (2000). Mechatronics design and control of hybrid electric vehicles, *IEEE ASME Transactions on Mechatronics*, 5(1), 58–72.

Bishop, R.H. (2002). *The Mechatronics Handbook*, Taylor & Francis, New York.

Boldea, I. and Nasar S.A. (2001). *Linear Motion Electromagnetic Devices*, Taylor & Francis, New York.

Bottauscio, O. et al. (2003). Diffusion and hysteresis in axisymmetric electromechanical devices, *IEEE Transactions on Magnetics*, 39(2), 990–997.

Bottauscio, O. et al. (2005). Advanced model for dynamic analysis of electromechanical devices, *IEEE Transactions on Magnetics*, 41(1).

Box, M.J. et al. (1969). *Non-Linear Optimization Techniques*, Oliver and Boyd, London.

Brauer, J.R. (1988). *What Every Engineer Should Know about Finite Element Analysis*, Marcel Dekker, New York.

Brauer, J.R. et al. (2000). Alternative dynamic electromechanical models of magnetic actuators containing eddy currents, *IEEE Transactions on Magnetics*, 36(4), 1333–1336.

Carpenter Technology Corporation (1989). Carpenter Specialty Alloys, Catalog 4-89/5M, Wyoming, PA.

Carsile, B.H. (1986). Neodymium challenges ferrite magnets, *Machine Design*, January 9, 24–30.

Chai, H.D. (1984). Cogging torque of PM step motors, in *Proceedings of IMCS Symposium*, University of Illinois Press, Champaign, pp. 163–166.

Chai, H.D. (1986). Permeance based step motor model revised, *Motion*, March/April, 14–28.

Chandran, K.B. (1986). Prosthetic heart valves, *Mechanical Engineering*, January, 53–58, 1986.

Chatterjee, M.S. et al. (2003). Manufacturing Technique for Multi-Layered Structure with Magnet Using an Extrusion Process, U.S. Patent 6,627,326.

Chirikjian, G.S. et al. (1999). Kinematic design and commutation of a spherical stepper motor, *IEEE/ASME Transactions on Mechatronics*, 4(4), December, 342–353.

Christensen, C. (1997). *The Innovator's Dilemma: When New Technologies Cause Great Firms to Fail*, Harvard University Press, Boston.

Coey, J.M. (1999). New Materials — New Applications, Proceedings of the NdFeB'99 Conference, Intertech, San Francisco, April 12–14, p. 5.

Coulomb, J. and Meunier, G. (1983). Finite element implementation of virtual work principle for magnetic or electric force and torque computation, *IEEE Transactions on Magnets*, MAG-20, 1894–1896.

Crnosija, P. et al. (2000). Microcomputer implementation of optimal algorithms for closed-loop control of hybrid stepper motors drives, *IEEE Transactions on Industrial Electronics*, 47(6), December.

Croat, J.J. (1985). High Coercivity Rare Earth-Iron Magnets, U.S. Patent 4,496,395.

Dąbrowski, M. (1971). *Magnetic Fields and Circuits of Electrical Machines* (in Polish), WNT, Warsaw.

Dąbrowski, M. (1977). *Construction of Electrical Machines* (in Polish), WNT, Warsaw.

Dąbrowski, M. (1980). Joint action of permanent magnets in electrical machines (in Polish), *PUT Elektryka*, 21, 7-17.

Daido Electronics (2003). Neoquench — DR, Radially Oriented Ring Magnets, Gifu, Japan.

Delphi Corp. (2002). Delphi MagneRide™ Suspension Technology Recognized by Industry Experts, press release retrieved from <http://www.delphi.com/news/pressRelises/pr13557-05302002>.

Demenko, A. (1994). Time stepping FE analysis of electric motors drives with semiconductor converters, *IEEE Transactions on Magnetics*, 30(5), 3264-3267.

Demenko, A. and Pietrowski, W. (2004). 3D edge element analysis of electromechanical transient in brushless motors with conductive permanent magnets, *Archives on Electrical Engineering*, 53(207-1), 23-33.

Demenko, A. and Sykulski, J. (2002). Network equivalents of nodal and edge elements in electromagnetics, *IEEE Transactions on Magnetics*, 38(2), 1305-1308.

DeNagel, S.F. et al. (1994). Solenoid Actuated Valve Assembly, U.S. Patent 5,353,991.

Eckhard, D. et al. (1992). Electromagnetic Control Apparatus for Varying the Driver Steering Effort of a Hydraulic Power Steering System, U.S. Patent 5,119,898, June 9.

Ellis, J.N. and Collins, F.A. (1980). Brushless Rotating Electrical Generators for Space Auxiliary Power Systems, NASA Report CR-54320, Section J.

Fletcher, R. (1987). *Practical Methods of Optimization*, 2nd ed., John Wiley & Sons, New York, 1987.

Floresta, J.G. (1990). The disc magnet stepper motor, *Electronic MotorTechnics*, January, 37-41, 1990.

Foster, D.A. (1988). *Developments in Wheel Speed Sensing*, Paper No. 880325, Society of Automotive Engineers, Detroit, MI.

Furlani, E.P. (2001). *Permanent Magnet and Electromechanical Devices: Materials, Analysis, and Applications*, Academic Press, San Diego.

Gasiorek, S. (1999). NdFeB high potential magnet material, proceedings of the NdFeB '99 Conference, Intertech, San Francisco, April 12-14, p. 6.

Gieras, J.F. and Wing, M. (1994). Design of synchronous motors with rare-earth surface permanent magnets, in *Proceedings of ICEM'94 (Paris)*, 1, 159-64.

Gieras, J.F. and Wing, M. (2002). *Permanent Magnet Motor Technology*, Marcel Dekker, New York, 2002.

Glinka, T. (1995). *Micromotors with Permanent Magnets* (in Polish), Silesian University of Technology, Wydawnictw. Politechniki Śląskiej, Gliwice, Poland.

Glinka, T. et al. (1995). System of the wheelchair (in Polish), in 2nd International Conference on Modern Supply Systems and Drives for Electrical Traction, Warsaw, Poland, pp. 101-105.

Glinka, T. et al. (2005). DC motors with permanent magnets (in Polish), in *Proceedings of XLI International Symposium on Electrical Machines*, Wydawnictwo Politechniki Opolskiej, Opole-Jarniów, June, pp. 196-201.

Graber, D.W. et al. (1989). Electromagnetic Control Apparatus for Varying the Driver Steering Effort of a Hydraulic Power Steering System, U.S. Patent 4,886,138, December 12.

Graber, D.W. et al. (1991). Rotary Actuator with Limited Angular Movement, U.S. Patent 5,038,063, August 6.

Guyton, A.C. (1977). *Basic Human Physiology: Normal Function and Mechanism of Disease*, W.B. Saunders, Philadelphia, pp. 145-156.

Hammond, P. (1978). *Applied Electromagnetism*, Pergamon Press, Oxford.

Hanitsch, R. (1994). Microactuators and micromotors — technologies and characteristics, *Proceedings of ICEM '94 (Paris)*, 1, 20-27.

Harris, M.R. et al. (1975). Static torque production in saturated doubly-salient toothed structures, *Proceedings of IEEE*, 122, 1121-1127, October.

Hennenberger, G. and Bork, M. (1997). Development of a new transverse flux motor, Proceedings of the IEE Colloquium on New Topologies of PM Machines, London, pp. 1/1-1/6.

Hill, N.A. (2003). *Magnetic Materials: Fundamentals and Applications*, Cambridge University Press, Cambridge, 2003.

Hitachi Metals Ltd. (1999). Hitachi Rare-Earth Magnets, China Grove, NC.

Iwasa, M. et al. (1981). Fracture of isotropic and textured hexaferrite, *Journal of the American Ceramic Society*, 64(7), 390–393.

Kasai, Y. (1992). MQ1, 2 & 3 Rings Applied to Motors, New Materials Research Labs, report, Daido Steel Co. Ltd., Gifu, Japan.

Kenjo, T. (1990). *Stepping Motors and Their Microprocessor Control*, Clarendon Press, Oxford.

Korane, K.J. (1997). Replacing the human heart, *Machine Design*, 9, 100–105.

Kuester, J.L. et al. (1973). *Optimization Techniques with Fortran*, McGraw-Hill, New York.

Kuo, B.C. (1982). *Design of Step Motors*, Step Motor Design Course, University of Illinois, Champaign, pp. 142–180.

Lee, J.H. et al. (2003). Experimental study of sliding mode control for a benchmark magnetic bearing system and artificial heart pump suspension, *IEEE Transactions on Control System Technology*, 11(1).

Lequesne, B. et al. (1996). Magnetic velocity sensors, *Transactions of IEEE/IAS*, 32(5), 1166–1175, 1996.

MacBain, J.A. (1981). A numerical analysis of time-dependent two-dimensional magnetic fields, *IEEE Transactions on Magnetics*, 17(6), 3259–3261.

Macoit, A.J. (1999). Growth opportunities for NdFeB in automotive applications, Proceedings of the NdFeB '99 Conference, Intertech, San Francisco, April 12–14.

Magnetic speed variable assist, *Automotive Industries*, August, 50, 1993.

Marinova, I. et al. (2000). A neural network inversion approach to electromagnetic device design, *IEEE Transactions on Magnetics*, 36(4).

Matsumoto, S. et al. (2004). A new concept for optimal design method considering modeling accuracy of electromagnetic devices, *IEEE Transactions on Magnetics*, 40(2), pp. 1232–1235.

Matsuura, Y. (1999). NEOMAX update '99, presented at the NdFeB '99 Conference, San Francisco, April 12–14, p. 4.

McRuer, D. (1974). *Analysis of Nonlinear Control Systems*, John Wiley & Sons, New York, 1974.

Melgoza, E. and Rodger D. (2002). Comparison of table models of electromagnetic actuators, *IEEE Transactions on Magnetics*, 38(2), 2002, 953–956.

Mercow, B.C. et al. (1990). A new high torque density permanent magnet machine configuration, in *Proceedings of the International Conference on Electrical Machines*, Part 3, MIT Press, Cambridge, MA, 1990, pp. 1046–1052.

Miller, T.J.E. (1989). *Brushless Permanent-Magnet and Reluctance Motor Drives*, Clarendon Press, Oxford, p. 63.

Mills, D.A. (1999). Coating technologies for magnetic materials, Proceeding of the NdFeB '99 Conference, San Francisco, April 12–14, p. 2.

Miyashita, K. et al. (1987). Features of a magnetic rotary encoder, *IEEE Transactions on Magnetics*, 23(5), 2182–2184.

Moulin, E.G. (1955). *The Principles of Electromagnetism*, Clarendon Press, Oxford, 1955.

Myers, S. and Marquis, D.G. (1996). *Successful Industrial Innovation*, Washington, D.C., National Science Foundation; MIT Press, Boston.

Navarra, P. (1990). Round Core Solenoid Optimization, Paper 905023, Society of Automotive Engineers, Detroit, MI.

Nehl, T.W. et al. (1988). A general purpose finite element package for computer aided design and analysis of electromagnetic devices, *IEEE Transactions on Magnetics*, 24(1), 385–462.

Nowak, L. (1989). Field diffusion in magnetic circuit containing moving parts, *Archiv für Elektrotechnik*, 72, 11–18.

Nowak, L. and Demenko, A. (2000). The 3D coupled field-circuit simulation of transient in converters with conducting solid parts, *IEEE Transactions on Magnetics*, 36(4), 1412–1416.

Ohshima, Y. and Akiyama, Y. (1989a). Magnetic and electrostatic motion system sensors, *Power Conversion and Intelligent Motion*, April, 56–60.

Ohshima, Y. and Akiyama, Y. (1989b). An overview of motor sensors, *Power Conversion and Intelligent Motion*, 15(7), May, 96–98.

Pawlak, A.M. (1984). Static and dynamic analysis of claw pole stepper motor with permanent magnet, in *Proceedings of 13th Annual Symposium on Incremental Motion Control Systems and Devices*, University of Illinois, Champaign, May, pp. 341–351.

Pawlak, A.M. (1986). A method for determining the inductance of claw pole stepper motor in dynamic operation, presented at International Conference on Electrical Machines Proceedings ICEM '86, Munich, West Germany, September 8–10, 1986, pp. 928–931.

Pawlak, A.M. (1989). Transient design optimization of solenoid actuators using finite elements, in *Proceedings of COMPUMAG, Conference on the Computation of Electromagnetic Fields*, AP33, Tokyo University, Tokyo, September 3–7, pp. 163–166.

Pawlak, A.M. (1990). Novel homopolar rotary actuators, in *Proceedings of ICEM '90 International Conference on Electrical Machines*, MIT, Cambridge, MA, August 13–15, pp. 72–78.

Pawlak, A.M. (1992a). Ring Shaped Variable Reluctance Speed Sensor, 104/Research Disclosure No. 33417, February.

Pawlak, A.M. (1992b). Claw pole rotary actuators, in *Proceedings of ICEM '92 International Conference on Electrical Machines*, Vol. 1, University of Manchester Press, Manchester, pp. 122–126.

Pawlak, A.M. (1992c). Sensing Steering Position and Rate with Magnetic Variable Assist System, 468/Research Disclosure No. 33855, June.

Pawlak, A.M. (1995). Magnets in modern rotary actuators, in *Proceedings of IEEE/IAS '95 Conference*, Orlando, FL, October 9–13, pp. 498–504.

Pawlak, A.M. (1996). Magnets in modern electromagnetic devices, in *Proceedings of the 10th Symposium on Micromachines and Servodrives*, Vol. 1, Wydawnictwo Politechniki Poznanskiej, Rydzyna, Poland, September 23–27, pp. 19–27.

Pawlak, A.M. (1999a). *Distributed Variable Reluctance Sensors*, Publ. No. 991039, Society of Automotive Engineers, Detroit.

Pawlak, A.M. (1999b). Electromagnetic devices with permanent magnets in the air gap, in *Proceedings of the NdFeB '99 Conference*, San Francisco, April 12–14.

Pawlak, A.M. (2000a). Magnets in modern automotive applications, in *Proceedings of the Permanent Magnet Systems Conference*, Atlanta, September 25–27.

Pawlak, A.M. (2000b). *Fostering Creativity in the New Millennium*, Research Technology Development, Vol. 43(6), Industrial Research Institute, The Sheridan Press, New York, pp. 32–35.

Pawlak, A.M. (2004). Hidden values of technology, in *Proceedings of ICEM '04 International Conference on Electrical Machines*, Technical University of Lodz, Krakow, Poland, September 6–9.

Pawlak, A.M. and Gruber, D.W. (1991). Electromagnetic Control Apparatus for Varying the Driver Steering Effort of a Hydraulic Power Steering System, U.S. Patent 5,070,956, December 10.

Pawlak, A.M. and Shirai, T. (1988). Variable Reluctance Sensor, Research Disclosure 29634, December.

Pawlak, A.M. and Young, D.B. (1989). Electromagnetically controlled heart valve, *IEEE/IAS Transactions*, San Diego, CA, October 1–5, pp. 177–183.

Pawlak, A.M. et al. (1988). Transient finite element modeling of solenoid actuators: coupled power electronics, mechanical, and magnetic field problem, *IEEE Transactions on Magnetics*, 24(1), 270–274.

Pawlak, A.M. et al. (1989). Electromagnetic Control Apparatus for Varying the Driver Steering Effort of a Hydraulic Power Steering System, U.S. Patent 4,886,137, December 12.

Pawlak, A.M. et al. (1991a). Variable Reluctance Rotation Sensor, U.S. Patent 5,023,546, June 11.

Pawlak, A.M. et al. (1991b). Variable Reluctance Rotation Sensor, U.S. Patent 5,023,547, June 11.

Pawlak, A.M. et al. (1991c). Claw Pole Rotary Actuator with Limited Angular Movement, U.S. Patent 5,038,066, August 6.

Pawlak, A.M. et al. (1991d). *Novel Variable Reluctance Sensors*, Paper 910902, Society of Automotive Engineers, Detroit, MI.

Pawlak, A.M. et al. (1992). Electronically Controlled Heart Valve, U.S. Patent 5,135,538, August 4.

Pawlak, A.M. et al. (1994a). *Magnetic Power Steering Assist System — MAGNASTEER*, Publ. No. 940867, Detroit, MI.

Pawlak, A.M. et al. (1994b). Magnetic Power Steering Assist System, in *SAE International Congress and Exposition*, SP1031, Society of Automotive Engineers, Detroit, MI.

Pawlak, A.M. et al. (1994c). Rotary actuators, in *Proceedings of IEEE/IAS '94 Conference*, Vol. 1, Denver, CO, October 2–6, pp. 361–367.

Pawlak, A.M. et al. (1995). Rotary actuators with multipole ring magnets, *IEEE/IAS Transactions on Industry Applications*, 31(6).

Pawlak, A.M. et al. (1996). Rotary Encoder with Neutral Position, U.S. Patent 5,491,632, February 13.

Pawlak, A.M. et al. (1997). Magnetically Latching Relay, U.S. Patent 5,703,550, December 30.

Pawlak, A.M. et al. (1999). Magnetically Latching Solenoid Apparatus, U.S. Patent 5,883,557, March 19.

Pickup, I.E.D. and Russell, A.P. (1979). Nonlinear model for predicting setting time and pull-in rate in hybrid motors, *Proceedings of IEEE*, 126(4), 230–237.

Piron, M. et al. (1999). Rapid computer-aided design method for fast-acting solenoid actuators, *IEEE Transactions on Industrial Applications*, 35(5), 991–999.

Podeswa, R. and Lachman, U. (1989). Differential Hall ICs for gear tooth sensing in hostile environments, *Sensors*, January, 34–38.

Pollack, S.H. (1980). An analysis and prediction of the mid-frequency resonance phenomenon in permanent magnet step motors, in *Proceedings of 9th Annual Symposium on Incremental Motion Control Systems and Devices*, Champaign, IL, pp. 29–54.

Rabinow, J. (1951). Magnetic Fluid Torque and Force Transmitting Device, U.S. Patent 2,575,360.

Rajagopal, K.R. et al. (2003). Optimal tooth-geometry for specific performance requirements of a hybrid stepper motor, *IEEE Transactions on Magnetics*, 39(5), 3013–3015.

Ramsden, E. (2001). *Hall Effect Sensors, Theory and Application*, Advanstar Communications Inc., New York.

Rashidi, S. (1982). Proliferation of rare earth magnets in computer peripheral devices, presented at the International Workshop on Rare Earth Magnets, Baden/Vienna, Austria, August 31.

Rashidi, S. (1999). NdFeB opening remarks, presented at NdFeB '99 Conference, San Francisco, April 12–14, p. 3.

Rashidi, S. (2003). Neo iron boron magnets evolving technology spawns new possibilities, presented at the Gorham Conference, Detroit, October 15.

Rischmuller, V. et al. (2000). 3D transient analysis of electromechanical devices using parallel BEM coupled to FEM, *IEEE Transactions on Magnetics*, 36(4), 1360–1363.

Robinson, D.T. (1969). Dynamic Analysis of Permanent Magnet Stepping Motors, NASA TN D-5094, Washington, D.C., March, pp. 1–63.

Robinson, D.T. and Taft, C.K. (1969). Dynamic analysis of magnetic stepping motors, *IEEE Transactions on Industrial and Control Instrumentation*, 1(2), 111–124.

Roel Ortiz, J.L. et al. (2001). Coupling static converter with loop control and non-linear electromagnetic devices, *IEEE Transactions on Magnetics*, 37(5), 3514–3517.

Roters, H.C. (1967). *Electromagnetic Devices*, 3rd ed., John Wiley & Sons, New York.

Rowley, J.W. and Stolfus, J.D. (1990). *Approaches to Solid-State Magnetic Sensors*, No. 900263, Society of Automotive Engineers, Detroit, MI.

Russell, A.P. and Lenhouts, A.C. (1980). An application-oriented approach to the prediction of pull-out/speed curves for permanent magnet stepping motors, in *Proceedings of 9th Annual Symposium on Incremental Motion Control Systems and Devices*, University of Illinois, Champaign, 1980, pp. 15–22.

Russell, A.P. and Pickup, I.E. (1982). Calculation of the pull-out torque of hybrid stepping motors in the half-step mode, *Electric Machines and Electromechanics*, 7, 103–114.

Sabonnadiere, E. et al. (1989). Two and three dimensional models of an electromagnetic velocity sensor, *IEEE Transactions on Magnetics*, 25(5), 3284–3286.

Saito, H. et al. (1988). *Wheel Rotation Sensor for Navigation System*, Paper No. 880409, Society of Automotive Engineers, Detroit, MI.

Schroeder, T. et al. (1990). High Sensitivity Magnetic Circuit, U.S. Patent 4,926,122, May 15.

Schroeder, T. et al. (1996). Three Sensor Rotational Position and Displacement Detection Apparatus with Common Mode Noise Rejection, U.S. Patent 5,568,048, October 22.

Shimizu, M. and Hirai, N. (1990). *Hitachi Metals Technical Bulletin* (in Japanese), 6, 33–36.

Shirai, T. and Pawlak, A.M. (1993). Variable Reluctant Sensor with Offset Magnets Having Improved Magnetic Flux Member, U.S. Patent 5,236,518, August 17.

Shirai, T. and Pawlak, A.M. (1995a). Variable Reluctance Integral Bearing Sensor, U.S. Patent 5,385,410, January 31.

Shirai, T. and Pawlak, A.M. (1995b). Variable Reluctance Integral Bearing Sensor, U.S. Patent 5,385,411, January 31.

Shirai, T. and Pawlak, A.M. (1996). Variable Reluctance Rotation Sensor with Leakage Magnetic Flux Sensing, U.S. Patent 5,510,708, April 23.

Silvester, P.P. and Ferrari, R.L. (1990). *Finite Elements for Electrical Engineers*, 2nd ed., Cambridge University Press, Cambridge.

Singh, G. (1974). *Mathematical Modeling of Step Motors in Theory and Applications of Step Motors*, Kuo, B.C., Ed., West Publishing Co., Champaign, IL, pp. 33–75.

Sykulski, J. et al. (1995). *Computational Magnetics*, Chapman & Hall, London.

Triantafyllou, M. et al. (1999). Mechatronics for automotive and industrial applications, *IEEE Transactions on Advanced Packaging*, 22(3).

Tung, S.C. et al. (2002). Wear Testing Development and Test Procedures for Evaluation of Seal Materials, Research Disclosure No. 457007, Defensive Disclosure Publication.

Tupper, E. (1999). Update on Anisotropic HDDR Powder, presented at NdFeB '99 Conference, Intertech, San Francisco, April 12–14, p. 8.

Vardaraian, I.R. et al. (2004). Wear testing of seals in magneto-rheological fluids, *Tribology Transactions*, 47, 23–28.

Weh, H. et al. (1990). Field control in synchronous machines with permanent magnet excitation in flux concentration mode, in *Proceedings of ICEM '90 International Conference on Electrical Machines*, MIT Press, Boston, 1990, pp. 143–148.

White, D.C. and Woodson, H.H. (1959). *Electromechanical Energy Conversion*, John Wiley & Sons, New York.

Yoon, S.B. et al. (1999). Robust shape optimization of electromechanical devices, *IEEE Transactions on Magnetics*, 35(3), 1710–1713.

Young, D. and Pawlak, A.M. (1990). An Electromagnetically Controlled Heart Valve Suitable for Chronic Implantation, presented at *Transactions of ASAIO American Society for Artificial Internal Organs Conference*, Washington, D.C., April 17–25, 1990, pp. M421–M425.

Young, D. and Pawlak, A.M. (1992). Drive System for Artificial Hearts and Left-Ventricular Assist Devices, U.S. Patent 5,089,017, February 18.

Zhao, L. et al. (1999). A new structure transcutaneous transformer for artificial heart system, *IEEE Transactions on Magnetics*, 35(5), 3550–3552.

Zuraski, J.A. et al. (1989). Electromagnetic Control Apparatus for Varying the Driver Steering Effort of a Hydraulic Power Steering System, U.S. Patent 4,871,040, October 3.

Index

A

ABS, *see* Antiskid braking system (ABS)
Absolute magnetic encoders, 22
AC, *see* Alternating current (AC)
Adams studies, 62
Advanced plastic-molding technology, 35
Aftonin studies, 1
Aging test, 330–332
Air gaps
 conical solenoids, 112
 conventional VR sensors, 31
 cylindrical rotary actuators, 321
 diesel fuel injector system, 132, 135
 front-mounted magnet sensors, 43, 44
 Hall-effect sensors, 3
 inserted-magnet sensors, 37, 42, 42
 magnetic-circuit analysis, 206
 magnetic forces, 97
 magnetic operating point, 208
 magnetic sensor analysis, 24
 magnetic speed sensors, 78, 79
 multiple magnet VR sensors, 53
 plunger solenoids, 108–109
 solid state sensors, 75, 76
 static torque analysis, 197
 stepper motor inductance, 242–249, 244
 temperature, 210
 transmission solenoids, 141, 141, 143
 U-shaped magnetic structure, 52, 53
 variable reluctance sensors, 2, 26
 VR sensor noise, 83–84, 84–85
Akiyama, Ohshima and, studies, 2, 21–22, 72
Alciatore and Histand studies, 1
Alexandridis studies, 281, 283
Alleghney studies, 9
Alnico magnets, 13
Alternating current (AC), 4, 11–12
Analog variable reluctance sensors, 3, *see also* Variable reluctance (VR) sensors
Analysis
 claw pole rotary actuators, 306–309, 308, 313
 cylindrical rotary actuators, 317–321, 322
 disk rotary actuators, 293–298, 294–297
 heart pump, 279, 281
 high-performance VR sensors, 33
 latching relays, 165–172, 165–173, 168–170, 169, 172, 173
 latching solenoids, 188, 188
 magnetic sensors, 22, 24–26, 27
 noise, 81–82

solid state sensors, 71–72
transmission solenoids, 141, 141–143, 143
U-shaped magnetic structure, 52, 53
Analytical simulations, *see* Simulations
Ando studies, 102
Anisotropic properties, 13–14
Annealing, 78, 79
Ansoft studies, 102, 291, 318, 322
Antiskid braking system (ABS)
 dual-magnet sensors, 61
 high-performance VR sensors, 35–36
 magnetic speed sensors, 78, 78
 MR fluid applications, 287
 multiple magnet VR sensors, 53
 two-magnet VR sensor signal calculation, 86–87
Apparent/real permeability, 247, 247
Applications, *see also* specific application
 common, 2
 diesel fuel-injection applications, 5
 latching linear actuators, 155
 latching solenoids, 189–190, 189–190
 linear solenoid actuators, 3–4, 89
 magnetic materials and technology, 16–19
 magnetic sensors, 77–80
 magnetic velocity sensors, 21
Application specific integrated circuit (ASIC), 191
Armatures
 heart pump, 276, 276, 277, 278
 linear solenoid actuators, 89, 90
 reaction effect, 210–211, 211
Aurora (Oldsmobile), 342, 347
Automatic transmissions, *see also* Transmission applications; Truck transmission applications
 ball-type solenoids, 110
 latching solenoids, 174, 189, 189
Automotive applications, *see also* specific type
 ball-type solenoids, 110
 cylindrical rotary actuator PM, 330
 high-performance VR sensors, 35
 magnetic sensor application, 77, 77
 magnetic speed sensor requirements, 77, 77
 PWM analysis, 98
 sensor market valuation, 2
 suspension, 8

B

Back air gap semicircular cylinder leakage, 246
Back walls “D” area, 255

Ball solenoids
 fast-acting actuators, 110, 111–113
 solenoid analysis and simulation, 102–103, 103, 105

Barriers criteria, 354

Battery, PWM analysis, 98

Baumann studies, 1

Bingham plastic, 283

Bipolar driver unit schematic, 193–194, 195

Bipolar latching relays
 assembly, 170, 170
 basics, 155, 159–163, 160–162, 164, 170
 components, 160
 control scheme, 156, 157
 conventional structure, 156
 structure, 160, 160

Bipolar sensors, 3

Bipolar stepper motors, 6, 193–194

Bishop studies, 1

Bistable solenoids, 4–5

Bobbinless technology, 35, 55

Boldea and Nasar studies, 3

Boldea studies, 89

Bonded magnets, 13–14

Bork, Hennenberger and, studies, 8, 291, 316–317

Bottauscio studies, 102, 292

Bottom line, 348

Box studies, 1, 102

Brauer studies, 102

Business attributes, 349, 353–354

Butt joint
 magnetic-circuit analysis, 202, 203, 205–206
 stepper motor inductance, 245, 245–246

C

Cadillac, 342, 354, *see also* MagneRide

Calculations, *see* Examples

Can-stack motors, *see* Claw pole stepper motors

Carpenter studies, 1, 120, 143, 179

Carsile studies, 17, 302, 328

Cartesian properties
 conventional latching relays, 155
 cylindrical rotary actuators, 318–321, 319

Center pole height, *see* Height

Center pole width, *see* Width

Ceramic magnets, 12

Chai studies, 197, 243, 307

Chandran studies, 262

Chatterjee studies, 11

Chevrolet Corvette, 342, 354

China, 18

Chirikjian studies, 191

Christensen studies, 351

Classification
 basics, 2
 latching solenoid actuators, 3–5
 linear actuators, 8
 linear solenoid actuators, 3–5
 magnetic sensors, 2–3

rotary actuators, 8
 special magnetic devices, 7–8
 stepper motors, 5–7

Claw pole rotary actuators
 analysis, 306–309, 308
 applications, 336–338, 336–339
 assembly, 313, 314
 basics, 8, 304–306, 306–307
 cross section, 192, 310, 311
 design, 309, 309
 distributed view, 309, 309
 electromagnet parts, 309, 310
 excitation electromagnetic circuit, 309–310, 310–311
 permanent magnets, 310, 311
 PM, 310–313, 312–314
 test results, 313–314, 314–315
 toothed magnetic part, 310, 311–312

Claw pole stepper motors
 basics, 6
 distributed view, 191, 192
 magnetic circuits, 202, 251
 mathematical model, 218–220

Closing magnetic moment, 268–269

Closing moment, 267

Coating technologies, 15

Cobalt-iron material, 11

Coercivity, 9

Coey studies, 12

Coil and coil configurations
 analog variable reluctance sensors, 3
 cylindrical rotary actuators, 332, 332
 diesel fuel injector system, 132, 136–137
 distributed VR sensors, 63, 65
 dual-magnet sensors, 55
 excitation electromagnetic circuit, 332, 332
 high-performance VR sensors, 35
 latching solenoids, 180, 182
 permanent magnets, 197, 197
 VR sensor noise, 83, 84

Collins, Ellis and, studies, 1, 6

Commercialization, 349

Commercial latching relays, 156, 156

Common-rail diesel fuel-injection applications, 5

Comparisons, magnetic valves, 272–273, 273

Competitiveness, 346–347

Components
 bipolar latching relays, 160
 claw pole stepper motors, 191, 192
 cylindrical rotary actuators, 316, 317
 disk rotary actuators, 302, 304
 latching relay analysis, 166, 167
 Magnasteer, 334, 335, 338, 340
 unipolar latching relay, 163–164, 164–165
 variable reluctance (VR) sensors, 21, 22

Concept stage, 350–351

Conical solenoids
 basics, 89, 90
 fast-acting actuators, 112, 113–115, 114

Continuous duty solenoids, 4

Control schemes, 156, 157

Conventional VR sensors
 basics, 23, 27–31, 28–32
 comparisons, 44, 45

Corrosion, *see* Coating technologies

Corvette (Chevrolet), 342, 354

Costs
 barriers, 19
 ceramic magnets, 12
 conventional VR sensors, 29
 distributed VR sensors, 67
 high-performance VR sensors, 32
 inserted-magnet sensors, 37
 latching relays, 169
 Magnasteer, 348
 magnetic speed sensors, 78
 magnetic velocity sensors, 21
 materials, 11
 permanent magnets wheels, 22
 product value, 352, 353
 rare-earth compounds, 18–19
 VR sensor noise, 83

Coulomb and Meunier studies, 117, 322

Crankshaft position sensor
 high-performance VR sensors, 36
 magnetic position sensors, 79–80, 80

Credibility, 348

Criteria weights, 349, 350, 355

Crnosija studies, 6

Croat studies, 6, 14

Cruise control, 81

Current characteristics
 claw pole rotary actuators, 313, 314–315, 338, 338
 diesel fuel injector system, 132, 134–135
 disk rotary actuators, 297, 297
 fast-acting actuators, 116, 117
 gasoline injectors, 127, 128
 heart pump, 277, 279
 latching relays, 157, 158, 170, 171–172
 latching solenoids, 180, 181–182, 186, 188
 solenoid analysis and simulation, 103, 105–106
 static torque, 215, 216
 stepper motors, 221, 221
 transmission solenoids, 141, 141, 141–143, 142, 146, 147

Current trends, automotive design, 19

Cylinder volume per cycle, 288–289

Cylindrical coordinates, 90, 91

Cylindrical rotary actuators
 analysis, 317–321
 applications, 338–342, 340–342
 basics, 8, 316–317, 316–317
 components, 316, 317
 design, 325–326
 excitation electromagnetic circuit, 332, 332
 PM, 326–332, 327–331
 test results, 322–324, 323–326
 three-dimensional (3D) analysis, 322–324, 323–326
 toothed magnetic structure, 332–333, 333
 two-dimensional (2D) analysis, 318–321, 319–320, 322

Cylindrical symmetry
 disk rotary actuators, 295, 296
 gasoline injectors, 128
 latching solenoids, 185

D

Dąbrowski studies, 1, 102, 243

Daido Electronics, 1, 14, 326, 352

“D” area, back walls, 255

DC, *see* Direct current (DC)

Deceleration, 234, 235–236

Delphi Corp., 1, 8, 281, 285–286

Demagnetization
 armature reaction, 258
 cylindrical rotary actuator PM, 328, 329–330, 330
 PM materials, 12, 13

Demenko, Nowak and, studies, 97

Demenko and Pietrowski studies, 97

Demenko and Sykulski studies, 97

Demenko studies, 102

DeNagel studies, 122

Design
 claw pole rotary actuators, 309, 309
 cylindrical rotary actuators, 325–326
 disk rotary actuators, 298
 heart pump, 275–281, 280
 heart valves, 265, 269–272
 high-performance VR sensors, 35–36
 latching solenoids, 178, 180, 185, 188
 magnetic sensors, 25
 magnetic valves, 264, 265
 solid state sensors, 72–75

Devices, *see specific type*

Diamagnets, 8

Diesel fuel injectors, 131–132, 132–137

Digital output, 3

Dimension, 271–272, 272

Diode model, 98–101, 100

Direct current (DC), 4, 11

Disadvantages, 13

Disk rotary actuators
 analysis, 293–298, 294–297
 applications, 335–336, 336
 assembly, 302, 304
 basics, 8, 90, 292–293, 292–304
 components, 302, 304
 configuration, 291–292, 292
 design, 298
 excitation electromagnetic circuit, 298–299, 299, 303
 PM, 300, 301–303, 302
 test results, 302–304, 304–305
 toothed magnetic part, 299, 300

Disk solenoids
 calculations, 149–151, 150
 fast-acting actuators, 106–107, 107–108

Displacement
 claw pole rotary actuators, 306, 307, 314, 315
 compressor solenoid valves, 137, 138, 138–140
 heart valves, 271–272, 272

- latching solenoids, 180, 181–182
 - transmission solenoids, 142
- Disruptive technology, 351–352
- Distance, heart pump, 277, 277–278
- Distributed VR sensors
 - basics, 32, 63–70, 64–67, 69
 - high-performance VR sensors, 35
- Drawbacks, variable reluctance sensors, 2
- Dual-magnet VR sensors
 - basics, 53–61, 54, 56–62
 - high-performance VR sensors, 32
- Dual sensor arrangement, 61–63, 63–64
- Duty cycle
 - basics, 4–5
 - latching solenoids, 190
 - linear solenoids, 5
 - PWM analysis, 97, 98
- Dynamic analysis
 - latching relays, 157–159, 158–159
 - latching solenoids, 185, 186
 - transmission solenoids, 147, 149
- Dynamic analysis, stepper motors
 - basics, 217
 - examples, 250–259
 - experimental results, performance, 231–232, 232
 - inductance, dynamic operation, 242–250, 243–245, 247–250
 - load torque effects, 237–241, 237–241
 - mathematical model, 218–220
 - parameter effects, 226–227, 227–231, 230
 - performance, 226–227, 230–232
 - simulation, dynamic, 221, 221–227, 223, 226
 - torque, 237–241
 - validation, dynamic model, 223, 223–227, 226
 - viscous damping coefficient evaluation, 233–235, 234–237, 237
- Dynamic applications, materials, 11
- Dynamic characteristics
 - ball-type solenoids, 110, 112
 - conical solenoids, 114, 114
 - diesel fuel injector system, 132, 134
 - disk solenoids, 107, 108
 - gasoline injectors, 123, 124
 - plunger solenoids, 109, 109
 - T-shaped plunger, 129, 129–131, 131
- Dynamic simulations, transmission solenoids, 143, 144
- Dynamometers, stepper motors, 231, 232

E

- Eckhard studies, 334
- Eddy current, 96, 247
- E-J* core calculations, 150–151
- Electrical network equations, 92–94, 92–94
- Electrical system architecture, trends, 19
- Electromagnetic devices, symmetrical analysis, 90–91, 91
- Electromotive force (EMF), 4
- Electronically controlled transmissions, *see* Transmission applications
- Electronic motor control, trends, 19

- Electrorheological fluids, applications, 8
- Ellis and Collins studies, 1, 6
- EMF, *see* Electromotive force (EMF)
- Encapsulation, 15
- Encoders, absolute magnetic, 22
- End effects, 77
- Equivalent electrical network model, 98, 99
- Equivalent magnetic circuits, 242, 243
- E-shaped magnetic structure
 - basics, 44–46, 45–46
 - examples, 85–86
 - front-mounted magnet sensors, 45
- Examples
 - cylinder volume per cycle, 288–289
 - dynamic analysis, stepper motors, 250–259
 - E-shaped magnetic structure, 85–86
 - heart pump, 288
 - heart valves, 287
 - linear actuators, 149–152
 - magnetic sensors, 85–88
 - rotary actuators, 342–344
 - special magnetic devices, 287–289
 - stepper motors, 250–259
 - temperatures, 288–289
- Excitation electromagnetic circuit
 - claw pole rotary actuators, 309–310, 310–311
 - cylindrical rotary actuators, 332, 332
 - disk rotary actuators, 298–299, 299, 303
- Excitation sequence, stepper motors, 191, 193, 200
- Exciter wheel, *see also* Teeth
 - analog variable reluctance sensors, 3
 - conventional VR sensors, 28, 31, 32
 - distributed VR sensors, 65, 67–69
 - dual-magnet sensors, 53–54, 54, 59, 60–61
 - front-mounted magnet sensors, 43, 43
 - high-performance VR sensors, 32–33, 35–36
 - inserted-magnet sensors, 37–38
 - permeance, 23, 23, 33
 - solid state sensors, 71–72
 - variable reluctance sensors, 26–27
 - VR sensor noise, 82, 82–83
- Experimental results, *see also* Test results
 - dynamic analysis, stepper motors, 231–232, 232
 - static analysis, stepper motor, 211–215, 212–216

F

- Fast-acting actuators
 - ball solenoids, 110, 111–113
 - basics, 106
 - conical solenoids, 112, 113–115, 114
 - disk solenoids, 106–107, 107–108
 - optimization, 115–117, 116–117
 - plunger solenoids, 108–109, 109–110
- FE, *see* Finite element (FE) method and models
- Ferrari, Silvester and, studies, 102
- Ferrite Ceramic 8, 313
- Ferrite magnets, 12
- Ferrites, 12
- Ferromagnets, 8–9
- Ferrous stainless steel, 11

Field distribution, 270
 Field regions, 90–91, 91
 Figures of merit, 29
 Financial attributes, 349, 354–355
 Finite element (FE) method and models
 assumptions and data input, 150–152
 conventional VR sensors, 29
 disk rotary actuators, 295, 298
 dual-magnet sensors, 58, 58, 61
 E-*I* core rectangular solenoid, 151–152
 fast-acting actuators, 89
 gasoline injectors, 122, 123
 heart pump, 276
 high-performance VR sensors, 35
 inserted-magnet sensors, 38, 39
 latching solenoids, 179
 magnetic operating point, 208
 magnetic sensors, 21, 25, 27
 PWM analysis, 97
 solenoid analysis and simulation, 102
 solid state sensors, 72
 U-shaped magnetic structure, 47, 48
 Fletcher studies, 1, 117
 Flexibility, development team, 348
 Flexible resin ring magnet, 66, 67
 Floresta studies, 191
 Flow, solenoid fuel pump, 119–120, 120
 Flow mode, 282, 282–283, 286
 Fluid pressure
 PWM analysis, 97, 98
 unipolar latching relay, 165–166, 166–168
 Flux and flux lines, *see also* Magnetic flux
 ball-type solenoids, 110, 113
 bipolar latching relay, 160–161, 161
 claw pole rotary actuators, 308, 308, 311, 313
 compressor solenoid valves, 139, 139
 conical solenoids, 114, 115
 conventional VR sensors, 28, 28
 cylindrical rotary actuators, 318–321, 319–320, 323, 323–324, 326
 diesel fuel injector system, 132, 133
 disk rotary actuators, 295, 296–297, 297
 disk solenoids, 107, 107
 distributed VR sensors, 64, 66, 67–68
 dual-magnet sensors, 54, 59–60, 60–61
 efficiency calculation, 86
 electrical network equations, 92–95, 93–94
 E-shaped magnetic structure, 45, 45
 front-mounted magnet sensors, 43
 gasoline injectors, 128, 128–130, 130
 heart pump, 277, 277–278
 heart valves, 269, 269
 inserted-magnet sensors, 37
 latching relay, 158, 158–159
 latching solenoids, 178, 178, 184–185, 187
 magnetic circuits, 202, 253–254
 magnetic forces, 96, 96
 magnetic position sensors, 79
 magnetic sensor analysis, 24–26
 magnetorheological fluid solenoid actuator, 284, 284

Multec fuel injector system, 122, 123
 plunger solenoids, 108, 110
 solenoid analysis and simulation, 102, 104
 solid state sensors, 72–75, 73–74
 static torque, 197–198, 200
 temperature, 210
 transmission solenoids, 147, 148
 unipolar latching relay, 165–166, 167–168
 VR sensor noise, 82

Force
 cylindrical rotary actuators, 321
 heart valves, 264–272
 latching relays, 168, 169
 linear solenoids, 5
 mechanical equations, 94–95, 95
 transmission solenoids, 141, 141

Foster studies, 2, 21
 Frequency, stepper motor inductance, 250, 250
 Front-mounted-magnet VR sensors
 basics, 43–44, 43–45
 comparisons, 44, 45
 dual-magnet sensors, 54–55
 high-performance VR sensors, 34, 34–35
 inserted-magnet sensors, 37
 magnetic position sensors, 79, 80
 U-shaped magnetic structure, 47, 47–48

Fuel injector system, 122–124, 131–132
 Fuel pump, *see* Solenoid fuel pump
 Furlani studies, 1, 6

G
 Gallium arsenite materials, 71
 Gasiorek studies, 14
 Gasoline injectors, 121–123, 122–125
 Gaussian effect, 70
 General Motors Research Lab, 14, 352
 Geometries
 conventional VR sensors, 30
 cylindrical rotary actuators, 323, 325
 disk rotary actuators, 300, 301, 302, 303
 fast-acting actuators, 115, 116
 FE analysis, 27
 high-performance VR sensors, 36
 inserted-magnet sensors, 37
 latching solenoids, 185, 187
 neodymium magnets, 326, 327
 symmetrical analysis, 91
 transmission solenoids, 147
 U-shaped magnetic structure, 51
 VR sensor noise, 83

Germanium materials, 71
 Giant magnetoresistive (GMR) sensors, 3
 Giers and Wing studies, 1, 14, 291, 316–317
 Glinka studies, 1, 14, 261
 Gruber, Pawlak and, studies, 291
 Gruber studies, 334
 Grease cover, 66, 67
 Guyton studies, 246

H

H, *see* Samarium-cobalt magnets (SmCo_{17})
 Half-steps, 7
 Hall-effect devices
 analog variable reluctance sensors, 3
 basics, 2, 21, 70
 materials, 71
 Hammond studies, 90
 Hanitsch studies, 1
 Hard magnetic materials and technology, 9, 12–13, 12–15, 16–17
 Harris studies, 291, 316
 HDDR (hydrogenation-disproportionation-desorption-recombination), 14
 Heart pump
 analytical simulations, 275–281, 276–281
 basics, 273–274
 configuration, 275–276, 276
 design concept, 274–275, 275
 example, 288
 optimized design, 275–281, 276–281
 requirements, 274–275, 275
 temperatures, 7
 Heart valves
 background, 262, 263
 basics, 7
 comparison, 272–273
 configurations, 265–266, 266
 design concept, 264, 265, 266
 disk type, 262, 263
 example, 287
 location, 262, 263
 optimized design, 263, 269–272, 272
 requirements, 262–265, 263–265
 temperatures, 7
 test results, 272–273, 273
 Height
 conventional VR sensors, 30–31, 31–32
 dual-magnet sensors, 58, 59
 E-shaped magnetic structure, 46, 46
 inserted-magnet sensors, 39, 40–41, 41
 U-shaped magnetic structure, 49, 50, 52
 Hennenberger and Bork studies, 8, 291, 316–317
 High magnetic induction, 11
 High performance VR sensors, 32–36, 33–34, 77
 High-temperature polyamide NdFeB injection molding materials, 14
 Hirai, Shimizu and, studies, 14
 Histanic, Alciatore and, studies, 1
 Hitachi Metals Ltd., 1, 12, 14, 326, 352
 Holding solenoids, 4
 HS, *see* Neodymium magnets
 Hybrid stepper motors, 6
 Hydrogenation-disproportionation-desorption-recombination (HDDR), 14

I

Incremental technology, 351
 Indium antimonite materials, 71

Inductance

 materials, 11
 static torque, 198
 stepper motors, 242–250, 243–245, 247–250

Industrial work solenoids, 4**Injector systems, 122–124****Inserted magnets**

 high-performance VR sensors, 33–34, 34
 signal value calculation, 88
 variable reluctance sensors, 36–42

Integral bearing speed sensors, 36**Intellectual property (IP), 352, 355****Intermediate distance, 277, 277****IP, *see* Intellectual property (IP)****Iron, 11**

 Iron-cobalt alloys, 11
 Iron-nickel alloys, 11–12
 Iron permeance, 246–249
 Iron powder metal material, 11
 Iron-silicon, 12
 Isotropic properties, 13–14
 Iterative design approach, 29
 Iwasa studies, 12–13, 352

J**Japan, 19****K**

Kasai studies, 1, 14, 352
 Kenjo studies, 191
 Korane studies, 7
 Kuester studies, 1, 117
 Kuo studies, 217

L

Lachman, Podeswa and, studies, 2, 21–22
 Laminations, 202, 203, 205–206
 Lap joint, 202, 203, 205–206
 Lap joint back air gap permeance, 246
 "L" area, side walls, 254
 Latching linear actuators, *see also specific type*
 analysis, 165–172, 165–173
 applications, 189–190, 189–190
 basics, 155
 bipolar type, 159–163, 160–162, 164, 170
 dynamics, 157–159, 158–159
 moving magnets, 174–180, 175–182
 relays, 155–172
 solenoids, 173–190
 stationary magnets, 182–188, 183–188
 unipolar type, 163–165, 163–168, 170

Latching relays, components, 166, 167**Latching solenoid actuators, 5****Lee studies, 261****Lenhouts, Russell and, studies, 6, 217****Lequesne studies, 21, 71****Linear actuators**

 ball solenoids, 110, 111–113

basics, 89, 90
classification, 8
compressor solenoid valves, 137–139, 138–140
conical solenoids, 112, 113–115, 114
diesel fuel injectors, 131–132, 132–137
disk solenoids, 106–107, 107–108
electrical network equations, 92–94, 92–94
electromagnetic devices, symmetrical analysis, 90–91, 91
examples, 149–152
fast-acting type, 106–117
gasoline injectors, 121–123, 122–125
long stroke solenoid fuel pumps, 118–121
magnetic forces, 95–96, 96–97
mathematical model, 89–103
mechanical equations, 94–96, 95
natural gasoline injectors, 125–131, 125–131
optimization, 115–117, 116–117
plunger solenoids, 108–109, 109–110
PWM analysis, 97–101, 98–101
solenoid actuator applications, 118–147
solenoid analysis and simulations, 102–103, 103–106
transmission solenoids, 140–147, 140–149

Linear solenoid actuators, 3–5
Linear solenoids, 4
Load speed, stepper motors, 227, 229–231
Load torque effects, 237–241, 237–241, *see also* Torque
Location, 34, 47, 48, 49
Long stroke solenoid fuel pumps, 118–121
Lorentzian forces, 70
Low-carbon steels, 11
Lumped element sensors, 62–63, 69, *see also* Dual sensor arrangement
Lumped-parameters model
calculations, 150–151
electrical network equations, 92, 92
PWM analysis, 98, 99

M

Macoit studies, 1, 17
MacPherson struts, 284, 285
Magnasteer system
assembly, 341, 342
claw pole rotary actuators, 338
components, 334, 335, 338, 340
concept, 347
cylindrical actuators, 338, 340
disk rotary actuator integration, 335–336, 336
disruptive technology, 352
flexibility, 348
requirements, 339, 341, 341
schematic, 334, 334
valve, 291
MagneQuench (MQ1, MQ2, MQ3)
claw pole rotary actuators, 313
cylindrical rotary actuator PM, 328, 331
latching relay analysis, 166
unipolar latching relay, 167–168

MagneRide, 279, 284–287, 286
Magnetic circuits
calculations, 251–252
claw pole stepper motors, 251
high-performance VR sensors, 32
intermediate calculations, 252
static analysis, stepper motor, 201, 201–207, 203–204, 207

Magnetic encoders, absolute, 22
Magnetic field distribution, 269, 270
Magnetic flux, *see also* Flux and flux lines
magnetic circuits, 254–256
static torque calculations, 256–257
stepper motors, 257–259
working point flux, 257

Magnetic forces
fast-acting actuators, 117, 117
mathematical model, 95–96, 96–97

Magnetic induction, 11

Magnetic latching solenoids, 5

Magnetic materials and technology
basics, 8–9
coating technologies, 15
hard type, 12–13, 12–15, 16–17
market and applications, 16–19, 18
soft type, 9–12, 10

Magnetic materials market and applications, *see* Applications; Market

Magnetic nanocomposites, 15

Magnetic position sensor applications, 77–78

Magnetic sensors, *see also* specific type
analysis, 22, 24–26, 27, 71–72
applications, 77–80
basics, 21–22
classification, 2–3
conventional type, 23, 27–31, 28–32
design, 72–75, 73–76
distributed type, 63–70, 64–67, 69
dual-magnet type, 53–61, 54, 56–62
dual sensor arrangement, 61–63, 63–64
E-shaped magnetic structure, 44–46, 45–46
examples, 85–88
front-mounted-magnet type, 43–44, 43–45
high performance type, 32–36, 33–34, 77
inserted magnets, 36–42
multiple magnets type, 53
noise, 81–84
solid state type, 70–76
test results, 75–76, 76–77
theory, 22–23, 23–24
U-shaped magnetic structure, 46–52, 47–53
variable reluctance type, 26–70

Magnetic valves
background, 262, 263
basics, 261–262
comparison, 272–273, 273
design concept, heart valves, 264, 265, 266
heart valve requirements, 262–265, 263–265
mathematical model and simulations, 265–269, 266–268, 270–271
optimized design, 263, 269–272, 272

- requirements, heart valves, 262–265, 263–265
- test results, 272–273, 273
- Magnetization
 - disk rotary actuators, 294, 295, 300, 301
 - laminations, 202–205, 204
 - neodymium magnets, 326, 327
 - permanent magnets, 208–209, 209
 - soft magnetic materials and technology, 9, 10
- Magnet materials, signals, 33, 34
- Magnetomotive force (MMF)
 - armature reaction effect, 210
 - claw pole rotary actuators, 308–309
 - cylindrical rotary actuators, 318, 328, 329
 - disk rotary actuators, 295, 302, 302, 303, 305
 - heart pump, 278, 279, 281
 - heart valves, 269, 270, 272
 - latching relays, 168, 169
 - magnetic circuits, 202–206, 253–256
 - magnetic operating point, 208
 - rotary actuators, 293
 - stepper motor inductance, 242, 248
 - U-shaped magnetic structure, 49
- Magnet operating point, 207, 207–210, 209
- Magnetoresistive (MR) devices
 - analog variable reluctance sensors, 3
 - basics, 2, 21
 - materials, 7
- Magnetorheological fluids, applications, 8
- Magnetorheological fluid solenoids
 - actuators, 283–284, 283–285
 - background, 281–283, 282–283
 - basics, 281
 - MagneRide fluid applications, 284–287, 286
- Magnets, function, 16–17
- Magnet working point, 207, 207
- Main air gap area, 255, *see also* Air gaps
- Manufacturing processes, 16–17, 19
- Marinova studies, 97
- Market
 - business attributes, 354
 - magnetic materials and technology, 16–19, 18
- Marquis, Myers and, studies, 349
- Mass production stage, 351
- Mathematical models
 - basics, 89
 - dynamic analysis, stepper motors, 218–220
 - electrical network equations, 92–94, 92–94
 - electromagnetic devices, symmetrical analysis, 90–91, 91
 - heart valves, 265–269, 266–268, 270–271
 - magnetic forces, 95–96, 96–97
 - magnetic valves, 265–269, 266–268, 270–271
 - mechanical equations, 94–96, 95
 - noise, 81–82
 - PWM analysis, 97–101, 98–101
 - solenoid analysis and simulations, 102–103, 103–106
- Matsumoto studies, 115, 117, 122
- Matsuura studies, 14, 17
- Maximum distance, 277, 277
- Maximum induction applications, 11
- Maxwell stress tensor
 - disk rotary actuators, 297
 - heart valves, 266
 - magnetic forces, 97
 - mechanical equations, 95
- McBain studies, 102
- McRuer studies, 220
- Mechanical equations, 94–96, 95
- Medical applications, temperatures, 7, *see also specific application*
 - Melgoza and Rodger studies, 102
 - Mercow studies, 291, 316
 - Meunier, Coulomb and, studies, 117, 322
 - Microsteps, 7
 - Miller studies, 332
 - Mills studies, 15
 - Minimum distance, 277, 278
 - Mitral valve replacement, 7, *see also* Heart valves
 - Miyashita studies, 22
 - MMF, *see* Magnetomotive force (MMF)
 - Modularity trends, 19
 - Motor control trends, 19
 - Motor technology trends, 19
 - Moulin studies, 246
 - Moving magnets, latching solenoids, 173–180, 175–182
 - MQ, *see* MagneQuench (MQ1, MQ2, MQ3)
 - MR, *see* Magnetoresistive (MR) devices
 - Multec port fuel injector system, 122, 122–124
 - Multiphase windings, stepper motors, 6–7
 - Multiple coatings, 15
 - Multiple coil configurations, 3
 - Multiple magnet VR sensors, 53
 - Myers and Marquis studies, 349

N

- Nanocomposites, magnetic, 15
- Nasar, Boldea and, studies, 3
- Natural gasoline injectors, 125–131, 125–131
- Navarra studies, 1, 117
- NdFeB, *see* Neodymium-iron-boron (NdFeB) magnets
- Nehl studies, 90, 102–103, 122, 266, 291, 318
- Neobond 50, 313
- Neodymium-iron-boron (NdFeB) magnets, 14
- Neodymium magnets, 326–327, 327
- Neodymium materials, 55
- Net mechanical powers, 96
- Newtonian rheological behavior, 283
- Noise
 - analysis, 81–82
 - basics, 81, 81
 - conventional VR sensors, 29
 - high-performance VR sensors, 36
 - mathematical model, 81–82
 - solutions, 82–84, 82–85
 - time characteristics, 81, 81
- No-load conditions, 230, 230
- No-load speed, 223, 225–227, 226
- Nominal load point, 212, 212, 215
- Nominal torque, 223, 226

Nonsupportive magnet configuration
calculation, 87
dual-magnet sensors, 56–57, 56–57
Novelty, technology, 351
Nowak and Demenko studies, 97
Nowak studies, 97

O

Ohmic terms, 96
Ohshima and Akiyama studies, 2, 21–22, 72
Oldsmobile Aurora, 342, 347
Omnipolar sensors, 3
Open frame solenoid configuration, 4
Opening moment, 267
Open-loop control system, 231, 232
Operation principles
 bipolar latching relay, 160–161, 161
 static analysis, stepper motor, 192–196
 stepper motors, 191–195, 192–196
Optimization
 bipolar latching relay, 161, 162, 163
 compressor solenoid valves, 139, 140
 conventional VR sensors, 29, 30
 E-shaped magnetic structure, 46, 46
 fast-acting actuators, 115–117, 116–117, 117, 118
 gasoline injectors, 123, 125
 heart pump, 275–281, 276–281
 heart valves, 263, 269–272, 272
 high-performance VR sensors, 33, 35
 inserted-magnet sensors, 38–39, 40–41
 magnetorheological fluid solenoid actuator, 284
 transmission solenoids, 143, 144
Outlet pressure, 119–120, 120
Output, solid state sensors, 71–72

P

Paramagnets, 8
Parameters
 dynamic analysis, stepper motors, 226–227, 227–231, 230
 stepper motors, 223, 223
Parasitic air gap area, 112, 255
Parasitic engine losses, 19
Partnership, technology development, 345–346
Passive solid-state magnetic (PSSM) sensors, 3
Pawlak, Shirai and, studies, 53, 63
Pawlak, Young and, studies, 7, 261–262, 264–265
Pawlak and Gruber studies, 291
Pawlak and Shirai studies, 53
Pawlak and Young studies, 261
Pawlak studies
 applications, 1
 claw pole rotary actuators, 304, 306
 cylindrical rotary actuators, 316, 318, 322, 334
 distributed VR sensors, 63
 electronically operated heart valve, 261
 fast-acting actuator optimization, 115
 gasoline injectors, 122, 155

latching and linear actuators, 8, 155
latching and linear solenoids, 5
magnetic materials, 11, 17
magnetic sensors, 2, 21–22
magnet operating point, 209
multiple magnet VR sensors, 53
PWM analysis, 97
rotary actuators, 8, 291–292
solenoid analysis and simulation, 103
stepper motors, 191, 242
technology valuation, 352
VR sensors, 26, 31, 53, 63
Performance
 compressor solenoid valves, 139, 140
 diesel fuel injector system, 132, 137
 dynamic analysis, stepper motors, 226–227, 230–232
 front-mounted magnet sensors, 43–44, 45
 hard magnetic materials and technology, 12, 12
 inserted-magnet sensors, 37, 37
 latching relays, 170, 170
 latching solenoids, 174–175, 177, 178–179, 180, 186, 190, 191
 permanent magnets, 302, 302, 313
 pulse-width, 125–126, 126, 128
 soft magnetic materials and technology, 9, 10
 transmission solenoids, 147, 147

Permalloy, 11–12

Permandur, 11

Permanent magnets (PM)

 cylindrical rotary actuators, 318
 demagnetization curves, 12, 13
 disk rotary actuators, 300, 301–303, 302
 dual-magnet sensors, 56–58, 59
 equivalent coil, 197, 197
 latching relays, 155, 156
 latching solenoids, 174, 177
 market, 17
 U-shaped magnetic structure, 47, 48, 49
 variable reluctance sensors, 26
 wheels, 21–22

Permanent magnets (PM), stepper motors

 basics, 6
 claw pole rotary actuators, 310–313, 312–314
 cylindrical rotary actuators, 326–332, 327–331
 disk rotary actuators, 300, 301–303, 302
 magnetic-circuit calculations, 250–251

Permeance

 conventional VR sensors, 28–29
 magnetic sensor theory, 23
 stepper motor inductance, 242–249, 244
 transmission solenoids, 147

Persistence, technology development, 347–348

Phosphorus-iron materials, 11

Pickup, Russell and, studies, 7, 217

Pickup and Russell studies, 217

Pietrowski, Demenko and, studies, 97

Piezoelectric effect, 7, *see also* Passive solid-state magnetic (PSSM) sensors

Piron studies, 1, 103

Plastic-molding technology, 35

Plunger solenoids
 basics, 89, 90
 fast-acting actuators, 108–109, 109–110

PM, *see* Permanent magnets (PM), stepper motors

Pneumatic artificial heart, 274, 274, *see also* Heart pump

Podeswa and Lachman studies, 2, 21–22

Poisson's equation, 102

Pole body leakage, 244–246

Pole head end leakage, 244–245

Pole side leakage, 244–245

Pollack studies, 217

Polymer materials, 7

Portable artificial heart, 275, 275, *see also* Heart pump

Port fuel injector system, 122, 122–124

Position, *see also* Location; Magnetic position sensor
 applications
 cylindrical rotary actuators, 323–324, 325–326
 disk actuator torque, 294, 294
 disk rotary actuators, 303, 305

Powder-metal materials and technology
 basics, 9
 dual-magnet sensors, 55
 high-performance VR sensors, 32
 inserted-magnet sensors, 37–38
 maximum induction, 11

Power flow, 93, 93–94

Power-generation technologies, 19

Power train transmissions, 82–83, 82–83

Preload requirements, latching solenoids, 178, 178

Product value, 352, 353

Proportional solenoids, 5

Prototypes, inserted-magnet sensors, 41–42, 42

Prototyping stage, 350–351

PSSM, *see* Passive solid-state magnetic (PSSM) sensors

Pull-back phenomena, 97

Pull-in curves, 223, 224–229, 226–227

Pull-in force, 4

Pull-in torque
 block schematic, 232, 232
 stepper motors, 226–229, 227

Pulse-width modulation (PMW)
 linear solenoids, 5
 mathematical model, 97–101, 98–101

Pulse-width performance, 125–126, 126, 128

Pump drive circuit, 120–121, 121

PWM, *see* Pulse-width modulation (PMW)

Q

Quantitative accuracy, 25

R

Rabinow studies, 25, 281

Radial air gaps, 53, *see also* Air gaps

Radially magnetized magnet, 174, 176

Rajagopal studies, 191

Ramsden studies, 21, 70

Rare earth, 14, 16–17, 17–18

Rashidi studies, 1, 15, 17

Reactive spring, 96

Rectangular coordinates, 90, 91

Redundancy, 3

Relative duty cycle, *see* Duty cycle

Relays, latching
 analysis, 165–172, 165–173
 basics, 155–156
 bipolar type, 159–163, 160–162, 164, 170
 dynamics, 157–159, 158–159
 unipolar type, 163–165, 163–168, 170

Requirements
 heart pump, 274–275, 275, 279, 280
 heart valves, 262–265, 263–265
 latching solenoids, 178, 178, 189, 189
 transmission solenoids, 142, 143

Resolvers, cost, 22

Results, *see also* Test results
 heart valves, 273, 273
 latching relays, 172, 173

Return path thickness, 51, 51

Rheological materials, 7

Ring magnets
 claw pole rotary actuators, 310–311, 312, 313
 high-performance VR sensors, 35
 latching solenoids, 174, 177

Ring structure, 63, 65–66

Rischmuller studies, 122

Robinson and Taft studies, 217, 221

Robinson studies, 217, 221

Rodger, Melgoza and, studies, 102

Roel Ortiz studies, 97

Rotary actuators
 analysis, 293–298, 306–309, 308, 317–321
 applications, 333–342
 basics, 291–292, 292
 classification, 8
 claw pole type, 307–314, 336–338
 cylindrical type, 316–333, 338–342
 design, 298, 309, 309, 325–326
 disk type, 292–304, 335–336
 examples, 342–344
 excitation electromagnetic circuit, 298–299, 309–310, 332

PM, 300, 302, 310–313, 326–332

test results, 302–304, 313–314, 322–324

three-dimensional (3D) analysis, 322–324, 323–326

toothed magnetic structure, 299, 310, 332–333

two-dimensional (2D) analysis, 318–321, 319–320, 322

Rotary solenoids, 4

Rotational speed, 221, 222

Rotation angle, 334, 335

Roters studies, 25, 243

Rowley and Stoflus studies, 3, 21, 72

Runge-Kutta integration, 220

Russell, Pickup and, studies, 217

Russell and Lenhouts studies, 6, 217

Russell and Pickup studies, 7, 217

S

Sabonnadiere studies, 25

Saito studies, 21
Samarium-cobalt magnets (SmCo_{17}), 14–15, 33
Samarium-cobalt materials, 55
Schroeder studies, 22, 73
Semicircular cylinder leakage, 245–246
Sensitivity, 37, 72–73, 73–74
Seville (Cadillac), 354
Sheer mode, 282, 282–283, 286
Shimizu and Hirai studies, 14
Shim thickness, 168, 169
Shirai, Pawlak and, studies, 53
Shirai and Pawlak studies, 53, 63
Shock absorber, 284
Side walls “L” area, 254
Signal performance and strength
 calculation, 86
 conventional VR sensors, 29, 29
 distributed VR sensors, 67–68, 69
 dual-magnet sensors, 55–58, 56–59
 front-mounted magnet sensors, 43, 44
 high-performance VR sensors, 33, 36
 inserted-magnet sensors, 37
 magnetic speed sensors, 78, 79
 magnet materials, 33, 34
 sensor noise, 81, 81
 U-shaped magnetic structure, 47, 48–52, 49
 variable reluctance sensors, 2
 VR sensor noise, 83, 84–85
Silicon-iron materials, 11
Silicon materials, 71
Silvester and Ferrari studies, 102
Simulations
 dynamic analysis, stepper motors, 221, 221–227, 223, 226
 heart pump, 275–281, 276–281
 heart valves, 265–269, 266–268, 270–271, 273, 273
 magnetorheological fluid solenoid actuator, 284
 stepper motor inductance, 249, 249
 transmission solenoids, 143, 144
Singh studies, 191, 217
Single-acting linear solenoids, 4
Sintered soft magnetic materials, 9–10
Sinusoidal field distribution, 198–199
Sketch lumped-parameters model, 150
Slot depth and width
 inserted-magnet sensors, 39, 40
 U-shaped magnetic structure, 47, 49
 SmCo_{17} , *see* Samarium-cobalt magnets (SmCo_{17})
Soft ferrites, 12
Soft iron, 9
Soft magnetic materials and technology, 9–12, 10
Solenoid fuel pump, 118–121, 119–121
Solenoids
 analysis and simulations, 102–103, 103–106
 magnetorheological fluid, 283–287
 pump drive circuit, 120–121, 121
 PWM analysis, 98–99, 98–99
Solenoids, actuator applications
 basics, 118
 compressor solenoid valves, 137–139, 138–140
 diesel fuel injectors, 131–132, 132–137
gasoline injectors, 121–123, 122–125
long stroke solenoid fuel pumps, 118–121
magnetorheological fluid, 283–284, 283–285
natural gasoline injectors, 125–131, 125–131
transmission solenoids, 140–147, 140–149
Solenoids, latching
 applications, 189–190, 189–190
 basics, 173
 moving magnets, 174–180, 175–182
 stationary magnets, 182–188, 183–188
Solid state sensors
 analysis, 71–72
 basics, 21, 70–71
 design, 72–75, 73–76
 output, 3
 test results, 75–76, 76–77
Solutions, noise, 82–84, 82–85
Special magnetic devices
 actuators, 283–284, 283–285
 analytical simulations, 275–281, 276–281
 background, 262, 263, 281–283, 282–283
 basics, 261
 classification, 7–8
 comparison, 272–273, 273
 design concepts, 264, 265, 266, 274–275, 275
 examples, 287–289
 heart pump, 273–281
 heart valve requirements, 262–265, 263–265
 MagneRide fluid applications, 284–287, 286
 magnetic valves, 261–273
 magnetorheological fluid solenoids, 281–287
 mathematical model and simulations, 265–269, 266–268, 270–271
 optimized design, 263, 269–272, 272, 275–281, 276–281
 requirements, 262–265, 263–265, 274–275, 275
 test results, 272–273, 273
Speed
 requirements and applications, 77–78, 77–79
 viscous damping coefficient, 234–235, 235–237, 237
Speedometer, 81
Speed sensor, 21, 22
Spool valve assembly, 174, 176
Squeeze mode, 282, 282–283
Stable equilibrium position, 293, 293
Stall torque, 223, 226
Stand-alone sensors, 32
Static analysis, stepper motor
 armature reaction effect, 210–211, 211
 basics, 196
 experimental results, performance, 211–215, 212–216
 magnetic-circuit analysis, 201, 201–207, 203–204, 207
 magnet operating point, 207, 207–210, 209
 operation principles, 192–196
 temperature effect, 210, 210
 torque, 196–200
Static torque calculations, 254–257
Stationary magnets, 173–174, 182–188, 183–188
Stator core structure, 6

Stator walls, 254–255

Stator winding design, 6–7

Steering assist, 334, 334–335, 338, 339, *see also* Magnasteer system

Stepper motors

- armature reaction effect, 210–211, 211
- back walls “D” area, 255
- basics, 191
- classification, 5–7
- “D” area, back walls, 255
- dynamic analysis and performance, 217, 217–250
- examples, 250–259
- experimental results, performance, 211–215, 212–216, 231–232, 232
- flux calculations, 253–254
- inductance, dynamic operation, 242–250, 243–245, 247–250
- “L” area, side walls, 254
- load torque effects, 237–241, 237–241
- magnetic-circuit analysis, 201, 201–207, 203–204, 207, 250–256
- magnetic flux, 254–259
- magnet operating point, 207, 207–210, 209
- main air gap area, 255
- mathematical model, 218–220
- MMF calculations, 253–256
- motor permeance, 256–257
- operation principles, 191–195, 192–196
- parameter effects, 226–227, 227–231, 230
- parasitic air gap area, 255
- performance, 226–227, 230–232
- PMs, magnetic calculations, 250–251
- schematic, 191, 193
- side walls “L” area, 254
- simulation, dynamic, 221, 221–227, 223, 226
- static analysis, 196–215
- static torque calculations, 256–257
- stator walls, 254–255
- temperature effect, 210, 210
- tooth area, 254
- torque, 196–200, 237–241
- validation, dynamic model, 223, 223–227, 226
- viscous damping coefficient evaluation, 233–235, 234–237, 237
- working point flux, 257

Stoflus, Rowley and, studies, 3, 21, 72

Strategic positioning criteria, 354

Stroke and stroke lengths, 4–5

Structure, unipolar latching relay, 163–164, 164–165

Sumitomo Corporation, 14

Supply considerations trends, 19

Supportive magnet configuration

- calculation, 87
- dual-magnet sensors, 54, 55–58, 56, 58

Sykulski, Demenko and, studies, 97

Sykulski studies, 102

Symbols, xi–xix

T

Taft, Robinson and, studies, 217, 221

TC, *see* Traction control (TC) systems

Technology and technology development

- basics, 345
- competitiveness, 346–347
- “coolness,” 351
- partnership, 345–346
- persistence, 347–348
- ranking, 355, 356
- technical attributes, 349–353, 351, 353
- technical growth, 348–349
- valuation, 349–355

Teeth, *see also* Exciter wheel; Width

- claw pole rotary actuators, 310, 311–312
- cylindrical rotary actuators, 332–333, 333
- disk rotary actuators, 297–299, 300
- distributed VR sensors, 64
- magnetic circuits, 202, 204, 205–206, 254
- solid state sensors, 75, 76

Temperatures

- barriers, 19
- cylindrical rotary actuator PM, 330
- dual-magnet sensors, 55
- example, 288–289
- Hall-effect sensors, 3
- heart pumps, 7, 277
- heart valves, 7, 263–264, 264
- high-performance VR sensors, 36
- latching solenoids, 180, 182
- multiple magnet VR sensors, 53
- polyamide NdFeB injection molding materials, 14
- samarium-cobalt magnets, 15
- static analysis, stepper motor, 210, 210
- variable reluctance sensors, 2

Test results, *see also* Experimental results; Results

- claw pole rotary actuators, 313–314, 314–315
- cylindrical rotary actuators, 321, 322, 322–324, 323–326
- disk rotary actuators, 302–304, 304–305
- dual-magnet sensors, 61, 62
- gasoline injectors, 127, 128
- heart pump, 279, 281
- heart valves, 272–273, 273
- latching relays, 168–170, 169, 172, 173
- latching solenoids, 188, 188
- solenoid analysis and simulation, 103, 105
- solid state sensors, 75–76, 76–77
- static torque, 214–216, 215
- transmission solenoids, 143, 144

TFMs, *see* Transverse flux motors (TFMs)

Theory, magnetic sensors, 22–23, 23–24

Thermoresponsive materials, 7

Thickness, *see also* Width

- cylindrical rotary actuator PM, 328, 328
- disk rotary actuators, 302, 303
- solid state sensors, 73–75, 74–76

Thin-can motors, *see* Claw pole stepper motors

Three-dimensional (3D) analysis

- cylindrical rotary actuators, 322–324, 323–326
- distributed VR sensors, 64
- high-performance VR sensors, 35
- magnetic sensors, 21

magnetorheological fluid solenoid actuator, 284
 VR sensor noise, 82

3M Corporation, 350, 351

Three-phase windings, stepper motors, 7

Time characteristics, *see also* Travel time
 conical solenoids, 114, 115
 conventional VR sensors, 29, 29
 diesel fuel injector system, 132, 134–137
 disk solenoids, 107, 107
 electrical network equations, 92–95, 93–94
 fast-acting actuators, 116, 116–117
 heart pump, 276, 276, 277, 279
 latching relay, 157, 158
 latching solenoids, 179, 179–180, 186, 188
 PWM analysis, 101, 101
 sensor noise, 81, 81
 solenoid analysis and simulation, 103, 105
 stepper motors, 221, 221–222
 transmission solenoids, 142, 146, 147, 148
 viscous damping coefficient, 233–234, 234–235

Time frame, business attributes, 353

Tooth area, *see* Teeth

Torque
 claw pole rotary actuators, 306–308, 307, 313–314, 314–315, 338, 338
 cylindrical rotary actuators, 318–321, 319, 322, 323–324, 324–326, 328, 329
 disk rotary actuators, 302, 302–303, 305
 dynamic analysis, stepper motors, 237–241
 rotary actuators, 334, 335
 static analysis, stepper motor, 196–200
 static torque, 196–200, 198–199, 201
 stepper motors, 221, 222, 237–241, 237–241
 unidirectional, production, 191, 192

Torque actuators and motors, 8, *see also* Linear actuators; Rotary actuators

Torquemeters, 231

Traction control (TC) systems
 high-performance VR sensors, 35–36
 MR fluid applications, 287
 VR sensor noise, 81

Transistor model, 98–101, 100

Transmission applications, *see also* Truck transmission applications
 ball-type solenoids, 110
 conventional VR sensors, 29
 latching solenoids, 189, 189
 linear solenoids, 5
 solenoid actuator applications, 140–147, 140–149
 speed sensors, 83, 83

Transverse flux linear actuator, 8

Transverse flux motors (TFMs), 317

Trapezoidal magnets, 55

Travel time, *see also* Time characteristics
 gasoline injectors, 123, 124
 latching solenoids, 179, 179–180
 transmission solenoids, 143–144, 145–146

Trends, automotive design, 19

Triantafyllou studies, 1

Truck transmission applications, 36–37, 38, *see also* Transmission applications
 T-shaped plunger configuration, 126–127, 127
 Tubular solenoids, 4

Tung studies, 282

Tupper studies, 14

Two-dimensional (2D) analysis
 cylindrical rotary actuators, 318–321, 319–320, 322, 323
 disk rotary actuators, 295
 fast-acting actuators, 89
 heart pump, 276
 high-performance VR sensors, 35
 magnetic operating point, 208
 magnetic sensors, 21, 25
 PWM analysis, 97
 solenoid analysis and simulation, 102
 solid state sensors, 76, 76

Two-directional linear solenoids, 4

Two-magnet VR sensor magnet configurations, 87

U

Unidirectional torque, 191, 192

Unipolar driver, 193–194, 194

Unipolar latching relays
 assembly, 170, 170
 basics, 155, 163–165, 163–168, 170
 components, 163–164, 164–165
 control scheme, 156, 157
 structure, 163–164, 164–165

Unipolar sensors, 3

Unipolar stepper motors, windings, 6, 191

U-shaped magnetic structure, 45–52, 47–53

V

Validation, dynamic model, 223, 223–227, 226

Valuation, technology
 basics, 349
 business attributes, 353–354
 financial attributes, 354–355
 technical attributes, 349–353, 351, 353
 technology ranking, 355, 356

Value distribution, technology, 355, 356

Value proposition, 353–354

Valve replacement, 7, *see also* Heart valves

Vardaraian studies, 282

Variable reluctance (VR) sensors
 basics, 2, 21, 22, 26–27
 comparisons, 44, 45
 components, 21, 22
 configurations, 27, 28
 conventional type, 23, 27–31, 28–32
 distributed type, 63–70, 64–67, 69
 drawbacks, 2
 dual-magnet type, 53–61, 54, 56–62
 dual sensor arrangement, 61–63, 63–64
 E-shaped magnetic structure, 44–46, 45–46
 front-mounted-magnet type, 43–44, 43–45
 high performance type, 32–36, 33–34, 77
 inserted magnets, 36–42

- multiple magnet type, 53
- U-shaped magnetic structure, 46–52, 47–53
- Variable reluctance (VR) stepper motors, 6
- Variation torque, 200
- Venture capital (VC) firms, 353, 355
- Vibration, 7, 37, 82
- Viscous damping
 - coefficient evaluation, 233–235, 234–237, 237
 - mechanical equations, 96
 - stepper motors, 227, 228–229
- Voltage
 - analog variable reluctance sensors, 3
 - diesel fuel injector system, 132, 134
 - fast-acting actuators, 116, 116
 - Hall-effect sensors, 3
 - latching relays, 170, 171–172
 - latching solenoids, 185, 187
 - PWM analysis, 97–101, 98, 98–101
 - stepper motors, 221, 221, 223, 224–229
 - transmission solenoids, 141–143, 142
 - variable reluctance sensors, 2
 - viscous damping coefficient, 233–234, 234
- VR, *see* Variable reluctance (VR) sensors

W

- Waveforms
 - bipolar driver unit, 194–195, 196
 - solenoid analysis and simulation, 102, 104
 - unipolar driver unit, 194
- Weh studies, 8, 291, 316–317
- Weighted criteria, 349, 350, 355

- White and Woodson studies, 1, 93
- Width
 - conventional VR sensors, 30, 31
 - dual-magnet sensors, 59, 60
 - E-shaped magnetic structure, 46, 46
 - inserted-magnet sensors, 38–39, 39, 40–41, 41
 - solid state sensors, 72, 73
 - U-shaped magnetic structure, 50, 51
- Winding design, 6–7, 191, 193, *see also* Coil and coil configurations
- Wing, Gieras and, studies, 1, 14, 291, 316–317
- Wire, 83, 84, *see also* Coil and coil configurations
- Woodson, White and, studies, 1, 93
- Working point
 - calculations, 253
 - cylindrical rotary actuator PM, 330, 330
 - flux, 257

Y

- YBM, *see* Ferrite magnets
- YCM, *see* Alnico magnets
- Yield stress, 283, 286
- Yoon studies, 1, 115, 122
- Young, Pawlak and, studies, 261
- Young and Pawlak studies, 7, 261–262, 264–265

Z

- Zhao studies, 7
- Zuraski studies, 335–336

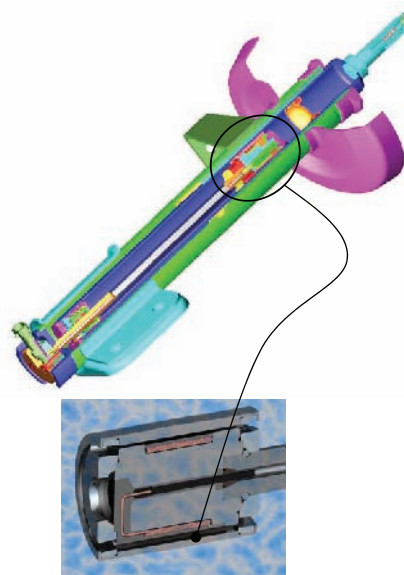
Related Titles

Handbook of Sensor Networks: Compact Wireless and Wired Sensing Systems
Edited by Mohammad Ilyas

The Mechatronics Handbook
Edited by Robert H. Bishop

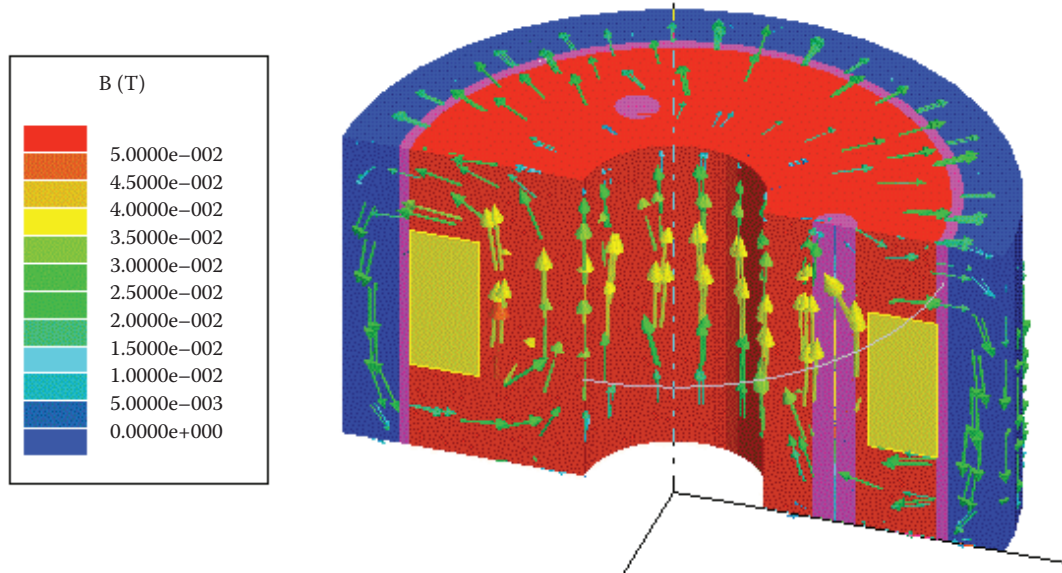
Mechatronics: An Integrated Approach
Clarence W. de Silva

Micromechatronics: Modeling, Analysis, and Design with MATLAB
Victor Giurgiutiu and Sergey Edward Lyshevski



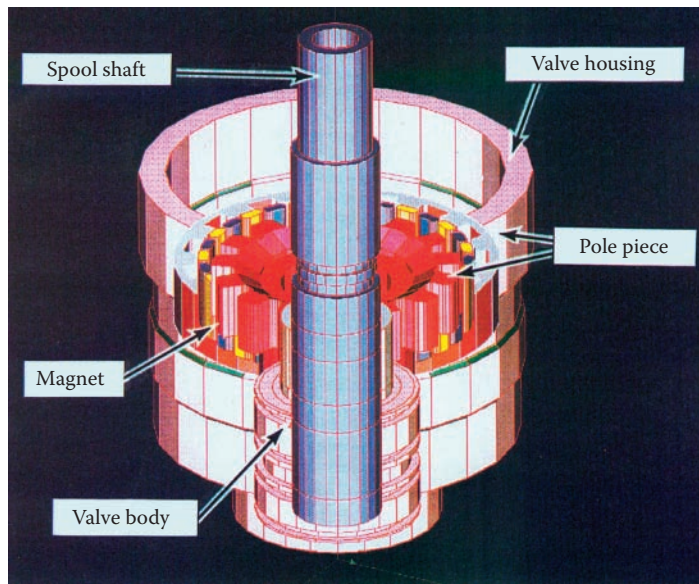
COLOR FIGURE 6.30

Cutaway of the MacPherson strut and cross section of the damper cylinder tube. (Courtesy of Delphi Corp.)



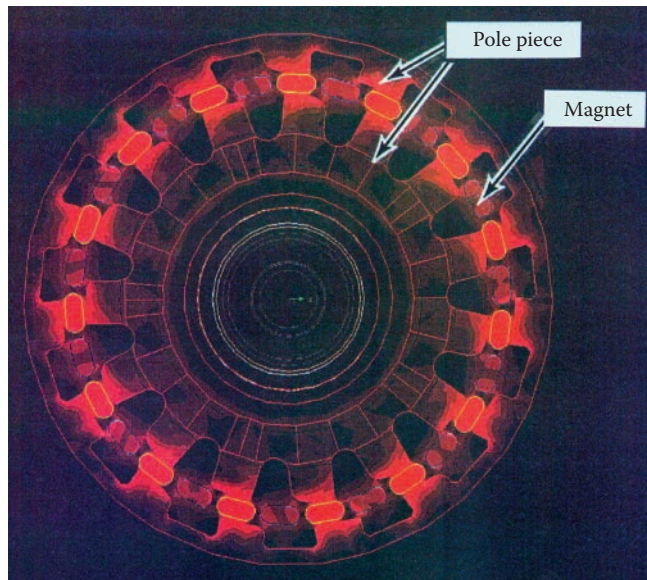
COLOR FIGURE 6.31

The 3D magnetic analysis of the magnetorheological fluid actuator. (Courtesy of Delphi Corp.)



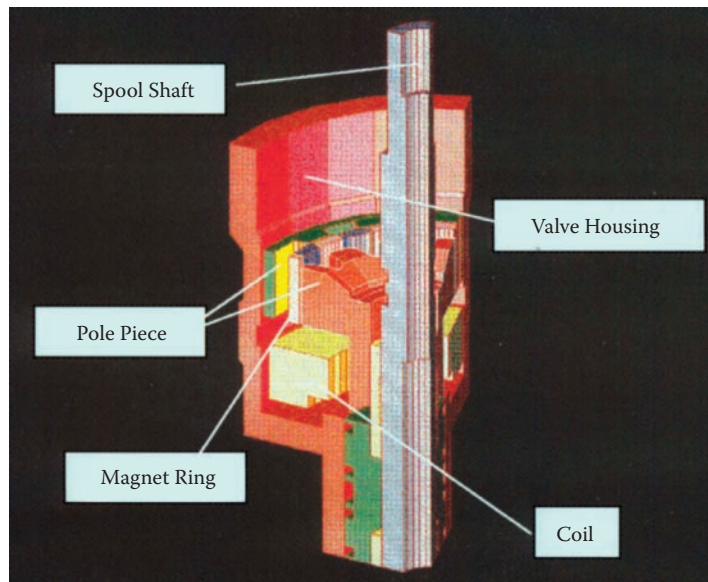
COLOR FIGURE 7.42

A 3D actuator geometry for the full model. (From Pawlak, A.M. et al., *Proceedings of the IEEE/IAS '94 Conference*, Vol. 1, Denver, CO, October 2-6, 1994. With permission.)



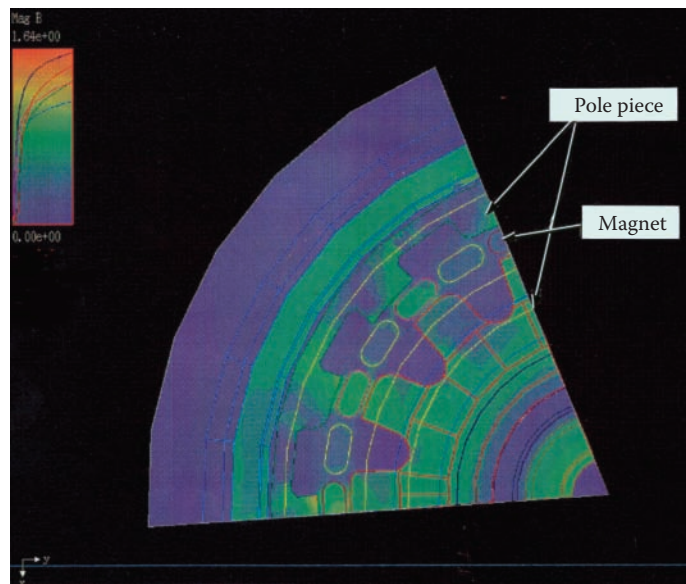
COLOR FIGURE 7.43

Full model flux-density distribution. (From Pawlak, A.M. et al., *Proceedings of the IEEE/IAS '94 Conference*, Vol. 1, Denver, CO, October 2-6, 1994. With permission.)



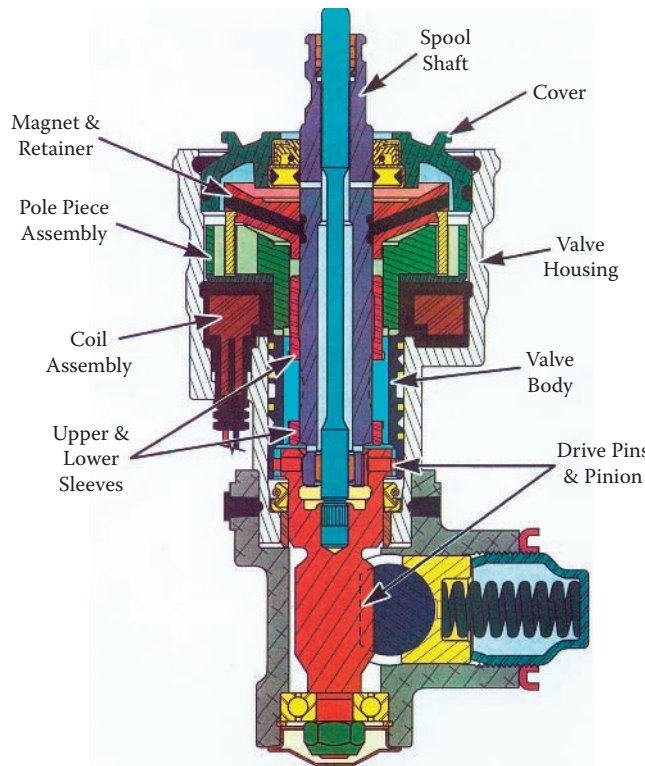
COLOR FIGURE 7.45

A 3D wedge model actuator geometry. (From Pawlak, A.M. et al., *Proceedings of the IEEE/IAS '94 Conference*, Vol. 1, Denver, CO, October 2–6, 1994. With permission.)



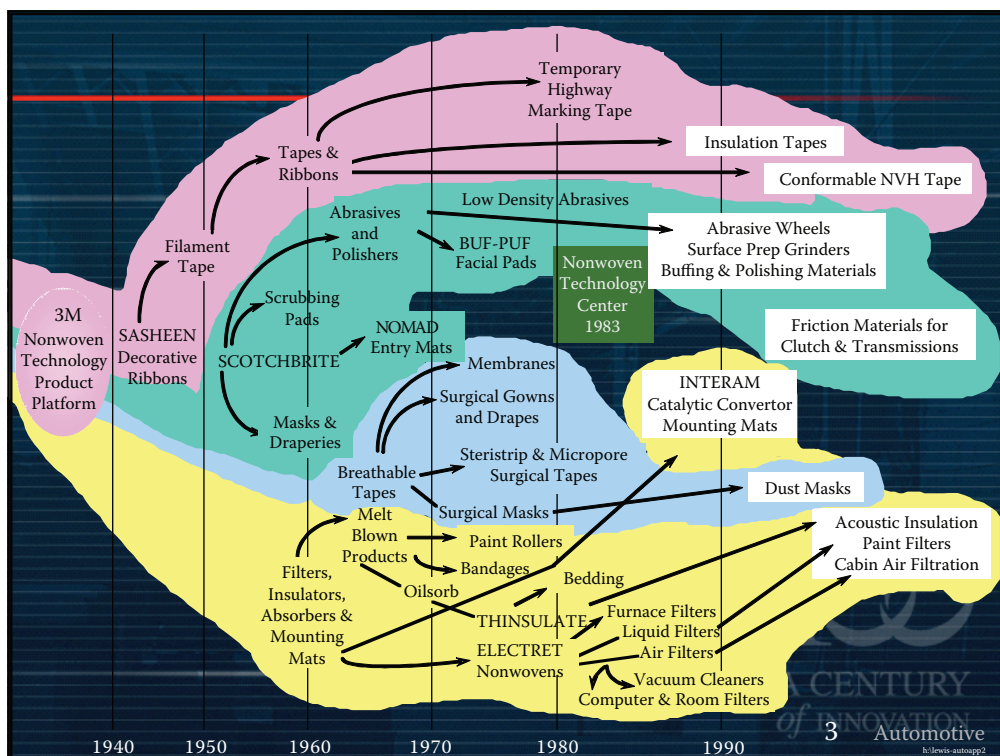
COLOR FIGURE 7.46

Wedge model flux density. (From Pawlak, A.M. et al., *Proceedings of the IEEE/IAS '94 Conference*, Vol. 1, Denver, CO, October 2–6, 1994. With permission.)



COLOR FIGURE 7.66

Magnasteer system components. (From Pawlak, A.M. et al., *Magnetic Power Steering Assist System — MAG-NASTEER*, Publ. No. 940867, Society of Automotive Engineers, Detroit, MI, 1994. With permission.)



COLOR FIGURE 8.1

Example of organic technology growth at the 3M Corporation. (Image published with permission of 3M.)